BİNGÖL ÜNİVERSİTESİ

BİNGÖL ÜNİVERSİTESİ FEN BİLİMLERİ ENSTİTÜSÜ 2009

e-ISSN 2149-6366

Cilt 12, Sayı 1, Mart 2023
Volume 12, Issue 1, March 2023

# TDFD
## TÜRK DOĞA ve FEN DERGİSİ

**TURKISH JOURNAL OF NATURE AND SCIENCE**

# TJNS

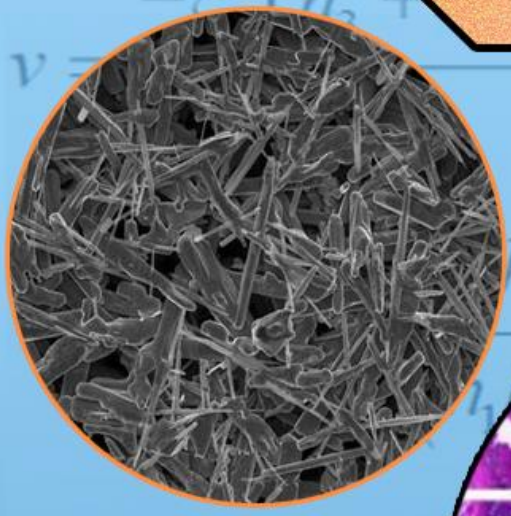

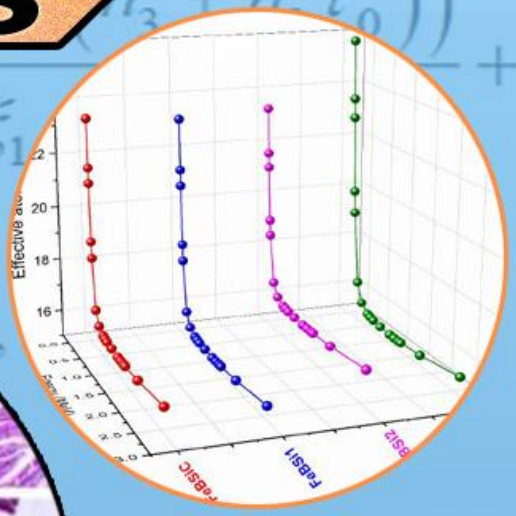

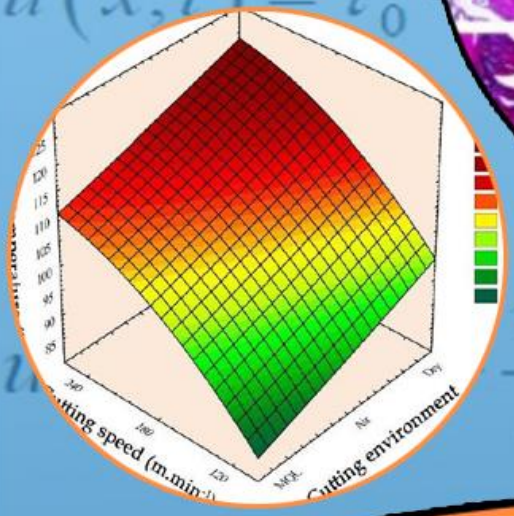


www.dergipark.gov.tr/tdfd

Bingöl Üniversitesi Fen Bilimleri Enstitüsü tarafından yayımlanmaktadır.
Published by Bingol University Institute of Science

ULAKBİM TR DİZİN

# TÜRK DOĞA VE FEN DERGİSİ

## Amaç

Türk Doğa ve Fen Dergisi, Dergipark tarafından yayınlanan Bingöl Üniversitesi Fen Bilimleri Enstitüsüne ait ulusal ve hakemli bir dergidir. Türk Doğa ve Fen Dergisi, Türkiye ve dünyanın her yerinden gelen doğa ve fen bilimlerinin her alanında özgün, yayımlanmamış, yayımlanmak üzere başka yere gönderilmemiş makale, derleme ve sempozyum değerlendirmesi gibi çalışmaların bilim alemine sunulması amacıyla kurulmuştur.

## Kapsam

Türk Doğa ve Fen Dergisinde Mühendislik, Ziraat, Veterinerlik, Fen ve Doğa Bilimleri alanlarından olmak üzere Türkçe ve İngilizce hazırlanmış orijinal makale, derleme ve sempozyum değerlendirmesi gibi çalışmalar yayımlanır. Türk Doğa ve Fen Dergisi sadece online sistemde yayınlanmakta olup ayrıca kağıt baskısı bulunmamaktadır.

## *Merhaba…*

Türk Doğa ve Fen Dergisi, Dergipark tarafından yayınlanmakta olup Bingöl Üniversitesi Fen Bilimleri Enstitüsüne aittir. Bahar ve güz dönemi olmak üzere yılda iki defa çıkarılan ulusal hakemli bir dergi olarak ilk sayısını 2012 bahar döneminde yayımlamıştır. Türk Doğa ve Fen Dergisi, Türkiye ve dünyanın her yerinden gelen doğa ve fen bilimlerinin her alanında özgün, yayımlanmamış, yayımlanmak üzere başka yere gönderilmemiş makale, derleme ve sempozyum değerlendirmesi gibi çalışmaların bilim alemine sunulması amacıyla kurulmuştur. İlk sayısından bugüne kesintisiz olarak faaliyetlerini sürdürmektedir.

Türk Doğa ve Fen Dergisi sadece online sistemde yayınlanmakta olup ayrıca kağıt baskısı bulunmamaktadır. Dergimize gelen her çalışma öncelikle Turnitin intihal programında taranmaktadır. Dergimizde editörlerin, hakemlerin ve yazarların, uluslararası yayım etik kurallarına uyması ve makalelerin yazım kurallarına uyumlu olması zorunluluğu vardır.

Yazarlar yayımlanmak üzere dergimize gönderdikleri çalışmaları ile ilgili telif haklarını zorunlu olarak Bingöl Üniversitesi Türk Doğa ve Fen Dergisi'ne devretmiş sayılırlar. Yazarlardan herhangi bir ücret talep edilmemektedir. Yazarların değerlendirmeleri, dergimizin resmi görüşü olarak kabul edilemez. Çalışmaların her türlü sorumluluğu yazarlarına aittir. Araştırma ürünleri için etik kurul raporu gerekli ise, çalışma üzerinde bu raporun alınmış olduğu belirtilmeli ve kurul raporu sisteme kaydedilmelidir. Araştırma ile ilgili intihal, atıf manipülasyonu, sahte veri uydurma vb. suistimallerin tespit edilmesi halinde yayım ve etik ilkelerine göre davranılır. Bu durumda çalışmanın yayımlanmasını önlemek, yayımdan kaldırmak ya da başka işlemler yapmak için gerekli işlemler takip edilmektedir.

Dergimizde, kaynak gösteriminde uluslararası Vancouver sistemine geçilmiştir. Ayrıca dergimiz, Creative Commons ile lisanslanmak suretiyle dergimizde yayımlanan makalelerin paylaşımı, kaynak gösterimi ve yayımlanmasında dergi ve yazar haklarını korumaya almıştır. 2018 yılı güz döneminden itibaren makaleler, uluslararası yazar kimlik numarası ORCID No'su ile yayımlanmaktadır.

Dergi ekibi, dergimizin ulusal ve uluslararası indekslerce taranan bir dergi olması yönünde çalışmalarını titizlikle sürdürmektedir. Dergimize gösterilen ilgi bu yönde bizleri teşvik etmeye devam edecektir.

Bingöl Üniversitesi Fen Bilimleri Enstitüsü tarafından yayımlanmaktadır

# EDİTÖRLER (YAYIN) KURULU

**Prof. Dr. Zafer ŞİAR**

Bingöl Üniversitesi, Fen-Edebiyat Fakültesi, Matematik Bölümü
E-Mail: zsiar@bingol.edu.tr

**Prof. Dr. Uğur ÇAKILCIOĞLU**

Munzur Üniversitesi, Pertek Sakine Genç Meslek Yüksekokulu, Bitki Morfolojisi ve Anatomisi Bölümü
E-Mail: ucakilcioglu@yahoo.com

**Doç. Dr. Kamuran DİLSİZ**

Bingöl Üniversitesi, Fen-Edebiyat Fakültesi, Fizik Bölümü
E-Mail: kdilsiz@bingol.edu.tr

**Doç. Dr. Şükran KONCA**

Bakırçay Üniversitesi, Mühendislik ve Mimarlık Fakültesi, Temel Bilimler, Matematik Bölümü
E-Mail: sukran.konca@bakircay.edu.tr

**Doç. Dr. İdris YAZGAN**

Kastamonu Üniversitesi, Fen Edebiyat Fakültesi, Biyoloji

E-Mail: idrisyazgan@gmail.com

**Doç. Dr. Abdulcabbar YAVUZ**

Gaziantep Üniversitesi, Mühendislik Fakültesi, Metalurji ve Malzeme Mühendisliği
E-Mail: ayavuz@gantep.edu.tr

**Doç. Dr. Bünyamin ALIM**

Bayburt Üniversitesi, Teknik Bilimler Meslek Yüksekokulu, Elektrik ve Enerji Bölümü
E-Mail: balim@bayburt.edu.tr

**Dr. Öğr. Üyesi Mustafa Şükrü KURT**

Erzurum Teknik Üniversitesi, Fen Fakültesi, Temel Bilimler
E-Mail: mustafa.kurt@erzurum.edu.tr

**Dr. Öğr. Üyesi Sinan SAĞIR**

Karamanoğlu Mehmetbey Üniversitesi, Fizik

E-Mail: sinansagir@kmu.edu.tr / sinan.sagir@cern.ch

**Doç. Dr. Murat AYDEMİR**

Erzurum Teknik Üniversitesi, Fen Fakültesi, Temel Bilimler

E-Mail: murat.aydemir@erzurum.edu.tr

## Mühendislik Bilimleri

**Doç. Dr. Özgür ÖZGÜN**

Bingöl Üniversitesi, Sağlık Bilimleri Fakültesi, İş Sağlığı ve Güvenliği Bölümü
E-Mail: oozgun@bingol.edu.tr

**Prof. Dr. Figen KOREL**

İzmir Yüksek Teknoloji Enstitüsü, Gıda Mühendisliği Bölümü
E-Mail: figenkorel@iyte.edu.tr

**Prof. Dr. Kubilay ASLANTAŞ**

Afyon Kocatepe Üniversitesi, Teknoloji Fakültesi, Makine Mühendisliği Bölümü
E-Mail: aslantas@aku.edu.tr

**Prof. Dr. Hamit Özkan GÜLSOY**

Marmara Üniversitesi, Teknoloji Fakültesi, Metalurji ve Malzeme Mühendisliği Bölümü
E-Mail: ogulsoy@marmara.edu.tr

**Prof. Dr. Ali Adnan HAYALOĞLU**

İnönü Üniversitesi, Mühendislik Fakültesi, Gıda Mühendisliği Bölümü
E-Mail: adnan.hayaloglu@inonu.edu.tr

**Prof. Dr. Barbara SAWICKA**

University of Life Sciences in Lublin, Department of Plant Production Technology and Commodities Sciences
E-Mail: barbara.sawicka@gmail.com

**Prof. Dr. İbrahim GÜNEŞ**

Giresun Üniversitesi, Mühendislik Fakültesi, İnşaat Mühendisliği Bölümü
E-Mail: ibrahim.gunes@giresun.edu.tr

**Doç. Dr. Sırma YEĞİN**

Ege Üniversitesi, Mühendislik Fakültesi, Gıda Mühendisliği Bölümü
E-Mail: sirma.yegin@ege.edu.tr

**Doç. Dr. Hasan OĞUL**

Sinop Üniversitesi, Mimarlık ve Mühendislik Fakültesi, Nükleer Enerji Mühendisliği
E-Mail: hogul@sinop.edu.tr

**Doç. Dr. Murat YILMAZTEKİN**

İnönü Üniversitesi, Mühendislik Fakültesi, Gıda Mühendisliği Bölümü
E-Mail: murat.yilmaztekin@inonu.edu.tr

**Doç. Dr. Ferhat AYDIN**

Sakarya Uygulamalı Bilimler Üniversitesi, Teknoloji Fakültesi, İnşaat Mühendisliği Bölümü
E-Mail: ferhata@subu.edu.tr

**Dr. Öğr. Üyesi Nurullah DEMİR**

Bingöl Üniversitesi, Mühendislik ve Mimarlık Fakültesi, Gıda Mühendisliği Bölümü
E-Mail: ndemir@bingol.edu.tr

**Dr. Öğr. Üyesi Ahmet GÜNER**

Bingöl Üniversitesi, Mühendislik ve Mimarlık Fakültesi, Elektrik ve Elektronik Mühendisliği Bölümü
E-Mail: aguner@bingol.edu.tr

**Dr. Öğr. Üyesi Tahir AKGÜL**

Sakarya Uygulamalı Bilimler Üniversitesi, Teknoloji Fakültesi, İnşaat Mühendisliği Bölümü
E-Mail: tahirakgul@subu.edu.tr

**Dr. Erhan Sulejmani**

University of Tetova, Faculty of Food Technology and Nutrition
E-Mail: erhan.sulejmani@unite.edu.mk

**Dr. Hacène Medjoudj**

Larbi Ben M'Hidi University of Oum El Bouaghi, Food Science Department
E-Mail: medjoudjh@yahoo.com

**Dr. Avinash Lakshmikanthan**

Nitte Meenakshi Institute of Technology, Department of Mechanical Engineering, Karnataka, India
E-Mail: avinash.laks01@gmail.com

**Dr. Manjunath Patel GC**

PES Institute of Technology and Management, Department of Mechanical Engineering, Karnataka, India
E-Mail: manju09mpm05@gmail.com

## Sağlık Bilimleri

**Doç. Dr. Aydın Şükrü BENGÜ**

Bingöl Üniversitesi, Sağlık Hizmetleri Meslek Yüksekokulu, Tıbbi Hizmetler ve Teknikler
E-Mail: abengu@bingol.edu.tr

**Dr. Öğr. Üyesi Dilhun Keriman ARSERİM UÇAR**

Bingöl Üniversitesi, Sağlık Bilimleri Fakültesi, Beslenme ve Diyetetik Bölümü
E-Mail: dkucar@bingol.edu.tr

**Dr. Öğr. Üyesi Abdullah TUNÇ**

Bingöl Üniversitesi, Sağlık Bilimleri Fakültesi, İş Sağlığı ve Güvenliği Bölümü
E-Mail: atunc@bingol.edu.tr

**Dr. Öğr. Üyesi Ramazan GÜNDOĞDU**

Bingöl Üniversitesi, Sağlık Hizmetleri Meslek Yüksekokulu, Eczane Hizmetleri
E-Mail: rgundogdu@bingol.edu.tr

**Dr. Alexander HERGOVICH**

UCL Cancer Institute, Faculty of Medical Sciences, Department of Cancer Biology, UCL, London, UK
E-Mail: a.hergovich@uc.ac.uk

**Dr. Valenti GOMEZ**

UCL Cancer Institute, Faculty of Medical Sciences, Department of Oncology, UCL, London, UK
E-Mail: valentin.gomez@ucl.ac.uk

## Veterinerlik Bilimleri

**Doç. Dr. Cüneyt ÇAĞLAYAN**

Bilecik Şeyh Edebali Üniversitesi, Tıp Fakültesi, Temel Tıp Bilimleri Bölümü, Tıbbi Biyokimya Anabilim Dalı
E-Mail: cuneyt.caglayan@bilecik.edu.tr

**Prof. Dr. Fatih Mehmet KANDEMİR**

Atatürk Üniversitesi, Veteriner Fakültesi, Veteriner Hekimliği Temel Bilimler
E-Mail: fmehmet.kandemir@atauni.edu.tr

**Doç. Dr. Akın KIRBAŞ**

Bozok Üniversitesi, Veteriner Fakültesi, Klinik Bilimler Bölümü
E-Mail: akindahiliye55@yahoo.com

**Doç. Dr. Emrah Hicazi AKSU**

Atatürk Üniversitesi, Veteriner Fakültesi, Klinik Bilimler Bölümü
E-Mail: emrahaksu@atauni.edu.tr

## Ziraat Bilimleri

**Dr. Öğr. Üyesi Zeynep DUMANOĞLU**

Bingöl Üniversitesi, Ziraat Fakültesi, Biyosistem Mühendisliği Bölümü
E-Mail: zdumanoglu@bingol.edu.tr

**Prof. Dr. Kağan KÖKTEN**

Bingöl Üniversitesi, Ziraat Fakültesi, Tarla Bitkileri Bölümü
E-Mail: kahafe1974@yahoo.com

**Prof. Dr. Mustafa SÜRMEN**

Adnan Menderes Üniversitesi, Ziraat Fakültesi, Tarla Bitkileri Bölümü
E-Mail: mustafa.surmen@adu.edu.tr

BİNGÖL ÜNİVERSİTESİ

Türk Doğa ve Fen Dergisi
Turkish Journal of Nature and Scienc
www.dergipark.gov.tr/tdfd

# İÇİNDEKİLER/CONTENTS

Araştırma Makalesi https://doi.org/10.46810/tdfd.1148326 Research Article

Türk Doğa ve Fen Dergisi
Turkish Journal of Nature and Science
www.dergipark.gov.tr/tdfd

# Seasonal Level Change and Overdraft of Water Wells

**Kürşat ŞEKERCİ[1*], M. Cihat TUNA[2], M. Şahin DOĞAN[3]**

[1]Bingöl University, Engineering and Archtitecture Faculty, Civil Engineering Department, Bingöl, Türkiye
[2]Fırat University, Engineering Faculty, Civil Engineering Department, Elazığ, Türkiye
[3]Aksaray University, Engineering Faculty, Civil Engineering Department, Aksaray, Türkiye
Kürşat ŞEKERCİ ORCID No: 0000-0001-9096-4644
M. Cihat TUNA No: 0000-0001-9005-1968
M. Şahin DOĞAN No: 0000-0002-3378-9955

**Corresponding author: ksekerci@bingol.edu.tr*

(Received: 25.07.2022, Accepted: 14.11.2022, Online Publication: 27.03.2023)

**Keywords**
Overdraft,
Observation Well,
Basin

**Abstract:** In the simplest terms an overdraft, can be expressed as a condition in which the water withdrawn from an underground water aquifer by pumping exceeds the amount that recharges the aquifer via deep percolation. Groundwater aquifers are fed by infiltration from precipitation, surface water bodies, such as rivers and lakes when they are hydraulically connected, and return flows from agricultural and urban uses. Groundwater overdraft is an unsustainable use of limited water resources. Less surface water availability due to rising temperatures and lack of precipitation, and pollution of aquifers are among reasons for excessive groundwater overdraft. In addition to such negative factors, uncontrolled agricultural irrigation also increases the effect of overdraft. For such reasons, it is important to protect the waters with the understanding of sustainable management. In this study, seasonal water heights in observation wells operated at the same water elevation in two different resorts located on the borders of the Uluova basin were examined and water level changes were examined. The periodic (seasonal) water heights of the observation wells in 2011 and 2018 were studied. The effect of overdraft was pointed out through the height changes in the observation wells.



# Su Kuyularının Mevsimsel Seviye Değişimi ve Aşırı Çekim

**Anahtar Kelimeler**
Aşırı Çekim,
Gözlem Kuyusu,
Havza

**Öz:** En basit ifadeyle aşırı çekim, bir yeraltı suyu akiferinden pompajla çekilen suyun, derin süzülme yoluyla akiferi yeniden dolduran miktarı aşması durumu olarak ifade edilebilir. Yeraltı suyu akiferleri, hidrolik olarak bağlı olduklarında nehirler ve göller gibi yüzeysel su kütleleri ve tarımsal ve kentsel kullanımlardan kaynaklanan geri dönüş akışları ile yağıştan sızma ile beslenir. Yeraltı suyu fazla çekimi, sınırlı su kaynaklarının sürdürülemez bir kullanımıdır. Artan sıcaklıklar ve yağış eksikliği nedeniyle daha az yüzey suyu mevcudiyeti ve akiferlerin kirlenmesi, aşırı yeraltı suyu aşırı çekiminin nedenleri arasındadır. Bu tür olumsuz faktörlerin yanı sıra kontrolsüz tarımsal sulama da aşırı çekimin etkisini artırmaktadır. Bu gibi nedenlerle suların sürdürülebilir yönetim anlayışı ile korunması önemlidir. Bu çalışmada Uluova havzası sınırlarında yer alan iki farklı beldede aynı su kotunda işletilen gözlem kuyularındaki mevsimsel su yükseklikleri incelenmiş ve su seviyesi değişimleri incelenmiştir. 2011 ve 2018 yıllarında gözlem kuyularının periyodik (mevsimsel) su yükseklikleri incelenmiştir. Gözlem kuyularındaki yükseklik değişiklikleri ile aşırı çekim etkisine dikkat çekilmiştir.

## 1. INTRODUCTION

Today, water; In addition to being of vital importance for human life, health and ecosystems, it is a basic need for the development of countries. Water scarcity is becoming an increasingly prominent and pervasive problem. Water quality is deteriorating rapidly in almost every country. This problem also causes many chained problems in terms of social and economic aspects. In terms of ensuring sustainable development, it is very important to ensure the balance of protection and use. All these elements can only be evaluated within the scope of sustainable water

management. The developing approach in terms of water resources management is to perform resource management on a basin basis and in an "integrated" manner with other natural resources. Integrated management of water resources, which is the driving force for major sectors of socioeconomic development such as energy, agriculture and health, is one of the basic components of sustainable development. Especially basin-based protection [1]. All developments and uses should be directed in a controlled manner while making plans [1]. In parallel with the increasing irrigation areas in our country, problems related to irrigation management have also increased and the realization rate of the expected benefits from irrigation has remained low. When this situation is combined with the policies followed, irrigation and irrigation management will become more efficient and more economical in this context. Today, irrigation management is generally carried out by irrigation unions, irrigation cooperatives, municipalities or village legal entities. As a result, the water crisis has become inevitable all over the world [2]. The growth of the population and the increase in water-based agriculture increase the dependence on groundwater [3-5].

The continuous increase in population, agriculture and industrial activities necessitates the use of more water in every period than in the past. And requires the continuation of water resources management [6]. The excessive use of groundwater due to recent high demand and drought has had sometimes irreversible effects on many aquifers around the world [7]. Wada et al. [8], reported that groundwater overdraft has doubled in the last 50 years in arid and semi-arid regions of the world. Doğan et al. investigated the effects of overdraft on groundwater in a study [9]. Therefore, hydro-economic models are needed to identify the areas most affected by groundwater overdraft and measures to reduce existing groundwater consumption. In this study, the effect of overdraft was investigated by examining 2 underground water observation wells in different locations in Uluova region of Turkey's Elazığ province.

Uluova micro-basin in Turkey's Elazig province is a region where important agricultural lands of the city are located. In addition, a significant part of the drinking and utility water of the city with a population of approximately 500.000 is provided from the wells drilled in this basin.

## 2. MATERIAL AND METHOD

This study was carried out on the underground water wells in the Yurtbaşı and Yazıkonak regions of Elazığ province. In the study, seasonal water measurements of wells operated for observation purposes in Yazıkonak and Yurtbaşı districts, one of the central districts of Elazığ, located within the boundaries of the Uluova basin, were used. In the period of 2011-2018, water level measurements were used for April, the month with the highest seasonal water level, and September, when the seasonal water level was the lowest. The effect of overdraft on the respective water wells has been specifically studied (Table 1).

**Table 1.** Seasonal water levels of observation wells

| Yurtbaşi Observation Well Data | | | Yazikonak Observation Well Data | | |
|---|---|---|---|---|---|
| Years | September | April | Years | September | April (m) |
| 2011 | -32.7 | -25.2 | 2011 | -22.1 | -17.3 |
| 2012 | -39.5 | -29.3 | 2012 | -27.5 | -21.3 |
| 2013 | -33.8 | -30.0 | 2013 | -29.3 | -24.4 |
| 2014 | -36.0 | -37.0 | 2014 | -30.8 | -27.7 |
| 2015 | -38.7 | -33.1 | 2015 | -33.2 | -29.0 |
| 2016 | -40.0 | -34.9 | 2016 | -34.8 | -30.8 |
| 2017 | -45.2 | -37.0 | 2017 | -38.2 | -32.5 |
| 2018 | -49.0 | -41.0 | 2018 | 0.00 | -37.4 |

An example diagram showing the urban and agricultural water demands with the Yazıkonak and Yurtbaşı observation wells is given in the figure below (Figure 1). As seen in the diagram, there is a flow feeding the groundwater reservoir. Afterward, water is transferred from the reservoir to the urban and rural water demand points, which are shown in different colors. In this study, since the example of Yazıkonak and Yurtbaşı wells as urban (rural) and agricultural underground water reservoirs is examined, these wells are shown in the network flow chart. There is a flow to the underground wells as shown by the brown arrow in the diagram. This brown arrow represents the flow that goes underground with precipitation. The purple arrows represent water delivered from the distribution point from underground wells to urban and agricultural areas. The gray arrows represent the flow returning from the urban and agricultural demand points by infiltration into the ground.



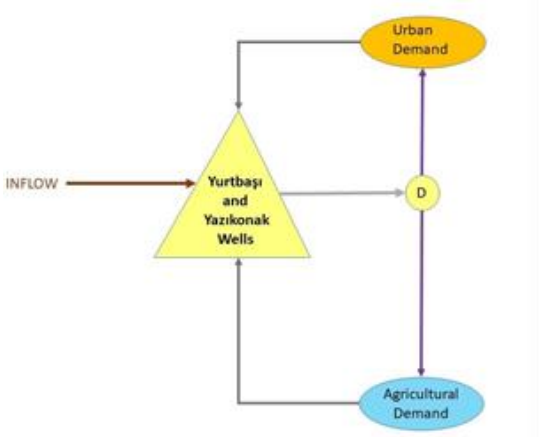


**Figure 1**.The link between urban and agricultural water demands and wells

In Table 2, the annual average precipitation values of the precipitation station including Yurtbaşı and Yazıkonak regions are given [10].

**Table 2.** Study area precipitation station data[10]

| Yurtbaşı And Yazıkonak Regions Precipitation Statistics | |
|---|---|
| Years | Annual Average Precipitaion (mm) |
| 2011 | 33.48 |
| 2012 | 29.00 |
| 2013 | 23.69 |
| 2014 | 27.29 |
| 2015 | 35.08 |
| 2016 | 23.96 |
| 2017 | 16.40 |
| 2018 | 35.36 |

In Figure 2, the study area where the observation wells are located is given [11].


**Figure 2.** Working area [11]

## 3. RESULTS

Seasonal water changes in Yazıkonak and Yurtbaşı observation wells in the relevant time period are examined from the graphs given in Figure 3, Figure 4 and Figure 5. In Figure 3, the water level changes of the Yazıkonak (B) observation well are examined. The black dashed line shows the water level changes in September of the relevant year, and the red dashed line shows the water level changes in April of the relevant year. In the column chart, the blue columns represent September, and the orange colored columns represent the April water level measurements.

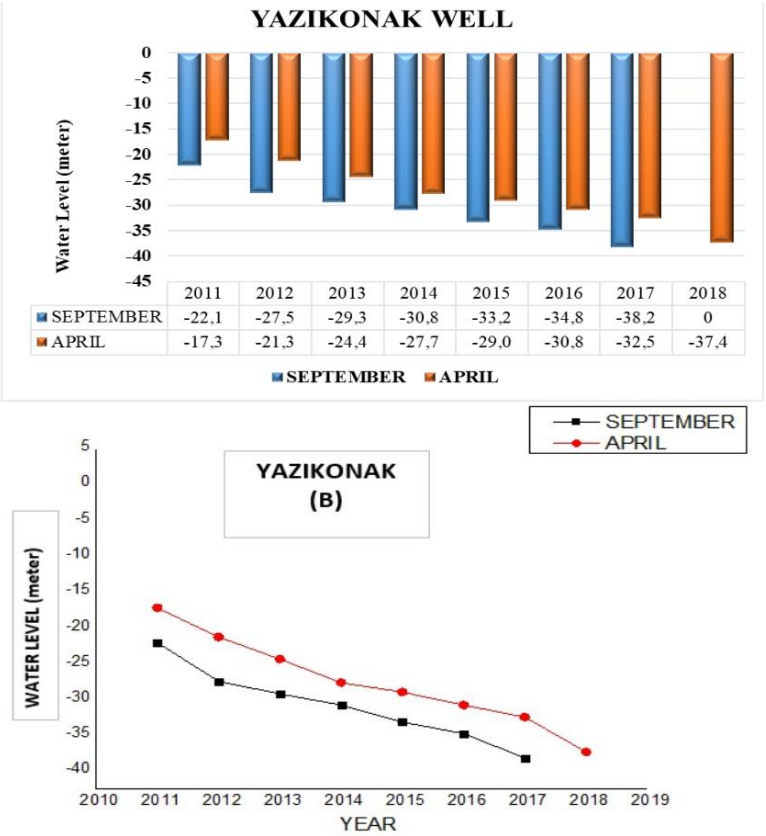


**Figure 3.** Yazıkonak observation well analysis results

In Figure 3, it was observed that the water level decreased every year from 2011 to 2018 in the Yazıkonak observation well. Due to the lack of water in the Yazıkonak well in September, when the water level was the lowest in 2018, the water level value is not given in the chart. Due to the lack of water in the Yazıkonak well in September, when the water level was the lowest in 2018, the water level value is not given in the chart. Although there was much more precipitation in the Yazıkonak region in 2018 compared to previous years, it is clearly seen that this precipitation did not have any positive effect on the well level. Again, despite the increased precipitation in 2015, the downward trend of the water level in the water well continued.

In Figure 4, the changes in the water levels of the Yurtbaşı (A) observation well are examined. The black dashed line shows the water level changes in September of the relevant year, and the red dashed line shows the water level changes in April of the relevant year. In the column chart, the blue columns represent September and the orange colored columns represent the April water level measurements.

In Figure 4, it is seen that the water level in the Yurtbaşı observation well decreases with each passing year compared to the previous year. It can be said that the water level measured in September and April 2014 is almost the same. This is probably due to the relatively increased rainfall in 2014 compared to the previous year. It has been observed that the level of the well has decreased by approximately 20 m in the period from 2011 to 2018.

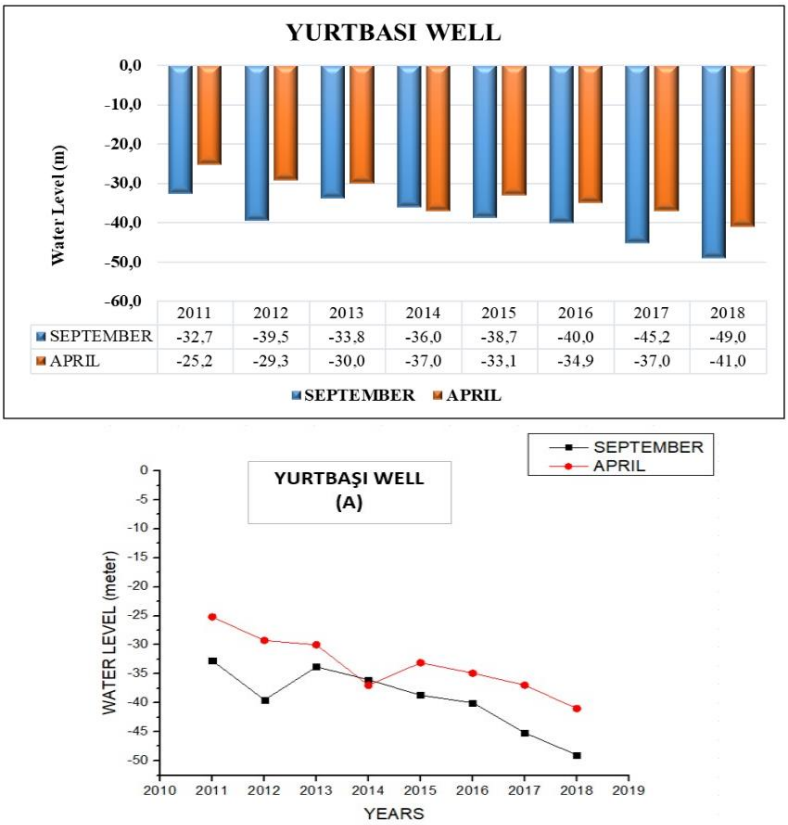


**Figure 4.** Yurtbaşı observation well analysis results

In Figure 5, the water level changes of the Yurtbaşı (A) and Yazıkonak (B) observation wells are examined together. In 2011, 2012, 2013, 2014, 2015, 2016, and 2017 April and September, it was observed that the water level in Yazıkonak well decreased less than the water level in the Yurtbaşı well. The reason for the decrease in the level in the wells is generally thought to be the decreasing rainfall and the increasing water demand due to the increase in population. However, despite the large increase in precipitation, especially in 2018, the water level continued to decrease in both wells. So much so that in September 2018, the water in the Yazıkonak well was completely exhausted. This is probably because most of the water from precipitation is lost as runoff before it enters the wells.



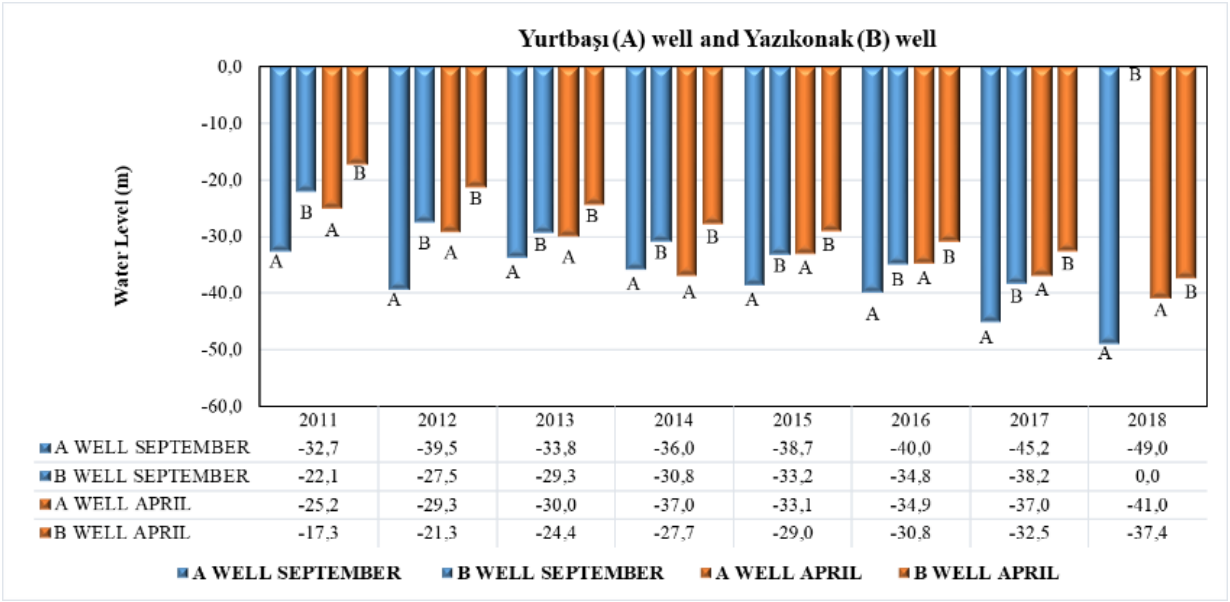


**Figure 5.** Yurtbaşı and yazıkonak well analysis results

## 4. DISCUSSION AND CONCLUSION

In the study in which seasonal water level changes and overdraft effect were examined in the period covering the years 2011-2018, the following issues were determined in the Yurtbaşı and Yazıkonak observation wells.

- It was observed that the overdraft was effective in both wells in the relevant time period.
- It has been determined that the seasonal water height changes at Yurtbaşı well are more striking in the other 7 years except for 2018.
- In both observation wells, it was observed that groundwater levels dropped significantly in September, the end of the dry period.
- It was observed that the water level in the Yurtbaşı observation well decreased more than the water level in the Yazıkonak observation well in April and September of all years.
- According to the water level values, it can be said that the overdraft effect in the Yurtbaşı observation well is more pronounced than in the Yazıkonak observation well.
- It was observed that the water height in Yazıkonak well decreased less than the set height in the Yurtbaşı well in both April and September of 2011,2012,2013,2014,2015,2016 and 2017.
- The decrease in water level has negative effects on agricultural and urban (rural) water use.
- It is suggested that global warming and drought in the region also have a significant share in the decrease in the water level in both observation wells.
- Increasing water demands every day also contribute significantly to the reduction of the water level in both observation wells over the years.
- As a result, it was clearly seen that the water level in both wells decreased every year compared to the previous year and was exposed to the overdraft effect.
- In future studies, it would be useful to include other underground observation wells in the basin and conduct a more detailed and comprehensive examination so that the results can be understood more clearly and their true dimensions can be seen. It is thought that it would be useful to create a comprehensive hydro-economic model for this.

## REFERENCES


[1] Sezer Güney, B. Havza Yönetimi Yaklaşımı Çerçevesinde Yeraltı Barajları. Su Kaynakları. 2020; 5 (1): 7-12.

[2] Özkan, E. , Aydın, B. , Hurma, H. & Aktaş, E. Su Kaynaklarının Sürdürülebilir Kullanımında Su Yönetiminin Önemi. Türk Bilimsel Derlemeler Dergisi. 2013;(1):150-153.

[3] Gorelick, S. M., and Zheng, C. M. Global change and the groundwater management challenge. Water Resources Research. 2015; (51): 3031–3051.

[4] Roddell, M., I. Velicogna, and J.S. Famiglietti. Satellite-based estimates of groundwater depletion in India. Nature. 2009; (460): 999-1002.

[5] Siebert, S., Burke, J., Faures, J. M., Frenken, K., Hoogeveen, J., Doll, P., and Portmann, F. T. Groundwater use for irrigation—A global inventory. Hydrology and Earth System Sciences. 2010; 14(10):1863–1880.

[6] T, Meriç. Su Kaynakları Yönetimi ve Türkiye. Jeoloji Mühendisliği Dergisi. 2004;28(1):27-38.

[7] Taylor, R.G., Scanlon, B., Döll, P., Rodell, M., Van Beek, R., Wada, Y., Longuevergne, L., Leblanc, M., Famiglietti, J.S., Edmunds, M. and Konikow, L. Ground water and climate change. Nature climate change. 2013; 3(4): 322-329.

[8] Wada, Y., van Beek, L. P., van Kempen, C. M., Reckman, J. W., Vasak, S., and Bierkens, M. F. Global depletion of groundwater resources. Geophysical Research Letters. 2010; 37(20):94-8276.

[9] Dogan, M. S., Buck, I., Medellin-Azuara, J., Lund, J. R. Statewide Effects of Ending Long-Term Groundwater Overdraft in California, *Journal of Water Resources Planning and Management.* 2019*;* 145(9), 04019035.

[10] MGM. Meteorolojik Veriler, T.C. Tarım ve Orman Bakanlığı Meteoroloji Genel Müdürlüğü 13. Bölge Müdürlüğü, 2020.

[11] Google Earth. Available from: https://earth.google.com/web/@38.60368148,39.3046644,876.60117685a,40512.39070184d,34.999335y,-0h,0t,0r, 2022.

Cilt 12, Sayı 1, Sayfa 6-11, 2023 Volume 12, Issue 1, Page 6-11, 2023

Araştırma Makalesi https://doi.org/10.46810/tdfd.1209680 Research Article

Türk Doğa ve Fen Dergisi
Turkish Journal of Nature and Science
www.dergipark.gov.tr/tdfd

# Experimental and Theoretical Analysis to Determine the Radiation Shielding Properties of Mortar Samples Prepared with Different Mineral Additives

**Adnan KÜÇÜKÖNDER[1], İbrahim ALKILINÇ[2], Seyma Biber TEMİRCİK[3], Başak ZENGİN[4*]**

[1] Kahramanmaras Sutcu Imam University Department of Physics, Kahramanmaras¸Türkiye
[2] Ekinözü Municipality, Kahramanmaras, Türkiye
[3]Kahramanmaras¸Türkiye
[4] Kahramanmaras Istiklal University, Department of Construction Technology, Kahramanmaras¸Türkiye
Adnan KÜÇÜKÖNDER ORCID:0000-0002-6582-2254
İbrahim ALKILINÇ ORCID :0000-0002-3027-7102
Şeyma Biber TEMİRCİK ORCID:0000-0003-1650-6666
Başak ZENGIN ORCID: 0000-0003-3719-9423

**Corresponding author: basakzengin@istiklal.edu.tr*

(Received: 24.11.2022, Accepted: 29.12.2022, Online Publication: 27.03.2023)

**Keywords**
Different Mortar Types, Mineral Additives, XCOM, Radiation Shielding.

**Abstract:** In this study, the Radiation Shielding properties of reinforced mortars whose matrices were made with different mineral materials were investigated. In order to predict the behavior of the mortar specimens against radiation, productions were made with using mineral additives of different properties in the mortar specimens. Perlite, colemanite, pumice, silica fume, fly ash, and ground blast furnace slag, which are widely used in the construction industry, were preferred. In order to study the radiation shielding properties of the prepared samples, the mass attenuation coefficients ($cm^2$ /g) were determined using the XCOM program at an energy of 59.543 keV. The rays were detected with a high resolution Si(Li) detector. Experimental results were compared with theoretical values.The comparison of the experimental results with the theoretical results, it was found that there was a satisfactory agreement between the two methods. In general, the calculated values differ by 4% from the experimental values.



# Farklı Mineral Katkı Oranlarına Göre Üretilen Harç Numunelerin Radyasyon Zırhlama Özelliklerinin Belirlenmesinde Deneysel ve Teorik Analiz

**Anahtar Kelimeler**
Farklı Harç Türleri, Mineral Katkılar, XCOM, Radyasyon Zırhlama

**Öz:** Bu çalışmada farklı mineral malzemelerle matrisleri hazırlanan takviyeli harçların radyasyon zırhlama özellikleri incelenmiştir. Harç numunelerinin radyasyona karşı gösterecekleri davranışı belirleyemek için harç numunelerinde farklı özelliklere sahip mineral katkılar kullanılarak üretimler yapılmıştır. Yapı sektöründe yaygın kullanılan perlit, kolemanit, pomza, silis dumanı, uçucu kül, öğütülmüş yüksek fırın cürufu tercih edilmiştir. Üretilen numunelerin radyasyon zırhlama özelliklerini araştırabilmek için ise kütle azaltma katsayıları (zırh) XCOM programında 59.543 keV enerjide hesaplanmıştır. Işınlar Yüksek çözünürlüklü bir Si(Li) dedektörü ile dedekte edildi. Deneysel sonuçlarla teorik sonuçlar karşılaştırıldığında ise iki yöntem arasında iyi bir uyum olduğu elde edilmiştir. Hesaplanan değerler ile deneysel veriler arasında ortalama %4 fark vardır.

## 1. INTRODUCTION

All living and non-living things on earth are exposed to natural radiation sources in the air, water, soil, and even within their own bodies, as well as artificial radiation sources produced by humans every day. In particular, it is necessary to develop radiation shields in order to adequately protect the bodies of employees and patients. Permanent tissue damage, acute radiation syndromes, cancers, and deaths have been observed in living beings exposed to radiation for a long time [1] [2]. To be protected from the harmful effects of radiation, three basic issues should be considered: time, distance and shielding. The longer the exposure time to the radiation

from the radioactive source or the closer to the radiating source, the higher the radiation dose to be received.
The radiation efficiency by certain radionuclides is so powerful that it can be exposed even when it is invisible even from miles away. The effects of such strong radioactive materials can only be protected by shielding. The parts that are included in the structure of the design that provides the formation of that design and its shaping in the process of use and that regulate the health and comfort of the person using the design are called building materials. After the nineteenth century, as a result of economic and social changes, material technology gained more importance, and solutions in the form of material combinations emerged in all designs instead of a single material [3].

Lead, iron, and materials containing both elements are the best examples of high-intensity radiation shields. Although these materials offer the desired protective feature, they are not preferred in the construction of buildings due to their durability and high costs. Also, lead is toxic to humans and the environment, making it less ideal. For this reason, inexpensive protective materials containing brick, concrete, cement, and sand are used, although they seem less effective. In studies, improving these materials or which ones are better were compared [4] [5]. Due to the popularity of the most widely used concrete building material in construction, studies have been carried out by changing factors such as the effect of aggregate types used in concrete production and the concentration amounts of chemical compounds of cement and water. In most studies, experimental and theoretical evaluation of radiation shielding properties of building materials has been made. Radiation attenuation coefficients were determined to estimate the radiation shielding properties of building materials and more commonly used materials.Thus, it is important to choose building materials that will reduce the effect of radiation on living things [6] [7] [8] [9].

The aim of this study is to compare the radiation protection capability of the produced mortars with the theoretical data in order to investigate the effects of different mineral solids, which are widely used in mortar production, on radiation shielding. For the theoretical calculation, the analysis made using XCOM was performed.

## 2. MATERIAL AND METHOD

### 2.1. Materials

#### 2.1.1. Cement

Chemical properties of CEM I 42.5R Portland Cement produced in Mersin Cement factory were used. The chemical analysis of the cement used is given in Table 1.

**Table 1**. Cement sample chemical analysis

| Chemical Test Results | |
|---|---|
| Constituents Parts | % |
| $SiO_2$ | 20.02 |
| $Al_2O_3$ | 4.87 |
| $Fe_2O_3$ | 3.44 |
| CaO | 62.49 |
| MgO | 2.81 |
| $Na_2O+K_2O$ | 0.91 |
| $SO_3$ | 2.86 |
| Free CaO | 0.48 |
| Loss on Ignition | 2.12 |

#### 2.1.2. Aggregate

0-4 mm Aksu sand, 4-16 mm and 16-32 mm crushed stone gravel, which was extracted from the Aksu river bed and sieved, was used. The maximum grain diameter of the aggregate used in the mortar samples was 32 mm, washed and used after drying in the drying-oven.

In this study, acidic pumice (AP), basic pumice (BP), blast furnace slag (Y), fly ash (U), silica fume (S), colemanite (K) and perlite (P) ground minerals were used. Materials used in the experimental study; ground blast furnace slag and ground basaltic pumice from Iskenderun Adana cement factory, ground colemanite Etimaden A.Ş. Bigadiç boron facility, perlite from Saftaş Mining, fly ash from Elbistan Thermal Power Station. The chemical analysis values of the mineral additives used in the study are given in Table 2.

**Table 2 .** Chemical analysis of mineral additives

| **Constituents Parts (%)** | **Asidic Pumice** | **Basic Pumice** | **B. Furnuce Slag** | **Fly Ash** | **Silica Fume** | **Colemanite** | **Perlite** |
|---|---|---|---|---|---|---|---|
| **$SiO_2$** | 66.12 | 47.63 | 43.71 | 35.84 | 79.62 | 4.00 | 72.93 |
| **$Al_2O_3$** | 15.23 | 15.99 | 11.14 | 15.90 | 2.01 | 0.40 | 13.98 |
| **$Fe_2O_3$** | 3.18 | 11.24 | 1.21 | 5.67 | 0.70 | 0.08 | 0.60 |
| **CaO** | 4.98 | 9.65 | 32.28 | 20.93 | 0.56 | 26.00 | 0.81 |
| **MgO** | 2.13 | 8.05 | 8.42 | 5.83 | 8.66 | 3.00 | 0.43 |
| **$SO_3$** | 0.38 | - | - | 3.31 | 0.23 | - | 0.03 |
| **$Na_2O+K_2O$** | 5.85 | 6.51 | - | 5.00 | 3.69 | 0.35 | 8.43 |
| **$TiO_2$** | 0.40 | 0.2 | | 0.64 | 0.30 | | 0.11 |
| **MnO** | 0.10 | | | | | | |
| **$SO_3$** | | | 1.33 | 2.85 | 0.42 | | |
| **SrSO** | - | - | - | | - | 1.50 | - |
| **$B_2O_3$** | - | - | - | - | - | 40.00 | - |
| **Loss on Ignition** | 1.63 | 0.73 | 1.91 | 4.03 | 3.81 | 24.67 | 2.68 |

## 2.2. Method

### 2.2.1. The method for preparing mortar samples

In this study, mineral additives, which are preferred in research and generally in mortar production, were used. In the production of mortar, mineral additives in different proportions were used instead of reducing the amount of cement. In the study, the preparation of mortar was made according to TS 802. Silica fume (S), perlite (P), blast furnace slag (Y), acidic pumice (AP), basaltic pumice (BP) and colemanite (K) were used as mineral additives.

Instead of cement in the mortar mix, silica fume (S), perlite (P) at the rates of 5, 10, 15, 20 and 25%, blast furnace slag (Y) at the rates of 10, 20, 30, 40, 50 percent, acidic pumice (AP), fly ash (U) and basaltic pumice (BP) and colemanite (K) at 0.5, 1.0, 1.5, 2.0 and 2.5 % were used. Mixture calculations were made for 36 types of mortar samples, including the control sample.The components used in 36 types of sample contents are given in Table 3.

**Table 3.** Mixing quantities of different types of mortars for 1 $m^3$[10]

| | Mixture Quatities | | | |
|---|---|---|---|---|
| **Samples** | **Cement** | **Water** | **Sand** | **Minerals** |
| | **(kg/m³)** | **(kg/m³)** | **(kg/m³)** | **(kg/m³)** |
| R | 450 | 225 | 1350 | 0 |
| AP10 | 405 | 225 | 1350 | 45 |
| AP20 | 360 | 225 | 1350 | 90 |
| AP30 | 315 | 225 | 1350 | 135 |
| AP40 | 270 | 225 | 1350 | 180 |
| AP50 | 225 | 225 | 1350 | 225 |
| BP10 | 405 | 225 | 1350 | 45 |
| BP20 | 360 | 225 | 1350 | 90 |
| BP30 | 315 | 225 | 1350 | 135 |
| BP40 | 270 | 225 | 1350 | 180 |
| BP50 | 225 | 225 | 1350 | 225 |
| Y10 | 405 | 225 | 1350 | 45 |
| Y20 | 360 | 225 | 1350 | 90 |
| Y30 | 315 | 225 | 1350 | 135 |
| Y40 | 270 | 225 | 1350 | 180 |
| Y50 | 225 | 225 | 1350 | 225 |
| U10 | 405 | 225 | 1350 | 45 |
| U20 | 360 | 225 | 1350 | 90 |
| U30 | 315 | 225 | 1350 | 135 |
| U40 | 270 | 225 | 1350 | 180 |
| U50 | 225 | 225 | 1350 | 225 |
| S5 | 427.5 | 225 | 1350 | 22.5 |
| S10 | 405 | 225 | 1350 | 45 |
| S15 | 382.5 | 225 | 1350 | 67.5 |
| S20 | 360 | 225 | 1350 | 90 |
| S25 | 337.5 | 225 | 1350 | 112.5 |
| K0.5 | 447.5 | 225 | 1350 | 2.25 |
| K1 | 445.5 | 225 | 1350 | 4.5 |
| K1.5 | 443.25 | 225 | 1350 | 6.75 |
| K2 | 441 | 225 | 1350 | 9 |
| K2.5 | 438.75 | 225 | 1350 | 11.25 |
| P5 | 427.5 | 225 | 1350 | 22.5 |
| P10 | 405 | 225 | 1350 | 45 |
| P15 | 382.5 | 225 | 1350 | 67.5 |
| P20 | 360 | 225 | 1350 | 90 |
| P25 | 337.5 | 225 | 1350 | 112.5 |

### 2.2.2. Experimental process for radiation shielding

In the experiment system, Canberra brand Si (Li) semiconductor solid-state detector preamplifier, ADC (Analog-Digital Converter), system 100 computer board with a resolution of 155eV at 5.9 keV was used. Ring sources of $^{241}$Am (59.543 keV) and $^{55}$Fe (5.9 keV) were used as radiation sources. $S_i$ ($L_i$) semiconductor solid-state detector is a detector with 2 mm thickness, 12.5 mm² active area, and 500 volts reverse supply voltage, with Lithium atoms diffusing into the lattice spaces of the semiconductor silicon crystal, and it is under vacuum (Canberra, 1995) [11].

It was immersed in liquid nitrogen (-196 ºC) in order to reduce electronic noise and to prevent the evaporation of conductivity-enhancing Lithium, which can evaporate at room temperature, and thermal equilibrium was achieved.

The pre-amplifier converts the characteristic X-rays reaching the detector into electrical pulses in the order of a few millivolts. From here, the electrical pulses reaching the amplifier are amplified to the order of 0-10 volts. These electrical pulses are converted to numerical values in the ADC. These values form peaks in channels suitable for their energies on the 4096-channel screen, depending on their size. In this way, pulses coming in different numbers and energies are displayed on the screen.gives the characteristic X-ray spectrum of the samples. (Figure 1).

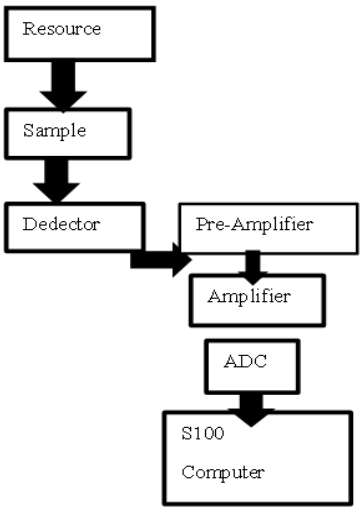


**Figure 1.** Experimental Setups

Using equation 1, radiation attenuation coefficients of the mortars were obtained using X-Ray fluorescence $^{241}$Am (59.543 keV) gamma beam sources.

$$\mu = \frac{log_e \frac{I_o}{I}}{t} \quad ,\mu_m = \frac{\mu}{\rho}\frac{cm^2}{g} \qquad (1)$$

After the 28-day strength of the mortar samples prepared as 12x12x2 $cm^3$, the radiation shielding test of the mortar samples was determineted.. By using 36 different mortar samples, $^{241}$Am (59.543 keV) source, linear attenuation coefficients (μ) and mass attenuation coefficients ($\mu_m$) of AP, BP, Y, U, S, K and P added mortar samples were obtained. The samples were weighed with precision scales and the mass amounts of the samples were obtained. The densities (ρ) of the samples were calculated based on the sample weights. The thickness of each of the samples was measured with the help of the

caliper (t). Before starting the experiment, when the system was empty, counting was made with a γ source of 59.543 keV for 1000 seconds and $I_0$ was found. Afterwards, the samples were placed in the sample holder, counted again at the same time and recorded (I).

$I_o$ = Incoming photon intensity with no sample
I = Incoming photon intensity with sample
t = Thickness of the sample
μ = Linear attenuation coefficient
ρ = Density
$\mu_m$ = Mass attenuation coefficient

### 2.3. XCOM Program Analysis

In the XCOM program, mass attenuation coefficients were found according to the radiation transmittance of the samples exposed to 59.543 keV energy. $I/I_0$ was found using the Beer-Lambert equation. This equation is as follows.

$$\mu = \frac{1}{x} In \frac{Io}{I} \quad (2)$$

*x* sample thickness

$I_0$ the peak area recorded with no sample between the source and the detector.

*I* peak area recorded with sample between source and detector.

The linear attenuation coefficients measured from the experiment and the mass attenuation coefficients finded out using the XCOM program were compared.References in sample thickness (*t*) and density (*ρ*) experiments were chosen as references for using XCOM.

## 3. DISCUSSION AND RESULTS

The data used to interpret the radiation shielding properties of 36 different mortar samples and the data obtained from the experiment are given in Table 4.

**Table 4.** Experimental data of samples according to 59.543 keV (Linear attenuation, mass attenuation coefficients) [10].

| Simples | t(cm) | ρ(g/cm$^3$) | μ(cm$^{-1}$) | μm(cm$^2$ /g) | $I/I_0$ |
|---|---|---|---|---|---|
| R | 2.10 | 2.02 | 0.54 | 0.27 | 0.32 |
| AP10 | 2.10 | 2.01 | 0.59 | 0.29 | 0.29 |
| AP20 | 2.20 | 1.92 | 0.56 | 0.29 | 0.29 |
| AP30 | 2.20 | 1.94 | 0.54 | 0.29 | 0.30 |
| AP40 | 2.20 | 1.84 | 0.53 | 0.29 | 0.31 |
| AP50 | 2.20 | 1.86 | 0.51 | 0.27 | 0.32 |
| BP10 | 2.20 | 1.39 | 0.44 | 0.32 | 0.38 |
| BP20 | 2.10 | 1.27 | 0.41 | 0.32 | 0.42 |
| BP30 | 2.05 | 1.30 | 0.42 | 0.32 | 0.42 |
| BP40 | 2.10 | 1.30 | 0.42 | 0.32 | 0.41 |
| BP50 | 2.10 | 1.29 | 0.42 | 0.33 | 0.41 |
| Y10 | 2.00 | 2.00 | 0.58 | 0.29 | 0.31 |
| Y20 | 2.10 | 2.00 | 0.57 | 0.29 | 0.30 |
| Y30 | 2.15 | 1.98 | 0.56 | 0.28 | 0.30 |
| Y40 | 2.20 | 1.82 | 0.55 | 0.30 | 0.30 |
| Y50 | 2.10 | 1.87 | 0.54 | 0.29 | 0.32 |
| U10 | 2.10 | 1.37 | 0.41 | 0.30 | 0.42 |
| U20 | 2.20 | 1.56 | 0.47 | 0.30 | 0.35 |
| U30 | 2.20 | 1.73 | 0.49 | 0.28 | 0.34 |
| U40 | 2.05 | 1.80 | 0.53 | 0.29 | 0.33 |
| U50 | 2.10 | 1.87 | 0.56 | 0.30 | 0.31 |
| S5 | 2.00 | 2.00 | 0.55 | 0.28 | 0.33 |
| S10 | 2.10 | 1.97 | 0.55 | 0.28 | 0.32 |
| S15 | 2.20 | 1.92 | 0.54 | 0.28 | 0.31 |
| S20 | 2.20 | 1.88 | 0.54 | 0.29 | 0.30 |
| S25 | 2.20 | 1.95 | 0.52 | 0.27 | 0.32 |
| K0.5 | 2.05 | 2.00 | 0.59 | 0.30 | 0.30 |
| K1.0 | 2.10 | 1.96 | 0.57 | 0.29 | 0.30 |
| K1.5 | 2.20 | 1.86 | 0.55 | 0.30 | 0.30 |
| K2.0 | 2.20 | 1.82 | 0.54 | 0.30 | 0.30 |
| K2.5 | 2.20 | 1.83 | 0.53 | 0.29 | 0.31 |
| P5 | 2.20 | 1.94 | 0.55 | 0.28 | 0.30 |
| P10 | 2.10 | 1.79 | 0.52 | 0.29 | 0.33 |
| P15 | 2.20 | 1.76 | 0.51 | 0.29 | 0.32 |
| P20 | 2.10 | 1.62 | 0.50 | 0.30 | 0.35 |
| P25 | 2.10 | 1.55 | 0.47 | 0.30 | 0.37 |

The linear attenuation coefficient at 59.543 keV was obtained at most from AP10 (0.59) and K0.5 (0.59), and at least from BP20(0.41) and U10 (0.41) samples. It was determined that the linear attenuation coefficient increased as the amount of fly ash increased in the mortar produced with the fly ash (U) mortar sample. In the samples of acidic pumice (AP), basic pumice (BP), blast furnace slag (Y), fly ash (U) silica fume (S), colemanite (K) and perlite (P) added additives, the energy rays of 59.543 keV are reduced by It has been obtained that it has undergone 20% of the radiation. It was found that the AP20 sample passed 28% radiation, while the BP30 sample passed 42% radiation. The mass attenuation coefficient is the highest in the BP50 (0.33) sample and the least in the S25 and AP50 (0.27) sample.

A theoretical study was created by adhering to the data in the experimental process. The theoretical mass absorption coefficients were obtained with the XCOM program. The experimental and theoretical mass absorption coefficients were compared. As can be seen in Figure 2, the experimental measurement results of the samples and the theorical/computed results are in good agreement. There is an average of 4% difference between the calculated values and the experimental data. Once the experimental and theoretical mass attenuation coefficients are compared, the closest average to each other is in the U mineral added samples at the rate of 0.3%. Whenever the experimental and theoretical data of the samples produced with P and S were compared, an average of 0.6% was estimanted, the samples produced with Y were compared, an average of 0.9% difference was obtained. As compared to the serial samples produced with A, an average difference of 1.5% was resuting. The difference in the average comparison rate of the serial samples produced with K is 9%. The experimental and theoretical data of the samples produced with BP were compared, a difference of 12% was obtained. In this case, the experimental and theoretical mass attenuation coefficients were compared, the greatest difference was found in the AP samples.

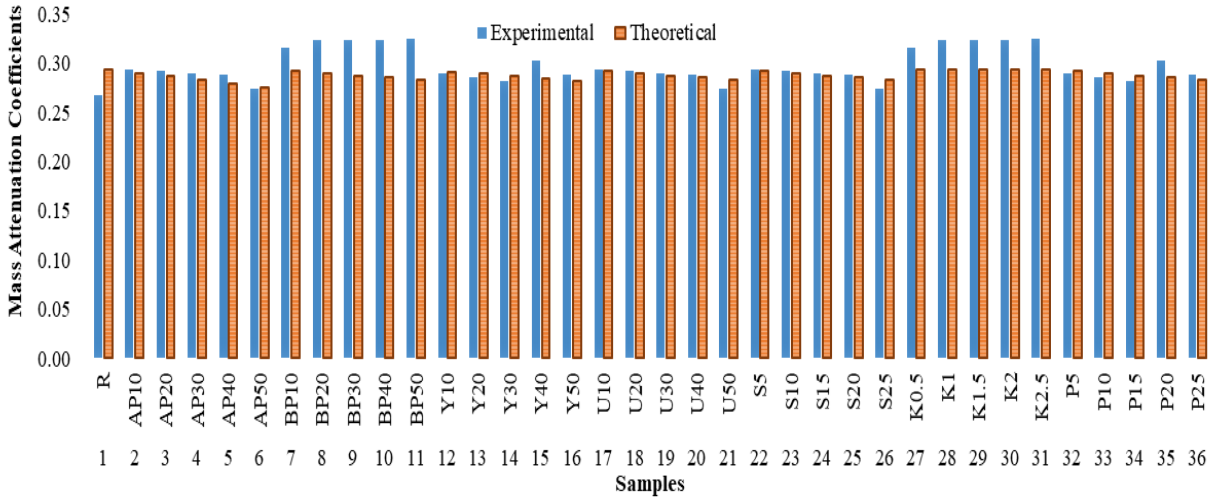


**Figure 2.** Experimental and theoretical comparison of mass attenuation coefficients of mortar samples



## 4. CONCLUSION

Radiation shielding properties of 36 different mortar samples produced with different minerals were obtained by experimental and theoretical methods, depending on the mass attenuation coefficients. According to the energy of 59.543 keV, the experimental study results and the theoretical data were compared with the mass attenuation coefficients. The closeness of the obtained theoretical data to the experimental data was determined. According to the study data:

- Silica fume (S), colemanite (K), and perlite (Acidic pumice (AP), basic pumice (BP), blast furnace slag (Y) and fly ash (U) added mortar samples) were analyzed according to 59,543 keV energy beams. In the mortar samples with the P) additive, it was determined that the P5 sample passed 29% of the energy, the P25 sample passed 37% of the energy, the AP20 sample absorbed 72% of the energy, and the BP30 sample absorbed 58% of the energy.

- The linear absorption coefficient at 59.543 keV is the highest in the AP10 sample and the least in the BP20 and U10 samples. It was determined that the linear attenuation absorption coefficient increased depending on the increase in the amount of fly ash (U).

- The linear absorption coefficients of fly ash (U), and basaltic pumice (BP) in mortar samples increased, and the number of additives in colemanite (K), acidic pumice (AP), blast furnace slag (Y), silica fume (S) and perlite (P) samples It was evaluated that as the linear attenuation coefficient increased, the linear absorption coefficients decreased.

- In the theoretical reckon of the samples, an average of 4% difference was obtained compared to the experimental data. Depending on this ratio, it has been determined that the radiation attenuation coefficients can be used in a healthy way when the product is made according to these minerals theoretically.

Considering that it is always difficult to conduct experiments according to the results above, it is obvious that theoretical data will be supported in the determination of radiation amounts of materials in building products with theoretical studies. It will be easier to work with XCOM or other software. Materials in the building can be easily evaluated for radiation-holding properties. As a result, environmental problems can be prevented in the construction industry.

## REFERENCES


[1] Aygün, B. High alloyed new stainless steel shielding material for gamma and fast neutron radiation. Nucl. Eng. Technol. 2020; 52: 647–653.

[2] Sayyed, M., Al-Hadeethi, Y., AlShammari, M., Ahmed, M. , Al-Heniti S., and Rammah, Y. Physical, optical and gamma radiation shielding competence of newly borotellurite based glasses: TeO2–B2O3–ZnO–Li2O3–Bi2O0. Ceram. Int. 2021;47: 611–618.

[3] Eriç, M. Building Physics and Materials. Literatür Press Istanbul 199: 367.

[4] Gökçe, H.S., Canbaz-Öztürk, B., Çam, N.F., Andiç-Çakır, Ö. Gamma-ray attenuation coefficients and transmission thickness of high consistency heavyweight concrete containing mineral admixture. Cem. Concr. Compos. 2018; 92: 56–69.

[5] Obaid, S. Gaikwad D. and Pawar, P. Determination of gamma ray shielding param-eters of rocks and concrete. Radiat. Phys. Chem. 2018;144:356–360.

[6] Gökce H. S. , Yalçınkaya Ç., Tuyan M. Optimization of reactive powder concrete by means of barite aggregate for both neutrons and gamma rays. Constr. Build. Mater. 2018;189:470–477.

[7] Sayyed, M. I. Tekin, H. O. Kılıcoglu, O. Agar, O. Zaid, M. H. M. Shielding features of concrete types containing sepiolite mineral:Comprehensive study on experimental, XCOM and MCNPX results M.I. Results in Physics. 2018; 11:40–45.

[8] Han D., Kim W, Lee S, Kim H., Romero P. Assessment of gamma radiation shielding properties of concrete containers containing recycled coarse aggregates. Constr Build Mater. 2018;38:122-163.

[9] Agar O. Study on gamma ray shielding performance of concretes doped with natural sepiolite mineral. Radiochim Acta. 2018;2981.

[10] Temircik, B. Ş. Investigation of Radiation Permeability and Engineering Properties of Building Material. KSU Graduate School of Natural and Applied Sciences Doctoral Thesis, (in Turkish), Kahramanmaras; 2015.

[11] Canberra, Edition Ten Product Catolog. Canberra Endustries, Inc Connecticut, USA, 1995.

Araştırma Makalesi https://doi.org/10.46810/tdfd.1022507 Research Article

BİNGÖL ÜNİVERSİTESİ

Türk Doğa ve Fen Dergisi
Turkish Journal of Nature and Science

www.dergipark.gov.tr/tdfd

# Proposal of New Dataset for Child Face Expression Recognition and Comparison of Deep Learning Models on The Proposed Dataset

**İrem SAYIN[1], Bekir AKSOY[2*]**

[1] Yıldız Technical University, Machine Faculty, Mechatronics Engineering Department, İstanbul, Türkiye
[2] Isparta University of Applied Sciences, Technology Faculty, Mechatronics Engineering Department, Isparta, Türkiye
İrem SAYIN ORCID No: 0000-0002-0627-8308
Bekir AKSOY ORCID No: 0000-0001-8052-9411

**Corresponding author: bekiraksoy@isparta.edu.tr*

(Received: 12.11.2022, Accepted: 4.01.2023, Online Publication: 27.03.2023)

**Keywords**
Child Facial Expression Recognition, Facial Expression Recognition, Deep Learning, Transfer learning

**Abstract:** With the developing technology, smart systems have started to take place in our daily lives. Accordingly, it is very important for the systems that will actively participate in social life to adapt to social life properly. One of the most important steps of adapting to social life is communication. Facial expressions are one of the most important parts of communication that usually supports verbal communication. For this reason, many studies have been carried out on identifying facial expressions. The vast majority of these studies were carried out using datasets containing only adult faces. Conducting studies that do not involve the elderly and children may lead to the creation and development of highly biased smart systems. Therefore, this article focuses on detecting children's facial expressions. In order to detect facial expressions in children, a data set was prepared with images collected from search engines using keywords. In the study, VGG16, ResNet50, DenseNet121, InceptionV3, InceptionResNetV2 and Xception artificial intelligence models were used on the data set prepared using transfer learning methods, and the success of the models at the end of the training was evaluated and compared. Obtained results were evaluated according to performance evaluation metrics. According to the evaluation results, the best result was obtained with the InceptionV3 model with an accuracy rate of 76.3% and an F1 score of 0.76.



# Çocuklarda Yüz İfadesi Tanımlama için Yeni Veri Seti Önerilmesi ve Veri Seti Üzerinde Derin Öğrenme Modellerinin Karşılaştırılması

**Anahtar Kelimeler**
Çocuklarda Yüz İfadesi Tespiti, Yüz İfadesi Tanıma, Derin Öğrenme, Transfer Öğrenme

**Öz:** Gelişen teknoloji ile akıllı sistemler günlük hayatımızda yer edinmeye başlamıştır. Sosyal hayatta aktif olarak katılacak sistem ve teknolojilerin sosyal hayata uyum sağlamaları oldukça önemlidir. Sosyal hayata uyum sağlamanın en önemli adımlarından birisi iletişimdir. Yüz ifadeleri genellikle sözlü olarak gerçekleştirilen iletişimi destekleyen iletişimin oldukça önemli parçalarından biridir. Bu nedenle son zamanlarda oldukça popüler bir alan olmuş olan yüz ifadelerini tanımlama üzerinde pek çok çalışma gerçekleştirilmiştir. Gerçekleştirilen bu çalışmaların büyük bir çoğunluğu yalnızca yetişkin yüzlerinin içeren veri setleri kullanılarak gerçekleştirilmiştir. Yaşlı ve çocukları içermeyen çalışmaların yapılması oldukça yanlı sistemlerin oluşturulması ve geliştirilmesine neden olabilir. Bu nedenle bu makalede ihmal edilen gruplardan bir tanesi olan çocuklar yüzleri üzerinde bir çalışma gerçekleştirilmiştir. Çalışmada arama motorlarında belirlenmiş olan anahtar kelimeler kullanılarak çocuk yüz ifadelerini içeren bir veri set hazırlanmıştır. Çalışmada transfer öğrenme yöntemleri kullanılarak hazırlanan veri seti üzerinde VGG16, ResNet50, DenseNet121, InceptionV3, InceptionResNetV2 ve Xception yapay zeka modelleri kullanılarak eğitim sonucunda modellerinin başarısı değerlendirilerek karşılaştırılmıştır. Elde edilen sonuçlar performans değerlendirme metriklerine göre değerlendirilmiştir. Değerlendirme sonuçlarına göre en iyi sonuç %76,3 doğruluk oranı ve 0,76 F1 puanı ile InceptionV3 modeli ile elde edilmiştir.

## 1. INTRODUCTION

Humans are social beings by nature. People communicate with each other to convey information, meet their social needs, and share their thoughts and feelings. This communication is usually carried out by verbal communication. Where verbal communication is insufficient, human expressions come into play. Facial Expressions have a very important place in human communication [1]. Understanding human expressions allows to determine the emotional state of the person at that moment. Deeper meanings can be extracted by combining the person's expressions and the emotions they reflect with their verbal expressions [2].

With the developing technology, simple verbal communications have begun to be used to assign simple tasks between humans and intelligent systems. The relationship between technology and people, which is expected to develop further in the future and take more place in daily life, needs to be developed. Intelligent technologies that will enter our lives will need to detect facial expressions of people, make mood analyses and communicate at a higher level. For this reason, facial expression recognition has become a very popular field and a lot of researches have been done on it and different datasets have been developed for this purpose

When the studies on expression recognition are examined, it is seen that the majority of the studies and the prepared data sets are mostly composed of adult faces. It is seen that the faces of children and the elderly are rarely included in the studies. In the study of Howard et al. on the bias of machine learning algorithms on facial expression detection, they stated that the old and young age groups and ethnic minorities were not adequately represented in the studies and data sets [3]. They stated that this causes machine learning algorithms to be biased. Guo et al.'s study on elderly faces found that elderly people's expressions were less exaggerated compared to adults. In addition, they stated that the loss of elasticity of the skin and wrinkles due to aging cause difficulty in detecting expression [4]. Similarly, Houstis and Kiliaridis examined the differences between children and adults in their study [5]. According to their study, they found differences in the way adult and child faces express emotions. They stated that vertical features in facial emotional expressions were not developed in children.

As a result of this unbalanced distribution in the field, it is likely that the systems to be developed in the future (smart home systems, assistive robots, etc.) will develop a bias towards a single age, gender and ethnic group. For example, in the study of Brandao and Martim on pedestrian identification algorithms, they found that the miss rate of female and child pedestrians was two times higher than that of male and adult pedestrians in the most successful algorithm [6]. In addition to the bias in the studies, the majority of the datasets containing facial expressions also consist of adults (Extended Cohn-Kanade Dataset/CK+, FER-2013, AffectNet, The Japanese Female Facial Expression Dataset/JAFFE, CMU MultiPIE). In addition to the small number of datasets created for children, these datasets generally consist of images collected in controlled environments. The majority of studies on the detection of child facial expressions use NIMH-ChEFS (The NIMH Child Emotional Faces Picture Set) [7] or CAFE (The Child Affective Facial Expression Set) [8] datasets.

In this study, a chil facial expression data set was created by collecting images from search engines for children between the ages of 2 and 10. While creating the data set, facial expressions belonging to 7 classes were collected, including angry, happy, disgusted, sad, scared, surprised and neutural, considering the 6 basic facial expressions presented by Ekman et al. [9]. Using this data set, different deep learning models were trained with the transfer learning method. The most successful model was determined by comparing the precision, recall, accuracy and F1 score values of the models.

In the second part, the main studies on child facial expression recognition are examined. In the third section, brief information is given about the models and data set. In the fourth section, comparisons of models are given according to precision, recall, F1 score and accuracy values. In the fifth and last chapter, the conclusion and plans for future studies are given.

## 2. RELATED WORKS

In the study carried out, academic studies on emotion analysis of children's facial expressions using artificial intelligence methods were examined in detail and discussed in detail below.

Rao et al., (2020) classified and evaluated the datasets of children and adults using the same model they developed in their study and investigated whether there are significant differences between adult and child faces for face detection [10]. They used the CK+ and CAFFE datasets to compare adult and child facial expressions. They identified sixty-eight key points using facial landmarks to be used in expression detection. They aimed to determine the minimum number of points required for adult and child faces by comparing the accuracy results they obtained with the DNN model they created. They tested the datasets with the DNN model using different facial landmark points. When all sixty-eight points were used with the CAFE dataset, they achieved an accuracy rate of 66%. in addition, the accuracy decreased to 49% when only twenty-three eye-brow points were used, and to 41% when only twenty-one lip points were used. In the CK+ dataset, they achieved an accuracy rate of 87% for all 68 points, 83% for eye-brow points, and 83% for lip points. They stated that the results they obtained support the hypothesis that there are differences in the ability of children and adults to express emotions. Finally, by analyzing the results of the CK+ dataset and maintaining the obtained accuracy, they tried to reduce the required number of facial points and reduced the eye-brow points to ten and the lip points to eight. For the CAFE dataset, they stated that the removal of facial points greatly affected the accuracy rate. They stated that children cannot display strong expressions as adults, and therefore

the same features may not be appropriate for children and adults.

Leo et al. developed an SVM-based expression recognition system to be used with the Robokind R25 robot to interact with children with Autism Spectrum Disorder (ASD) in their study [11]. With the proposed system, they aimed to automatically manage the medical protocol aimed at improving the capacity of children affected by ASD to associate emotions with facial expressions. The protocol performed is based on the imitation of the emotion shown by the robot by the child. The emotion imitated by the child was detected and analyzed by the robot with the model developed in the study. In the first step of the developed model, after the face identification process, the HOG vectors of these images were extracted with the Directed Gradient Histogram algorithm. These extracted HOG vectors were given as input to the SVM classifier and they performed the classification process. The training of this developed model was carried out using a subset of the CK+ dataset. As a result of the training, they obtained an accuracy rate of 97.5% with the model CK+ data set.

Nagpal et al., (2019) stated that children's faces are not adequately represented in expression identification studies [12]. In their study, they proposed a new learning model called Mean Supervised Deep Boltzmann Machine/ms-DBM in order to classify children's facial expressions. In the model they proposed, they enabled the model to learn the distinguishing features by minimizing the intra-class variations and maximizing the inter-class variations according to the average feature vectors. In their study, they trained and tested the model not only on children's faces but also on adult faces. For this reason, in addition to the Radbound Faces dataset, which includes both adult and child expressions, they used CAFE emotion datasets consisting only of child expressions. In order to perform expression recognition on children's faces, a pre-training was carried out with the images of 1197 adult facial expressions in the Radbound Faces dataset. As a result of their study, they obtained a better result by approximately 3.3% than the models they compared with the msDBM model on the Radboud dataset with an accuracy rate of 75%. On the CAFE dataset, they achieved an accuracy rate of 48%, which was approximately 14% better than the other models. They stated that the reason why this ratio is very different from the Radboud Faces dataset is that the images of children in the Radboud dataset consist of adolescent children, while the images in the CAFE dataset consist of images of younger children (2-8) years old. In the classification of adult expressions, they achieved an accuracy rate of 85.9% with the msDBM model.

Witherow et al., (2019) suggested using the transfer learning method for facial expression recognition in children [13]. With the method they proposed, they offered a solution to the model education problem that emerged due to the datasets containing the child expressions, which are very few in number. They used the CNN model they designed in the study. After training the CNN model they developed with the CK+ dataset consisting of adult face images, they fine-tuned it using the CAFFE dataset. Using the model they created, they conducted training in five different combinations. These combinations are;

1. Combination: Training and testing the model with the CK+ dataset.
2. Combination: Training and testing the model with the CAFE dataset.
3. Combination: Testing the model trained with CK+ with the CAFE dataset.
4. Combination: Creating a model using the weights of the model trained with the CK+ dataset and testing the model by training with the CAFE dataset.
5. Combination: Fine-tuning the model trained with the CK+ dataset using the CAFE dataset.

As a result of all these trainings, they obtained test accuracy rates of approximately 93% for the first case, approximately 63% for the second case, approximately 46% for the third case, approximately 62% for the fourth case, and approximately 76% for the fifth case. According to the results obtained, the best accuracy rate for the CAFE dataset was obtained with the model trained on the CK+ dataset, fine-tuned and tested using the CAFE dataset.

Lopez-Rincon (2019) performed facial expression recognition in children using the NAO robot in their study [14]. A four-layer CNN model was created to be used in the study and the created CNN model was compared with the Facial Action Coding System (FACS) based AFFDEX SDK classifier. The hyperparameters of the created model were determined and adjusted according to the results of bayesian optimization and trained using a subset of the AffectNet dataset. As a result of the training, they achieved an accuracy rate of 68.4% on the AffectNet validation dataset. In order to increase the accuracy of the same model on the CAFE dataset, it has been fine-tuned by training the model with the NIHM-ChEF dataset.



## 3. DATASET AND MODELS

In this section, information about the data set prepared in the study is given. In addition to that, the training parameters of the models used for comparison are also presented in this section.

### 3.1. Data Set

The data set prepared in this study was created by collecting the images from various search engines with bulk download tools using keywords. The data set used consists of child facial expressions and includes a total of seven expression classes. Images that are similar and do not contain human faces among the collected images were deleted and cleaned. All images were reviewed by three adult individuals and reclassified according to dominant expression to ensure that the images obtained were classified correctly. The faces in the classified images were detected using HaarCascade, and the cut images were resized to 128 x 128. Some sample images of the data set are given in Figure 1.

**Figure 1.** Examples from the data set

A total of 6364 images were obtained. However, in order to prevent the imbalance between classes in the data set, the amount of data in the classes was reduced to be close to the number of data contained in the 'disgust expression' class, where the least image was obtained. As a result of this process, all classes were arranged and the total number of data was reduced to 4002. The dataset was divided into three as 80% training, 10% validation and 10% test dataset. The training, validation and test data set distributions for all classes are given in Table 1.

**Table 1.** Distribution of the classes in the Data Set in the training, validation and test sets

| Class Name | Training Dataset | Validation Dataset | Test Dataset | Total Data |
|---|---|---|---|---|
| Angry | 467 | 54 | 54 | 575 |
| Disgusted | 416 | 48 | 48 | 512 |
| Happy | 500 | 58 | 58 | 616 |
| Neutural | 455 | 52 | 52 | 559 |
| Sad | 451 | 52 | 52 | 555 |
| Scared | 483 | 56 | 56 | 595 |
| Surprised | 478 | 56 | 56 | 590 |
| Total | 3 250 | 376 | 376 | 4 002 |

Evaluation of the models was carried out using the test data set. Methods were used to increase the amount of data used. For this purpose, random rotation, horizontal flip, horizontal and vertical scrolling operations were performed on the data set.

### 3.2. Models

In this study, 6 deep learning models, namely VGG16, ResNet50, DenseNet121, InceptionV3, InceptionResNetV2 and Xception, which were previously trained on ImageNet dataset, were used in order to train by transfer learning. The models were trained by fine tuning through freezing the weights in some layers. The most successful configuration obtained with the model as a result of many different trainings is presented in the study. All models were trained using early stopping according to the validation loss rate. Using Modelcheckpoint, validation accuracy and validation loss were tracked during the training of the models, and the models with the lowest validation loss and the highest validation accuracy were recorded.

The VGG16 model was first used to train the VGG16 in the study. The last layers of the model were removed and replaced with Global average pooling layer, dropout layer with 0.7 drop rate and 7 unit Softmax layers. Layers added to VGG16 are given in Figure 2. The weights of all layers except the last six layers were frozen. It was trained for 67 epochs using 128 batch size, $10^{-4}$ learning rate and Adam optimizer.

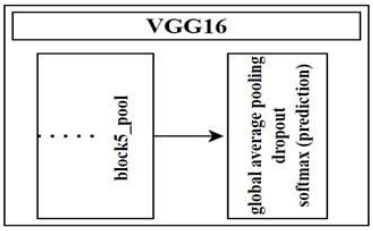


**Figure 2.** Layers added to the VGG16 model

Instead of the upper layers removed in the ResNet50 model, Global average pooling, dropout layer with 0.7 drop rate and 7 unit Softmax layer has been added as VGG16. Layers added to ResNet50 are given in Figure 3. Only the last 50 layers are trained using Batch size of 128, learning rate and Adam optimizer.

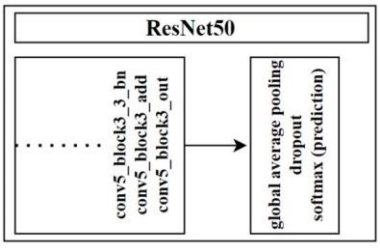


**Figure 3.** Layers added to the ResNet50 model

In the DenseNet121 model, the upper layers have been replaced with 0.7 dropout layer, global average pooling, 514 unit fully connected layer and 7 unit softmax layer. Layers added to DenseNet121 are displayed in Figure 4. 64 batch sizes were trained for 39 epochs using the Adam optimizer. When the validation loss plateus learning rate divided and decresed with factor 0.2 initial learning rate was determined as , and learning rate was reached at the end of the training.

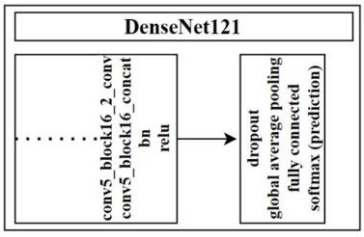


**Figure 4.** Layers added to the DenseNet121 model

In the InceptionV3 model, the upper layers have been replaced with global average pooling, 0.5 dropout layer, 1028 unit fully connected layer and 7 unit softmax layer. Layers added to InceptionV3 are given in Figure 5. Training was performed for 24 epochs using 64 batch size,

Adam optimizer. When the validation loss plateus learning rate divided and decresed with factor 0.2 initial learning rate was determined as , and learning rate was reached at the end of the training.

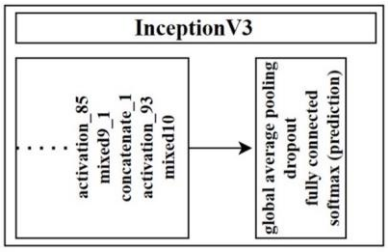


**Figure 5.** Layers added to the InceptionV3 model

In the InceptionResNetV2 model, the upper layers have been replaced with global average pooling and 7 softmax layers. Layers added to InceptionResNetV2 are presented in Figure 6. Training was carried out for 36 epochs using 64 batch size, Adam optimizer. When the validation loss plateus learning rate divided and decresed with factor 0.2 initial learning rate was determined as, a learning rate of was reached at the end of the training.

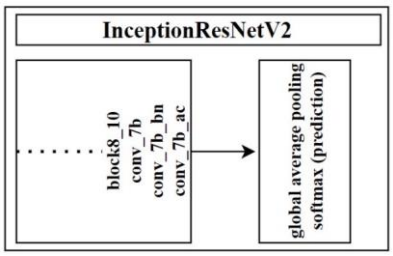


**Figure 6.** Layers added to the InceptionResNetV2 model

In the Xception model, the upper layers are replaced with global average pooling, 0.5 dropout layer, and 7 unit softmax layer. The layers added to Xception are given in Figure 7. Training was carried out for 36 epochs using 64 batch size, Adam optimizer. When the validation loss plateus learning rate divided and decresed with factor 0.2 initial learning rate was determined as $10^{-3}$, a learning rate of $4.10^{-5}$ was reached at the end of the training.

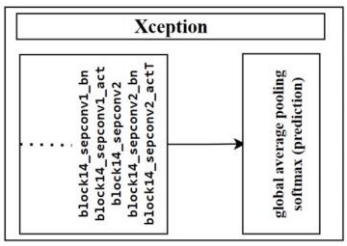


**Figure 7.** Layers added to the Xception model

The model that gave the most accurate result on the test data set among the checkpoint models recorded as a result of the training of all models was used for comparison.

## 4. COMPARISON OF TRAINING RESULTS AND MODELS

The models, which were trained by fine-tuning with the transfer learning method, were evaluated on the test data set as a result of the training. Precision, recall, accuracy and F1 scores obtained by the models on the test data were calculated and compared.

As a result of the evaluation made on the test data set for the VGG16 model, it was obersed that the best result was obtained with the model that gave the highest accuracy rate during the training, and this model was preferred for comparison. The complexity matrix showing the success of the VGG16 model in classifying the test data set is given in Figure 8.

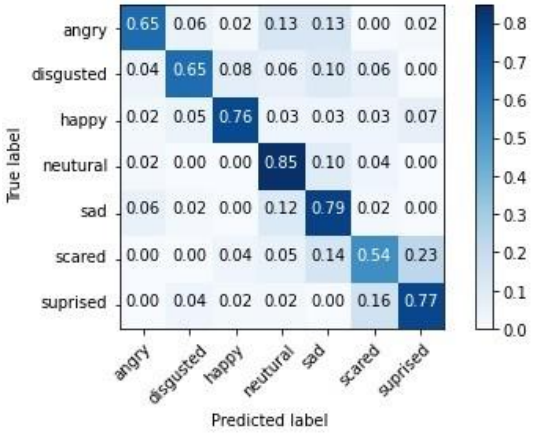


**Figure 8.** Confusion matrix of VGG16

When the complexity matrix given in Figure 8 is examined, it is seen that the VGG16 architecture classifies the neutral class as the most successful and the fear class as the most unsuccessful. Using the predictions made by the model on the test data set, accuracy, precision, sensitivity and F1 score values were calculated to evaluate the architecture and are given in Table 2.

**Table 2.** Accuracy, precision, sensitivity and F1 score results of VGG16 architecture

| | Accuracy (Test Data) | Precision | Recall | F1 Score |
|---|---|---|---|---|
| VGG16 | 0.712 | 0.723 | 0.712 | 0.711 |

Although the trained VGG16 architecture achieved the highest accuracy rate of 72% on the accuracy dataset, this rate was found to be 71% on the test dataset. Again, on the test data set, 0.723 precision, 0.712 sensitivity and 0.711 F1 score values were obtained.

For the ResNet50 model, the best result on the test data set was obtained with the model that gave the highest accuracy rate recorded with the checkpoint. Therefore, the comparison was made over this model. The complexity matrix showing the success of the ResNet50 model in classifying the test data set is given in Figure 9.

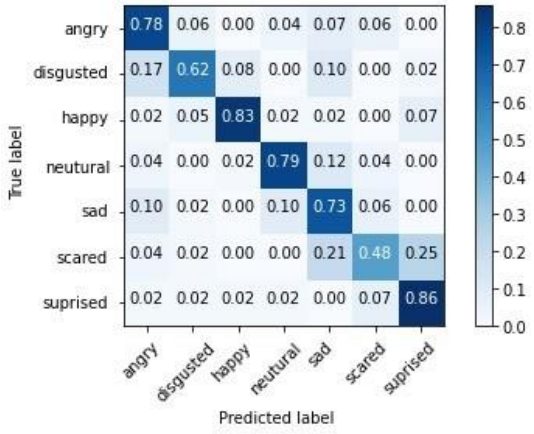


**Figure 9.** Confusion matrix of ResNet50

When the complexity matrix of the ResNet50 model is examined, it is seen that the model classifies the happy class as the most successful and the fear class as the most unsuccessful. Using the predictions made by the model on the test dataset, accuracy, precision, sensitivity and F1 score values were calculated to evaluate the architecture. The values calculated for the ResNet50 architecture are given in Table 3.

**Table 3.** Accuracy, precision, sensitivity and F1 score results of ResNet50 architecture

| | **Accuracy (Test)** | **Precision** | **Recall** | **F1 Score** |
|---|---|---|---|---|
| ResNet50 | 0.728 | 0.735 | 0.726 | 0.724 |

The highest accuracy rate of 72% was obtained on the trained ResNet50 architecture accuracy dataset. Again, an accuracy rate of 72% was obtained on the test data set. In addition, 0.735 precision, 0.726 sensitivity and 0.724 F1 score values were obtained on the test data set.

As a result of the evaluation made on the test data set with the DenseNet121 model, it was seen that the best result was obtained with the model obtained as a result of the whole training, and this model was used for comparison. The test data set complexity matrix of the DenseNet121 model is shown in Figure 10.

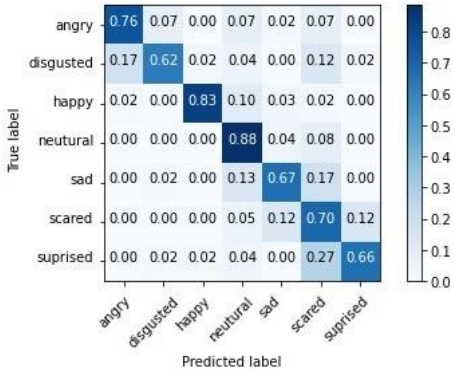


**Figure 10.** Confusion matrix of DenseNet121

When the complexity matrix is examined, it is seen that the DenseNet121 architecture classifies the neutral class as the most successful and the disgust class as the most unsuccessful. Using the predictions made by the model on the test dataset, accuracy, precision, sensitivity and F1 score values were calculated to evaluate the architecture. The values calculated for the DenseNet121 architecture are given in Table 4.

**Table 4.** Accuracy, precision, sensitivity and F1 score results of DenseNet121 architecture

| | **Accuracy (Test)** | **Precision** | **Recall** | **F1 Score** |
|---|---|---|---|---|
| DenseNet121 | 0.734 | 0.762 | 0.732 | 0.738 |

Although the trained DenseNet121 architecture achieved the highest accuracy rate of 74% on the accuracy dataset, this rate was found to be 73% on the test dataset. Again, on the test data set, 0.762 precision, 0.732 sensitivity and 0.738 F1 score values were obtained.

For the InceptionV3 model, the best result on the test data set was obtained with the model that gave the highest accuracy rate recorded with checkpoint, and this model was used for comparison. The test data set complexity matrix of the InceptionV3 model is shown in Figure 11.

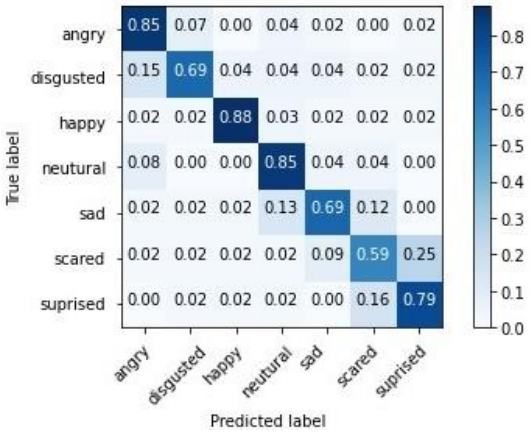


**Figure 11.** Confusion matrix of InceptionV3

When the complexity matrix shown in Figure 10 is examined, it is seen that the InceptionV3 architecture classifies the happiest class as the most successful and the fear class as the most unsuccessful. Using the predictions made by the model on the test data set, accuracy, precision, sensitivity and F1 score values were calculated to evaluate the architecture and are presented in Table 5.

**Table 5.** Accuracy, precision, sensitivity and F1 score results of InceptionV3 architecture

| | **Accuracy (Test)** | **Precision** | **Recall** | **F1 Score** |
|---|---|---|---|---|
| InceptionV3 | 0.763 | 0.764 | 0.761 | 0.760 |

Although the highest accuracy rate of 74% was obtained on the accuracy dataset with the trained InceptionV3 architecture, this rate was found to be 76% on the test dataset. Again, on the test data set, 0.764 precision, 0.761 sensitivity and 0.760 F1 score values were obtained.

As a result of the evaluation made on the test data set for the InceptionResNetV2 model, it was seen that the best result was obtained with the model obtained as a result of the whole training, and this model was used for

comparison. The test data set complexity matrix of the InceptionResNetV2 model is shown in Figure 12.

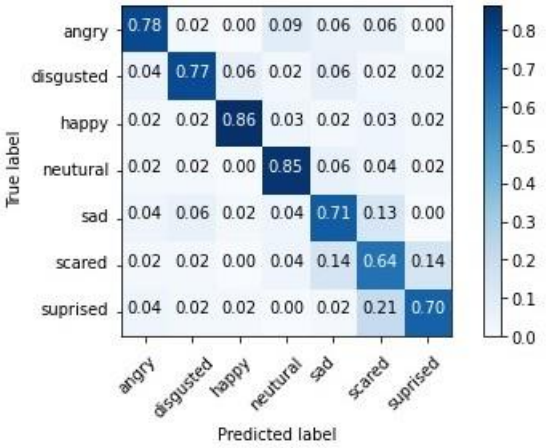


**Figure 12.** Confusion matrix of InceptionResNet50

When the complexity matrix given in InceptionResNetV2 is examined, it is seen that the InceptionResNetV2 architecture classifies the happiest class as the most successful and the fear class as the most unsuccessful. Using the predictions made by the model on the test dataset, accuracy, precision, sensitivity and F1 score values were calculated to evaluate the architecture. The calculated values for the InceptionResNetV2 architecture are given in Table 6.

**Table 6.** Accuracy, precision, sensitivity and F1 score results of InceptionResNetV2 architecture

| | **Accuracy (Test)** | **Precision** | **Recall** | **F1 Score** |
|---|---|---|---|---|
| InceptionResNetV2 | 0.757 | 0.764 | 0.758 | 0.760 |

Although the highest accuracy rate of 71% was obtained on the accuracy dataset with the trained InceptionResNetV2 architecture, this rate was obtained as 75% on the test dataset. Again, on the test data set, 0.764 precision, 0.758 sensitivity and 0.760 F1 score values were obtained.

As a result of the evaluation made on the test data set for the Xception model, the best result was obtained with the checkpoint model with the lowest validation loss during the training. Confusion matrix obtained from the test data set using this model is given in Figure 13.

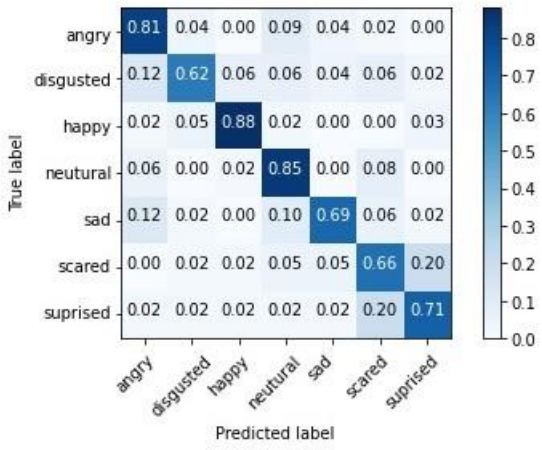


**Figure 13**. Confusion matrix of Xception

When the complexity matrix is examined, it is seen that the Xception architecture classifies the happy class as the most successful and the disgust class as the most unsuccessful. Using the predictions made by the model on the test dataset, accuracy, precision, sensitivity and F1 score values were calculated to evaluate the architecture. The values calculated for the Xception architecture are given in Table 7.

**Table 7.** Xception architecture accuracy, precision, sensitivity and F1 score results

| | **Accuracy (Test)** | **Precision** | **Recall** | **F1 Score** |
|---|---|---|---|---|
| Xception | 0.75 | 0.755 | 0.747 | 0.747 |

The highest accuracy rate of 73% was obtained on the trained Xception architecture accuracy dataset. In the test data set, the accuracy rate was found to be 75%. Again, on the test data set, 0.755 precision, 0.747 sensitivity and 0.747 F1 score values were obtained. The evaluation results of all models are given in Table 8.

**Table 8.** Evaluation results of models

| **Evaluation criteria** | **Models** | **Value** |
|---|---|---|
| Recall | VGG16 | 0.712 |
| | ResNet50 | 0.726 |
| | DenseNet121 | 0.732 |
| | **InceptionV3** | **0.761** |
| | InceptionResNetV2 | 0.758 |
| | Xception | 0.747 |
| Precision | VGG16 | 0.723 |
| | ResNet50 | 0.735 |
| | DenseNet121 | 0.762 |
| | **InceptionV3** | **0.764** |
| | **InceptionResNetV2** | **0.764** |
| | Xception | 0.755 |
| Accuracy | VGG16 | 71% |
| | ResNet50 | 73% |
| | DenseNet121 | 73.40% |
| | **InceptionV3** | **76.30%** |
| | InceptionResNetV2 | 75.70% |
| | Xception | 75% |
| F1 score | VGG16 | 0.711 |
| | ResNet50 | 0.724 |
| | DenseNet121 | 0.738 |
| | **InceptionV3** | **0.760** |
| | **InceptionResNetV2** | **0.760** |
| | Xception | 0.747 |

When the precision, recall, acuracy and F1 score values calculated from the test data are examined; It is seen that the highest recall and accuracy values are obtained with the InceptionV3 model. In F1 score and precision values, it is seen that InceptionV3 and InceptionResNetV2 models are very close to each other or give the same results.

## 5. RESULTS AND DISCUSSION

In the study, it was tried to perform emotion analysis by predicting children's facial expressions with artificial intelligence models. In the study carried out, it was tried to compare the models by using different artificial intelligence models in describing facial expressions.

Although there are many studies on facial expression recognition in the literature, expression recognition studies on children's faces are very limited. For this purpose, it was aimed to detect expression on children's faces in this study. For this purpose, images of search results made using keywords on search engines were collected. Face detection was performed on the collected images, and the images were divided into seven classes according to the expressions they displayed: angry, disgusted, happy, neutral, sad, afraid and surprised.

Using 6 different deep learning models and transfer learning on the prepared data set, the model that gave the best results on the data set was determined. All the models used were able to achieve over 70% accuracy in the test dataset. Inception-based models seem to give very successful results.

When the F1 score values of the models given in Figure 14 are examined according to the classes, it is seen that all models are quite successful in detecting the happy class. In addition, it is seen that there is a decrease in all models in the detection of scared, surprised and sad classes. It is thought that this may be due to the fact that the pictures in the fear and surprise classes are largely similar to each other.

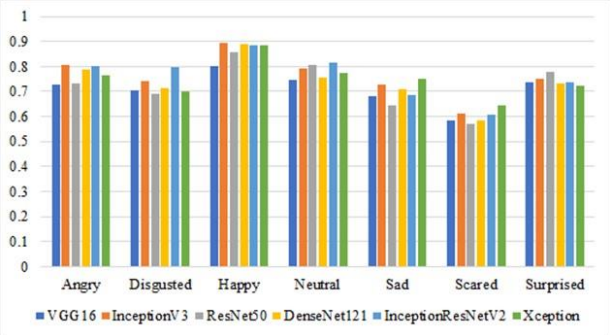


**Figure 14.** Class-based F1 scores of models

Since facial expression recognition is a very difficult and complex task, it is very important to have a large number of data in order to increase the success of the models. For this reason, datasets containing limited number of child facial expressions should be increased. Increasing the number of data of scared, sad and surprised facial expressions, which have low identification rates, will greatly benefit the success of the models.

In future studies, it is planned to expand the data set and detect real-time images. In addition, it is thought that training the models by using adult and child data sets together will increase the detection success of the models.

## Acknowledgement

We would like to thank the open access websites for making the images available on different websites and allowing us to use them in the study.

## Authors Contributions

The study was produced from the master thesis made by İrem SAYIN under the supervision of Bekir AKSOY

## REFERENCES

[1] Jack R.E., Schyns P.G. The Human Face as a Dynamic Tool for Social Communication. Curr Biol. 2015; 25:R621–R634. https://doi.org/10.1016/j.cub.2015.05.052.
[2] DeVito Jospeh A. Human Communication. Boston: Pearson; 2002.
[3] Howard A., Zhang C., Horvitz E. Addressing bias in machine learning algorithms: A pilot study on emotion recognition for intelligent systems. 2017 IEEE Workshop on Advanced Robotics and its Social Impacts, ARSO 2017. Austin, TX, USA; 2017. https://doi.org/10.1109/ARSO.2017.8025197.
[4] Guo G., Guo R., Li X. Facial expression recognition influenced by human aging. IEEE Trans. Affect. Comput. 2013; 4: 291–298. https://doi.org/10.1109/T-AFFC.2013.13.
[5] Houstis O., Kiliaridis S. Gender and age differences in facial expressions. Eur. J. Orthod. 2009; 31: 459–466. https://doi.org/10.1093/ejo/cjp019.
[6] Brandao M., Age and gender bias in pedestrian detection algorithms. arXiv Prepr. arXiv:1906.10490, 2019.
[7] Egger H.L., Pine D.S., Nelson E., Leibenluft E., Ernst M., Towbin, K.E., et al. The NIMH Child Emotional Faces Picture Set (NIMH-ChEFS): a new set of children's facial emotion stimuli. Int. J. Methods Psychiatr. Res. 2011; 20: 145–156. https://doi.org/10.1002/mpr.343.
[8] Lobue V., Thrasher C., Kret M.E. The Child Affective Facial Expression (CAFE) set: validity and reliability from untrained adults. Front. Psychol. 2015; 5: 1532. https://doi.org/10.3389/fpsyg.2014.01532.
[9] Ekman P., Friesen W. V., EllsWorth P. Emotion in the Human Face. 1st ed. Pergamon Press; 1972. https://doi.org/10.1016/C2013-0-02458-9.
[10] Rao A., Ajri S., Guragol A., Suresh R., Tripathi S. Emotion Recognition from Facial Expressions in Children and Adults Using Deep Neural Network. Int. J. Intell. Syst. 2020; 43–51. https://doi.org/10.1007/978-981-15-3914-5_4.

[11] Leo M., Del Coco M., Carcagnì P., Distante C., Bernava M., Pioggia G., et al. Automatic Emotion Recognition in Robot-Children Interaction for ASD Treatment. IEEE International Conference on Computer Vision, ICCV 2015. Santiago, Chile: 2015.p 537–545. https://doi.org/10.1109/ICCVW.2015.76.

[12] Nagpal, S., Singh, M., Vatsa, M., Singh, R., Noore, A. Expression classification in children using mean supervised deep Boltzmann Machine. IEEE/CVF Conference on Computer Vision and Pattern Recognition Workshops, CVPR 2019. California: 2019.

[13] Witherow, M. A., Samad, M. D.,Iftekharuddin, K. M. Transfer learning approach to multiclass classification of child facial expressions. SPIE Optical Engineering + Applications. San Diego, California, United States: 2019. p. 1113911

[14] Lopez-Rincon A. Emotion recognition using facial expressions in children using the NAO robot. 2019 International Conference on Electronics, Communications and Computers , CONIELECOMP 2019. Cholula, Mexico:IEEE; 2019.p.146-153. 10.1109/CONIELECOMP.2019.8673111

Cilt 12, Sayı 1, Sayfa 21-29, 2023 Volume 12, Issue 1, Page 21-29, 2023

Araştırma Makalesi https://doi.org/10.46810/tdfd.1113610 Research Article

Türk Doğa ve Fen Dergisi
Turkish Journal of Nature and Science
www.dergipark.gov.tr/tdfd

# Trace Element Analysis of some Medicinal and Aromatic Plant Taxa by ICP-MS

**Ebubekir İZOL[1*], İsa ÇİÇEK[2], Lütfi BEHÇET[2], Enes KAYA[1], Abbas TARHAN[3]**

[1] Bingöl University, Bee and Natural Products R&D and P&D Application and Research Center, Bingöl, Türkiye
[2] Bingöl University, Scıence and Art Faculty, Molecular Bıology and Genetıcs Department, Bingöl, Türkiye
[3] Dicle University, Science and Technology Application and Research Center, Diyarbakır, Türkiye
Ebubekir İZOL ORCID No: 0000-0003-0788-4999
İsa ÇİÇEK ORCID No: 0000-0001-7241-6599
Lütfi BEHÇET ORCID No: 0000-0001-8334-7816
Enes KAYA ORCID No: 0000-0003-3973-168X
Abbas TARHAN ORCID No: 0000-0001-5196-3892

**Corresponding author: eizol@bingol.edu.tr*

(Received: 7.05.2022, Accepted: 20.01.2023, Online Publication: 27.03.2023)

**Keywords**
ICP-MS,
Çermik,
Trace element analysis,
Plants,
Minerals

**Abstract:** In this study, analysis of trace elements (Al, V, Cr, Ni, Cu, Zn, As, Ag, Cd, Sn, Hg, Pb) in medicinally important taxa, such as *Alkanna trichophila* Hub.-Mor. var. *trichophila*, *Anchusa azurea* Mill. var. *azurea* (Boraginaceae), *Achillea biebersteinii* Afan., *Centaurea iberica* Trev. ex Sprengel (Asteraceae), *Ajuga vestita* Boiss. (Endemic), *Teucrium polium* L. (Lamiaceae), collected in Çermik district of Türkiye's Diyarbakır province, was conducted quantitatively and qualitatively using the ICP-MS technique. Today, ICP-MS technology is one of the most sensitive metal analysis methods. As a result of the analysis, Sn, Hg, and Pb elements in the studied plant taxa could not be determined since they were below the LOD value. It is essential for consumers that these three toxic elements are not specified in plant species. In general, it was determined that the concentrations of heavy metals, which have harmful effects on health, were low in the investigated plants. Of all the elements, Al (26.04-193.5 mg/kg) had the highest concentration in the studied taxa. As a consequence, several trace elements were characterized, and their concentrations were identified in the studied medicinal and aromatic six ethnobotanically important plant species.



# Bazı Tıbbi ve Aromatik Bitki Taksonlarının ICP-MS ile Eser Element Analizi

**Anahtar Kelimeler**
ICP-MS,
Çermik
Eser element analizleri,
Bitkiler,
Mineraller

**Öz:** Bu çalışmada Türkiye'nin Diyarbakır ilinin Çermik ilçesinde toplanmış, folklorik veya tıbbi amaçlar için kullanılan *Anchusa azurea* Mill. var. *azurea* (Boragınaceae), *Achillea biebersteinii* Afan. (Asteraceae), *Ajuga vestita* Boiss. (Endemik) (Lamıaceae), *Teucrium polium* L. (Lamıaceae), *Alkanna trichophila* Hub.-Mor. (Boragınaceae), *Centaurea iberica*Trev. ex Sprengel (Asteraceae) bitki türlerinin ICP-MS tekniği ile eser element (Al, V, Cr, Ni, Cu, Zn, As, Ag, Cd, Sn, Hg, Pb) analizi kantitatif ve kalitatif olarak yapılmıştır. ICP-MS teknolojisi günümüzde en hassas metal analiz yöntemlerindendir. Yapılan analiz sonucunda altı bitki türünün tamamında Sn, Hg, Pb elementleri LOD değerinin altında kaldığından belirlenememiştir. Toksik olan bu üç elementin bitki türlerinde belirlenmemesi tüketiciler için önemlidir. Genel olarak araştırılan bitkilerde sağlığa zararlı etkileri olan ağır metal konsantrasyonlarının düşük olduğu belirlenmiştir. En yüksek konsantrasyon ise Al (26,04-193,5 mg/kg) elementinde belirlenmiştir. Sonuç olarak, etnobotanik açıdan önemli altı tıbbi ve aromatik bitki türünde çeşitli eser elementlerin karekterizasyonu ve konsantrasyonları belirlenmiştir.

## 1. INTRODUCTION

For centuries, plants have been used for medicinal purposes to treat various diseases, including enteritis [1]. The development, regulation and application of traditional or herbal medicines in distinct parts of the world often present challenges. Common challenges in many countries are those connected to regulatory status, quality control, assessment of safety and effectiveness, safety monitoring, and insufficient knowledge of customary, complementary/alternative and herbal medicines within public drug regulatory authorities [2]. Metals with a density of more than 5 g / $cm^3$ are defined as "heavy metals". In another definition, metals that are harmful when they enter the body in high concentrations are called toxic metals or heavy metals. More than 60 metals are in this group, including Pb, Cr, Cd, Co, Ni, Cu, Zn, Hg and Fe. Due to their nature, these elements are generally found in stable compounds or silicates in the form of oxide, carbonate, sulfur and silicate in the earth crust. To maintain their everyday activities, all living things need heavy metals in the environment. Iron (Fe), copper (Cu), manganese (Mn), cadmium (Cd), molybdenum (Mo), silicon (Si) and boron (B) are heavy metals required for plant metabolism. Cu, Co, Fe, Mn, Mo, Zn, Se, and I are also heavy metals needed for animals. Co, Cu, Cr, Fe, Mn, Ni, Mo, Zn, U, V are also toxic substances. The primary sources of heavy metals are mineral fertilizers, some base stones, sewage wastes, biocides, wastewater, urban wastes, motor vehicle exhaust gases and mining [3].

Trace elements play an essential role in the formation of active chemicals in medicinal plants and are also responsible for the toxicity of medicinal plants [4]. The grade of toxic heavy metals in plants can be affected by the geochemical parameters of the soil, air, water pollution and the ability of plants to amass certain elements selectively. Besides, metals may be connected to the geographical origin, harvest or gathering of these plant materials. Some metals (such as Fe, Cr, Mo, Ni Zn, Co, Mn, Cu, Al) are essential plant nutrients, but at higher concentrations, they are phytotoxic. However, most heavy metals are initially micronutrients, namely, they are necessary (in small amounts) for the expected growth of plants and animals. Manganese (Mn), molybdenum (Mo), copper (Cu), zinc (Zn), and nickel (Ni) are heavy metals required for higher plants. For humans and animals, copper (Cu), Manganese (Mn), cobalt (Co), chromium (Cr), molybdenum (Mo), zinc (Zn), vanadium (V), and selenium (Se) are micronutrient heavy metals. Iron (Fe), which is not generally considered a heavy metal, is essential for both plants and animals. Several other elements, including cadmium (Cd), lead (Pb), arsenic (As), and tin (Sn), could play a significant role at very low concentrations. Toxicities and deficiencies of micronutrients adversely affect animal and plant health, causing declines in growth rate (and yield), obvious physiological stress symptoms, and, in extreme cases, the death of the animal or plant [5]. The consumption of plants is significant for humanity. Commonly consumed plants may be needed for their chemical content, and they may need to be avoided due to their harmful chemicals. [6]. For example, onion and garlic (*Allium* species) are widely consumed worldwide. Scientific studies have shown that these plants are beneficial, but they can be harmful due to their highly toxic element contents.

One of the most effective methods used to determine the amounts of elements in plants is the inductively coupled plasma-mass spectrometry (ICP-MS) method, an analytical technique in which the molecular bonds are broken, and atoms are ionized by sending argon to a high-temperature plasma. The sample is generally delivered as a solution to the nebulizer and spray chamber via the sample intake system. Here, thanks to the high-velocity argon flow, the sample solution is fogged. Only tiny droplets move into the argon plasma, and others go directly to waste. Plasma at temperatures of 7000 $^oK$ evaporates and ionizes the sample. Ion flow goes from atmospheric pressure to a high vacuum environment through sample and skimmer cones. The ion stream is then directed through the ion lenses to the mass filter, focusing on the quadruple. Ions are separated in the mass spectrometer according to their mass to charge ratio and are measured by the detector [7]. Essential components of ICP-MS are sample entry system, ICP torch, interface, vacuum system, lenses, DRC (Dynamic reaction cell), quadruple, detector, data processing and system controller [8]. ICP-MS is suitable for the determination of trace elements in solution with its fast analysis rate and convenient mass range. Simple spectra, low detection limit and compatibility with isotope ratios are the features that make ICP-MS attractive. The detection limit for most elements is below ng/L. Thanks to its ability to determine multiple elements, it is used in qualitative analysis and determination of isotope ratios, as well as in the quantitative and semi-qualitative analysis of the majority of the elements in the periodic table, including metallic elements, in various samples. Calibration graphs can be drawn between pg/L and mg/L for many elements. For this reason, many elements with different concentrations can be determined at the same time. Since the development of different sample introduction systems, the ICP-MS technique has been able to analyze solid samples as well as liquid samples. ICP-MS is widely used in wastewater, drinking water, food, hydrogeology, geochemistry, geology, and petrochemistry [9].

When the metal content of plants is considered, the concentrations of the elements must be determined in order not to exceed the concentration limits set by WHO, to be evaluated as a medicinal plant or food, to be used as a herbal drug and to be utilized ethnobotanically.

In this study, the trace element concentrations of six ethnobotanically important plant species (*A. trichophila*, *A. azurea*, *A. biebersteinii*, *C. iberica*, *A. vestita*, *T. polium*) were determined by inductively coupled plasma-mass spectrometry (ICP-MS) technique. Following is detailed information on the studied plant taxa.

*Anchusa azurea*: The local name of the plant is Gurız or Gelızvan. It is called by various local names in different

geographies. The gathering periods are between April and May. Above ground parts are used for food and treatment purposes [10]. In the literature, its leaves and flowering branches, known as wound healing externally, are used widely as they are suitable for kidney diseases and lip cracking and have urinary-enhancing effects. The leaves can be used as a decoction or infusion as a diaphoretic, urinary enhancer and ulcer remedy. As an antidote against snake bites by crushing the leaves, the water obtained from boiling the leaves and flowers can be used in the treatment of eczema, and the above-ground parts can be used as decoction in asthma [11-20].

*Achillea biebersteinii*: The regional name of the plant is Gihaye Zerg. Likewise, it is called by various local names in different geographies. The gathering periods are between May and June. Flower parts are used for treatment [10]. In the use of the literature, the main used part of the plant is flower conditions, but it is found in the stem and leaf in the drugs sold, albeit a little. It effectively relieves abdominal pain in treating asthma, kidney pain, skin spots, urine enhancer, as an appetizer, and in treating gynaecological diseases. In the form of infusion against urinary tract inflammations (5%), rheumatic illnesses, anti-inflammatory, menstrual, hepatitis, sinusitis, menstrual pain, toothache, shortness of breath, abdominal pain, asthma as a decoction of all parts, flowers and leaves are powdered after drying. It can be used in wound treatments by pouring it on the wound and leaving the leaves on the wound when fresh. In the treatment of decoction ulcers prepared from the above-ground parts, the infusion trained from the above-ground parts can be used as a urinary tract antiseptic, including the infusion prepared from the flowering parts (capitula) [20-26].

*Ajuga vestita*: The local name of the plant is Abamayasıl herb. The gathering periods are between April and May. Above ground, parts are used for treatment. There is no use of literature in ethnobotanical terms. It is a plant that is collected when fresh, and eaten raw and brewed after drying due to its bitter taste and drunk with various sweeteners to reduce sugar in case of diabetes [10].

*Teucrium polium* L.: The local name of the plant is Meryemhot and Meyero. Likewise, in different geographies, it is named with many various local names and these names take place in the literature. The gathering periods are between May-June. Above ground, parts are used for treatment and belief [10]. In the literature, they are used to relieve headache and ear pain, wound healing, pain-relieving, stimulant, appetite, stomach ailments, digestive and excretory system ailments, stomach aches, appetite and diabetes, intestinal inflammation and laziness. It is also used in the treatment of tuberculosis, relieving stomach pain, cancer treatment, rheumatic pain, colds and diabetes [27-35].

*Alkanna trichophila*: The local name of the plant is Gurız Dervin. It is also included in the literature with different names. The gathering periods are between April and May. Root parts are used for treatment. Its roots are used as an expectorant to heal stomach and intestinal ulcers [10].

*Centaurea iberica*: The vernacular name of the plant is Kerbeşık, Çavbelok. Like other plants, they are named with many vernacular names in different geographies and these names are included in the literature. The gathering periods are between March-May. Fresh and young parts of above-ground parts are used for food and treatment purposes. In the use of the literature, the decoction of flowers and branches is prepared and used against rheumatic pain, malaria, antipyretic, menstrual, constipation, appetite, against goitre disease, stomach pain, snake and scorpion bites and malaria. It is also used in the treatment of sugar reducers, infusions, and internal antipyretics, wounds and boils [36-39].

## 2. MATERIAL AND METHODS

### 2.1. Preparation of plant samples

Plant taxa were collected from the Çermik district in Diyarbakir province of Turkey. The plants collected were identified and recorded in the herbarium of Bingöl University. The names of the species, their herbarium numbers and the collection sites and times were given in Table 1.

**Tablo 1.** Names of plants species, place and time of gathering, herbarium numbers

| Name of Plant taxa | Collection localities | Herbarium numbers | Collection period |
|---|---|---|---|
| *Alkanna trichophila* | Diyarbakır | BIN9405 | Apr-May 2017 |
| *Centaurea iberica* | Diyarbakır | BIN9406 | March-May 2017 |
| *Anchusa azurea* | Diyarbakır | BIN9402 | Apr- May 2017 |
| *Achillea biebersteinii*. | Diyarbakır | BIN9401 | May- June 2017 |
| *Ajuga vestita*. | Diyarbakır | BIN9404 | Apr- May 2017 |
| *Teucrium polium* L. | Diyarbakır | BIN9403 | May- June 2017 |

### 2.2. Reagents

Ultrapure water (18.3 MΩ cm − 1 obtained from the Human power I device) was used in all of the experimental stages. Agilent Technologies (USA) brand multi-element calibration standard was used as the calibration standard for the elements determined for analysis reliability. In addition to the calibration standard, the internal standard Agilent Technologies brand standard internal mix is used. The nitric acid used is 65% Supra pure Merck (Darmstadt, Germany) brand.

### 2.3. Digestion of The Samples

The dissolution process was done before the samples were analyzed with the ICP-MS device. For this, the ground samples were weighed 1 g, and 6 mL of supra pure nitric acid and 2 mL of hydrogen peroxide were added. The prepared samples were dissolved in CEM brand MARS6 ONE TOUCH (USA) model microwave shredder oven. The dissolved samples were diluted to 50

mL with 1% supra pure nitric acid prepared with ultrapure water [40]. Additional dilution was made so that the prepared samples coincided with the standard calibration range.

### 2.4. Instrumentation and Statistical Analysis

Standard solutions were prepared with 1% supra pure nitric acid at the concentrations given in Table 2.

**Table 2**. Calibration Standards

| | | | | |
|---|---|---|---|---|
| **1.Sd** | **1 (µg/kg)** | **4.Sd** | **50 (µg/kg)** | **Internal Sd** |
| **2.Sd** | **10 (µg/kg)** | **5.Sd** | **100 (µg/kg)** | |
| **3.Sd** | **25 (µg/kg)** | **6.Sd** | **200 (µg/kg)** | |
| **Analytes** | $^{27}$Al, $^{51}$V, $^{52}$Cr, $^{60}$Ni, $^{63}$Cu, $^{66}$Zn | | | $^{45}$Sc |
| | $^{75}$As, $^{107}$Ag, $^{111}$Cd, $^{118}$Sn, $^{202}$Hg, $^{208}$Pb | | | $^{89}$Y |

Sd: Standard

Quantitative and qualitative analyses were performed with the ICP-MS (Agilent 7700X (Tokyo, Japan)) device. Before the sample analysis, the ICP-MS device was brought to optimum conditions and calibrated. $^{45}$Sc, $^{89}$Y elements are used as internal standards. After the calibration charts were created, the elements were analyzed with the ICP-MS device. A high level of helium gas is used to prevent interference. Samples diluted in the standard calibration range were sent to the cyclonic spray chamber with a peristaltic pump, high purity argon gas flow. Besides, for the reliability of the analysis, standard analysis and device calibration was performed after each sample. The operating parameters of the ICP-MS device are given in Table 3.

**Table 3.** ICP-MS device operating parameters

| Parameter | Description / Value |
|---|---|
| **Plasma gas** | Ar X50S 5.0 |
| **Makeup gas** | 0.9 L/min |
| **Carrier gas (inner)** | 1.1 L/min |
| **Plasma gas flow (Ar)** | 15 L/min |
| **Radio frequency power** | 1550 W |
| **Radio frequency matching** | 1.80 V |
| **Radio frequency** | 27.12 MHz |
| **Injector** | 2.0 mm |
| **Cones** | Ni |
| **Nebulizer pump** | 0.1 rps |
| **Background** | <5 cps (9 amu) |
| **Short-term stability** | <3% RSD |
| **Long-term stability** | <4% RSD/2 h |
| **Resolution m/z** | 244 amu |
| **Spray chamber temperature** | 2°C |
| **Rinse time** | 45 sec |
| **Sample intake** | 0.5 mL/min |

In the analysis, linear range, regression and correlation coefficient (R) values, detection limit (LOD) and measurement limit (LOQ) of the calibration chart drawn under optimal operating conditions for twelve elements are shown in Table 4. The LOD and LOQ values of the studied metal elements were calculated using 10 independent blank solutions. LOD and LOQ were found as 3.σ and 10.σ, respectively.

**Table 4**. Analytical parameters of the ICP-MS method

| Element | Linear range (µg/kg) | Regression | Correlation coefficient (r) | Limit of Detection (µg/kg) | Limit of Quantification (µg/kg) |
|---|---|---|---|---|---|
| Al | 0–200 | y=0.006x -0.004 | 0.9983 | 1.1637 | 3.4911 |
| V | 0–200 | y=0.002x -0.004 | 0.9989 | 0.0100 | 0.0300 |
| Cr | 0–200 | y=0.002x -0.005 | 0.9990 | 0.0115 | 0.0345 |
| Ni | 0–200 | y=0.001x -0.002 | 0.9994 | 0.0328 | 0.0984 |
| Cu | 0–200 | y=0.004x -0.007 | 0.9995 | 0.0683 | 0.2049 |
| Zn | 0–200 | y=0.054x +0.000 | 0.9885 | 0.4126 | 1.2378 |
| As | 0–200 | y=0.004x +0.002 | 0.9999 | 0.0747 | 0.2241 |
| Ag | 0–200 | y=0.003x +0.041 | 0.9747 | 0.0358 | 0.1074 |
| Cd | 0–200 | y=0.001x -0.002 | 0.9991 | 0.0607 | 0.1821 |
| Sn | 0–200 | y=0.001x -0.005 | 0.9987 | 0.0195 | 0.0585 |
| Hg | 0–200 | y=0.004x -0.001 | 0.9999 | 0.1355 | 0.4065 |
| Pb | 0–200 | y=0.014x -0.076 | 0.9952 | 0.0427 | 0.1281 |

Values expressed are means ±standard deviation of three parallel measurements ($p < 0.05$).

## 3. RESULTS AND DISCUSSION

The concentration results of the analyzed elements are given in Table 5 with the average of three parallel readings and standard deviation values.

**Table 5.** Elemental analysis results of plants by ICP-MS[a]

| Sample Id | Al 27 (mg/kg) | V 51 (µg/kg) | Cr 52 (µg/kg) |
|---|---|---|---|
| *Alkanna trichophila* | 38.2±0.8 | 97.0±2.1 | 163.0±3.5 |
| *Centaurea iberica* | 38.3±0.6 | 2041.7±99 | 969.8±27.9 |
| *Anchusa azurea* | 83.1±1.2 | 234.5±11 | 202.7±11.2 |
| *Achillea biebersteinii* Afan. | 193.5±3.5 | 474.5±17 | 1000.6±33.5 |
| *Ajuga vestita*. | 191.6±2.7 | 387.1±13 | 677.9±21.7 |
| *Teucrium polium* L. | 26.04±0.7 | 97.0±9.3 | 79.4±3.5 |
| | **Ni 60 (mg/kg)** | **Cu 63 (mg/kg)** | **Zn 66 (mg/kg)** |
| *Alkanna trichophila* Hub.-Mor. | 0.83±0.05 | 2.74±0.08 | 23.8±1.5 |
| *Centaurea iberica* Trev. ex Sprengel | 1.66±0.07 | 4.02±0.09 | 20.1±1.3 |
| Anchusa azurea Mill. var. azurea | 1.52±0.06 | 4.46±0.09 | 15.2±1.1 |
| *Achillea biebersteinii* Afan. | 6.27±0.11 | 3.79±0.09 | 63.1±2.3 |
| *Ajuga vestita* Boiss. | 3.75±0.07 | 5.87±0.11 | 14.1±1.3 |
| *Teucrium polium* L. | 0.69±0.03 | 6.73±0.13 | 17.8±1.7 |

[a] Results are the mean ± standard deviation of three parallel measurements. ($p < 0.05$).

**Table 5.** Elemental analysis results of plants by ICP-MS[a] (continuation)

| Sample Id | As 75 (µg/kg) | Ag 107 (µg/kg) | Cd 111 (µg/kg) |
|---|---|---|---|
| *Alkanna trichophila* | 8.7±0.03 | 75.1±5 | 230.5±15 |
| *Centaurea iberica* | 20.6±0.11 | 53.6±3 | <LOD |
| *Anchusa azurea* | 29.3±0.15 | 33.3±3 | 31.9±4 |
| *Achillea biebersteinii* | 67.0±4.5 | 163.2±11 | 17.8±1 |
| *Ajuga vestita* | 30.6±1.2 | 7.31±0.9 | 81.3±7 |
| *Teucrium polium* L. | <LOD | 89.3±7 | 24.2±2 |
| | **Sn 118 (µg/kg)** | **Hg 202 (µg/kg)** | **Pb 208 (µg/kg)** |
| *Alkanna trichophila* | <LOD | <LOD | <LOD |
| *Centaurea iberica* | <LOD | <LOD | <LOD |
| *Anchusa azurea* | <LOD | <LOD | <LOD |
| *Achillea biebersteinii* | <LOD | <LOD | <LOD |
| *Ajuga vestita*. | <LOD | <LOD | <LOD |
| *Teucrium polium* L. | <LOD | <LOD | <LOD |

[a] Results are the mean ± standard deviation of three parallel measurements. ($p < 0.05$).

In the literature review, it was determined that among the plant species, *Anchusa azurea* Mill., which was collekted only in Iraq, was analyzed by ICP-OES. In this study by Peshawa S. Osw and Faiq H.S. Hussain [41], Al concentration was found in the range of 25-303 mg/kg in seed, stem, branch and leaf. It was determined that the result we found (83.1 ± 1.2 mg/kg) was within this range. V concentration was determined in the range 0.1-1.7 mg / kg. It was found to be close to the result we found (0.2 mg/kg). While the element Cr was found in the range of 0.4-1.8 mg/kg, we found it to be 0.2 mg/kg. While Ni was found to be 0.9-6.5 mg / kg, we found it 1.52 mg / kg. The concentrations of Cu, Zn, As, Ag, Cd elements we found were determined to be below the values found in this study. While Pb could not be determined in our study, it was found below 1 mg/kg in this study. It was seen that the values in the study were performed to a large extent and the results in our study were close to each other [41].

Aluminum (Al) is a heavy metal taken into the human body from drinking water and other sources. Its excess accumulation in the body increases the possibility of getting Alzheimer. It has been determined that the amount of Al in the brains of Alzheimer's patient increases [42]. Besides, adverse effects on the nervous system and lungs were detected [43]. For these reasons, it is an element that is important for human health. In his study, Yener found the concentration of the element Al in plants in the range of 30-1424 mg/kg [4]. In this study, the Al concentration range in plant species was 26-193 mg/kg. It was determined that the plant with the lowest Al concentration was *Teucrium polium* L. and the highest was *Achillea biebersteinii* Afan.

Studies have shown that vanadium (V) has both positive and negative effects on human health. It has been determined that the compounds it creates cause hypoglycemia by causing low blood sugar in humans. It has also been stated that it may be an antineoplastic agent against cancer [44]. The concentration range of vanadium element in the plants studied was found to be 97-2041 µg / kg. At the same time, the highest concentration was observed in *Centaurea iberica*Trev. ex Sprengel plant, the lowest concentration was found in *Alkanna trichophila* Hub.-Mor. and *Teucrium polium* L. plants.

Chromium (Cr) element is crucial for human health. It acts as a cofactor in the synthesis of the insulin hormone and cholesterol. In a study, it was determined that Cr concentration varies between 0.15-4.8 mg/kg. In a different study, the Cr concentration was found in the range of 2-35 mg/kg [45]. According to WHO data, toxicity values for arsenic, lead, chromium and cadmium in wild plants were determined as 5, 10, 2 and 0.3 mg/kg, respectively [46, 47]. The range of values we found was determined as 79-1000 µg / kg. It was seen that the values found were below the WHO data. While the highest measurement was observed in *Achillea biebersteinii* Afan. plant, the lowest measure was found in *Teucrium polium* L. plant species.

Nickel (Ni) is a metal whose concentration is limited by WHO in consumed plants. WHO data reported that the limit of Ni element in edible plants was 1.63 mg/kg [46]. It has been stated that the Ni concentration needed for human health can vary between 80-100 µg / day. In general, the Ni content of foods is desired to be less than 0.5 mg/kg, but it has been reported that some foods may be higher [48]. A study determined that the Ni limit in plants was 0.5-10 mg/kg. In another study, Ni concentration was reported to range from 24-4740 µg / kg [45]. Ni concentration in our study was found in the range of 0.6-6 mg/kg. It was seen that these values were both above and below the WHO limit. It was determined that the highest concentration was in the *Achillea biebersteinii* Afan. plant species, and the lowest concentration was in the *Teucrium polium* L. plant.

Copper (Cu) is a heavy metal that is toxic when taken in excess. Also, it has been reported that copper can reduce hypertension and increase the infertility effect of lead [49]. Cu is a micronutrient element for plants [50]. In the study of Akgüç et al., They found the Cu limits in plants as 4-15 mg/kg [51]. In one study, Cu values were found as 0.2-24 mg/kg [45]. In this research, Cu levels in plants were found to be 2-6 mg/kg. It was determined that these values are below the WHO data.

Plants need nutrients containing trace elements found in the soil. Zinc (Zn) is an essential component for plant growth [52]. WHO has determined the Zn limit as 27.4 mg/kg in edible plants [46]. In the study of Potortì et al., They found the Zn concentration range as 1-5240 mg/kg. In this study, it was determined that the Zn concentration in plants was in the range of 14-23 mg/kg. The results we found were determined to be below the WHO limit.

Arsenic (As) is generally found in foods. Its source is legumes, vegetables, grains and herbs. Due to its toxic effect, the amount of exposure to human is important. Therefore, it needs to be controlled [53]. In the study on *Allium* species, As concentration was found in the range of 13-325 µg / kg [54]. The concentration of As in the *Murraya koenigii* plant grown for medicinal purposes in different cities of India was found in the range of 55-111 µg / kg [55]. Since the concentration of As in *Teucrium*

*polium* L. plant remained below the lod value, it could not be determined. The As range of other species was determined to be 8-67 µg / kg.

The concentration range for the silver (Ag) metal element was determined to be 7-163 µg / kg. The concentration varies according to the plant species. Tin (Sn) metal element could not be detected since it is below the loq value in all plant species. In a study on cadmium (Cd) metal, the concentration range was found to be 20-9000 µg / kg [46]. A different study determined that it was above 0.25 mg/kg [56]. WHO reported the Cd limit as 200 µg / kg in edible plants [46],[57]. Cd could not be determined in plant *Centaurea iberica*Trev. ex Sprengel. In other plant species, the Cd range is found as 17-230 µg / kg. *Alkanna trichophila* Hub.-Mor. while exceeding the plant, other species were determined to be below the limit.

Mercury (Hg) is a harmful metal for human health. It has been reported that the nervous system, in particular, has a high sensitivity to Hg compounds. Studies have shown that it causes severe damage to the brain and kidneys. The source of Hg can be industrial and thermal power plants, in particular, mercury-filled thermometers and amalgam fillings in homes [58]. According to WHO data, the Hg limit is specified as 0.2-0.5 mg/kg. The Hg concentration could not be determined in all plant species.

Lead (Pb) must rise to a certain level to have a toxic effect on the human body. Pb concentration in the blood varies due to many factors such as age, physiological conditions and nutrition. [59]. It has been stated that it may negatively affect the nervous system in the range of 100-1000 µg / L Pb limit in the blood [60]. It has also been reported to cause health problems such as diarrhoea, headache, anaemia, behavioural disorders, mental retardation and tremors [61]. WHO specified the 10 mg/kg limit for Pb [46],[57]. States such as the Republic of Korea and China have set a toxic metal limit in the range of 20-30 mg/kg [46]. In a study, the concentration of Pb in plants is 20-5100 µg / kg, 0.22-1.15 mg/kg in a different study [4] were found in the range. In this study, it could not be determined because the Pb concentration was below the LOD value.

The accumulation and absorption of trace elements in plant tissue depend on several factors [62]. Differences in concentrations of heavy metal elements are due to differences in the structure of certain parts of the plant and the chemical composition of the soil in distinct regions [63]. Besides, the uptake and transfer of heavy metals may vary, counting on the elements' properties and the structure and species of the plant [64],[65].

One of the most advanced techniques in heavy metal and mineral analysis is ICP-MS technology. With the advantage of wide concentration, the analysis of low concentrations is more reliable and sensitive than other techniques [66]. For this reason, quantitative and qualitative metal element analyzes of plants were made with ICP-MS.

## 4. CONCLUSION

Al, V, Cr, Ni, Cu, Zn, As, Ag, Cd, Sn, Hg, Pb trace element analysis of aromatic and medicinally consumed plant species *Anchusa azurea* Mill. var. azurea, *Achillea biebersteinii* Afan., *Ajuga vestita* Boiss., *Teucrium polium* L., *Alkanna trichophila* Hub.-Mor., *Centaurea iberica* Trev. ex Sprengel was determined quantitatively and qualitatively with this study. It is vital to use the studied plant species, especially for medicinal purposes. In the studied species, the highest concentration was detected in element Al. Failure to determine the toxic properties of Sn, Hg, and Pb heavy metals in all plants is critical in consumption and has reduced risk factors. Since Cd element exceeds WHO limit in *Alkanna trichophila* Hub.-Mor. plant, attention should be paid to its consumption. In other species, it was determined to be below the WHO limit. As the ace element limits cannot be determined for *Teucrium polium* L. plant species, it is found below the WHO limit. Even if it is by the literature data on other plant species, it should be cautious in its consumption and used in low limits because it exceeds the WHO data. Concentration limits of other elements were determined to be following WHO data. Metal concentrations can have positive and negative effects on human health. While high concentrations of some metals have a harmful effect, insufficient intake of some metals causes the same effect. The fact that metals act as catalysts in many biological reactions also makes them valuable. In this study, the heavy metal characterization and concentrations of these species used as medicinal and aromatic plants were determined, and thus it was stated that it was a significant study for consumers.



## REFERENCES

[1] Essawi, T., and M. Srour. “Screening of Some Palestinian Medicinal Plants for Antibacterial Activity.” Journal of Ethnopharmacology. 2000; 70 (3): 343–349. doi:10.1016/S0378-8741(99)00187-7.

[2] WHO Expert Committee on Biological Standardization. WHO Technical Report Series 927. Fifty-Fourth Report. Annex1 WHO Guidelines on Nonclinical Evaluation of Vaccines; 2005.

[3] Özbek, Z. Investigation of the Applicability of Limit Values for Heavy Metals in Soil. Master Thesis, 9(1): 76–99; 2010.

[4] Yener, İ. “Trace Element Analysis in Some Plants Species by Inductively Coupled Plasma Optical Emission Spectrometry (ICP-OES).” 2019; doi:10.21597/jist.

[5] Alloway, Brian J. “Heavy Metals and Metalloids as Micronutrients for Plants and Animals.” In. 2013; 195–209. Springer, Dordrecht. doi:10.1007/978-94-007-4470-7_7.

[6] İzol, E., H. Temel, M.A. Yilmaz, I. Yener, O.T. Olmez, E. Kaplaner, et al. A Detailed Chemical and Biological Investigation of Twelve Allium Species from Eastern Anatolia with Chemometric Studies. Chemistry & Biodiversity. 2021; 18, no. 1 (January 8): e2000560. doi:10.1002/cbdv.202000560.

[7] İzol, E. and İnik, O. Current Analysis Methods of Heavy Metals in Soil. European Journal of Science and Technology. 2022; (36), 116-120. Doi: 10.31590/ejosat.1111496.
[8] Önder, S. Investigation of Heavy Metal Pollution in Agricultural Fields Irrigated with Wastewater. Master Thesis, 66; 2012.
[9] Baba, B. Quantitative Determination of Arsenic (As) in Hot Springs of Biga Peninsula (Çanakkale) by Voltammetry and Inductively Coupled Plasma-Mass Spectrometer (Icp-Ms) Techniques. Master Thesis; 2007.
[10] Çiçek, İ. Ethnobotanical Characteristics of Çermik District and Its Villages (Diyarbakır). Bingol University Institute of Science and Technology, Master Thesis; 2019.
[11] Özturk, M., and H. Özcelik. Useful plants of Eastern Anatolia. Semih Offset Printing Facilities, Ankara; 1991.
[12] Özçelik, H., G. Ay, and M.Öztürk. Some economically important plants of Eastern and Southeastern Anatolia. X. National Biology Congress, Proceedings, 18–20 July, Erzurum; 1990. p. 1-10.
[13] Gümüş, İ. Local names and uses of some useful plants growing in Ağrı region. Turkish Journal of Botany, 18: 107-112; 1994.
[14] Işık, S., A. Gonuz, Ü. Arslan, and M. Ozturk. Ethnobotanical Characteristics of Some Species in Afyon (Turkey). Journal of Herb Systematic Botany. 1995; 2 (1): 161-166.
[15] Honda G, E. Yeşilada, M. Tabata, E. Sezik, T. Fujita, Y. Takeda, et al. Traditionalmedicine in Turkey VI. folk medicinei in west Anatolia: Afyon, Kütahya, Denizli, Muğla, Aydın provinces. Journal of Ethnopharmacology. 1996; 53: 75-87.
[16] Yeşilada, E., G. Honda, E. Sezik, M. Tabata, T. Fujita, T. Tanaka, et al. Traditional Medicine in Turkey. V. Folk Medicine in the Inner Taurus Mountains. Journal of Ethnopharmacology. 1995; 46, no. 3 (June 5): 133–152.doi:10.1016/0378-8741(95)01241-5.
[17] Çakılcıoğlu, U. Türkoğlu and İ. M. Kursat. Ethnobotanical features of Harput (Elazig) and its surroundings. Eastern Anatolia Region Studies (Daum) Journal. 2007; 5(2): 22-28 .
[18] Yapıcı, İ.Ü., H. Hoşgören, and Ö. Saya. Ethnobotanical Features of Kurtalan (Siirt) District. Journal of Dicle University Ziya Gökalp Faculty of Education. 2009; Vol. 12.
[19] Deniz, L., A. Serteser, and M. Kargioglu. Local Names and Ethnobotanical Characteristics of Some Plants in Uşak University and Its Neighborhood. AKU Journal of Science and Technology. 2010; 10, no. 01: 57–72.
[20] Melikoğlu, G., S. Kurtoğlu, and Ş. Culture.. Herbs Traditionally Used in Asthma Treatment in Turkey. Marmara Pharmaceutical Journal. 2015; 19, no. 1: 1–11.
[21] Altundağ E. Public Use of Natural Plants of Iğdır Province (Eastern Anatolia Region). Istanbul University Institute of Health Sciences, PhD Thesis; 2009.
[22] Güldaş, N. Determination of Usage Areas of Some Plants with Ethnobotanical Value in Adiyaman Province. Fırat University, Institute of Science and Technology. Master's Thesis; 2009.
[23] Tetik, F. A Research on Plants with Ethnobotanical Value of Malatya Province. Fırat University Institute of Science and Technology, Master Thesis; 2011.
[24] Polat, R., S. Selvi, U. Çakılcıoğlu, and M. Açar. Ethnobotanical investigation of wild plants sold in Bingöl neighborhood markets. Biological Diversity and Conservation. 2012; 5(3): 155-161.
[25] Yiğit SŞ. Plants Sold in Gaziantep Province Herbalists and Ethnobotanical Characteristics. Gaziantep University Department of Biology, Master's Thesis; 2014.
[26] Doğan, A. Ethnobotanical researches in Pertek (Tunceli) region. M.U. Institute of Health Sciences, Ph.D. Thesis; 2014.
[27] Tonbul,S., and Y. Altan. Some plants used by the people for various purposes in the Elazig region. Fırat University Journal (Social Sciences). 1989; 3(2): 267-278.
[28] Ayanoğlu, F., A. Mert, D.A. Kaya. Detection and Collection of Some Important Medicinal and Fragrant Plants Used by the People in the Hatay Region. Mustafa Kemal University, Journal of the Faculty of Agriculture. 1999; 4(1-2): 101-116.
[29] Özçelik, H. and C. Balabanlı.. Medicinal and aromatic plants of Burdur province. I. Burdur Symposium, Burdur; 2005. p. 1127-1136
[30] Çakılcıoğlu, U. Türkoğlu and İ. M. Kursat. Ethnobotanical features of Harput (Elazig) and its surroundings. Eastern Anatolia Region Studies (Daum) Journal. 2007; 5(2): 22-28 .
[31] Çimen, O.D. Ethnobotanical studies on folk remedies used in Konya. Gazi University Institute of Health Sciences, Master's thesis; 2007.
[32] Yeşil, Y. An ethnobotanical research in Kürecik (Akçadağ/Malatya) subdivision. Istanbul University Institute of Health Sciences, Master Thesis, p. 275; 2007.
[33] Doğan G., and E. Bağcı. Plants used by the people in some settlements of Elazığ based on their traditional ecological knowledge and their ethnobotanical features. Firat Univ. Journal of Science. 2011; 23(2): 77-86
[34] Kaval, İ. Ethnobotanical Characteristics of Geçitli (Hakkari) and Its Surroundings Yüzüncü Yıl University, Institute of Science and Technology, Master Thesis, p. 279; 2011.
[35] Mükemre, M. Ethnobotanical Characteristics of Konalga, Sırmalı, Dokuzdam Villages (Çatak-Van) and Their Surroundings. Yüzüncü Yıl University Graduate School of Natural and Applied Sciences, Department of Biology, Master's Thesis, 53(9): 1689–1699; 2013.
[36] Yazıcıoğlu, A., and E.Tuzlacı. Folk medicinal plants of Trabzon (Turkey). Fitoterapia, 67(4): 307-318; 1996.
[37] Baytop, T. Herbal Treatment in Turkey; Past And Today. Nobel Medical Bookstores Ltd. Sti, p. 480 Istanbul; 1999.

[38] Tuzlacı, E. For Healing - herbal folk remedies of Turkey. Alfa Publications, Istanbul; 2006.
[39] Kıran, Ö. Medicinal plants in the flora of Kozan region and their use in folk medicine. Department of Deontology and History of Medicine Çukurova University Institute of Health Sciences, M.Sc., p. 66; 2006.
[40] İzol, E., E. Kaya, and D. Karahan. Investigation of Some Metals in Honey Samples Produced in Different Regions of Bingöl Province by ICP-MS. Mellifera. 2021; 21, no. 1: 1–17.
[41] Osw, P.S., and F.H.S. Hussain. EAJSE Inductively Coupled Plasma-Optical Emission Spectrometric Determination of Some Elements from Anchusa Azurea Mill . Collected in Iraqi Kurdistan Region. 2020; 6, no. 2: 21–30.
[42] Dissanayake, C. B., and R. Chandrajith. "Sri Lanka-Madagascar Gondwana Linkage: Evidence for a Pan-African Mineral Belt." Journal of Geology. 1999;107 (2): 223–235.
[43] Cherian, M.G., and M. Nordberg. Cellular Adaptation in Metal Toxicology and Metallothionein. Toxicology. 1983; 28, no. 1–2 (September 1): 1–15. Elsevier: 1–15. doi:10.1016/0300-483X(83)90101-4.
[44] Evangelou, Angelos M. "Vanadium in Cancer Treatment." Critical Reviews in Oncology/Hematology. 2002;42 (3): 249–265. doi:10.1016/S1040-8428(01)00221-9.
[45] Potortì, A.G., V. Lo Turco, and G. Di Bella. Chemometric Analysis of Elements Content in Algerian Spices and Aromatic Herbs. 2021; LWT 138 (March): 110643. doi:10.1016/j.lwt.2020.110643.
[46] WHO. World Health Organization guidelines for assessing quality of herbal medicines with reference to contaminants and residues. Department of Technical Cooperation for Essential Drugs and Traditional Medicine. Geneva: World Health Organization; 2007.
[47] Pereira, João B., and Kelly G.F. Dantas. "Evaluation of Inorganic Elements in Cat's Claw Teas Using ICP OES and GF AAS." Food Chemistry. 2016; 196 (April). Elsevier Ltd: 331–337. doi:10.1016/j.foodchem.2015.09.057.
[48] Ebdon L., L. Pitts, R. Cornelis, H.Crews, OFX. Donard. Trace Element Speciation for Environment, Food and Health, Royal Society of Chemistry. 2001; p: 300.
[49] Vitali, D., I. Vedrina Dragojević, and B. Šebečić. "Bioaccessibility of Ca, Mg, Mn and Cu from Whole Grain Tea-Biscuits: Impact of Proteins, Phytic Acid and Polyphenols." Food Chemistry. 2008;110 (1). Food Chem: 62–68. doi:10.1016/j.foodchem.2008.01.056.
[50] Brun, L. A., J. Maillet, P. Hinsinger, and M. Pépin. "Evaluation of Copper Availability to Plants in Copper-Contaminated Vineyard Soils." Environmental Pollution. 2001; 111 (2). Elsevier Ltd: 293–302. doi:10.1016/S0269-7491(00)00067-1.
[51] Akguc, N., I. I. Ozyigit, U. Yasar, Z. Leblebici, and C. Yarci. "Use of Pyracantha Coccinea Roem. as a Possible Biomonitor for the Selected Heavy Metals." International Journal of Environmental Science and Technology. 2010; 7 (3): 427–434. doi:10.1007/BF03326152.
[52] Taha, K. K., Mona I. Shmou, Maisoon H. Osman, and M. H. Shayoub. "Soil-Plant Transfer and Accumulation Factors for Trace Elements at the Blue and White Niles." 2013.
[53] Matos-Reyes, M. N., M. L. Cervera, R. C. Campos, and M. de la Guardia. "Total Content of As, Sb, Se, Te and Bi in Spanish Vegetables, Cereals and Pulses and Estimation of the Contribution of These Foods to the Mediterranean Daily Intake of Trace Elements." Food Chemistry. 2010; 122 (1). Elsevier Ltd: 188–194. doi:10.1016/j.foodchem.2010.02.052.
[54] Varhan Oral, E., Ö. Tokul-Ölmez, İ. Yener, M. Firat, Z. Tunay, P. Terzioğlu, et al. Trace Elemental Analysis of Allium Species by Inductively Coupled Plasma-Mass Spectrometry (ICP-MS) wit0h Multivariate Chemometrics. Analytical Letters. 2019; 52, no. 2: 320–336. doi:10.1080/00032719.2018.1460376.
[55] Choudhury, R Paul, and A N Garg. "Variation in Essential, Trace and Toxic Elemental Contents in Murraya Koenigii-A Spice and Medicinal Herb from Different Indian States."; 2021. Accessed May 15. doi:10.1016/j.foodchem.2007.02.013.
[56] Saglam, C. Heavy Metal Accumulation in the Edible Parts of Some Cultivated Plants and Media Samples from a Volcanic Region in Southern Turkey. Ekoloji; 2013. 22(86): 1-8.
[57] Dubale, A.A., B.S. Chandravanshi, and K.F. Gebremariam. Levels of Major and Trace Metals in the Leaves and Infusions of Croton Macrostachyus. Bulletin of the Chemical Society of Ethiopia. 2015; 29, no. 1 (January 18): 11–26. doi:10.4314/bcse.v29i1.2.
[58] Soydemir, E. Determination of Mercury in 2.5 PM Air Particles by Solid Sampling High Resolution Electrothermal Atomic Absorption Spectrophotometer. Istanbul Technical University Institute of Science and Technology, Master Thesis, 5-7. 2013.
[59] Caglarirmak N., AZ. Hepcimen. Effect of Heavy Metal Soil Pollution on Food Chain and Human Health. Review Paper, Academic Food. 2010; 8 (2): 31-35.
[60] WHO (World Health Organization). Depleted Uranium: Sources, Exposure and Health Effects—Executive Summary; 2001.
[61] Terzioğlu, P., S. Yücel, and M. Öztürk. Application of Box-Behnken Design for Modeling of Lead Adsorption onto Unmodified and NaCl-Modified Zeolite NaA Obtained from Biosilica. Water Science and Technology. 2017; 75, no. 2 (January 1): 358–365. doi:10.2166/wst.2016.526.
[62] Kumar Sharma, R., M. Agrawal, and F. Marshall. Heavy Metal Contamination of Soil and Vegetables in Suburban Areas of Varanasi, India. Ecotoxicology and Environmental Safety. 2007;66, no. 2 (February): 258–266. doi:10.1016/j.ecoenv.2005.11.007.

[63] Ražić, S., A. Onjia, and B. Potkonjak. Trace Elements Analysis of Echinacea Purpurea - Herbal Medicinal. Journal of Pharmaceutical and Biomedical Analysis. 2003;33, no. 4 (November 24): 845–850.doi:10.1016/S0731-7085(03)00338-8.

[64] Chauhan, R.P., and A. Kumar. Soil to Plant Transfer of Alpha Activity in Potato Plants: Impact of Phosphate Fertilizers. Journal of Environmental Health Science and Engineering. 2015;13, no. 1 (December 16): 45 doi:10.1186/s40201-015-0200-4

[65] Gulsoy, E., Tarhan, A., Izol, E., Cokran, B. D., Simsek, M. A research on the chemical, mineral and fatty acid compositions of two almond cultivars grown as organic and conventional in southeastern Turkey. Grasas y Aceites, 2022; 73(3), e477-e477.

[66] Bengü, A. Ş., Üstek, M. A., İzol, E. Determination of Mineral Contents of Rock Salts Provıded by the Market by ICP-MS Technique. Bingol University Health Journal, 2020; 1(2): 42-52

Araştırma Makalesi https://doi.org/10.46810/tdfd.1225384 Research Article

BİNGÖL ÜNİVERSİTESİ

Türk Doğa ve Fen Dergisi
Turkish Journal of Nature and Science
www.dergipark.gov.tr/tdfd

# Effects of Nutrient Media Including Heavy Metals at Different Concentrations in *In Vitro* Conditions on the Growth of Squash (*Cucurbita pepo* L.)

**Zeki MANCAK[1], Gökhan BAKTEMUR[2*]**

[1]Sivas Bilim ve Teknoloji Üniversitesi Lisansüstü Eğitim Enstitüsü, Tarım Bilimleri Anabilim Dalı, Sivas, Türkiye
[2]Sivas Bilim ve Teknoloji Üniversitesi Tarım Bilimleri ve Teknoloji Fakültesi, Bitkisel Üretim ve Teknolojileri Bölümü, Sivas, Türkiye
Zeki MANCAK ORCID No: 0000-0001-9017-7085
Gökhan BAKTEMUR ORCID No: 0000-0002-0362-5108

**Corresponding author: gbaktemur@gmail.com*

(Received: 28.12.2022, Accepted: 07.02.2023, Online Publication: 27.03.2023)

**Keywords**
Heavy metals, *Cucurbita pepo* L., Plant tissue culture, Seed

**Abstract:** Squash (*Cucurbita pepo* L.) is a vegetable species that is appreciated and consumed in the Türkiye world and in the world. Its cultivation is carried out both in the open field and greenhouse. Heavy metals create adverse conditions for all living things due to their toxic effects. In this study, key heavy metals like aluminum (Al), cadmium (Cd), cobalt (Co), lead (Pb) and nickel (Ni) were added to the nutrient medium (Murashige and Skoog-MS)at different concentrations (0, 100, 200, 300, 400 and 500 µM). Squash seeds were germinated under *in vitro* conditions. During the research, the number of leaves and roots, stem and root lengths were determined. According to the results, the number of leaves was the highest in the control group for all heavy metals. The number of roots decreased as the heavy metal concentration increased. While stem length reached the highest number in all heavy metals in the control group, root lengths had the lowest levels at 400 and 500 µM doses. Considering these results, it has been revealed that as the dose of heavy metals increases, the growth of the plant is retarded.



# *In Vitro* Koşullarda Değişik Konsantrasyonlarda Ağır Metaller İçeren Besin Ortamlarının Kabak (*Cucurbita pepo* L.) Bitkisi Gelişimi Üzerine Etkileri

**Anahtar Kelimeler**
Ağır metal, *Cucurbita pepo* L., Bitki doku kültürü, Tohum

**Öz:** Kabak (*Cucurbita pepo* L.), dünyada ve ülkemizde sevilerek tüketilen bir sebzedir. Yetiştiriciliği, hem açıkta hem de örtüaltında yapılmaktadır. Ağır metaller, toksik etki yayması sebebiyle tüm canlılar için olumsuz durumlar oluşturmaktadırlar. Bu çalışmada, *in vitro* koşullar altında değişik konsantrasyonlarda (0, 100, 200, 300, 400 ve 500 µM) hazırlanmış alüminyum (Al), kadmiyum (Cd), kobalt (Co), kurşun (Pb) ve nikel (Ni) ağır metalleri Murashige ve Skoog (MS) besin ortamına eklenerek kabak tohumları kültüre alınmıştır. Araştırmada yaprak ve kök sayısı, gövde ve kök uzunlukları tespit edilmiştir. Yaprak sayısı tüm ağır metaller için kontrol grubunda en fazla olurken, ağır metal konsantrasyonu arttıkça kök sayıları azalmaya başlamıştır. Gövde uzunluğu ağır metallerin tamamında kontrol grubunda en fazla sayıya ulaşırken, kök uzunlukları 400 ve 500 µM dozlarında en düşük seviyeleri görmüştür. Bu sonuçlar dikkate alındığında, ağır metal dozu arttıkça bitki gelişiminin gerilediği ortaya çıkmıştır.

## 1. INTRODUCTION

Squash (*Cucurbita pepo* spp.) is one of the first cultivated plant species and are native to North and South America [1]. It has been proven as a result of archaeological studies that squash, which can adapt to many ecologies, has been cultivated in Mexico, North America and East Asia since ancient times [2]. Squash is a vegetable species belonging to the Cucurbitaceae family, which consists of about 130 species cultivated almost all over the world. All anatomical parts of the plant are edible, but the seeds and pulp are particularly important for food processing and nutrition [3,4,5]. It has low protein, fat and carbohydrate content. In addition, squash with orange flesh contains

high levels of carotenoids, especially beta-carotene and lutein [6,7,8,5]. The world squash production amount is 27.962.742 tons, and squash production in Türkiye is 771.651 tons per year [9]. Common squash areas in Türkiye are Mediterranean (459.270 tons), West Anatolia (74.766 tons), East Marmara (72.348 tons) and Aegean (60.254 tons) regions, respectively [10]. Heavy metals have a very high toxic content and pose a threat to humans and the environment. Heavy metals significantly affect plant growth and development [11,12]. High heavy metal concentrations in the environment can be harmful to various living species Onundi et al. [13], Heavy metals are in the class of substances that pollute the environment due to their toxic effects on plants, animals and humans. Heavy metal contamination of soil is caused by natural as well as anthropogenic activities. Anthropogenic activities, such as mining, smelting, and agriculture, raise the levels of heavy metals such as Cd, Co, Cr, Pb, As and Ni in the soil to locally dangerous levels. Heavy metals are persistent in nature, so they accumulate in the soil and plants. Heavy metals interfere with the physiological activities of plants. High amounts cause reductions in photosynthesis, gas exchange, plant growth, dry matter accumulation and yield. Heavy metals also interfere with antioxidant levels in plants and reduce their nutritional value [14]. However, most heavy metals such as cadmium, silver and mercury are toxic to plants. With the rapid development of industry and manufacturing, large amounts of heavy metal ores are processed, which gradually causes serious environmental pollution. Heavy metals in the soil are absorbed by plant roots and accumulate in plant tissues, seriously delaying many physiological and molecular processes [15,16,12]. Plant tissue culture, which is one of the vegetative propagation methods; It is called the creation of new plants or plants from plant particles in sterile conditions. Plant tissue culture aims to protect species that are in danger of extinction, to obtain disease and virus-free materials, to reproduce difficult-to-produce species, to be able to produce twelve months of the year without being tied to any season, and to produce a large number of plants in a short time. The aim of this study is to determine the effects of key heavy metals like aluminum, cadmium, cobalt, lead and nickel prepared in different concentrations (0, 100, 200, 300, 400 and 500 µM) under *in vitro* conditions on plant growth in squash seeds.

## 2. MATERIAL AND METHOD

The experiment was carried out in the plant tissue culture laboratory of Sivas University of Science and Technology, Faculty of Agricultural Sciences and Technology in 2022. Seeds of MRS 9029 variety (Manier Seed Company, Türkiye) were used in the experiment.

### 2.1. Nutrient Media Preparation

MS [17] nutrient medium was used in the study. Within the scope of the experiment, nutrient media were prepared by adding different concentrations of aluminum, cadmium, cobalt, lead and nickel heavy metals (0, 100, 200, 300, 400 and 500 µM). A heavy metal-free MS nutrient medium was also used as a control group (Table 1). The pH of the nutrient medium was adjusted to be 5.8, and it was sterilized by autoclave for 15 minutes at a temperature of 121 °C and a pressure of 1.2 atmospheres.



**Table 1.** Nomenclature of heavy metals

| Concentrations | Heavy Metals | | | | |
|---|---|---|---|---|---|
| | **Aluminyum** | **Cadmium** | **Cobalt** | **Lead** | **Nicel** |
| **Control** | Al-K | Cd-K | Co-K | Pb-K | Ni-K |
| **100 µM** | Al-1 | Cd-1 | Co-1 | Pb-1 | Ni-1 |
| **200 µM** | Al-2 | Cd-2 | Co-2 | Pb-2 | Ni-2 |
| **300 µM** | Al-3 | Cd-3 | Co-3 | Pb-3 | Ni-3 |
| **400 µM** | Al-4 | Cd-4 | Co-4 | Pb-4 | Ni-4 |
| **500 µM** | Al-5 | Cd-5 | Co-5 | Pb-5 | Ni-5 |

### 2.2. Sterilization of Seeds

The squash seeds used in the study were kept in a 20% sodium hypochlorite solution for 20 minutes, then washed 4-5 times with autoclaved distilled water to ensure sterilization of the materials. Seeds were planted into sterile petri dishes in a sterile bench as 5 seeds in each petri dish (100 seeds in each application). After sowing, the petri dishes were cultured in the growth chamber at 25 ± 2°C with 16 hours of light and 8 hours of darkness photoperiod condition.

### 2.3. Measurements Performed During the Study

***Number of Leaves:*** It was determined by counting the number of leaves formed on each plant.
***Number of Roots:*** It was determined by counting the number of roots formed in each plant.
***Stem Length:*** With the formation of shoots in each plant, it was measured as mm with the help of a caliper.
***Root Length:*** With the formation of roots in each plant, it was measured as mm with the help of a caliper.
Measurements were carried out for 1 month with the germination of the seeds.

### 2.4. Experimental Design and Statistical Analysis

The experiment was carried out according to the randomized plot design, with 4 replications and 5 petri dishes in each replication. Statistical analyzes were performed using the JMP 8.0.1 program.

## 3. RESULTS AND DISCUSSION

### 3.1. Effect of Aluminum on Squash Plant Growth

The effect of different doses of aluminum on the growth parameters of the squash plant was found to be statistically significant (Table 2). It was determined that the highest values in terms of root length, stem length, root number and leaf number were in the control

medium (79.88 mm, 63.98 mm, 14.71, 5.00, respectively). This was followed by the AI-1 medium. It was found that the plants grown in Al-1 medium had a root length of 49.29 mm, a stem length of 46.93 mm, 11.57 roots and 4.57 leaves. The lowest values for all parameters were obtained from Al-4 and Al-5 media.

Kara et al. [18], reported that the pepper plant did not grow in the nutrient medium including 500 µM aluminum and the plants died. Baran et al. [19], reported that aluminum did not have a significant effect on shoot growth in cucumber plants. [20] found that the effect of aluminum on the number of leaves in white cabbage was not significant. They stated that up to 300 µM doses had positive effects on root length, root number and shoot length. Sevim et al. [21], in their study on plant growth in sorghum plant, the heavy metals they prepared at different concentrations *in vitro* conditions determined the highest plant height in aluminum heavy metal in the control group (11.06 cm).

**Table 2.** Effect of aluminum on root length (mm), stem length (mm), root number (number) and number of leaves (number) in squash plant

| Heavy Metals | Root Length (mm) | Stem Length (mm) | Number of Roots (number) | Number of Leaves (number) |
|---|---|---|---|---|
| **Al-K** | 79.88 a | 63.98 a | 14.71 a | 5.00 a |
| **Al-1** | 49.29 b | 43.93 b | 11.57 b | 4.57 a |
| **Al-2** | 40.00 c | 34.85 c | 8.86 c | 3.50 c |
| **Al-3** | 34.38 d | 31.81 c | 6.86 d | 3.57 b |
| **Al-4** | 31.71 d | 21.60 d | 4.29 e | 2.57 c |
| **Al-5** | 19.35 e | 16.46 d | 2.50 f | 2.67 c |
| **LSD** | 5.48*** | 7.91*** | 1.51*** | 0.63*** |

LSD: least significant difference; *P < 0.05; **P ≤ 0.01; ***P ≤ 0.001

### 3.2. Effect of Cadmium on Squash Plant Growth

Cadmium (Cd) causes phytotoxic effects at high concentrations Pereira et al. [22], When it reaches high levels in the soils, it is easily assimilated by plants [23]. In addition to affecting photosynthesis, transpiration, root growth, dry weight, shoot length and nutrient accumulation, this element has an inhibitory or toxic effect on the metabolic activity of living systems [24,25] Acila et al. [26], reported that heavy metals (Cd, Cu) had a phytotoxic effect on the growth of squash seedlings and affected the elongation of young squash seedlings. The effects of different concentrations of cadmium on stem length, leaf number, stem length and root number in squash are given in Table 3. All of the parameters examined for the effect of cadmium were found to be statistically significant. When the effect on root length was examined, differences were found between applications.

Although the differences among Cd-K, Cd-1, Cd-2 and Cd-3 were not statistically significant, the longest-rooted plants were obtained with an average of 62.89 mm in Cd-K medium. It was observed that root length decreased significantly in Cd-4 and Cd-5 media. Deng et al. [27], investigated the effects of heavy metals; copper, mercury and cadmium under 20 and 40 °C temperatures in their study to determine the effects on the germination status of corn seeds. They determined that increasing concentrations of heavy metals and heat stress cause water accumulation in seeds and promote germination. Nouri et al. [28], found that increasing cadmium concentrations suppressed the root growth of *H. vulgare* and *H. distichum*. Baran et al. [19], found that cadmium had a negative effect on the root length of the cucumber plant and the highest values were obtained from the control medium. Kara et al. [18], reported that different doses of cadmium affected the root length of pepper plants negatively.

When the effects of cadmium on stem length were examined, it was determined that there were differences between the media. Plants with the longest stems were formed with a media of 51.64 mm and 46.83 mm, respectively in the Cd-K and Cd-3 media, and these two media were statistically in the same group. This was followed by Cd-1 (42.64 mm), Cd-5 (37.24 mm) and Cd-2 (57.56 mm) media, respectively. The shortest stem plants were obtained from Cd-4 medium with an average of 26.80 mm. Kara et al. [18], reported that cadmium had a significant negative effect on stem length in pepper plants. [20] found that cadmium reduced shoot length in white cabbage plants. In their study, the shoot length was found to be 29.60 mm in control medium, while it ranged from 22.56 to 12.18 mm in media containing different doses of cadmium. Baran et al. [19], reported that the effect of cadmium on the shoot length of the cucumber plant was statistically significant, but did not reduce the shoot length at high rates and the length varied between 5.08 and 4.03 cm. When the effect of cadmium on root development was examined, it was noted that the number of roots decreased with an increase in the cadmium dose. It was determined that the medium with the highest number of roots was Cd-K (10.78). It was observed that the plants with the lowest number of roots among the media used were in Cd-4 (4.22) medium. [20] found that cadmium had a reducing effect on the number of roots in the white cabbage plants.

When the effect of cadmium on leaf formation in squash plants was examined, it was determined that although the differences between the media were statistically significant, there was no significant difference in practice. The number of leaves varied between 2.00 and 3.33 on average. Kara et al. [29], reported that the effect of cadmium on the number of leaves in melon plants was not significant.

**Table 3.** Effect of cadmium on root length (mm), stem length (mm), root number (number) and leaf number (number) in squash plant

| Heavy Metals | Root Length (mm) | Stem Length (mm) | Number of Roots (number) | Number of Leaves (number) |
|---|---|---|---|---|
| **Cd-K** | 62.89 a | 51.64 a | 10.78 a | 3.33 a |
| **Cd-1** | 55.52 a | 42.64 ab | 7.89 b | 3.22 ab |
| **Cd-2** | 57.56 a | 35.17 bc | 6.00 c | 2.78 ab |
| **Cd-3** | 53.63 a | 46.83 a | 5.56 cd | 2.56 bc |
| **Cd-4** | 35.33 b | 26.80 c | 4.22 d | 2.00 c |
| **Cd-5** | 38.08 b | 37.24 b | 4.56 cd | 3.00 ab |
| **LSD** | 12.01*** | 9.48*** | 1.67*** | 0.69** |

LSD: least significant difference; *P < 0.05; **P ≤ 0.01; ***P ≤ 0.001

### 3.3. Effect of Cobalt on Squash Plant Growth

The effect of five different doses of cobalt on the growth parameters of squash plants is given in Table 4. According to Table 4, the effect of the applications on plant growth was found to be statistically significant. It is evident that the effect of cobalt on root length is quite significant. While the average root length was 116.84 mm in Co-K medium, significant reductions in root length occurred in the other media containing heavy metals. It was determined that the plants with the lowest root length were found in Co-4 (38.11 mm) and Co-5 (20.74 mm) media. It was observed that the increase in the dose of cobalt adversely affected the root length. Kara et al. [18], reported that the effect of cobalt on root length in pepper plants was significant and that a dose of 200 µM cobalt increased the root length.

When the effect of cobalt on stem length in squash was examined, it was determined that the plants with the longest stems were in Co-K (52.18 mm) and Co-2 (49.28 mm) media. These two media were followed by Co-3 with 41.18 mm and Co-1 with 39.93 mm, respectively. The shortest plant stems were obtained from Co-4 (21.37 mm) and Co-5 (18.23 mm) media. It was determined that 400 and 500 µM doses of cobalt had a reducing effect on the elongation of the stem Li et al. [30]. reported that cobalt concentrations limited the shoot growth of barley (*Hordeum vulgare* L.), oilseed rapeseed (*Brassica napus* L.) and tomato (*Lycopersicon esculentum* L.) plants with its increase. Baran et al. [19], reported that 500 µM dose of cobalt slowed down shoot growth in cucumber plants.

When the changes in the number of roots of squah plants in six media with or without cobalt at different doses were examined, the differences between the media were found to be statistically significant. While the medium with the highest number of roots was Co-K (14.22), the lowest number of roots was obtained from Co-4 (3.38) and Co-5 (3.00). Kara et al. [29], determined that the lowest number of roots in the melon plant was in Co-4 and Co-5 media.

When the effect of cobalt on the number of leaves was examined, the highest number of leaves was obtained from Co-K (4.33) medium, followed by Co-1 (2.11) and Co-3 (2.22) media. The least number of leaves was obtained from Co-4 and Co-5 media (2.00). Kara et al. [18], reported that the effect of cobalt on the number of leaves in the pepper plant was significant and that the dose of 200 µM cobalt had a positive effect on leaf formation. [20] found that cobalt did not affect the number of leaves in white cabbage plants up to a 200 µM dose.



**Table 4.** Effect of cobalt on root length (mm), stem length (mm), root number (number) and leaf number (number) in squash plant

| Heavy Metals | Root Length (mm) | Stem Length (mm) | Number of Roots (number) | Number of Leaves (number) |
|---|---|---|---|---|
| **Co-K** | 116.84 a | 52.18 a | 14.22 a | 4.33 a |
| **Co-1** | 57.36 c | 39.93 b | 5.89 c | 2.11 c |
| **Co-2** | 77.11 b | 49.28 a | 8.44 b | 2.67 b |
| **Co-3** | 49.86 c | 41.18 b | 5.78 c | 2.22 c |
| **Co-4** | 38.11 d | 21.37 c | 3.38 d | 2.00 c |
| **Co-5** | 20.74 e | 18.23 c | 3.00 d | 2.00 c |
| **LSD** | 10.21*** | 6.59*** | 1.76*** | 0.44*** |

LSD: least significant difference; *P < 0.05; **P ≤ 0.01; ***P ≤ 0.001

### 3.4. Effect of Lead on Squash Plant Growth

It has been determined that the effects of different doses of lead on the development of squash plants are important (Table 5). The plants with the highest root length (77.16 mm), stem length (49.44 mm), root number (16.57) and leaf number (6.00) were obtained from Pb-K medium. This was followed by the Pb-1 medium (root length 47.09 mm, stem length 39.30 mm, root number 10.86 and leaf number 4.57). The lowest values for all parameters were obtained from Pb-4 and Pb-5 media.

Pb, one of the main inorganic pollutants in our environment, causes toxic symptoms such as chlorosis and subcellular toxicity with its effects on plant respiration, mitosis, water use and nutrient intake [31,32]. [33] found that the root length of rice plants decreased with the increase of lead concentration in their study. Ayhan et al. [34], determined that root length decreased as a result of increasing lead concentration in some maize cultivars. [35] planted squash seeds under *in vitro* conditions with different doses of lead heavy metals and reported that the germination rate of the seeds decreased at 400 and 800 mg $L^{-1}$ doses. Baran et al. [19], determined that different doses of lead did not affect the root length of the cucumber plant. Kara et al.

[18], reported that lead had different effects on the development of pepper plants and determined that the highest number of leaves and root length were in Pb-3 medium. [36] reported that the plants with the longest shoots, the highest number of roots and the highest number of leaves were obtained from the heavy metal-free control media (Pb-K) in the arugula plant. Kara et al. [29], determined that the effect of lead on root length and shoot length was not statistically significant in melon plants.

**Table 5.** Effect of lead on root length (mm), stem length (mm), root number (number) and number of leaves (number) in squash plant

| Heavy Metals | Root Length (mm) | Stem Length (mm) | Number of Roots (number) | Number of Leaves (number) |
|---|---|---|---|---|
| **Pb-K** | 77.16 a | 49.44 a | 16.57 a | 6.00 a |
| **Pb-1** | 47.09 b | 39.30 b | 10.86 b | 4.57 b |
| **Pb-2** | 49.36 b | 35.54 b | 9.00 c | 3.14 c |
| **Pb-3** | 32.03 c | 29.35 c | 5.67 d | 4.00 b |
| **Pb-4** | 26.53 c | 21.41 d | 5.33 d | 2.00 d |
| **Pb-5** | 18.49 d | 16.88 e | 2.67 e | 2.00 d |
| **LSD** | 6.40*** | 4.06*** | 1.03*** | 0.59*** |

LSD: least significant difference; *P < 0.05; **P ≤ 0.01; ***P ≤ 0.001

### 3.5. Effect of Nickel on Squash Plant Growth

The effects of five different doses of nickel on squash plants are given in Table 6. According to the table, the effects of nickel on root and stem length as well as leaf and root number were found to be statistically significant. The highest and the lowest root length was obtained from Ni-K (87.69 mm) and Ni-4 (16.81 mm) media, respectively. It is evident that as the nickel dose increased, the root length decreased significantly. Nickel at doses of 200 µM and above decreased the root length of the squash plant. Peralta et al. [37], determined that low doses of nickel promote germination in oats, but its development slows down as a result of increasing concentrations. [38] reported that increasing doses of nickel adversely affected germination in sunflowers. [39] determined the effects of nickel on germination and early seedling growth parameters in spinach and found that nickel had a toxic effect at higher doses during the germination stage compared to the seedling stage. Kara et al. [18], reported that 100 and 200 µM doses of nickel promoted root length in pepper plants.

When the effect of nickel on the stem length was observed, the best results were obtained in Ni-K (49.64 mm) medium. Increasing doses of nickel had an inhibitory effect on shoot length as well as root length. It was determined that the stem length was the lowest in the Ni-5 (10.80 mm) medium. Kara et al. [18], reported that the shoot length of the pepper plant was the lowest in the Ni-5 medium. Kara and Baktemur [20], obtained the highest shoot length of white cabbage plants from the control medium.

The effect of nickel on the root number was found to be statistically significant. The highest number of roots was obtained from Ni-K (13.78) medium. This was followed by Ni-1 (11.38) medium. The other media were statistically included in the same group, and there were significant decreases in root numbers compared to the control medium.

The highest number of leaves was determined in Ni-K (4.29) medium. This was followed by Ni-2 (3.50) medium. The difference between other media was not found to be statistically significant. Kara et al. [18], determined that 100 and 200 µM doses of nickel had an effect on increasing the number of leaves in the pepper plant. Kara and Baktemur [20] reported that the effect of nickel on the number of leaves in white cabbage plants was not statistically significant.



**Table 6.** Effect of nickel on root length (mm), stem length (mm), root number (number) and number of leaves (number) in squash plant

| Heavy Metals | Root Length (mm) | Stem Length (mm) | Number of Roots (number) | Number of Leaves (number) |
|---|---|---|---|---|
| **Ni-K** | 87.69 a | 49.64 a | 13.78 a | 4.29 a |
| **Ni-1** | 80.53 b | 39.55 b | 11.38 b | 2.11 c |
| **Ni-2** | 21.02 cd | 18.61 d | 3.00 c | 3.50 b |
| **Ni-3** | 27.32 c | 23.35 c | 3.56 c | 2. 00 c |
| **Ni-4** | 16.81 d | 17.03 d | 2.56 c | 2. 00 c |
| **Ni-5** | 18.29 d | 10.80 e | 2.33 c | 2. 00 c |
| **LSD** | 7.12*** | 4.22*** | 1.33*** | 0.34*** |

LSD: least significant difference; *P < 0.05; **P ≤ 0.01; ***P ≤ 0.001

## 4. CONCLUSION AND RECOMMENDATIONS

In this study, the effects of heavy metals at different concentrations on the development of squash plants under *in vitro* conditions were investigated. Heavy metals, which have very negative effects on nature, also seriously slow down plant growth. In this context, considering the research results, it was observed that the growth of plants decreased as the heavy metal concentration increased. In the study, a total of 25 different nutrient media were used by adding five different heavy metals and their five different concentrations to the MS nutrient medium. In addition, no heavy metal was applied to five of the nutrient media used as control group for each studied heavy metal. Furthermore, the effects of heavy metals in plants were examined and it was found that the lowest number of

leaves, root number, stem length and root length in the media with aluminum were determined in Al-5 medium. When plant growth was examined in media prepared with cadmium, the lowest levels were determined in Cd-4 medium. Similarly, the lowest levels were found in the Co-5 medium for cobalt. Considering the nutrient media prepared with heavy metals (lead and nickel), it was determined that the growth slowed down as the plant growth increased to 400 and 500 µM doses.

## REFERENCES


[1] Heiser CB. Seed to civilization: The story of man's food. W. H. Freeman and Company, San Francisco 1973;243 p.

[2] Robinson RW, Decker-Walters DS. Cucurbits In Crop Production Science In Horticultures Series. CAB international Depertmant of Horticultural Science. Cornell University and D.S. Decker-Walters. 1997;The Cucurbit Network.U.S.A.

[3] Yadav M, Jain S, Tomar R, Prasad GB, Yadav H. Medicinal and biological potential of pumpkin: An updated review. Nutr. Res. Rev. 2010;23,184–190.

[4] Kwiri R, Winini C, Musengi A, Mudyiwa M, Nyambi C, Muredzi P, Malunga A. Proximate composition of pumpkin gourd (*Cucurbita pepo*) seeds from Zimbabwe. Int. J. Food Sci. Nutr. 2014;3,279–283.

[5] Kulczyński B, Gramza-Michałowska A. The profile of secondary metabolites and other bioactive compounds in Cucurbita pepo L. and Cucurbita moschata pumpkin cultivars. *Molecules*, 2019;24(16),2945.

[6] Azevedo-Meleiro CH, Rodriguez-Amaya DB. Qualitative and Quantitative di_erences in carotenoid composition among *Cucurbita moschata*, *Cucurbita maxi*ma, and *Cucurbita pepo*. J. Agric. Food Chem. 2007;55,4027–4033.

[7] Kulaitiene J, Jariene E, Danilcenko H, Cerniauskiene J, Wawrzyniak A, Hamulka J, Jukneviciene E. Chemical composition of pumpkin (Cucurbita maximaD.) flesh flours used for food. J. Food Agric. Environ. 2014;12,61–64.

[8] Seleim MAA, Ali HM, Hassan MAM. Comparative study of the beta-carotene, alpha-Tocopherol and pectin calues from three cultivars of pumpkin (*Cucurbita maxima*). World J. Dairy Food. Sci. 2015;10,132–140.

[9] FAO, 2020. Food and Agriculture Organization of the United Nations. FAOSTAT. http://faostat.fao.org/ (Accessed: 20.12.2022)

[10] TÜİK, 2021. Turkish Statistical Institute. http://www.tuik.gov.tr (Accessed: 20.12.2022)

[11] Nagajyoti PC, Lee KD, Sreekanth TVM. Heavy metals, occurrence and toxicity for plants: a review. Environ Chem Lett. 2010;8(3):199–216. DOI:10.1007/s10311-010-0297-8.

[12] Zhu T, Li L, Duan Q, Liu X, & Chen M. Progress in our understanding of plant responses to the stress of heavy metal cadmium. *Plant Signaling & Behavior*, 2021;16(1),1836884.

[13] Onundi YB, Mamun AA, Al Khatib MF, Ahmed YM. Adsorption of copper, nickel and lead ions from synthetic semiconductor industrial wastewater by palm shell activated carbon. Int. J. Environ. Sci. Tech. 2010;7(4):751-758.

[14] Sharma RK, Agrawal M. Biological effects of heavy metals: an overview. *Journal of Environmental Biology*, 2005;26(2),301-313.

[15] Broadley MR, White PJ, Hammond JP, Zelko I, Lux A. Zinc in plants: tansley review. New Phytologist. 2007;173:677–702.

[16] Zhang S, Song J. Geochemical cadmium anomaly and bioaccumulation of cadmium and lead by rapeseed (*Brassica napus* L.) from noncalcareous soils in the Guizhou Plateau. Sci Total Environ. 2018;644(10):624–634. DOI:10.1016/j.scitotenv.2018.06.230

[17] Murashige T, & Skoog F. A revised medium for rapid growth and bio assays with tobacco tissue cultures. Physiologia plantarum, 1962;15(3), 473-497.

[18] Kara E, Sarıkaya MF, Çilesiz Y, Akkaş F, Karaköy T. & Baktemur, G. Determination of the Effects of Heavy Metals Applied at Different Doses *In vitro* Conditions on the Development of Pepper (*Capsicum annuum*) Plant. Turkish Journal of Agricultural and Natural Sciences. 2022a;9 (4), 957-967. DOI: 10.30910/turkjans.1141400

[19] Baran O, Kara E, Karaköy T, Baktemur G. Determination of the Effects of Some Heavy Metals Applied *in vitro* Conditions on the Development of Cucumber (*Cucumis Sativus* L.). 8 th International Mardin Artuklu Scientific Researches Conference. 2022;June 4-6, 1296-1314/ Mardin, Turkey.

[20] Kara E, Baktemur G. Determining the Effects of Some Heavy Metal Applications on White Cabbage (*Brassica Oleracea* var. *Capitata F. Alba*) in *In vitro* Condıtıons. Ege 6th International Conference on Applied Sciences. September 2022;10-11, 2022/ İzmir pp.,254-262.

[21] Sevim A, Yüce İ, Bekiş P, Çilesiz Y, Karaköy T. Determination of the effects of some heavy metals applied *in vitro* conditions on the development of sorghum (*Sorghum bicolor* L.) 8th International Mardin Artuklu Scientific Researches Conference 2022;June 4-6, 2022, 1283-1295. Mardin, Turkey

[22] Pereira GJG, Molina SMG, Lea PJ, Azevedo RA. Activity of antioxidant enzymes in response to cadmium in *Crotalaria juncea* Plant Soil, 2002;239 pp.123-132.

[23] Guo Y, Marschner H. Uptake, distribution and binding of cadmium and nickel in different plant species J. Plant Nutr. 1995;18 pp.2691-2706

[24] Boussama N. Ouariti O. Ghorbal MH. Changes in growth and nitrogen assimilation in barley seedlings under cadmium stress J. Plant Nutr. 1999;22.731-752

[25] Khudsar T, Mahmooduzzafar, Iqbal M.. Cadmium-induced changes in leaf epidermis, photosynthetic rate and pigment concentration in Cajanus cajan Biol. Plant. 2001;44pp. 59-64

[26] Acila S, Derouiche S, Allioui N. Embryo growth alteration and oxidative stress responses in germinating *Cucurbita pepo* seeds exposed to

cadmium and copper toxicity. Research Square; 2022;DOI: 10.21203/rs.3.rs-2189796/v1.

[27] Deng B, Yang K, Zhang Y, Li Z. Can heavy metal pollution defend seed germination against heat stress? Effect of heavy metals (Cu(2+), Cd(2+) and Hg(2+)) on maize seed germination under high temperature. Environ Pollut. 2016;Sep;216:46-52. DOI: 10.1016/j.envpol.2016.05.050. Epub 2016 May 26.PMID: 27239687.

[28] Nouri M, El Rasafi T, & Haddioui A. Responses of Two Barley Subspecies to In vitro-Induced Heavy Metal Stress: Seeds Germination, Seedlings Growth and Cytotoxicity Assay. Agriculture/Pol'nohospodárstvo, 2019;65 (3):107−118.

[29] Kara E, Çilesiz Y, Karaköy T, Baktemur G. 'Determination of the Response of Melon (*Cucumis melo*) Plant to Some Heavy Metals *In vitro* Conditions' International Anatolian Congress on Multidiciplinary Scientific Research. 2022b;12-13 August 2022- Mardin/Türkiye. pp., 105-119.

[30] Li HF, Gray C, Mico C, Zhao FJ, and Mc Grath SP. Phytotoxicity and bio availability of cobaltto plantsin arange of soils. Chemosphere. 2009;75, 979 – 986. DOI:10.1016/j. Chemosphere.2008.12.068

[31] Tatar E, Mihucz V, Vaarga A, Faray G, Cseh E. Effect of lead, nickel and vanadium on organic acid transport in xylem sap of cucumber J. Inorg. Biol. 1999;75 pp.219-355

[32] Tabaldi LA, Ruppenthal R, Cargnelutti D, Morsch VM, Pereira LB, Schetinger MRC. Effects of metal elements on acid phosphatase activity in cucumber (*Cucumis sativus* L.) seedlings, Environmental and Experimental Botany. 2007;Volume 59,Issue 1, Pages 43-48,ISSN 0098-8472, DOI:10.1016/j.envexpbot.2005.10.009.

[33] Verma S, Dubey RS. Lead toxicity induces lipid peroxidation and alters the activities of antioxidant enzymes in growing rice plants. Plant Science, 2003;164, 645-655. DOI:10.1016/S0168-9452(03)00022-0

[34] Ayhan B, Ekmekçi Y, Tanyolaç D. Investigatin of the Tolerance to Heavy Metal (Cadmium and Lead ) Stress of some Maize Culivars at Early Seedling Stage. Anadolu University Journal of Science and Technology. 2007;8(2), 411-422.

[35] Akıncı İE, Çalışkan Ü. Effect o f Lead on Seed Germination and Tolerance Levels in Some Summer Vegetables. Ecology. 2010;19(74),164-172.DOI: 10.5053/ekoloji.2010.7420

[36] Baktemur G. Determination of the Effects of Lead (Pb) Heavy Metal Prepared at Different Concentrations under *in Vitro* Conditions on the Growth of Arugula (*Eruca sativa* L.) Plant. ISPEC Journal of Agricultural Sciences 2022;6(4), 828-834.

[37] Peralta JR, Gardea Torresdey JL, Tiemann KJ, Gomez E, Arteaga S, Rascon E, Parsons JG. Uptake and effects of five heavy metals on seed germination and plant growth in alfalfa (*Medicago sativa*) L. Bulletin of Environmental Contamination and Toxicology 2001;66 (6):727-734.

[38] Jadia CD, Fulekar, MH. Phytoremediation: The application of vermicompost to remove zinc, cadmium, copper, nickel and lead by sunflower plant. Environmental Engineering and Management Journal 2008;7(5):547-558.

[39] Akıncı S, Akıncı İE. Effect of Nickel on Germination and Some Seedling Growth Parameters in Spinach (*Spinacia oleracea*). Ecology 2011;20, 79, 69-76.DOI: 10.5053/ekoloji.2011.799

Cilt 12, Sayı 1, Sayfa 37-43, 2023 Volume 12, Issue 1, Page 37-43, 2023

Araştırma Makalesi https://doi.org/10.46810/tdfd.1225756 Research Article

Türk Doğa ve Fen Dergisi
Turkish Journal of Nature and Science
www.dergipark.gov.tr/tdfd

# Classification of Scenes in Aerial Images with Deep Learning Models

**Özkan İNİK**[1*]

[1] Department of Computer Engineering, Tokat Gaziosmanpasa University, Tokat, Türkiye
ORCID No: 0000-0003-4728-8438

**Corresponding author: ozkan.inik@gop.edu.tr*

(Received: 28.12.2022, Accepted: 08.02.2023, Online Publication: 27.03.2023)

**Keywords**
Aerial images classification, Deep learning, CNN pruning, VGG19

**Abstract:** Automatic classification of aerial images has become one of the topics studied in recent years. Especially for the use of drones in different fields such as agricultural applications, smart city applications, surveillance and security applications, it is necessary to automatically classify the images obtained with the camera during autonomous mission execution. For this purpose, researchers have created new data sets and some computer vision methods have been developed to achieve high accuracy. However, in addition to increasing the accuracy of the developed methods, the computational complexity should also be reduced. Because the methods to be used in devices such as drones where energy consumption is important should have low computational complexity. In this study, firstly, five different state-of-the-art deep learning models were used to obtain high accuracy values in the classification of aerial images. Among these models, the VGG19 model achieved the highest accuracy with 94.21%. In the second part of the study, the parameters of this model were analyzed and the model was reconstructed. The number of 143.6 million parameters of the VGG19 model was reduced to 34 million. The accuracy of the model obtained by reducing the number of parameters is 93.56% on the same test data. Thus, despite the 66.5% decrease in the parameter ratio, there was only a 0.7% decrease in the accuracy value. When compared to previous studies, the results show improved performance.



# Havasal Görüntülerdeki Sahnelerin Derin Öğrenme Modelleri ile Sınıflandırılması

**Anahtar Kelimeler**
Havasal görüntü sınıflandırma, Derin Öğrenme, ESA budama, VGG19

**Öz:** Havadan alınan görüntülerin otomatik olarak sınıflandırılması son yıllarda üzerinde yoğun çalışılan konulardan biri haline gelmiştir. Özellikle dronların tarımsal uygulamalar, akıllı şehir uygulamaları, gözetleme ve güvenlik uygulamaları gibi farklı alanlarda kullanımında otonom görev icrası sırasında kamera ile elde edilen görüntülerin otomatik olarak sınıflandırılması gerekmektedir. Bu amaçla araştırmacılar yeni veri setleri oluşturmuş ve yüksek doğruluk elde etmek için bazı bilgisayarlı görü yöntemleri geliştirilmiştir. Ancak geliştirilen yöntemlerin doğruluğunun artırılmasının yanı sıra hesaplama karmaşıklığının da azaltılması gerekmektedir. Çünkü dron gibi enerji tüketiminin önemli olduğu cihazlarda kullanılacak yöntemlerin düşük hesaplama karmaşıklığına sahip olması gerekmektedir. Bu çalışmada, öncelikle hava görüntülerinin sınıflandırılmasında yüksek doğruluk değerleri elde etmek için beş farklı derin öğrenme modeli kullanılmıştır. Bu modeller arasında en yüksek doğruluğu %94.21 ile VGG19 modeli elde etmiştir. Çalışmanın ikinci bölümünde bu modelin parametreleri analiz edilerek model yeniden yapılandırılmıştır. VGG19 modelinin 143.6 milyon olan parametre sayısı 34 milyona düşürülmüştür. Parametre sayısının azaltılmasıyla elde edilen modelin doğruluğu aynı test verileri üzerinde %93.56'dır. Böylece parametre oranındaki %66.5'lik azalmaya karşın doğruluk değerinde sadece %0.7'lik bir azalma olmuştur. Elde edilen sonuçlar önceki çalışmalarla karşılaştırıldığında, daha iyi sonuçların elde edildiği görülmüştür.

## 1. INTRODUCTION

The development of aerial vehicles and remote sensing methods has led to the studies for the autonomous implementation of many new applications. In particular, studies have been carried out on aerial control security systems, agricultural applications, control of smart cities, and the identification of scenes in aerial images in the movie industry. For example, an autonomous tracking

drone is used to shoot any scene on a movie set. In another example, aerial imagery is used to detect an environmental disaster from satellite photos. For this reason, researchers in the literature have initially created benchmark data sets for artificial intelligence-based vision systems to be developed in this field [1-5]. Deep learning-based methods were developed on these datasets [6-12]. Deep learning is a sub-branch of artificial intelligence and first attracted attention with the ImageNet competition in 2012. Deep learning, which was recognized for its high accuracy in this competition, has been used in many studies such as classification [13, 14], detection [15, 16], segmentation [17-20] and prediction [21]. The details of some of the deep learning-based studies used for the classification of scenes in aerial images are given below.

In [6], a deep learning method for aerial image classification using Residual Network v2 (IRV2) with Inception and a multilayer perceptron (MLP) model is proposed. The method includes preprocessing, feature extraction and classification of the images acquired by the UAV. The proposed method uses IRV2 for feature extraction and MLP for classification. The effectiveness of this method, called DLIRV2-MLP, was tested on a comparative aerial imagery dataset and was found to have an accuracy and precision of 90% and above. In [7] a semi-supervised center-based discriminative adversarial learning framework called SCDAL is proposed to address the labeling problem, which is the biggest time consuming issue in supervised classification of aerial images. The SCDAL framework is tested on two large aerial image datasets and shown to be superior to most existing domain adaptation methods with at least a 3% improvement in overall accuracy. Work [8] proposes a prototype-based memory network for recognizing multiple scenes in a single aerial image. The network consists of a prototype learning module, a prototype-hosting external memory, and a multi-head attention-based memory retrieval module. In the study, a puplic dataset is also created and the effectiveness of the proposed method on other datasets is demonstrated in experimental results. In [9] a deep learning system is proposed to classify objects and facilities into 63 different classes from high-resolution, multi-spectral satellite images. The proposed method achieved an overall accuracy of 83%, an F1 score of 0.797, and classified 15 of the classes with 95% or higher accuracy. Study [10] proposes a transfer learning based technique for aerial scene classification using a layer selection strategy called ReLu Based Feature Fusion (RBFF). In RBFF, a pre-trained MobileNetV2 deep learning model is used for feature discovery. The extracted features are dimensionally reduced with dimension reduction algorithms and classification is performed with support vector machine. With the result obtained, it is stated that it outperforms the studies conducted in recent years. In [11] proposed a method that all grains, one scheme (AGOS). The method is a method for extracting discriminative information from multi-granular representations of data proposed. It consists of three components: MGP, which preserves extended convolutional features from the backbone used for feature extraction; MBMIR, which highlights key examples in the multi-granular representation using multiple examples learning; and SSF, which allows the method to learn the same scene diagram from multi-granular instance representations and combine them for optimization. The AGOS method has been tested on three public datasets and has been reported to perform well. In [12], it is stated that objects in birds eye view images are more complex than objects in natural view, and therefore the discriminative features of scenes are difficult. To overcome this problem, a solution was sought by designing a new representation set called instance representation bank (IRB). The performance of the proposed method on three different datasets is very competitive compared to its competitors. Although new methods have been developed for classifying scenes in aerial images, these methods need to have low computational complexity. Because they need to be used on hardware with less energy-consuming processors. Especially deep learning-based methods need high capacity computing resources due to the high number of parameters. In order to overcome this situation, some studies [22-25] should be carried out to reduce the number of parameters of deep learning architectures. In this study firstly, the state of the art deep learning models Googlenet [26], Alexnet [27], Vgg19 [28], resnet-50, and Resnet-101 [29] were used to achieve high accuracy in the classification of scenes in aerial images. Applications were made on the popular Aerial Image data set (AID) [5]. Secondly, the effect of the feature maps in the VGG19 model, which gives the highest accuracy among these models, was investigated and the features with little effect were deleted. In this way, the VGG19 model was able to achieve results close to the same success with fewer parameters.



In the remaining sections of this paper is Section 2, the architecture and parameters of the VGG19 model are described. Also, the AID dataset is described in this section. Finally, the proposed method is presented. Section 3 describes the experimental studies, the results obtained by testing the models and comparing them with each other. Section 4 presents the conclusions of the study

## 2. MATERIAL AND METHOD

### 2.1. VGG19

The VGG19 model was developed by Karen Simonyan and Andrew Zisserman for the ImageNet competition in 2014. The goal of this model is to use convolution filters of smaller size for deeper model design. The architecture of the model and its values at each layer are given in Figure 1. When we look at the number of parameters of the model, it is seen that the most parameters are in the last convolution layer. The number of parameters here constitutes approximately 86% of the total number of parameters of the model. The aim of this study is to find the best features in the feature maps in this layer and achieve high accuracy with fewer features

Figure 1. The layer architecture of the VGG19 model and parameter values in each layer [30]

### 2.2. Data Set

The dataset was created by Xia et al. from google earth images [5]. The dataset consists of 30 classes in total. It consists of a total of 1000 images, with an average of 333 images for each class. A sample image of the dataset is given in Figure 2. The number of images in each class and class names are given in Table 1.

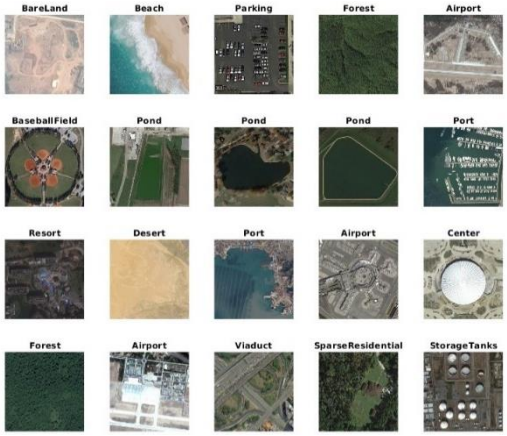


**Figure 2.** An example representation of the images in the AID dataset

### 2.3. Proposed Method

In this study, the VGG19 model was used along with other deep learning models to classify scenes in aerial images. Although the VGG19 model achieves high accuracy values, it has high parameter values. This increases the computational complexity of this model during the training and testing phase. To overcome this situation, the number of features in the flattening layer, which is the bottleneck of the model, has been reduced. The flow diagram of the proposed method is given in Figure 3. First, the dataset is divided into two parts, 50% training and 50% testing. The VGG19 model was trained with 50% of the dataset. After the training process, the feature map in the trained model was analyzed. In the analysis, the features obtained by the last convolution layer of the model were tested one by one on the test data and their effect on the result was calculated. The features with low impact were deleted from the VGG19 model. The VGG19 model was recoded according to the deleted features and retrained with the training data. After the training process, it was tested with test data and its final success was measured.

**Table 1.** Classes in the AID dataset and the number of images in each class

| Class name | Number of images | Class name | Number of images |
|---|---|---|---|
| Airport | 360 | Mountain | 340 |
| BareLand | 310 | Park | 350 |
| BaseballField | 220 | Parking | 390 |
| Beach | 400 | Playground | 370 |
| Bridge | 360 | Pond | 420 |
| Center | 260 | Port | 380 |
| Church | 240 | RailwayStation | 260 |
| Commercial | 350 | Resort | 290 |
| DenseResidential | 410 | River | 410 |
| Desert | 300 | School | 300 |
| Farmland | 370 | SparseResidential | 300 |
| Forest | 250 | Square | 330 |
| Industrial | 390 | Stadium | 290 |
| Meadow | 280 | StorageTanks | 360 |
| MediumResidential | 290 | Viaduct | 420 |

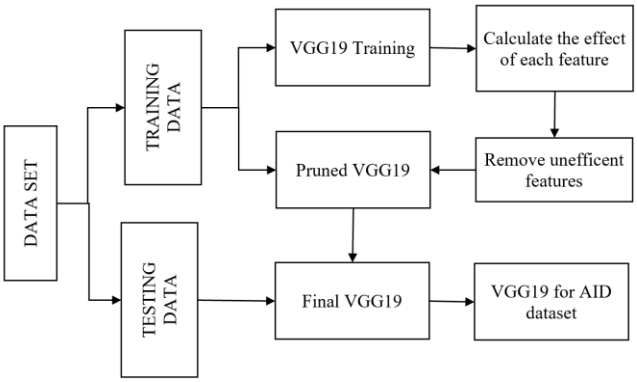


**Figure 3.** Flow diagram of the proposed method for reducing the number of parameters of the VGG19 model.

## 3. EXPARIMENTAL STUDIES

In the experimental studies, training and testing of the Googlenet, VGG19, Alexnet, Resnet-50, and Resnet-101 models were carried out. In addition, the VGG19 model, which has the highest number of parameters, was pruned and the training and testing of the adapted VGG19 model was carried out. Deep Learning toolbox of Matlab 2022b software was used in all experimental studies. The applications were performed on Nvidia 2080TI GeForce graphics cards.

### 3.1. Performance Criteria

In this study, the confusion matrix shown in Figure 4 was used to measure the performance of the models. The accuracy value obtained using the confusion matrix and given in Equation-1 was used to compare the models.

| | | PREDICT CLASS | |
|---|---|---|---|
| | | Positives | Negatives |
| TRUE CLASS | Positives | True Positive **(TP)** | False Positive **(FP)** |
| | Negatives | False Negative **(FN)** | True Negative **(TN)** |

**Figure 4.** Confusion matrix [18]

$$Accuracy = \frac{TP + TN}{TP + FP + FN + TN} \quad (1)$$

### 3.2. Training and Testing Results

The training parameters of the models are given in Table 2. All models are trained according to the same parameters.

**Table 2.** Parameters used in training the models

| Parameter Name | Parameter Value |
|---|---|
| Optimization algorithm | SGDM |
| Initial learning rate | 0.001 |
| Epoch | 50 |
| Batch size | 64 |
| Learning rate drop factor | 0.8 |
| Learning rate drop period | 10 |

The performances of the models were performed on the AID dataset, 50% of which was used for training and the rest for testing. In the training phase, the test data was used as validation data. In this way, it was examined whether the model overfitting in training. Some statistical information about the dataset is given in Table3.

**Table 3.** Some statistical information calculated on the AID dataset

| Information | Value |
|---|---|
| Class number | 30 |
| Total number of images | 10000 |
| Average number of images per class | 333 |
| Number of images of the class with the fewest images | 220 |
| Number of images of the class with the most images | 420 |
| Standard deviation of the number of images in classes | 57.79 |
| Number of images reserved for training | 5000 |
| Number of images reserved for testing | 5000 |

The convergence graphs obtained by the VGG19 model when trained with the training dataset are given in Figure 5. It reached 100% accuracy in the training phase with a total of 30 classes and 5000 images. In the validation data, the accuracy values after the 12th epoch were 93-94%.

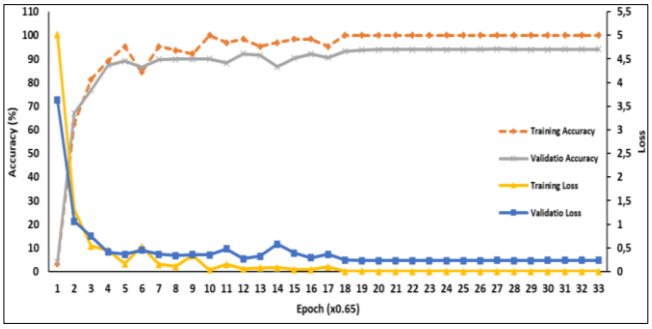


**Figure 5.** Convergence graphs obtained by the original VGG19 model in the training phase

The convergence graphs obtained by the pruned VGG19 model on the training data are given in Figure 6. Looking at the figure, it is expected that the accuracy and loss values are close to the previous result since the model was previously trained with the same data set. The most important reason for retraining the model is to rediscover the features in the last convolution layer. Because there were 512 filters in this layer, 449 of which were deleted. The features discovered by the remaining 63 filters were used to determine the model success.

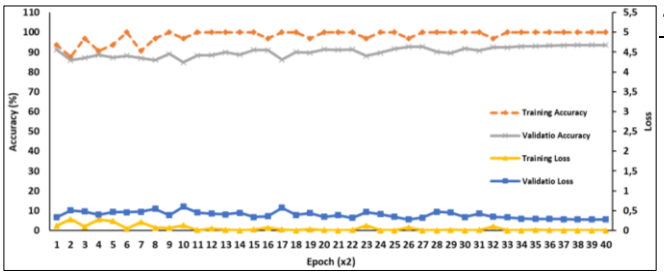


**Figure 6.** Convergence plots obtained by the pruned VGG19 model in the training phase

The confusion matrix obtained by the original VGG19 model in the test data is given in Figure 7. The confusion matrix of the pruned VGG19 model obtained by modifying the model with the proposed method is given in Figure 8. The model achieved an accuracy of 90.10% at this stage. After the modification, there were 63 features in the last feature layer of the Pruned VGG19 model. When the model was retrained and tested with the training dataset to retrieve these features, the confusion matrix in Figure 9 was obtained. When Figure 7-9 is analyzed, it is seen that the class most affected by the deleted 449 features is "BaseballField". With the retraining of the model, it was seen that this class was classified with the desired accuracy.

In addition to the VGG19 model, Alexnet, Googlenet, Resnet-50, Resnet-101 models, which are state-of-the-art models in the field of deep learning, were also tested on the AID dataset. Confusion matrices obtained for these

models are given in Figure 10-13 respectively. The comparison of all models is given in Table 4.

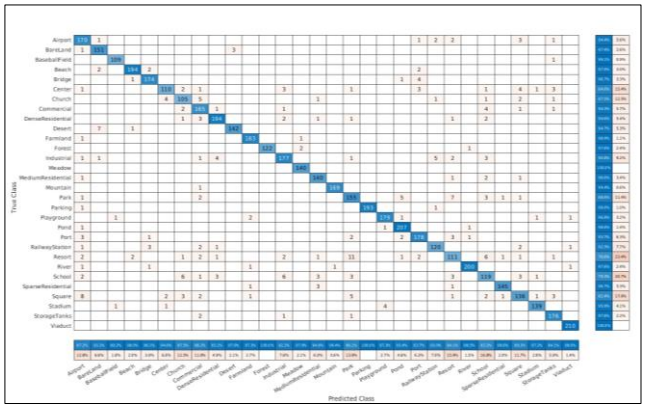

**Figure 7.** Confusion matrix obtained by the original VGG19 on test data

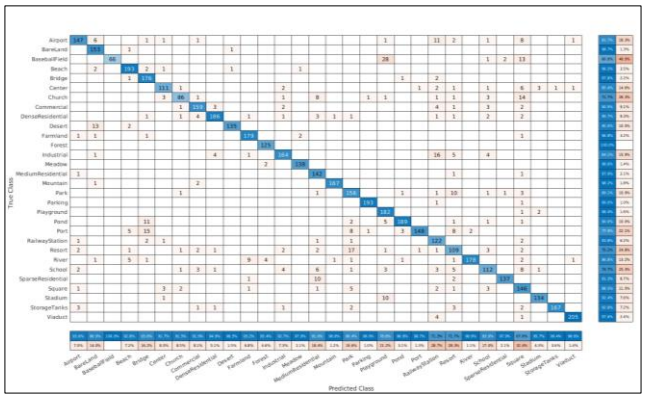

**Figure 8.** Confusion matrix obtained by the pruned VGG19 on test data

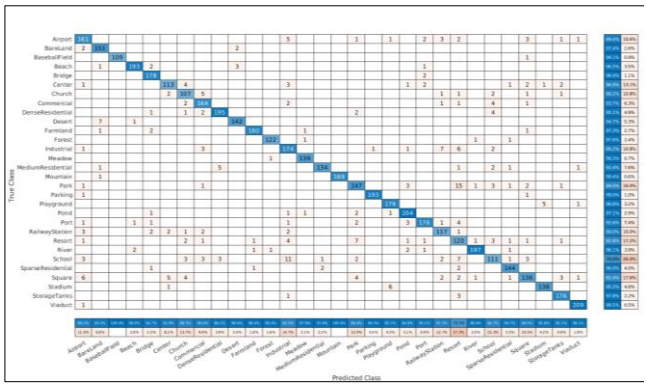

**Figure 9.** Confusion matrix obtained by the pruned VGG19 model on test data after retraining with training data

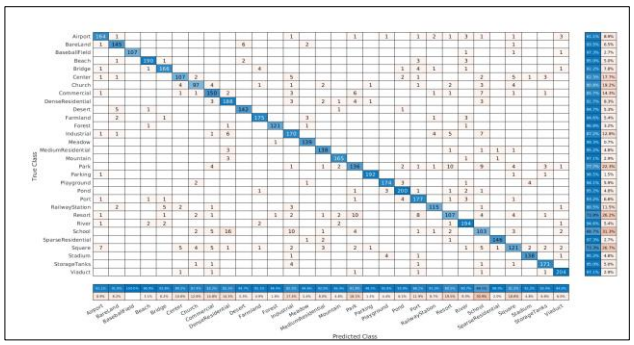

**Figure 10.** Confusion matrix obtained by Alexnet on test data

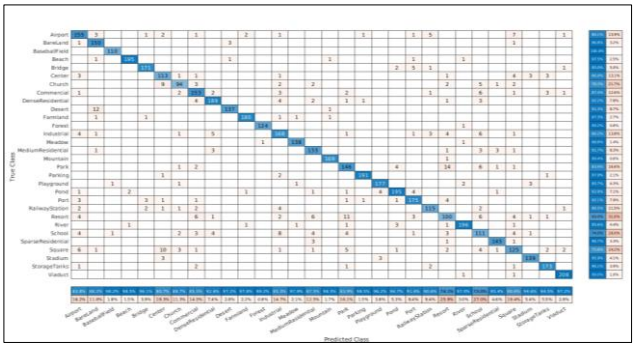

**Figure 11.** Confusion matrix obtained by Googlenet on the test data

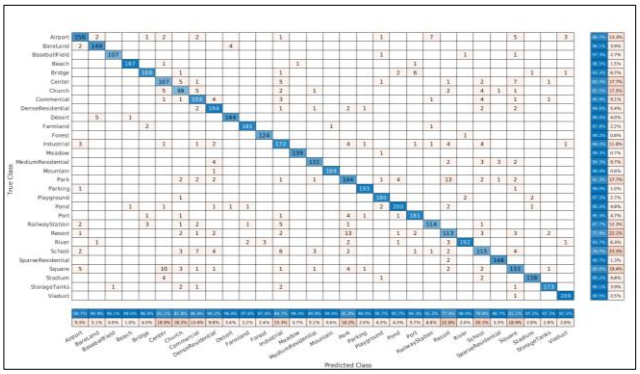

**Figure 12.** Confusion matrix obtained by Resnet-50 on the test data

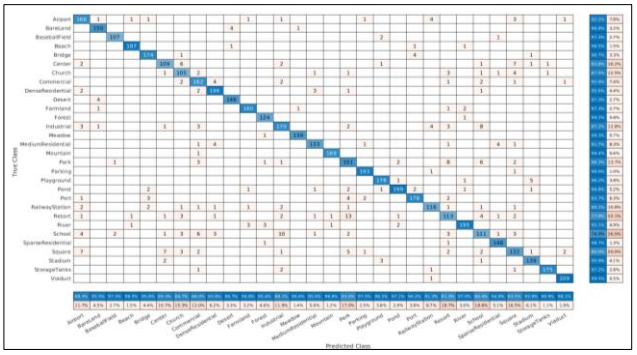

**Figure 13.** Confusion matrix obtained by ResNet-101 on the test data.

**Table 4.** Number of parameters, layer depth, and accuracy of the deep learning models on the AID dataset.

| Model Name | Accuracy (%) | Number of Parameters (Million) | Number of Layers |
|---|---|---|---|
| Resnet-50 | 92.58 | 25.5 | 177 |
| Resnet-101 | 93.28 | 42.6 | 347 |
| Googlenet | 91.50 | 6.9 | 144 |
| Alexnet | 90.84 | 60.9 | 25 |
| VGG19 | 94.26 | 143.6 | 47 |
| Pruned VGG19 | 93.56 | 48.1 | 47 |

Looking at Table 4, it is seen that the best accuracy value among the models is obtained by the VGG19 model with a value of 94.26%. However, the parameter value of this model is higher than all other models. On the contrary, the Pruned VGG19 model has 95.5 million fewer parameters than its original version and gave the second best result.

### 3.3. Comparison with Other Methods

Many studies have been carried out in the literature on the AID dataset. The results obtained in these studies and the result obtained with the proposed VGG19 model are given in Table 5. In the table, while the baseline is 68.96% in the AID data set, an accuracy value of 93.56% was obtained with Pruned VGG19. It has been observed that the results obtained with the proposed method have significantly improved the accuracy values compared to other studies.

**Table 5.** Comparison of the results of previous studies in the AID dataset with the proposed study.

| Authors/Reference | Method | Accuracy (%) |
|---|---|---|
| Xia, G.-S., et al.[5] | PLSA (SIFT) | 63.07 |
| Xia, G.-S., et al.[5] | BoVW (SIFT) | 68.37 |
| Xia, G.-S., et al.[5] | LDA (SIFT) | 68.96 |
| Han, X., et al [31] | SPP with Alexnet | 91.45 |
| Anwer, R.M., et al [32] | TEX-Net with VGG | 90.00 |
| Ilse, M., et al.[33] | Gated Attention | 92.01 |
| Bi, Q., et al.[34] | MIDC-Net CS | 92.95 |
| Bi, Q., et al.[35] | RADC-Net | 92.35 |
| Cao, R., et al.[36] | VGG VD16 + SAFF | 93.83 |
| Arefeen, M.A., et al.[10] | RBFF (3 6 13) + PCA (600) + LDA + SVM | 93.73 |
| Cheng, G., et al.[37] | D-CNN with AlexNet | 94.47 |
| Proposed | VGG19 | 94.26 |
| Proposed | Pruned VGG19 | 93.56 |

## 4. CONCLUSION

In this study, deep learning models are used to classify scenes from aerial images. First, the state-of-the-art deep learning models AlexNet, VGG19, Googlenet, Resnet-50, and Resnet-101 were used on the AID dataset. The accuracy values obtained by each model are 90.84%, 94.26%, 91.50%, 92.58%, and 93.28% respectively. Secondly, the model was pruned by selecting the effective features among the features discovered in the VGG19 model and deleting the remaining features. The total number of parameters of the original model is 143.6 million and the accuracy is 94.26%, while the total number of parameters of the pruned version is 48.1 million and the accuracy is 93.56%. Thus, although the number of parameters of the VGG19 model is reduced by 66.5%, the loss in accuracy is only 0.7%. The pruned VGG19 model was found to achieve better results than the other four models. Future studies are planned to use multi-objective optimization algorithms to prune CNN models according to accuracy and number of parameters.

## REFERENCES


[1] Zou, Q., et al., Deep learning based feature selection for remote sensing scene classification. IEEE Geoscience and Remote Sensing Letters, 2015. 12(11): p. 2321-2325.

[2] Xia, G.-S., et al. Structural high-resolution satellite image indexing. in ISPRS TC VII Symposium-100 Years ISPRS. 2010.

[3] Yang, Y. and S. Newsam. Bag-of-visual-words and spatial extensions for land-use classification. in Proceedings of the 18th SIGSPATIAL international conference on advances in geographic information systems. 2010.

[4] Cheng, G., J. Han, and X. Lu, Remote sensing image scene classification: Benchmark and state of the art. Proceedings of the IEEE, 2017. 105(10): p. 1865-1883.

[5] Xia, G.-S., et al., AID: A benchmark data set for performance evaluation of aerial scene classification. IEEE Transactions on Geoscience and Remote Sensing, 2017. 55(7): p. 3965-3981.

[6] Minu, M. and R.A. Canessane, Deep learning-based aerial image classification model using inception with residual network and multilayer perceptron. Microprocessors and Microsystems, 2022. 95: p. 104652.

[7] Zhu, R., et al., Semi-supervised center-based discriminative adversarial learning for cross-domain scene-level land-cover classification of aerial images. ISPRS Journal of Photogrammetry and Remote Sensing, 2019. 155: p. 72-89.

[8] Hua, Y., et al., Aerial scene understanding in the wild: Multi-scene recognition via prototype-based memory networks. ISPRS Journal of Photogrammetry and Remote Sensing, 2021. 177: p. 89-102.

[9] Pritt, M. and G. Chern. Satellite image classification with deep learning. in 2017 IEEE Applied Imagery Pattern Recognition Workshop (AIPR). 2017. IEEE.

[10] Arefeen, M.A., et al. A lightweight relu-based feature fusion for aerial scene classification. in 2021 IEEE International Conference on Image Processing (ICIP). 2021. IEEE.

[11] Bi, Q., et al., All Grains, One Scheme (AGOS): Learning Multi-grain Instance Representation for Aerial Scene Classification. arXiv preprint arXiv:2205.03371, 2022.

[12] Yi, J. and B. Zhou, Learning Instance Representation Banks for Aerial Scene Classification. arXiv preprint arXiv:2205.13744, 2022.

[13] İnik, Ö., CNN hyper-parameter optimization for environmental sound classification. Applied Acoustics, 2023. 202: p. 109168.

[14] 14. Falaschetti, L., et al., A CNN-based image detector for plant leaf diseases classification. HardwareX, 2022. 12: p. e00363.

[15] Girshick, R. Fast r-cnn. in Proceedings of the IEEE international conference on computer vision. 2015.

[16] İnik, Ö., et al., A new method for automatic counting of ovarian follicles on whole slide histological images based on convolutional neural network. Computers in biology and medicine, 2019. 112: p. 103350.

[17] İnik, Ö., et al., MODE-CNN: A fast converging multi-objective optimization algorithm for CNN-based models. Applied Soft Computing, 2021. 109: p. 107582.

[18] Inik, Ö. and E. Ülker, Optimization of deep learning based segmentation method. Soft Computing, 2022. 26(7): p. 3329-3344.
[19] Ronneberger, O., P. Fischer, and T. Brox. U-net: Convolutional networks for biomedical image segmentation. in Medical Image Computing and Computer-Assisted Intervention–MICCAI 2015: 18th International Conference, Munich, Germany, October 5-9, 2015, Proceedings, Part III 18. 2015. Springer.
[20] Genze, N., et al., Deep learning-based early weed segmentation using motion blurred UAV images of sorghum fields. Computers and Electronics in Agriculture, 2022. 202: p. 107388.
[21] Orhan, İ., et al., Soil Temperature Prediction with Long Short Term Memory (LSTM). Türk Tarım ve Doğa Bilimleri Dergisi. 9(3): p. 779-785.
[22] Mondal, M., et al., Adaptive CNN filter pruning using global importance metric. Computer Vision and Image Understanding, 2022. 222: p. 103511.
[23] Pattanayak, S., S. Nag, and S. Mittal, CURATING: A multi-objective based pruning technique for CNNs. Journal of Systems Architecture, 2021. 116: p. 102031.
[24] Ide, H., et al., Robust pruning for efficient CNNs. Pattern Recognition Letters, 2020. 135: p. 90-98.
[25] Yang, C. and H. Liu, Channel pruning based on convolutional neural network sensitivity. Neurocomputing, 2022. 507: p. 97-106.
[26] Szegedy, C., et al. Going deeper with convolutions. in Proceedings of the IEEE conference on computer vision and pattern recognition. 2015.
[27] Krizhevsky, A., I. Sutskever, and G.E. Hinton, Imagenet classification with deep convolutional neural networks. Communications of the ACM, 2017. 60(6): p. 84-90.
[28] Simonyan, K. and A. Zisserman, Very deep convolutional networks for large-scale image recognition. arXiv preprint arXiv:1409.1556, 2014.
[29] He, K., et al. Deep residual learning for image recognition. in Proceedings of the IEEE conference on computer vision and pattern recognition. 2016.
[30] Matlab_2022b. Get Started with Deep Network Designer. 2022 [cited 2022 23.12.2022]; Available from: https://www.mathworks.com/help/deeplearning/gs/get-started-with-deep-network-designer.html.
[31] Han, X., et al., Pre-trained alexnet architecture with pyramid pooling and supervision for high spatial resolution remote sensing image scene classification. Remote Sensing, 2017. 9(8): p. 848.
[32] Anwer, R.M., et al., Binary patterns encoded convolutional neural networks for texture recognition and remote sensing scene classification. ISPRS journal of photogrammetry and remote sensing, 2018. 138: p. 74-85.
[33] Ilse, M., J. Tomczak, and M. Welling. Attention-based deep multiple instance learning. in International conference on machine learning. 2018. PMLR.
[34] Bi, Q., et al., A multiple-instance densely-connected ConvNet for aerial scene classification. IEEE Transactions on Image Processing, 2020. 29: p. 4911-4926.
[35] Bi, Q., et al., RADC-Net: A residual attention based convolution network for aerial scene classification. Neurocomputing, 2020. 377: p. 345-359.
[36] Cao, R., et al., Self-attention-based deep feature fusion for remote sensing scene classification. IEEE Geoscience and Remote Sensing Letters, 2020. 18(1): p. 43-47.
[37] Cheng, G., et al., When deep learning meets metric learning: Remote sensing image scene classification via learning discriminative CNNs. IEEE transactions on geoscience and remote sensing, 2018. 56(5): p. 2811-2821.

Cilt 12, Sayı 1, Sayfa 44-52, 2023 Volume 12, Issue 1, Page 44-52, 2023

Araştırma Makalesi https://doi.org/10.46810/tdfd.1219070 Research Article

Türk Doğa ve Fen Dergisi
Turkish Journal of Nature and Science
www.dergipark.gov.tr/tdfd

# Rapid Suppression of Superconductivity in $Co_3O_4$ Nanoparticles-added Bi-2212 Ceramics

**Mehmet GÜRSUL**[1*]

[1] Çukurova University, Faculty of Sciences and Arts, Department of Physics, Adana, Türkiye
Mehmet GÜRSUL ORCID No: 0000-0002-3025-2183

**Corresponding author: mgursul@cu.edu.tr*

(Received: 14.12.2022, Accepted: 15.02.2023, Online Publication: 27.03.2023)

**Keywords**
HTSCs,
XRD,
SEM,
Magnetic Hysteresis,
Critical Current Density

**Abstract:** This study concerns the remarkable variations in the crystalline quality, phase compositions, superconducting properties, and pinning force in the Bi-2212 ceramics through the addition of $Co_3O_4$ nano-particles with the x % weight for x = 0, 0.5, 1, and 2, respectively. From XRD analysis, it is deduced that $Co_3O_4$-inclusions give rise to the XRD peaks to expand, degrade the crystal quality together with a decrement in the Bi-2212 amount. From SEM images, it is seen that there is an evolution from rod-like structure to plate-like structure with $Co_3O_4$ addition. The critical transition temperature ($T_c$) value which is determined from *M-T* measurement is 82 K in the pure sample, it drops gradually and takes the value 65 K and 42 K for the 0.5% Co sample and 1% Co sample respectively, and eventually, the superconductivity is lost in the 2% Co sample. From *M-H* measurements, it is clear that the hysteresis loop gets narrower with $Co_3O_4$ addition and temperature. Accordingly, critical current densities ($J_c$) and pinning forces ($F_p$) reduce due to deteriorations in the connectivity between superconducting grains induced by the augmentation in $Co_3O_4$ content.



# $Co_3O_4$ Nanoparçacıklarıyla Ekli Bi-2212 Seramiklerinde Süperiletkenliğin Hızlı Bastırılması

**Anahtar Kelimeler**
HTSCs,
XRD,
SEM,
Manyetik Histerezis,
Kritik Akım Yoğunluğu

**Öz:** Bu çalışma, sırasıyla x = 0, 0.5, 1 ve 2 için % x ağırlıkça $Co_3O_4$ nano-parçacıklarıyla eklenmiş Bi-2212 seramiğindeki kristal kalitesi, faz bileşimleri, süperiletken özellikler ve çivileme kuvvetindeki dikkate değer değişimlerle ilgilidir. XRD analizinden $Co_3O_4$-içeriğinin XRD piklerinde genişlemeye, kristal kalitesinin düşmesine ve Bi-2212 miktarının azalmasına yol açtığı sonucuna varılır. SEM görüntülerinden $Co_3O_4$ ilavesiyle çubuksu yapıdan plakamsı yapıya doğru bir evrilme olduğu görülmektedir. Kritik geçiş sıcaklığı ($T_c$), *M-T* ölçümlerinden saf örnekte 82 K olarak bulunmuş ve % 0.5 Co örneğinde 65 K'ye % 1 Co örneğinde 42 K'ye kademeli olarak düştükten sonra süperiletkenlik % 2 Co örneğinde kaybolmuştur. *M-H* ölçümlerinden, histerezis eğrilerinin $Co_3O_4$ eklenmesi ve sıcaklıkla birlikte daraldığı görülmektedir. Buna bağlı olarak, kritik akım yoğunlukları ($J_c$) ve çivileme kuvvetleri ($F_p$), $Co_3O_4$ içeriğindeki artışın neden olduğu süper iletken tanecikler arasındaki bağlantıdaki bozulmalar nedeniyle azalmıştır.

## 1. INTRODUCTION

The superconductivity was revitalized in 1986 thanks to the discovery of superconductivity in the copper-oxide based Ba−La−Cu−O system by Bednorz and Muller [1]. Prior to this progress, superconductivity was seen as a subject confined to temperatures near absolute zero and well explained by Bardeen–Cooper–Schrieffer (BCS) theory based on the electron-phonon interaction with a limit of critical transition temperature ($T_c$) of around 30 K [2]. However, after this discovery, superconductor studies accelerated tremendously and various high-$T_c$ superconductors (HTSCs) such as Y-Ba-Cu-O (YBCO, $T_c$=90K) [3], Bi-Sr-Ca-Cu-O (BSCCO, $T_c$=110K) [4], and Tl–Ca/Ba–Cu–O (TBCCO, $T_c$= 120 K) [5] emerged within a year. What makes these discoveries important is that the critical temperature values are above the boiling point (77 K) of liquid nitrogen, which is accepted as the psychological and technological barrier of superconductivity. Among these high temperature superconductors, the BSSCO system is one of the most studied one and is represented by the general formula $Bi_2Sr_2Ca_{n-1}Cu_nO_{2n+4+y}$. This system has Bi-2201 (n=1),

Bi-2212 (n=2), and Bi-2223 (n=3) phases, depending on the value of n, which shows the number of $CuO_2$ layers in the unit cell. As the $CuO_2$ layer in the structure increases, $T_c$ values increase and are 20, 85 and 110 K for Bi-2201, Bi-2212, and Bi-2223, respectively [6]. Although the Bi-2201 phase without Ca was discovered first and led to the emergence of Bi-2212 and Bi-2223, it does not attract attention due to its low $T_c$. On the other hand Bi-2212 has attracted much attention due to its lesser weak link problems, lower fabrication cost, much easier manufacturability, and better thermodynamic stability compared to the Bi-2223 [7-8].

Since the discovery of BSCCO [9], chemical doping, which can be in the form of addition or substitution, has become one of the most used methods to enhance $T_c$ and critical current density ($J_c$) or to uncover its physical and magnetic properties [10-16]. In addition to chemical doping, many synthesis routes are available to produce BSCCO bulk materials including solid state reaction [17], co-precipitation [18], sol-gel [19], and polymer matrix method [20]. Among these aforementioned methods, solid state one is frequently used by researchers owing to its advantages such as simplicity, cheapness, and reasonable reproducibility [14].

When a magnetic field applied to a Type-II superconductor is larger than the lower critical field ($H_{c1}$) and less than the upper magnetic field ($H_{c2}$), the superconductor exhibits a state called a mixed state (also known as vortex state or Shubnikov phase) where the magnetic field penetrates the superconductor in the configuration of quantized magnetic vortices carrying the magnetic flux quantum ($\phi_0$). When a current density ($\boldsymbol{J}$) is applied to the material, a Lorentz force ($\boldsymbol{F}_L = (1/c)\, \boldsymbol{J} \times \phi_0$) emerges causing resistance by forcing vortices to move. The tools that struggle with the Lorentz force in the material are expressed as pinning centers. A pinning center can be formed naturally by defects such as stack faults, dislocations, and twin planes, or it can be constructed artificially via chemical doping or neutron radiation [21-22]. Basically, chemical doping attracts a lot of attention as it is an easy-to-control, non-destructive and effective method of producing pinning centers [23]. Doping of nano-sized particles to the BSCCO system has been proposed as a workable approach and many nanoparticles such as MgO [24], $Al_2O_3$ [25], $ZrO_2$ [26], $Fe_3O_4$ [27], and $NiFe_2O_4$ [28] have been tested.

In the current work, it is aimed to investigate the effect of $Co_3O_4$ nano-particles on the structural, superconducting, and magnetic properties of Bi-2212. Parenthetically, $Co_3O_4$ nanoparticles have multifunctional properties and are used in many applied areas such as energy storage [29], resistive switching devices [30], and biomedical technologies [31]. $Co_3O_4$ is an intrinsic antiferromagnetic material having a Neel temperature of 40 K with weak ferromagnetic behavior due to the presence of both $Co^{2+}$ and $Co^{3+}$ cations and uncompensated surface spins or finite size effect [32]. Considering these multifunctional properties of $Co_3O_4$, it will be interesting to test whether $Co_3O_4$ nanoparticles have the capability to form effective pinning centers in BSCCO. In this regard, $Co_3O_4$ nanoparticles were produced using sol-gel auto combustion method described in detail elsewhere [33, 34] and added to Bi-2212 for different weights. Characterizations of the prepared samples were performed with conventional methods, viz., X-ray diffraction (XRD), scanning electron microscope (SEM), magnetization-temperature, and magnetic hysteresis techniques.

## 2. MATERIAL AND METHOD

$Bi_2Sr_2Ca_1Cu_2O_y$+x % weight for x=0, 0.5, 1, and 2 % polycrystalline specimens were synthesized from the high purity commercial powders of $Bi_2O_3$, $SrCO_3$, $CaCO_3$, and CuO via the standard solid state reaction technique. These starting powders are exactly weighted in the molar proportion by an electronic balance and are well mixed and milled. Then, the resultant mixture was calcined twice for 12 h at 750°C and 800°C together with intermediate grinding in an agate mortar using a pestle for about 25 min. After the calcination process, the obtained homogenous powders were pressed into tablets with 0.9 mm thick and 0.5 cm in diameter applying pressure of 5000 kg-force/cm$^2$ at room temperature. Then these pressed samples are sintered at 860°C for 60 h followed by cooling to 800°C and quenching to room temperature in air to provide a large amount of Bi-2212 phase. After this heat treatment process, $Co_3O_4$ nanoparticles obtained by sol-gel auto-combustion method corresponding to the x% weight of Bi-2212 was added to the specimens and the thermal treatment steps described above were carried out once more and finally, all samples were made ready for the characterization process. Throughout the paper, the prepared samples with nominal ratios of $Bi_2Sr_2Ca_1Cu_2O_y$+ x weight % $Co_3O_4$ where x= 0, 0.5, 1, and 2 % are named as 0 % Co, 0.5 % Co, 1 % Co, and 2 % Co, respectively. As for XRD analysis, PANalytical Empyrean diffractometer with Cu-Kα target (λ= 1.54 Å) was used at room temperature. Microstructural features of the samples were investigated by FEI-Quanta FEG 650 SEM. The magnetic measurements namely magnetization as a function of temperature (*M-T*) and magnetization versus magnetic field (*M-H*) were conducted using a 7304 model Lake Shore VSM system.

## 3. RESULTS AND DISCUSSION

Figure 1 represents XRD patterns between 20 and 50° at room temperature of the pristine and $Co_3O_4$ added Bi-2212 ceramics. Most of the diffractions peaks can be indexed to Bi-2201, Bi-2212, and Bi2223 labeled by 1, 2 and 3, respectively. In addition to these peaks secondary phases shown by asterisk are also observed in all samples. Although these peaks are not $Co_3O_4$ peaks, they have not been clearly defined and probably belong to non-superconducting phases such as $CaCuO_2$ or $CaBi_2O_4$ combined with $Co_3O_4$. To make a quantitative analysis, the relative phase abundance of each phase can be calculated by the equations given below;

$$f_{2212} = \frac{\sum I_{2212}}{\sum I_{2223} + \sum I_{2212} + \sum I_{2201} + \sum I_{other}} \times 100\% \quad (2)$$

$$f_{2201} = \frac{\sum I_{2201}}{\sum I_{2223} + \sum I_{2212} + \sum I_{2201} + \sum I_{other}} \times 100\% \quad (3)$$

$$f_{other} = \frac{\sum I_{other}}{\sum I_{2223} + \sum I_{2212} + \sum I_{2201} + \sum I_{other}} \times 100\% \quad (4)$$

where $f$ is the phase percentage and $I$ corresponds to the peak intensity of the related phase [6]. According to calculations embedded in Table 1, a considerable decrease in superconducting phases with the introduction of $Co_3O_4$. In particular, the amount of the Bi-2212 phase decreases from 74.4 to 46.6 % with only 2% $Co_3O_4$ addition. Besides, the Bi-2223 phase, which was around 8.5 % in the pure sample, completely disappeared in the 2% $Co_3O_4$-added sample. In addition, the Bi-2201 phase, which is around 11-12% in other samples, reached its smallest value of 9.2% in the 2% Co sample. More interestingly, non-superconducting secondary phases increased dramatically with the increase in $Co_3O_4$, taking a value of 44.2 % in the 2% Co sample. It should also be stated that the inclusions of $Co_3O_4$ in the system caused the XRD peaks to expand, reduce the crystal quality of the structure and thereby undermine the growth of the Bi-2212 phase. Moreover, observed peaks can be assigned to the tetragonal structure with space group $P_{4/mmm}$ and cell parameters can be determined through the equation [12]:

$$\frac{1}{d^2} = \frac{h^2}{a^2} + \frac{k^2}{b^2} + \frac{l^2}{c^2} \quad (5)$$

where d is the interlayer distance, h, k, and l are the Miller indices and a, b, and c are the lattice constants. As seen from the obtained values provided in Table 1, both a and c parameters reduce with $Co_3O_4$ addition; however, the decrease in c is more pronounced. The shrinkage of c cell germinates from the variation in the stability of oxygen level in the Bi-O stacks owing to the charge neutrality mechanism [6]. Furthermore, the average crystallite size of the samples can be deduced using Debye-Scherrer equation given as [35];

$$L = \frac{0.941\,\lambda}{\beta\,\cos\theta_\beta} \quad (6)$$

where $L$ is the crystallite-size, $\lambda$ the X-ray wavelength used in the diffractometer, $\beta$ is the full width at half maximum of the peak, and $\theta_\beta$ is the Bragg diffraction angle. The most intense peaks around 23.03°, 24.85°, 27.41°, 30.94°, and 33.11° corresponding to planes of

$$f_{2223} = \frac{\sum I_{2223}}{\sum I_{2223} + \sum I_{2212} + \sum I_{2201} + \sum I_{other}} \times 100\% \quad (1)$$

(008), (013), (015), (017), and (110) are used in the estimation of the average crystallite size. As clear from Table 2, the average crystallite size declines monotonically with the increment in $Co_3O_4$-content in Bi-2212 reflecting that $Co_3O_4$ additions scupper crystallinity of the Bi-2212. Put succinctly, $Co_3O_4$ inclusions raise the crystallization activation energy ($E_a$) of the Bi-2212 phase and expedite the nucleation rates of the secondary phases [36].

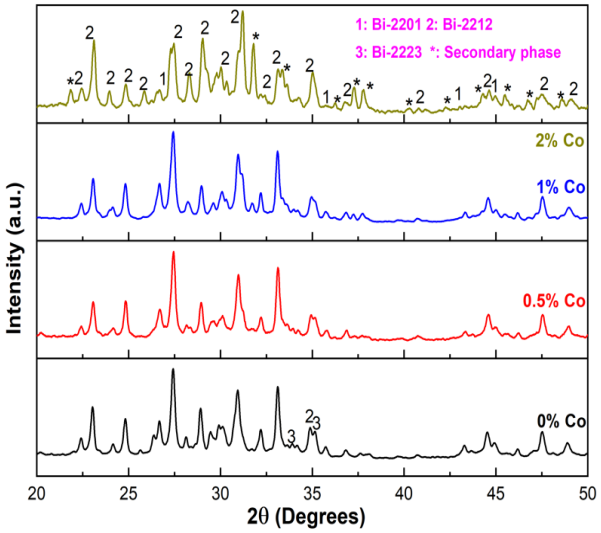


**Figure 1.** XRD patterns of $Co_3O_4$ nanoparticles-added Bi-2212 ceramics

The morphological properties of the samples were examined with SEM images taken at 1000X magnification in the secondary electron mode and obtained photographs are given in Figure 2. In the light of the first browses made to the photographs, it is seen that the addition of $Co_3O_4$ % significantly changes crystallinity and morphological characteristics of the samples. Namely, if one pays attention to the images in the pure sample (Figure 2a), while the rod- and needle-like grains constitute the microstructure forming a tight union by contacting each other, these structures have decreased in the $Co_3O_4$–added samples and the flaky structures and plate-like structures have emerged due to the expansion in the melting regions. The added $Co_3O_4$ accumulates at the boundaries of these rod-like grains forming the Bi-2212 structure causing the formation of melt regions in the structure, impairing the crystal quality, and breaking the connection between the superconducting grains. These variations in the morphological properties of the samples can be correlated with the serious decrement in the Bi-2212 percentages addressed in XRD discussions.

**Table 1**. Phase fractions and lattice parameters of the samples

| Sample | Bi-2223 % | Bi-2212 % | Bi-2201 % | Other % | a (Å) | c (Å) |
|---|---|---|---|---|---|---|
| **%0 Co** | 8.5 | 74.4 | 11.1 | 6.0 | 5.4093 | 30.8879 |
| **%0.5 Co** | 6.2 | 68.8 | 12.1 | 12.9 | 5.4061 | 30.8444 |
| **%1 Co** | 2.8 | 64.0 | 12.1 | 21.1 | 5.4082 | 30.8442 |
| **%2 Co** | 0.0 | 46.6 | 9.2 | 44.2 | 5.3781 | 30.7945 |

**Table 2.** Determination of average crystallite size estimated from the Debye-Scherrer relation using the reflections at 2θ= 23.03°, 24.85° 27.41°, 30.94°, and 33.11°

| 2θ (Degrees) | 0% Co (nm) | 0.5% Co (nm) | 1% Co (nm) | 2% Co (nm) |
|---|---|---|---|---|
| **23.03** | 56.99 | 52.54 | 53.67 | 53.41 |
| **24.85** | 51.41 | 60.42 | 52.55 | 47.80 |
| **27.41** | 68.19 | 42.24 | 45.16 | 51.65 |
| **30.94** | 52.41 | 46.06 | 46.86 | 44.04 |
| **33.11** | 67.98 | 64.11 | 61.08 | 15.75 |
| **Average Crys.Size (L)** | 59.40 | 53.07 | 51.86 | 42.53 |

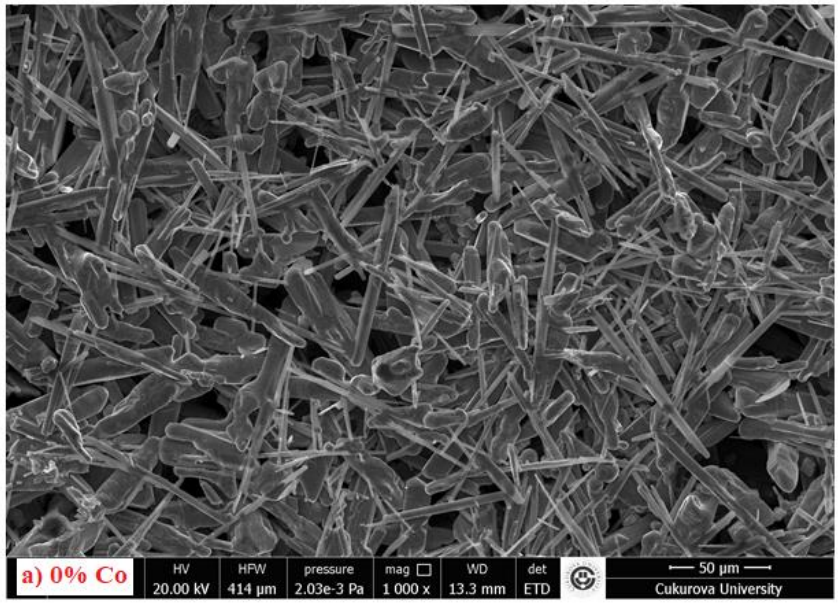


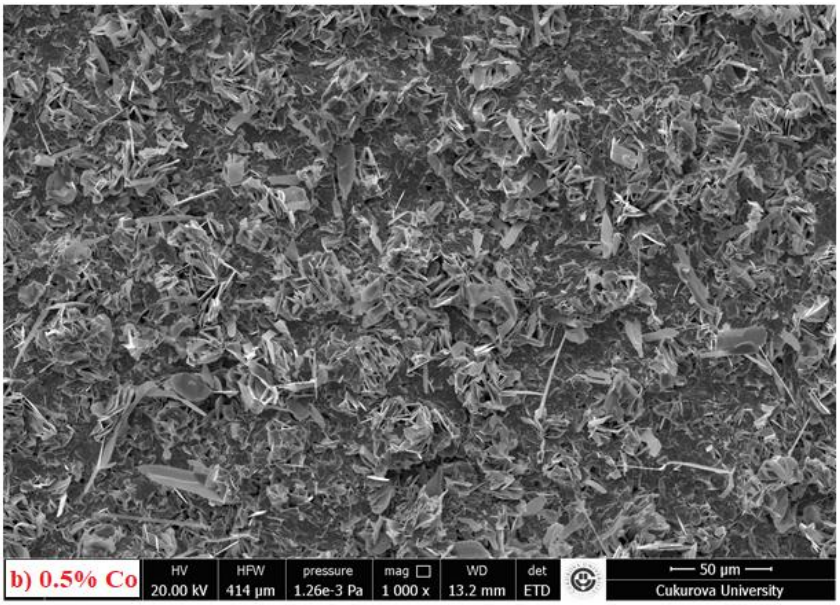

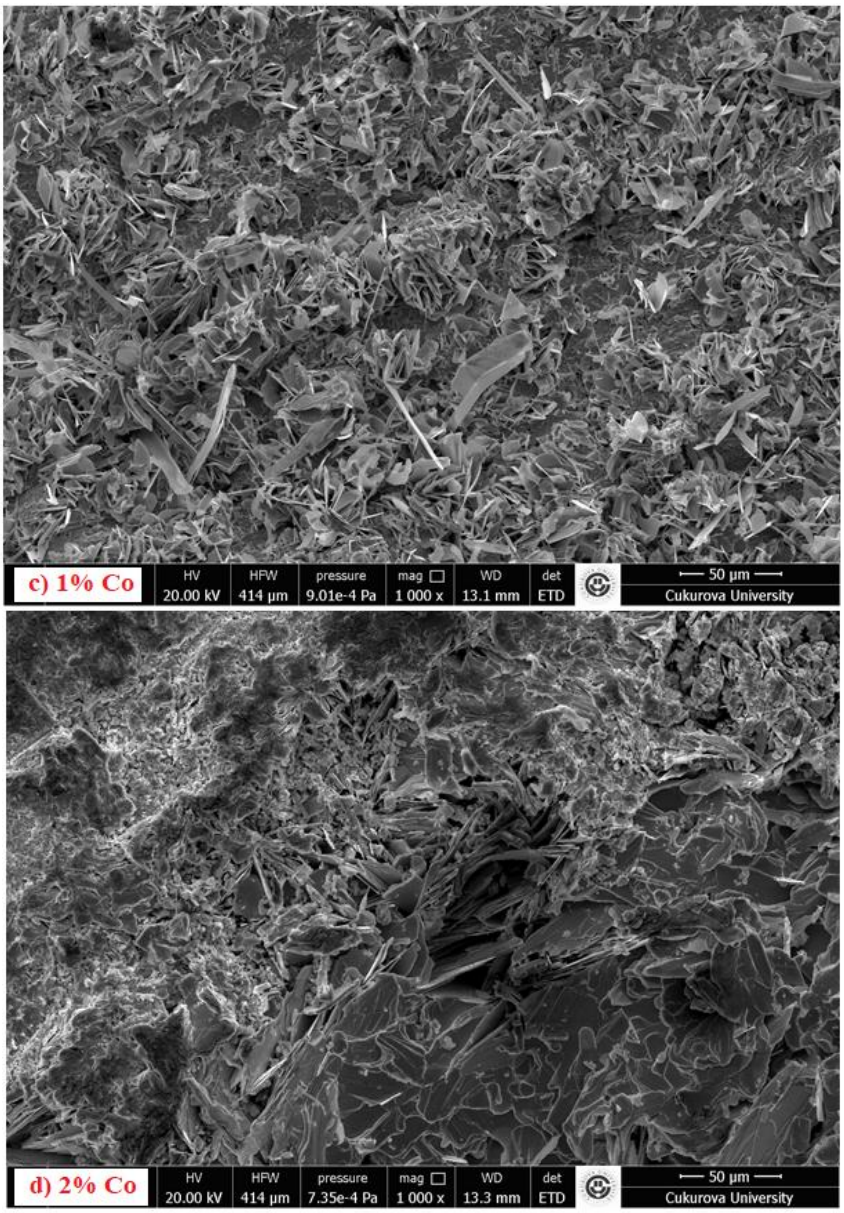


**Figure 2.** SEM images for a) 0% Co, b) 0.5% Co, c) 1% Co and, d) 2% Co samples

Magnetization versus temperature curves at the applied field of 100 Oe is given in Figure 3. The transition temperature ($T_c$) which corresponds to beginning point of diamagnetic signals decreases harshly with the addition of $Co_3O_4$. To put it numerically, the $T_c$ value in the pure sample is 82 K, while in the 0.5% Co sample it drops sharply, takes the value 65 K. The critical temperature value reduces to 42 K in the 1% sample and the superconductivity is lost in the 2% sample. This dramatic decrease in $T_c$ values can be elucidated within the framework of the pair-breaking theory suggested by Abrikosov and Gor'kov [37, 38]. Namely, as a consequence of the interaction of the electrons of the magnetic impurities and the Cooper pairs, the spins of the electrons change and the Cooper-pairs breakage occurs. More specifically, the significant decrease in $T_c$ values is associated with the increase of the Gennes factor ($G=(g-1)^2 J (J+1)$), including Lande g factor and the total angular momentum due to magnetic impurities [38]. According to the Abrikosov-Gor'kov theory [37] the reduction of $T_c$ values due to magnetic impurities is given by the relation;

$$\ln\frac{T_{c0}}{T_c} = \psi\left[\frac{1}{2}+\frac{\Gamma}{2\pi k_B T_C}\right]-\psi\left[\frac{1}{2}\right] \qquad (7)$$

where $T_{c0}$ is the transition temperature of the pure material (without magnetic impurity), $\psi$ is the digamma function, and $\Gamma$ is the pair-breaking parameter proportional to the magnetic impurity concentration [39]. If we relate to our case, it can be said that the $Co_3O_4$-impurities gradually actualize pair-breaking in Bi-2212 leading to a decrement in $T_c$ values. However it can be emphasized that doping with non-magnetic impurities in cuprates can also degrade their $T_c$ as in the case of Zn-doped [40] or Y-doped BSCCO [41]. The vanquishing of superconductivity in the non-magnetic impurity containing BSCCO can be expounded that random impurity potentials evolve due to enhancement of nonmagnetic disorder leading to the localization of

electronic states at the Fermi level [39, 41, 42]. Hence another scenario of the rapid decrement in $T_c$ is the result of new permanent crystallinity disorders such as porosity, defects, cracks, and grain boundary coupling problems evolving with the addition of $Co_3O_4$ [6]. Eventually, 2% Co doping level exterminate the superconductivity in Bi-2212 system resulting in a metal-insulator type transition (MIT) [40, 43].

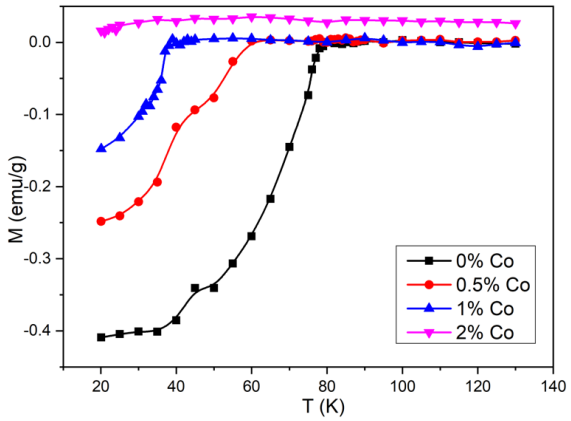


**Figure 3**. Magnetization versus temperature curves of the samples.

Magnetic field dependence of magnetization of the samples (*M-H*) measured at 10, 15, and 20 K between $\pm$ 1 T are illustrated in Figure 4. It is clear that the area of the magnetic hysteresis gets narrower with addition of $Co_3O_4$ and with increasing temperature. This is stem from the fact that the addition of $Co_3O_4$ and increasing temperature reduce the pinning ability of Bi-2212. Similarly, $H_{c1}$ values for the samples where magnetization-magnetic field curves deviate from linearity and vortices emerge show a decreasing trend as $Co_3O_4$ enters the system. For example, $H_{c1}$ of the pure sample at 10 K is 1611 Oe, while $H_{c1}$ of the 1% Co sample decreases to 1242 Oe. In addition, $M_r$ values which we call remanent magnetization and represent the flux trapping in the system decreased with increasing amount of $Co_3O_4$. The change of $H_{c1}$ and $M_r$ values are given in Table 3 for different $Co_3O_4$-content at temperatures of 10, 15 and 20 K, respectively.

Using magnetization versus magnetic field data, the intra-grain critical current densities, $J_c$, in A/cm$^2$, of all samples can be calculated using Bean's model given as [44,45];

$$J_c = 20\Delta M/[a(1 - a/3b)] \quad (8)$$

where ΔM is the difference between the magnetization values of up and down fields measured in emu/cm$^3$ and, a and b (a<b) are the dimensions of the samples. Obtained $J_c$ values of the samples are depicted in Figure 5 for temperatures of 10, 15, and 20 K. It can be seen from the graphs that the negativity on the superconducting properties with $Co_3O_4$ is also reflected in the critical current densities decreased significantly with the increasing amount of $Co_3O_4$. As the amount of $Co_3O_4$ rises, the amount of the Bi-2212 phase reduces and the connectivity of superconducting grains weakens, causing serious drops in the critical current densities of the samples.

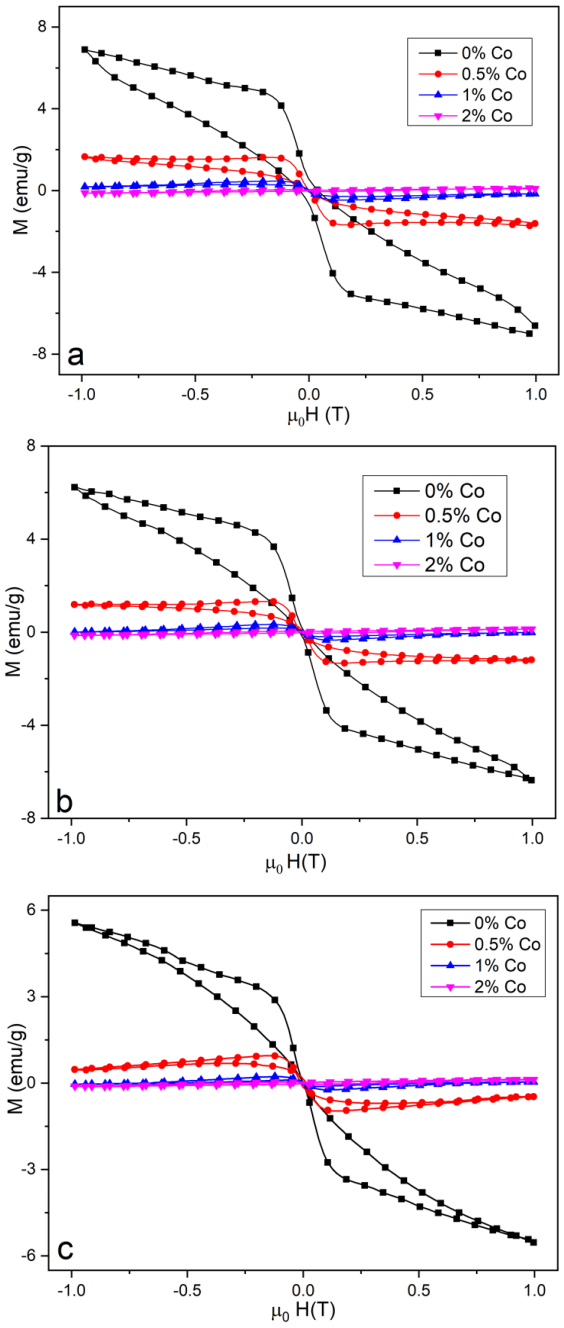


**Figure 4.** Magnetization versus magnetic field for a) 10 K, b) 15 K, and c) 20 K

As the final calculation, the volume pinning force ($F_p$) of the samples can be determined using the equation below [45].

$$F_P = J_C \times B \quad (9)$$

Calculated $F_p$ values as a function of the magnetic field for all samples are given in Figure 6. If the figure is examined, it can be deduced that $F_P$ values decline with increasing temperature and $Co_3O_4$-content. The maximum $F_p$ was calculated to be approximately 4.2 × 10$^6$ N/m$^3$ in the pristine sample at 10 K. However with the increment in $Co_3O_4$, this value reduces to 0.8 × 10$^6$ in 0.5% $Co_3O_4$ sample for the applied field of 0.8 T.

All in all, it can be deduced that introducing $Co_3O_4$ nanoparticles to the Bi-2212 superconductor undermines the pinning ability of the superconductor.

**Table 3**. $H_{c1}$ and $M_r$ values of the samples at 10, 15, and 20 K.

| Sample | $H_{c1}$ (Oe) at 10 K | $M_r$ (emu/gr) at 10 K | $H_{c1}$ (Oe) at 15 K | $Mr$ (emu/gr) at 15 K | $H_{c1}$ (Oe) at 20 K | $M_r$ (emu/gr) at 20 K |
|---|---|---|---|---|---|---|
| **0% Co** | 1611 | 0.560 | 1478 | 0.750 | 1305 | 0.025 |
| **0.5% Co** | 1376 | 0.041 | 1297 | 0.023 | 1112 | ~0 |
| **1% Co** | 1242 | 0.027 | 1141 | 0.009 | 1065 | ~0 |
| **2%Co** | ~0 | ~0 | ~0 | ~0 | ~0 | ~0 |

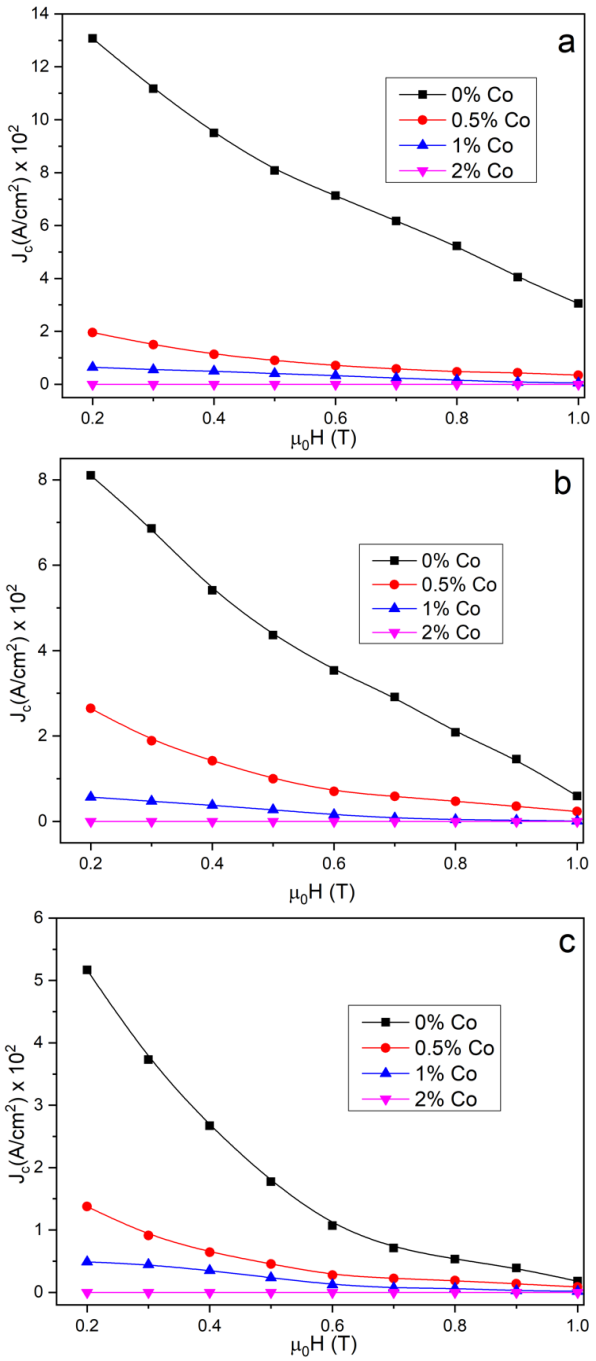


**Figure 5.** Critical current density versus magnetic field for a) 10 K, b) 15 K, and c) 20 K

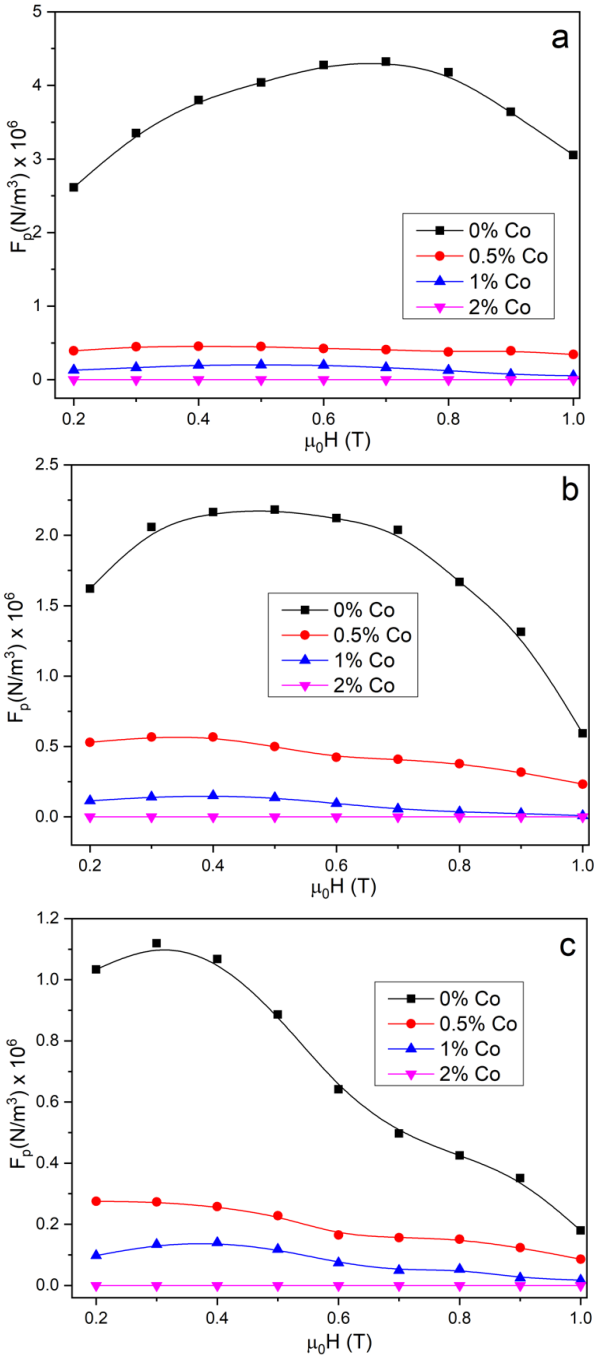


**Figure 6.** Variation of pinning force against magnetic field for a) 10 K, b) 15 K, and c) 20 K



## 4. CONCLUSION

In the current study, the influence of $Co_3O_4$-nanoparticle addition on the phase distributions including Bi-2201, Bi-2212, and Bi-2223, average crystallite size, morphological and microstructural features, superconducting and magnetic hysteresis properties of $Bi_2Sr_2CaCu_2O_y$ + x wt % $Co_3O_4$ (x=0, 0.5, 1, 2) ceramics prepared by classical solid state reaction technique are investigated with the aid of XRD, SEM,

magnetization-temperature, and magnetization-magnetic field experiments. XRD surveys reveal that Bi-2212 phase reduces considerably and some non-superconducting secondary phases prominently enhance with the introducing of $Co_3O_4$. Besides, it can be detected from the SEM images that there is a transformation from rod-like structure to plate-like structure in the microstructure with $Co_3O_4$-content. From *M-T*, it seems that there is a rapid reduction in $T_c$ values due to pair-breaking effect and localization of charge carriers through $Co_3O_4$ doping. From *M-H*, it is evident that hysteresis loop gets narrower with $Co_3O_4$ addition and temperature. In relation to this, $M_r$ value at 10 K representing flux pinning ability of the samples is 0.560 emu/gr for 0% Co sample and harshly drops to 0.027 emu/gr in 1% Co sample. Moreover, it is determined that critical current densities ($J_c$) and pinning forces ($F_p$) of the samples also reduce as a consequence escalation of structural problems and weakening of the connectivity between the superconducting clusters induced by $Co_3O_4$-doping. All in all, the discussions mentioned throughout the text plainly reveal that $Co_3O_4$ nanoparticles play an inhibitory role in creating effective pinning centers in Bi-2212 system.

**Acknowledgement**

The author expresses his deep gratitude to Prof. Dr. Bekir Özçelik for the valuable suggestions and discussions. The author dedicates this work to his children Furkan, Hakan and Ayça.

**REFERENCES**

[1] Bednorz J G, Müller K.A. Possible high Tc superconductivity in the Ba−La−Cu−O system. Z. Physik B - Condensed Matter. 1986; 64: 189–193.

[2] Bardeen J, Cooper L N., Schrieffer J R, Microscopic Theory of Superconductivity. Phys. Rev. 1957; 106: 162.

[3] Wu M K, Ashburn J R, Torng C J, Hor P H, Meng R. L., Gao L, Huang Z J, Wang Y Q, Chu C W, Superconductivity at 93 K in a new mixed-phase Y-Ba-Cu-O compound system at ambient pressure. Phys. Rev. Lett. 1987; 58: 908.

[4] Maeda H, Tanaka Y., Fukutomi M, Asano T, Togano K, Kumakura H, Uehara M, Ikeda S, Ogawa K, Horiuchi S, Matsui Y, New high-Tc superconductors without rare earth element. Physica C 1988; 153–155: 602–607.

[5] Sheng Z, Hermann A, Bulk superconductivity at 120 K in the Tl–Ca/Ba–Cu–O system. Nature. 1988; 332, 138–139.

[6] Ulgen A T, Yildirim G, Degradation in fundamental characteristic features of Bi-2212 superconducting ceramic material with Sr/Ti partial substitution. J Mater Sci: Mater Electron. 2019; 30: 8268–8277.

[7] Biju A , Aloysius R P , Syamaprasad U, Enhanced critical current density in Gd-added (Bi, Pb)-2212 bulk superconductor. Supercond. Sci. Technol. 2005; 18:1454-1459.

[8] Yildirim G, Determination of optimum diffusion annealing temperature for Au surface-layered Bi-2212 ceramics and dependence of transition temperatures on disorders, Journal of Alloys and Compounds. 2017; 699: 247-255.

[9] Maeda H, Tanaka Y, Fukutomi M, Asano T, A New High-Tc Oxide Superconductor without a Rare Earth Element Jpn. J. Appl. Phys. 27, L209.

[10] Biju A, Vinod K, Aloysius RP, Syamaprasad U, Improved superconducting properties by La addition in (Bi, Pb)-2212 bulk superconductor. J. Alloys Compd. 2007; 431: 49–55.

[11] Özçelik B, Gündoğmuş H, Yazıcı D, Effect of (Ta/Nb) co-doping on the magnetoresistivity and flux pinning energy of the BPSCCO superconductors. J Mater Sci: Mater Electron. 2014; 25: 2456–2462.

[12] Guner S B, Zalaoglu Y, Turgay T, Ozyurt O, Ulgen AT, Dogruer M, Yildirim G, A detailed research for determination of Bi/Ga partial substitution effect in Bi-2212 superconducting matrix on crucial characteristic features. Journal of Alloys and Compounds. 2019; 772: 388-398.

[13] Sedky A, Al-Battat W, Effect of Y substitution at Ca site on structural and superconducting properties of Bi:2212 superconductor. Physica B: Condensed Matter. 2013; 410: 227-232.

[14] Fallah-Arani H, Baghshahi S, Sedghi A, Stornaiuolo D, Tafuri F, Riahi-Noori N, Enhancement in superconducting properties of $Bi_2Sr_2Ca_1Cu_2O_{8+\theta}$ (Bi-2212) by means of boron oxide additive. Physica C: Superconductivity and its Applications. 2018; 548: 31-39.

[15] Ozabaci M, Sotelo A, Madre M.A, Yakinci M A, Effect of Fe Substitution for Cu on Microstructure and Magnetic Properties of Laser Floating Zone (LFZ) Grown Bi-2212 Rods. J Supercond Nov Magn 2013; 26: 1143–1149.

[16] Lu T., Zhang C, Guo S, Wu Y, Li C, Zhou L, The influence of critical current density of Bi-2212 superconductors by defects after Yb-doping, Physica C: Superconductivity and its Applications, 2015; 519:24-27.

[17] Türk N, Gündoğmuş H, Akyol M, Yakıncı Z D, Ekicibil A, Özçelik B, Effect of Tungsten (W) Substitution on the Physical Properties of Bi-(2223) Superconductors. J Supercond Nov Magn. 2014; 27: 711–716.

[18] Hamadneh I, Halim S A. Lee, C K, Characterization of $Bi_{1.6}Pb_{0.4}Sr_2Ca_2Cu_3O_y$ ceramic superconductor prepared via coprecipitation method at different sintering time. J Mater Sci. 2006; 41: 5526–5530.

[19] Li D., Zhang H, Gao X, Yang S, Chen Q, Effect of the fabrication process on the electrical properties of polycrystalline $Bi_{1.7}Pb_{0.3}Sr_2Ca_2Cu_3O_{10}$. Ceramics International. (2016) 42(1): 1728-1732.

[20] Gürsul M, Ekicibil A, Özçelik B, Sotelo A, Madre M A, Sintering Effects in Na-Substituted Bi-(2212) Superconductor Prepared by a Polymer Method. J Supercond Nov Magn 2015; 28: 1913–1924.

[21] Yazici D, Erdem M, Ozcelik B, Improvement of the Intergranular Pinning Energy in the $(BiPb)_2Sr_2Ca_2Cu_3O_{10+\delta}$ Superconductors Doped with High Valancy Cations. J Supercond Nov Magn. 2012; 25:725–729.

[22] Trastoy J, Rouco V, Ulysse C, Bernard R, Faini G, Lesueur J, Briatico J, Villegas J E, Nanostructuring of high-TC superconductors via masked ion irradiation for efficient ordered vortex pinning. Physica C 2014; 506:195-200.

[23] Boudjadja Y, Amira A, Saoudel A, Varilci A, Altintas S P, Terzioglu C, Structural and electrical properties of cerium doped Bi(Pb)-2212 phases. Physica B: Condensed Matter 2014; 443:130-135.

[24] Wei W, Schwartz J, Goretta K C, Balachandran U, Bhargava A, Effects of nanosize MgO additions to bulk $Bi_{2.1}Sr_{1.7}CaCu_2O_x$. Physica C: Superconductivity. 1998; 298(3-4): 279-288.

[25] Aftabi A, Mozaffari M, Intergranular Coupling, Critical Current Density, and Phase Formation Enhancement of Polycrystalline $Bi_{1.6}Pb_{0.4}Sr_2Ca_2Cu_3O_{10-y}$ Superconductors by α-$Al_2O_3$ Nanoparticle Addition. J Supercond Nov Magn. 2015; 28: 2337–2343.

[26] Zouaoui M, Ghattas A, Annabi M, Azzouz F B, Salem, M B, Effect of nano-size $ZrO_2$ addition on the flux pinning properties of (Bi, Pb)-2223 superconductor. Supercond. Sci. Technol. (2008); 21(12):125005.

[27] Abd-Shukor R, Kong W, Magnetic field dependent critical current density of Bi–Sr–Ca–Cu–O superconductor in bulk and tape form with addition of $Fe_3O_4$ magnetic nanoparticles. J. Appl. Phys. 2009; 105: 07E311.

[28] Kong W, Abd-Shukor R, Enhanced Electrical Transport Properties of Nano $NiFe_2O_4$-added $(Bi_{1.6}Pb_{0.4})Sr_2Ca_2Cu_3O_{10}$ Superconductor. J Supercond Nov Magn. 2010; 23:257.

[29] Liu Y, Mi C, Su L, Zhang X, Hydrothermal synthesis of $Co_3O_4$ microspheres as anode material for lithium-ion batteries, Electrochimica Acta, 2008; 53(5): 2507-2513.

[30] Younis A, Chu D, Lin X, Lee J, Li S, Bipolar resistive switching in p-type $Co_3O_4$ nanosheets prepared by electrochemical deposition. Nanoscale Res Lett. 2013; 8: 36.

[31] Santra S, Wang K, Tapec R, Tan W, Development of novel dye-doped silica nanoparticles for biomarker application. J. Biomed. Opt. 2001.

[32] Bindu Duvuru H, Alla S K, Shaw S K, Meena S S, Gupta N, Vara Prasad B.B.V.S., Kothawale M M, Kumar M K, Prasad N K, Magnetic and dielectric properties of Zn substituted cobalt oxide nanoparticles. Ceramics International. 2019; 45(13):16512-16520.

[33] Wicaksono Y A, Puspitasari P, Pratama M M A., A. Permanasari A, Sukarni S, Synthesis and characterisation of cobalt oxide ($Co_3O_4$) using sol-gel auto combustion method with stirring time variations. AIP Conference Proceedings. 2022; 2489:030031.

[34] Razavi F S, Sobhani A, Amiri O, Ghiyasiyan-Arani M, Salavati-Niasari M, Green sol-gel auto-combustion synthesis, characterization and investigation of the electrochemical hydrogen storage properties of barium cobalt oxide nanocomposites with maltose. International Journal of Hydrogen Energy. 2020; 45 (35): 17662-17670.

[35] Cullity B D, Element of X-ray Diffraction (Addition-Wesley, Reading, 1978).

[36] Dogruer M, Yildirim G, Terzioglu C, Evolution of electrical, superconducting, crystallinity and structural features with aliovalent Nd/Sr replacement in Bi-2223 ceramics. Materials Chemistry and Physics. 2022; 288: 126350.

[37] Abrikosov A A, Gor'kov L P, Contribution to the theory of superconducting alloys with paramagnetic impurities. Zh. Eksp. Teor. Fiz. 1960; 39:1781–1796.

[38] Zalaoglu Y, Yildirim G, Buyukuslu H, Saritekin N K, Varilci A, Terzioglu C, Gorur O, Important defeats on pinning of 2D pancake vortices in highly anisotropic Bi-2212 superconducting matrix with homovalent Bi/La substitution. Journal of Alloys and Compounds. 2015; 631: 111-119.

[39] Nkum R K, Punnett A, Datars W R, Substitution of 3d metals for Cu in $(Bi, Pb)_2Sr_2Ca_2Cu_3O_y$. Physica C. 1992: 20; 371-378.

[40] Maeda A, Yabe T, Takebayashi S, Hase M., Uchinokura K, Substitution of 3d metals for Cu in $Bi_2(Sr_{0.6}Ca_{0.4})_3Cu_2O_y$. Phys. Rev. B 1989; 41: 4112.

[41] Singh S, Suppression of superconductivity in Sm and Co substituted Bi Sr Ca Cu O system. Physica C. 1998; 294: 249–256.

[42] Jayaram B, Lanchester P C, Weller M T, Localization and interaction effects during superconductor-insulator transition of $Bi_2Sr_2Ca_{1-x}Gd_xCu_2O_{8+d}$, Phys. Rev. B 1991; 43: 5444.

[43] Yildirim G, Beginning point of metal to insulator transition for Bi-2223 superconducting matrix doped with Eu nanoparticles, Journal of Alloys and Compounds. 2013; 578: 526-535.

[44] Bean C P, Magnetization of Hard Superconductors. Phys. Rev. Lett. 1962; 8: 250.

[45] Gursul M, Ozcelik B, Liu M, Boltalin A I, Morozov I V, Structural and physical properties of Na-substituted $K_{0.8}Fe_{2-y}Se_2$ single crystal. Journal of Alloys and Compounds, 2019; 777: 1074-1079.

Cilt 12, Sayı 1, Sayfa 53-60, 2023 Volume 12, Issue 1, Page 53-60, 2023

Araştırma Makalesi https://doi.org/10.46810/tdfd.1235560 Research Article

Türk Doğa ve Fen Dergisi
Turkish Journal of Nature and Science
www.dergipark.gov.tr/tdfd

# Determination of Gamma Radiation Shielding Characteristics for Some Iron-Based Metallic Glasses

**Ferdi AKMAN**[1*]

[1]Bingöl University, Vocational School of Social Sciences, Department of Property Protection and Security, Program of Occupational Health and Safety, 12000, Bingöl, Türkiye
Ferdi AKMAN ORCID No: 0000-0002-8838-1762

**Corresponding author: fakman@bingol.edu.tr*

(Received: 15.01.2023, Accepted: 15.02.2023, Online Publication: 27.03.2023)

**Keywords**
Metallic glass, Gamma shielding, WinXCOM, GEANT4, FLUKA

**Abstract:** In this study, the gamma radiation shielding characteristics of metallic glasses having Fe81B13.5Si3.5C2, Fe79B16Si5, Fe78B13Si9 and Fe40Ni38B18Mo4 components and coded as FeBSiC, FeBSi1, FeBSi2 and FeNiBMo were investigated. In order to investigate, the mass attenuation coefficients for metallic glasses in the photon energies range of 0.060 MeV to 2.614 MeV were calculated with the help of WinXCOM program and GEANT4 and FLUKA simulation codes. The linear attenuation coefficient, half and tenth value layers, mean free path, effective atomic number and electron density parameters were calculated with the help of the calculated mass attenuation coefficients. Variations of the calculated gamma radiation shielding parameters with photon energy were discussed. It was observed that mass and linear attenuation coefficients, effective atomic number and electron density parameters decreased with increasing photon energy, while half and tenth value layers and mean free path parameters increased with increasing photon energy. It has been observed that metallic glasses have better gamma shielding capabilities in the low photon energy region, and metallic glass coded as FeNiBMo has better gamma radiation shielding capacity than other studied metallic glasses.



# Demir Tabanlı Bazı Metalik Camlar İçin Gama Radyasyonu Zırhlama Karakteristiklerinin Belirlenmesi

**Anahtar Kelimeler**
Metalik cam, Gama zırhlama, WinXCOM, GEANT4, FLUKA

**Öz:** Sunulan bu çalışmada, Fe81B13.5Si3.5C2, Fe79B16Si5, Fe78B13Si9 ve Fe40Ni38B18Mo4 içeriklerine sahip ve FeBSiC, FeBSi1, FeBSi2 ve FeNiBMo olarak kodlanan metalik camların gama radyasyonu zırhlama karakteristikleri incelenmiştir. İnceleme yapmak için WinXCOM programı ve GEANT4 ve FLUKA simülasyon kodları yardımıyla 0.060 MeV ila 2.614 MeV foton enerjileri aralığında metalik camların kütle azaltma katsayıları hesaplanmıştır. Hesaplanan kütle azaltma katsayıları yardımıyla lineer azaltma katsayıları, yarı ve onda-bir kalınlık değerleri, ortalama serbest yol, etkin atom numarası ve elektron yoğunluğu parametreleri hesaplanmıştır. Hesaplanan gama radyasyonu zırhlama parametrelerinin foton enerjisi ile değişimleri irdelenmiştir. Kütle ve lineer azaltma katsayıları, etkin atom numarası ve elektron yoğunluğu parametrelerinin artan foton enerjisi azaldığı gözlemlenirken, yarı ve onda-bir kalınlık değerleri ve ortalama serbest yol parametrelerinin artan foton enerjisi ile arttığı gözlemlenmiştir. Düşük foton enerjisi bölgesinde metalik camların daha iyi gama zırhlama kabiliyetlerine sahip olduğu ve FeNiBMo olarak kodlanan metalik camın incelenen diğer metalik camlara göre daha iyi gama radyasyonu zırhlama kapasitesinin olduğu gözlemlenmiştir.

## 1. INTRODUCTION

Glass generally has an amorphous, non-crystalline structure, produced from silica ($SiO_2$) and oxides of metals such as Al, Mg, Ca, K and Na. Rapid cooling of silicate and metallic oxides is provided to prevent crystallization in glasses. During this rapid cooling process, the atoms in the liquid cannot rearrange themselves into the regular periodic structure, that is, as a crystalline solid. On the other hand, the term metallic glass refers to an amorphous metallic alloy prepared by rapid solidification of the molten metallic alloy. Metallic glasses are used in electricity and

electronics because of their high electrical resistance, in nuclear reactor engineering for the preparation of magnets in nuclear waste disposal containers and fusion reactors because their magnetic properties do not change under radiation, and in the biomedical industry because they can be used as cutting, making and prosthetic materials of surgical instruments due to their high resistance to corrosion. In addition, iron (Fe) and cobalt (Co) based metallic glasses generally show ferromagnetic properties.

Today, radiation is used to benefit humanity in medicine, industry, academic studies and electricity generation. In addition, radiation has useful applications in many fields such as agriculture, space exploration, geology and archaeology. Ionizing radiation exposure causes chemical damage to body tissues. Just as with exposure to any toxic chemical, the human body can tolerate radiation up to a point without causing any injury. However, high levels of exposure can cause serious problems such as skin burns, hair loss, internal bleeding, anemia and immune system involvement. Even very high exposure increases the risk of cancer.

The guiding principle for radiation protection is the ALARA "As Low As Reasonably Achievable" concept. The three main principles that will help this concept for radiation protection are time, distance and shielding. There is a linear relationship between the time spent near a radioactive source and the exposed radiation dose. The greater distance between the radiation source and the living thing, the less dose will be exposed. So, exposure is inversely proportional to the square of the distance. When the distance from the source is doubled, the exposure level will be four times less. In these two principles, exposure to radiation is seen as inevitable. In shielding, radiation exposure can be kept to a minimum. Today, lead aprons, mobile lead shields, lead glasses or lead barriers are generally preferred for protection from ionizing radiation. Due to the known toxic effects of lead and some problems arising from its weight, the search for new radiation shielding materials as an alternative to lead has gained momentum. Glasses [1-3], alloys [4-6], concretes [7-9], composites [10-12] and minerals [13,14] are included in the search new alternative products to lead. In addition to these, the choice of metallic glasses is a new alternative for use in this field, as their elements are adjustable up to a certain point.

Olarinoye and Oche [15] determined some radiation shielding parameters using XCOM and auto-Zeff programs in the energy range of 15 keV to 15 MeV to investigate the radiation shielding properties of titanium-based two metallic glasses. As a result of the calculations, they suggested that metallic glasses $Ti_{32.8}Zr_{30.2}Ni_{5.3}Cu_9Be_{22.7}$ and $Ti_{31.9}Zr_{33.4}Fe_4Cu_{8.7}Be_{22}$ could be good radiation shielding materials. Tekin et al. [16] investigated the radiation shielding capacities of metallic glasses having eight different concentrations in $Cu_xZr_{100-x}$ (x=35 ($Cu_{35}Zr_{65}$)-70($Cu_{70}Zr_{30}$)) combination using MCNPX simulation and Phy-X/PSD interface. For this purpose, they calculated the linear and mass attenuation coefficients, half value layer, tenth value layer, mean free path, effective atomic number and electron density parameters in the energy range of 0.015 to 15 MeV. They reported that $Cu_{70}Zr_{30}$ metallic glass is a better radiation shielding material than others. Perişanoğlu [17] investigated the alpha, proton, neutron and gamma radiation shielding capabilities of $Zr_{65}Al_{7.5}Ni_{10}Cu_{17.5}$, $Ti_{40}Zr_{26}Be_{28}Fe_6$, $Cu_{49}Hf_{42}Al_9$, $Pd_{40}Ni_{40}P_{20}$, $Ni_{50}Pd_{30}P_{20}$ and $Ca_{65}Mg_{15}Zn_{20}$ metallic glasses. He noted that among the studied metallic glasses, the $Cu_{49}Hf_{42}Al_9$ sample had better alpha, proton, neutron and gamma-ray shielding ability than the others. Tamam et al. [18] investigated the effect of Cu on gamma, charged particle and neutron shielding in metallic glasses with xCu-(20-x)Ge-40Se-40Te ($0<x\leq20$) structure with the help of FLUKA simulation. They noted that 20% Cu-doped metallic glass shielded gamma, charged particles and neutrons better than the others. As can be seen from the literature review, the examination of the radiation shielding capabilities of metallic glasses is a very current issue and there are few studies on such samples.

There are two classes of metallic glasses as metal-metal and metal-metalloid. In the present study, Fe81B13.5Si3.5C2, Fe79B16Si5, Fe78B13Si9 and Fe40Ni38B18Mo4 metallic glasses belonging to the metal-metalloid class were preferred. In this study, Fe, Ni and Mo are metallic, while B, Si and C are metalloids. Gamma radiation shielding capabilities of the specified metallic glasses at energies (in the range of 0.060-2.614 MeV, 18 different energies) emitted from the most preferred radioactive sources in the literature were investigated with the help WinXCOM program [19], GEANT4 [20] and FLUKA [21] simulation codes. To compare the gamma radiation shielding capabilities of the specified metallic glasses, the mass and linear attenuation coefficients, half and tenth value layers, mean free paths, effective atomic numbers and electron densities were calculated.

## 2. MATERIAL AND METHODS

The gamma radiation shielding capacities of the specified metal-metalloid metallic glasses were investigated with the help of WinXCOM program, GEANT4 and FLUKA simulation codes. In order to estimate shielding performance, the chemical contents and densities of the metallic glasses presented in Table 1 were used.

**Table 1.** Codes, chemical compositions and densities of metallic glasses

| Sample Code | Chemical Composition (%) | | | | | | Density (g cm$^{-3}$) |
|---|---|---|---|---|---|---|---|
| | Fe | B | Si | C | Ni | Mo | |
| **FeBSiC [22]** | 81.0 | 13.5 | 3.5 | 2.0 | - | - | 7.32 |
| **FeBSi1 [23]** | 79.0 | 16.0 | 5.0 | - | - | - | 7.28 |
| **FeBSi2 [24]** | 78.0 | 13.0 | 9.0 | - | - | - | 7.18 |
| **FeNiBMo [25]** | 40.0 | 18.0 | - | - | 38.0 | 4.0 | 7.90 |

XCOM [26] is an online platform that gives partial cross-sections such as photoelectric, Compton scattering, pair production, triple production as well as attenuation coefficients of the elements, compounds or mixtures in the photon energy range from 1 keV to 100 GeV. WinXCOM is a Windows version of XCOM. GEANT4 is a code that simulates the passage of particles or photons through matter. With this code, operations such as geometry manipulation, tracking, run management and visualization can also be done. This code, which is generally used in high energy physics, is also preferred in space exploration, medical applications where radiation interactions are simulated, investigating radiation effects in semiconductors and nuclear physics. FLUKA is a code that simulates the interaction and propagation of sixty different particles, such as photons, electrons, neutrinos with matter in the energy range for 1 keV to thousands of TeV. FLUKA has usage areas such as radiation shielding studies, cosmic rays, neutrinos, detector design and dosimetry. In the presented paper, studies were carried out at photon energies of 0.060, 0.081, 0.088, 0.122, 0.136, 0.239, 0.356, 0.511, 0.569, 0.583, 0.662, 0.835, 1.063, 1.173, 1.275, 1.333, 1.770 and 2.614 MeV emitted from $^{22}$Na, $^{54}$Mn, $^{57}$Co, $^{60}$Co, $^{109}$Cd, $^{133}$Ba, $^{137}$Cs, $^{207}$Bi, $^{228}$Th and $^{241}$Am radioactive sources that are frequently used in the literature, industry, medicine and research laboratories. In the simulation codes, the interactions that can occur when ten million photons are radiated on the material are simulated. Detailed information about the simulation process has been reported in previous studies [27-28].

The mass attenuation coefficients of materials containing more than one element such as alloy, mineral, compound can be determined theoretically by the mixture rule method. In this method, the weight fraction of each element in the material and the mass attenuation coefficient of that element are multiplied to determine the contribution of the materials' total mass attenuation coefficient. After determining these additives for each element, they are summed to determine the mass attenuation coefficient of the material. The mixing rule is mathematically expressed in the equation below.

$$\left(\mu/\rho\right)_{material} = \sum_i W_i \left(\mu/\rho\right)_i \quad (1)$$

Here, $W_i$ and $(\mu/\rho)_i$ are weight fraction and the mass reduction coefficient of the $i^{th}$ element. The weight fraction of elements in a material can be determined using the following equation.

$$W_i = \frac{n_i A_i}{\sum_j n_j A_j} \quad (2)$$

In the equation, $n_i$ and $A_i$ express the element number and atomic weight of the $i^{th}$ element in the material. The mass attenuation coefficient is a parameter independent of the density and phase state of the material. The linear attenuation coefficient is a parameter that changes with the density and phase state of the material and can be calculated from the mathematical multiply of the mass attenuation coefficient and the density of the material.

With the help of linear attenuation coefficient, half value layer (HVL), tenth value layer (TVL) and mean free path (MFP) parameters can be determined. They are defined as the material thickness that passes 50%, 10% and 36.8% of the initial radiation intensity, respectively, and these parameters can be determined with the help of the below equations.

$$HVL = \frac{ln2}{\mu} = \frac{0.693}{\mu} \quad (3)$$

$$TVL = \frac{ln10}{\mu} = \frac{2.303}{\mu} \quad (4)$$

$$MFP = \frac{1}{\mu} \quad (5)$$

The molecular, atomic and electronic cross-sections can be determined with the help of the mass attenuation coefficient. The molecular cross-section is determined by the following equation.

$$\sigma_{t,m} = \frac{1}{N}\left(\mu/\rho_{mater}\right)\sum_i (n_i A_i) \quad (6)$$



Here, N, $(\mu/\rho)_{mater}$, $n_i$ and $A_i$ are the Avogadro number, the total mass attenuation coefficient of the material, the element number and atomic weight of the $i^{th}$ element in the material, respectively. The relationship between the molecular cross-section and the atomic cross-section is shown in equation 7.

$$\sigma_{t,a} = \sigma_{t,m}/\sum_i n_i \quad (7)$$

The electronic cross-section could be obtained using equation 8.

$$\sigma_{t,e} = \frac{1}{N}\sum_i \frac{f_i A_i}{Z_i}\left(\mu/\rho\right)_i \quad (8)$$

Here, $f_i$, $(\mu/\rho)_i$ and $Z_i$ express the abundance fraction, mass attenuation coefficient and atomic number of the $i^{th}$ element in the material, respectively. The effective atomic number is a parameter that can be obtained by dividing the atomic cross-section with electronic cross-section, and its mathematical representation is presented below.

$$Z_{eff} = \frac{\sigma_{t,a}}{\sigma_{t,e}} \quad (9)$$

Finally, the effective electron density can be

determined with the help of the equation 10.

$$N_E = \frac{Z_{eff}}{A_{tot}}(Nn_{tot}) \quad (10)$$

Here, $A_{tot}$ ve $n_{tot}$ are the total atomic weight and number of elements in the material, respectively.

## 3. RESULTS AND DUSCUSSION

In the present study, gamma radiation shielding parameters of metallic glasses, whose codes, chemical components and densities are given in Table 1, were investigated in the photon energy range of 0.060 MeV to 2.614 MeV using WinXCOM program, GEANT4 and FLUKA simulation codes.

On this purpose, first of all, the mass attenuation coefficients of metallic glasses were determined by using the specified program and simulation codes. In Figure 1, the variation of the mass attenuation coefficients of the investigated metallic glasses according to the photon energy is presented, and in Table 2 the results of the mass attenuation coefficients of WinXCOM, GEANT4 and FLUKA are listed. When Figure 1 and Table 2 are examined, it is seen that the mass attenuation coefficients decrease exponentially with increasing photon energy and this parameter varies according to the elements in the metallic glasses. As seen in Figure 1, while the mass attenuation coefficients show a sharp decrease in the low energy region, this decrease is lower in the medium and high energy region. The reductions in these energy regions can be explained by the interaction events of the photon with matter. The dominant interaction process in the low energy region is the photoelectric event, while the dominant processes in the medium and high energy regions are Compton scattering and pair production events, respectively. Photoelectric cross-section depends on photon energy and atomic number as $E^{-3.5}$ and $Z^{4-5}$, respectively. While the relationship between Compton scattering cross-section between energy and atomic number is $E^{-1}$ and Z, these dependencies are E and $Z^2$ for the pair production cross-section. Considering these proportionalities, the exponential decrease in the change of the mass attenuation coefficients with the photon energy is better understood. As can be seen in Figure 1 and Table 2, coded as FeNiBMo metallic glass containing nickel and molybdenum instead of low iron ratio has higher mass attenuation coefficients, especially in the low energy region. Therefore, this metallic glass has better gamma radiation shielding than other studied metallic glasses.

The linear attenuation coefficient, which is determined by the mass attenuation coefficient and the density of the material, is a more important gamma radiation shielding parameter in terms of usability. The graph of the linear attenuation coefficients depending on the photon energy for the investigated metallic glasses is shown in Figure 2.



**Table 2**. The mass attenuation coefficient results of WinXCOM, GEANT4 and FLUKA ($cm^2\ g^{-1}$) for metallic glasses

| Energy (MeV) | FeBSiC | | | FeBSi1 | | | FeBSi1 | | | FeNiBMo | | |
|---|---|---|---|---|---|---|---|---|---|---|---|---|
| | WinX. | GEANT4 | FLUKA | WinX. | GEANT4 | FLUKA | WinX. | GEANT4 | FLUKA | WinX. | GEANT4 | FLUKA |
| 0.060 | 1.012 | 0.929 | 1.150 | 0.993 | 0.911 | 0.995 | 0.989 | 0.907 | 0.991 | 1.256 | 1.159 | 1.545 |
| 0.081 | 0.499 | 0.452 | 0.556 | 0.492 | 0.445 | 0.492 | 0.490 | 0.443 | 0.490 | 0.603 | 0.550 | 0.720 |
| 0.088 | 0.420 | 0.380 | 0.464 | 0.414 | 0.374 | 0.414 | 0.413 | 0.373 | 0.413 | 0.502 | 0.456 | 0.594 |
| 0.122 | 0.239 | 0.216 | 0.256 | 0.236 | 0.214 | 0.237 | 0.236 | 0.214 | 0.236 | 0.271 | 0.246 | 0.307 |
| 0.136 | 0.206 | 0.187 | 0.219 | 0.204 | 0.186 | 0.205 | 0.204 | 0.186 | 0.204 | 0.230 | 0.209 | 0.256 |
| 0.239 | 0.124 | 0.117 | 0.126 | 0.123 | 0.117 | 0.123 | 0.124 | 0.117 | 0.124 | 0.129 | 0.122 | 0.149 |
| 0.356 | 0.099 | 0.096 | 0.100 | 0.099 | 0.096 | 0.099 | 0.099 | 0.096 | 0.099 | 0.101 | 0.098 | 0.103 |
| 0.511 | 0.083 | 0.082 | 0.083 | 0.083 | 0.082 | 0.083 | 0.083 | 0.082 | 0.083 | 0.084 | 0.083 | 0.090 |
| 0.569 | 0.079 | 0.078 | 0.079 | 0.079 | 0.078 | 0.079 | 0.079 | 0.078 | 0.079 | 0.080 | 0.079 | 0.082 |
| 0.583 | 0.078 | 0.077 | 0.079 | 0.078 | 0.077 | 0.078 | 0.078 | 0.077 | 0.078 | 0.079 | 0.078 | 0.082 |
| 0.662 | 0.073 | 0.073 | 0.073 | 0.073 | 0.073 | 0.073 | 0.074 | 0.073 | 0.074 | 0.074 | 0.074 | 0.076 |
| 0.835 | 0.066 | 0.066 | 0.066 | 0.066 | 0.066 | 0.066 | 0.066 | 0.066 | 0.076 | 0.066 | 0.066 | 0.069 |
| 1.063 | 0.058 | 0.058 | 0.058 | 0.058 | 0.058 | 0.058 | 0.058 | 0.058 | 0.058 | 0.058 | 0.058 | 0.059 |
| 1.173 | 0.055 | 0.055 | 0.055 | 0.055 | 0.055 | 0.055 | 0.055 | 0.055 | 0.055 | 0.056 | 0.056 | 0.056 |
| 1.275 | 0.053 | 0.053 | 0.053 | 0.053 | 0.053 | 0.053 | 0.053 | 0.053 | 0.053 | 0.053 | 0.053 | 0.054 |
| 1.333 | 0.052 | 0.052 | 0.052 | 0.052 | 0.052 | 0.052 | 0.052 | 0.052 | 0.052 | 0.052 | 0.052 | 0.052 |
| 1.770 | 0.045 | 0.045 | 0.045 | 0.045 | 0.045 | 0.045 | 0.045 | 0.045 | 0.045 | 0.045 | 0.045 | 0.046 |
| 2.614 | 0.038 | 0.038 | 0.038 | 0.038 | 0.038 | 0.038 | 0.038 | 0.038 | 0.038 | 0.038 | 0.038 | 0.038 |

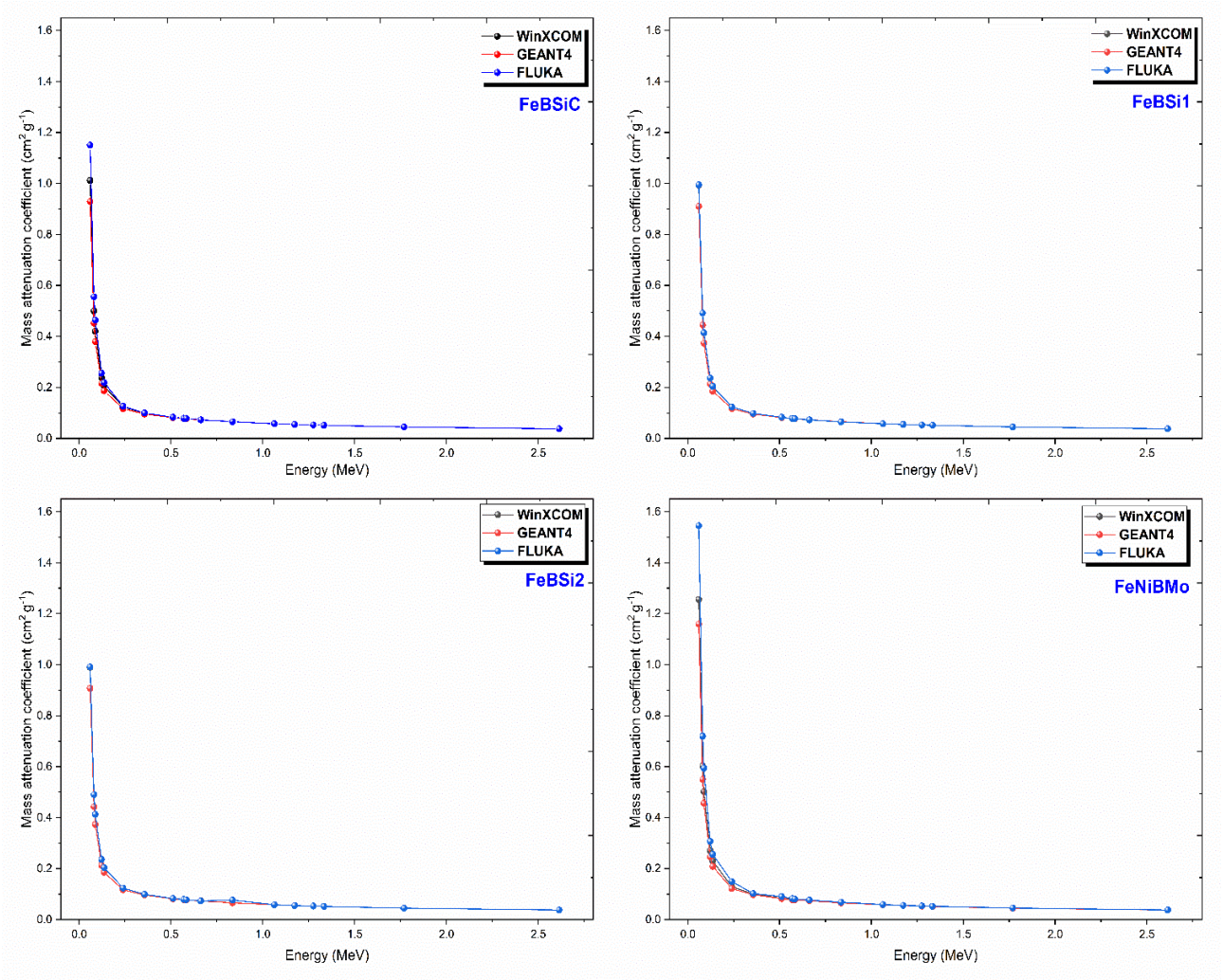


**Figure 1.** Variation of mass attenuation coefficients with photon energy for the studied metallic glasses

As can be seen in Figure 2, the variation of linear attenuation coefficients with energy shows a similar trend as the variation of mass attenuation coefficients with energy. That is, the linear attenuation coefficients decrease exponentially with increasing photon energy. At 0.060 MeV, linear attenuation coefficients of FeBSiC, FeBSi1, FeBSi2 and FeNiBMo metallic glasses are 7.4086, 7.2310, 7.1031 and 9.9196 cm$^{-1}$, respectively, while these values are 0.5372, 0.5338, 0.5280 and 0.5842 cm$^{-1}$ at 0.662 MeV, respectively. It is seen that the difference between the linear attenuation coefficients decreases as the photon energy increases. This can be explained by photon-matter interaction processes as interpreted by the mass attenuation coefficients in the low, medium and high energy regions. While the investigated metallic glasses show good gamma radiation shielding properties in the low energy region, coded as FeNiBMo metallic glass with high linear attenuation coefficients and density has higher gamma radiation shielding capacity than the others.

Other parameters that are important for material usability are half and tenth value layers and mean free path. The variation of these parameters with photon energy is shown in Figures 3-5, respectively. As can be seen from Equation 3-5, these parameters are inversely proportional to the linear attenuation coefficient and these parameters are important parameters as they indicate the absorber thickness required to reduce certain amounts of radiation intensity.

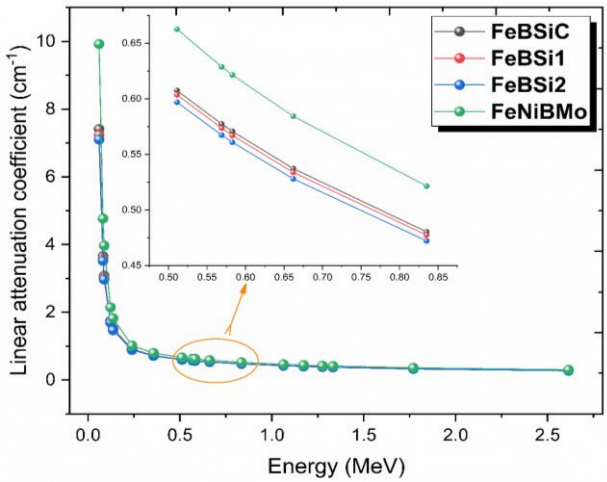


**Figure 2.** Variation of linear attenuation coefficients with photon energy for the studied metallic glasses

It can be seen from Figures 3-5 that these parameters increase with increasing photon energy since they are

inversely proportional to the linear attenuation coefficient. At 0.060 MeV, the half value layers of FeBSiC, FeBSi1, FeBSi2 and FeNiBMo metallic glasses are 0.0936, 0.0959, 0.0976 and 0.0699 cm, respectively, according to WinXCOM results, while these values are 1.2902, 1.2985, 1.3127 and 1.1864 cm, respectively at 0.662 MeV. So, in order to reduce half of the incident radiation intensity at photon energies of 0.060 and 0.662 MeV, the investigated metallic glasses must have the above-mentioned thicknesses. When the half value layers at the mentioned energies above and Figures 3-5 are examined, coded as FeNiBMo metallic glass has lower half and tenth value layers and mean free path values. Therefore, this metallic glass is a better gamma radiation shielding material than others.

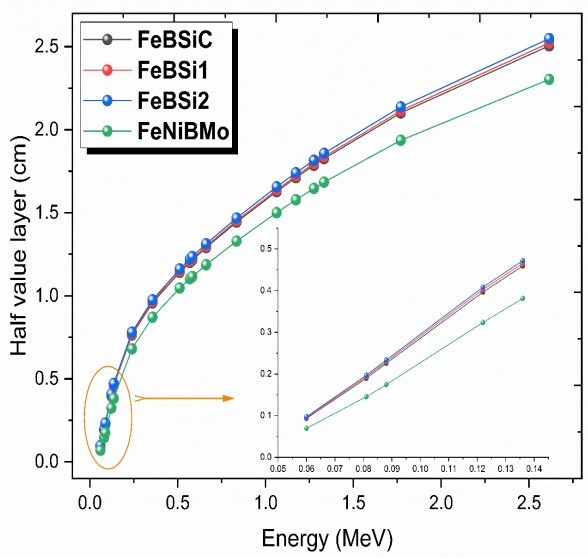


**Figure 3.** Variation of half value layers with photon energy for the studied metallic glasses

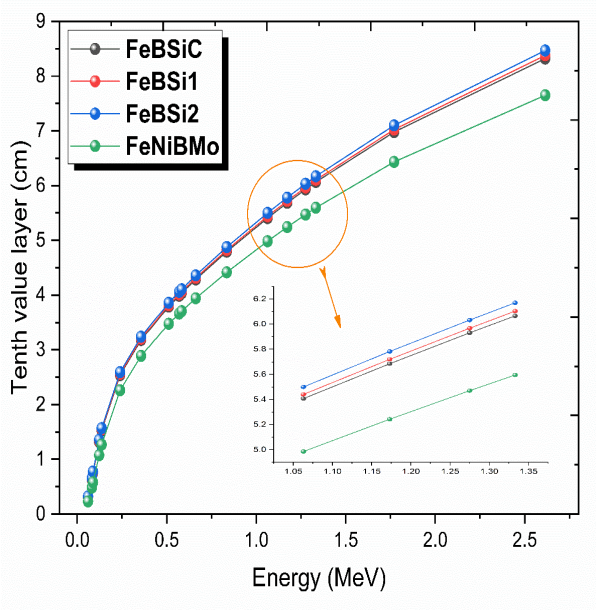


**Figure 4.** Variation of tenth value layers with photon energy for the studied metallic glasses

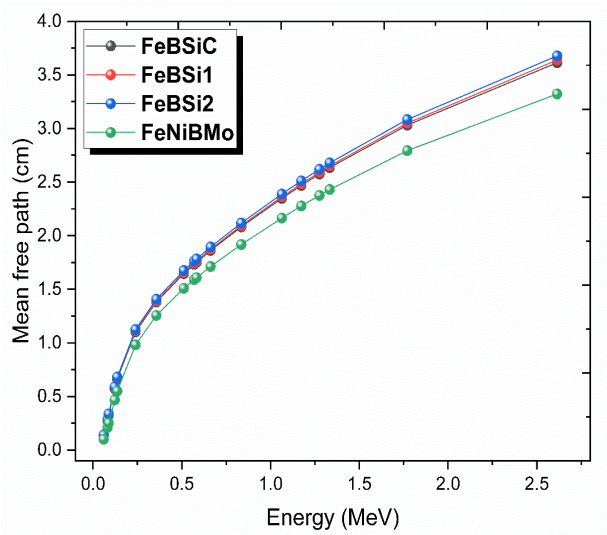


**Figure 5.** Variation of mean free path with photon energy for the studied metallic glasses

The determined another parameter using the mass attenuation coefficient is the effective atomic number. The large values of the effective atomic number indicate that the material is a good gamma radiation shielding material. The variation of the effective atomic numbers with the photon energy for the investigated metallic glasses is seen in Figure 6. As seen from the figure, the effective atomic numbers of metallic glasses are listed as FeNiBMo>FeBSiC>FeBSi2>FeBSi1. Also, as seen in Figure 6, the effective atomic number decreases exponentially with photon energy. Changes in different energy regions can be interpreted according to photoelectric, Compton scattering and pair production cross-sections, as explained in other parameters.



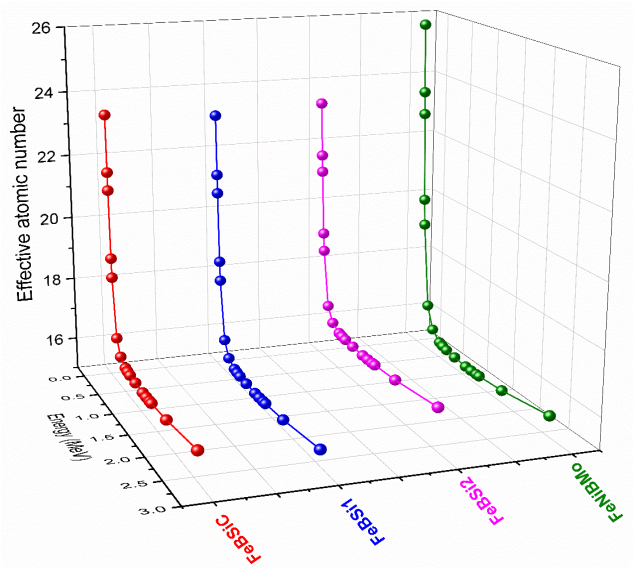


**Figure 6.** Variation of effective atomic number with photon energy for the studied metallic glasses

The effective electron density is a parameter related to the effective atomic number and their variation with photon energy is presented in Figure 7. According to

this figure, the effective electron densities are listed as FeNiBMo>FeBSiC>FeBSi1>FeBSi2. When Equation 10 is examined, there is a direct proportionality between the effective atomic number and the effective electron density. So, as the effective atomic number increases, the effective electron density also increases, or vice versa. This proportionality can be seen in Figure 8. However, the effective electron density is directly proportional to the total number of atoms in the material and inversely proportional to the sum of the atomic weights of the elements in the material, except for the effective atomic number. The effective atomic number of FeBSi2 sample is greater than that of FeBSi1 sample, but the effective electron density of FeBSi2 is smaller than that of FeBSi1. This difference is due to the number or atomic weights of the elements in the metallic glass. When the figures for effective number and electron density are examined, FeNiBMo metallic glass has better gamma radiation shielding than other metallic glasses.

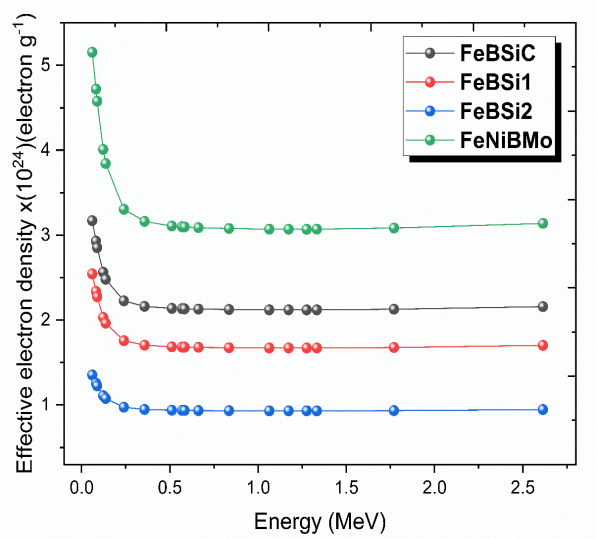


**Figure 7.** Variation of effective electron density with photon energy for the studied metallic glasses

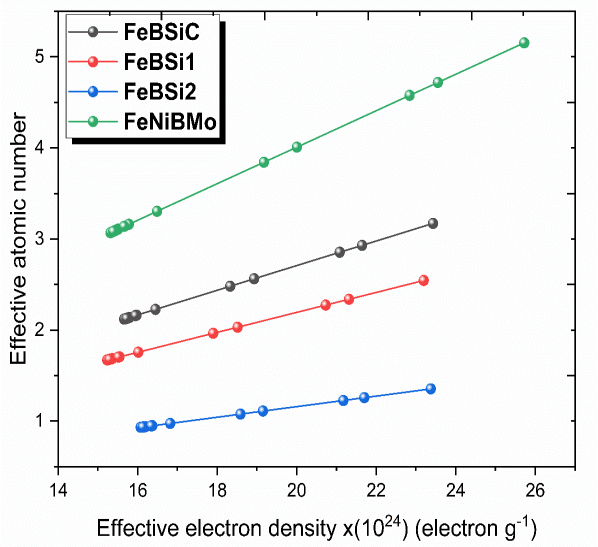


**Figure 8.** Variation of effective atomic number with effective electron density

## 4. CONCLUSIONS

In the present study, the gamma radiation shielding capacities of Fe81B13.5Si3.5C2, Fe79B16Si5, Fe78B13Si9 and Fe40Ni38B18Mo4 metallic glasses were investigated in the photon energies range of 0.060 to 2.614 MeV (18 different energies). For this, WinXCOM program, GEANT4 and FLUKA simulation codes are used. It was observed that mass and linear attenuation coefficients, effective atomic number and electron density parameters decreased with increasing photon energy, while half and tenth value layers and mean free path parameters increased with increasing photon energy for the investigated metallic glasses. When all the calculated gamma radiation shielding parameters were examined, it was observed that all metallic glasses had good gamma radiation shielding characteristics in the low energy region, and metallic glass coded as FeNiBMo had better gamma shielding capacity than other metallic glasses. The investigated metallic glasses can be used in electrical and electronics, nuclear waste disposal containers, nuclear reactors in terms of shielding gamma radiation, as well as radiation-related units of hospitals, space research and laboratories where radiation studies are carried out.

## REFERENCES

[1] Halimah MK, Azuraida A, Ishak M, Hasnimulyati L. Influence of bismuth oxide on gamma radiation shielding properties of boro-tellurite glass. J Non-cryst Solids. 2019; 512: 140-7.

[2] Al-Buriahi MS, Sriwunkum C, Arslan H, Tonguc BT, Bourham MA. Investigation of barium borate glasses for radiation shielding applications. Appl Phys A-Mater. 2020; 126(1): 1-9.

[3] El-Sharkawy RM, Shaaban KS, Elsaman R, Allam EA, El-Taher A, Mahmoud ME. Investigation of mechanical and radiation shielding characteristics of novel glass systems with the composition xNiO-20ZnO-60B2O3-(20-x) CdO based on nanometal oxides. J Non-cryst Solids. 2020; 528: 119754.

[4] Kaur T, Vermani YK, Al-Buriahi MS, Alzahrani JS, Singh T. Comprehensive investigations on radiation shielding efficacy of bulk and nano Pb-Sn-Cd-Zn alloys. Phys Scripta. 2022; 97(5): 055009.

[5] Turhan MF, Akman F, Taşer A, Dilsiz K, Oğul H, Kacal MR, et al. Gamma radiation shielding performance of CuxAg (1-x)-alloys: Experimental, theoretical and simulation results. Prog Nucl Energ. 2022; 143: 104036.

[6] Alzahrani JS, Alrowaili ZA, Eke C, Mahmoud ZM, Mutuwong C, Al-Buriahi MS. Nuclear shielding properties of Ni-, Fe-, Pb-, and W-based alloys. Radiat Phys Chem. 2022; 195: 110090.

[7] Zeyad AM, Hakeem IY, Amin M, Tayeh BA, Agwa IS. Effect of aggregate and fibre types on ultra-high-performance concrete designed for radiation shielding. J Build Eng. 2022; 58: 104960.

[8] Kharita MH, Takeyeddin M, Alnassar M, Yousef S. Development of special radiation shielding concretes using natural local materials and evaluation of their shielding characteristics. Prog Nucl Energ. 2008; 50(1): 33-6.
[9] Makarious AS, Bashter II, Abdo AES, Azim MSA, Kansouh WA. On the utilization of heavy concrete for radiation shielding. Ann Nucl Energy. 1996; 23(3): 195-206.
[10] Cherkashina NI, Pavlenko VI, Noskov AV. Radiation shielding properties of polyimide composite materials. Radiat Phys Chem. 2019; 159: 111-7.
[11] Saleh HM, Bondouk II, Salama E, Esawii HA. Consistency and shielding efficiency of cement-bitumen composite for use as gamma-radiation shielding material. Prog Nucl Energ. 2021; 137: 103764.
[12] Okafor CE, Okonkwo UC, Okokpujie IP. Trends in reinforced composite design for ionizing radiation shielding applications: a review. J Mat Sci. 2021; 56(20): 11631-55.
[13] Özdemir HG, Demirkol İ, Erkoyuncu İ, Yılmaz M, Kaçal MR, Akman F. Bazı Tungsten İçerikli Minerallerin Gama Zırhlama Özelliklerinin Geniş Enerji Aralığında İncelenmesi. J Inst Sci Tech. 2022; 12(4): 2175-87.
[14] Turhan MF, Akman F, Kaçal MR, Durak R. Calculation of Absorption Parameters for Some Selected Minerals in the Energy Range of 1 keV to 100 GeV. Int J Sci Eng Res. 2019; 10(9): 56-61.
[15] Olarinoye O, Oche C. Gamma-ray and fast neutron shielding parameters of two new titanium-based bulk metallic glasses. Iran J Med Phys. 2021; 18(2): 139-147.
[16] Tekin HO, ALMisned G, Susoy G, Zakaly HM, Issa SA, Kilic G, et al. A detailed investigation on highly dense CuZr bulk metallic glasses for shielding purposes. Open Chem. 2022; 20(1): 69-80.
[17] Perişanoğlu U. Assessment of nuclear shielding and alpha/proton mass stopping power properties of various metallic glasses. Appl Phys A-Mater. 2019; 125(11): 1-11.
[18] Tamam N, Alrowaili ZA, Elqahtani ZM, Somaily HH, Alwadai N, Sriwunkum C, et al. Significant influence of Cu content on the radiation shielding properties of Ge-Se-Te bulk glasses. Radiat Phys Chem. 2022; 193: 109981.
[19] Gerward L, Guilbert N, Jensen KB, Levring H. WinXCom—a program for calculating X-ray attenuation coefficients. Radiat Phys Chem. 2004; 71(3-4): 653-4.
[20] Agostinelli S, Allison J, Araujo H, Arce P, Asai M, Axen D, et al. GEANT4-a simulation toolkit. Nucl Instrum Meth A. 2003; 506 (3): 250-303.
[21] Böhlen TT, Cerutti F, Chin MPW, Fassò A, Ferrari A, Ortega PG, et al. The FLUKA code: developments and challenges for high energy and medical applications. Nucl Data Sheets. 2014; 120: 211-4.
[22] Goodfellow [Internet]. [cited 2023 Feb 05] Available from: https://www.goodfellow.com/uk/en-gb/displayitemdetails/p/fe80-fl-000150/iron-boron-silicon-foil
[23] Goodfellow [Internet]. [cited 2023 Feb 05] Available from: https://www.goodfellow.com/uk/en-gb/displayitemdetails/p/fe82-fl-000150/iron-boron-silicon-foil
[24] Goodfellow [Internet]. [cited 2023 Feb 05] Available from: https://www.goodfellow.com/uk/en-gb/displayitemdetails/p/fe81-fl-000150/iron-boron-silicon-foil
[25] Goodfellow [Internet]. [cited 2023 Feb 05] Available from: https://www.goodfellow.com/uk/en-gb/displayitemdetails/p/fe83-fl-000150/iron-nickel-boron-foil
[26] Gerward L, Guilbert N, Jensen KB, Levring H. X-ray absorption in matter. Reengineering XCOM. Radiat Phys Chem. 2011; 60(1-2): 23-4.
[27] Kilicoglu, O, Akman F, Oğul H, Agar O, Kara U. Nuclear radiation shielding performance of borosilicate glasses: Numerical simulations and theoretical analyses. Radiat Phys Chem. 2023; 204: 110676.
[28] Ozdogan, H, Kilicoglu O, Akman F, Agar O. Comparison of Monte Carlo simulations and theoretical calculations of nuclear shielding characteristics of various borate glasses including Bi, V, Fe, and Cd. Appl Radiat Isotopes. 2022; 189: 110454.

Cilt 12, Sayı 1, Sayfa 61-67, 2023 Volume 12, Issue 1, Page 61-67, 2023

Araştırma Makalesi https://doi.org/10.46810/tdfd.1162900 Research Article

Türk Doğa ve Fen Dergisi
Turkish Journal of Nature and Science
www.dergipark.gov.tr/tdfd

# Effects of Dietary Momordica Charantia Supplementations on Broiler Performance, Blood Parameters, Meat Quality and Intestinal Morphology

**Güler YENİCE[1*], Mustafa ATASEVER[2a], Adem KARA[3], Seçkin ÖZKANLAR[4], Sevda URÇAR GELEN[2b], Semin GEDİKLİ[5]**

[1] Atatürk University, Faculty of Veterinary Medicine, Department of Animal Nutrition and Nutritional Disorders, Erzurum, Türkiye
[2] Atatürk University, Faculty of Veterinary Medicine, Department of Food Hygiene and Technology, Erzurum, Türkiye
[3] Erzurum Technical University, Faculty of Science, Department of Molecular Biology and Genetics, Erzurum, Türkiye
[4] Atatürk University, Faculty of Veterinary Medicine, Department of Biochemistry, Erzurum, Türkiye
[5] Atatürk University, Faculty of Veterinary Medicine, Department of Histology and Embryology, Erzurum, Türkiye
Güler YENİCE ORCID No: 0000-0003-0819-8843
Mustafa ATASEVER ORCID No: 0000-0002-1627-5565
Adem KARA ORCID No: 0000-0002-5766-6116
Seçkin ÖZKANLAR ORCID No: 0000-0001-7717-797X
Sevda URÇAR GELEN ORCID No: 0000-0002-1852-3614
Semin GEDİKLİ ORCID No: 0000-0001-8238-7226

**Corresponding author: gulerata@atauni.edu.tr*

(Received: 17.08.2022, Accepted: 17.02.2023, Online Publication: 27.03.2023)

**Keywords**
Phytoextract, Momordica charantia, Broiler, Performance, Intestinal morphology

**Abstract:** Momordica charantia (MC) is one of the most often used medicinal plants, a rich source of vitamins and minerals. This study aimed to assess the effects of a food supplementation of MC extract at various doses (0, 0.15, 0.30, 0.45 g $kg^{-1}$) on the performance, carcass yield, meat quality, intestinal morphology, and some blood parameters in broilers. A total of 288 Ross 308 broiler chicks (1 day old) were used in the experiment. Animals were divided into 4 groups with 6 replicates. Feed intake (FI), daily weight gain (DWG), feed conversion rate (FCR), and carcass yield were unaffected by MC extract supplementations. The group treated with a high dosage of MC extract had significantly lower serum phosphor (P) levels than the other groups ($P<0.05$). In the small intestine sections of the MC supplemented groups, goblet cell number (GCN), crypt depth (CD), villus length (VL), and epithelial height (EH) had significantly increased ($P<0.05$). Conversely, MC had a quite limited and variable effect on meat quality parameters. In conclusion, the MC extract doses studied in the study have no significant effect on the performance of the broiler. Furthermore, contrasting several dosages in different housing and health conditions plans can be essential.



# Momordica Charantia Katkısının Broilerde Performans, Biyokimyasal Parametreler, Et Kalitesi ve Bağırsak Morfolojisi Üzerine Etkileri

**Anahtar Kelimeler**
Bitkisel ekstrakt, Momordica charantia, Broiler, Performans, Bağırsak morfolojisi

**Öz:** açısından zengin, yaygın olarak kullanılan tıbbi bitkilerden biridir. Sunulan çalışmada, etlik piliçlerde rasyona farklı seviyelerde MC ekstraktı (0, 0.15, 0.30, 0.45 g $kg^{-1}$) takviyesinin performans, karkas verimi, et kalitesi, bağırsak morfolojisi ve bazı kan parametreleri üzerine etkileri değerlendirilmiştir. Çalışmada toplam 288 adet Ross 308 etlik civciv (1 günlük) kullanılmıştır. Hayvanlar altı tekerrürlü dört gruba ayrıldı. MC ekstraktı takviyesi yem tüketimi, günlük canlı ağırlık artışı, yemden yararlanma oranı ve karkas verimini etkilememiştir. Yüksek doz MC ekstraktı ilave edilen grupta serum P seviyeleri, diğer gruplardan önemli ölçüde daha düşüktü ($P<0.05$). MC ekstraktı ilave edilen grupların ince bağırsak bölümlerinde, goblet hücre sayısı, kript derinliği, villus uzunluğu ve epitel yüksekliği önemli ölçüde artış göstermiştir ($P<0.05$). Bununla birlikte MC'nin et kalite parametreleri üzerinde oldukça sınırlı ve değişken bir etkisi oldu. Sonuç olarak, çalışmada kullanılan dozlarda MC ekstraktının Broiler'de performans üzerine herhangi bir etkisi olmamıştır. Farklı barınma ve sağlık koşullarında farklı doz rejimlerini karşılaştırmak gerekli olabilir.

## 1. INTRODUCTION

Momordica charantia L. (MC) is a plant used for food and medicine that generally grows in tropical regions. The fruit and leaves of MC are rich in minerals and vitamins, and also contain numerous chemicals such as glycosides, saponins, alkaloids, fixed oils, triterpenes, proteins, and steroids, which are biologically active compounds [1,2]. Anti-diabetic [3,4], antimalarial [5], antiviral [6], anthelmintic [7], antitumor [8,9], antifungal, and antimicrobial [10] properties of MC are reported. Also, it is reported that MC extract has sanitizer properties and can be used as a preservative/sanitizer in the food industry [11]. Shahadat et al. [7] reported that, besides its anthelmintic effect, MC extract (30 g/liter drinking water) provides live weight gain in chickens infected with Ascaridia galli. Likewise, it has been reported that extract of MC improved the body weight of broiler chickens as feed additives, reduced liver function enzymes, and changed the lipid profile [12]. Nevertheless, comprehensive studies on the effect of MC on poultry performance are not enough. Thus, it is not clear whether MC has any growth-promoting effects on broiler chicken. This study was conducted to investigate the effects of adding MC extract to broiler rations at different doses on performance, carcass characteristics, some biochemical parameters, meat quality, and intestinal histopathology.

## 2. MATERIAL AND METHOD

The Atatürk University Animal Experiments Local Ethics Committee authorized the study's experimental procedure in its decision dated 30 June 2016 and numbered 113.

### 2.1. Experimental Design

A total of 288 Ross 308 male broiler chicks (1 day old) were used in the experiment. Animals were divided into 4 groups with 6 replicates and 12 animals in each replicate. The first group was separated as control and MC extract was added to the basal ration in other groups respectively 0.15, 0.30, and 0.45 g kg-1. All groups were fed ad libitum with broiler starter feed (22% crude protein, 12.2 MJ ME kg-1) between 1-21 days and broiler grower-finisher feed (19% crude protein, 13.4 MJ ME kg-1) between 22-42 days. The diet formulation meets the nutritional requirements of the National Research Council (NRC) for broiler chickens [13]. The ambient temperature was kept at 32-35 °C during the first week, then gradually lowered to 22 °C until the end of the experiment. During the trial period, fluorescent lighting was applied 23 hours a day.

### 2.2. Performance Parameters

The experiment lasted for 42 days, and weekly (7, 14, 21, 28, 35, and 42. days) feed intake (FI), and body weights (BW) were determined by weighing. Daily weight gains (DWG) and feed conversion rates (FCR) were determined by calculation (FCR=Total feed consumption/Total weight gain). At the end of the experiment, 15 broilers from each group (3 broilers from each subgroup) were slaughtered to determine the carcass yield.

### 2.3. Histopathological Analysis

At the end of the study, animals were sacrificed then for histological analysis of duodenum, jejunum, and ileum tissues were excised. The tissues were fixed in 10% buffered formol solution for 48 hours. Then, the tissues were passed through alcohol and xylol series with standard histological methods and embedded in paraffin blocks. Sections of 5 µm thickness taken from paraffin blocks with a Leica RM2125RT microtome (Leica Microsystems, Wetzlar, Germany) were stained with Crossman's triple staining to evaluate the crypt depth (CD), villus length (VL), and epithelial height (EH). In order to determine the distribution and histochemical structure of goblet cells, Periodic Acid Shift (PAS) staining was applied to transversal serial sections of 5-7 µm taken from each block.

For this purpose, goblet cells were counted in the villi and crypt epithelium of the 30000 µm (20 lenses) long region in the villi and crypts in serial sections taken from each block. Goblet cell averages falling to 1 mm were measured manually by Cameram SLR 6.1 image analysis program (Mikro Sistem Ltd., Turkey) and their arithmetic averages were calculated.

### 2.4. Meat Quality Analysis



Drumstick and breast meat were removed from broilers that had been slaughtered and brought to the lab under sanitary circumstances, and they were kept for nine days at 4°C. On meat samples taken on the first, third, fifth, seventh, and ninth days of storage chemical analyses were carried out such as water activity (aw), pH, thiobarbituric acid reactive substances (TBARS), and colors [L* (relative lightness), a* (relative redness), and b* (relative yellowness)]. Micrococcus/Staphylococcus, Pseudomonas spp., TMAB (total mesophyll aerobic bacteria), TPAB (total psychrophile aerobic bacteria), and the number of Coliform group bacteria were all measured to assess microbiological characteristics.

The aw value was determined using the Aqualab 4TE (USA) instrument. After homogenization, pH values were assessed using a pH meter (WTW Inolab, Germany) [14].

The findings of the analysis of TBARS, which was done as Lemon [15] specified, are presented in µmol malonaldehyde/kg (µmolMDA/kg).

The samples' cross-sectional surface color intensities (L *, a *, and b *) were measured using by Minolta colorimeter (CR-200, Minolta Co, Osaka, Japan).

### 2.5. Biochemical Analyses

The blood samples collected during the sacrifice process of the animals were centrifuged at 1500 rpm for 5

minutes, and the serum samples obtained were stored at -80 °C until biochemical analyses. In blood serum samples, alkaline phosphatase (ALP), triglyceride (TG), cholesterol, high-density lipoprotein (HDL), low-density lipoprotein (LDL), calcium (Ca), phosphor (P), total protein, albumin, glucose, creatinine, and uric acid were analyzed using commercial kits on the Beckman Coulter AU5800 (Beckman Coulter Inc., USA) auto analyzer.

### 2.1. Statistical Analysis

With the aim of determining the statistical significance between the groups, analysis of variance (ANOVA) was performed using the SPSS 20.00 package program (IBM Inc, NY, USA), and the statistical difference between the groups ($p<0.05$) was determined according to the Duncan Post Hoc test.

## 3. RESULTS AND DISCUSSION

Most medicinal plants can successfully boost animals' growth performance, which makes them more valuable and popular in the poultry industry. Due to its bioactive components such as sterol and saponin triterpenoids, saponins, polypeptides, flavonoids, alkaloids, and sterols, MC has antidiabetic, antiviral, antimalarial, anthelmintic, antitumor, antioxidant and antimicrobial properties [16]. Nevertheless, comprehensive studies on the effect of MC on poultry performance are not enough. A limited number of previous studies have reported that the addition of 3% MC extract to drinking water improves body weight in broilers [12] and increases body weight in Ascaridia galli-infected chickens [7]. The results obtained in the current study showed that MC supplementation improved FCR depending on the dose and reduced FI. Nevertheless, it has no significant effect ($P>0.05$) on final BW, FI, DWG, FCR, and carcass yield (Table 1).

**Table 1.** Performance parameters and carcass yield.

| Days | Parameters | Control | MC-15 | MC-30 | MC-45 | SEM | *P-values* |
|---|---|---|---|---|---|---|---|
| | Initial BW (g) | 56.3 | 55.9 | 55.9 | 56.0 | 0.001 | ns |
| | Final BW (g) | 2839.17 | 2669.53 | 2597.49 | 2738.76 | 33.69 | ns |
| 0-21 | DWG | 0.046 | 0.045 | 0.044 | 0.046 | 0.001 | ns |
| | FI | 0.067 | 0.065 | 0.065 | 0.064 | 0.001 | ns |
| | FCR | 1.468 | 1.47 | 1.478 | 1.399 | 0.038 | ns |
| 21-42 | DWG | 0.087 | 0.08 | 0.077 | 0.082 | 0.002 | ns |
| | FI | 0.192 | 0.167 | 0.173 | 0.174 | 0.007 | ns |
| | FCR | 2.215 | 2.088 | 2.245 | 2.126 | 0.048 | ns |
| 0-42 | DWG (g) | 66.3 $^{a}$ | 62.2 $^{ab}$ | 60.5 $^{b}$ | 63.9 $^{ab}$ | 0.001 | * |
| | FI (g) | 129.6 | 116.2 | 118.8 | 119.1 | 0.004 | ns |
| | FCR | 1.957 | 1.867 | 1.966 | 1.865 | 0.046 | ns |
| | Carcass Yield (%) | 68.2 | 66.8 | 68.7 | 70.0 | 0.855 | ns |

$^{a, b, c}$: Different superscripted means within the same row differ significantly. *: ($p<0.05$). ns: not significant ($p>0.05$). FI: feed intake, BW: body weight, DWG: daily weight gain, FCR: feed conversion rate. MC-15, MC-30, MC-45: basal diet supplemented with MC at 0.15, 0.30, 0.45 g $kg^{-1}$respectively.

It is observed that the supplementation of MC to the diet did not make a significant difference in the biochemical parameters studied (Table 2).

**Table 2.** Biochemical parameters.

| | Control | MC-15 | MC-30 | MC-45 | SEM | *P-values* |
|---|---|---|---|---|---|---|
| ALP (U $L^{-1}$) | 2392.71$^{a}$ | 1337.29$^{b}$ | 1754.14$^{ab}$ | 1439.43$^{b}$ | 266.262 | * |
| Triglyceride (mg $dL^{-1}$) | 32.29$^{ab}$ | 41.43$^{a}$ | 29.57$^{ab}$ | 23.00$^{b}$ | 3.935 | * |
| Cholesterol (mg $dL^{-1}$) | 117.71 | 103.43 | 109.86 | 114.71 | 7.749 | ns |
| HDL (mg $dL^{-1}$) | 80.14 | 69.43 | 76.14 | 80.71 | 4.984 | ns |
| LDL (mg $dL^{-1}$) | 61.71 | 52.00 | 53.00 | 56.57 | 4.682 | ns |
| Ca (mg $dL^{-1}$) | 8.34 | 8.14 | 7.74 | 8.26 | 0.34 | ns |
| P (mg $dL^{-1}$) | 6.14$^{a}$ | 6.27$^{a}$ | 5.99$^{a}$ | 5.10$^{b}$ | 0.254 | * |
| Total Protein (g $dL^{-1}$) | 2.89 | 2.53 | 2.74 | 2.73 | 0.178 | ns |
| Albumin (g $dL^{-1}$) | 0.99 | 0.88 | 0.93 | 0.93 | 0.06 | ns |
| Glucose (mg $dL^{-1}$) | 218.29 | 233.29 | 210.14 | 214.14 | 10.201 | ns |
| Creatinine (mg $dL^{-1}$) | 0.00 | 0.01 | 0.01 | 0.03 | 0.014 | ns |
| Uric Acid (mg $dL^{-1}$) | 2.66 | 3.89 | 2.57 | 3.54 | 0.522 | ns |

$^{a, b, c}$: Different superscripted means within the same row differ significantly. *: ($p<0.05$). ns: not significant ($p>0.05$). ALP: alkaline phosphatase, HDL: high-density lipoprotein, LDL: low-density lipoprotein, Ca: calcium, P: phosphor. MC-15, MC-30, MC-45: basal diet supplemented with MC at 0.15, 0.30, 0.45 g $kg^{-1}$respectively.

There was no difference in blood serum parameters except ALP, TG, and P levels among the groups. Serum P levels in the high dose of MC extract-treated group were significantly lower than the other groups ($P<0.05$). Also, all the treatment groups showed varying degrees of reduction in serum ALP levels compared to the control group. It has been reported that MC has the potential to reduce hepatic triglyceride and cholesterol concentration [17], and this effect is related to the mechanism of inhibiting lipid metabolism of the sterile glycoside fraction which is the active ingredients in mainly methanolic extracts [18]. In the study, it was observed that TG, cholesterol, HDL, and LDL levels showed a decreasing tendency in the MC groups, but this decrease was not statistically significant. MC has a hypoglycemic effect due to its content of phyto-constituent called charantin, insulin-like peptides, and alkaloids [2,9,19]. Studies on the hypoglycemic effect of MC have

generally been conducted in rats and humans with diabetes [3,4,20]. However, the current study results show that MC has no effect on the blood glucose level in broiler (Table 2).

There was no previous study on the effects of MC on intestinal morphology. In the current study light microscopically, there was no significant change in the intestinal villi surface epithelium of all groups (Figure 1). Histological staining showed that goblet cells in the villi and crypts of the duodenum, jejunum, and ileum give a positive reaction with PAS staining (Figure 2). It was observed that GCN was higher in the ileum compared to the duodenum and jejunum, and the number of goblet cells increased in parallel with the increase in MC dose (Figure 2).

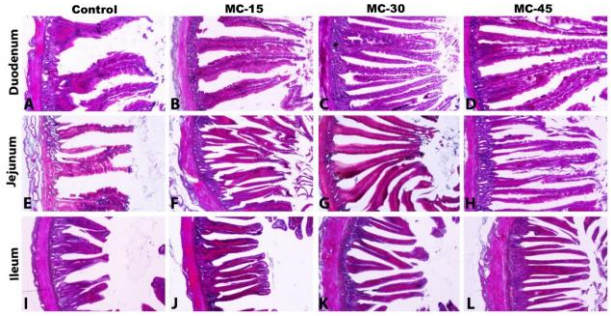


**Figure 1.** General view of duodenum, jejunum and ileum sections. With Crossman's modified triple stain. MC-15, MC-30, MC-45: basal diet supplemented with MC at 0.15, 0.30, 0.45 g $kg^{-1}$respectively.

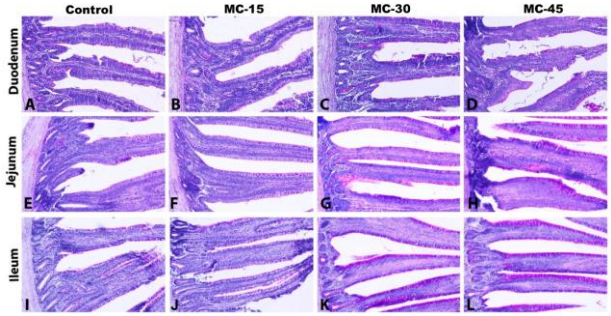


**Figure 2.** Figure showing PAS reaction and increased staining of duodenum, jejunum, and ileum sections. MC-15, MC-30, MC-45: basal diet supplemented with MC at 0.15, 0.30, 0.45 g $kg^{-1}$respectively.

Depending on the dose, it was observed that the GCN, CD, VL, and EH values in the duodenum, jejunum, and ileum tissues increased statistically significantly in the MC-supplemented groups compared to the control group ($p<0.05$) (Table 3, Figure 3). MC contains flavonoids, phenolic compounds, and saponins compounds such as momordin, momordicoside, momordicin, kuguacin, karavilsodie, and karavilagenin [21,22]. As it is known, saponins and flavonoids have a beneficial effect on intestinal health. Prihambodo et al. [23] reported that flavonoid supplementation has a positive effect on small intestine morphology and villus length increased the in the small intestine of the broiler. According to researchers, due to the antibacterial properties of flavonoids, they reduce pathogenic bacteria that may damage the villi in the intestines, and a low pathogen community stimulates intestinal villi growth and regeneration. Similarly, Youssef et al. [24] reported that the dietary supplements of saponins enhanced intestinal morphology, and increased the villus height in broilers.

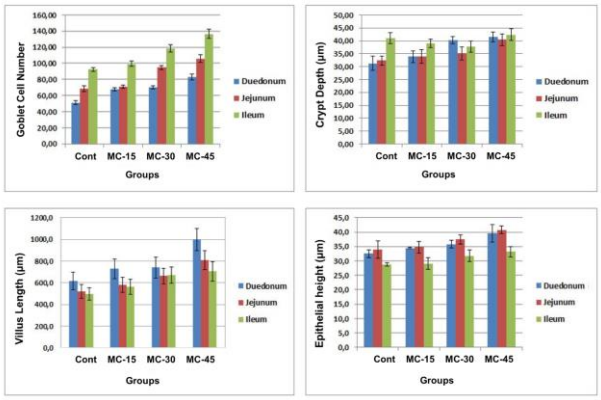


**Figure 3.** Average epithelial height, goblet cell number, crypt depth, and villus length by intestinal sections and groups. MC-15, MC-30, MC-45: basal diet supplemented with MC at 0.15, 0.30, 0.45 g $kg^{-1}$respectively.



**Table 3.** Histometric measurement results of intestinal sections.

| | | Control | MC-15 | MC-30 | MC-45 | *P-values* |
|---|---|---|---|---|---|---|
| **Duodenum** | GCN (number 1000µm$^{-1}$) | 51.2±2.4$^{a}$ | 67.8±1.9$^{b}$ | 70.43±2.1$^{b}$ | 83.3±3.5$^{c}$ | * |
| | CD (µm) | 31.2±2.7$^{a}$ | 33.9±2.3$^{a}$ | 40.2±1.4$^{b}$ | 41.5±1.9$^{b}$ | * |
| | VL (µm) | 617.3±80.3$^{a}$ | 728.2±92.1$^{b}$ | 740.5±95.6$^{b}$ | 999.0±103.3$^{c}$ | * |
| | EH (µm) | 32.5±1.3$^{a}$ | 34.5±0.2$^{a}$ | 35.8±1.4$^{a}$ | 39.6±3.1$^{b}$ | * |
| **Jejunum** | GCN (number 1000µm$^{-1}$) | 68.54±3.4$^{a}$ | 71.1±1.9$^{a}$ | 94.8±2.6$^{b}$ | 105.9±4.6$^{c}$ | * |
| | CD (µm) | 32.3±1.7$^{a}$ | 34.0±2.7$^{a}$ | 35.1±2.5$^{a}$ | 40.5±2.2$^{b}$ | * |
| | VL (µm) | 521.3±63.4$^{a}$ | 582.3±69.5$^{a}$ | 662.4±72.9$^{b}$ | 810.3±87.3$^{c}$ | * |
| | EH (µm) | 33.9±2.9$^{a}$ | 34.8±2.0$^{a}$ | 37.4±1.5$^{a}$ | 40.8±1.4$^{b}$ | * |
| **Ileum** | GCN (number 1000µm$^{-1}$) | 92.4.2±2.5$^{a}$ | 99.5±3.1$^{b}$ | 118.7±4.2$^{c}$ | 136.3±5.7$^{d}$ | * |
| | CD (µm) | 41.0±2.1$^{a}$ | 38.9±1.7$^{b}$ | 37.8±2.2$^{b}$ | 42.4±2.3$^{a}$ | * |
| | VL (µm) | 497.3±55.8$^{a}$ | 562.0±69.1$^{b}$ | 670.2±76.4$^{c}$ | 706.0±90.2$^{d}$ | * |
| | EH (µm) | 28.8±0.6$^{a}$ | 29.0±2.0$^{a}$ | 31.7±2.1$^{b}$ | 33.2±1.9$^{b}$ | * |

The values are given as mean ± SEM. $^{a, b, c}$: Different superscripted means within the same row differ significantly. *: ($p<0.05$). GCN: Number of goblet cells (in 1000 µm area), CD: Crypt depth, VL: Villus length, EH: Epithelial height. MC-15, MC-30, MC-45: basal diet supplemented with MC at 0.15, 0.30, 0.45 g $kg^{-1}$respectively.

Physical and chemical properties of meat affect meat quality such as color, odor, flavor, texture, and pH are the basic parameters. The microbial load is one of the factors that determine meat quality and shelf life in meat production. The findings of the present study showed

that MC has a quite limited and variable effect on these parameters of breast and drumstick meat during the storage period (Table 4-7).

**Table 4.** Quality parameters in chicken breast meat during the storage period.

| Days | Groups | pH | *Aw* | TBARS (*μmolMDA kg$^{-1}$*) | *L** | a* | b* |
|---|---|---|---|---|---|---|---|
| 1 | Control | 5.75±0.01 | 0.991±0.001$^{b}$ | 4.55±0.20 | 53.26±0.41$^{a}$ | 3.66±0.39 | 5.28±0.89 |
| | MC-15 | 5.83±0.03 | 0.990±0.001$^{ab}$ | 4.59±0.13 | 55.24±0.75$^{b}$ | 3.48±0.60 | 7.14±0.47 |
| | MC-30 | 5.90±0.05 | 0.998±0.001$^{a}$ | 4.56±0.06 | 49.55±0.78$^{a}$ | 3.98±0.51 | 5.58±0.74 |
| | MC-45 | 5.76±0.07 | 0.988±0.001$^{b}$ | 4.35±0.04 | 53.36±1.22$^{a}$ | 3.21±0.30 | 7.00±1.03 |
| | *P-values* | ns | * | ns | ** | ns | ns |
| 3 | Control | 5.75±0.02 | 0.993±0.000$^{a}$ | 4.70±0.05 | 56.20±0.72 | 3.89±0.73 | 6.98±0.62 |
| | MC-15 | 5.69±0.12 | 0.987±0.001$^{b}$ | 5.05±0.25 | 57.02±2.92 | 2.20±0.33 | 6.55±1.42 |
| | MC-30 | 5.79±0.04 | 0.987±0.000$^{b}$ | 5.07±0.07 | 57.24±0.79 | 2.94±0.63 | 8.13±1.02 |
| | MC-45 | 5.78±0.02 | 0.989±0.002$^{b}$ | 4.53±0.17 | 54.82±0.46 | 4.41±0.30 | 7.50±0.68 |
| | *P-values* | ns | * | ns | ns | ns | ns |
| 5 | Control | 5.95±0.03$^{a}$ | 0.990±0.000 | 5.30±0.12 | 50.26±2.12 | 3.16±0.82 | 4.78±0.30 |
| | MC-15 | 5.73±0.02$^{c}$ | 0.993±0.001 | 4.84±0.02 | 50.94±1.04 | 3.39±0.64 | 9.95±0.56 |
| | MC-30 | 5.89±0.00$^{ab}$ | 0.989±0.001 | 5.24±0.56 | 50.56±0.25 | 3.59±0.50 | 6.14±1.70 |
| | MC-45 | 5.86±0.02$^{b}$ | 0.991±0.002 | 5.01±0.24 | 52.92±0.50 | 2.90±0.60 | 6.57±1.77 |
| | *P-values* | ** | ns | ns | ns | ns | ns |
| 7 | Control | 5.77±0.02 | 0.990±0.001 | 5.36±0.14 | 52.89±1.38 | 1.84±0.04 | 8.17±0.35$^{a}$ |
| | MC-15 | 5.59±0.01 | 0.991±0.001 | 4.88±0.17 | 53.82±0.70 | 3.25±0.48 | 9.18±0.39$^{a}$ |
| | MC-30 | 5.70±0.04 | 0.991±0.002 | 5.35±0.13 | 52.48±0.55 | 2.66±0.61 | 7.85±1.10$^{a}$ |
| | MC-45 | 6.11±0.26 | 0.993±0.002 | 5.11±0.21 | 52.54±0.38 | 2.66±0.59 | 4.13±0.36$^{b}$ |
| | *P-values* | ns | ns | ns | ns | ns | *** |
| 9 | Control | 6.04±0.05 | 0.991±0.001 | 5.39±0.35$^{ab}$ | 51.01±1.95$^{ab}$ | 3.22±0.91 | 7.66±0.66$^{a}$ |
| | MC-15 | 6.08±0.22 | 0.990±0.001 | 4.93±0.04$^{b}$ | 54.29±1.15$^{a}$ | 2.39±0.32 | 6.20±0.75$^{ab}$ |
| | MC-30 | 6.10±0.07 | 0.995±0.005 | 6.23±0.46$^{a}$ | 48.09±0.86$^{b}$ | 3.39±0.21 | 5.09±0.52$^{b}$ |
| | MC-45 | 5.96±0.02 | 0.993±0.002 | 6.16±0.24$^{a}$ | 53.24±1.50$^{a}$ | 4.58±1.37 | 7.93±0.50$^{a}$ |
| | *P-values* | ns | ns | * | * | ns | * |

The values are shown as mean ± SEM. $^{a, b, c}$: Different superscripted means within the same column differ significantly. *: ($p<0.05$), **: ($p<0.01$) ***: ($p<0.001$). ns: not significant ($p>0.05$). aw: water activity, TBARS: thiobarbituric acid reactive substances, L*: relative lightness, a*: relative redness, b*: relative yellowness. MC-15, MC-30, MC-45: basal diet supplemented with MC at 0.15, 0.30, 0.45 g kg$^{-1}$respectively.

**Table 5.** Quality parameters in chicken drumstick meat during the storage period.

| Days | Groups | pH | *Aw* | TBARS (*μmolMDA kg$^{-1}$*) | *L** | a* | b* |
|---|---|---|---|---|---|---|---|
| 1 | Control | 6.01±0.01 | 0.994±0.001 | 4.03±0.07$^{b}$ | 57.07±2.30 | 5.34±0.51 | 5.46±0.83 |
| | MC-15 | 6.21±0.14 | 0.992±0.001 | 4.13±0.07$^{b}$ | 56.74±0.71 | 4.55±0.92 | 3.48±0.57 |
| | MC-30 | 6.12±0.06 | 0.989±0.001 | 4.50±0.13$^{a}$ | 52.55±0.92 | 6.81±1.05 | 6.14±1.36 |
| | MC-45 | 6.17±0.10 | 0.993±0.007 | 4.20±0.10$^{b}$ | 55.75±1.25 | 7.30±0.93 | 5.07±0.99 |
| | *P-values* | ns | ns | * | ns | ns | ns |
| 3 | Control | 5.84±0.53 | 0.992±0.002 | 4.28±0.13 | 57.81±0.42 | 4.59±0.06 | 1.79±0.51$^{a}$ |
| | MC-15 | 6.25±0.05 | 0.992±0.002 | 4.58±0.30 | 56.36±1.23 | 3.24±0.20 | 3.99±0.48$^{ab}$ |
| | MC-30 | 6.19±0.02 | 0.989±0.000 | 4.56±0.16 | 54.20±0.84 | 3.81±0.79 | 5.92±1.46$^{b}$ |
| | MC-45 | 6.40±0.04 | 0.994±0.006 | 4.64±0.20 | 55.55±0.94 | 5.29±0.77 | 5.19±0.96$^{b}$ |
| | *P-values* | ns | ns | ns | ns | ns | * |
| 5 | Control | 6.10±0.15 | 0.991±0.001 | 4.94±0.13 | 55.32±2.40 | 4.04±0.19 | 6.28±0.83 |
| | MC-15 | 6.36±0.05 | 0.997±0.010 | 4.83±0.03 | 57.46±3.04 | 4.62±0.34 | 3.37±1.59 |
| | MC-30 | 6.26±0.02 | 0.997±0.002 | 4.71±0.05 | 44.35±0.45 | 5.24±0.56 | 5.40±0.93 |
| | MC-45 | 6.00±0.06 | 0.992±0.001 | 4.70±0.08 | 59.08±0.95 | 5.81±1.39 | 4.39±1.17 |
| | *P-values* | ns | ns | ns | ns | ns | ns |
| 7 | Control | 5.98±0.03 | 0.989±0.001 | 4.84±0.11 | 52.11±6.15 | 4.75±1.04 | 5.152±0.77 |
| | MC-15 | 5.76±0.07 | 0.995±0.003 | 5.13±0.22 | 58.83±0.85 | 5.11±0.54 | 5.25±0.28 |
| | MC-30 | 6.17±0.02 | 0.990±0.000 | 4.81±0.10 | 55.64±0.45 | 3.82±0.87 | 5.90±0.58 |
| | MC-45 | 6.00±0.23 | 0.993±0.002 | 4.76±0.13 | 55.06±1.17 | 4.87±0.29 | 3.14±1.14 |
| | *P-values* | ns | ns | ns | ns | ns | ns |
| 9 | Control | 6.46±0.14$^{ab}$ | 0.999±0.002 | 4.97±0.07 | 50.76±1.58$^{b}$ | 5.54±0.35 | 3.90±0.86 |
| | MC-15 | 6.15±0.00$^{c}$ | 0.992±0.000 | 5.50±0.40 | 55.49±1.37$^{a}$ | 4.63±0.37 | 3.13±1.19 |
| | MC-30 | 6.19±0.04$^{bc}$ | 0.993±0.010 | 5.40±0.19 | 55.78±0.40$^{a}$ | 4.83±0.35 | 5.16±0.96 |
| | MC-45 | 6.58±0.05$^{a}$ | 0.993±0.001 | 5.26±0.29 | 51.15±1.17$^{b}$ | 6.54±1.09 | 4.44±0.47 |
| | *P-values* | * | ns | ns | * | ns | ns |

The values are shown as mean ± SEM. $^{a, b, c}$: Different superscripted means within the same column differ significantly. *: ($p<0.05$). ns: not significant ($p>0.05$). aw: water activity, TBARS: thiobarbituric acid reactive substances, L*: relative lightness, a*: relative redness, b*: relative yellowness. MC-15, MC-30, MC-45: basal diet supplemented with MC at 0.15, 0.30, 0.45 g kg$^{-1}$respectively.

**Table 6.** Microbial counts in chicken breast meat during the storage period. (log cfu $g^{-1}$).

| Days | Groups | TMAB | *Coliform* | *Lactobacillus* spp. | *Micrococcus-Staphylococcus* | Pseudomonas spp. | Yeast-Mould | TPAB |
|---|---|---|---|---|---|---|---|---|
| 1 | Control | 4.94±0.10 | 3.21±0.07 | 4.20±0.20$^{c}$ | 4.23±0.28 | 4.27±0.16 | 2.54±0.06$^{b}$ | 3.67±0.29 |
| | MC-15 | 5.40±0.45 | 3.73±0.25 | 4.96±0.15$^{ab}$ | 4.29±0.01 | 4.37±0.23 | 3.39±0.09$^{a}$ | 4.09±0.09 |
| | MC-30 | 5.82±0.09 | 3.30±0.30 | 5.11±0.05$^{a}$ | 4.39±0.09 | 4.18±0.70 | 3.27±0.27$^{a}$ | 4.58±0.10 |
| | MC-45 | 5.56±0.30 | 3.39±0.01 | 4.47±0.13$^{bc}$ | 4.66±0.17 | 4.46±0.01 | 3.467±0.01$^{a}$ | 3.83±0.00 |
| | *P-values* | ns | ns | * | ns | ns | * | ns |
| 3 | Control | 6.03±0.05$^{a}$ | 3.60±0.00$^{b}$ | 4.68±0.68 | 4.42±0.42 | 4.30±0.05 | 3.02±0.02$^{c}$ | 4.61±0.02$^{b}$ |
| | MC-15 | 5.45±0.15$^{b}$ | 4.51±0.13$^{a}$ | 5.26±0.30 | 5.28±0.02 | 4.72±0.22 | 3.63±0.06$^{b}$ | 4.22±0.08$^{c}$ |
| | MC-30 | 5.94±0.04$^{a}$ | 3.59±0.21$^{b}$ | 5.44±0.13 | 4.39±0.39 | 4.32±0.11 | 3.80±0.05$^{a}$ | 5.25±0.07$^{a}$ |
| | MC-45 | 6.19±0.11$^{a}$ | 3.87±0.05$^{b}$ | 4.66±0.10 | 4.89±0.41 | 4.49±02.4 | 3.53±0.02$^{b}$ | 4.53±0.02$^{b}$ |
| | *P-values* | * | * | ns | ns | ns | *** | *** |
| 5 | Control | 6.29±0.69 | 3.74±0.74 | 4.87±0.04 | 4.59±0.11$^{b}$ | 5.65±0.69 | 3.04±0.04 | 5.39±0.39 |
| | MC-15 | 6.99±0.37 | 4.73±0.46 | 5.28±0.28 | 5.36±0.11$^{a}$ | 5.21±0.06 | 3.61±0.17 | 5.98±0.57 |
| | MC-30 | 6.02±0.32 | 3.66±0.18 | 5.69±0.25 | 5.42±0.08$^{a}$ | 5.87±0.53 | 3.83±0.68 | 5.43±0.17 |
| | MC-45 | 6.21±0.32 | 3.89±0.11 | 4.68±0.02 | 5.59±0.02$^{a}$ | 4.98±0.28 | 3.55±0.02 | 5.54±0.11 |
| | *P-values* | ns | ns | ns | ** | ns | ns | ns |
| 7 | Control | 6.34±0.30 | 3.94±0.34 | 4.94±0.04$^{b}$ | 5.18±0.09 | 5.98±0.03$^{ab}$ | 3.30±0.30 | 6.22±0.27 |
| | MC-15 | 7.03±0.14 | 5.32±0.00 | 5.60±0.10$^{a}$ | 5.52±0.31 | 6.41±0.21$^{a}$ | 4.05±0.10 | 6.61±0.01 |
| | MC-30 | 6.71±0.37 | 3.81±0.09 | 5.82±0.08$^{a}$ | 5.76±0.23 | 6.09±0.04$^{a}$ | 4.91±0.43 | 6.24±0.20 |
| | MC-45 | 6.29±0.36 | 4.09±0.61 | 5.15±0.11$^{b}$ | 5.93±0.23 | 5.58±0.05$^{b}$ | 4.30±0.18 | 6.45±0.15 |
| | *P-values* | ns | ns | ** | ns | * | ns | ns |
| 9 | Control | 6.84±0.01$^{b}$ | 5.64±0.21$^{a}$ | 5.13±0.25$^{b}$ | 6.45±0.42 | 7.47±0.03$^{b}$ | 4.11±0.16$^{b}$ | 6.37±0.29 |
| | MC-15 | 7.40±0.10$^{a}$ | 6.09±0.09$^{a}$ | 5.73±0.13$^{ab}$ | 5.78±0.04 | 7.64±0.03$^{ab}$ | 4.47±0.06$^{ab}$ | 7.55±0.29 |
| | MC-30 | 7.52±0.05$^{a}$ | 4.32±0.02$^{b}$ | 6.18±0.04$^{a}$ | 6.27±0.04 | 7.76±0.08$^{a}$ | 5.31±0.14$^{a}$ | 6.32±0.14 |
| | MC-45 | 6.53±0.07$^{c}$ | 5.00±0.53$^{ab}$ | 5.63±0.16$^{ab}$ | 6.19±0.34 | 6.14±0.02$^{c}$ | 5.19±0.36$^{a}$ | 7.46±0.40 |
| | *P-values* | *** | * | * | ns | *** | * | ns |

The values are shown as mean ± SEM. $^{a, b, c}$: Different superscripted means within the same column differ significantly. *: (p<0.05), **: (p<0.01), ***: (p<0.001). ns: not significant (p>0.05). TMAB: total mesophyll aerobic bacteria, TPAB: total psychrophile aerobic bacteria. MC-15, MC-30, MC-45: basal diet supplemented with MC at 0.15, 0.30, 0.45 g $kg^{-1}$respectively.

**Table 7.** Microbial counts in chicken drumstick meat during the storage period. (log cfu $g^{-1}$).

| Days | Groups | TMAB | *Coliform* | *Lactobacillus* spp. | *Micrococcus/ Staphylococcus* | Pseudomonas spp. | Yeast-Mould | TPAB |
|---|---|---|---|---|---|---|---|---|
| 1 | Control | 6.39±0.07 | 3.30±0.30 | 5.22±0.09 | 5.18±0.18 | 4.19±0.11 | 2.74±0.04 | 3.71±0.06$^{b}$ |
| | MC-15 | 6.03±0.19 | 3.52±0.44 | 4.68±0.28 | 4.48±0.48 | 4.69±0.25 | 3.35±0.01 | 4.31±0.01$^{a}$ |
| | MC-30 | 6.32±0.43 | 3.18±0.03 | 4.48±0.43 | 5.55±0.14 | 4.64±0.21 | 3.31±0.53 | 4.45±0.20$^{a}$ |
| | MC-45 | 5.72±0.21 | 3.24±0.06 | 4.57±0.28 | 5.29±0.51 | 4.39±0.24 | 2.77±0.07 | 4.59±0.19$^{a}$ |
| | *P-values* | ns | ns | ns | ns | ns | ns | * |
| 3 | Control | 6.63±0.23 | 3.59±0.11 | 5.23±0.24 | 5.28±0.04 | 4.58±0.08$^{c}$ | 3.04±0.04$^{d}$ | 4.53±0.35 |
| | MC-15 | 6.16±0.35 | 3.90±0.30 | 5.09±0.09 | 5.43±0.05 | 5.19±0.07$^{ab}$ | 3.84±0.00$^{a}$ | 5.89±0.89 |
| | MC-30 | 6.53±0.17 | 3.47±0.23 | 4.62±0.11 | 5.77±0.05 | 5.45±0.22$^{a}$ | 3.55±0.01$^{b}$ | 5.22±0.04 |
| | MC-45 | 6.25±0.37 | 3.37±0.05 | 4.84±0.84 | 5.35±0.31 | 4.90±0.06$^{bc}$ | 3.31±0.01$^{c}$ | 4.94±0.28 |
| | *P-values* | ns | ns | ns | ns | * | *** | ns |
| 5 | Control | 6.97±0.01 | 3.65±0.05$^{c}$ | 5.46±0.11 | 5.79±0.09 | 5.57±0.16 | 3.15±0.15 | 5.83±0.08 |
| | MC-15 | 6.15±0.15 | 4.06±0.06$^{b}$ | 5.48±0.07 | 6.30±0.04 | 6.12±0.23 | 4.04±0.04 | 5.95±0.15 |
| | MC-30 | 6.62±0.37 | 4.87±0.01$^{a}$ | 5.63±0.15 | 5.62±0.21 | 5.68±0.77 | 3.96±0.66 | 5.64±0.19 |
| | MC-45 | 6.27±0.08 | 3.53±0.11$^{c}$ | 5.04±0.07 | 5.69±0.20 | 5.84±0.58 | 3.64±0.64 | 6.20±0.08 |
| | *P-values* | ns | *** | ns | ns | ns | ns | ns |
| 7 | Control | 6.78±0.00 | 4.70±0.40 | 5.45±0.22$^{b}$ | 6.31±0.04$^{b}$ | 6.09±0.29 | 4.00±0.30 | 6.380.38 |
| | MC-15 | 6.24±0.28 | 5.37±0.31 | 5.64±0.02$^{b}$ | 6.73±0.10$^{a}$ | 6.69±0.11 | 4.26±0.22 | 6.80±0.00 |
| | MC-30 | 6.79±0.30 | 5.31±0.30 | 6.29±0.07$^{a}$ | 5.88±0.14$^{b}$ | 5.94±0.25 | 4.51±0.00 | 6.37±0.03 |
| | MC-45 | 6.31±0.12 | 4.57±0.27 | 5.44±0.01$^{b}$ | 6.16±0.12$^{b}$ | 5.88±0.54 | 4.21±0.31 | 6.41±0.26 |
| | *P-values* | ns | ns | * | * | ns | ns | ns |
| 9 | Control | 7.13±0.62 | 4.72±0.24$^{b}$ | 5.49±0.27$^{b}$ | 6.33±0.15$^{b}$ | 7.44±0.31 | 4.20±0.15 | 7.16±0.02 |
| | MC-15 | 7.24±0.04 | 5.66±0.14$^{a}$ | 5.84±0.16$^{ab}$ | 7.23±0.08$^{a}$ | 7.84±0.10 | 4.43±0.13 | 7.03±0.01 |
| | MC-30 | 7.77±0.27 | 5.44±0.10$^{a}$ | 6.41±0.03$^{a}$ | 6.62±0.19$^{b}$ | 7.59±0.36 | 4.58±0.20 | 7.09±0.01 |
| | MC-45 | 6.52±0.52 | 4.75±0.03$^{b}$ | 5.58±0.01$^{b}$ | 6.33±0.07$^{b}$ | 6.59±0.17 | 4.80±0.50 | 7.38±0.33 |
| | *P-values* | ns | * | * | * | ns | ns | ns |

The values are shown as mean ± SEM. $^{a, b, c}$: Different superscripted means within the same column differ significantly. *: (p<0.05), ***: (p<0.001). ns: not significant (p>0.05). TMAB: total mesophyll aerobic bacteria, TPAB: total psychrophile aerobic bacteria. MC-15, MC-30, MC-45: basal diet supplemented with MC at 0.15, 0.30, 0.45 g $kg^{-1}$respectively.

## 4. CONCLUSION

This study is among the first to look into how MC extract affects the performance, intestinal morphology, and meat quality of broilers. In conclusion, despite the improving effect on intestinal morphology MC extract had quite a limited effect on performance in Broiler in the doses used in the study. Furthermore, contrasting several dosages in different housing and health conditions plans can be essential.

## REFERENCES

[1] Grover JK, Yadav SP. Pharmacological actions and potential uses of Momordica charantia: A review. J Ethnopharmacol. 2004;93(1):123–32.

[2] Sharma Y. A chemical and medicinal potency of Momordica charantia. 2019;8(6):531–6.

[3] Miura T, Itoh C, Iwamoto N, Kato M, Kawai M, Park SR, et al. Hypoglycemic activity of the fruit of

the Momordica charantia in type 2 diabetic mice. J Nutr Sci Vitaminol (Tokyo). 2001;47(5):340–4.
[4] Kar A, Choudhary BK, Bandyopadhyay NG. Comparative evaluation of hypoglycaemic activity of some Indian medicinal plants in alloxan diabetic rats. J Ethnopharmacol. 2003 Jan 1;84(1):105–8.
[5] Singh RK, Dhiman RC, Mittal PK. Mosquito larvicidal properties of Momordica charantia Linn (Family: Cucurbitaceae). J Vector Borne Dis. 2006;(June):88–91.
[6] Jiratchariyakul W, Wiwat C, Vongsakul M, Somanabandhu A, Leelamanit W, Fujii I, et al. HIV Inhibitor from Thai Bitter Gourd. Planta Med. 2001;67(04):350–3.
[7] Shahadat HM, Mostofa M, Mamun MAA, Hoque ME, Awal MA. Comparative efficacy of korolla (Momordica charantia) extract and IvermecÂ® pour on with their effects on certain blood parameters and body weight gain in indigenous chicken infected with Ascaridia galli. Bangladesh J Vet Med. 2008;6(2):153–8.
[8] Sur S, Ray RB. Bitter melon (Momordica charantia), a nutraceutical approach for cancer prevention and therapy. Cancers (Basel). 2020;12(8):1–22.
[9] Bortolotti M, Mercatelli D, Polito L. Momordica charantia, a nutraceutical approach for inflammatory related diseases. Vol. 10, Frontiers in Pharmacology. 2019.
[10] Mahmood MS, Rafique A, Younas W, Aslam B. Momordica charantia L. (bitter gourd) as a candidate for the control of bacterial and fungal growth. Pakistan J Agric Sci. 2019;56(4):1031–6.
[11] Abdelkarim H, Rukayadi Y, Abdulkarim SM, Sulaiman R. Effect of dried and extrudate of bitter gourd fruit on epithelial microflora in raw chicken legs meat. Int Food Res J. 2017;24(5):2253–8.
[12] Zuhra FT, Paul AK, Riad MM, Ahmed MS. Effects of Probiotics and Phytoextracts on Growth and Immunomodulating Performances of Broiler Chickens. Bangladesh J Vet Med. 2018;16(1):13–21.
[13] NRC. Nutrient Requirements of Poultry. Nutr Requir Poult. 9th ed. 1994;1994.
[14] Gökalp HY, Kaya M, Tülek Y, Zorba O. Guide for quality control and laboratory application of meat products. Erzurum: Atatürk Univ. Publ. (751); 2001.
[15] Lemon D. An improved TBA test for rancidity new series circular, No: 51. Halifax, NS, Canada Halifax-Laboratory [Internet]. 1975;0–3. Available from: http://icnaf.nafo.int/docs/1974/res-07.pdf
[16] Jia S, Shen M, Zhang F, Xie J. Recent Advances in Momordica charantia : Functional Components and Biological Activities. Int J Mol Sci [Internet]. 2017;18(12):2555. Available from: https://www.mdpi.com/1422-0067/18/12/2555/htm
[17] Senanayake GVK, Maruyama M, Shibuya K, Sakono M, Fukuda N, Morishita T, et al. The effects of bitter melon (Momordica charantia) on serum and liver triglyceride levels in rats. J Ethnopharmacol. 2004;91(2–3):257–62.
[18] Ng TB, Wong CM, Li WW, Yeung HW. A steryl glycoside fraction from Momordica charantia seeds with an inhibitory action on lipid metabolism in vitro. Biochem Cell Biol. 1986;64(8):766–71.
[19] Kumar KPS, Bhowmik D. Traditional medicinal uses and therapeutic benefits of Momordica charantia Linn. Int J Pharm Sci Rev Res. 2010;4(3):23–8.
[20] Xu B, Li Z, Zeng T, Zhan J, Wang S, Ho CT, et al. Bioactives of Momordica charantia as Potential Anti-Diabetic/Hypoglycemic Agents. Molecules. 2022;27(7):1–17.
[21] Nair MNB. Medicinal plants for Home herbal gardens , Institutional gardens and animal health.
[22] Tan SP, Kha TC, Parks SE, Roach PD, Tan SP, Kha TC, et al. Bitter melon ( Momordica charantia L .) bioactive composition and health benefits : A review. Food Rev Int [Internet]. 2016;32(2):181–202. Available from: http://dx.doi.org/10.1080/87559129.2015.1057843
[23] Prihambodo TR, Sholikin MM, Qomariyah N, Jayanegara A, Batubara I, Utomo DB, et al. Effects of dietary flavonoids on performance , blood constituents , carcass composition and small intestinal morphology of broilers : a meta-analysis. 2021;34(3):434–42.
[24] Youssef IMI. Effect of essential oils or saponins alone or in combination on productive performance , intestinal morphology and digestive enzymes ' activity of broiler chickens. 2020;(July):1–9.

Cilt 12, Sayı 1, Sayfa 68-75, 2023 Volume 12, Issue 1, Page 68-75, 2023

Araştırma Makalesi https://doi.org/10.46810/tdfd.1184478 Research Article

Türk Doğa ve Fen Dergisi
Turkish Journal of Nature and Science
www.dergipark.gov.tr/tdfd

# Prototype Design of Solar Collector Hybrid Heating System and Testing of Triethylene Glycol Nanofluid

**Muhammed BABALIOGLU[1], Hakan BUYUKPATPAT[2], Abdullah GENC[1*]**

[1]Isparta University of Applied Sciences, Faculty of Technology, Department of Mechatronics Engineering, Isparta, Türkiye

[2]Bartin University, Faculty of Engineering, Architecture and Design, Department of Computer Engineering, Bartın, Türkiye

Muhammed BABALIOGLU ORCID No: 0000-0002-3852-5932
Hakan BUYUKPATPAT ORCID No: 0000-0003-3277-8653
Abdullah GENC ORCID No: 0000-0002-7699-2822

**Corresponding author: abdullahgenc@isparta.edu.tr*

(Received: 7.10.2022, Accepted: 20.02.2023, Online Publication: 27.03.2023)

**Keywords**
Solar energy, Solar collector, Hybrid heating system, Triethylene glycol, Nano fluid, Heat transfer fluid

**Abstract:** The inclusion of solar energy, which is a renewable energy source, in heating systems in buildings provides significant advantages. To make heating with solar energy sufficient and efficient, nanofluids are used in solar collectors. In this study, a hybrid heating prototype is produced, a control mechanism controlling the operation of the hybrid system is established and tests are carried out by including monoethylene glycol, propylene glycol, aluminum oxide, copper oxide, titanium dioxide, especially triethylene glycol-based nanofluids in the system. Finally, a new nanofluid is obtained by mixing triethylene glycol with aluminum oxide and is tested on the prototype. With the tests carried out under the same conditions, the temperature differences of the nanofluids in a certain time period are observed and recorded. In the experiments, the mixtures are examined for heating in the solar collector in the range of 0-90 minutes, and the 1st, 2nd, 3rd, 4th, 5th, 6th, 7th, and 8th mixtures show 12.5°C, 13.4°C, 18.4°C, 8.6°C, 21°C, 15.4°C, 18.0°C, and 16.4°C temperature changes, respectively. According to the results, it is observed that the 5th mixture, the pure water, and aluminum oxide mixture, is the fastest heating liquid with a temperature change of 21°C. The 4th mixture containing water, and triethylene glycol is the mixture that heats up the slowest with a temperature change of 8.6°C. Although the water and triethylene glycol mixture performs more inefficiently than other mixtures, it is thought that it can be used for heat storage since it heats up for a long time and cools down for a long time.



# Güneş Kollektörlü Hibrit Isıtma Sisteminin Prototip Tasarımı ve Trietilen Glikollü Isı Transfer Sıvısının Test Edilmesi

**Anahtar Kelimeler**
Güneş enerjisi, Güneş kollektörü, Hibrit ısıtma sistemi, Trietilen glikol, Nanoakışkan, Isı transfer sıvısı

**Öz:** Yenilenebilir enerji kaynağı olan güneş enerjisinin, binalardaki ısıtma sistemlerine dâhil edilmesi önemli avantajlar sağlamaktadır. Güneş enerjisi ile ısıtmanın yeterli ve verimli hale gelebilmesi için güneş kollektörlerinin içerisinde ısı transfer sıvıları kullanılmaktadır. Bu çalışmada hibrit bir ısıtma prototipi üretilerek, hibrit sistemin çalışmasını denetleyen kontrol mekanizması oluşturulmuş ve trietilen glikol esaslı ısı transfer sıvısı başta olmak üzere mono etilen glikol, propilen glikol, alüminyum oksit, bakır oksit, titanyum dioksit sisteme dahil edilerek testler yapılmıştır. Son olarak trietilen glikol ile alüminyum oksit birbirine karıştırılarak yeni bir ısı transfer sıvısı elde edilmiş ve prototip üzerinde test edilmiştir. Aynı şartlar altında gerçekleştirilen testler ile ısı transfer sıvılarının belirli zaman diliminde sıcaklık farkları gözlemlenerek kaydedilmiştir. Yapılan deneylerde 0-90 dakika aralığında karışımlar güneş kollektöründe ısıtılmak üzere denenmiş ve karışımlar sırasıyla; 1. karışım 12.5°C, 2. karışım 13.4 °C, 3. karışım 18.4°C, 4. karışım 8.6°C, 5. karışım 21°C, 6. karışım 15.4°C, 7. karışım 18.0°C, 8. karışım 16.4°C sıcaklık değişimi göstermiştir. Sonuçlara göre 5. karışım olan saf su ve alüminyum oksit karışımı 21°C derece sıcaklık değişimi ile en hızlı ısınan sıvı olduğu gözlemlenmiştir. 4. karışım olan su ve trietilen glikol karışımı ise 8.6°C sıcaklık değişimi ile en yavaş ısınan karışım olduğu gözlemlenmiştir. Su ve trietilen glikol karışımı diğer karışımlara göre daha verimsiz bir performans sergilese de uzun sürede ısınıp uzun sürede soğuduğu için ısının depolanması amacıyla kullanılabileceği düşünülmektedir.

## 1. INTRODUCTION

Most of the energy sources used to supply the heat needs of buildings in Turkey and in the world consists of fossil fuels. The problem of global warming and air pollution, which is significantly affected by fossil energy sources, reveals the common problem of all humanity. With the use of fossil fuels, the amount of greenhouse gases released into the atmosphere increases considerably. Global warming is increasing with the accumulation of greenhouse gases in the atmosphere, and therefore, the glaciers are melting, and climate changes occur. Air pollution, which negatively affects humans and all other living things, reduces the quality of life, and causes various diseases [1].

Many meteorological and hydrological differences have been identified, especially in the last century, with the completion of the industrial revolution and the increase in the use of fossil fuels. In Figure 1, the increase in the amount of carbon dioxide ($CO_2$) gas in the atmosphere, which is one of these differences, is given according to the years.

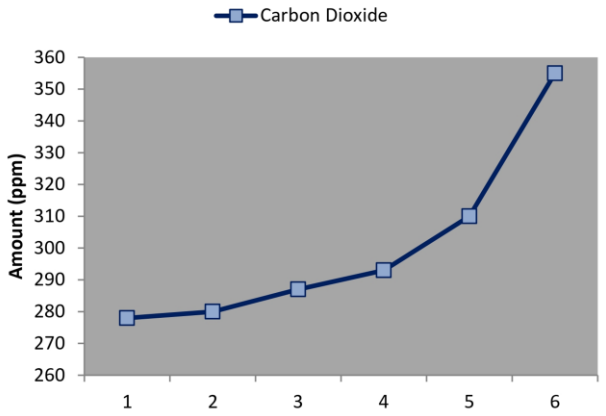


**Figure 1.** Graph of carbon dioxide increase according to years [2]

The accumulation of carbon dioxide gas, which is one of the greenhouse gases, in the atmosphere and its increase since the beginning of the 2000s brings along global problems. The accumulation of carbon dioxide gas and other greenhouse gases in the atmosphere causes the problem of global warming. The global average temperature increase is given in Figure 2.

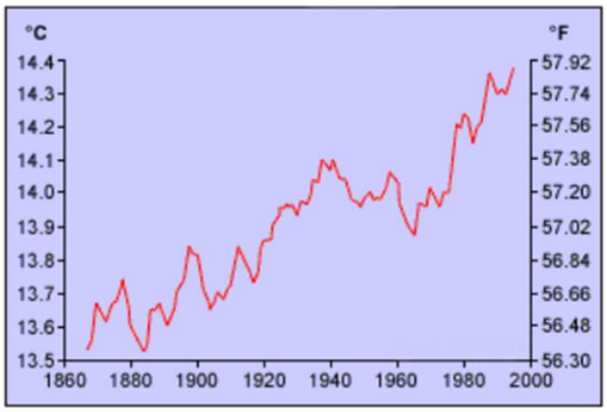


**Figure 2.** Global average temperature increase [2]

It is seen that the graph of the increase in carbon dioxide and other greenhouse gases accumulating in the atmosphere and the graph of the global average temperature increase depend on the cause-effect relationship. Greenhouse gases that cause global warming trigger global warming at the rate they accumulate in the atmosphere. One of the most common renewable energy methods that can be used as an alternative to fossil fuel use is solar energy [3]. There are studies on the evaluation of the energy from the sun in many areas [4]. Figure 3 shows the atlas of Turkey's solar energy potential. Considering the location of Turkey and the amount of solar radiation, it should be noted that it has an ideal level of sunshine.

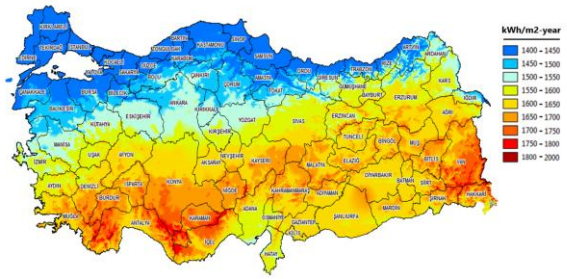


**Figure 3.** Turkey's solar energy potential atlas [5]

Turkey has a total annual sunshine duration of 2,737 hours and an average of 7.5 hours of sunshine per day [6]. Especially Turkey's Mediterranean, Eastern Anatolia, Southeastern Anatolia, as well as Central Anatolia, and southern parts of the Aegean have high levels of sunshine. Supplying the heating needs by utilizing solar energy according to Turkey's sunshine potential has a positive impact on problems such as global warming, air pollution, and the current account deficit arising from energy imports by reducing the use of fossil fuels [6]. Solar collector water heating systems, which are widely used to supply hot water need, are also used to supply the heat needs of the buildings in the hot regions of Turkey. Systems with solar collectors, which cannot perform water heating in rainy and cloudy weather in winter, operate as a hybrid with fossil fuels, which are the existing heat source [7-8].

The properties of the heat transfer fluid used in circulation and heating in solar energy systems working with heat transfer fluid are very important. There are many studies on nanofluids in collectors and heat transfer systems. Bohne et al. [9] are carried out to determine parameters such as thermal conductivity and density because of the mixture (mix.) of ethylene glycol, which is widely used among heat transfer fluids, with water.

Ogut and Dilki [10] in their study performed the process of adding nanoparticle $SiO_2$ (Silicon dioxide) to the water fluid and increasing the volume ratio of the nanoparticle. As a result of the test, they observed that it improved the heat transfer and increased the average Nusselt number. They have stated that an improvement of around 18% is achieved in the average Nusselt number compared to the base fluid. As a result of their study, Akcay and Akdag obtained velocity and

temperature distributions in the pipe for continuous and pulsatile flow conditions. As a result of the analysis, it has been seen that the best heat transfer performance is obtained for $SiO_2$-water nanofluid for $R_e$ = 500 and $\varphi$ = 3%. In another study, a heat transfer fluid consisting of $TiO_2$ (titanium dioxide) nanofluid and pure water is obtained. It is observed that the metal oxide particles in this heat transfer fluid increase the conductivity of the working fluid, resulting in an increase of approximately 11.76% in the efficiency of the heat pipe [11]. In their study, Dagdevir and Ozceyhan [12] revealed that the modeling of nanofluid with a single-phase model in numerical analysis is in great agreement with the literature in terms of both heat transfer and hydraulic performance.

Morever, Kilic et al. [13] carried out an experiment with $TiO_2$/water nanofluid mix. in a flat plate solar collector in a pulsed ultrasonic bath for a certain time. The results they obtained were found to be 48.67% more efficient for $TiO_2$/water and 36.20% more efficient for pure water compared to water. Verma et al. [14] performed the performance analysis of water-based MWCNTs with CuO and MgO nanofluids in a flat plate solar collector in their study. In the study, the exergetic and energetic efficiency of the solar collector was obtained with different efficiency values of CuO and MgO in certain parameters compared to water. In another study [15], solar collector performance was investigated by using water, $Al_2O_3$, and CuO nanofluids. The results obtained in the study showed that $Al_2O_3$ and CuO nanofluids increased the thermal efficiency compared to water.

Michael Joseph Stalin et al. [16] used water and $CeO_2$/water nanofluid in their study and compared them according to Energy, economic and environmental factors. In the experiment with $CeO_2$/water nanofluid, approximately 28% more efficient system was obtained compared to water, while it was stated that a 24.52% reduction could be achieved in the size of flat plate solar collectors using the same capacity water with $CeO_2$/water nanofluid. In addition, it has been observed that approximately 300 MJ energy savings, 175 kg less $CO_2$ emission, and approximately 2.1 years earlier payback time can be achieved with $CeO_2$/water nanofluid. Akram et al. [17] on the other hand, used carbon and metal oxides-based nanofluids. Density, viscosity, and specific heat capacity of nanofluids were evaluated in the study. The results obtained from the experiment were compared with f-GNPs, ZnO, and $SiO_2$ in the collector compared to water, and an increase in efficiency of 17.45%, 13.05%, and 12.36% was observed, respectively. In a study [18], the exergy and energy efficiency of DWCNTs-$TiO_2$/water nanofluid with an innovative geometric structure were evaluated. It was observed that the energy and exergy efficiency increased by 22.19% and 23.26%, respectively, under the most ideal conditions, according to the Re, PR, and Nuave values. Also, Özbaş [19], carried out a study on the use of waste vegetable oils in solar heating systems. This study is aimed to evaluate waste vegetable oils and increase the efficiency of solar heating systems. In another study [20], the heat transfer and flow behavior of ionic-based nanofluids under magnetic influence is investigated. Unlike the literature, it is carried out by simulating with the ANSYS Fluent program.

The control mechanisms of solar collector heating systems with hybrid systems have of great importance. Positive effects on efficiency can be achieved with the algorithmic structure used in the design of the control mechanism. The correct determination of the heating conditions reduces the use of fossil fuels and increases the efficiency of the system. The heat transfer fluid in the solar collector and the installation can increase the amount of energy gain to be obtained from the sun per unit of time and can provide it to the heating installation with minimum loss.

In this study, a hybrid heating prototype is produced and a control mechanism controlling the operation of the hybrid system is established. In the prototype system, monoethylene glycol, propylene glycol, aluminum oxide, copper oxide, and titanium dioxide, especially triethylene glycol-based nanofluid, are included in the system and their efficiency on the system has been tested. As a novelty, a new nanofluid is obtained by mixing triethylene glycol with aluminum oxide and tested on the produced prototype. As a result of the tests carried out under the same conditions, the temperature differences of the nanofluids over time are observed and recorded. This study is organized in three parts. Section 1 includes the introduction, Section 2 includes the designed systems and methods, Section 3 includes the findings of the study, and the last includes evaluation and results.



## 2. MATERIAL AND METHOD

### 2.1. Solar Collectors

Solar collectors are used to absorb the heat energy from the sun and transfer the absorbed heat energy to the nanofluid. Solar collectors are positioned to make the best use of the angle of incidence of the sun's rays [21]. Planar solar collectors consist of glass, absorber plate, liquid pipes, and an insulated zone to prevent heat loss. Planar solar collectors are positioned with an inclination between 30°-45° and absorb the heat energy from the sun [22]. The expression of the heat energy absorbed by the absorber plate is given in Equation 1 [23].

$$\dot{Q}_{abs} = \tau a A G \quad (1)$$

where $\tau$, $a$, $A$ ($m^2$), and $G$ ($W/m^2$) is indicated the transmittance property of the glass, absorptivity of the absorber plate, the area of the collector surface, and the solar radiation incident per unit surface area, respectively. Some of the heat energy obtained from the sun is emitted to the air around the collector by convection, and some to the atmosphere by radiation. The heat energy lost through convection and radiation is given in Equation 2 [23].

$$\dot{Q}_{loss} = UA(T_c - T_a) \quad (2)$$

where $U$ (W/m$^2$.°C), $T_c$ (°C), and $T_a$ (°C) indicate heat loss coefficient, average collector temperature, and air temperature, respectively. The part of the heat energy from the sun transmitted to the heat transfer fluid in the solar collector is expressed as useful heat energy. Useful heat energy is equal to the difference between the total heat energy absorbed and the heat energy lost. In Equation 3, the expressions used in calculating the amount of useful heat are given [23].

$$\begin{aligned}\dot{Q}_{useful} &= \dot{Q}_{abs} - \dot{Q}_{loss} \\ &= \tau aAG - UA(T_c - T_a) \\ &= A[(\tau aG - U(T_c - T_a)]\end{aligned} \quad (3)$$

where $\dot{Q}_{abs}$ is the total absorbed heat energy and $\dot{Q}_{loss}$ is the lost heat energy. In addition, the amount of useful heat energy can be obtained with the mass flow rate of the heat transfer fluid used in the solar collector with Equation 4 [23].

$$\dot{Q}_{useful} = \dot{m}c_p(T_{w,out} - T_{w,in}) \quad (4)$$

where $\dot{m}$, $c_p$ (J/kg.°C), $T_{w,out}$ and $T_{w,in}$ indicate the mass flow rate, the specific heat of water, the inlet water temperature, and the outlet water temperature, respectively. The efficiency of a solar collector is obtained by the ratio of the useful heat energy to the total radiation energy coming to the solar collector. The efficiency of the solar collector is expressed in Equation 5 [23].

$$Q\eta_c = \frac{\dot{Q}_{useful}}{\dot{Q}_{incident}} = \frac{\tau aAG - UA(T_c - T_a)}{AG} \quad (5)$$

$$= \tau a - U\frac{(T_c - T_a)}{G}$$

where $\dot{Q}_{useful}$ is the useful heat energy and $\dot{Q}_{incident}$ is the total radiation energy.

### 2.2. Prototype Design of Solar Collector Hybrid Heating System

The prototype of the hybrid heating system with a solar collector is given in Figure 4. In the creation of the prototype planar solar collector, tank, radiator, pump, resistance, and control panel are used. Outdoor temperatures are recorded with LM35 temperature sensors, tank liquid temperature is recorded with a NTC temperature sensor. Arduino Mega 2560 is used as a microcontroller in the control of the hybrid heating system. The Arduino Mega 2560 is an open-source Atmega2560 based microprocessor board built on the foundations of the development environment that implements a simple I/O board and processing language. It has 54 digital input/output pins (14 of which can be used as PWM outputs), 16 analog inputs, 4 UARTs (hardware serial ports), a 16 MHz crystal oscillator, a USB connector, a power jack, an ICSP connector, and it consists of a reset button.

With the planar solar collector, the heat energy taken from the sun is transferred to the nanofluids and stored. When the stored liquid reaches the set value according to the air temperature value, it is sent to the radiator. When the nanofluid cannot reach the desired temperature level, it is heated with the help of a resistance. The efficiency of the results relative to each other is tested by considering only the solar energy of the nanofluids and the temperature changes in the tank.

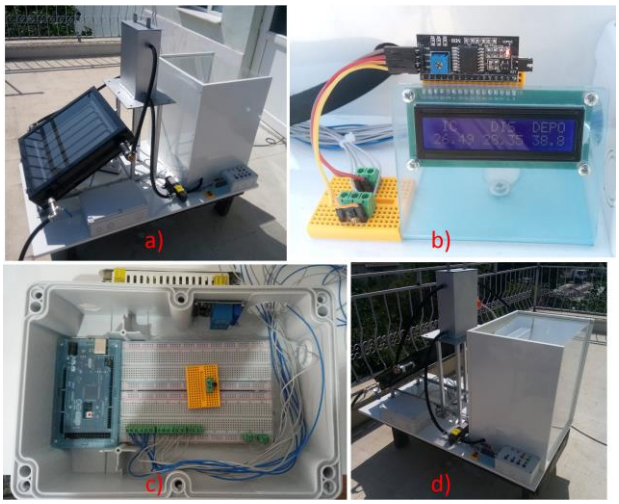


**Figure 4.** (a) Front view of the hybrid heating system prototype, (b) panel control, (c) electronic design, and (d) back view of the hybrid heating system prototype

The flow diagram of the hybrid working algorithm of the produced prototype is given in Figure 5. The flow chart is the presentation of the algorithm that makes the system work in algorithmic order and rule using visual elements.

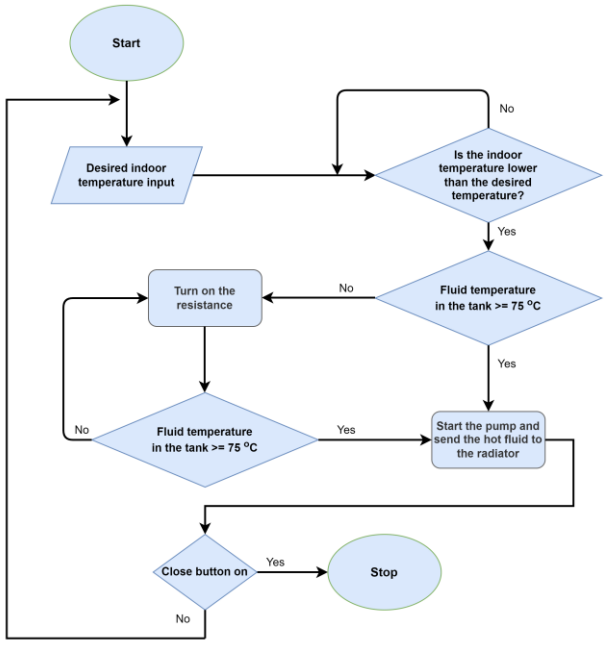


**Figure 5.** Flow chart of the hybrid heating model

### 2.3. Preparation of Nanofluids

Nanofluids are prepared at the rates determined to be tested and kept in 5-liter bottles. nanofluids, each

prepared as 10 liters, are put into the fluid tank for testing on the prototype. The contents and ratios of the prepared mixes are given in Table 1. The bottles in which the nanofluid mix. are prepared are given in Appendix A.

**Table 1**. Mixing ratios and contents of nanofluids

| Mixture | Chemical component | Volume ratio (%) |
|---|---|---|
| 1 | Water<br>Benzotriazole | 99.8%<br>0.2% |
| 2 | Water<br>Monoethylene glycol<br>Benzotriazole | 49.9%<br>49.9%<br>0.2% |
| 3 | Water<br>Propylene glycol<br>Benzotriazole | 49.9%<br>49.9%<br>0.2% |
| 4 | Water<br>Triethylene glycol<br>Benzotriazole | 49.9%<br>49.9%<br>0.2% |
| 5 | Pure Water<br>Aluminum Oxide<br>Benzotriazole | 99.0%<br>0.8%<br>0.2% |
| 6 | Pure Water<br>Copper Oxide<br>Benzotriazole | 99.0%<br>0.8%<br>0.2% |
| 7 | Pure Water<br>Titanium Dioxide<br>Benzotriazole | 99.0%<br>0.8%<br>0.2% |
| 8 | Water<br>Triethylene Glycol<br>Pure Water<br>Aluminum Oxide<br>Benzotriazole | 49.5%<br>24.95%<br>24.95%<br>0.4%<br>0.2% |

## 3. RESULTS

The findings obtained with the experimental studies are given in this section. The performance of nanofluids mixed at certain ratios according to time is investigated.

### 3.1. Test Results of Nanofluid Mixtures (1st-8th mix.)

Temperature changes till ninety minutes are recorded as a result of the tests performed with water, and benzotriazole (1st mix.), water, monoethylene glycol, and benzotriazole (2nd mix.), water, propylene glycol, and benzotriazole (3rd mix.) water, triethylene glycol, and benzotriazole (4th mix.) mixtures. The results obtained are shown in Figure 6.

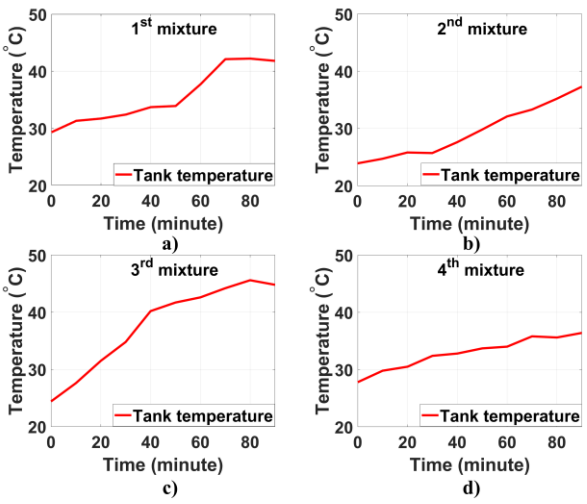


**Figure 6.** The variations of tank temperatures for (a) 1st mix., (b) 2nd mix., (c) 3rd mix., and (d) 4th mix.

Temperature changes are recorded with the tests performed with pure water, aluminum oxide, and benzotriazole (5th mix.), pure water, copper oxide, and benzotriazole (6th mix.), pure water, titanium dioxide, and benzotriazole (7th mix.), water, triethylene glycol, pure water, and aluminum oxide (8th mix.) mixtures. The results obtained are shown in Figure 7.

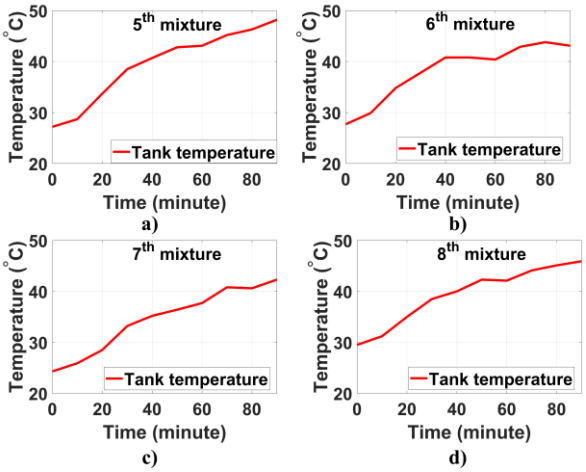


**Figure 7.** The variations of tank temperatures for (a) 5th mix., (b) 6th mix., (c) 7th mix., and (d) 8th mix.

In this work, all measurements are carried out between 1 and 10 July 2022 in Mihalgazi district of Eskişehir province in Turkey. As aforementioned before, the efficiency of the solar collector value is found by dividing $Q_{useful}$ value by the $Q_{incident}$ value as expressed in Equation 5. The symbols in this equation can be expressed as follows. $\tau$ is heat transmittance of glass, $\alpha$ is the absorptivity of the absorber plate, $A$ is the surface area of the collector, $U$ is the heat loss coefficient and $G$ is the solar radiation incident per unit surface area. $G$ value has nearly calculated the values given in Figure 8 for Eskişehir province. Since temperature change of the 5th mix. is maximum, the efficiency is calculated for only 5th mix., and the efficiency depending on collector temperature change is given in Figure 8d. According to the measurement setup in this study, $\tau$ = 0.89, $\alpha$ = 0.92, $U$=10.1 W.°C$^{-1}$m$^{-2}$ for 3 mm single glazed aluminum frame material, $A$= 0.5×0.5 m$^2$ and $T_a$=27.2 °C. $T_c$ for 5th mix. varies from 24 °C to 48.2 °C. We can calculate $G$ value by dividing the value in July in Figure 8a (6.01 KWh.m$^{-2}$.day) by the value in July in Figure 8b (10.52 hours). It should be noted that according to the efficiency value obtained in Figure 8d, the designed system provides sufficient requirements.

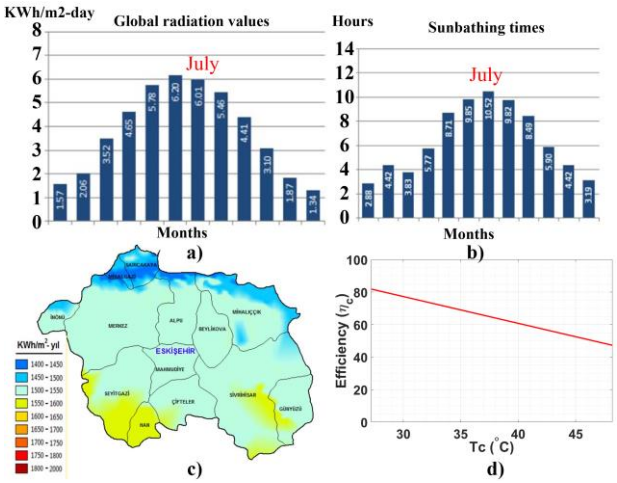


**Figure 8.** a) Global radiation values, b) sunbathing times in Eskişehir province, c) total solar radiation of Eskişehir province and d) efficiency of collector for the 5th mix.

### 3.2. The Comparison of Mixtures Made with Nanofluids

As a result of the tests, the temperature is increased by 12.5°C in the 1st mix., 13.4°C in the 2nd mix., 18.4°C in the 3rd mix. and 8.6°C in the 4th mix. in the range of 0-90 minutes. In similar tests, the temperature increases by 21°C in the 5th mix., 15.4°C in the 6th mix., 18.0°C in the 7th mix., and 16.4°C in the 8th mix. In Figure 9, the heating performances of the mixtures are given together.

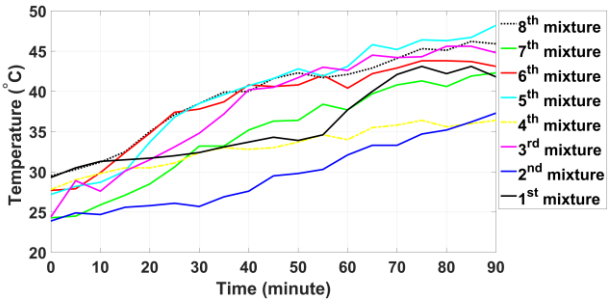


**Figure 9.** The comparison of tank temperatures

- It is observed that the mix. showing the lowest heating rate with a temperature increase of 8.6°C has water, triethylene glycol mix., and the mix. showing the highest heating rate with a temperature increase of 21°C has pure water and aluminum oxide mix.
- Water, propylene glycol mix., and pure water, titanium dioxide mix., which are the mixtures that heat up the most after pure water, aluminum oxide mix., provided positive results when used in solar collectors.
- In the 8th mix., water, pure water, triethylene glycol and aluminum oxide mix. is made and tested. As a result of the tests, a temperature increase of 16.4 degrees is observed in the range of 0-90 minutes.
- With the test results obtained, it is observed that triethylene glycol performs negatively only when mixed with water, and it heats up 2 times more when mixed with aluminum oxide.
- It is seen that it has not appropriate to use a water, triethylene glycol mix. as a heating fluid in solar collectors, but it has appropriated to use pure water, aluminum oxide mix. in solar collectors.
- When the studies in the literature are examined, the heat transfer rates of nanofluids and ethylene glycol groups in solar collectors are investigated. Unlike the studies in the literature, the heat transfer rates of triethylene glycol and triethylene glycol + aluminum oxide mixtures are experimentally investigated in this study. Moreover, the temperature of the pure water + aluminum oxide mix. increased from 27.2 °C to 48.2 °C within 90 minutes, resulting in a 21 °C temperature increase. In the experiment, which is carried out with only water without mixing, the temperature of the water increased from 29.3 °C to 41.8 °C within 90 minutes, resulting in a temperature increase of 12.5 °C. According to the results obtained, it is determined that the pure water + aluminum oxide mixture heated 59.52% more than the normal unmixed water. In another study, it is observed that the pure water + aluminum oxide mixture is 61.1% more efficient than the normal unmixed water in the yield value calculated according to the ASHRAE 93-2003 standard [24].

## 4. DISCUSSION AND CONCLUSION

In this study, a prototype of a hybrid heating system with a solar collector is produced and eight different nanofluids are tested on the prototype. Nanofluid containing triethylene glycol is compared with other nanofluids and its effects on solar collector are investigated. Eight different nanofluids are tested under the same conditions and their thermal performance is evaluated according to each other. As a result of the tests, it has been seen that triethylene glycol had the lowest heating rate. It has been shown that triethylene glycol, which does not transfer heat quickly, can be efficient if it is used as a storage of heat energy obtained as a result of stable performance. It is also observed that the highest temperature increase is achieved with the 21°C temperature increase of the pure water, aluminum oxide mix. In future studies, it is aimed to be used in cases where a low heating rate is desired in accordance with the characteristic features of triethylene glycol.

### Acknowledgement

Authors would like to thank Mr. Ercument BOSTANCI for contributing to the realization of this study and TUBITAK for its support within the scope of 2209-A University Students Research Projects Support Program (Project No: 1919B012006220).

### REFERENCES

[1] Kilic FC. Solar energy, its recent status in turkey and production Technologies. Engineering and Machine. 2015;52(617):94-106.
[2] General Directorate of Meteorology. Effects of Global Warming and Climate Change [Internet]. 2021 [cited 2021 Oct 15]. Available from: https://www.mgm.gov.tr/genel/meteorolojiyegir.aspx?s=19
[3] Gencoglu MT. Importance of renewable energy resources for Turkey. Firat University Journal of Science and Engineering. 2002;14(2):57-64.

[4] Saglam S. Türkiye'nin güneş enerjisi potansiyelinin ve kullanım alanlarının incelenmesi. [M.S. thesis]. Istanbul: Graduate School of Science and Engineering, Marmara University; 2000.
[5] General Directorate of Renewable Energy. Solar Potential Atlas [Internet]. 2021 [cited 2021 Oct 17]. Available from: http://www.gepa.enerji.gov.tr/MyCalculator/
[6] Seydiogullari HS. Renewable energy for sustainable development. Planning Journal. 2013;23(1):19-25.
[7] Ertekin C, Evrendilek F, Kulcu R. Modeling spatio-temporal dynamics of optimum tilt angles for solar collectors in Turkey. Sensors. 2008;8(5): 2913-2931.
[8] Gundogdu K, Kabadayi HS, Ozturk A. Photovoltaic solar panels for you follow a simple and economic system design. Düzce University Journal of Science & Technology. 2016;4(2):634-639.
[9] Bohne D, Fischer S, Obermeier E. Thermal, conductivity, density, viscosity, and prandtl-numbers of ethylene glycol-water mixtures. Reports of the Bunsen Society for Physical Chemistry, 1984;88(8):739-742.
[10] Ogut E, Dilki S. Dalgalı trapez plakalı ısı eşanjörü içindeki nanoakışkanların akış ve ısı transfer karakteristiklerinin incelenmesi. Dicle University Engineering Faculty Journal of Engineering. 2018;10(3):933-943.
[11] Akcay S, Akdag U. Parametric investigation of effect on heat transfer of pulsating flow of nanofluids in a tube using circular rings. Pamukkale University Journal of Engineering Sciences. 2018;24(4):597-604.
[12] Dagdevir T, Ozceyhan V. Investigation of the effect of using water based hybrid nanofluid on thermal and hydraulic performance in a heat exchanger. Erciyes University Institute of Science Journal of Science. 2021;37(1):61-73.
[13] Kilic F, Menlik T, Sözen A. Effect of titanium dioxide/water nanofluid use on thermal performance of the flat plate solar collector. Sol. Energy, 2018;164:101-108.
[14] Verma SK, Tiwari AK, Tiwari S, Chauhan DS. Performance analysis of hybrid nanofluids in flat plate solar collector as an advanced working fluid. Sol. Energy, 2018;167:231-241.
[15] Tong Y, Lee H, Kang W, Cho H. Energy and exergy comparison of a flat-plate solar collector using water, $Al_2O_3$ nanofluid, and CuO nanofluid. Appl. Therm. Eng. 2019;159:113959.
[16] Michael Joseph Stalin P, Arjunan TV, Matheswaran MM, Dolli H, Sadanandam N. Energy, economic and environmental investigation of a flat plate solar collector with $CeO_2$/water nanofluid. J. Therm. Anal. Calorim. 2020;139(5):3219-3233.
[17] Akram N, Montazer E, Kazi SN, Soudagar MEM, Ahmed W, Sarsam W. Experimental investigations of the performance of a flat-plate solar collector using carbon and metal oxides based nanofluids. Energy. 2021;227:120452.
[18] Khetib Y, Alzaed A, Tahmasebi A, Sharifpur M, Cheraghian G. Influence of using innovative turbulators on the exergy and energy efficacy of flat plate solar collector with DWCNTs-$TiO_2$/water nanofluid. Sustainable Energy Technol. Assess. 2022;51:101855.
[19] Özbaş, E. Güneş enerjili su ısıtma sistemleri için termosifon tip ısı borusunda çalışma akışkanı olarak bitkisel atık yağ kullanımının deneysel incelenmesi. Avrupa Bilim ve Teknoloji Dergisi, 2022;(45), 131-134.
[20] Şakirali E. İyonik sıvı bazlı nanoakışkanların (iyonanoakışkan) manyetik alan altındaki akış ve ısı transferi davranışlarının sayısal olarak incelenmesi [M.S. thesis]. Karabük Üniversitesi, Lisansüstü Eğitim Enstitüsü; 2022.
[21] Yilanci A, Atalay O, Kocar G, Eryasar A. Determination of thermal performance of a solar collector by using dynamic test method. Pamukkale University Journal of Engineering Sciences. 2019;25(4):417-422.
[22] Tezcan M. Flat plate solar collectors and efficiency calculation [M.S. thesis]. Istanbul: Graduate School of Science and Engineering, Istanbul Technical University; 2001.
[23] Cengel YA, Boles MA. Introduction and Basic Concepts In: Thermodynamics: an Engineering Approach. McGraw-Hill Companies; 2011. p. 445-460.
[24] Budak N. Güneş kollektörlerinde nanoakışkan kullanımının ısıl verime etkisinin deneysel olarak incelenmesi. [dissertation]. Elâzığ: Firat University; 2016.

## Appendices

**Appendix A.** Photos of Eight Different Mixtures

**1.**

(Water + Benzotriazole)

**2.**

(Water + Monoethylene glycol + Benzotriazole)

**3.**

(Water + Propylene Glycol + Benzotriazole)

**4.**

(Water + Triethylene glycol + Benzotriazole)

**5.**

(Pure water + Aluminum oxide + Benzotriazole)

**6.**

(Pure water + Copper oxide + Benzotriazol)

**7.**

(Pure water + Titanium dioxide + Benzotriazole)

**8.**

(Water + Triethylene glycol + Pure water + Aluminum oxide + Benzotriazole)

Araştırma Makalesi https://doi.org/10.46810/tdfd.1193469 Research Article

BİNGÖL ÜNİVERSİTESİ

Türk Doğa ve Fen Dergisi
Turkish Journal of Nature and Science
www.dergipark.gov.tr/tdfd

# Determination of Self-absorption Correction Factors of Some Algae Samples: An Experimental Study

**Reyhan OZAYDIN OZKARA[1], Canel EKE[2*]**

[1] Akdeniz University, Vocational School of Technical Sciences, Nuclear Technology and Radiation Safety, Antalya Türkiye
[2] Akdeniz University, Faculty of Education, Department of Mathematics and Science Education, Antalya, Türkiye
Reyhan OZAYDIN OZKARA ORCID No: 0000-0003-2699-1060
Canel EKE ORCID No: 0000-0002-6672-6467

**Corresponding author: ceke@akdeniz.edu.tr, caneleke@hotmail.com*

(Received: 23.10.2022, Accepted: 21.02.2023, Online Publication: 27.03.2023)

**Keywords**
Algae,
Self-absorption correction factors,
Gamma-ray spectrometry,
HPGe detector

**Abstract:** The purpose of this study to examine experimentally self-absorption correction factors (SACFs) of some algae samples using gamma-ray spectrometry. Various algae samples were collected from Boğaçay in Antalya, Turkey. Collected algae samples were dried, and masses of the samples were calculated. Then densities of the samples were calculated. Each of algaes was counted with and without point sources which are $^{22}$Na, $^{60}$Co, $^{133}$Ba, and $^{137}$Cs about 1000 seconds using high purity germanium detector. The SACFs of algae samples were determined between 80 keV and 1332 keV gamma-ray energies. As a result, SACFs of studied algae samples generally reduce as gamma-ray energy enhances. SACFs of some algae samples are higher at low photon energies because cross section of the photoelectric effect is higher at low photon energies.



# Bazı Alg Örneklerinin Öz-soğurma Düzeltme Faktörünün Belirlenmesi: Deneysel Bir Çalışma

**Anahtar Kelimeler**
Alg,
Öz soğurma düzeltme faktörleri,
Gama-ışını spektrometresi,
HPGe dedektör

**Öz:** Bu çalışmanın amacı bazı alg örneklerinin öz soğurma faktörünü deneysel olarak gama spektroskopisini kullanarak belirlemektir. İncelenen alg örnekler Antalya ili Boğaçay bölgesinden toplanmıştır. Toplanan alg örnekleri kurutulmuş ve kütleleri hesaplanmıştır. Daha sonra örneklerin özkütleleri hesaplanmıştır. Her bir alg örneği yüksek saflıkta germanium dedektörü kullanılarak $^{22}$Na, $^{60}$Co, $^{133}$Ba, and $^{137}$Cs noktasal kaynaklar olmadan ve bu noktasal kaynaklar ile birlikte 1000 s sayılmıştır. Alg örneklerinin öz-soğurma düzeltme faktörü 80 keV ile 1332 keV gama enerji aralığında belirlenmiştir. Sonuç olarak, çalışılan alg örneklerinin öz-soğurma düzeltme faktörü değerleri genellikle gama enerjisi arttıkça azalmaktadır. Ayrıca, alg örneklerinin öz-soğurma düzeltme faktörü değerleri düşük foton enerjilerinde fotoeleketrik olayın tesir kesitinin düşük enerjilerde daha yüksek olmasından dolayı daha büyüktür.

## 1. INTRODUCTION

Nuclear weapons testing, authorized discharge of radioactive waste to shore, erosion, river transport, dissolution, diffusion, and wind-blown particles, in addition to naturally occurring radionuclides from the atmosphere, have all resulted in worldwide investigations of the radioactivity content of waters and the high seas [1]. When radioactive materials interact aquatic environment for a variety of reasons, they may remain in solution or suspension, precipitate at the bottom, or be consumed by organisms. As a result, they may cause radioactive contamination in the aquatic ecosystem.

Algaes are an important component of the marine ecosystem. Algaes are ubiquitous in the water system and have colonized almost every part of the globe [2]. Since ancient times, they have been used for food, feed, fertilizer, and medicine all over the world, and they are still used in skin care products today. They also contain a high concentration of biofunctional metabolites with potential health benefits [3]. Algaes are biological pointers of contaminants in the sea habitats due to their ability to accumulate radioisotopes, including low-level radionuclides in water [4]. As a result, analyzing marine organisms has become influential method for assessing

the quality of the marine environment. The existence of radionuclides in the sea habitat is the greatest concern because their existence may ascend ecological danger. Various studies have been carried out to investigate the activity concentration of naturally occurring radionuclides found in algaes [4-7].

Using high resolution gamma-ray spectrometry is a simple and influential method for precisely quantifying the natural radionuclide activity concentration of environmental materials like algaes in the scientific literature [8]. High-purity germanium (HPGe) detectors are widely utilized in gamma-ray spectrometry for activity measurements at low radioactivity levels and small sample amounts [9]. The primary superiority of HPGe detector is its high energy resolution, which provides discrimination among near-energy (several keV) emissions [10]. The efficiency curve for a fixed source-sample location is typically optimized in HPGe detector models [11]. The activity concentration of radionuclides connected with a gamma line is calculated by precisely determining its energy peak yield. The total energy peak efficiency of a sample can be calculated experimentally or numerically [12]. Different types of detector efficiency corrections must be applied for each measurement setup to achieve adequate analytical accuracy in gamma-ray spectrometry [13, 14].

Self-attenuation correction factors (SACFs) are of particular interest in sensitive gamma-ray spectrometry. Correction of photon attenuation of studied samples is a critical parameter in volumetric gamma-ray spectrometry [15,16]. The SACF is dependent on the physical properties of studied material. Some information about structure of the studied material can be evaluated by measuring this factor, which is distinguishing feature of the studied material. The self-absorption of gamma rays occurs in gamma spectrometry of environmental samples, reducing counting efficiency [17]. Therefore, determination of SACF of each sample is critical [18]. Furthermore, activity concentrations calculated for radionuclides with gamma emission energies in the small energy range may deviate significantly from expected values if self-absorption effects are not corrected for when the composition and densities of the actual sample differ greatly from those of the reference sample [19, 20]. Especially, at energies lower than 100 keV, the attenuation of gamma rays by the absorber material causes reducing of the photopic intensity in the spectrum [8, 21].

The elemental composition of samples with densities close to that of the reference sample is the primary source of count loss [22]. The bigger gamma-ray absorption is observed at the higher the atomic number of the substance [23].

As photons travel through the material, they interact with material in the form of scattering, absorption, or energy loss. Many factors influence the value of gamma-ray self-absorption. These are the contents of the components of the sample, its atomic density, its weight, and its dependence on gamma emission energy. [17, 24, 22]. Self-attenuation correction can be determined experimentally [13, 23, 24, 26], numerically [14, 27,], or analytically [14,15, 28].
Many researchers investigated the effect of SACF to calculate accurate activity concentration of the samples using gamma-ray spectrometry. [8, 21, 23, 29, 30-33]. The peak count ratio for given energy in a gamma-ray spectrum can easily be used to calculate the intensity of gamma rays at that energy.

The goal of this research is to determine SACFs of eight algae samples collected from Boğaçay in Antalya, Turkey. The SACFs of algae samples will be experimentally determined using the transmission method proposed by Cutshall et al [34].

## 2. MATERIAL AND METHOD

### 2.1. Locations of the Collected Algae Samples

Boğaçay is formed by the combination of the Doyran and Çandır Streams from Antalya Province Konyaaltı Region and the Karaman Stream from the North in Turkey. Eight algae samples from Boğaçay were collected. Table 1 and Figure 1 show coordinates of collected algaes and a mapping of the studied region based on the coordinates.

**Table 1**. Coordinates of the collected algae samples

| Sample Name | Latitude | Longitude |
|---|---|---|
| A1 | 36° 52' 01" | 30° 37' 07" |
| A2 | 36° 51' 58" | 30° 37' 06" |
| A3 | 36° 51' 56" | 30° 37' 06" |
| A4 | 36° 51' 49" | 30° 37' 07" |
| A5 | 36° 51' 43" | 30° 37' 04" |
| A6 | 36° 51' 28" | 30° 37' 06" |
| A7 | 36° 51' 27" | 30° 37' 16" |
| A8 | 36° 51' 20" | 30° 37' 25" |

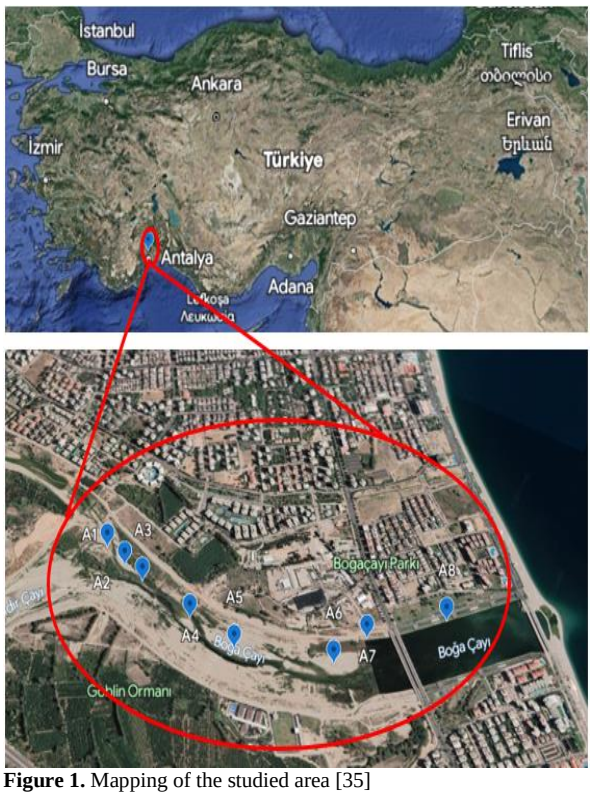


**Figure 1.** Mapping of the studied area [35]

### 2.2. Preparation of the Algae Samples

Eight algae samples were dried in environment for a week before being ground separately and passing through a 2 mm sieve. To calculate density of the of the algae samples, they were dried 24 hours at 80°C in vacuum oven. After drying of the algae samples, the samples were placed in 30 ml plastic containers and then the densities of the samples were calculated. Calculated bulk densities of studied algae samples are presented in Table 2. The bulk density or apparent density is calculated as $\rho = {}^{M}/_{V}$ where $M$ is the oven-dry mass of the sample and $V$ is the total volume of the sample [36, 37]. The bulk densities of the algae samples range from 0.154999 g/cm$^3$ to 0.626192 g/cm$^3$.

**Table 2**. Bulk densities of studied algae samples

| Sample Name | Density (g/cm$^3$) |
|---|---|
| A1 | 0.487575 |
| A2 | 0.396929 |
| A3 | 0.527853 |
| A4 | 0.626192 |
| A5 | 0.20778 |
| A6 | 0.248792 |
| A7 | 0.154999 |
| A8 | 0.230077 |

### 2.3. Counting of the Algae Samples by the HpGe Dedector

The SACFs of the algae samples were obtained using a HPGe detector by using four-point sources which were $^{22}$Na, $^{60}$Co, $^{133}$Ba, and $^{137}$Cs. The point sources were placed on the empty container and algaes samples, respectively to count of the gamma-rays about 1000 s. Schematic view of the experimental setup (see Fig.2) After analyzing of the obtained gamma-ray spectra using the MC$^2$ Analyzer Program [38].

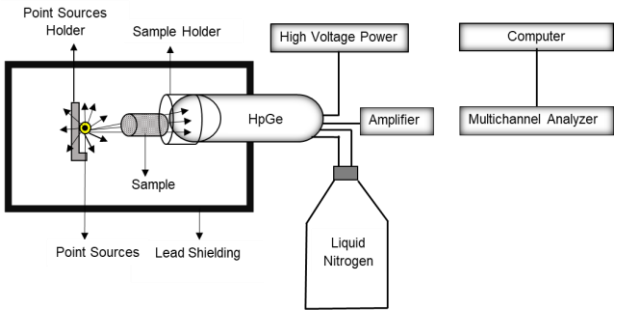


**Figure 2.** Schematic view of the experimental setup

### 2.4. Determination of the SACFs for the Algae Samples

The SACFs of algae samples were carried out experimentally using Cutshall's transfer model [34] is base of the SACFs calculations. Radioactive point sources are used to experimentally determine the SACFs using the Cutshall Method [23, 24]. The Cutshall's transmission method presumes that gamma rays disseminated by the sample have a parallel track for both sample and transmission measurements [39]. Therefore, following formula is used for parallel beams to obtain experimentally SACF of the studied samples [9, 25].

$$SACF = \frac{\ln \frac{I}{I_0}}{\frac{I}{I_0} - 1} \quad (1)$$

where $I$ is the number of counts of the point sources with algae samples and $I_0$ is the number of counts of the point sources with air sample.

## 3. RESULTS

The SACFs of studied algaes dependent with gamma-ray energies vary as illustrated in Figure 3.

Obtained experimentally SACFs of A1, A2, A3 and A4 samples were fitted using exponential function (see Eq.2) and those of A5, A6 and A7 were fitted using power function (See Eq.3) as following functions (see eqs: 2 and 3):

$$y = a + b\exp^{(-cx)} \quad (2)$$

$$y = a + bx^{(c)} \quad (3)$$

Where $a$, $b$ and $c$ are fit parameters, $x$ is related gamma-ray energy and $y$ is the SACFs. The fit parameters and $R^2$ values of algaes (see Table 3).

The $R^2$ values of A1, A2, A3 and A4 are very high, and this value shows that the exponential fit model is suitable for experimental data of algae samples. The SACFs relative to air versus the energy for the A5, A6, A7 and A8 could not be fitted very well using exponential function therefore A5, A6 and A8 were fitted using power function. As illustrated in Figure 3, the SACFs of the A7 which vary nearly constant is not fitted using exponential or power functions. This situation can be explained that densities and elemental composition of the studied algae samples. Because the SACFs of the algae samples modify with elemental composition and density of the samples [22, 23, 40].

At low photon energies, the SACFs of algae samples are higher and at higher photon energies the SACFs of the algae samples are lower and they tend to be steady. Because the large atomic number of sample is the higher the interaction of the gamma-rays with it gets, and the cross section of the photoelectric effect of the samples is higher in the low photon energies and at middle photon energies, Compton scattering is effective [40, 41]. At higher photon energies, pair production is dominant [42].

Consequently, this study is an experimental study for the application of the Cutshall's transmission method and this method is fundamentally based on the normal incidence radiation hypothesis, which states that all gamma radiation reaching the detector follows a straight line through the source.

**Table 3**. Fit parameters and $R^2$ for the SACFs of algae samples relative to air sample

| Sample No | *a* | *b* | *c* | $R^2$ |
|---|---|---|---|---|
| A1 | 1.04269±0.00285 | 0.19242±0.01563 | 0.00509±5.27791E-4 | 0.97947 |
| A2 | 1.03083±0.0056 | 0.12789±0.02312 | 0.00378±0.00101 | 0.90138 |
| A3 | 1.04807±0.00539 | 0.26541±0.04076 | 0.00673±0.00124 | 0.93952 |
| A4 | 1.04698±0.00459 | 0.30602±0.04005 | 0.00751±0.00117 | 0.95975 |
| A5 | 1.04239±0.00689 | -8.9595E-7±7.04026E-6 | 1.43857±1.06852 | 0.86551 |
| A6 | 1.05113±0.01472 | -6.0585E-6±6.23221E-5 | 1.19927±1.28356 | 0.72248 |
| A7 | Not fitted. | | | |
| A8 | 1.03949±0.01214 | -9.11523E-7±1.42105E-5 | 1.41712±2.1189 | 0.60941 |

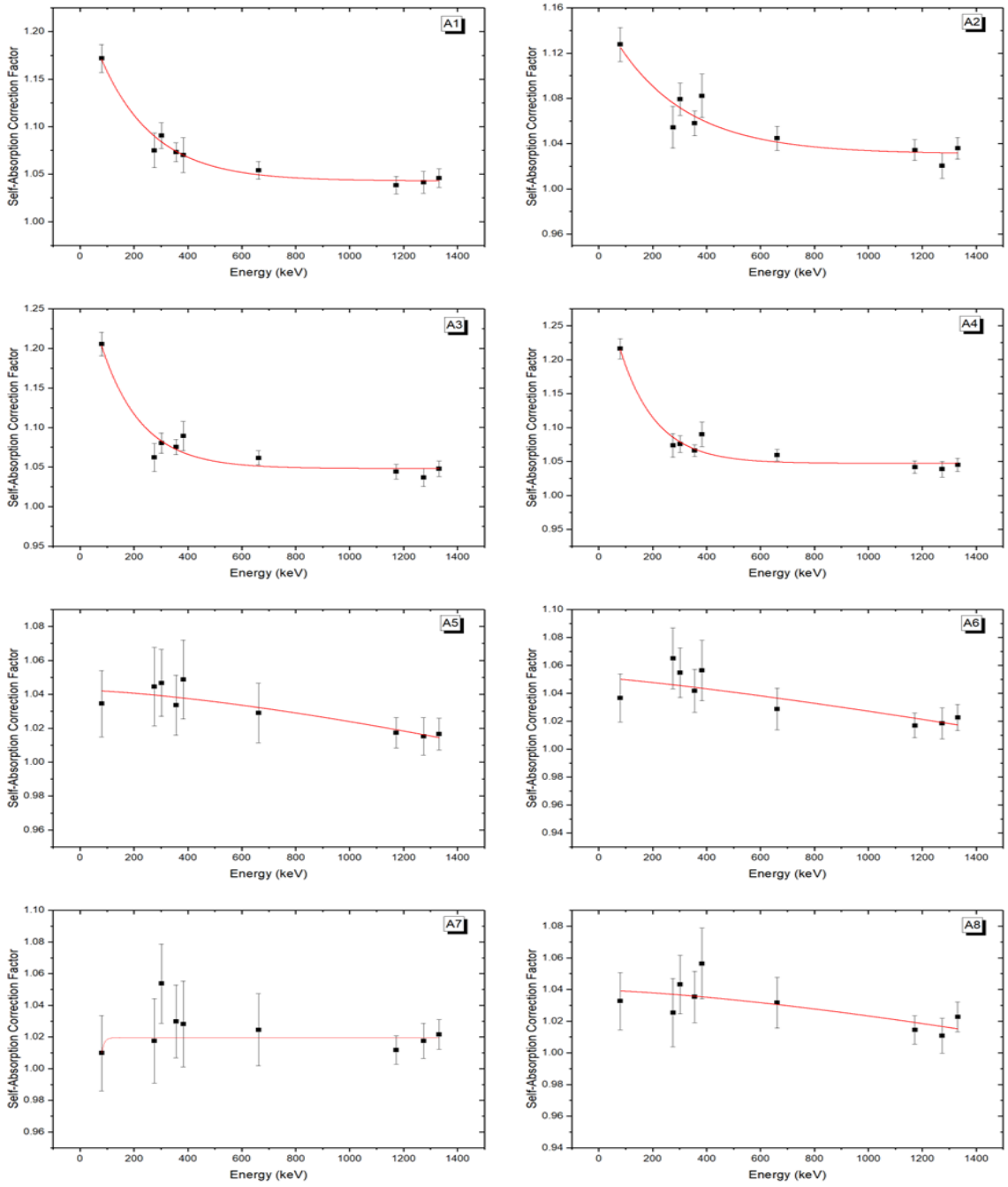


**Figure 3.** Variation of the SACFs relative to air of studied algae samples with photon energies

The path of gamma radiation within the source is determined by the source's origin and direction of emission [43]. This method determines the attenuated intensity of the source, as well as the difference

between the peak count rate at a given energy and the weldless working sample for a point source placed above the working sample.

## 4. DISCUSSION AND CONCLUSION

In this study, the SACFs of the algae samples collected from Boğaçay in Antalya, Turkey were determined experimentally using HPGe detector. Determination of the SACFs of the samples are significant to obtain accurate activity concentration of the samples if the geometry of the sample and reference material are different. The SACFs of the A1, A2, A3 and A4 are fitted exponential function and they are fitted power function for A5, A6 and A8 samples. As the density of the samples increase, the SACFs of the samples enhance. The significant differences can be found samples A1-A4 and A5, A6 and A8. These are due to the density of the composition of the studied algae samples. Besides, particularly, the SACFs of the algae samples are significant at low photon energies. At higher photon energies, the SACFs of the algae samples are lower and nearly steady due to the interactions of the gamma-ray with matter as photoelectric effect, Compton scattering and pair production. As a result, this paper is a new experimental example for determination of the SACs of algae samples using Cutshall's transmission method.

**Acknowledgement**

This paper was presented as oral presentation in 6th International Conference on Advances in Natural and Applied Sciences (ICANAS 2022), 11-13 October 2022, Ağrı/Türkiye.

## REFERENCES

[1] Linsley G, Sjöblom KL, Cabianca T. Overview of the point sources of anthropogenic radionuclides in the oceans, in: Marine Radioactivity. Radioactiv. Environm. H.D. Livingston (Ed.). 2004;6.

[2] Peng C, Ma Y, Ding Y, He X, Zhang P, Lan T, et al. Influence of Speciation of Thorium on Toxic Effects to Green Algae Chlorella pyrenoidosa. Int. J. Mol. Sci. 2017; 18:795.

[3] Barrow C, Shahidi F. Marine nutraceuticals and functional foods. CRC Press, Boca Raton. 2007; 512.

[4] Tejera A, Pérez-Sánchez L, Guerra G, Arriola-Velásquez A, Alonso H, Arnedo M, et al. Natural radioactivity in algae arrivals on the Canary coast and dosimetry assessment. Sci. Total Environ. 2009; 658:122-131.

[5] Khandaker M, Heffny NAB, Amin YM, Bradley DA. Elevated concentration of radioactive potassium in edible algae cultivated in Malaysian seas and estimation of ingestion dose to humans. Algal Research. 2019; 38:101386.

[6] Uddin S, Bebhehani M, Sajid S, Karam Q. Concentration of 210Po and 210Pb in macroalgae from the northern Gulf, Mar. Pollut. Bull. 2019; 145:474-479.

[7] Shigeoka Y, Myose H, Akiyama S, Matsumoto A, Hirakawa N, Ohashi H, et al. Temporal Variation of Radionuclide Contamination of Marine Plants on the Fukushima Coast after the East Japan Nuclear Disaster. Environ. Sci. Technol. 2019; 53(16):9370-9377.

[8] Robu E, Giovani C. Gamma-ray self-attenuation corrections in environmental samples. Rom. Rep. Phys. 2009;61(2):295.

[9] Gouda MM, Hamzawy A, Badawi MS, El Hatib AM, Thabet AA, Abbas MI. Mathematical method to calculate full-energy peak efficiency of detectors based on transfer technique. Indian J Phys. 2016; 90:201–210.

[10] Guerra JG, Rubiano JG, Winter G, Guerra AG, Alonso H, Arnedo MA. Computational characterization of HPGe detectors usable for a wide variety of source geometries by using Monte Carlo simulation and a multi-objective evolutionary algorithm. Nucl. Instrum. Methods. Phys. Res. A. 2017; 858:113-122.

[11] Subercaze A, Sauzedde T, Domergue C, Destouches C, Philibert H, Fausser C, et al. Effect of the geometrical parameters of an HPGe detector on efficiency calculations using Monte Carlo methods, Nuclear Instruments and Methods in Physics Research Section A: Nucl. Instrum. Methods Phys. Res. A. 2022; 1039:167096.

[12] Mohebian M, Pourimani R, Modarresi SM. Using MCNP Simulation for Self-absorption Correction in HPGe Spectrometry of Soil Samples. Iran J Sci Technol Trans Sci. 2019; 43:3047–3052.

[13] Barba-Lobo A, Bolívar JP. A practical and general methodology for efficiency calibration of coaxial Ge detectors. Measurement. 2022; 197:111295.

[14] Sostaric M, Babic D, Petrinec B, Zgorelec Z. Determination of gamma-ray self-attenuation correction in environmental samples by combining transmission measurements and Monte Carlo simulations. Appl. Radiat. Isot. 2016; 113:110-116.

[15] Jodłowski P. Self-absorption correction in gamma-ray spectrometry of environmental samples - an overview of methods and correction values obtained for the selected geometries. Nukleonika. 2006;51(2): 21–25.

[16] Khater AEM, Ebaid YY. A simplified gamma-ray self-attenuation correction in bulk samples. Appl. Radiat. Isot. 2008; 66:407–413.

[17] Pourimani R, Mohebian M, Modarresi SM. Assessment of the Soil Self-Attenuation Correction Factor to Determine the Efficiency of a High-Purity Germanium Detector. Iran J Sci Technol Trans Sci. 2020; 44:311–317.

[18] Eke C, Boztosun I. Gamma-ray spectrometry for the self-attenuation correction factor of the sand samples from Antalya in Turkey. J Radioanal Nucl Chem. 2014; 301:103–108.

[19] Barba-Lobo A, Mosqueda F, Bolívar JP. A general function for determining mass attenuation

coefficients to correct self-absorption effects in samples measured by gamma spectrometry. Radiat. Phys. Chem. 2021; 179:109247

[20] McMahon CA, Fegan MF, Wong J, Long SC, Ryan TP, Colgan PA. Determination of self-absorption corrections for gamma analysis of environmental samples: comparing gamma-absorption curves and spiked matrix-matched samples. Appl. Radiat. Isot. 2004; 60 (2–4):571-577.

[21] Millsap DW, Landsberger S. Self-attenuation as a function of gamma ray energy in naturally occurring radioactive material in the oil and gas industry. Appl. Radiat. Isot. 2015; 97:21-23.

[22] Dziri S, Nachab A, Nourreddine A, Sellam A, Pape A. Elemental composition effects on self-absorption for photons below 100 keV in gamma-ray spectrometry. Nucl Instrum Methods Phys Res B. 2014: 330:1-6.

[23] Bonczyk M. Determination of 210Pb concentration in NORM waste – An application of the transmission method for self-attenuation corrections for gamma-ray spectrometry. Radiat. Phys. Chem. 2018; 148:1-4.

[24] Barros LF, Pecequilo BRS. Self-attenuation factors in gamma-ray spectrometry of select sand samples from Camburi Beach, Vitória, Espírito Santo, Brazil. Radiat. Phys. Chem. 2014; 95:339-341.

[25] Misiak R, Hajduk R, Stobiński M, Bartyzel M, Szarłowicz K, Kubica B. Self-absorption correction and efficiency calibration for radioactivity measurement of environmental samples by gamma-ray spectrometry. Nukleonika. 2011; 56:23-28.

[26] Bouisset P, Lefèvre O, Cagnat X, Kerlau G, Ugron A, Calmet D. Direct gamma-X spectrometry measurement of 129I in environmental samples using experimental self-absorption corrections. Nucl. Instrum. Methods Phys. Res.,Sect. A. 1999; 437(1):114-127.

[27] Eke C, Yildirim A. Experimental and Simulation Results of the Self-Absorption Correction Factors of Some Chemical Fertilizers in the Energy Range from 80 to 1332 keV. Bull. Russ. Acad. Sci. Phys. 2020; 84:1012–1021.

[28] Pilleyre T, Sanzelle S, Miallier D, Fain D, Courtine F. Theoretical and experimental estimation of self-attenuation corrections in determination of 210Pb by γ-spectrometry with well Ge detector. Radiat. Meas. 2006; 41(3):323-329.

[29] Bolivar JP, García-León M, García-Tenorio R. On self-attenuation corrections in gamma-ray spectrometry. Appl. Radiat. Isot. 1997; 48(8):1125-1126.

[30] Eke C, Agar O, Boztosun I, Aslan A, Emsen B. Determination of self-attenuation correction factor for lichen samples by using gamma-ray spectrometry. Kerntechnik. 2017; 82 (1):136-139.

[31] Cessna JT, Golas DB, Bergeron DE. Source self-attenuation in ionization chamber measurements of 57Co solutions. Appl. Radiat. Isot. 2016; 109:402-404.

[32] Boshkova T, Minev L. Corrections for self-attenuation in gamma-ray spectrometry of bulk samples Appl. Radiat. Isot. 2001; 54:777-783.

[33] Al-Masri MS, Hasan M, Al-Hamwi A, Amin Y, Doubal AW. Mass attenuation coefficients of soil and sediment samples using gamma energies from 46.5 to 1332 keV. J. Environ. Radioact. 2013; 116:28-33.

[34] Cutshall NH, Larsen IL, Olsen CR. Direct analysis of 210Pb in sediment samples: self-absorption corrections. Nucl Instrum Methods Phys Res.1983; 206:309-312.

[35] Google Earth; (2023) [cited 16 March 2023]. Available from: https://www.google.com/intl/tr/earth/

[36] Al-Shammary AAG, Kouzani AZ, Kaynak A, Khoo SY, Norton M, Gates W. Soil Bulk Density Estimation Methods: A Review. Pedosphere. 2018; 28(4): 581-596.

[37] Han Y, Zhang J, Mattson KG, Zhang W, Weber TA. (2016), Sample Sizes to Control Error Estimates in Determining Soil Bulk Density in California Forest Soils. Soil Sci. Soc. Am. J. 2018; 80: 756-764.

[38] MC2 Analyzer; (2022) [cited 2022 October 12]. Available from: https://www.caen.it/products/mc2analyzer/

[39] Lurian AR, Millward GE, Sima O, Taylor A, Blake W. Self-attenuation corrections for Pb-210 in gamma-ray spectrometry using well and coaxial HPGe detectors. Appl. Radiat. Isot. 2018; 134:151-156.

[40] Ba VN, Thien BN, Loan TTH. Effects of element composition in soil samples on the efficiencies of gamma energy peaks evaluated by the MCNP5 code. Nucl. Eng. Technol., (2021); 53: 337-343.

[41] Barba-Lobo A, Mosqueda F, Bolivar JP. A general function for determining mass attenuation coefficients to correct self-absorption effects in samples measured by gamma spectrometry. Radiat. Phys. Chem. 2022; 179: 109247.

[42] Gilmore GR. Practical Gamma-Ray Spectroscopy. 2nd ed. Warrington: Wiley; 2008.

[43] Barrera M, Suarez-Llorens A, Ruiz MC, Alonso JJ, Vidal J. Theoretical determination of gamma spectrometry systems efficiency based on probability functions. Application to self-attenuation correction factors. Nucl. Instrum. Methods. Phys. Res. A. 2017; 854:31-39.

Cilt 12, Sayı 1, Sayfa 82-90, 2023 Volume 12, Issue 1, Page 82-90, 2023

Araştırma Makalesi https://doi.org/10.46810/tdfd.1211012 Research Article

Türk Doğa ve Fen Dergisi
Turkish Journal of Nature and Science
www.dergipark.gov.tr/tdfd

# Effects on Machinability of Minimum Quantity Lubrication Strategy during Milling of ST52 Steel

**Serhat ŞAP**[1*]

[1] Bingöl University, Technical Sciences Vocational School, Electricity and Energy Department, Bingöl, Türkiye
Serhat Şap ORCID No: 0000-0001-5177-4952

**Corresponding author: ssap@bingol.edu.tr*

(Received: 28.11.2022, Accepted: 22.02.2023, Online Publication: 27.03.2023)

**Keywords**
ST52 steel,
Machinability,
Minimum quantity lubrication,
Taguchi technique

**Abstract:** This study focuses on milling under sustainable cutting conditions of ST52 steel, frequently used in the manufacturing industry. ST52 steel is a good candidate as a workpiece because it is inexpensive and readily available. The cutting zone minimum quantity lubrication technology was used during processing to achieve sustainable conditions. The experiments used three cutting speeds (120-180-240 m min-1), three feed rates (0.12-0.18-0.24 mm rev-1), and a constant depth of cut (0.5 mm). Taguchi $L_9$ orthogonal array was used to reduce repetitions. The response parameters are surface roughness, flank wear, and cutting temperature. As a result, compared to the dry environment, the minimum quantity lubrication environment improved surface roughness by approximately 62.37%, flank wear by about 9.95%, and cutting temperature by about 13.82%. In addition, the most effective control factors on response parameters were determined by statistical analysis.



# ST52 Çeliğinin Frezelenmesi Sırasında Minimum Miktarda Yağlama Stratejisinin İşlenebilirliğe Etkileri

**Anahtar Kelimeler**
ST52 çelik,
İşlenebilirlik,
Minimum miktarda yağlama,
Taguchi tekniği

**Öz:** Bu çalışma, imalat sanayisinde sıklıkla kullanılan ST52 çeliğinin sürdürülebilir kesme koşulları altında frezelenmesine odaklanmaktadır. ST52 çeliği, ucuz olması ve kolayca bulunabilmesi nedeniyle iş parçası olarak iyi bir adaydır. Sürdürülebilir koşullara ulaşmak için işleme sırasında kesme bölgesinde minimum miktarda yağlama teknolojisi kullanıldı. Deneylerde üç kesme hızı (120-180-240 m $dk^{-1}$), üç ilerleme hızı (0.12-0.18-0.24 mm $dev^{-1}$) ve sabit kesme derinliği (0.5 mm) seçilmiştir. Tekrarları azaltmak için Taguchi $L_9$ ortogonal dizisi kullanıldı. Yanıt parametreleri; yüzey pürüzlülüğü, kenar aşınması ve kesme sıcaklığıdır. Sonuç olarak minimum miktarda yağlama yapılan ortamda kuru ortama göre yüzey pürüzlülüğünde yaklaşık % 62.37, yanak aşınmasında yaklaşık % 9.95 ve kesme sıcaklığında yaklaşık % 13.82 oranında iyileşme sağlanmıştır. Ayrıca yanıt parametreleri üzerinde en etkili kontrol faktörleri istatistiksel analizlerle belirlenmiştir.

## 1. INTRODUCTION

With the advancement of technology, the number of organizations in the industrial sector is increasing. Thus, the demand for many materials in the production sector is expanding daily [1]. ST52 steel is one of the most demanded products by companies in the industrial sector all over the world. ST52 structural steels are known as steels containing up to 0.2% carbon [2]. In other words, it can also be called steel with a tensile strength of at least 52 kg $mm^{-1}$. It can be used in machine parts exposed to constant and variable loads. ST52 steel is frequently preferred, especially in the automotive industry. This material is needed in the industrial sector due to its good applicability. Due to its easy formability, it has a usage area in almost every field.

The process of transforming the raw material into the desired product is called manufacturing. Many different methods can be used in the manufacturing process. These methods can be called machining and chipless manufacturing. In machining methods, machining can be done by removing chips from the workpiece with techniques such as turning, milling, and planing [3, 4]. The chip removal mechanism is a very complex operation. The cutting tool can be exposed to very high internal stress and excessive heat during machining [5].

These stresses and high temperatures cause different wear mechanisms on the cutting tool. Deformations and wear during machining adversely affect the cutting tool and workpiece [6]. Conventional cutting fluids are used in machining to prevent these unfavorable circumstances [7]. These fluids are soluble in water. Although conventional cutting liquids lower the temperatures in the cutting area, they have many negative aspects. These liquids are dangerous to the environment and workers' health. In addition, because they are applied in the form of flood cooling, their costs are high. Many researchers have been drawn to the minimum quantity lubrication (MQL) strategy as an alternative to traditional liquids in recent years [8-11]. The MQL system aims to increase productivity by using high-efficiency cutting fluids sensitively and economically [12]. This technology is highly efficient when compared to flood cooling. Compared to traditional cutting fluids, the MQL strategy is economical and environmentally friendly, especially in machine tools [13]. There are many studies in the literature using the MQL cooling strategy [14-17]. For example, Hadad and Sadeghi [18] investigated the machinability of AISI 4140 steel in an MQL environment. They claimed that when milling AISI 4140 material with MQL, the temperature at the tool-chip interface was around 350 °C lower than in a dry environment. Muhammed and Choudhury [19] used an MQL environment in the milling of AISI 4340. They discovered that using liquids with low viscosity in the MQL environment is more beneficial. They also reported that with the MQL technique, wastes could be reduced, and an environmentally friendly sustainable production could be made. Salur et al. [20] investigated machinability properties by milling AISI 1040 steel in dry and MQL conditions. They reported that the MQL environment outperformed the dry environment, with improvements in all processing parameters.

In this study, different machining parameters and different cooling/lubrication strategies were used during the milling of ST52, which is widely used in the manufacturing industry. There are limited studies in the literature on the processing of ST52 steel with environmentally friendly cooling/lubrication strategies. However, the limited number of studies supports the original side of the article. Three different cutting speeds (120-180-240 m $min^{-1}$), three different feed rates (0.12-0.18-0.24 mm $rev^{-1}$), and three different cooling/lubrication environments were used in the experiments (dry-air-MQL). To reduce the number of experiments and costs, the Taguchi $L_9$ orthogonal array was used. Obtained results were analyzed comparatively.

## 2. MATERIAL AND METHOD

In this study, ST52 material, which is a commercially available low-carbon steel, was used as the workpiece. This material has usage areas in almost every field of the industrial sector. Sample dimensions are in the form of a 50x50x5 mm plate. Table 1 shows the chemical compositionof the workpiece.



**Table 1.** Chemical composition of ST52 [21]

| Material | Carbon (wt.%) | Silicon (wt.%) | Manganese (wt.%) | Phosphorus (wt.%) | Sulfur (wt.%) | Chromium (wt.%) | Molybdenum (wt.%) |
|---|---|---|---|---|---|---|---|
| **ST52** | max 0.20 | max 0.21 | 1.2 | 0.01 | max 0.035 | 0.008 | max 0.005 |

The experiments were carried out on a computer numerically controlled milling machine (DAHLIH MCV-860). As cutting tools, AlTiN-coated carbide inserts were used. Cutting speed (120-180-240 m $min^{-1}$), feed rate (0.12-0.18-0.24 mm $rev^{-1}$), and cutting environment were all variables (dry-air-MQL). The cutting depth was calculated to be 0.50 mm. The machinability parameters were determined by considering the characteristics of the workpiece and the recommendations of the cutting tool manufacturer. Three different parameters were selected to cool/lubricate the chip tool interface. Air cooling and MQL system compared to a dry environment. Air cooling is done with the help of a compressor connected to the machine tool. The MQL environment was implemented through a Werte Micro Stn-15 model system. The cutting fluid in the MQL system is delivered to the cutting environment in the form of pressure and mist at regular intervals. The cutting tool and workpiece are therefore effectively cooled with a small amount of coolant. The nozzle was placed at a distance of 40 mm from the cutting zone, taking into account the manufacturer's recommendations (7 bar compressor pressure, liquid flow rate 45 mL $h^{-1}$, spray angle 40°). Pressurized oil was transferred to the cutting zone in a pulverized manner from a 5 mm diameter nozzle. After the experiment, the wear amount and images of the cutting tool were determined with the help of the Insize ISM-PM200SA Digital Microscope. Temperatures in the cutting zone during tests were measured by means of a thermal imager (Testo 871). To get an idea about the surface integrity of the processed material, a TIME3200 model surface roughness measuring device was preferred. The arithmetic mean was taken by measuring five times in each sample.

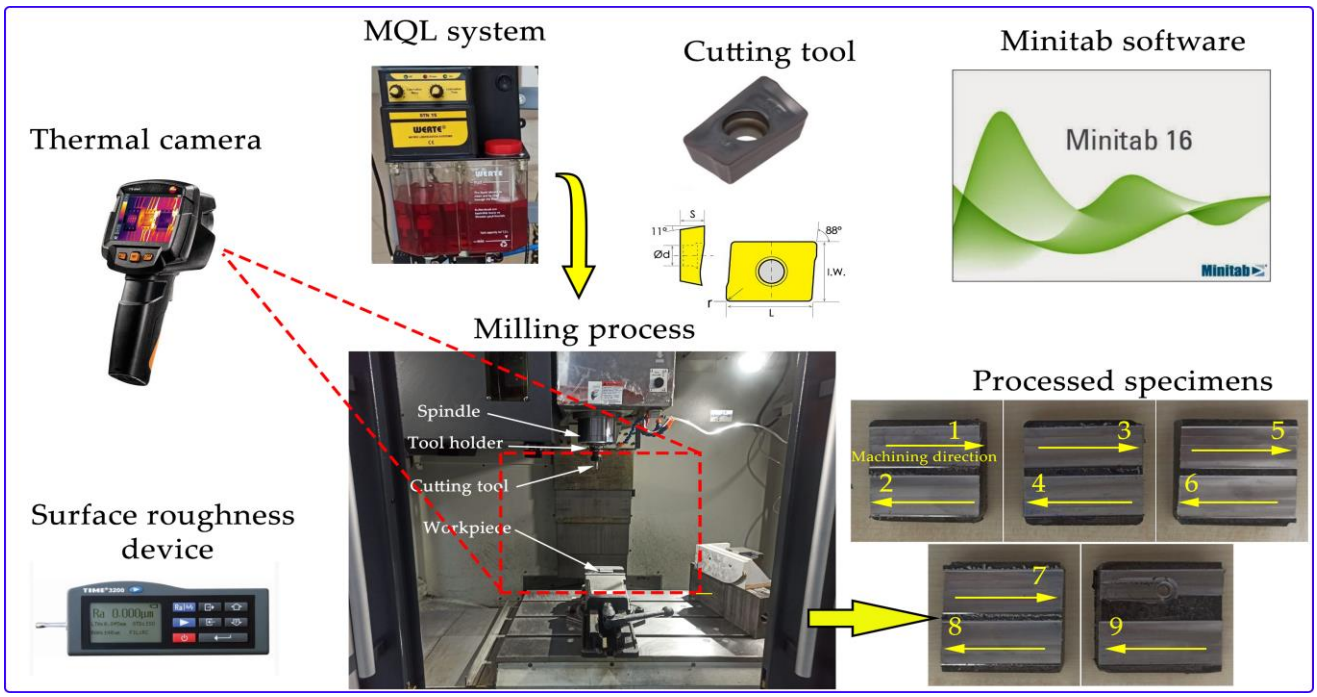


**Figure 1.** Experimental setup

Taguchi $L_9$ orthogonal array is designed to obtain more results with a minimum number of experiments. To cut expenses and discover the most effective parameters, many researchers choose the Taguchi approach. In Table 2, the Taguchi $L_9$ design is given. The process conditions and stages are shown in Table 3. An equation is applied to establish a relationship between the experimental results obtained in the Taguchi technique and the desired values. This equation is converted into a signal-to-noise (S/N) ratio via Minitab software. Since the smallest values are better in the results of the machinability experiments, the "smaller is better" equation was used. S/N ratios were found with the help of the Equation 1.

$$S/N = -10 \log \left[ \frac{1}{n} \sum_{i=1}^{n} (y^2) \right] \quad (1)$$

Here y; response parameters n; the repeating number for the test conditions, i; It represents n repetition times.

**Table 2.** Taguchi $L_9$ ($3^3$) design

| Exp. number | Cutting speed (m min$^{-1}$) | Feed rate (mm rev$^{-1}$) | Cooling/ Lubrication |
|---|---|---|---|
| 1 | 120 | 0.12 | Dry |
| 2 | 120 | 0.18 | Air |
| 3 | 120 | 0.24 | MQL |
| 4 | 180 | 0.12 | Air |
| 5 | 180 | 0.18 | MQL |
| 6 | 180 | 0.24 | Dry |
| 7 | 240 | 0.12 | MQL |
| 8 | 240 | 0.18 | Dry |
| 9 | 240 | 0.24 | Air |

**Table 3.** Variables and steps of process

| Milling parameters | Unit | Levels | | |
|---|---|---|---|---|
| | | 1 | 2 | 3 |
| Cooling conditions | - | Dry | Air | MQL |
| Cutting speed, ($V_c$) | m min$^{-1}$ | 120 | 180 | 240 |
| Feed rate, ($f_n$) | mm rev$^{-1}$ | 0.12 | 0.18 | 0.24 |



## 3. RESULTS AND DISCUSSION

Milling studies on ST57 were carried out in a variety of cutting conditions and with different processing settings. The findings of surface roughness, tool wear, cutting temperature, and statistical analysis were carefully analyzed.

### 3.1. Surface Roughness Analysis

Surface integrity is very important in machinability studies. Therefore, it is necessary to fully understand the surface roughness values in the surface integrity of the test sample. Figure 2 depicts 3D surface graphs illustrating the relationship between various cutting conditions, cutting environments, and surface quality. The lowest surface roughness values were measured as 1.996 µm in a dry environment, 1.256 µm in the air environment, and 0.751 µm in the MQL environment. It seems that the best cutting environment is MQL. It was determined that the MQL environment provides an improvement of approximately 62.37% compared to the dry environment and approximately 40.20% compared to the air environment. With MQL environment, cooling and lubrication processes are carried out in the cutting zone [22]. In this way, surface roughness can also be reduced. In dry machining conditions, cutting temperatures can reach maximum levels. Therefore, some wear occurs on the cutting tool. Due to these adverse conditions, the surface roughness may deteriorate. Cutting variables and cutting

environments can have a significant impact on surface roughness. When the 3D visuals are inspected, it is clear that the surface roughness rises as the cutting speed increases and reduces when the feed rate increases. As a result, the obtained results can be said to be in line with previous research.

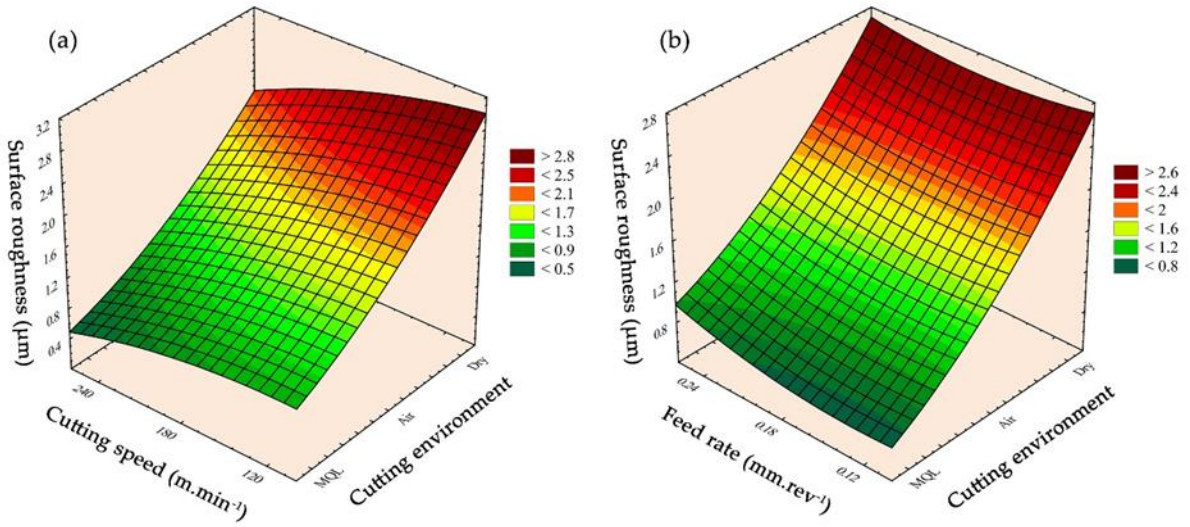


**Figure 2.** 3D surface plots showing the relationship of surface roughness with various conditions; a) Cutting speed-Cutting environment, b) Feed rate-Cutting environment

### 3.2. Flank Wear Analysis

Tool wear is a phenomenon that severely affects all parameters in machining. It is a parameter that must be monitored to maintain tool life and surface integrity [23]. Figure 3 depicts 3D surface plots that demonstrate the effects of various cutting conditions (cutting speed, feed rate) and cutting environments (dry, air, MQL) on flank wear. The lowest flank wear values; were 462 µm in the dry environment, 437 µm in air, and 416 µm in the MQL environment. MQL environment has an improvement of approximately 9.95% compared to the dry environment and about 4.80% compared to the air environment. When evaluated in terms of flank wear, it is seen that the best cutting environment is MQL. High temperatures in the cutting zone in a dry environment can cause plastic deformation and cause severe damage to the cutting tool [24]. Therefore, the amount of flank wear increases more in dry conditions. When cutting parameters were evaluated, an increase in flank wear values was seen as cutting speed was increased (Figure 3a). The opposite is true for feed rate. The flank wear, on the other hand, diminishes when the feed rate increases.



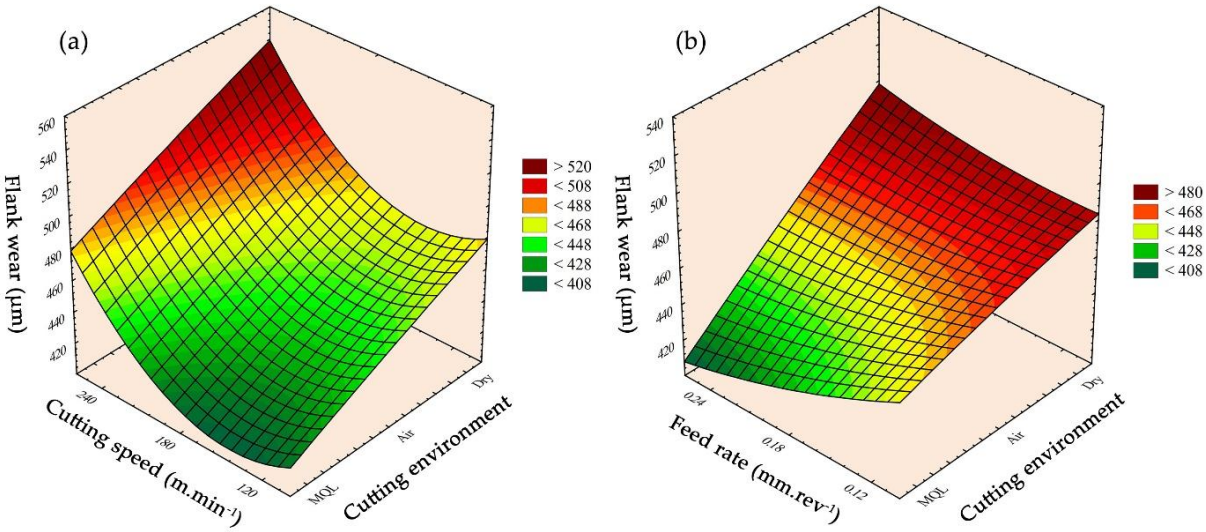


**Figure 3.** 3D surface plots showing the relationship of flank wear with various conditions; a) Cutting speed-Cutting environment, b) Feed rate-Cutting environment

Figure 4 depicts the wear dimensions of cutting tools following milling experiments at various cutting conditions, feed rates, and cutting speeds of 120 m $min^{-1}$. According to the photographs obtained from the optical images, it is seen that the amount of flank wear decreases as you go from the dry environment to the MQL environment. Furthermore, it was revealed that when the feed rate increased, the flank wear values reduced.

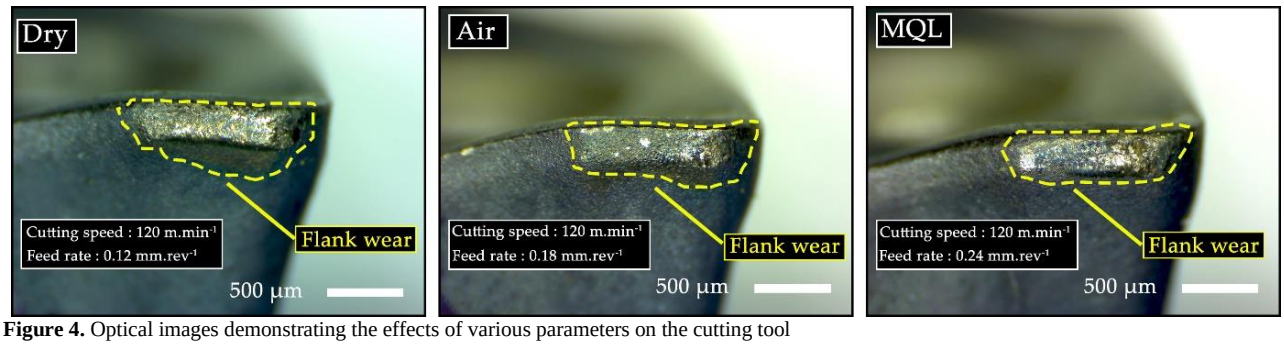


**Figure 4.** Optical images demonstrating the effects of various parameters on the cutting tool

### 3.3. Cutting Temperature Analysis

In machining, cutting temperature is one of the most critical parameters determining cutting tool wear and surface roughness. Heat is generated on the workpiece and cutting tool during machining owing to friction. However, this temperature can reach very high levels in the tool-chip interface. The temperatures measured in this study are those in the cutting zone between the cutting tool and the workpiece. Temperatures occurring at the tool-chip interface cannot be reduced by conventional coolants. Because high cutting and feed rates might make fluid penetration into the cutting zone harder [25]. Figure 5 shows 3D surface graphs that show the influence of different processing settings on cutting temperature. As can be seen from the 3D graphics, it is seen that the cutting temperature decreases as you go from the dry environment to the MQL environment. The cutting fluid may be effectively transferred to the chip tool interface in a pressured and pulverized state thanks to the MQL system. Thus, high temperatures caused by the friction of hard particles breaking off from both the cutting tool and the workpiece in the cutting zone are reduced. The lowest cutting temperature; was determined as 104.9 °C in a dry environment, 95.6 °C in an air environment, and 90.4 °C in an MQL environment. It was revealed that in the MQL environment, the cutting temperature reduced by approximately 13.82% when compared to the dry environment and by roughly 5.43% when compared to the air environment. The cutting temperature, on the other hand, rises as the cutting speed and feed rate rise. Because more friction occurs as the cutting speed and feed rate increase, plastic deformation increases and the temperature rises to higher levels.



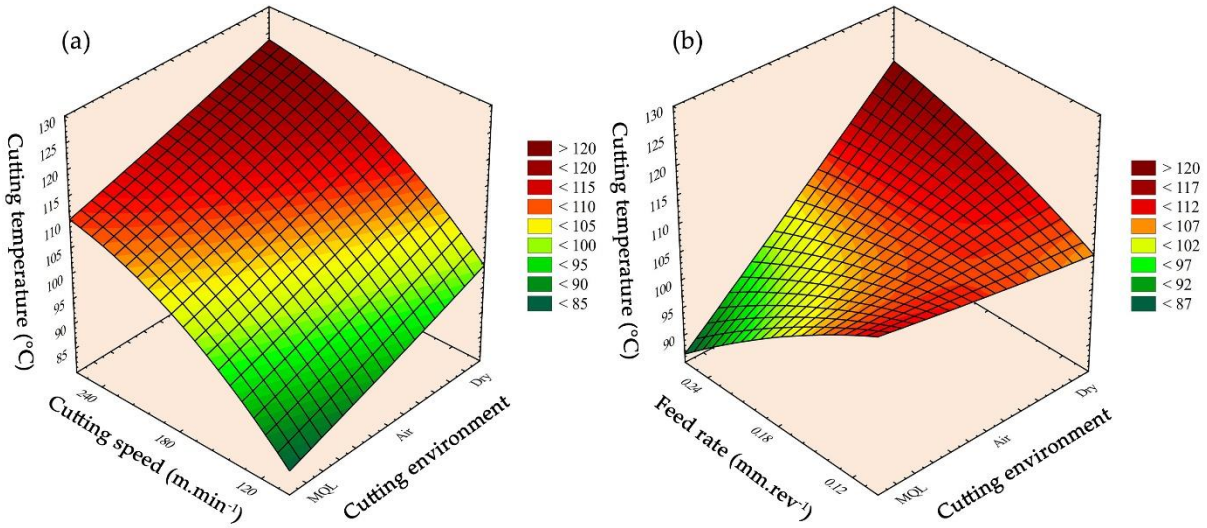


**Figure 5.** 3D surface plots showing the relationship of cutting temperature with various conditions; a) Cutting speed-Cutting environment, b) Feed rate-Cutting environment

### 3.4. Statistical Analysis

For researchers, experiments can often be difficult and costly. The higher the number of experiments, the higher the cost and burden. In this method, which was invented by a researcher named Taguchi, the number of experiments can be reduced by using the loss function resulting from the mean target deviations. In the Taguchi method, response parameters are defined in the first place, and then a standard way is followed by choosing the S/N ratios [26]. Response parameters; surface roughness ($R_a$), Flank wear ($V_b$) and Cutting temperature ($T_c$). Table 4 displays the experimental results as well as the S/N ratios. The Taguchi method focuses on the S/N ratio since noise has an effect on the response parameters. Maximum S/N ratios are required for positive results of response parameters. Therefore, the S/N ratios are; It is based on 1.5454 dB for $R_a$, -52.3819 dB for $V_b$ and -39.1234 dB for $T_c$.

**Table 4.** S/N percentages and tests data

| Experiment number | $R_a$ (µm) | $V_b$ (µm) | $T_c$ (°C) | S/N for $R_a$ (dB) | S/N for $V_b$ (dB) | S/N for $T_c$ (dB) |
|---|---|---|---|---|---|---|
| 1 | 2.565 | 471 | 104.9 | -8.1817 | -53.4604 | -40.4155 |
| 2 | 1.859 | 437 | 95.6 | -5.3855 | -52.8096 | -39.6092 |
| 3 | 1.047 | 418 | 90.4 | -0.3989 | -52.4235 | **-39.1234** |
| 4 | 1.402 | 459 | 112.2 | -2.9349 | -53.2363 | -40.9999 |
| 5 | 0.837 | 416 | 103.9 | **1.5454** | **-52.3819** | -40.3323 |
| 6 | 2.705 | 462 | 110.4 | -8.6433 | -53.2928 | -40.8594 |
| 7 | 0.751 | 464 | 110.1 | 2.4872 | -53.3304 | -40.8357 |
| 8 | 1.996 | 517 | 123.7 | -6.0032 | -54.2698 | -41.8474 |
| 9 | 1.256 | 481 | 113.4 | -1.9797 | -53.6429 | -41.0923 |

Figure 6 depicts main effect graphs created with Minitab software that show the effects of response parameters on control factors. The larger the impact of the control factor on the response parameter, the steeper the lines in the graphs. It is observed that the cutting environment line is more vertical in the surface roughness and flank wear graphics. According to this, the most effective control factor in surface roughness and flank wear is the cutting environment. In terms of cutting temperature, however, the cutting speed control factor was found to be more upright. As can be observed, cutting speed is the most efficient temperature control component. On all response characteristics, the feed rate was shown to be the least effective control factor.

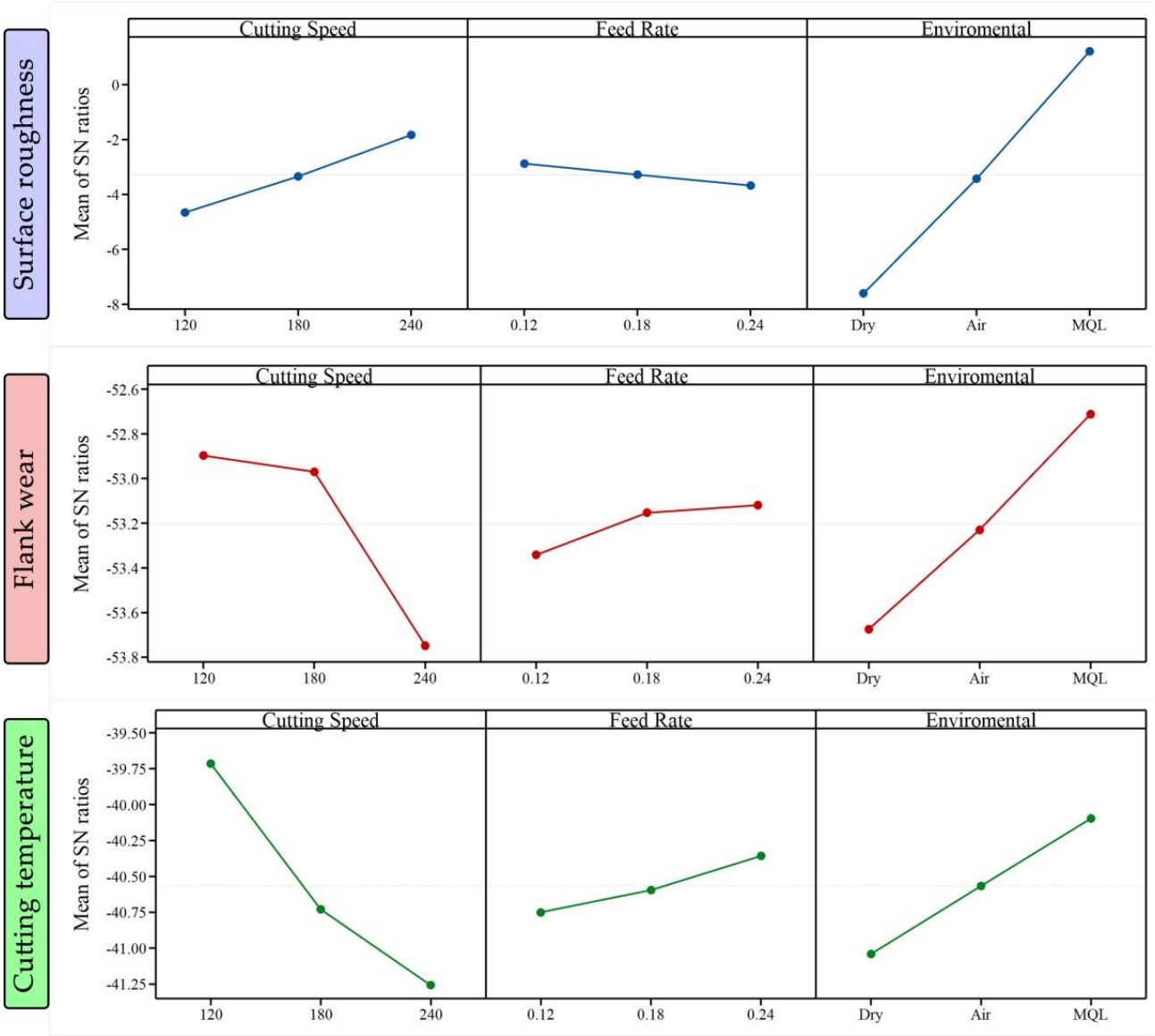


**Figure 6.** Plots of main effects of control factors on response parameters

Table 5 shows the analysis of variance (ANOVA) table for all response parameters and contribution rates. ANOVA provides information on the importance of control factors based on the averages of response parameters in different combinations. The analysis was based on the level of significance. For example, a P value of 0.05 in the table is deemed significant. Adj SS corrected the sum of squares, Adj MS corrected the mean squares, and F and P values in the table demonstrate the significance of control variables. The contribution rates of the most influential factors specified in the main impact graphs are given as numerical values in this table. According to the table, the cutting environment was the most effective factor for surface roughness (88.971%), the cutting environment was the most effective factor for flank wear (48.678), and the cutting speed was the most effective factor for cutting temperature (69.048). According to the table, the significance levels of the most effective control factors are; It was determined as 0.013 for surface roughness, 0.034 for flank wear, and 0.022 for cutting temperature. Since all control factors were <0.05, the analysis can be said to be significant.

**Table 5.** ANOVA table for factors affecting response parameters and contribution rates

| Source | DF | Seq SS | Adj SS | Adj MS | F | P | Contribution rate (%) |
|---|---|---|---|---|---|---|---|
| **Surface roughness** | | | | | | | |
| Cutting speed (m min$^{-1}$) | 2 | 11.978 | 11.978 | 5.9892 | 7.73 | 0.115 | 9.123 |
| Feed rate (mm rev$^{-1}$) | 2 | 0.954 | 0.954 | 0.4771 | 0.62 | 0.619 | 0.727 |
| Environmental | 2 | 116.817 | 116.817 | 58.4083 | 75.42 | **0.013** | **88.971** |
| Residual Error | 2 | 1.549 | 1.549 | 0.7744 | - | - | 1.180 |
| Total | 8 | 131.298 | - | - | - | - | 100.000 |
| **Flank wear** | | | | | | | |
| Cutting speed (m min$^{-1}$) | 2 | 1.33177 | 1.33177 | 0.66589 | 26.81 | 0.036 | 46.569 |
| Feed rate (mm rev$^{-1}$) | 2 | 0.08626 | 0.08626 | 0.04313 | 1.74 | 0.365 | 3.016 |
| Environmental | 2 | 1.39209 | 1.39209 | 0.69605 | 28.03 | **0.034** | **48.678** |
| Residual Error | 2 | 0.04967 | 0.04967 | 0.02483 | - | - | 1.737 |
| Total | 8 | 2.85979 | - | - | - | - | 100.000 |
| **Cutting temperature** | | | | | | | |
| Cutting speed (m min$^{-1}$) | 2 | 3.68712 | 3.68712 | 1.84356 | 44.36 | **0.022** | **69.048** |
| Feed rate (mm rev$^{-1}$) | 2 | 0.23405 | 0.23405 | 0.11703 | 2.82 | 0.262 | 4.383 |
| Environmental | 2 | 1.33563 | 1.33563 | 0.66782 | 16.07 | 0.059 | 25.012 |
| Residual Error | 2 | 0.08312 | 0.08312 | 0.04156 | - | - | 1.557 |
| Total | 8 | 5.33993 | - | - | - | - | 100.000 |



Figure 7 represents graphs comparing experimental results of response parameters with results estimated by ANOVA. As seen from the graphs, surface roughness shows 98.82% accuracy, flank wear 98.26%, and cutting temperature 98.44% accuracy. Statistical analysis accepts it when the success rate is 85% and above. It is understood that high success rates were achieved in this study.

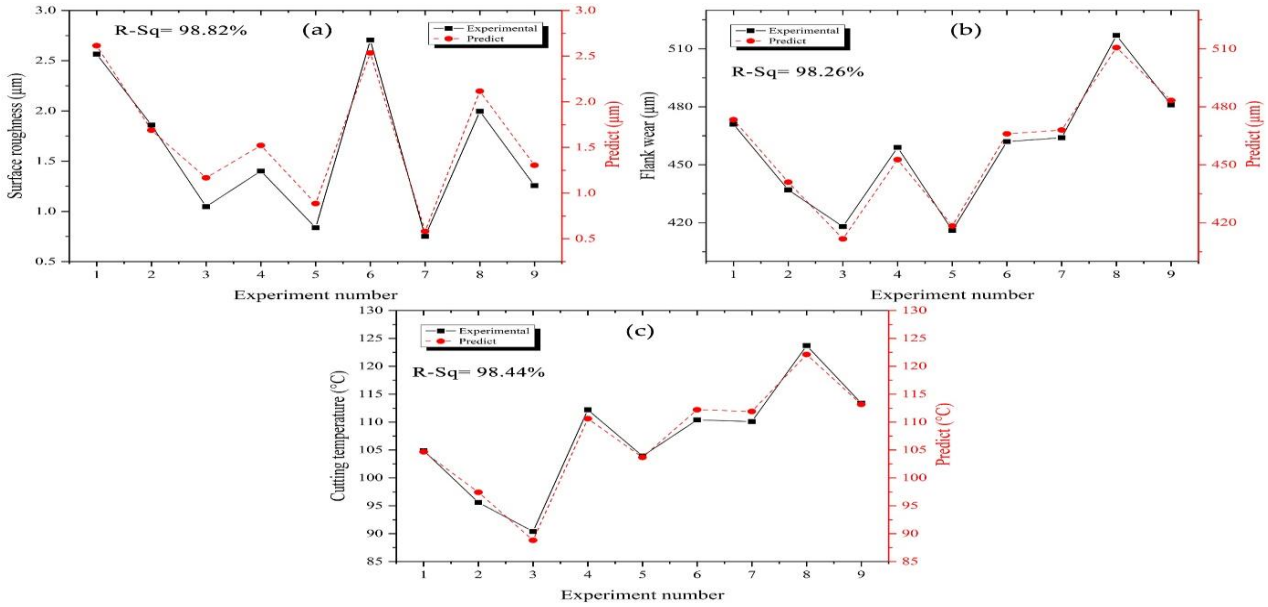


**Figure 7.** Comparison of experimental and projected findings for the response parameters

## 4. CONCLUSION

This study investigated the milling of ST52 steel under different cooling/lubrication conditions. For this purpose, surface roughness, flank wear, and cutting temperature were analyzed. In addition, Taguchi analysis was performed to reduce the number of experiments and costs. The results are as follows.

- In the surface roughness test, the MQL environment produced the lowest value (0.751 m). The MQL environment improved by roughly 62.37% as compared to the dry environment.

- The lowest flank wear value was obtained as a result of machining in the MQL environment and recorded as 416 µm. Flank wear is reduced by approximately 9.95% compared to a dry environment.

- The MQL environment had the lowest temperature (90.4 °C) in the cutting temperature experiments. When compared to the dry environment, the MQL environment reduced the cutting temperature by approximately 13.82%.

- The most effective control factors on the response parameters were determined by statistical analysis; it was determined the cutting environment for surface roughness (88.971%) and flank wear (48.678), and cutting speed (69.048) for cutting temperature.

## REFERENCES


[1] Salur E. Understandings the tribological mechanism of Inconel 718 alloy machined under different cooling/lubrication conditions. Tribol Int. 2022;174:107677.

[2] Ekinovic S, Prcanovic H, Begovic E. Investigation of Influence of MQL Machining Parameters on Cutting Forces During MQL Turning of Carbon Steel St52-3. Procedia Eng. 2015;132:608-14.

[3] Şap S, editor Ultra Yüksek Mukavemetli S1100 Çeliğinin MQL koşullarında Frezelenmesinin Takım Aşınması Üzerindeki Etkileri. 4 th International Conference on Applied Engineering and Natural Sciences; 2022 November 10-13, 2022; Konya/Turkey.

[4] Meddour I, Yallese MA, Khattabi R, Elbah M, Boulanouar L. Investigation and modeling of cutting forces and surface roughness when hard turning of AISI 52100 steel with mixed ceramic tool: cutting conditions optimization. Int J Adv Manuf Technol. 2015;77(5):1387-99.

[5] Usca ÜA, Uzun M, Şap S, Giasin K, Pimenov DY, Prakash C. Determination of machinability metrics of AISI 5140 steel for gear manufacturing using different cooling/lubrication conditions. J Mater Res Technol. 2022;21:893-904.

[6] Mia M, Gupta MK, Singh G, Królczyk G, Pimenov DY. An approach to cleaner production for machining hardened steel using different cooling-lubrication conditions. J Clean Prod. 2018;187:1069-81.

[7] Şap S, Usca ÜA, Uzun M, Kuntoğlu M, Salur E. Performance evaluation of AlTiN coated carbide tools during machining of ceramic reinforced Cu-based hybrid composites under cryogenic, pure-minimum quantity lubrication and dry regimes. J Compos Mater. 2022;56(22):3401-21.

[8] Boswell B, Islam MN, Davies IJ, Ginting YR, Ong AK. A review identifying the effectiveness of minimum quantity lubrication (MQL) during conventional machining. Int J Adv Manuf Technol. 2017;92(1):321-40.

[9] Chetan, Ghosh S, Rao PV. Comparison between sustainable cryogenic techniques and nano-MQL cooling mode in turning of nickel-based alloy. J Clean Prod. 2019;231:1036-49.

[10] Debnath S, Reddy MM, Yi QS. Environmental friendly cutting fluids and cooling techniques in machining: a review. J Clean Prod. 2014;83:33-47.

[11] Dureja JS, Singh R, Singh T, Singh P, Dogra M, Bhatti MS. Performance evaluation of coated carbide tool in machining of stainless steel (AISI 202) under minimum quantity lubrication (MQL). Int J Precis Eng Manuf. 2015;2(2):123-9.

[12] Şap S, Usca ÜA, Uzun M, Kuntoğlu M, Salur E, Pimenov DY. Investigation of the Effects of Cooling and Lubricating Strategies on Tribological Characteristics in Machining of Hybrid Composites. Lubricants. 2022;10(4):63.

[13] Usca ÜA, Şap S, Uzun M. Evaluation of Machinability of Cu Matrix Composite Materials by Computer Numerical Control Milling under Cryogenic LN2 and Minimum Quantity Lubrication. J Mater Eng Perform. 2022:1-15.

[14] Gupta MK, Sood PK, Sharma VS. Investigations on Surface Roughness Measurement in Minimum Quantity Lubrication Turning of Titanium Alloys Using Response Surface Methodology and Box–Cox Transformation. J Manuf Sci Eng. 2016;16(2):75-88.

[15] Khan MMA, Mithu MAH, Dhar NR. Effects of minimum quantity lubrication on turning AISI 9310 alloy steel using vegetable oil-based cutting fluid. J Mater Process Technol. 2009;209(15):5573-83.

[16] Korkmaz ME, Gupta MK, Boy M, Yaşar N, Krolczyk GM, Günay M. Influence of duplex jets MQL and nano-MQL cooling system on machining performance of Nimonic 80A. Manuf Process. 2021;69:112-24.

[17] Makhesana MA, Patel KM, Khanna N. Analysis of vegetable oil-based nano-lubricant technique for improving machinability of Inconel 690. Manuf Process. 2022;77:708-21.

[18] Hadad M, Sadeghi B. Minimum quantity lubrication-MQL turning of AISI 4140 steel alloy. J Clean Prod. 2013;54:332-43.

[19] Muaz M, Choudhury SK. Experimental investigations and multi-objective optimization of MQL-assisted milling process for finishing of AISI 4340 steel. Measurement. 2019;138:557-69.
[20] Salur E, Kuntoğlu M, Aslan A, Pimenov DY. The Effects of MQL and Dry Environments on Tool Wear, Cutting Temperature, and Power Consumption during End Milling of AISI 1040 Steel. Metals. 2021;11(11):1674.
[21] Farzin YA, Najafizadeh A, Nejad EH. Effect of temperature in intercritical treatment on microstructure, tensile properties and hardness in dual phase ST52 steel. Journal of Materials and Environmental Science. 2015;5:1716-22.
[22] Şap E, Usca ÜA, Uzun M. Machining and optimization of reinforced copper composites using different cooling-lubrication conditions. J Braz Soc Mech Sci & Eng. 2022;44(9):399.
[23] Şap S, Uzun M, Usca ÜA, Pimenov DY, Giasin K, Wojciechowski S. Investigation of machinability of Ti–B-SiCp reinforced Cu hybrid composites in dry turning. J Mater Res Technol. 2022;18:1474-87.
[24] Sarıkaya M, Güllü A. Multi-response optimization of minimum quantity lubrication parameters using Taguchi-based grey relational analysis in turning of difficult-to-cut alloy Haynes 25. J Clean Prod. 2015;91:347-57.
[25] Dhar NR, Islam MW, Islam S, Mithu MAH. The influence of minimum quantity of lubrication (MQL) on cutting temperature, chip and dimensional accuracy in turning AISI-1040 steel. J Mater Process Technol. 2006;171(1):93-9.
[26] Dutta S, Narala SKR. Optimizing turning parameters in the machining of AM alloy using Taguchi methodology. Measurement. 2021;169: 108340.

Cilt 12, Sayı 1, Sayfa 91-98, 2023

Volume 12, Issue 1, Page 91-98, 2023

Araştırma Makalesi https://doi.org/10.46810/tdfd.1224967 Research Article

Türk Doğa ve Fen Dergisi
Turkish Journal of Nature and Science
www.dergipark.gov.tr/tdfd

# A Field Study on Determination of Nematode Diversity in Canola Fields in Tekirdağ

**Lerzan ÖZTÜRK**[1*]

[1] Tekirdağ Viticulture Research Institute, Tekirdağ, Türkiye
Lerzan ÖZTÜRK ORCID No: 0000-0003-2199-6807

*Corresponding author: lerzanozturk@gmail.com*

(Received: 27.12.2022, Accepted: 28.02.2023, Online Publication: 27.03.2023)

**Keywords**
Nematode diversity, Canola, Tekirdağ, Türkiye

**Abstract:** Soil samples were collected from 28 canola fields in Malkara, Süleymanpaşa, Muratlı, Hayrabolu, and Ergene districts of Tekirdağ to study nematode faunal structure. Soil samples were taken from 0-60 cm depth in each field, and a total of 28 genera of nematodes were extracted by the modified Baermann Funnel method. Eight of these nematodes were bacterivores, three were fungivores, five were omnivores, three were predators, and the rest were plant-parasitic species. Nematodes in survey areas had colonizer-persister values ranging from 1 to 5. The maturity and community indices were also calculated, and four were found as follows: Enrichment (E): 34.6±15.2; Maturity (MI): 2.68±0.05; Plant parasite (PPI): 2.69±0.39; Shannon's diversity (H'): 1.80±0.26. The predominant taxa were *Filenchus* (100%), *Mesodorylaimus* (92%), and *Ditylenchus* (85.1%). In terms of density in 100 $cm^3$ soil, the highest values were found in the genus *Acrobeloides* (192 individuals/100 $cm^3$ soil), and the number of *Ditylenchus* (57 individuals/100 $cm^3$ soil), *Filenchus* (180 individuals/100 $cm^3$ soil), and *Mesodorylaimus* (165 individuals/100 $cm^3$ soil) individuals were also found high in some soils. The plant parasitic nematodes identified in canola fields include *Boleodorus tylactus*, *Filenchus cylindricus*, *F. sheri*, *F. thornei*, *Geocenamus brevidens*, *Helicotylenchus digonicus*, *Malenchus fusiformis*, *Paratylenchus variabilis*, *Pratylenchoides alkani*, *Rotylenchus robustus*, *Tylenchorhynchus annulatus*, and *T. cylindricus*.



# Tekirdağ İli Canola Tarlalarında Nematod Çeşitliliğinin Belirlenmesi Üzerine Bir Arazi Çalışması

**Anahtar Kelimeler**
Nematod çeşitliliği, Kanola, Tekirdağ, Türkiye

**Öz:** Tekirdağ'da Malkara, Süleymanpaşa, Muratlı, Hayrabolu ve Ergene ilçelerinde 28 kanola tarlasından alınan toprak örnekleri nematod faunasının belirlenmesi için incelenmiştir. Her tarlada 0-60 cm derinlikten toprak örneği alınmış ve bu örneklerden modifiye Baermann Funnel metoduyla 28 cinse ait nematod türleri toplanmıştır. Bunlardan 8 tanesi bakteri ile beslenen, 3 tanesi fungus ile beslenen, 5 tanesi omnivor, 3 tanesi predatör ve kalanı bitki paraziti türlerdir. Sürvey alanlarındaki nematodların colonizer-persister değerleri 1 ile 5 arasında değişmiştir. Maturity ve kommunite indeksleri de hesaplanmış ve 4 tanesi şu değerleri almıştır: Enrichment (E): 34.6±15.2; Maturity (MI): 2.68±0.05; Plant parasite (PPI): 2.69±0.39; Shannon's diversity (H'): 1.80±0.26. En yaygın cinsler *Filenchus* (100%), *Mesodorylaimus* (92 %), ve *Ditylenchus* (85.1 %) olmuştur. 100 $cm^3$ toprakta yoğunluk bakımından en yüksek değer *Acrobeloides* (192 birey/100 $cm^3$ toprak)'te bulunmuş, bazı topraklarda ise *Ditylenchus* (57 birey/100 $cm^3$ toprak), *Filenchus* (180 birey/ 100 $cm^3$ toprak) ve *Mesodorylaimus* (165 birey/100 $cm^3$ toprak) birey sayısıda yüksek bulunmuştur. Kanola tarlalarında teşhis edilen bitki paraziti nematodlar ise *Boleodorus tylactus, Filenchus cylindricus, F. sheri, F. thornei, Geocenamus brevidens, Helicotylenchus digonicus, Malenchus fusiformis, Paratylenchus variabilis, Pratylenchoides alkani, Rotylenchus robustus, Tylenchorhynchus annulatus,* ve *T. cylindricus*'tur.

## 1. INTRODUCTION

Canola (*Brassica napus* L. var. *napus* ) is an annual herbaceous plant with winter and summer-grown varieties. It is classified in the Brassicaceae family and Brassica (Cruciferae) genus. Canola is among the plants grown as a source of vegetable oil from 240 plant species in this genus. Canola plant has been produced with the

breeding studies of rapeseed, which is the third largest vegetable oil source and the second largest protein meal source in the world with the seeds it produces [1]. Plant seeds contain 38-50% oil and 16-24% protein [32]. Prohibited from cultivation in the past because of containing erucic acid, which is harmful to human health, and glucosinolate, toxic to animal health, canola is now grown in many countries [27]. The pulp of this plant, whose seeds are used in oil production for human consumption, is also used to make animal feed and biofuel.

Canola is grown on 73.776.943 hectares of land in the world, and Canada, China, India, Germany, France, Australia, and Poland are world leaders in terms of production [34]. Türkiye has a 37.601 ha cultivation area, and, Tekirdağ ranks first with a 12.261 ha area in terms of production [4]. Although it is grown in all districts in Tekirdağ province, the production is more intensive in Çorlu, Hayrabolu, Marmara Ereğlisi, Malkara, Muratlı, and Süleymanpaşa.

The soil micro and macrofauna include several pests, insects, and microorganisms. Members from phylum Nematoda constitute almost the majority of the total organisms. The phylum includes animal-plant parasites and marine and free-living non-parasitic nematodes. Dozens of species with different feeding habitats, such as plant parasites (e.g. Meloidogyne spp.), bacterivores (e.g. Acrobeles spp.), omnivores (e.g. Dorylaimus spp.), or predatory (e.g. Seinura spp.), and fungivores (e.g. Mononchus sp.) live in agricultural areas [20].

There are limited studies on nematode diversity associated with canola in a limited number of countries and Türkiye as well [29, 9]. Therefore a study in canola fields in Tekirdağ is planned. The study aimed at the determination of free-living and plant parasitic nematodes. Nematode genera in the surveyed fields were determined. Nematodes were grouped based on feeding style and feeding habitat. The maturity and community indices were calculated. Plant parasitic nematode species were described based on morphometric characteristics.

## 2. MATERIAL AND METHOD

### 2.1. Study Area Information

The study was conducted in the province of Tekirdag, located northwest of Turkey, on the coast of the Marmara Sea. Viticulture, sunflower, and wheat cultivation are the most common agricultural activity in the region. Canola is also grown in all districts in Table 1 and is cultivated in rotation with sunflower and wheat.

**Table 1.** Canola production area, districts, total production in 2021 [4]

| DISTRICTS | TOTAL PRODUCTION AREA (ha) | TOTAL PRODUCTION (ton) |
|---|---|---|
| ÇERKEZKÖY | 2.3 | 9 |
| ÇORLU | 2.200 | 7.900 |
| ERGENE | 700 | 2.800 |
| HAYRABOLU | 1325 | 4.630 |
| KAPAKLI | 9.6 | 24 |
| MALKARA | 1800 | 7.010 |
| MARMARA | 1.550 | 5.950 |
| EREĞLİSİ | | |
| MURATLI | 1750 | 6.970 |
| SARAY | 250 | 1.000 |
| SÜLEYMANPAŞA | 2.250 | 8.300 |
| ŞARKÖY | 425 | 4.250 |

### 2.2. The Survey, Soil Collection, and Nematode Recovery

Within the scope of the study, canola fields in Malkara, Muratlı, Hayrabolu, Marmara ereğlisi, Çorlu, Süleymanpaşa, and Şarköy districts were surveyed in May, and soil samples were collected from 28 fields (Figure 1). Soils taken from 0-60 cm depth in the root zone of 5 randomly selected plants in each field were collected, and approximately 1 kg of soil was arranged per field. While sampling, attention was paid to ensure at least a 1 km distance between each field.

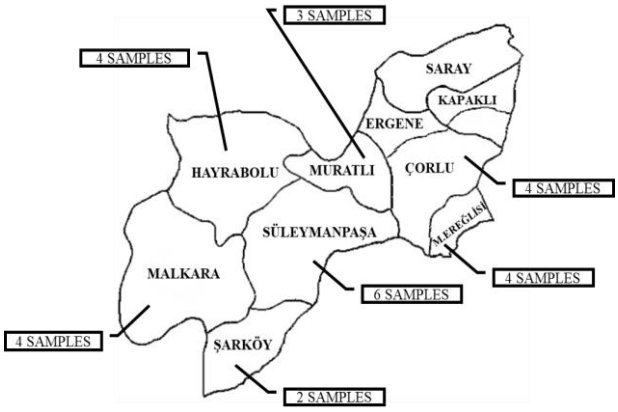


**Figure 1.** Map of the study area with the number of samples

Nematodes were isolated from the collected soils by the sugar centrifugation method of Jenkins [10]. In this method, 200 g of each sample was taken into a bowl, and water was added. This thoroughly mixed mixture was first passed through a 200, then 400 mesh sieve and the nematodes remaining at the bottom of the 400 mesh sieve were collected into the tube. The collected nematode suspension was first centrifuged at 1750 rpm for 5 minutes, then a solution containing 475 g/l sugar was added instead of water and centrifuged again for 1 minute. In the last step, the suspension was passed through a 400 mesh sieve, and the remaining nematodes were washed with tap water and collected.

### 2.3. Nematode identifications, the diversity, and ecologic indices of nematodes

Species identifications were carried out from female nematodes. Slides of females were prepared by heat-

killing (at 60ºC) and fixing in a double-strengthened TAF (Trietmanolamine-formalin) solution [22]. The classifications were conducted based on [24]. Plant parasitic nematodes were identified on a species level, and the morphometric parameters were determined based on de Man [7].

The feeding habitat and colonizer-persister values (c-p value 1-5) of each nematode species were determined [6, 33]. The frequency of occurrence (f %) of species was calculated by dividing the number of samples in which the total number of samples recorded the species/genera. Shannon's diversity index (H'), Evenness index (J'), Enrichment (EI), Structure index (SI), Channel index (CI), Basal index (BI), Maturity index (MI), Maturity index 2-5, and Plant parasitic index (PPI) were calculated [23, 26, 8].

## 3. RESULTS AND DISCUSSION

In this study, a total of 28 taxa of nematodes were found in canola fields. Identified nematodes were divided into two groups free-living non-parasites and plant parasites. All identified taxa were classified based on feeding habitat as bacterivores, fungivores, herbivores, omnivores, and predators. Free-living nematodes included bacterivores, fungivores, omnivores, and predator species. Their c-p values ranged between 1 to 5 (Figure 2).

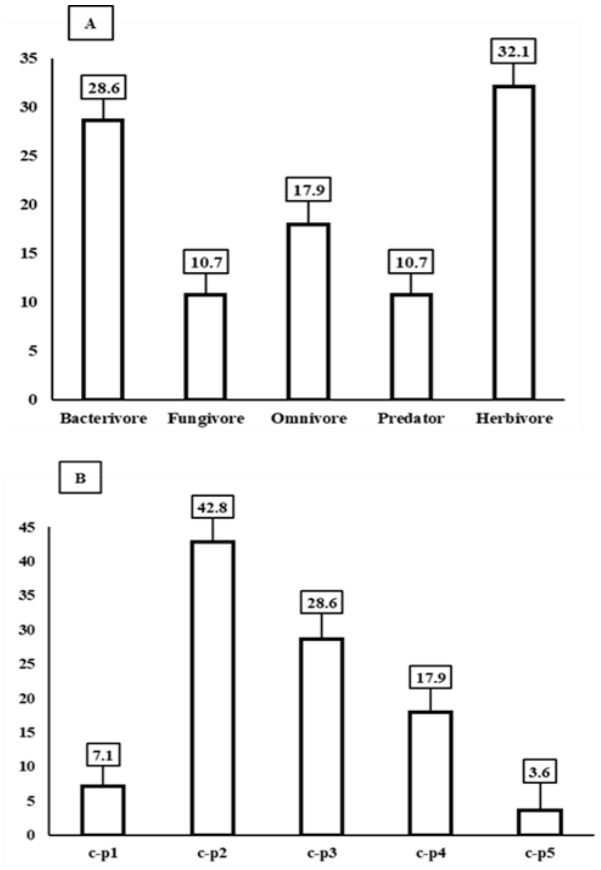


**Figure 2.** A. The proportion of nematode taxa in terms of feeding habitat B. The proportion of nematode taxa in terms of colonizer-persister (c-p) values

Diversity indices were determined for 28 fields, and mean values were in Table 1. Significant variations in indices were observed in 28 fields. The Channel indices (CI) that reach 100 in some locations indicate the dominance of fungivore nematodes and a higher rate of organic decomposition. Due to the higher presence of bacterivore c-p1 and fungivore c-p2 species, an Enrichment (E) value of 59.65 is calculated in one field. The Maturity index (MI) values in canola fields in Tekirdağ were between 2-3.48. Values above three were obtained from soils with good soil structure, and an MI index higher than three indicates high organic matter.

**Table 1.** Indices of diversity for canola fields in Tekirdağ

| Indices | Mean | Minimum-maximum |
|---|---|---|
| Basal (BI) | 30.4±17.3 | 5.31-53.73 |
| Channel (CI) | 93.03±12.6 | 64.7-100 |
| Evenness (J') | 0.8±0.12 | 0.6-0.92 |
| Enrichment (E) | 34.6±15.2 | 12.5-59.65 |
| Maturity (MI) | 2.68±0.05 | 2-3.48 |
| Maturity 2-5 | 2.69±0.51 | 2-3.55 |
| Plant parasite (PPI) | 2.69±0.39 | 2-3 |
| Structure (SI) | 67.4±21.7 | 40-94.24 |
| Shannon's diversity (H') | 1.8±0.26 | 1.44-2.21 |

The lowest nematode population in 100 $cm^3$ soil was counted as 23, and the highest as 476. The number of nematodes was determined to be the lowest in arid soils. However, only some nematodes were isolated from soils taken from heavy, stony fields.



The most common nematode taxa in Tekirdağ were bacterivore species. In some soils, the rate of bacterivore species reached 57.3%, while in some, it remained at the level of 3%. The percentages of herbivores, bacterivores, omnivores, fungivores, and predators varied between 8.1-45.6%, 3-56.1%, 7.6-65.9%, 4.3-46.8, and 1.9-38.6% respectively. Predators were the least common, and their incidence was below 25%. *Acrobeloides*, *Mesodorylaimus*, and *Ditylenchus* were leading taxa in frequency and density (Table 2).

Twelve species belonging to nine genera in the Tylenchida order were determined as plant parasites. (Table 3). Migratory ectoparasites were predominant, and endoparasite *Pratylenchoides alkani* was present only in eight fields.

When species density at 100 $cm^3$ was considered, individuals were generally found below the economic loss threshold in species like *Helicotylenchus digonicus* and *P. alkani*. Species' morphometrics and morphologic parameters also fit published descriptions (Table 3-5). The classification and frequency of occurrence are given in Table 6 and Table 7.

**Table 3.** Morphometrics of *Helicotylenchus digonicus*, *Rotylenchus robustus*, *Tylenchorhynchus cylindricus*, *Filenchus sheri.* Measurements except for L in µm. mean± (SD) range.

| | ***Helicotylenchus digonicus*** | [35] | ***Rotylenchus robustus*** | [37] | ***Tylenchorhynchus cylindricus*** | [2] | ***Filenchus sheri*** | [13] |
|---|---|---|---|---|---|---|---|---|
| **n** | 7 | 18 | 7 | 1 | 5 | 13 | 6 | 5 |
| **L** | 0.71±0.04 (0.69-0.77) | 0.64-0.76 | 0.93±0.01 (0.90-0.95) | 0.91-1.10 | 0.93±0.01 (0.91-0.93) | 0.65-0.99 | 0.45±0.02 (0.41-0.47) | 0.46-0.51 |
| **a** | 27.6±0.93 (26.3-28.4) | 20-25 | 31.15±2.33 (28.5-34.9) | 24-29 | 33.5±1.50 (32.1-35.65) | 28-35 | 30.4±0.94 (29.1-31.2) | 31-38 |
| **b** | 4.93±0.12 (4.8-5.1) | 5.3-6.1 | 7.3±0.13 (7.3-7.58) | 6.3-7.9 | 5.73±0.12 (5.6-5.91) | 4.2-6 | 6.53±0.12 (6.4-6.7) | 5-6 |
| **c** | 42.1±4.59 (36.8-48) | 38-51 | 65.6±3.39 (61.4-69.7) | 50-82 | 20.5±0.70 (19.6-21.3) | 13-20 | 6.11±0.02 (6-6.2) | - |
| **c'** | 1.04±0.23 (0.85-1.37) | - | 0.84±0.02 (0.81-0.90) | - | 2.56±0.12 (2.4-2.7) | - | 6.9±0.34 (6.51-7.35) | 6.7-7.6 |
| **Stylet** | 24±0.85 (24-25.1) | 26-29 | 30.8±0.48 (29.2-30.4) | 33-40 | 22.3±0.2 (22.1-22.6) | 24-27 | 10 | 7-8 |
| **Tail** | 15.9±2.12 (14.3-18.9) | - | 14.2±0.71 (13.6-15.2) | 20-28 | 47.1±1.87 (44.4-49.4) | - | 71.2±3.43 (67.2-75.6) | - |
| **Vulva %** | 62.5±0.5 (62-63) | 60-64 | 59.3±0.94 (58-60) | 55-58 | 54±1.63 (52-56) | 54-64 | 65 | 61-63 |

**Table 4.** Morphometrics of *Boleodorus tylactus*, *Filenchus thornei*, *Filenchus cylindricauda*, *Pratylenchoides alkani*, Measurements except for L in

| | ***Boleodorus tylactus*** | [30] | ***Filenchus thornei*** | [13] | ***Filenchus cylindricauda*** | [13] | ***Pratylenchoides alkani*** | [36] |
|---|---|---|---|---|---|---|---|---|
| **n** | 9 | - | 9 | 1 | 5 | 1 | 8 | - |
| **L** | 0.54±0.02 (0.52-0.59) | 0.5 | 0.72±0.09 (0.66-0.79) | 0.73 | 0.88±0.02 (0.88-0.91) | 1 | 0.75±0.02 (0.72-0.75) | 0.82-1.21 |
| **a** | 36.4±0.78 (35.2-37) | 21 | 36.4±0.78 (35.2-37) | 36.7 | 35.5±1.2 (33.19-37) | 40 | 28.8±0.6 (28-29.44) | 29-35 |
| **b** | 6.5±0.37 (5.9-6.9) | 5 | 6.5±0.37 (5.9-6.9) | 7.8 | 5.92±0.17 (5.68-6.10) | 6.5 | 5.17±0.2 (4.97-5.45) | 4-4.9 |
| **c** | 4.6±0.04 (4.58-4.68) | 10 | 4.2±0.42 (3.9-5) | 3.95 | 6.46±0.28 (6.23-6.86) | 6.5 | 18.6±0.94 (17.9-20) | 14-17 |
| **c'** | 6.1±0.28 (5.68-6.48) | - | 12.3±0.94 (11.3-13.6) | - | 9.32±0.02 (9.21- 9.43) | - | 2.94±0.2 (2.69-3.26) | - |
| **Stylet** | 11.4±1.16 (10-13) | 12-14 | 10.7±0.76 (9.5-11.6) | 10.5 | 11.6 | 13 | 17.2±0.84 (16-18.5) | 22-25 |
| **Tail** | 45.3±4.3 (41.2-51.6) | 63.5-71.5 | 176±4.6 (169-181) | 187 | 136±3.74 (132-141) | - | 46.9±2.24 (43.9-49.8) | - |
| **Vulva %** | 60 | 69 | 60 | 58.1 | 69±0.81 (68-70) | 64 | 55.2±0.74 (55-56) | 55 |

µm. mean± (SD) range.

**Table 5.** Morphometrics of *Malenchus fusiformis*, *Paratylenchus variabilis*, *Geocenamus brevidens*, *Tylenchorhynchus annulatus*, Measurements except for L in µm. mean± (SD) range

| | ***Malenchus fusiformis*** | [31] | ***Paratylenchus variabilis*** | [21] | ***Geocenamus brevidens*** | [2] | ***Tylenchorhynchus annulatus*** | [25] |
|---|---|---|---|---|---|---|---|---|
| **n** | 2 | 1 | 2 | 3 | 6 | 11 | 5 | - |
| **L** | 0.33-0.36 | 0.35 | 277-295 | 296.1±23.2 (247.7-336.2) | 0.67±0.01 (0.65-0.67) | 0.54-0.69 | 0.93±0.03 (0.89-0.96) | 0.75-0.91 |
| **a** | 27.2-30 | 17 | 17.7-24.6 | 22.8±1.4 (20.5-25.0) | 23.9±1.96 (21.3-25.6) | 23-27 | 32.6±1.61 (30.5-34.4) | 26.8-35.9 |
| **b** | 4.8-5 | 5 | 3.95-4.21 | 4.2±0.4 (3.8-4.9) | 3.66±1.24 (3.5-3.8) | 4.2-5.2 | 5.26±0.24 (5-5.58) | 5.3-6.8 |
| **c** | 5 | 5.1 | 10.22-14.14 | 12.9±1.6 (9.1-15.0) | 12±0.65 (11.3-12.9) | 11-13 | 16.6±0.69 (16.3-17.6) | 15.6-19.1 |
| **c'** | 6.4-6.5 | - | 2.46-2.54 | 2.6±0.4 (2.0–3.4) | 2.74 (2.73-2.75) | - | 2.64±0.06 (2.55-2.7) | 2.2-3.4 |
| **Stylet** | 10 | 10 | 17.9-21.3 | 17.6±0.8 (16.3-19.0) | 13.2±0.9 (12.2-14.9) | 14-16 | 18.4±0.95 (17.6-19.8) | 17.7-21.8 |
| **Tail** | 67-72 | - | 27.1-27.9 | 23.3±3.3 (16.5-31.7) | 55±4.4 (49-59.2) | - | 55±3.26 (51-59) | 41.4-53.6 |
| **Vulva %** | 65 | 64 | 85 | 83.9±1.0 (82.4-85.4) | 55±2.44 (55-58) | - | 55±1.24 (55-57) | 52.2-57.5 |

**Table 6.** Free-living nematode taxa identified from canola fields in Tekirdağ

| **Species/genus** | **Order** | **Family** | **c-p class** | **Feeding type** | **Frequency of occurence** | **Abundance in 100 cm$^3$** |
|---|---|---|---|---|---|---|
| *Achromadora* Cobb, 1913 | Chromadorida | Achromadoridae | 3 | Bacterivore | 23 | 1-4 |
| *Acrobeles* Cobb, 1924 | Rhabditida | Cephalobidae | 2 | Bacterivore | 26.9 | 3-21 |
| *Acrobeloides* von Linstow, 1877 | Rhabditida | Cephalobidae | 2 | Bacterivore | 85.7 | 5-192 |
| *Aporcelaimellus* Heyns, 1965 | Dorylaimida | Aporcelaimidae | 5 | Omnivore | 7.1 | 2-9 |
| *Aphelenchoides sacchari* Hooper, 1958 | Aphelenchida | Aphelenchoididae | 2 | Fungivore | 21.4 | 2-57 |
| *Aphelenchoides obtusus* Thorne & Malek, 1968 | Aphelenchida | Aphelenchoididae | 2 | Fungivore | 7.1 | 2-4 |
| *Aphelenchus avenae* Bastian,1865 | Aphelenchida | Aphelenchoididae | 2 | Fungivore | 25 | 1-5 |
| *Cephalobus* Bastian, 1865 | Rhabditida | Cephalobidae | 2 | Bacterivore | 57.7 | 5-8 |
| *Clarkus* Jairajpuri, 1970 | Mononchida | Mononchidae | 4 | Predator | 25 | 3-5 |
| *Ditylenchus myceliophagus* Goodey, 1958 | Tylenchida | Anguinidae | 2 | Fungivore | 85.1 | 3-57 |
| *Dorylaimus* Dujardin, 1845 | Dorylaimida | Dorylaimidae | 4 | Omnivore | 25 | 3 |
| *Eudorylaimus* Andrássy, 1959 | Dorylaimida | Dorylaimidae | 4 | Omnivore | 38.4 | 6-7 |
| *Mesodorylaimus* Andrassy 1959 | Dorylaimida | Dorylaimidae | 4 | Omnivore | 92 | 4-170 |
| *Mesorhabditis* Osche, 1952 | Rhabditida | Rhabditidae | 1 | Bacterivore | 21.4 | 3-11 |
| *Monhystera* Bastian, 1865 | Monhysteria | Monhysteridae | 2 | Bacterivore | 13.3 | 2 |
| *Prodorylaimus* Fuchs, 1930 | Dorylaimida | Dorylaimidae | 4 | Omnivore | 7.1 | 4-8 |
| *Rhabditis* Dujardin, 1845 | Rhabditida | Rhabditidae | 1 | Bacterivore | 15.4 | 6-10 |
| *Seinura* Fuchs, 1931 | Aphelenchida | Aphelenchoididae | 2 | Predator | 10.7 | 7-28 |
| *Tripyla* Bastian, 1865 | Triplonchida | Tripylidae | 3 | Predator | 17.9 | 1-4 |
| *Wilsonema* Cobb, 1913 | Plectida | Plectidae | 3 | Bacterivore | 3.6 | 2 |

**Table 7.** Herbivore nematode species identified from canola fields in Tekirdağ, c-p values, feeding strategies, occurrence, and abundance rates

| Family | Genus | Species | c-p | Feeding strategy | Frequency of occurrence | Abundance in 100 cm$^3$ |
|---|---|---|---|---|---|---|
| Boleodorinae | *Boleodorus* | *Boleodorus tylactus* Thorne, 1941 | 2 | M2 | 17.8 | 4-7 |
| Belanolaimidae | *Tylenchorhynchus* | *Tylenchorhynchus annulatus* (Cassidy, 1930) Golden, 1971 | 3 | M2 | 32.1 | 2-7 |
| | | *Tylenchorhynchus cylindricus* Cobb, 1913 | 3 | M2 | 21.4 | 2-4 |
| Hoplolaimidae | *Helicotylenchus* | *Helicotylenchus digonicus* Perry, Darling Thorne, 1959 | 3 | M2 | 46.4 | 4-8 |
| | *Rotylenchus* | *Rotylenchus robustus* deMan, 1876 | 3 | M2 | 21.4 | 2-70 |
| Paratylenchidae | *Paratylenchus* | *Paratylenchus variabilis*, Raski, 1975 | 2 | M2 | 7.1 | 18 |
| Pratylenchidae | *Pratylechoides* | *Pratylenchoides alkani* Yüksel, 1977 | 3 | M1 | 28.5 | 6-8 |
| Telotylenchidae | *Geocenamus* | *Geocenamus brevidens* (Allen, 1955) Siddiqi | 3 | M2 | 53.7 | 20-48 |
| Tylenchidae | *Filenchus* | *Filenchus sheri* Siddiqi, 1986 | 2 | M2 | 50 | 2-77 |
| | | *Filenchus thornei* Andrassy, 1963 | 2 | M2 | 25 | 3-24 |
| | | *Filenchus cylindricus* Thorne & Malek, 1968) Niblack & Bernard, 1985 | 2 | M2 | 35.7 | 2-40 |
| | *Malenchus* | *Malenchus fusiformis* (Thorne and Malek, 1968) Siddiqi, 1979 | 2 | M2 | 3.6 | 75 |

M1: Migratory endoparasite M2: Migratory ectoparasite

The results obtained from this study indicate the presence of different free-living nematode species in canola fields. Free-living nematodes play an essential role in the nutrient cycle in the soil and contribute to the improvement of soil permeability and texture. Some species can also feed on pathogens or other pests that are parasitic on plants [28]. In this study, herbivore plant-parasitic nematodes, which do not cause economic yield loss in canola, were detected and were therefore called weak parasites. Virus vector species such as *Xiphinema*, *Longidorus*, and *Trichodorus* were also not found.

Our results were compatible with other researchers' studies. In rapeseed fields in Italy, nematodes belonging to 24 genera were identified. Free-living bacterivores (50.18%) and fungivores (42.90%) took the first two places regarding the occurrence rate. The most abundant genera were *Aphelenchus* (23.71%), *Acrobeloides* (20.49%), and *Aphelencoides* (19.18%) [14]. Additionally, nematodes such as *Aphelenchoides limberi, A. daubichaensis, A. delhiensis, A. confusus, A. rutgersi, D. dipsaci, P. thornei*, and *P. neglectus* have been detected in canola fields in several countries [5, 9]. Growth anomalies and damage have been reported in canola seedlings due to *D. dipsaci* feeding [29]. On the contrary, symptoms like plant damage caused by nematodes were not observed in the canola fields surveyed in this study in Tekirdağ.

On the contrary, in our study, species belonging to *Boleodorus, Filenchus, Geocenamus, Helicotylenchus, Malenchus, Paratylenchus, Pratylenchoides*, and *Rotylenchus* genera were determined in canola fields in Tekirdağ. *Boleodorus* and *Filenchus* species are known as one of the most common root hair-feeding, highly proliferative nematodes on earth with a short life cycle [15, 16]. Similarly, in our study in Tekirdağ, *Filenchus* was the most common (100% occurrence) and abundant (in highly infested fields 98 individuals/ 100 cm$^3$). Additionally, the ability of *Filenchus* species to feed with fungal species such as *Rhizoctonia solani, Fusarium oxysporum*, and *Pythium ultimum* has been clarified in several studies [17, 18]. *Ditylenchus myceliophagus, Aphelenchus avenae, Aphelenchoides sacchari*, and *A. obtusus*, extracted from canola fields in Tekirdağ, were the other nematodes of which fungal feeding behavior was determined in laboratory studies. Meanwhile, *Geocenamus brevidens, Pratylenchoides alkani, Tylenchorhynchus annulatus*, and *T. cylindricus* species in this study found in canola fields have previously been extracted from orchards and vegetable growing areas [12].



The number of plant-parasitic species identified in canola-growing areas in the world was low. The glucosinolate component secreted from canola was reported to have a nematode suppressive effect on many plant-parasitic species [11]. For instance, it has been reported that the population of *Pratylenchus thornei*, a significant pest in wheat, is considerably reduced when canola is planted in the field [19]. As in other studies in the world, in this study in Tekirdağ, only a few species of plant parasitic nematodes were detected. The low number of plant-parasitic species in canola fields in Tekirdağ may be attributed to the result of some nematicidal components secreted from the plant.

This study was the most recent pioneer study conducted on nematode biodiversity one of the provinces where canola is grown most extensively in Türkiye. As a result of the study, it was determined that there were no harmful nematode species such as *Meloidogyne* in the canola fields, and the populations of the detected species were not at a level that would cause harm.

## 4. CONCLUSION

In a study covering canola fields in Tekirdağ, Turkey, nematodes from different trophic groups were identified. They were classified as free-living non-plant parasitics and plant parasitics. Free-living nematodes belong to 19 genera, while plant parasitics belong to 9 genera. Most free-living were bacterivores, and plant parasitics were ectoparasite species. None of the plant-parasitic species was quarantined pests. Except for *Pratylenchoides alkani*

and *Rotylenchulus robustus*; the rest of the species did not cause significant plant damage, even under higher populations. It is unknown whether the role of the plant's allelochemical secretions is responsible for the low nematode richness. More studies must be conducted to reveal the interaction between the canola plant and nematode population growth.

## REFERENCES


[1] AAFC. Agriculture and Agri-Food Canada – Regulatory Directive DIR 94-09: The Biology of *Brassica napus* L. (Canola/ Rapeseed). 1994;11.

[2] Allen MW. A review of the nematode genus *Tylenchorhynchus*. Uni Calif Pub Zool. 1955;61:129-166.

[3] Andrássy I. Revision der Gattung *Tylenchus* Bastian, 1865 (Tylenchidae, Nematoda). Acta Zool. Hung. 1954;1:5-42.

[4] Anonymous. Turkish Statistical Institute; 2021. Available from: https://www.tuik.gov.tr.

[5] Baadl S, Mahdikhani Moghadam E, Rouhani H. Identification of *Aphelenchoides* Fischer, 1849 species (Nematoda: Aphelenchoididae) collected from rapeseed fields in North Khorasan province. Journal of Iranian Plant Protection Research. 2016;29(4):558-570. doi: 10.22067/jpp.v29i4.32940.

[6] Bongers R. The maturity index: An ecological measure of environmental disturbance based on nematode species composition. Oecologia. 1990;83:14-19.

[7] De Man JG. Onderzoekingen over vrij in de aarde levende Nematoden. Tijdschrift Nederlandsche voor de Dierkunde Vereen. 1876;2:78-196.

[8] Elliot CA. Diversity indices. – In Hunter MLJr Wildlife, forests, and forestry. Prentice Hall. Engelwood Cliffs, N.J. 1990; 297-302.

[9] Fatemy S, Abootorabi E, Ebrahimi N, Aghabeigi F. First report of *Pratylenchus neglectus* and *P. thornei* infecting canola and weeds in Iran. Plant Dis. 2006;90(12):1555. doi: 10.1094/PD-90-1555B. PMID: 30780991.

[10] Jenkins W RA. Rapid centrifugal-flotation technique for separating nematodes from soil. Plant Dis Rep.1964;48:692.

[11] Jing GN, Halbrendt MG. Nematicidal compounds from rapeseed (*Brassica napus* and B. campestris). Journal of the Pennsylvania Academy of Science. 1994;68(1):29-33. JSTOR, http://www.jstor.org/stable/44148985.

[12] Kepenekci İ. Plant parasitic nematodes (Tylenchida, Nematoda) in Turkey. Pakistan Journal of Nematology. 2014; 32 (1): 11-31.

[13] Khan M, Khan S. Two new and a known species of *Tylenchus* Bastian (Nematoda: Tylenchinae) from Afghanistan. Nematol. Mediterr. 1978;6:213-221.

[14] Manachini B, Landi S, Tomasini V. Biodiversity of nematofauna of oilseed rape (*Brassica napus* L.). Commun Agric Appl Biol Sci. 2005;70(4):927-35. PMID: 16628940.

[15] Munawar M., Yevtushenko DP., Castillo P. Overview of the genus *Boleodorus* and first reports of *Boleodorus thylactus* and *B. volutus* from Southern Alberta, Canada. Animals 2021; 11:1760. https://doi.org/10.3390/ ani11061760

[16] Munawar M., Castillo P., Yevtushenko DP. Description of *Filenchus* species from agroecosystem of Southern Alberta, Canada. *Agronomy*. 2022; 12(3):690. https://doi.org/10.3390/agronomy12030690

[17] Okada H., Harada, H., Kadota I. Fungal-feeding habits of six nematode isolates in the genus *Filenchus*. *Soil Biol. Biochem.* 2005; 37: 1113–1120.

[18] Okada H., Kadota I. Host status of 10 fungal isolates for two nematode species, *Filenchus misellus* and *Aphelenchus avenae*. Soil Biol. Biochem. 2003; 35: 1601–1607

[19] Owen KJ, Clewett TG, Thompson JP. Pre-cropping with canola decreased *Pratylenchus thornei* populations, arbuscular mycorrhizal fungi, and yield of wheat. Crop and Pasture Science. 2010;61:399-410. https://doi.org/10.1071/CP09345.

[20] Potter, J. W. and McKeown, A. W. 2003. Nematode biodiversity in Canadian agricultural soils. Can. J. Soil Sci. 83: 289–302.

[21] Rosmaninho T, Mota M, Inácio ML, Eisenback JD, Gutiérrez-Gutiérrez C. Six first reports of pin nematodes from Portugal, with an update of the systematics, genetic diversity, and phylogeny of the genus *Paratylenchus* (Nematoda: Tylenchulidae). Horticulturae. 2022;8:343. https://doi.org/10.3390/ horticulturae8040343.

[22] Seinhorst JW. A rapid method for the transfer of nematodes from fixative to anhydrous glycerin. Nematologica. 1959;4(1):67-69. https://doi.org/10.1163/187529259X0038.

[23] Shannon CE. A mathematical theory of communication. The Bell System Technical Journal. 1948;27:379-423. https://doi.org/10.1002/j.1538-7305.1948.tb01338.x.

[24] Siddiqi MR. Tylenchida: parasites of plants and insects. 2nd edition. Wallingford Oxon: CAB International; 2000:833 pp.

[25] Simon ACM, Lopez-Nicora HD, Ralston TI, Richer EA, Niblack TL, Paul PA. First report of stunt nematode (*Tylenchorhynchus annulatus*) on corn in Ohio. Plant disease.2020;104:2527. doi: 10.1094/PDIS-02-20-0429-PDN.

[26] Simpson EH. Measurement of diversity. Nature. 1949;163:688. http://dx.doi.org/10.1038/163688a0.

[27] Süzer S. Kanola Tarımı. Edirne, 2001;Yayın No:77-78.

[28] Taher, I. E., Ami, S. N., Haleem, R. A., & Shareef, B. (2017). First record of mycetophagous nematode *Aphelenchus avenae* In Iraq with description and testing their propagatıon on different fungus culture. *Bulletin of The Iraq Natural History Museum*, 14, 251-259. 10.26842/binhm.7.2017.14.3.0251.

[29] Taylor S, Szot D. First record of damage to canola caused by the oat race of stem nematode (*Ditylenchus dipsaci*). Australasian Plant Pathology. 2000;29:153. https://doi.org/10.1071/AP00027.

[30] Thorne G. Some nematodes of the family Tylenchidae which do not possess a valvular median

esophageal bulb. Great Basin Naturalist. 1941;2(2):1.
[31] Thorne G, Malek RB. Nematodes of the northern Great Plains. Part I. Tylenchida (Nemata: Secernentea). Tech. Bull. S. Dak. Agric. Exp. Stn. 1968;1:72-76.
[32] Tıraş M. Türkiye'de kanola tarımı. Doğu Coğrafya Dergisi. 2011;14(21):159-172. Retrieved from https://dergipark.org.tr/tr/pub/ataunidcd/issue/2436/31181.
[33] Yeates GW, Bongers T, de Goede RGM, Freckman DW, Georgieva SS. Feeding habits in soil nematode families and genera-an outline for soil ecologists. Journal of Nematology. 1993;25:315-331.
[34] Yilmaz H, Avkiran B. Analysis of canola (rapeseed) production cost and income in context of oilseeds production support policies: A case study from Trakya region of Turkey. Ekonomika poljoprivrede. 2020;67:483-493. 10.5937/ekoPolj2002483Y.
[35] Yuen PH. Four new species of *Helicotylenchus* Steiner (Hoplolaiminae: Tylenchida) and a redescription of *H. canadensis* Waseem, 1961. Nematologica.1964;10(3):373-387.
[36] Yüksel HŞ. *Pratylenchoides alkani* n. sp. and *P. erzurumensis* n. sp. (Nematoda: Tylenchoidea) from soil in Turkey. Proceedings of the Helminthological Society of Washington.1977;44:185-188.
[37] Wouts WM, Sturhan D. Descriptions of *Rotylenchus* species from New Zealand, including *R. labiodiscus* sp. n. (Nematoda: Hoplolaimidae), New Zealand Journal of Zoology. 1999;26(4):395-404. doi: 10.1080/03014223.1999.9518202.

Cilt 12, Sayı 1, Sayfa 99-107, 2023 Volume 12, Issue 1, Page 99-107, 2023

Araştırma Makalesi https://doi.org/10.46810/tdfd.118657 Research Article

Türk Doğa ve Fen Dergisi
Turkish Journal of Nature and Science
www.dergipark.gov.tr/tdfd

# Türkiye's Offshore Hybrid Energy Potential and Cost Estimation in the Eastern Mediterranean

**Soner ÇELİKDEMİR[1*], Mahmut Temel ÖZDEMİR[2]**

[1] Bitlis Eren University, Adilcevaz Vocational High School, Electric and Energy Department, Bitlis, Türkiye
[2] Firat University, Engineering Faculty, Electrical and Electronics Engineering Department, Elazığ, Türkiye
Soner ÇELİKDEMİR ORCID No: 0000-0002-1419-3398
Mahmut Temel ÖZDEMİR ORCID No: 0000-0002-5795-2550

**Corresponding author: celikdemirsoner@gmail.com*

(Received: 09.10.2022, Accepted: 02.03.2023, Online Publication: 27.03.2023)

**Keywords**
Offshore Renewable Energy Sources, Hydrogen Production, Hydrogen Transmission, Cost Analysis

**Abstract:** In this study, for the first time, the focus is on determining the potential of renewable energy-derived hybrid energy in the Eastern Mediterranean region and conducting cost analysis for sample locations. The most important motivation of this study is that the Eastern Mediterranean zone has a significant hydrocarbon potential in addition to its geopolitical value, energy lines, and being a transportation route. Providing the energy needs of hydrocarbon platforms to be established in the region constitutes the main framework. For this, 6 zones determined were examined. Wind, solar, and wave energy potentials of these zones have been determined. If the energy is produced more than the needs of the platforms, it is planned to produce hydrogen by electrolysis. In this case, cost analyses of the system were carried out taking into account the situation of the hydrogen produced being transmitted to the mainland by different transport methods in the form of liquids or gases. According the results of the analyzes, it has been shown that the Eastern Mediterranean has a very high wind, solar, and wave energy potential due to the fact that Crete and Rhodes Islands form a natural strait. As a conclusion different transmission scenarios of the hydrogen to the mainland shows that the energy required by the platforms can be provided by renewable energy sources, regardless of their power.



# Türkiye'nin Doğu Akdeniz'deki Açık Deniz Hibrit Enerji Potansiyeli ve Maliyet Tahmini

**Anahtar Kelimeler**
Açık Deniz Yenilenebilir Enerji Kaynakları, Hidrojen Üretimi, Hidrojen Taşınması, Maliyet Analizi

**Öz:** Bu çalışmada ilk kez Doğu Akdeniz bölgesinde yenilenebilir enerji kaynaklı hibrit enerji potansiyelinin belirlenmesi ve örnek lokasyonlar için maliyet analizi yapılmasına odaklanılmıştır. Bu çalışmanın en önemli motivasyonu, Doğu Akdeniz bölgesinin jeopolitik değeri, enerji hatları ve ulaşım güzergahı olmasının yanında önemli bir hidrokarbon potansiyeline sahip olmasıdır. Bölgede kurulacak hidrokarbon platformlarının enerji ihtiyacının karşılanması ana çerçeveyi oluşturmaktadır. Bunun için belirlenen 6 bölge incelenmiştir. Bu bölgelerin rüzgar, güneş ve dalga enerjisi potansiyelleri belirlenmiştir. Platformların ihtiyacından fazla enerji üretilmesi durumunda elektroliz ile hidrojen üretilmesi amaçlanmıştır. Bu durumda üretilen hidrojenin farklı taşıma yöntemleriyle sıvı veya gaz halinde anakaraya iletilmesi durumları dikkate alınarak sistemin maliyet analizleri yapılmıştır. Analiz sonuçlarına göre Girit ve Rodos Adaları'nın doğal bir boğaz oluşturması nedeniyle Doğu Akdeniz'in çok yüksek bir rüzgar, güneş ve dalga enerjisi potansiyeline sahip olduğu gösterilmiştir. Sonuç olarak, hidrojenin anakaraya farklı iletim senaryoları, platformların ihtiyaç duyduğu enerjinin, gücü ne olursa olsun yenilenebilir enerji kaynakları ile sağlanabileceğini göstermektedir.

## 1. INTRODUCTION

Nowadays, the desire for energy is increasing worldwide. This reality leads increase the importance of Renewable Energy Sources (RES), which can produce energy through natural cycles and low negative environmental impacts [1–3]. The main kinds of RES can be listed as; wind, solar, wave, geothermal, and biomass energy. These

energy sources vary according to geographical and geological characteristics. Many studies have been carried out to determine the potentials of energy resources, especially by running the techno-economic analysis of single or multiple resources, and then find alternative solutions to increase their overall efficiency.

Hybrid use of renewable energy sources may have very different purposes. Especially hydrogen-producing systems have been discussed by many researchers in recent years. Today, different hydrogen production methods are involved. The most common method is 'gray' hydrogen, which is derived from natural gas and produces significant carbon emissions. Less harmful than this method is 'blue' hydrogen. The production process is similar to gray hydrogen. The difference is that it makes use of carbon capture and storage. Unlike these methods, it is defined as 'green' hydrogen produced by RES's [4–19].

Although the past studies were mostly carried out for onshore wind power plants, some studies dealt with the amount of hydrogen production from offshore wind power plants [15,17,20,21]. Similarly, techno-economic analyses of hydrogen production from solar power plants were carried out [22,23]. Wave power plants, another renewable energy source, have also been discussed for different regions [24]. In addition to this situation, the hybrid operation of different renewable energy sources has been examined using commercial softwares [25–27]. By using hybrid energy systems together, energy potentials for selected regions and therefore hydrogen production potentials can be determined [13,16,28]. Hydrogen energy, as one of the RES, is of increasing interest due to its positive characteristics as an energy carrier [1,7]. As a result, it is an alternative for countries to diversify their energy resources.

### *The Motivation of The Study*

Türkiye has a developing economy and its energy needs are constantly increasing. Türkiye is going through the process of developing energy resources. For this reason, the Eastern Mediterranean Exclusive Economic Zone (EEZ) is very important in terms of its potential. Hydrocarbon exploration is currently underway in the Eastern Mediterranean Barbaros Hayreddin Pasha and Oruç Reis Seismic Research vessels operating in the region, and Yavuz and Fatih Drilling also continue their exploration activities. In case of possible reserves, oil and gas platforms will be established in the region. The main motivation of this study is to supply the energy needs of these platforms and to produce green hydrogen.

The extraction of offshore hydrocarbon resources and the meeting of the energy needs of refined processes with RES is an issue considered by the researchers [24,28–33]. Despite this, it has that the determination of the RES potential of Türkiye's Eastern Mediterranean continental shelf and its cost analysis have not been investigated before. This is a very important deficiency that needs to be examined in detail.

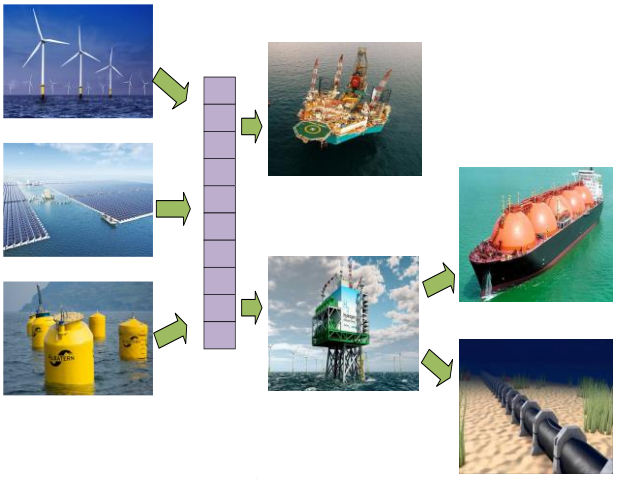

**Figure 1.** Systematic View of the Study

Offshore oil and gas platforms have different characteristics. These features are; varies depending on various features such as size, site conditions, and various features. These platforms have high power demands ranging from 1 MW to 100 MW [28,34]. These power demands are often met by stand-alone electrical systems using multiple redundant gas turbines when available at oil or gas exploration sites. These systems have higher fuel usage and lower efficiency. In addition, such a situation negatively affects the carbon footprint [29].

Firstly, information about the region is given in the study. In addition, wind, solar and wave energy potentials were investigated for six different regions. Designed to provide platform energy with existing renewable energy potential. Then the green hydrogen production situation is discussed with the excess energy that can be produced by RESs. In conclusion part, different transmission scenarios of the hydrogen produced to the mainland were examined. As a result, it has been seen that the energy required by the platforms can be provided by RES, regardless of their power. It has also been shown that there is much greater power generation potential. The systematic view details of the study are given in Fig. 1.

## 2. ECONOMIC EXCLUSIVE ZONE AND RENEWABLE ENERGY POTENTIAL

Considering the geography where Türkiye is located, the region has rich oil and natural gas reserves. In addition, the gas reserves found in the Eastern Mediterranean basin to date have further increased the geopolitical and geostrategic importance of the region. As a result, a Memorandum of Understanding was signed between the Government of the Republic of Türkiye and the Government of the State of Libya on 27$^{th}$ of November 2019, for the determination of the maritime jurisdiction areas in the Mediterranean Sea in Istanbul [35]. The working zone is given in Fig. 2.

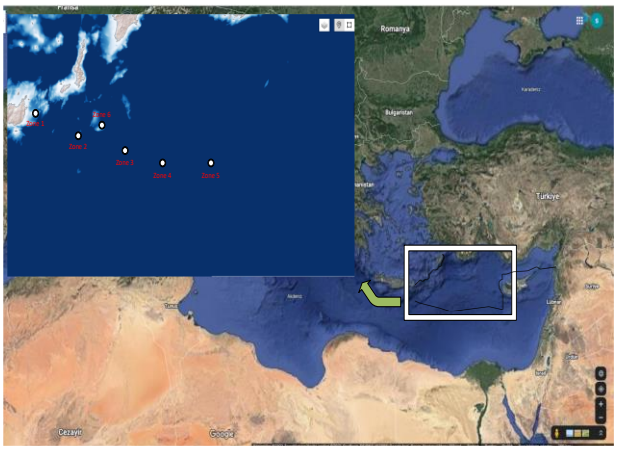


**Figure 2.** Exclusive Economic Zone of Türkiye and Working Zones

## 2.1. Wind Energy Potential

Obtaining Weibull distributions from field data is the first stage in determining the wind energy potential of regions [4,5,36–39]. In the next stage, energy density is calculated. If an original design is to be carried out, the annual amount of energy is calculated taking into account all parameters of the plant. In general, turbines of many brands and models that have already been manufactured and tried in different projects are taken into account. For those suitable from these turbines, Weibull distribution is applied and the amounts of energy to be produced for each different turbine are calculated. Then, the unit energy costs are found. As a result, the shape and scale parameters, capacity factors, and therefore energy amounts of each turbine will be different. In the literature, studies have been carried out to develop solutions with optimum energy costs for different sites. In these studies, different hybrid solutions such as wind-solar, wind-wave, wind-solar-hydrogen are discussed.

Wind speed is directly proportional to the height from the ground. As it approaches the Earth, it decreases due to the effect of friction force. The speed of the wind at a given altitude can be estimated by measuring the speed at any altitude. The most commonly used correlation for this is the Hellmann Equation [36]. Wind speed measurements are carried out at an altitude of 10 meters determined by the World Meteorological Organization. Rotor blades are directly effective in the transformation from wind energy to mechanical energy. The kinetic energy difference in cases where the wind touches the wings and leaves the wings is equal to the amount of wind energy that transforms into kinetic energy. Kinetic energy equations are used in the calculation of this power. The amount of energy that can be obtained from a wind turbine is given in Eq. (1).

$$E_e = \frac{\mathrm{q}\, A}{2} v^3 \qquad (1)$$

Where; q is the air density (kg $m^{-3}$), A is the swept area of the wind turbine ($m^2$), v is the wind speed value at the tower height (m $s^{-1}$), and t is the time (s).

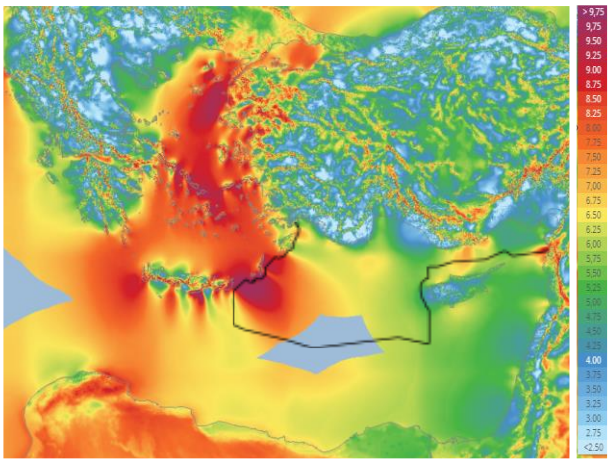

**Figure 3.** EEZ Wind Speed Map

The average wind speed of the determined areas at an altitude of 100 m is seen in Fig. 3 where the value is above 6 m $s^{-1}$. In addition, wind speed values are seen to be higher in the eastern region of Crete Island. The average monthly and hourly wind speed values of the regions are given in Fig. 4 and Fig. 5.

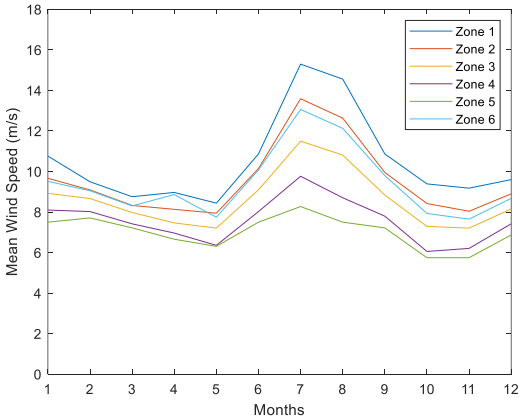


**Figure 4.** Average Monthly Wind Speeds

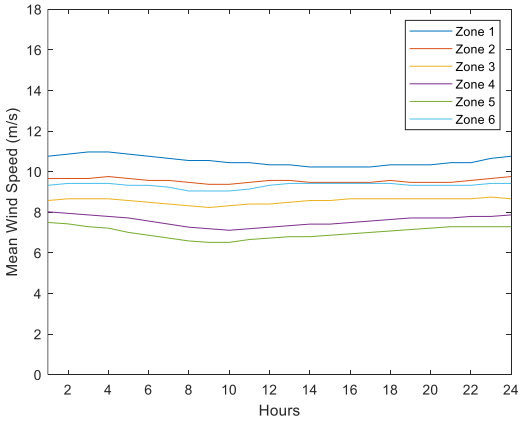


**Figure 5.** Average Hourly Wind Speeds

According to these values, the monthly and hourly wind speed values of Zone 1 are higher than than that in the other regions. In addition, it is seen that the average wind speed values of the regions in the summer months are higher than in other seasons. The characteristic information of the regions is given in Table 1.

**Table 1.** Information about the Zones

| Zone | Lat. | Lon. | Mean Wind Speed (m sn$^{-1}$) | Water Depth (m) | Power Density (W m$^{-2}$) | Energy Density (MWh m$^{-2}$ year) |
|---|---|---|---|---|---|---|
| Zone 1 | 35.14 | 26.38 | 10.55 | -382 | 1245 | 10906.20 |
| Zone 2 | 34.83 | 27.16 | 9.57 | -2216 | 897 | 7857.72 |
| Zone 3 | 34.52 | 27.79 | 8.58 | -2558 | 618 | 5413.68 |
| Zone 4 | 34.50 | 28.26 | 7.57 | -2571 | 449 | 3933.24 |
| Zone 5 | 34.40 | 29.11 | 7.01 | -2683 | 364 | 3188.64 |
| Zone 6 | 34.95 | 27.45 | 9.33 | -618 | 799 | 6999.24 |

According to these data, the wind energy potential of the zones varies between 364 W m$^{-2}$ and 1245 W m$^{-2}$. As a result of this, the eastern region of Crete Island, which is located in EEZ, has an assessable wind energy potential.

## 2.2. Solar Energy Potential

Solar energy, which is the source of many RES, is the radiation energy formed by the fusion process in the sun core. The energy production of a solar module depends on external factors as well as its structure. Solar radiation, cell temperature, and shading values are the main factors affecting the efficiency of solar modules. These factors should be taken into account when designing. The amount of energy to be obtained annually from a solar module is estimated using Eq. (2).

$$E_e = A_{tp} . A_v . \eta_f . GHI \quad (2)$$

Where, '$E_e$' the annual electricity generation of the solar module (kWh year$^{-1}$), '$A_{tp}$' the area of the total solar module (m$^2$), '$A_v$' the availability of the solar module, '$\eta_f$' the efficiency of the solar module and '$GHI$' refers to the annual amount of global horizontal radiation (kWh m$^{-2}$). The annual efficiency of solar modules varies regionally. But, the efficiency of offshore modules is greater than onshore modules. This value may be over 95% [28]. The surface solar radiation information of the EEZ examined in the study is given in Fig. 6 [40].

**Table 2.** Annual Irradiation Values of Zones

| Zone | DNI (kWh m$^{-2}$) | GHI (kWh m$^{-2}$) | DIF (kWh m$^{-2}$) | GTI (kWh m$^{-2}$) |
|---|---|---|---|---|
| Zone 1 | 1933.3 | 1874 | 647.3 | 2069.8 |
| Zone 2 | 2023.3 | 1939.3 | 650.2 | 2150.4 |
| Zone 3 | 2036.7 | 1959.4 | 661 | 2172.7 |
| Zone 4 | 2049.2 | 1967.2 | 661.5 | 2184.4 |
| Zone 5 | 2053.1 | 1972.4 | 663.9 | 2190.6 |
| Zone 6 | 2038.7 | 1942.7 | 649 | 2158.8 |

In addition, the direct normal irradiation (DNI), Spherical horizontal irradiation (GHI), diffuse horizontal irradiation (DIF), and spherical oblique irradiation at optimum angle (GTI) values of the zones specified in the EEZ are given in Table 2.

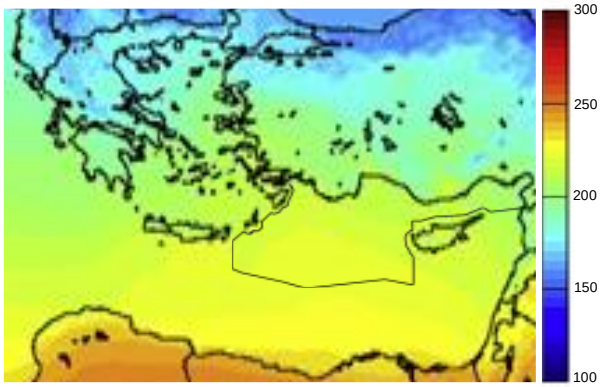


**Figure 6.** EEZ Solar Radiation Map



**Table 3.** Annual Direct Irradiation Values of Zone 5 (Wh m$^{-2}$)

| Hr. / M. | Jan. | Feb. | Mar. | Apr. | May. | Jun. | Jul. | Aug. | Sep. | Oct. | Nov. | Dec. |
|---|---|---|---|---|---|---|---|---|---|---|---|---|
| 0 - 1 | | | | | | | | | | | | |
| 1 - 2 | | | | | | | | | | | | |
| 2 - 3 | | | | | | | | | | | | |
| 3 - 4 | | | | | | | | | | | | |
| 4 - 5 | | | | | | | | | | | | |
| 5 - 6 | | | | 1 | 47 | 108 | 68 | 9 | | | | |
| 6 - 7 | | | 29 | 139 | 289 | 395 | 374 | 262 | 176 | 64 | 3 | |
| 7 - 8 | 57 | 113 | 233 | 335 | 433 | 549 | 545 | 488 | 436 | 317 | 175 | 69 |
| 8 - 9 | 254 | 300 | 374 | 454 | 541 | 658 | 667 | 622 | 575 | 467 | 366 | 271 |
| 9 - 10 | 367 | 389 | 475 | 547 | 620 | 736 | 753 | 716 | 669 | 557 | 471 | 376 |
| 10 - 11 | 419 | 461 | 537 | 612 | 669 | 784 | 804 | 776 | 727 | 614 | 534 | 432 |
| 11 - 12 | 448 | 492 | 567 | 636 | 698 | 805 | 827 | 802 | 751 | 629 | 546 | 442 |
| 12 - 13 | 448 | 496 | 569 | 631 | 690 | 808 | 829 | 803 | 752 | 623 | 535 | 434 |
| 13 - 14 | 436 | 480 | 546 | 609 | 675 | 785 | 815 | 783 | 724 | 595 | 494 | 408 |
| 14 - 15 | 392 | 437 | 524 | 558 | 635 | 748 | 775 | 733 | 666 | 530 | 418 | 358 |
| 15 - 16 | 311 | 363 | 445 | 479 | 563 | 682 | 704 | 652 | 573 | 415 | 297 | 254 |
| 16 - 17 | 131 | 246 | 333 | 382 | 463 | 588 | 605 | 539 | 430 | 209 | 94 | 67 |
| 17 - 18 | | 31 | 134 | 226 | 327 | 455 | 463 | 356 | 155 | 3 | | |
| 18 - 19 | | | | 17 | 77 | 160 | 180 | 45 | | | | |
| 19 - 20 | | | | | | | | | | | | |
| 20 - 21 | | | | | | | | | | | | |
| 21 - 22 | | | | | | | | | | | | |
| 22 - 23 | | | | | | | | | | | | |
| 23 - 24 | | | | | | | | | | | | |

Solar energy potential values of the determined zones vary between 1933 kWh $m^{-2}$ and 2053 kWh $m^{-2}$. When these data are taken into account, it is seen that the studied region has a potential that can be evaluated in terms of solar energy. Although the energy densities of the zones are close to each other, the energy density of the 5th Zone is higher than the other zones. The monthly average energy density graph of the 5th Zone among the zones is given in Fig. 7 and the hourly average direct irradiation values are given in Table 3.

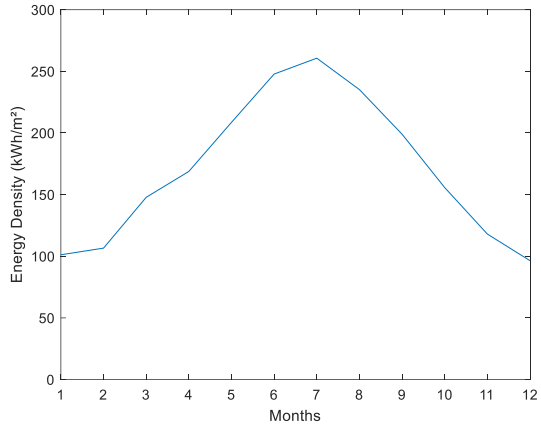


**Figure 7.** The Average Monthly Energy Density of Zone 5

## 2.3. Wave Energy Potential

Wave energy is an energy source generated by wind, seafloor movements, solar and moon gravitational forces, human activities, and different mass movements on the surface of the water. In general, the wave energy source is defined as the average wave power per unit of peak length. The wave energy source expression is given in Eq. 3.

$$E_w = \frac{\rho g^2}{64\pi} \sum_{i=1}^{N} \sum_{j=1}^{M} H_s^2 \, T_E \, f_{ij} \tag{3}$$

Where; ρ seawater density (kg $m^{-3}$), g refers to gravitational acceleration (m $s^{-2}$), $H_s$ is the wave height (m), $T_E$ is the energy period (s), $f_{ij}$ is the wave formation frequency, and $E_w$ is the wave energy. Accordingly, the average annual energy of the resulting wave is indicated by $E_{ij}$ and given in Eq. (4).

$$E_{ij} = \frac{\rho g^2}{64\pi} H_s^2 T_E f_{ij} \tag{4}$$

**Table 4.** Annual Wave Energy Values

| Zone | Average Wave Height (m) | Period (s) | Power Density (kW $m^{-1}$) | Energy Density (MWh $m^{-1}$) |
|---|---|---|---|---|
| Zone 1 | 1.11 | 4.7 | 8.9 | 77.964 |
| Zone 2 | 1.12 | 4.6 | 9.3 | 81.468 |
| Zone 3 | 1.05 | 4.6 | 8.95 | 78.402 |
| Zone 4 | 1.03 | 4.5 | 8.9 | 77.964 |
| Zone 5 | 1.00 | 4.45 | 8.01 | 70.1676 |
| Zone 6 | 1.07 | 4.6 | 8.97 | 78.5772 |

There are two important components that determine the value of wave energy [41]. These are the wave height and the wave period value. These two components should be considered when examining the wave energy potential of a zone.

There are two important components that determine the value of wave energy [41]. These are the wave height and the wave period value. These two components should be considered when examining the wave energy potential of a zone.

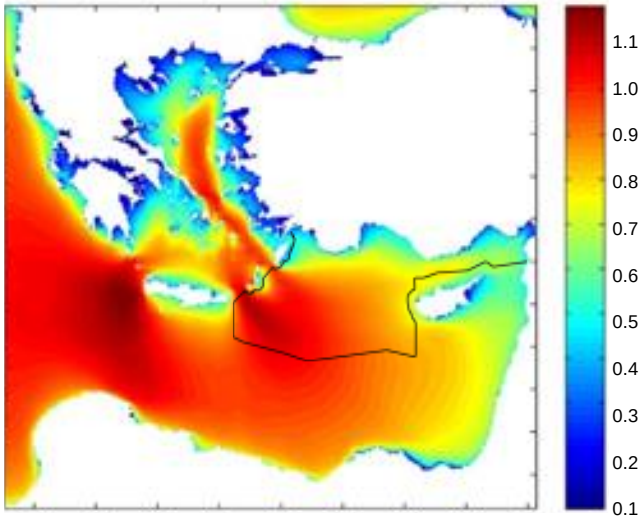


**Figure 8.** EEZ Wave Height Map

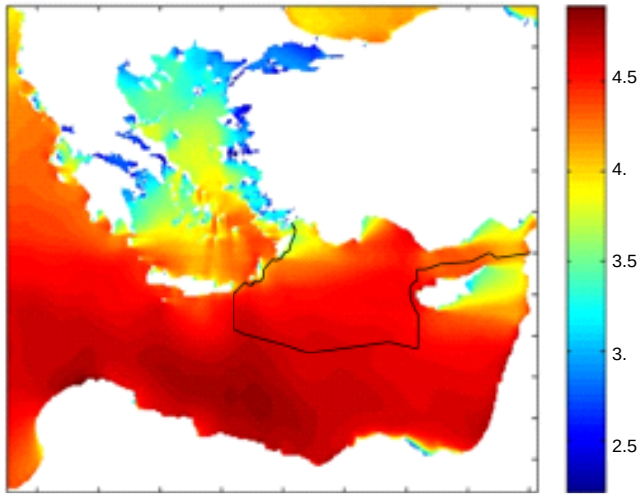


**Figure 9.** EEZ Wave Period Map

Wave height data is given in Fig. 8 [41]. Accordingly, the highest wave values are seen on the east and west coasts of Crete Island.

The average wave height for the investigated EEZ is 1.12 meters. Similarly, the wave period is given in Fig. 9. Accordingly, although the highest wave period values are on the African coasts, the lowest wave period values are on the Turkish coasts. In addition, wave energy data of the zones determined in EEZ are given in Table 4.

In the southern region of Crete Island, the wave period value varies between 4.45-4.7 seconds. When wave height and wave period value are taken into account together for

wave energy potential, it is seen that the region in question has an assessable potential.

## 3. HYDROGEN ENERGY

It was stated by Dinçer [42] that the Hydrogen age started with the Covid-19 pandemic. In addition, the global hydrogen economy is predicted to be $155 billion in 2022 [18]. Therefore, hydrogen production has now emerged as an important engineering application. Although hydrogen is abundant in nature, it is not easily found because it is dependent on other molecules [6]. Therefore, it must be produced before it can be used. There are various methods in the literature to produce hydrogen. However, in order to be an alternative energy source, it must have a renewable and sustainable structure. In this stduy, the water electrolysis method is the most applicable technology to produce large-capacity 'green and clean' hydrogen [19]. Water electrolysis is the process of decomposing water into oxygen and hydrogen with the effect of direct current. The water electrolysis method has many advantages such as high efficiency and the use of RES [14]. This has revealed the necessity of examining and investigating renewable energy-based hydrogen production in the Eastern Mediterranean region, which has high renewable energy potential. This situation has been the most important motivation of the study.

There are many electrolysis technologies in the literature. In this study, the most advanced and widely used Polymer Electrolyte Membrane (PEM) electrolysis is referenced [43]. PEMs have many advantages. These advantages can be listed as high efficiency, adaptability to electrical fluctuations, low pressure hydrogen generation and direct storage without the need to compress the produced hydrogen [5,44]. Details of the cost of producing hydrogen using PEM electrolysis are given in Table 5 [45].

**Table 5.** Hydrogen Costs for PEM Electrolysis

| | | Electricity Cost ($ kWh$^{-1}$) | Capacity Factor (%) | System CAPEX ($ W$^{-1}$) | $H_2$ Cost ($ kg$^{-1}$) |
|---|---|---|---|---|---|
| Ongrid | Low | 0.050 | 90.0 | 1.0-1.5 | 5.13-4.37 |
| | High | 0.070 | 90.0 | 1.0-1.5 | 6.27-5.50 |
| | PV 1 | 0.032 | 31.8 | 1.0 | 6.09 |
| | PV 2 | 0.029 | 35.1 | 1.0 | 5.54 |
| Offgrid | Onshore Class 6 | 0.038 | 38.0 | 1.0 | 5.76 |
| | Onshore Class 1 | 0.028 | 52.1 | 1.0 | 4.22 |
| | Offshore | 0.120 | 51.0 | 1.5 | 8.34 |
| | Low | 0.050 | 90.0 | 1.0-1.5 | 5.13-4.37 |

Today, the hydrogen produced is transported by using different methods. The produced hydrogen produced can be transported as compressed/liquefied by pipelines and cargo ships [46]. In addition, if there is natural gas that can be extracted in the region, it can be mixed with natural gas and transmitted to the mainland. In general, pipeline transportation is the most economical method. However, it requires high installation costs and low maintenance-operation costs [47]. The main limitation in liquid hydrogen transport is the high energy required for disposal [48]. Therefore, it can be said that pipelines are preferred for large-scale applications [49].

## 4. COST ANALYSIS

The RES potential of the regions determined in the Eastern Mediterranean EEZ is detailed in Section 2. In this section, the energy needs of the hybrid power plant to be established in the region and the platforms to be probable hydrocarbon extraction are examined. In addition, the scenarios of producing hydrogen and moving to the mainland from the excess energy produced are detailed. The installed power and cost values of the hybrid RES plant for 6 determined zones are approximately the same. For this reason, the cost of a zone is given in Table 6. Cost information was obtained from literature studies of regions with very similar geographical features [24,50,51]. In addition, unit costs were examined in the study.

**Table 6.** Hybrid System Installed Power and Cost Values

| RES | Installed Power (MW) | Total Cost (M$) | Unit Power Cost ($ kW$^{-1}$) | Energy (GWh) | Unit Energy Cost ($ kWh$^{-1}$) |
|---|---|---|---|---|---|
| Wind[50] | 500 | 2264.062 | 4528.125 | 2095.210 | 1.080 |
| Wave[24] | 150 | 192.093 | 1280.620 | 2.346 | 81.881 |
| Solar [51] | 10 | 9.364 | 936.400 | 3.810 | 2.457 |
| Total | 660 | 2465.520 | 3735.636 | 2101.370 | 1.173 |

Accordingly, the hybrid power plant consisting of a 500 MW wind power plant, 150 MW wave power plant, and 10 MW solar power plant in the region will produce an average of 2101.369 GWh of energy per year. Although the solar Photovoltaic (PV) power plant value is seen to be very low when the unit cost of installed power is taken into account, it is seen that wind energy is much more advantageous when considering the unit cost of energy produced annually. Power consumption in hydrocarbon platforms during the year is approximately constant. Daily power consumption ranges from 22 MW to 35 MW. It can be considered that the daily consumption for an average day is approximately 27 MW. In this case, a hydrocarbon platform with an average size is considered to have an average energy consumption of 237 GWh per year [24]. Thus, the rest of the energy produced from RESs, 1864.359 GWh, can be used in hydrogen production. In this case, while it is 39 kWh km$^{-1}$ for 100% efficiency, the efficiency is around 70% in today's conditions. When this efficiency is taken into account, energy consumption is 49 kWh kg$^{-1}$. According to this energy value, 38.048x10$^{6}$ kg of hydrogen can be produced annually.

In addition, different scenarios are discussed to transmit increased energy from existing platforms to the mainland. These scenarios include pipelines, freighters and finally transporting the hydrogen produced to the mainland by mixing it with natural gas if natural gas reserves are in the region. In this case, if the hydrogen produced is transported by cargo ships, there are two different methods. These are transported as compressed or liquefied hydrogen. While the cost of transporting liquefied hydrogen is 0.584 M$ km$^{-1}$, the cost of transporting compressed hydrogen is 0.14 M$ km$^{-1}$. The

cost is 0.96 M$ $km^{-1}$ if it comes to transportation by pipelines [8].

## 5. DISCUSSION AND CONCLUSION

In this study, for the first time, its cost estimation was carried out by examining the RES potential of the Eastern Mediterranean zone. The wind, solar and wave energy potentials of the 6 zones determined for this purpose were examined. It is seen that wind energy densities are high due to the fact that the zones are located between low pressure and high-pressure air currents and Crete and Rhodes islands are a natural strait. In determining solar energy potential, it is seen that the energy density of the zones is high when the latitude effect and daily irradiation are taken into account as the main criterion. Likewise, the energy density is high due to the offshore characteristics of the wave energy potential. Although the unit cost of the wind power plant is high as Although the unit cost of the wind power plant is high, the amount of energy produced is also higher than other RESs. However, although the unit cost of the solar power plant is low, the amount of energy produced is also low. Considering the high unit energy produced cost of the wave power plant, a RES hybrid study was proposed in the zone. In this case, the hybrid power plant consisting of a 500 MW wind power plant, 150 MW wave power plant, and 10 MW solar power plant in the determined zones will produce an average of 2101.369 GWh of energy per year. When the possible platforms in the zone have an average energy consumption of 237 GWh per year, the rest of the energy produced, 1864.359 GWh, can be used in hydrogen production. In this case, there is an energy consumption of 49 kWh $km^{-1}$ for 70% efficiency. According to this energy value, $38.048x10^6$ kg of hydrogen can be produced annually. The transport of this hydrogen energy to the mainland has been examined for two different scenarios. While the cost of transporting liquefied hydrogen is 0.584 M$ $km^{-1}$, the cost of transporting compressed hydrogen is 0.14 M$ $km^{-1}$. The cost is 0.96 M$ $km^{-1}$ if it comes to transportation by pipelines. Since the distance of the zones to the mainland is 250 km, it is more economical to transport as compressed hydrogen by cargo ships.

Some important contributions of this research are given below,

• The RES potential of sample 6 zones in the Eastern Mediterranean region was examined,

• cost estimation was made for the hybrid RES,

• It was shown that RES can meet the energy needs of hydro-carbon platforms such as oil/gas and that hydrogen will be produced with excess energy,

• cost estimation of the conditions of transport of hydrogen produced to the mainland were made for different scenarios,

and as a result, the region has been shown to have a high energy potential. This situation will enable it to become an important center where hydrogen, the fuel of the future, is produced.

## REFERENCES

[1] Dincer I, Javani N, Karayel GK. Hydrogen farm concept: A Perspective for Turkey. Int J Energy Res. 2021 Jul 27;39(1):er.7086.

[2] Acar C, Dincer I. Comparative assessment of hydrogen production methods from renewable and non-renewable sources. Int J Hydrogen Energy. 2014 Jan;39(1):1–12.

[3] Karmendra Kumar Agrawal, Shibani Khanra Jha, Ravi Kant Mittal SV. Assessment of floating solar PV (FSPV) potential and water conservation: Case study on Rajghat Dam in Uttar Pradesh, India. Energy Sustain Dev. 2022;(66):287–295.

[4] Rezaei M, Mostafaeipour A, Qolipour M, Arabnia H-R. Hydrogen production using wind energy from sea water: A case study on Southern and Northern coasts of Iran. Energy Environ. 2018 May 2;29(3):333–357.

[5] Siyal SH, Mentis D, Mörtberg U, Samo SR, Howells M. A preliminary assessment of wind generated hydrogen production potential to reduce the gasoline fuel used in road transport sector of Sweden. Int J Hydrogen Energy. 2015 Jun;40(20):6501–11.

[6] Abdalla AM, Hossain S, Nisfindy OB, Azad AT, Dawood M, Azad AK. Hydrogen production, storage, transportation and key challenges with applications: A review. Energy Convers Manag. 2018 Jun;165:602–627.

[7] Dincer I. Green methods for hydrogen production. Int J Hydrogen Energy. 2012 Jan;37(2):1954–71.

[8] Çelikdemir S, Özdemir MT. Turkey's Offshore Hybrid Energy Potential and Techno-Economic Analysis in the Eastern Mediterranean. In: 5 th International Hydrogen Technologies Congress (IHTEC-2021). Niğde; 2021. p. 140–142.

[9] Çelikdemir S, Özdemir MT. Techno-Economic Analysis of Onshore and Offshore Wind Power Plant. In: TÜBA World Conference on Energy Science and Technology. İstanbul; 2021. p. 201–203.

[10] Çelikdemir S, Özdemir MT. A New Alternative Solution for Wind Power Plants. In: The International Conference series on Alternative Fuels, Energy and Environment: Future and Challenges (ICAFEE). Kayseri; 2021. p. 177–180.

[11] Çelikdemir S, Özdemir MT. A new approach in the cost estimation of a hydroelectric power plants in Türkiye based on geographical features. Int J Energy Res. 2022 Nov 15;46(14):20858–72.

[12] Zodiatis G, Galanis G, Nikolaidis A, Kalogeri C, Hayes D, Georgiou GC, et al. Wave energy potential in the Eastern Mediterranean Levantine Basin. An integrated 10-year study. Renew Energy. 2014 Sep;69:311–323.

[13] Nematollahi O, Alamdari P, Jahangiri M, Sedaghat A, Alemrajabi AA. A techno-economical assessment of solar/wind resources and hydrogen production: A case study with GIS maps. Energy. 2019 May;175:914–930.

[14] Gökçek M, Kale C. Techno-economical evaluation of a hydrogen refuelling station powered by Wind-PV hybrid power system: A case study for İzmir-Çeşme. Int J Hydrogen Energy. 2018 Jun;43(23):10615–25.

[15] Loisel R, Baranger L, Chemouri N, Spinu S, Pardo S. Economic evaluation of hybrid off-shore wind power and hydrogen storage system. Int J Hydrogen Energy. 2015 Jun;40(21):6727–39.

[16] Armijo J, Philibert C. Flexible production of green hydrogen and ammonia from variable solar and wind energy: Case study of Chile and Argentina. Int J Hydrogen Energy. 2020 Jan;45(3):1541–58.

[17] Calado G, Castro R. Hydrogen Production from Offshore Wind Parks: Current Situation and Future Perspectives. Appl Sci. 2021 Jun 16;11(12):5561.

[18] Sun F, Qin J, Wang Z, Yu M, Wu X, Sun X, et al. Energy-saving hydrogen production by chlorine-free hybrid seawater splitting coupling hydrazine degradation. Nat Commun. 2021 Dec 7;12(1):4182.

[19] Proost J. State-of-the art CAPEX data for water electrolysers, and their impact on renewable hydrogen price settings. Int J Hydrogen Energy. 2019 Feb;44(9):4406–13.

[20] Peters R, Vaessen J, Meer R van der. Offshore Hydrogen Production in the North Sea Enables Far Offshore Wind Development. In: Day 4 Thu, May 07, 2020. OTC; 2020.

[21] Dinh VN, Leahy P, McKeogh E, Murphy J, Cummins V. Development of a viability assessment model for hydrogen production from dedicated offshore wind farms. Int J Hydrogen Energy. 2021 Jul;46(48):24620–31.

[22] Sellami MH, Loudiyi K. Electrolytes behavior during hydrogen production by solar energy. Renew Sustain Energy Rev. 2017 Apr;70:1331–5.

[23] Mohamed B, Ali B, Ahmed B, Ahmed B, Salah L, Rachid D. Study of hydrogen production by solar energy as tool of storing and utilization renewable energy for the desert areas. Int J Hydrogen Energy. 2016 Dec;41(45):20788–806.

[24] Oliveira-Pinto S, Rosa-Santos P, Taveira-Pinto F. Electricity supply to offshore oil and gas platforms from renewable ocean wave energy: Overview and case study analysis. Energy Convers Manag. 2019 Apr;186:556–69.

[25] Ishaq H, Dincer I. Comparative assessment of renewable energy-based hydrogen production methods. Renew Sustain Energy Rev. 2021 Jan;135:110192.

[26] Ishaq H, Dincer I. A comparative evaluation of OTEC, solar and wind energy based systems for clean hydrogen production. J Clean Prod. 2020 Feb;246:118736.

[27] Yuksel YE, Ozturk M, Dincer I. Development and assessment of a novel geothermal power-based multigenerational system with hydrogen and ammonia production options. Energy Convers Manag. 2021 Sep;243:114365.

[28] Oliveira-Pinto S, Rosa-Santos P, Taveira-Pinto F. Assessment of the potential of combining wave and solar energy resources to power supply worldwide offshore oil and gas platforms. Energy Convers Manag. 2020 Nov;223:113299.

[29] Haces-Fernandez F, Li H, Ramirez D. Assessment of the Potential of Energy Extracted from Waves and Wind to Supply Offshore Oil Platforms Operating in the Gulf of Mexico. Energies. 2018 Apr 27;11(5):1084.

[30] Yıldız S, Gunduz H, Yildirim B, Özdemir MT. An islanded microgrid energy system with an innovative frequency controller integrating hydrogen-fuel cell. Fuel. 2022 Oct;326:125005.

[31] Daghan IH, Gencoglu MT, Ozdemir MT. Chaos Embedded Particle Swarm Optimization Technique for Solving Optimal Power Flow Problem. In: 2021 18th International Multi-Conference on Systems, Signals & Devices (SSD). IEEE; 2021. p. 725–31.

[32] Özdemir MT. Optimal parameter estimation of polymer electrolyte membrane fuel cells model with chaos embedded particle swarm optimization. Int J Hydrogen Energy. 2021 Apr;46(30):16465–80.

[33] Özdemir MT. A novel optimum PI controller design based on stability boundary locus supported particle swarm optimization in AVR system. Turkish J Electr Eng Comput Sci. 2021 Jan 27;29(1):291–309.

[34] He W, Uhlen K, Hadiya M, Chen Z, Shi G, del Rio E. Case Study of Integrating an Offshore Wind Farm with Offshore Oil and Gas Platforms and with an Onshore Electrical Grid. J Renew Energy. 2013;2013:1–10.

[35] Tuna F. Türk Dış Politikasında Realist Yaklaşım: Türkiye'nin Doğu Akdeniz ve Libya Politikası. Uluslararası Hukuk ve Sos Bilim Araştırmaları Derg. 2020;2(1):74–87.

[36] Çelikdemir S, Özdemir MT. Adilcevaz Bölgesinde Rüzgar Enerji Potansiyelinin İncelenmesi. Bitlis Eren Üniversitesi Fen Bilim Derg. 2020 Mar 13;9(1):204–14.

[37] Nezhad MM, Groppi D, Marzialetti P, Fusilli L, Laneve G, Cumo F, et al. Wind energy potential analysis using Sentinel-1 satellite: A review and a case study on Mediterranean islands. Renew Sustain Energy Rev. 2019 Jul;109:499–513.

[38] Onea F, Deleanu L, Rusu L, Georgescu C. Evaluation of the wind energy potential along the Mediterranean Sea coasts. Energy Explor Exploit. 2016 Sep 26;34(5):766–92.

[39] Soukissian T, Denaxa D, Karathanasi F, Prospathopoulos A, Sarantakos K, Iona A, et al. Marine Renewable Energy in the Mediterranean Sea: Status and Perspectives. Energies. 2017 Sep

29;10(10):1512.

[40] Alexandri G, Georgoulias AK, Meleti C, Balis D, Kourtidis KA, Sanchez-Lorenzo A, et al. A high resolution satellite view of surface solar radiation over the climatically sensitive region of Eastern Mediterranean. Atmos Res. 2017 May;188:107–21.

[41] Nikolaidis G, Karaolia A, Matsikaris A, Nikolaidis A, Nicolaides M, Georgiou GC. Blue Energy Potential Analysis in the Mediterranean. Front Energy Res. 2019 Jun 25;7:1–12.

[42] Dincer I. Covid-19 coronavirus: Closing carbon age, but opening hydrogen age. Int J Energy Res. 2020 Jun 25;44(8):6093–7.

[43] Nikolaidis P, Poullikkas A. A comparative overview of hydrogen production processes. Renew Sustain Energy Rev. 2017 Jan;67:597–611.

[44] Dagdougui H, Ouammi A, Sacile R. A regional decision support system for onsite renewable hydrogen production from solar and wind energy sources. Int J Hydrogen Energy. 2011 Nov;36(22):14324–34.

[45] Vicker J, Peterson D, Randolph K. Cost of Electrolytic Hydrogen Production with Existing Technology. Am Deparment Energy United Staes Am. 2020;

[46] Singh S, Jain S, PS V, Tiwari AK, Nouni MR, Pandey JK, et al. Hydrogen: A sustainable fuel for future of the transport sector. Renew Sustain Energy Rev. 2015 Nov;51:623–33.

[47] Reuß M, Grube T, Robinius M, Preuster P, Wasserscheid P, Stolten D. Seasonal storage and alternative carriers: A flexible hydrogen supply chain model. Appl Energy. 2017 Aug;200:290–302.

[48] Balat M. Potential importance of hydrogen as a future solution to environmental and transportation problems. Int J Hydrogen Energy. 2008 Aug;33(15):4013–29.

[49] Liu H, Almansoori A, Fowler M, Elkamel A. Analysis of Ontario's hydrogen economy demands from hydrogen fuel cell vehicles. Int J Hydrogen Energy. 2012 Jun;37(11):8905–16.

[50] Effiom SO, Nwankwojike BN, Abam FI. Economic cost evaluation on the viability of offshore wind turbine farms in Nigeria. Energy Reports. 2016 Nov;2:48–53.

[51] Goswami A, Sadhu P, Goswami U, Sadhu PK. Floating solar power plant for sustainable development: A techno-economic analysis. Environ Prog Sustain Energy. 2019 Nov 5;38(6).

Cilt 12, Sayı 1, Sayfa 108-116, 2023 Volume 12, Issue 1, Page 108-116, 2023

Araştırma Makalesi https://doi.org/10.46810/tdfd.1218818 Research Article

Türk Doğa ve Fen Dergisi
Turkish Journal of Nature and Science
www.dergipark.gov.tr/tdfd

# Pointwise Quasi Hemi-Slant Submanifolds of Cosymplectic Manifolds

**Selahattin BEYENDİ**[1*]

[1]Inonu University Education Faculty, Department of Mathematics, Malatya, Türkiye
Selahattin BEYENDİ ORCID No: 0000-0002-1037-6410

**Corresponding author: selahattin.beyendi@inonu.edu.tr*

(Received: 14.12.2022, Accepted: 03.03.2023, Online Publication: 27.03.2023)

**Keywords**
Pointwise quasi hemi-slant, cosymplectic manifold, Totally geodesic foliation

**Abstract:** The object of this manuscript is to investigate related to the geometry of distributions on pointwise quasi hemi-slant submanifolds (abbr. PQHS) in cosymplectic manifolds. In this context, the preconditions for such distributions to be integrable, totally geodesic foliation, totally geodesic and mixed totally geodesic are obtained. In addition, we are going to present several examples to guarantee these new types of submanifolds in cosymplectic manifolds.

# Kosimplektik Manifoldların Noktasal Yarı-Eğimli Alt Manifoldları

**Anahtar Kelimeler**
Noktasal yarı eğimli, kosimplektik manifold, Tamamen jeodezik yapraklanma

**Öz:** Bu makalenin amacı, kosimplektik manifoldlarda noktasal yarı-eğimli alt manifoldlar (kısaltılmış PQHS) üzerindeki dağılımların geometrisiyle ilgili araştırma yapmaktır. Bu bağlamda, bu tür dağılımların integrallenebilir olması, tamamen jeodezik yapraklanma, tamamen jeodezik ve karışık tamamen jeodezik olması için ön koşullar elde edilmektedir. Ek olarak, kosimplektik manifoldlarda bu yeni alt manifold tiplerini garanti etmek için birkaç örnek sunacağız.



## 1. INTRODUCTION

Differential geometry has been one of the most outstanding branches of mathematics and physics since the earliest times. Among the most outstanding topics in the field of differential geometry in recent years is the contact geometry. Contact geometry has a very important place in physical and other mathematical structure. Sophus Lie first mentioned contact structures in his work on partial differential equations [1]. In recent years, the geometry of contact Riemannian manifolds has received great attention. In contact geometry, there have been many classes of manifolds considered as odd-dimensional analogs of Kähler spaces, the most important ones being cosymplectic and Sasakian spaces. An odd-dimensional equivalent of a Kähler manifold can be presented by a cosymplectic manifold, locally a product of a Kähler manifold having a line or a circle [2]. An obvious instance of a cosymplectic manifold can be presented with the product of 1-dimensional manifold with (2n)-dimensional Kähler manifold.

On the other side, submanifold theory has got outstanding characteristics in Mathematical, Mechanics and Physics. In the recent twenty years, Kähler manifold applications are widely known (in particular, in the target spaces for non-linear $\sigma$ -models having supersymmetry). Today, submanifolds theory has an important place in computer design, image processings, economic modelling. Submanifolds geometry concept has started with the concept of the extrinsic geometry of the surface and it is developed for ambient space with time. In this context, the submanifolds of a cosymplectic manifold have been studied by G. D. Ludden [3]. Later on, A. Cabras et al. [4] has given the proof of the fact that in a cosymplectic manifold there is not ant extrinsic sphere which is tangent to the structure vector fields. In 1990, Chen has put forward the notion of slant submanifold, which totally real submanifolds and generalizes holomorphic [5]. Then, the theory of submanifolds is investigated by many geometers like [6-14]. As a generalization of slant submanifolds; semi-slant submanifolds, hemi-slant submanifolds, bi-slant submanifolds, quasi bi-slant submanifolds, quasi hemi-slant submanifolds, pointwise quasi bi-slant submanifolds, PQHS submanifolds [15-29] and many

others. In 2013, B. Şahin defined the concept of pointwise semi-slant submanifolds [30]. In 2014, K. S. Park has given the concept of pointwise almost h-semi- slant submanifolds and pointwise almost h-slant submanifolds in an almost quaternionic Hermitian manifold [31-32]. In 2020, Akyol et al. [33] initiated the study of quasi bi-slant submanifolds of an almost contact metric manifold by generalizing slant, semi-slant, hemi-slant and bi-slant submanifolds (See also: [34]). Motivated by all those work in the present article, we are going to investigate PQHS submanifolds of cosymplectic manifolds.

The layout of the manuscript can be given as follows: In the second section, the fundamental descriptions and formulae about cosymplectic manifolds and the geometry of submanifolds are given. The third section gives the definition of PQHS submanifolds of cosymplectic manifolds and we obtained some results for the next sections. In the fourth section, we deals with main theorems related to the geometry of distributions. Finally in the last section, we proved two examples of such submanifolds.

## 2. SOME BASIC CONCEPTS

This section presents a cosymplectic manifold definition and some fundamentals about submanifolds theory.

An almost contact structure $(\varphi, \xi, \eta)$ on a $(2m+1)$-dimensional manifold $N$ is defined by a (1,1) tensor field $\varphi$, a vector field $\xi$ and a 1-form $\eta$ satisfying the following conditions:

$$\varphi^2 = -I + \eta \otimes \xi, \ \ \eta(\xi) = 1, \ \eta o \varphi = 0, \ \ \varphi\xi = 0. \quad (1)$$

One can always find a Riemannian metric $<,>$ on an almost contact manifold $N$ which satisfies the conditions given below

$$\begin{gathered} <\varphi U, \varphi V> = <U, V> - \eta(U)\eta(V) \\ \eta(U) = <U, \xi>, \end{gathered} \quad (2)$$

where $U, V$ are vector fields on $N$.

It is said that an almost contact structure $(\varphi, \xi, \eta)$ is normal when the almost complex structure $J$ on the product manifold $N \times \mathbb{R}$ is given by

$$J(U, f\frac{d}{dt}) = (\varphi U - f\xi, \eta(U)\frac{d}{dt}),$$

in which $f$ is a $C^\infty$-function on $N \times \mathbb{R}$ without torsion i.e., $J$ is integrable. The condition for normality in terms of $\varphi, \xi$ and $\eta$ is $[\varphi, \varphi] + 2d\eta \otimes \xi = 0$ on $N$, in which $[\varphi, \varphi]$ is the Nijenhuis tensor of $\varphi$. Lastly, the fundamental two-form $\Phi$ is defined $\Phi(U, V) = <U, \varphi V>$.

If the almost contact structure $(\varphi, \xi, \eta, <,>)$ is normal and both $\Phi$ and $\eta$ are closed, then this structure can be expressed as cosymplectic [3, 35-37]. From the point of the covariant derivative of $\varphi$, the cosymplectic condition can be specified by

$$(\nabla_U \varphi)V = 0, \quad (3)$$

for every $U, V$ tangent to $N$, in which $\nabla$ stands for the Riemannian connection of the metric $<,>$ on $N$. Furthermore, for cosymplectic manifold

$$\nabla_U \xi = 0. \quad (4)$$

Let $N$ be a Riemannian manifold isometrically immersed in $\widetilde{N}$ and induced Riemannian metric on $N$ is described by the $<,>$ throughout this manuscript. Let $h$ and $\mathcal{A}$ denote second fundamental form and the shape operator, respectively, of immersion of $N$ into $\widetilde{N}$. If $\nabla$ is the induced Riemannian connection on $N$, then the Gauss and Weingarten formulae are presented by [5]

$$\widetilde{\nabla}_U V = \nabla_U V + h(U, V) \quad (5)$$

and

$$\widetilde{\nabla}_U V = -\mathcal{A}_V U + \nabla^\perp_U V, \quad (6)$$

for any $U, V \in \Gamma(TN)$, $V \in \Gamma(T^\perp N)$ and $\nabla^\perp$ stands for the connection on the normal bundle $T^\perp N$ of $N$.

If $N$ is totally geodesic, then $h(U, V) = 0$ for all $U, V \in \Gamma(TN)$.

At this point, one has the following description from [38]:

**Definition 2.1** A submanifold N of an almost Hermitian manifold $\widetilde{N}$ is known pointwise slant if, for every point $p \in N$, the Wirtinger angle $\theta(U)$ is independent of the selection of nonzero vector $U \in T_p^*N$, where $T_p^*N$ is the tangent space of nonzero vectors. Under these conditions, $\theta$ is known slant function of N.

**Definition 2.2** A submanifold N is known (i) $(\mathfrak{D}_1, \mathfrak{D}_2)$-mixed totally geodesic if $h(Z, W) = 0$, for any $Z \in \Gamma(\mathfrak{D}_1)$ and $W \in \Gamma(\mathfrak{D}_2)$ (ii) $\mathfrak{D}$-totally geodesic if it is $(\mathfrak{D}, \mathfrak{D})$-mixed totally geodesic [34].

## 3. POINTWISE QUASI HEMI-SLANT SUBMANIFOLDS OF COSYMPLECTIC MANIFOLDS

In this section, we are going to present basic definitions and lemmas related to PQHS submanifolds of cosymplectic manifolds.

**Definition 3.1** A submanifold N of cosymplectic manifolds $(\widetilde{N}, \varphi, \xi, \eta, <,>)$ is known PQHS if there exist distributions $\mathfrak{D}$, $\mathfrak{D}_\theta$ and $\mathfrak{D}^\perp$ such that

(i) $TN = \mathfrak{D} \oplus \mathfrak{D}_\theta \oplus \mathfrak{D}^\perp \oplus <\xi>$.

(ii) The distribution $\mathfrak{D}$ is invariant, i.e. $\varphi\mathfrak{D} = \mathfrak{D}$.

(iii) For a vector field which is different from zero $U \in (\mathfrak{D}_\theta)_p$, $p \in N$, the angle $\theta$ between $\varphi U$ and $(\mathfrak{D}_\theta)_p$ is slant function and is independent of the choice of the point $p$ and $U$ in $(\mathfrak{D}_\theta)_p$.

(iv) The distribution $\mathfrak{D}^{\perp}$ is anti-invariant, i.e., $\varphi\mathfrak{D}^{\perp} \subseteq T^{\perp}N$.

The $\theta$ is known as a PQHS angle of $N$. A PQHS submanifold $N$ is known proper if its pointwise-slant function satisfies $\theta \neq 0, \frac{\pi}{2}$, and $\theta$ is not constant on $N$.

If we represent by $k_1$, $k_2$ and $k_3$ the dimension of $\mathfrak{D}$, $\mathfrak{D}_\theta$ and $\mathfrak{D}^{\perp}$, respectively, thus with the usage of generalized PQHS submanifold definition, one can easily see the following particular cases;

(i) $N$ is pointwise hemi-slant submanifold when $k_1 = 0$,

(ii) $N$ is semi-invariant submanifold when $k_2 = 0$,

(iii) $N$ is pointwise semi-slant submanifold when $k_3 = 0$.

Let $N$ be a PQHS submanifold of a cosymplectic manifold $\widetilde{N}$. Thus, for any $U \in \Gamma(TN)$, one has

$$U = PU + QU + RU + \eta(U)\xi, \tag{7}$$

in which $P, Q$ and $R$ stands for the projections on the distributions $\mathfrak{D}$, $\mathfrak{D}_\theta$ and $\mathfrak{D}^{\perp}$, respectively.

$$\varphi U = TU + FU, \tag{8}$$

where FU and TU are normal and tangential components on $N$, respectively. By using (7) and (8), we get immediately

$$\varphi U = TPU + FPU + TQU + FQU + TRU + FRU,$$

in which due to the fact that $\varphi\mathfrak{D} = \mathfrak{D}$, one has $FPU = 0$. Therefore, one gets

$$\varphi(TN) = \mathfrak{D} \oplus T\mathfrak{D}_\theta \oplus F\mathfrak{D}_\theta \oplus \varphi\mathfrak{D}^{\perp}$$

and

$$T^{\perp}N = F\mathfrak{D}_\theta \oplus \varphi\mathfrak{D}^{\perp} \oplus \mu,$$

in which $\mu$ stands for the orthogonal complement of $F\mathfrak{D}_\theta \oplus \varphi\mathfrak{D}^{\perp}$ in $T^{\perp}N$ and $\varphi\mu = \mu$. At the same time, for every $Z \in T^{\perp}N$, one has

$$\varphi Z = BZ + CZ, \tag{9}$$

in which $BZ \in \Gamma(\mathfrak{D}_\theta \oplus \mathfrak{D}^{\perp})$ and $CZ \in \Gamma(\mu)$.

When the condition (iii) given in Definition 3.1 is used together with (8) and (9), one obtains the followings:

$T\mathfrak{D} = \mathfrak{D}$, $T\mathfrak{D}_\theta = \mathfrak{D}_\theta$, $T\mathfrak{D}^{\perp} = \{0\}$, $BF\mathfrak{D}_\theta = \mathfrak{D}_\theta$, $BF\mathfrak{D}^{\perp} = \mathfrak{D}^{\perp}$.

When Eqs. (8) and (9) are used, one obtains the following Lemma.

**Lemma 3.2** Let N be a PQHS submanifold of an almost contact metric manifold $\widetilde{\mathrm{N}}$. Therefore, one has

$(a)\ T^2U = -(\cos^2\theta)U$, $(b)\ BFU = -(\sin^2\theta)U$,

$(c)\ T^2U + BFU = -U$, $(d)\ FTU + CFU = 0$,

for any $U \in \mathfrak{D}_\theta$.

With the help of (3), (8) and (9) and Definition 3.1, one obtains the following Lemma.

**Lemma 3.3** Let N be a PQHS submanifold of an almost contact metric manifold $\widetilde{\mathrm{N}}$. Then, we have

(i) $< TU, TV >= (\cos^2\theta) < U, V >$,

(ii) $< FU, FV >= (\sin^2\theta) < U, V >$,

for any $U, V \in \Gamma(\mathfrak{D}_\theta)$.

**Proof.** One can follow a similar way presented in Proposition 2.8 of [38].

When Eqs. (3), (5), (6), (8) and (9) are used and the normal and tangential components are compared, one has the following:

**Lemma 3.4** Let N be a PQHS submanifold of a cosymplectic manifold $\widetilde{\mathrm{N}}$. Therefore, one obtains

$$\nabla_U TV - A_{FV}U - T\nabla_U V - Bh(U,V) = 0$$

and

$$h(U,TV) + \nabla^{\perp}_U FV - F(\nabla_U V) - Ch(U,V) = 0,$$

for all $U, V \in \Gamma(TN)$.

**Lemma 3.5** Let N be a PQHS submanifold of a cosymplectic manifold $\widetilde{\mathrm{N}}$. Thus, one has

$$(\widetilde{\nabla}_U T)V = A_{FV}U + Bh(U,V),$$

$$(\widetilde{\nabla}_U F)V = Ch(U,V) - h(U,TV),$$

for any $U, V \in \Gamma(TN)$.

**Lemma 3.6** N be PQHS submanifold of a cosymplectic manifold $\widetilde{\mathrm{N}}$. Thus, one has

$$T([U,V]) = A_{\varphi V}U - A_{\varphi U}V$$

and

$$F([U,V]) = \nabla^{\perp}_U \varphi V - \nabla^{\perp}_V \varphi U,$$

for any $U, V \in \mathfrak{D}^{\perp}$.

**Proof.** Let $U, V \in \Gamma(\mathfrak{D}^{\perp})$, then

$$(\widetilde{\nabla}_U \varphi)V = \widetilde{\nabla}_U \varphi V - \varphi(\widetilde{\nabla}_U V).$$

Taking into account of (3) in the above equation, we have

$$-A_{\varphi V}U + \nabla^{\perp}_U \varphi V - T\nabla_U V - F\nabla_U V - Bh(U,V) - Ch(U,V) = 0.$$

When the normal and tangential parts are compared in the equation given above, one obtains

$$-A_{\varphi V}U - T\nabla_U V - Bh(U,V) = 0 \tag{10}$$

and

$$\nabla^{\perp}_{U}\varphi V - F\nabla_{U}V - Ch(U,V) = 0. \quad (11)$$

From equations (10) and (11), one may conclude the the statement of Lemma 3.6.

**Lemma 3.7** Let N be a PQHS submanifold of a cosymplectic manifold $\tilde{N}$. Under these assumptions, we have

(i) $< [U,V], \xi >= 0,$

(ii) $< \tilde{\nabla}_{U}V, \xi >= 0,$

for all $U,V \in (\mathfrak{D} \oplus \mathfrak{D}_{\theta} \oplus \mathfrak{D}^{\perp})$.

## 4. BASIC RESULTS

**Theorem 4.1** Let N be a PQHS submanifold of a cosymplectic manifold $\tilde{N}$. Then, $\mathfrak{D}$ is integrable if and only if

$$< h(V,TU), FQZ > - < h(U,TV), FZ >$$
$$= < \nabla_{U}TV - \nabla_{V}TU, TQZ >$$
$$+ < T\nabla_{V}TU + Bh(V,TU), RZ >,$$

where $U,V \in \Gamma(\mathfrak{D}), Z = QZ + RZ \in \Gamma(\mathfrak{D}_{\theta} \oplus \mathfrak{D}^{\perp})$.

**Proof.** The distribution $\mathfrak{D}$ is integrable on $N$ if and only if

$$< [U,V], \xi >= 0 \quad and \quad < [U,V], Z >,$$

for all $U,V \in \Gamma(\mathfrak{D})$, $Z = QZ + RZ \in \Gamma(\mathfrak{D}_{\theta} \oplus \mathfrak{D}^{\perp})$. For any $V \in \Gamma(\mathfrak{D})$ , one has $< V, \xi >= 0$ . Taking the covariant derivative of (4) along $U$, one has

$$< \tilde{\nabla}_{U}V, \xi > + < V, \tilde{\nabla}_{U}\xi >= 0. \quad (12)$$

From the equations (4) and (12), we obtain

$$< [U,V], \xi >= < \tilde{\nabla}_{U}V, \xi > - < V, \tilde{\nabla}_{U}\xi, >= 0.$$

Next, for every $U,V \in \Gamma(\mathfrak{D})$ and $Z = QZ + RZ \in \Gamma(\mathfrak{D} \oplus \mathfrak{D}_{\theta})$. Using (5), (8) and $FV = 0$ for all $V \in \Gamma(\mathfrak{D})$, we get

$$< [U,V], Z >= < \tilde{\nabla}_{U}\varphi V, \varphi Z > - < \tilde{\nabla}_{V}\varphi U, \varphi Z >$$
$$= < \tilde{\nabla}_{U}TV, TQZ + FQZ > + < \tilde{\nabla}_{U}TV, FRZ >$$
$$- < \tilde{\nabla}_{V}TU, \varphi QZ + \varphi RZ >.$$

By using (9) in the above equation, we have

$$< [U,V], Z >= < \nabla_{U}TV, TQZ > + < h(U,TV), FQZ >$$
$$+ < h(U,TV), FRZ > + < \varphi(\tilde{\nabla}_{V}TU), RZ >$$
$$- < \tilde{\nabla}_{V}TU, TQZ + FQZ >$$
$$= < \nabla_{U}TV - \nabla_{V}TU, TQZ > + < h(U,TV), FZ >$$
$$+ < T\nabla_{V}TU + Bh(V,TU), RZ >$$
$$- < h(V,TU), FQZ > \quad (13)$$

The proof comes from (13).

**Theorem 4.2** Let N be a PQHS submanifold of a cosymplectic manifold $\tilde{N}$. Then, $\mathfrak{D}_{\theta}$ is integrable if and only if

$$\sin(2\theta)\, Z(\theta) < U,V > - cos^{2}\theta < \nabla_{Z}U, V >$$
$$= < A_{CFU}V - \nabla_{V}BFU, Z >$$
$$+ < \nabla_{V}TU, TPZ) - < \nabla_{Z}BFU, V >,$$

where $U,V \in \Gamma(\mathfrak{D}_{\theta}), Z = PZ + RZ \in \Gamma(\mathfrak{D} \oplus \mathfrak{D}^{\perp})$.

**Proof.** For every $U,V \in \Gamma(\mathfrak{D}_{\theta}), Z = PZ + RZ \in \Gamma(\mathfrak{D} \oplus \mathfrak{D}^{\perp})$, utilizing (2), (3), (8) and (9), one has

$$< [U,V], Z >= < \tilde{\nabla}_{U}V, Z > - < \tilde{\nabla}_{V}U, Z >$$
$$= - < \tilde{\nabla}_{Z}\varphi U, \varphi V > - < [U,Z], V >$$
$$- < \tilde{\nabla}_{V}\varphi U, \varphi Z >$$
$$= < \tilde{\nabla}_{Z}T^{2}U, V > + < \tilde{\nabla}_{Z}FTU, V >$$
$$+ < \tilde{\nabla}_{Z}BFU + CFU, V > - < [U,Z], V >$$
$$- < \tilde{\nabla}_{V}TU, \varphi Z > - < \tilde{\nabla}_{V}FU, \varphi Z >. \quad (14)$$

On the other hand, taking into account of Lemmma 3.2, using (5), (6), equation (14)

$$< [U,V], Z > = \sin(2\theta)\, Z(\theta) < U,V >$$
$$+ \cos^{2}\theta \ < \tilde{\nabla}_{U}V, Z > - \sin^{2}\theta < [U,Z], V >$$
$$+ < \nabla_{Z}BFU, V > - < \nabla_{V}TU, TPZ >$$
$$+ < \nabla_{V}BFU - A_{CFU}V, Z >$$
$$= \sin(2\theta) Z(\theta) < U,V > - cos^{2}\theta < \nabla_{Z}U, V >$$
$$+ < \nabla_{Z}BFU, V > - < \nabla_{V}TU, TPZ >$$
$$+ < \nabla_{V}BFU - A_{CFU}V, Z >. \quad (15)$$

The proof comes from (15).

**Theorem 4.3** Let N be a PQHS submanifold of a cosymplectic manifold $\tilde{N}$. Then, $\mathfrak{D}^{\perp}$ is integrable if and onl if

$$< T([U,V]), TPZ - QZ >= < BF([U,V]), QZ >,$$

where $U,V \in \Gamma(\mathfrak{D}^{\perp})$, $Z = PZ + QZ \in \Gamma(\mathfrak{D} \oplus \mathfrak{D}_{\theta})$.

**Proof.** For any $U,V \in \Gamma(\mathfrak{D}^{\perp})$, $Z = PZ + QZ \in \Gamma(\mathfrak{D} \oplus \mathfrak{D}_{\theta})$, by using (2), (3), (6), one obtains

$$< [U,V], Z >= < \tilde{\nabla}_{U}\varphi V, \varphi Z > - < \tilde{\nabla}_{V}\varphi U, \varphi Z >$$
$$= < -A_{\varphi V}U + \nabla^{\perp}_{U}\varphi V, \varphi PZ >$$

$$+< \varphi(A_{\varphi V}U - \nabla^{\perp}_{U}\varphi V), QZ >$$

$$+< A_{\varphi U}V - \nabla^{\perp}_{V}\varphi U, TPZ >$$

$$+< \varphi(\nabla^{\perp}_{V}\varphi U - A_{\varphi U}V), QZ >. \quad (16)$$

By virtue of (8) and (9), equation (16)

$$< [U,V], Z >=< A_{\varphi U}V - A_{\varphi V}U, TPZ >$$

$$+< T(A_{\varphi V}U - A_{\varphi U}V), QZ >$$

$$+< B(\nabla^{\perp}_{V}\varphi U - \nabla^{\perp}_{U}\varphi V), QZ >.$$

From Lemma 3.6, one has

$$< [U,V], Z >=< T([U,V]), TPZ - QZ >$$

$$-< BF([U,V]), QZ >. \quad (17)$$

Hence the proof follows from (17).

**Theorem 4.4** Let N be a PQHS submanifold of a cosymplectic manifold $\widetilde{N}$. Then, $\mathfrak{D}$ defines a totally geodesic foliation on N if and only if

$$< T\nabla_{U}TV + Bh(U,TV), QZ >=< h(U,TV), FRZ >$$

and

$$< \nabla_{U}V, TBW >=< F\nabla_{U}V + Ch(U,V), CW >,$$

where $U,V \in \Gamma(\mathfrak{D})$, $Z = QZ + RZ \in \Gamma(\mathfrak{D}_{\theta} \oplus \mathfrak{D}^{\perp})$ and $W \in \Gamma(TN)^{\perp}$.

**Proof.** For every $U,V \in \Gamma(\mathfrak{D})$, $Z = QZ + RZ \in \Gamma(\mathfrak{D}_{\theta} \oplus \mathfrak{D}^{\perp})$, utilizing (2), (5), (8) and (9), one has

$$< \widetilde{\nabla}_{U}V, Z >=< \widetilde{\nabla}_{U}\varphi V, \varphi Z >$$

$$=< \widetilde{\nabla}_{U}TV, \varphi QZ > +< \widetilde{\nabla}_{U}TV, \varphi RZ >$$

$$= -< \varphi\big(\nabla_{U}TV + h(U,TV)\big), QZ >$$

$$+< h(U,TV), \varphi RZ >$$

$$= -< T\nabla_{U}TV + Bh(U,TV), QZ >$$

$$+< h(U,TV), FRZ >. \quad (18)$$

Now, for all $W \in \Gamma(TN)^{\perp}$ and $U,V \in \Gamma(\mathfrak{D})$, we get

$$< \widetilde{\nabla}_{U}V, W >=< \widetilde{\nabla}_{U}\varphi V, BW + CW >$$

$$= -< \widetilde{\nabla}_{U}V, \varphi BW + \varphi CW >$$

$$= -< \nabla_{U}V, TBW > +< \varphi\widetilde{\nabla}_{U}V, CW >$$

$$= -< \nabla_{U}V, TBW >$$

$$+< F\nabla_{U}V + Ch(U,V), CW >. \quad (19)$$

Thus from (18) and (19), which achieves the proof.

**Theorem 4.5** Let N be a PQHS submanifold of a cosymplectic manifold $\widetilde{N}$. Then, $\mathfrak{D}_{\theta}$ defines a totally geodesic foliation on N if and only if

$$\cos^2\theta < [U,Z], V > + \sin(2\theta)\, Z(\theta) < U,V >$$

$$=< T\nabla_{Z}TU + Bh(Z,TU), V >$$

and

$$< FA_{FV}U, W >=< C\nabla^{\perp}_{U}FV + \nabla^{\perp}_{U}FTV, W >,$$

where $U,V \in \Gamma(\mathfrak{D}_{\theta}), Z = PZ + RZ \in \Gamma(\mathfrak{D} \oplus \mathfrak{D}^{\perp})$ and $W \in \Gamma(TN)^{\perp}$.

**Proof.** For every $U,V \in \Gamma(\mathfrak{D}_{\theta})$, $Z = PZ + RZ \in \Gamma(\mathfrak{D} \oplus \mathfrak{D}^{\perp})$, utilizing (2), (5), (8) and (9), we have

$$< \widetilde{\nabla}_{U}V, Z >= U < V, Z > -< V, \widetilde{\nabla}_{U}Z >$$

$$= -< [U,Z], V > -< \widetilde{\nabla}_{Z}\varphi U, \varphi V >$$

$$-< \widetilde{\nabla}_{Z}FU, \varphi V >$$

$$= -< [U,Z], V > +< T\nabla_{Z}TU, V >$$

$$+< Bh(Z,TU), V > +< \widetilde{\nabla}_{Z}BFU, V >$$

$$+< \widetilde{\nabla}_{Z}CFU, V >.$$

Then from (6), Lemma 3.2 and using the property of slant function, we get

$$< \widetilde{\nabla}_{U}V, Z >= -< [U,Z] + T\nabla_{Z}TU + Bh(Z,TU), V >$$

$$-< \widetilde{\nabla}_{Z}\sin^2\theta U - A_{CFU}Z, V >$$

$$= -\sin(2\theta)Z(\theta) < U,V > -\sin^2\theta < \widetilde{\nabla}_{Z}U, V >$$

$$-< [U,Z] + T\nabla_{Z}TU + Bh(Z,TU), V >. \quad (20)$$

From (20), we obtain

$$\cos^2\theta < \widetilde{\nabla}_{U}V, Z >= -\cos^2\theta < [U,Z], V >$$

$$-\sin(2\theta)Z(\theta) < U,V >$$

$$+< T\nabla_{Z}TU + Bh(Z,TU), V >. \quad (21)$$

Now, for every $W \in \Gamma(TN)^{\perp}$, with the help of (2), (6), (8) and Lemma 3.2, we have

$$< \widetilde{\nabla}_{U}V, W >=< \widetilde{\nabla}_{U}\varphi V, \varphi W >$$

$$= -< \widetilde{\nabla}_{U}T^2V - \widetilde{\nabla}_{U}FTV, W >$$

$$-< \varphi(-A_{FV}U + \nabla^{\perp}_{U}FV), W >,$$

which gives

$$\sin^2\theta < \widetilde{\nabla}_{U}V, W >=< FA_{FV}U - \nabla^{\perp}_{U}FTV - C\nabla^{\perp}_{U}FV, W >. \quad (22)$$

Thus from (21) and (22), which achieves the proof .

**Theorem 4.6** Let N be a PQHS submanifold of a cosymplectic manifold $\widetilde{N}$. Then, $\mathfrak{D}^{\perp}$ defines a totally geodesic foliation on N if and only if

$$< A_{FV}U, TQZ > =< \nabla^{\perp}_{U}FV, FQZ >$$

and

$$< A_{FV}U, BW > =< \nabla^{\perp}_{U}FV, CW >,$$

where $U, V \in \Gamma(\mathfrak{D}^{\perp})$, $Z = PZ + QZ \in \Gamma(\mathfrak{D} \oplus \mathfrak{D}_{\theta})$ and $W \in \Gamma(TN)^{\perp}$.

**Proof.** For all $U, V \in \Gamma(\mathfrak{D}^{\perp})$, $Z = PZ + QZ \in \Gamma(\mathfrak{D} \oplus \mathfrak{D}_{\theta})$, using (2), (6) and (8), one has

$$\begin{aligned} < \widetilde{\nabla}_{U}V, Z > &=< \widetilde{\nabla}_{U}\varphi V, \varphi Z > \\ &=< \widetilde{\nabla}_{U}\varphi V, \varphi PZ + \varphi QZ > \\ &=< -A_{\varphi V}U + \nabla^{\perp}_{U}\varphi V, FPZ > \\ &+< -A_{FV}U + \nabla^{\perp}_{U}FV, TQZ + FQZ > \\ &= -< A_{FV}U, TQZ > +< \nabla^{\perp}_{U}FV, FQZ >. \end{aligned} \quad (23)$$

Now, for every $U, V \in \Gamma(\mathfrak{D}^{\perp})$ and $W \in \Gamma(TN)^{\perp}$, utilizing (2), (6), (9), we get

$$\begin{aligned} < \widetilde{\nabla}_{U}V, W > &=< \widetilde{\nabla}_{U}FV, BW + CW > \\ &= -< A_{FV}U, BW > +< \nabla^{\perp}_{U}FV, CW >. \end{aligned} \quad (24)$$

The proof comes from (23) and (24).

**Theorem 4.7** Let N be a PQHS submanifold of a cosymplectic manifold $\widetilde{N}$. Then, $\mathfrak{D}$ is totally geodesic if and only if

$$\begin{aligned} &< T\nabla_{U}V + Bh(U,V), BW > \\ &= -< F\nabla_{U}V + Ch(U,V), CW >, \end{aligned}$$

where $U, V \in \Gamma(\mathfrak{D})$ and $W \in \Gamma(TN)^{\perp}$.

**Proof.** For any $U, V \in \Gamma(\mathfrak{D})$ and $W \in \Gamma(TN)^{\perp}$, by using (2), (5) , (8) and (9), we have

$$\begin{aligned} < (h(U,V), W > &=< \widetilde{\nabla}_{U}\varphi V, \varphi W > \\ &=< \varphi\widetilde{\nabla}_{U}V, BW > +< \varphi\widetilde{\nabla}_{U}V, CW > \\ &=< T\nabla_{U}V + Bh(U,V), BW > \\ &+< F\nabla_{U}V + Ch(U,V), CW >. \end{aligned} \quad (25)$$

The proof comes from (25).

**Theorem 4.8** Let N be a PQHS submanifold of a cosymplectic manifold $\widetilde{N}$. Then, $\mathfrak{D}_{\theta}$ is totally geodesic if and only if

$$< A_{W}U, BFV > =< \nabla^{\perp}_{U}W, CFV + FTV >,$$

where $U, V \in \Gamma(\mathfrak{D}_{\theta})$ and $W \in \Gamma(TN)^{\perp}$.

**Proof.** For any $U, V \in \Gamma(\mathfrak{D}_{\theta})$ and $W \in \Gamma(TN)^{\perp}$, by using (2) and (8), we get

$$\begin{aligned} < h(U,V), W > &= -< \widetilde{\nabla}_{U}\varphi W, \varphi V > \\ &=< \widetilde{\nabla}_{U}W, \varphi TV > +< \widetilde{\nabla}_{U}W, \varphi FV > \\ &=< \widetilde{\nabla}_{U}W, T^{2}V + FTV > \\ &+< \widetilde{\nabla}_{U}W, BFV + CFV >. \end{aligned} \quad (26)$$

Taking into account of (6) and from Lemma 3.2, equation (26)

$$\begin{aligned} < h(U,V), W > &= \cos^{2}\theta < \widetilde{\nabla}_{U}V, W > \\ &+< \nabla^{\perp}_{U}W, FTV + CFV > \\ &-< A_{W}U, BFV >. \end{aligned} \quad (27)$$

From (27), we obtain

$$\begin{aligned} \sin^{2}\theta < \widetilde{\nabla}_{U}V, W > &=< \nabla^{\perp}_{U}W, FTV + CFV > \\ &-< A_{W}U, BFV >. \end{aligned}$$

This implies

$$\begin{aligned} < h(U,V), W > = \csc^{2}\theta\{&< \nabla^{\perp}_{U}W, FTV + CFV > \\ &-< A_{W}U, BFV >\}. \end{aligned} \quad (28)$$

Thus from (28), which achieves the proof.



**Theorem 4.9** Let N be a PQHS submanifold of a cosymplectic manifold $\widetilde{N}$. Then, $\mathfrak{D}^{\perp}$ is totally geodesic if and only if

$$< B\nabla^{\perp}_{U}W - TA_{W}U, TV > =< FA_{W}V - C\nabla^{\perp}_{U}W, FV >,$$

where $U, V \in \Gamma(\mathfrak{D}^{\perp})$ and $W \in \Gamma(TN)^{\perp}$.

**Proof**. For any $U, V \in \Gamma(\mathfrak{D}^{\perp})$ and $W \in \Gamma(TN)^{\perp}$, by using (2), (6), (8) and (9), we have

$$\begin{aligned} < h(U,V), W > &= -< \widetilde{\nabla}_{U}\varphi W, \varphi V > \\ &= -< \varphi(-A_{W}U + \nabla^{\perp}_{U}W), \varphi V > \\ &=< TA_{W}U - B\nabla^{\perp}_{U}W, TV > \\ &+< FA_{W}V - C\nabla^{\perp}_{U}W, FV >. \end{aligned} \quad (29)$$

The proof comes from (29).

**Theorem 4.10** Let N be a PQHS submanifold of a cosymplectic manifold $\widetilde{N}$. Then, $\mathfrak{D} - \mathfrak{D}_{\theta}$ mixed totally geodesic if and only if

$$< FA_{FV}U - \nabla^{\perp}_{U}FTV - C\nabla^{\perp}_{U}FV, W > = 0,$$

where $U \in \Gamma(\mathfrak{D})$, $V \in \Gamma(\mathfrak{D}_{\theta})$ and $W \in \Gamma(TN)^{\perp}$.

**Proof.** For any $U \in \Gamma(\mathfrak{D})$, $V \in \Gamma(\mathfrak{D}_\theta)$ and $W \in \Gamma(TN)^\perp$, by using (2), (5), (6), (8), (9) and from Lemma 3.2, one can obtain

$$< h(U,V), W >=< \tilde{\nabla}_U \varphi V, \varphi W >$$
$$=< \tilde{\nabla}_U TV, \varphi W > +< \tilde{\nabla}_U FV, \varphi W >$$
$$=< \tilde{\nabla}_U T^2 V + FTV, W > -< \varphi \tilde{\nabla}_U FV, W >$$
$$= \cos^2\theta < \tilde{\nabla}_U V, W > -< \nabla^\perp_U FTV, W >$$
$$-< \varphi \tilde{\nabla}_U FV, W >. \quad (30)$$

From equation (30), we have

$$\sin^2\theta < h(U,V), W >$$
$$=< FA_T VU - \nabla^\perp_U FTV - C\nabla^\perp_U FV, W >,$$

which gives

$$< h(U,V), W >$$
$$= \csc^2\theta\{< FA_{FV}U - \nabla^\perp_U FTV - C\nabla^\perp_U FV, W >\},$$

which completes the proof.

**Theorem 4.11** Let N be a PQHS submanifold of a cosymplectic manifold $\tilde{N}$. Then, $\mathfrak{D} - \mathfrak{D}^\perp$ mixed totally geodesic if and only if

$$\nabla_V BW - A_{CW}V \in \Gamma(\mathfrak{D}^\perp),$$

where $U \in \Gamma(\mathfrak{D})$, $V \in \Gamma(\mathfrak{D}^\perp)$ and $W \in \Gamma(TN)^\perp$.

**Proof.** For every $U \in \Gamma(\mathfrak{D})$, $V \in \Gamma(\mathfrak{D}^\perp)$ and $W \in \Gamma(TN)^\perp$, by using (2), (5), (6), (8) and (9), we get

$$< h(U,V), W >= -< \tilde{\nabla}_V \varphi W, \varphi U >$$
$$= -< \tilde{\nabla}_V BW + CW, TU >$$
$$= -< \nabla_V BW - A_{CW}V, TU >. \quad (31)$$

The proof comes from (31).

**Theorem 4.12** Let N be a PQHS submanifold of a cosymplectic manifold $\tilde{N}$. Then, $\mathfrak{D}_\theta - \mathfrak{D}^\perp$ mixed totally geodesic if and only if

$$< A_{FV}U, BW >=< \nabla^\perp_U FV, CW >,$$

where $U \in \Gamma(\mathfrak{D}_\theta)$, $V \in \Gamma(\mathfrak{D}^\perp)$ and $W \in \Gamma(TN)^\perp$.

**Proof.** For every $U \in \Gamma(\mathfrak{D}_\theta)$, $V \in \Gamma(\mathfrak{D}^\perp)$ and $W \in \Gamma(TN)^\perp$, by using (2), (5), (6), (8) and (9), one has

$$< h(U,V), W >=< \tilde{\nabla}_U \varphi V, \varphi W >$$
$$=< \tilde{\nabla}_U FV, BW + CW >$$
$$=< \nabla^\perp_U FV, CW > -< A_{FV}U, BW >. \quad (32)$$

The proof comes from (32).

Finally, we mention the following examples.

## 5. EXAMPLES

**Example 5.1** For $\theta \in (0, \frac{\pi}{2})$, consider a submanifold N of a cosymplectic manifold $\tilde{N}$ described by immersion f as follows:

$$f(\theta,u,w,s,m,n,z) =$$
$$\left(\frac{\sqrt{3}}{2}w, 0, 0, -\frac{w}{2}, u^2, -\sin\theta, u^2, \cos\theta, s, 0, u^2, -\sin\theta, u^2, \cos\theta, m, n, z\right).$$

By aid of simple calculations, one can easily control that the tangent bundle of $N$ is spanned by the set $\{X_1, X_2, X_3, X_4, X_5, X_6, X_7\}$, where

$$X_1 = -\cos\theta \frac{\partial}{\partial y_3} - \sin\theta \frac{\partial}{\partial y_4} - \cos\theta \frac{\partial}{\partial y_6} - \sin\theta \frac{\partial}{\partial y_7},$$

$$X_2 = 2u\frac{\partial}{\partial x_3} + 2u\frac{\partial}{\partial x_4} + 2u\frac{\partial}{\partial x_6} + 2u\frac{\partial}{\partial x_7},$$

$$X_3 = \frac{\sqrt{3}}{2}\frac{\partial}{\partial x_1} - \frac{1}{2}\frac{\partial}{\partial y_2}, \qquad X_4 = \frac{\partial}{\partial x_5},$$

$$X_5 = \frac{\partial}{\partial x_8}, \qquad X_6 = \frac{\partial}{\partial y_8}, \qquad X_7 = \frac{\partial}{\partial z}.$$

$\varphi$ be the (1,1) tensor field defined by

$$\varphi\left(\frac{\partial}{\partial x_i}\right) = -\frac{\partial}{\partial y_i}, \quad \varphi\left(\frac{\partial}{\partial y_j}\right) = \frac{\partial}{\partial x_j},$$

$$\varphi\left(\frac{\partial}{\partial z}\right) = 0, \quad 1 \le i,j \le 8.$$

If the linearity of $\varphi$ and $<,>$ is used, one has

$$\varphi^2 = -I + \eta \otimes \xi, \qquad \varphi\xi = 0, \qquad \eta(\xi) = 1,$$
$$< \varphi U, \varphi V >=< U, V > -\eta(U)\eta(V),$$

for every $U, V \in \Gamma(T\tilde{N})$. Hence $(\tilde{N}, \varphi, \xi, \eta, <,>)$ is almost contact metric manifold. At the same time, one can easily illustrate that $(\tilde{N}, \varphi, \xi, \eta, <,>)$ is a cosymplectic manifold of dimension 17. Thus we have

$$\varphi X_1 = -\cos\theta \frac{\partial}{\partial x_3} - \sin\theta \frac{\partial}{\partial x_4} - \cos\theta \frac{\partial}{\partial x_6} - \sin\theta \frac{\partial}{\partial x_7},$$

$$\varphi X_2 = -2u\frac{\partial}{\partial y_3} - 2u\frac{\partial}{\partial y_4} - 2u\frac{\partial}{\partial y_6} - 2u\frac{\partial}{\partial y_7},$$

$$\varphi X_3 = -\frac{\sqrt{3}}{2}\frac{\partial}{\partial y_1} - \frac{1}{2}\frac{\partial}{\partial x_2}, \qquad \varphi X_4 = -\frac{\partial}{\partial y_5},$$

$$\varphi X_5 = -\frac{\partial}{\partial y_8}, \qquad \varphi X_6 = \frac{\partial}{\partial x_8}, \qquad \varphi X_7 = 0.$$

With simple computations, one can obtain $\mathfrak{D} = Span\{X_5, X_6\}$ is an invariant, $\mathfrak{D}_\theta = Span\{X_1, X_2\}$ is a pointwise slant with slant function $-\cos^{-1}(\frac{\sin 2\theta}{\sqrt{2}})$ and

$\mathfrak{D}^{\perp} = Span\{X_3, X_4\}$ is anti-invariant. Thus $f$ defines a proper 7 -dimensional PQHS submanifold in cosymplectic manifold $\widetilde{N}$.

**Example 5.2** For $\theta \in (0, \frac{\pi}{2})$ and $k \in R$ consider a submanifold N of a cosymplectic manifold $\widetilde{N}$ described by immersion $\gamma$ as follows:

$$\gamma(u,v,w,\theta,s,t,q) = (u, w, 0, \frac{s}{\sqrt{2}}, 0, \frac{t}{\sqrt{2}}, 0, v,$$

$$\cos(\theta + k), -\sin(\theta + k), 0, \frac{s}{\sqrt{2}}, 0, \frac{t}{\sqrt{2}}, q).$$

One can obviously observe the fact that the tangent bundle of N is spanned by the tangent vectors

$$Z_1 = \frac{\partial}{\partial x_1}, \qquad Z_2 = \frac{\partial}{\partial y_1}, \qquad Z_3 = \frac{\partial}{\partial x_2},$$

$$Z_4 = \cos(\theta + k)\frac{\partial}{\partial y_2} - \sin(\theta + k)\frac{\partial}{\partial y_3},$$

$$Z_5 = \frac{1}{\sqrt{2}}(\frac{\partial}{\partial x_4} + \frac{\partial}{\partial y_5}), \quad Z_6 = \frac{1}{\sqrt{2}}(\frac{\partial}{\partial x_6} + \frac{\partial}{\partial y_7}),$$

$$Z_7 = \frac{\partial}{\partial z}.$$

One can describe (1,1)-tensor field $\varphi$ as

$$\varphi(\frac{\partial}{\partial x_i}) = \frac{\partial}{\partial y_i}, \quad \varphi(\frac{\partial}{\partial y_j}) = -\frac{\partial}{\partial x_j}, \quad \forall i, j = 1, \ldots, 7.$$

When the linearity of $\varphi$ and $<,>$, one has

$$\varphi^2 = -I + \eta \otimes \xi, \qquad \varphi\xi = 0, \qquad \eta(\xi) = 1,$$

$$< \varphi U, \varphi V > = < U, V > -\eta(U)\eta(V),$$

for every $U, V \in \Gamma(T\widetilde{N})$ . Hence $(\widetilde{N}, \varphi, \xi, \eta, <,>)$ is almost contact metric manifold. At the same time, it can be obviously seen that $(\widetilde{N}, \varphi, \xi, \eta, <,>)$ is a cosymplectic manifold of dimension 15. Thus we have

$$\varphi Z_1 = \frac{\partial}{\partial y_1}, \qquad \varphi Z_2 = -\frac{\partial}{\partial x_1}, \qquad \varphi Z_3 = \frac{\partial}{\partial y_2},$$

$$\varphi Z_4 = -\cos(\theta + k)\frac{\partial}{\partial x_2} + \sin(\theta + k)\frac{\partial}{\partial x_3},$$

$$\varphi Z_5 = \frac{1}{2}(\frac{\partial}{\partial y_4} - \frac{\partial}{\partial x_5}), \quad \varphi Z_6 = \frac{1}{2}(\frac{\partial}{\partial y_6} - \frac{\partial}{\partial x_7}),$$

$$\varphi Z_7 = 0.$$

Now, let the distributions $\mathfrak{D} = Span\{Z_1, Z_2\}$ , $\mathfrak{D}_\theta = Span\{Z_3, Z_4\}$, $\mathfrak{D}^{\perp} = Span\{Z_5, Z_6\}$. Then obviously $\mathfrak{D}$, $\mathfrak{D}_\theta$ and $\mathfrak{D}^{\perp}$ satisfy the definition of pointwise quasi hemi slant of a cosymplectic manifold. Thus $\gamma$ defines a proper 7-dimensional PQHS submanifold of $R^{15}$ with pointwise slant function $(\theta + k)$.

## 6. CONCLUSION

In this paper, we have presented a novel class of submanifolds of cosymplectic manifolds that may be seen as a generalization of quasi hemi-slant, hemi-slant, slant etc. submanifolds. Moreover, conditions for such distributions to be integrable, totally geodesic foliation, totally geodesic and mixed totally geodesic are obtained.

## REFERENCES


[1] Lie S. Geometrie der Berührungstransfor-mationen. B. G. Teubner, Leipzig. 1896.

[2] Blair DE and Goldber SI. Topology of almost contact manifolds. J. Differential Geom. 1967;1:347-354.

[3] Ludden GD. Submanifolds of cosymplectic manifolds. J. Differential Geom. 1970;4:237-244.

[4] Cabras A, Ianus S and Pitis GH. Extrinsic spheres and parallel submanifolds in cosymplectic manifolds. Toyama Math. J. 1994;17:31-53.

[5] Chen BY. Slant immersions. Bull. Aust. Math. Soc. 1990;41(1):135-147.

[6] Cabrerizo JL, Carriazo A, Fernandez LM and Fernandez M. Semi-slant submanifolds of a Sasakian manifold. Geom. Dedicata. 1999;78(2):183-199.

[7] Chen BY. Geometry of slant submanifolds. Katholieke Universiteit Leuven. 1990.

[8] Lotta A. Slant submanifolds in contact geometry. Bull. Math. Soc. Sci. Math. Roumanie. 1996;39:183-198.

[9] Matsumoto K, Mihai I, Tazawa Y. Ricci tensor of slant submanifolds in complex space forms. Kodai Math. J. 2003;26:85-94.

[10] Şahin B. Slant submanifolds of an almost product Riemannian manifold. J. Korean Math. Soc. 2006;43(4):717-732.

[11] Şahin B. Slant submanifolds of quaternion Kaehler manifolds. Commum. Korean Math. Soc. 2007;22(1):123-135.

[12] Şahin B and Keleş S. Slant submanifolds of Kaehler product manifolds. Turkish J. Math. 2007;31(1):65-77

[13] Taştan HM, Şahin B and Yanan Ş. Hemi-slant submanifolds. Mediterr. J. Math. 2016;13(4):2171-2184.

[14] Uddin S, Khan VA, Özel C. Classification of totally umbilical $\xi^{\perp}$ CR-submanifolds of cosymplectic manifolds. Rocky Mountain J. Math. 2015;45(1):361-369.

[15] Akyol MA, Beyendi S, Fatima T and Ali A. Pointwise quasi bi-slant submanifolds. Filomat. 2022;36(19):6687-6697.

[16] Beyendi S, Akyol MA, Stanković MS. Pointwise quasi hemi-slant submanifolds. Filomat. 2023;37(1):127-138.

[17] Carriazo A. New developments in slant submanifolds theory. Narasa Publishing Hause New Delhi, India. 2002.

[18] Chen BY and Uddin S. Warped product pointwise bi-slant submanifolds of Kaehler manifolds. Publ. Math. Debrecen. 2018;92(1-2):183-199.

[19] Etayo F. On quasi-slant submanifolds of an almost Hermitian manifold. Publ. Math. Debrecen. 1998;53:217-223.
[20] Lone MA, Lone MS and Shahid MH. Hemi-slant submanifolds of cosymplectic manifolds. Cogent Math. 2016;3(1):120-143.
[21] Papaghuic N. Semi-slant submanifold of Kaehlerian manifold. An. Ştiint. Univ. A1. I. Cuza. Iaşi. Math. (N.S.). 1994;9:55-61.
[22] Prasad R, Verma SK and Kumar S. Quasi hemi-slant submanifolds of Sasakian manifolds. J. Math. Comput. Sci. 2020;10(2):418-435.
[23] Prasad, R, Singh PK and Rai AK. On quasi hemi-slant submanifolds of nearly Kaehler manifolds. Differ. Geom. Dyn. Syst. 2021;23:188-202.
[24] Prasad R, Verma SK, Kumar S and Chaubey SK. Quasi hemi-slant submanifolds of cosymplectic manifolds. Korean J. Math. 2020;28(2):257-273.
[25] Prasad R, Shukla SS, Haseeb A and Kumar S. Quasi hemi-slant submanifolds of Kaehler manifolds. Honam Math. J. 2020;42(4);795-809.
[26] Prasad R, Akyol MA, Singh PK, Kumar S. On quasi bi-slant submersions from Kenmotsu manifolds onto any Riemannian manifolds. Journal of Mathematical Extension. 2022;16(6):1-25.
[27] Siddesha MS, Praveena MM and Bagewadi CS. On quasi hemi-slant submanifolds of LP-cosymplectic manifolds. Math., Anal., Appl. 2021;3(3):39-49.
[28] Şahin B. Non-existence of warped product semi-slant submanifolds of Kaehler manifolds. Geom. Dedicata. 2006;117:195-202.
[29] Uddin S, Chen BY and Al-Solamy FR. Warped product bi-slant immersions in Kaehler manifolds. Mediterr. J. Math. 2017;14(2):1-10.
[30] Şahin B. Warped product pointwise semi-slant submanifolds of Kaehler manifolds. Port. Math. 2013;70(3):252-268.
[31] Park KS. Pointwise slant and pointwise semi-slant submanifolds in almost contact metric manifolds. Mathematics. 2020;8(6):1-33.
[32] Park KS. On the pointwise slant submanifolds. In Hermitian-Grassmannian Submanifolds. Suh, Y., Ohnita, Y., Zhou, J., Kim, B., Lee, H., Eds.; Springer Proceedings in Mathematics and Statistics. 203; Springer: Singapore. 2017.
[33] Akyol MA and Beyendi S. A note on quasi bi-slant submanifolds of cosymplectic manifolds. Commun. Fac. Sci. Univ. Ank. Ser. A1 Math. Stat. 2020;69(2):1508-1521.
[34] Perktaş SY, Blaga AM and Kılıç E. Almost bi-slant submanifolds of an almost contact metric manifold. J. Geom. 2021;112(2):1-23.
[35] Blair DE. Contact manifolds in Riemannian geometry. Lecture Notes in Mathematic. Vol: 509, Springer-Verlag, Berlin. 1976.
[36] Akyol MA. Conformal anti-invariant submersions from cosymplectic manifolds. Hacet. J. Math. Stat. 2017;46:177–192.
[37] Blair DE. The theory of quasi-Sasakian structure. J. Differential Geom. 1. 1967;3(4):331-345.
[38] Chen BY and Garay OJ. Pointwise slant submanifolds in almost Hermitian manifolds. Turkish J. Math. 2012;36(4):630-640.

Cilt 12, Sayı 1, Sayfa 117-124, 2023 Volume 12, Issue 1, Page 117-124, 2023

Araştırma Makalesi https://doi.org/10.46810/tdfd.1242764 Research Article

Türk Doğa ve Fen Dergisi
Turkish Journal of Nature and Science
www.dergipark.gov.tr/tdfd

# Purification and Charcterızatıon Glutathione S-Transferase from Chicken Liver

**Hakan YILMAZ[1], Mehmet ÇİFTCİ[*2], Yusuf TEMEL[3]**

[1]Kimya Bölümü / Fen Bilimleri Enstitüsü, Bingöl Üniversitesi, Türkiye
[2]Temel Bilimler Bölümü / Veteriner Fakültesi, Bingöl Üniversitesi, Türkiye
[3]Tıbbi Hizmetler ve Teknikler Bölümü/ Solhan Sağlık Hizmetleri MYO, Bingöl Üniversitesi, Türkiye
Hakan YILMAZ ORCID No: 0000-0003-3518-1473
Mehmet ÇİFTCİ ORCID No: 0000-0002-1748-3729
Yusuf TEMEL ORCID No: 0000-0001-8148-3718

**Corresponding author: mciftci@bingol.edu.tr*

(Received: 26.01.2023, Accepted: 05.03.2023, Online Publication: 27.03.2023)

**Keywords**
Glutathione S-transferase, Chicken liver, Purification

**Abstract:** In this study, the glutathione S-transferase enzyme (GST; EC 2.5.1.18) was purified with 8.35 EU/mL specific activity, 24.56 times 8% yield, from chicken liver, using ammonium sulfate precipitation and glutathione-agarose affinity chromatography. In order to control the purity of the enzyme, SDS-PAGE was performed and a single band was obtained. The molecular mass of the subunit was calculated as approximately 30.9 kDa. In addition, the optimum pH value of the enzyme (8.5 in Tris-HCl); optimum ionic strength (150 mM with Tris-HCl); optimum temperature (70 °C); stable pH value (8.5 with Tris-HCl) was determined. The $K_M$ value for the GSH substrate of the enzyme was 0.802 mM, the Vmax value was 1.833 EU/mL; For CDNB, the $K_M$ value was calculated as 3.6 mM and the Vmax value was calculated as 2.829 EU/mL.



# Tavuk Ciğerinden Glutatyon S-Transferazın Saflaştırılması ve Karakterizasyonu

**Anahtar Kelimeler**
Glutatyon S-transferaz, Tavuk karaciğeri, Saflaştırma

**Öz:** Bu çalışmada glutatyon S-transferaz enzimi (GST; EC 2.5.1.18) tavuk karaciğerinden amonyum sülfat çöktürmesi ve glutatyon-agaroz afinite kromatografisinden yararlanılarak 8,35 EÜ/mL spesifik aktivitesine sahip olan enzim, %8 verimle 24,56 kat saflaştırıldı. Saflaştırılan enzimin saflığının kontrol edilmesi maksadıyla SDS-PAGE işlemi yapıldı ve tek bant elde edildi. Alt birimin molekül kütlesi yaklaşık olarak 30,9 kDa olarak hesaplandı. Ayrıca enzimin optimum pH değeri (Tris-HCl içinde 8,5), optimum iyonik şiddeti (Tris-HCl ile 150 mM), optimum sıcaklığı (70 °C), stabil pH değeri (Tris-HCl ile 8,5) tespit edildi. Enzimin GSH substratı için $K_M$ değeri 0,802 mM, Vmax değeri 1,833 EÜ/mL; CDNB için de $K_M$ değeri 3,6 mM ve Vmax değeri 2,829 EÜ/mL olarak hesaplandı.

## 1. INTRODUCTION

Enzymes are indispensable macroproteins for the metabolic activities of living things. Many enzymes play important roles alone or with their derivatives in animal, plant and human cells [1-3]. One of these is the glutathione S-transferase (GST) (EC.2.5.1.18) enzyme, which provides the internal balance of the body by catalyzing the first step of mercapturic acid, which is the end product of the detoxification systems developed by the body against the environmental, chemical and radioactive effects that the body is exposed to. In the detoxification system, which consists of three phases in total, the glutathione s transferase enzyme appears in the Phase II phase produced by conjugation reactions [1-6]. The first place where the glutathione S-transferase enzyme, which has a weight of about 27 kDa and consists of subunits of 229 amino acids, was purified by Boyland et al., form rat liver [7].

GST enzyme group is named as microsomal, cytosolic and mitochondrial according to their positions, mostly cytosolic in the cell [4]. The fact that this enzyme does not lose its activity for a long time under certain conditions, contains a large number of isoenzymes and has parts that bind water and substrates has made it included in many research topics. These properties allow reduced glutathione to be conjugated with many different

compounds and to catalyze substrates with different structures [4,8].

GST enzyme can only be activated by the presence of reduced glutathione. GST, which is selective about the substrate, shows partial specificity with this behavior. Apart from providing homeostasis in the body's defense, the GST enzyme plays a preventive role by preventing the microparticles in the body from combining with the toxic structures entering the body and posing a threat [7,9,10]. Enzymes are made of proteins, and their components are made up of amino acids. The type of amino acids found in enzymes is very important according to the enzyme's function. Although the GST enzyme does not contain the same amino acids in every living thing, the most similar component type is found in humans and rats. The amino acids found in common in human and rat GST enzymes are aspartic acid, glutamic acid, and leucine. Tryptophan and cysteine amino acids are only found in trace amounts in rats, unlike humans [10,11].

In this study, it was aimed to purify and characterize the GST enzyme from chicken liver tissue for the first time.

## 2. MATERIAL AND METHOD

### 2.1. Chemicals

Reduced Glutathione (GSH), 1-chloro 2,4 dinitrobenzene (CDNB), Sephadex G-150, acrylamide, coomassie brilliant blue G-250, bromine thymol blue, sodium dodecyl sulfate (SDS), ammonium persulfate, beta-mercaptoethanol used in our study, standard bovine serum albumin, N,N,N',N'-tetramethyl ethylenediamine (TEMED), glutathione agarose, glutathione acetate, glycine, glycerine, potassium bisphosphate, potassium phosphate, trihydroxymethylaminomethane (Tris), NaOH, NaCl, HCl, $H_3PO_4$, $C_2H_5OH$, $CH_3OH$, $CH_3COOH$, $NaCH_3COO$, isopropanol were obtained from Sigma Chemical Comp.

### 2.2. Preparation of Homogenate

Chicken livers used during the experiment were obtained fresh from Bingöl Meat and Milk Institution according to cold chain rules. Tissues brought to the laboratory were cut into small pieces and 10 grams of tissue was taken and powdered with liquid nitrogen in a mortar. The pulverized tissue was suspended in 10 mL of 50 mM Tris-HCl (pH: 7.5) buffer. The resulting suspension was then centrifuged at 13.000 rpm for one hour to precipitate tissue and cell particles. The supernatant was carefully taken with a dropper and used in the study, and these processes were carried out at +4°C [12].

### 2.3. Ammonium Sulphate Precipitation and Dialysis

Ammonium sulfate precipitation was made in the ranges of 0-20%, 20-40%, 40-60%, 60-80%, 80-100% in the homogenate obtained, and the interval at which the enzyme precipitated was determined. Centrifugation was carried out at 10.000 rpm for 20 minutes at each stage. The activity of the supernatant and precipitate was measured each time. Then, the thin transparent cylindrical dialysis bag was opened, knotted from the bottom, and poured into the mixture obtained as a result of precipitation, and another knot was tied in such a way that there was no air on it. Dialysis was performed against dialysis buffer (10 mM K-Phosphate, 1 mM EDTA and pH 7.5) for about 2 hours by changing the water on the magnetic stirrer every hour and the temperature was kept at +4ºC during the procedures.

### 2.4. Purification of Glutathione S-Transferase

Affinity chromatography technique, which is one of the most popular and efficient methods among enzyme purification techniques, was preferred for this study and enzyme purification was performed from affinity chromatography using the glutathione-agarose. First, 1 g of dry glutathione-agarose solid was weighed and washed with 200 mL of water, and the small solid particles were removed. After washing, the gel was swelled and the gel was suspended by adding buffer solution (0.05 M K-phosphate, pH: 7.4, 1 mM EDTA and 1 mM DTT), which functions as balancing, packaging and washing. The glutathione agarose affinity column was adjusted to correspond to a flow rate of 60 mL per hour by means of a peristaltic pump. Against the risk of cracking the column, the buffer was added up to 1-2 cm above the gel. First, the column was regenerated with 0.5 M NaCl and 0.1 boric acid (pH: 8.5) and 0.1 M sodium acetate and 0.5 M NaCl (pH: 4.5) buffers, and 10 mM $KH_2PO_4$ and 150 mM equilibrated with NaCl (pH:7.4) buffer. Then, ammonium sulfate and enzyme sample obtained after dialysis processes were applied and washing was performed with 0.05 M K-phosphate, pH: 7.4, 1 mM EDTA and 1 mM DTT buffer. After washing, the enzyme sample was eluted with 50 mM Tris-HCl buffer (pH: 9.5) containing 2.5 mM, 5 mM and 10 mM GSH solution into three mL tubes [13,14].

### 2.5. Measuring Enzyme Activity

Activity measurement of GST enzyme was measured spectrophotometrically according to the method of Habig et al. This method is based on the absorbance of dinitrobenzene 5-glutathione at 340 nm, which is formed in the reaction catalyzed by the GST enzyme [15].

### 2.6. Protein Determination

#### 2.6.1. Qualitative Protein Determination

The qualitative determination of proteins is based on the principle that tyrosine and tryptophan amino acids, which are the amino acids present in the structure of proteins, show a maximum absorbance value at 280 nm [16].

#### 2.6.2. Quantitative Protein Determination

The amount of protein (quantitative) at all stages throughout the study was made using the Bradford method. This method works on the basis that Coommassie Brilliant Blue G-250 reagent rapidly binds to protein and shows maximum absorbance at 595 nm. [17].

### 2.7. Control of GST Enzyme Purity via SDS-PAGE

The purity of the GST enzyme was checked by batch SDS-Polyacrylamide Gel Electrophoresis (SDS-PAGE) with a range of 3-8% using the technique proposed by Laemmli [18].

### 2.8. Characterization Studies

#### 2.8.1. Determination of Optimum pH

In order to determine the optimum pH of the glutathione S-transferase enzyme obtained from chicken liver, the pH values from potassium phosphate buffer were 5.5, 6.0, 6.5, 7.0, 7.5 and 8.0; Tris-HCl buffer solutions were prepared at pH ranges of 7.5, 8.0, 8.5, and 9.0. The activity of the enzyme was calculated with each of these buffers separately. pH-activity graphs were drawn in order to determine the optimum pH.

#### 2.8.2. Stable pH Determination

In order to determine the pH value at which the enzyme exhibits optimal stability; $KH_2PO_4$ with pH values of 5.5, 6.0, 6.5, 7.0, 7.5 and 8.0 and 7.5, 8.0, 8.5 and 9 prepared. Activity measurements were made with these prepared buffers every 24 hours for 3 days. As a result of the activity measurements, graphs were drawn to determine the stable pH of the enzyme.

#### 2.8.3. Determination of Optimum Ionic Strength

In order to determine the optimum ionic strength of the enzyme, activity measurements were made with 50, 100, 150, 160, 170, 200 and 250 mM Tris-HCl solutions.

#### 2.8.4. Determination of Optimum Temperature

In order to determine the optimum temperature value of the enzyme, an activity measurement was carried out at every 10ºC between 0ºC and 90ºC using optimum pH, optimum ionic strength and the mentioned buffer.

#### 2.8.5. Kinetic Studies

First of all, 1/V-1/[S] graph was drawn by measuring the activities at the fixed concentration of GSH and 5 different suitable concentrations of CDNB, and $K_M$ and $V_{max}$ values for CDNB were calculated from these graphs. Then, the same procedures were performed for the fixed concentration of CDNB and the GSH substrate at 5 different appropriate concentrations of GSH [19].

## 3. RESULTS

A standard graph was prepared for the determination of protein amounts in homogenate, ammonium sulfate precipitate and purified enzyme solution and shown in Figure 1.

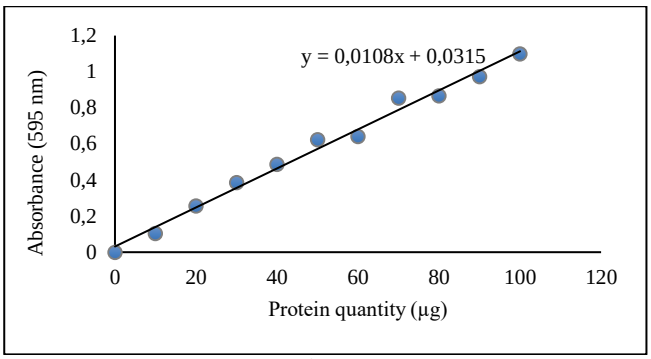


**Figure 1.** Standard graph obtained for quantitative protein determination

The ammonium sulfate precipitation procedure was performed as described in the Materials and Methods section, and the results are shown in Table 2.

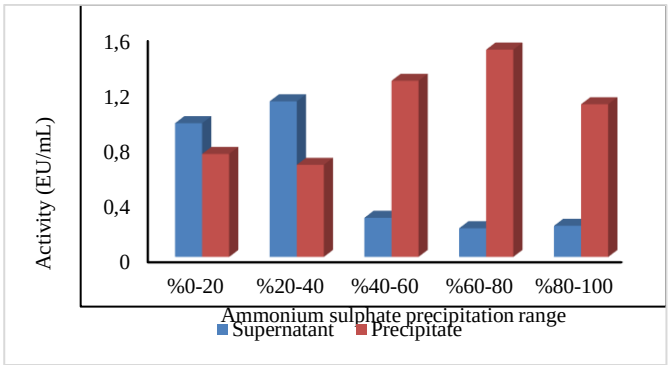


**Figure 2.** Ammonium sulfate precipitation interval graph

Purification of the enzyme was performed as described in the Materials and Methods section, and the specific activity, yield%, activity, total activity, protein, total protein and purification coefficient values were calculated and indicated in Table 1. As seen in the Table 1, 8.35 EU/mg GST enzyme with protein specific activity was purified with 24.56 fold and 8% yield.

**Table 1.** Purification results of glutathione S-transferase enzyme

| Steps | Total Volume (mL) | Activity (EU/mL) | Total Activity (EU/mL) | Protein (mg/mL) | Total Protein (mg) | Specific Activity | Yield % | Purification Coficient |
|---|---|---|---|---|---|---|---|---|
| Homogenate | 20 | 1,633 | 32,66 | 4,809 | 96,18 | 0,340 | 100 | 1 |
| Ammonium Sulfate Precipitation (40-100%) | 8 | 2,470 | 19,76 | 5,735 | 45,88 | 0,430 | 60 | 1,26 |
| Affinity Chromatography | 6 | 0,440 | 2,640 | 0,052 | 0,316 | 8,350 | 8 | 24,56 |

As mentioned in the Materials and Methods section, the activity values of the eluates after performing the gradient elution process are shown in Figure 3.

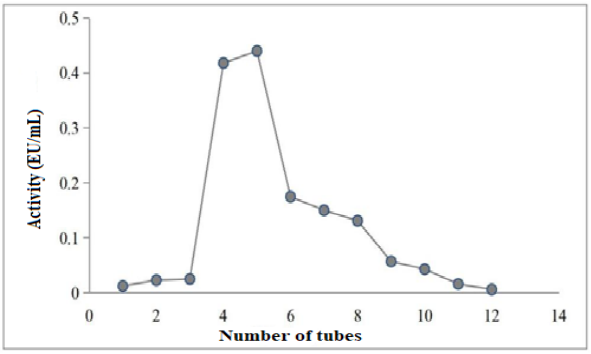


**Figure 3.** Elution graph obtained in the purification process

SDS-PAGE was performed as described in the Materials and Methods section, and its photograph was taken and shown in Figure 4. In addition, using the SDS-PAGE photograph in Figure 4, the $R_f$-Log MK graph was drawn to determine the molecular mass of the subunit of the enzyme and shown in Figure 5.

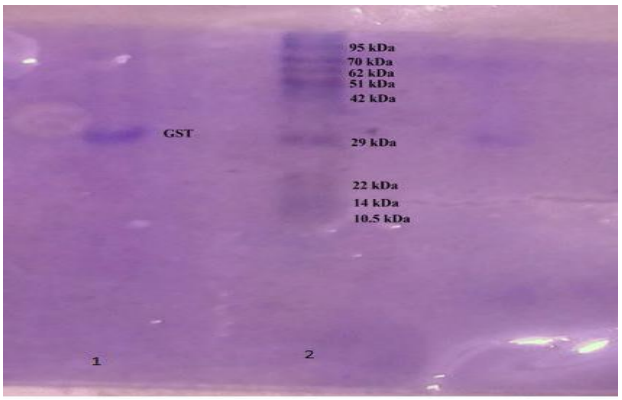


**Figure 4.** SDS-PAGE photograph. well 1 pure enzyme, 2 well standard proteins

As described in the materials and methods section, optimum pH determination studies were performed and is shown in Figure 5.

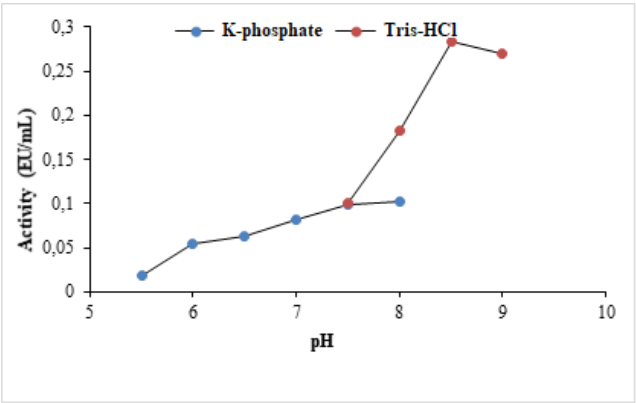


**Figure 5.** pH-activity plot using Tris HCl and K-Phosphate buffers

Stable pH studies with K-phosphate and Tris-HCl buffers as described in the materials and methods section are shown in Figure 6 and Figure 7.

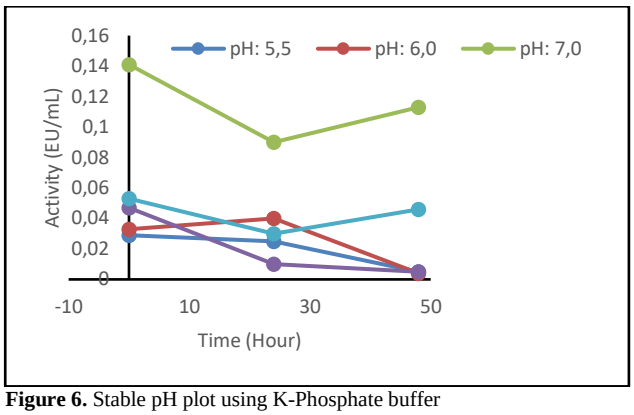


**Figure 6.** Stable pH plot using K-Phosphate buffer

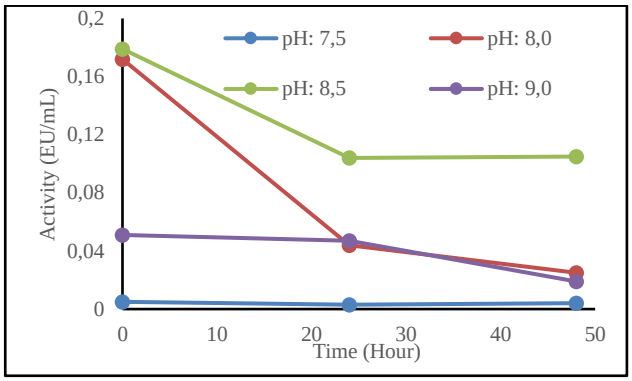


**Figure 7.** Stable pH plot using Tris-HCl buffer

Optimum ionic strength studies were performed as described in the Materials and Methods section, and the results were shown in Figure 8.

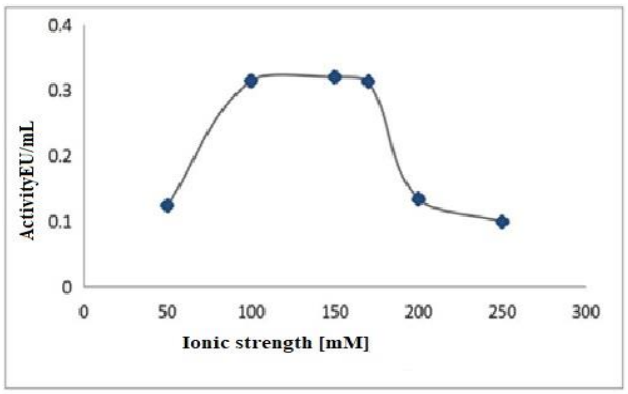


**Figure 8.** Optimum ionic strength graph

Optimum temperature studies are performed as described in the Materials and Methods section, and the results are shown in Figure 10.

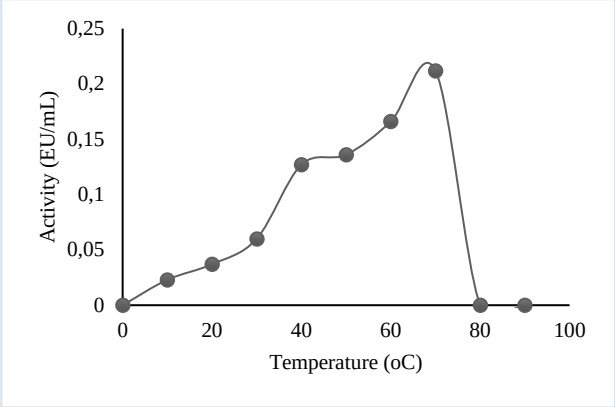


**Figure 9.** Optimum temperature graph

As described in the Materials and Methods section, 1/V-1/[S] graphs were drawn to calculate the $K_M$ and Vmax values for CDNB and GSH, which are the substrates of the enzyme, and are shown in Figure 10 and Figure 11.

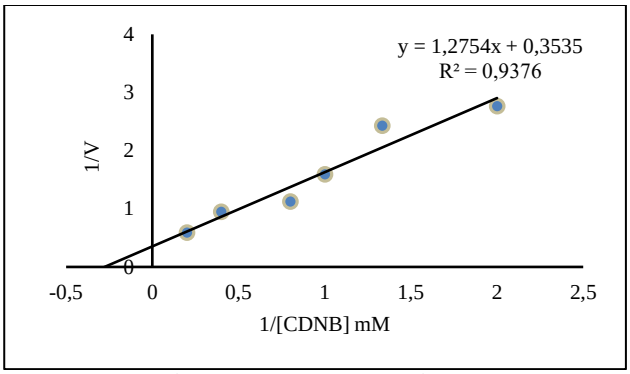


**Figure 10.** Graph of 1/V to 1/[CDNB] obtained for CDNB substrate

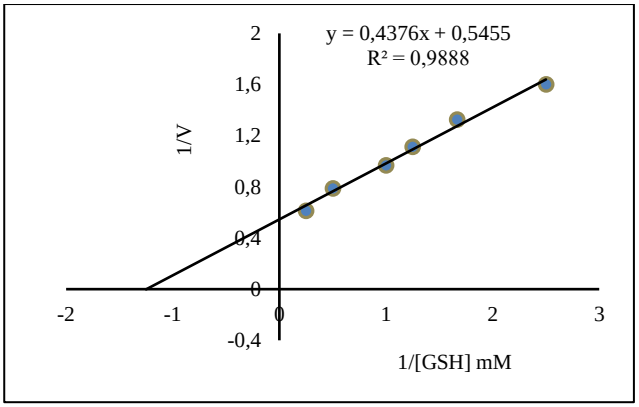


**Figure 11.** Graph of 1/V-1/[GSH] obtained for the GSH substrate

## 4. DISCUSSION AND CONCLUSION

Glutathione S-Transferase enzymes especially act as phase-II detoxification enzymes. Although they generally perform their functions in the cytosol, they also have functions such as conjugation of electrophilic substrates to glutathione. Cytosolic mammalian GST enzymes have been characterized and classified as α, μ, π, and θ. A few new classifications have also been made in non-mammalian organisms. Living organisms are exposed to many chemicals, xenobiotics, toxic and carcinogenic substances during feeding. In the last century, this threat has increased due to the chemicals thrown into the environment. Against all these threats, systems created in living things automatically activate and eliminate harmful substances. If the threats are not eliminated, serious problems arise. One of the most important substances used for the elimination of xenobiotics involved in metabolism is the GSH molecule. GSH provides conversion by making conjugate with the substances in question under the catalysis of GST enzymes. This results in a reduction of hydroperoxides. In addition to their catalytic properties, GST enzymes are enzymes with broad ligand binding properties [20-25].

Considering the above-mentioned features of the GST enzyme, it seems to be a very important metabolic enzyme. Therefore, within the scope of this study, the GST enzyme was purified from chicken liver and characterized.

Measuring the amount of protein in the samples during the purification studies is very important for the study. Protein determination was performed according to the Bradford method. The sensitivity of this method is high and it is less affected by the disturbing factors in the environment [17].

As can be seen from Figure 2, it is seen that the majority of the protein to be purified does not precipitate in the precipitation process between 0-20% and 20-40%. While the amount of enzyme precipitated increases in the range of 40-60%, it seems that the amount of precipitation reaches a maximum in the range of 60-80%. These ranges were evaluated and the precipitation range was accepted as 40-80%. This precipitation range was found to be 20-80% in quail liver and in some studies, ammonium sulfate precipitation was not performed [21,22].

In the literature, it is seen that the GST enzyme is purified from many living tissues by using some chromatographic methods. For example, the GST enzyme was purified using DEAE-cellulose anion exchange chromatography [26], CM-cellulose G-75 affinity chromatography [27], in another study using DEAE-cephagel and glutathione agarose affinity column [28]. In this study, glutathione-agarose affinity chromatography was used in terms of short purification time, high yield and low consumption of chemicals. As it can be seen from Table 1, GST enzyme with 8.35 EU/mg protein specific activity was purified from chicken liver with 8% yield as 24.56 fold in our study. With a similar method, the enzyme (with a specific activity of 11344,83 EU/mg.protein) was purified 1543.5 times from the gills of Lake Van pearl mullet with a yield of 82.25% [21]. In another study with quail liver, the GST enzyme with 15.86 EU/mg.protein specific activity was purified 46.1-fold with a yield of 12.36% [2]. While the specific activity, % yield and purification coefficient obtained in our study are lower than Zaric's study, they are similar to Taysi's study results [21,22].

Looking at Figure 3, it is seen that the enzyme is eluted from the 3rd tube. In the 3rd tube, there is no significant activity and the enzyme activity is the highest in 4.5.6.7.

and 8 tubes. Therefore, in kinetic studies 4.5.6.7. and 8th tubes were combined and used.

As seen in Figure 4, the presence of a single band in the first well of the SDS-PAGE photograph obtained after the SDS-PAGE process shows that the enzyme was obtained pure. In addition, the molecular mass of the enzyme, obtained under denaturing conditions, was found to be 30.9 kDa, with the help of the graphic obtained by using this photograph and shown in Figure 5. In the literature, this value was 25.1 kDa for quail liver [22], 22.5 kDa for *E.coli* GST enzyme [28], 26 kDa for rat liver GST enzyme [29], 23 kDa for GST enzyme for mullet liver [30], 22.3 kDa for human liver GST enzyme [31], and 27 kDa [32] for bovine brain GST enzyme, 25.2 kDa for rat erythrocyte GST enzyme [41] . It is seen that the molecular mass found in this study is close to the values found in the literature.

As seen in Figure 6, Tris-HCl with pH 7.5 8.0, 8.5 and 9.0 and pH 5.5, 6.0, 6.5, 7.0, 7.5 A graph was obtained by measuring enzyme activities in K-phosphate buffers of pH 8.0. As seen from the graph, the highest activity was obtained in Tris-HCl buffer at pH= 8.5. Therefore, the optimum pH was accepted as 8.5 in Tris-HCl buffer. Similar results were obtained in quail liver (pH= 8.5, Tris-HCl) [22], for E. coli (pH= 7.0) [28], in albus fish liver pH= 7.0-7.5 [33], in human blood serum (pH= 5.5) [34], in Lake Van fish (pH= 7.3) [21].

As can be seen from Figures 7 and 8, it is seen that the maximum activity for the enzyme in stable pH studies with K-phosphate and Tris-HCl buffers is obtained at pH= 8.5 in Tris-HCl buffer, which is the best maintained pH for 48 hours. Therefore, the pH value of the enzyme was accepted as 8.5. Similar results were found for gill GST enzyme of Lake Van fish [21], 8.5 [22] for quail liver, 8.0 [35] for rainbow trout liver.
As can be seen from Figure 9, when the activity measurements measured with various concentrations of Tris-HCl buffer are examined, it is seen that the highest activity is 150 mM. Therefore, the optimum ionic strength was accepted as 150 mM. In the literature review, this value was found to be 1400 mM [22] in quail liver and 120 mM [21] in Lake Van fish. The result we found is close to the optimum ionic strength value for Lake Van fish.

In order to find the optimum temperature, the enzyme activity was measured every 10ºC in the 0-90°C temperature range and shown in Figure 9. As seen in Figure 10, the highest activity was obtained as 70°C. Therefore, the optimum temperature was accepted as 70ºC. In the literature researches; It was found as 35 °C [21] in Lake Van fish, 35ºC [33] in albus fish, 30°C [36] in rainbow trout erythrocytes, 55 °C [22] in quail liver, 50ºC [28] for *E. coli*, 65°C [34] in human blood serum. As can be seen from these results, the temperature we found has a higher value than all those found in the literature. Since this situation is related to the amino acid sequence and the environment, it is normal for it to vary from living thing to living thing and from tissue to tissue.

It is extremely important to find the $K_M$ and $V_{max}$ values for an enzyme's substrates. As seen in Figures 10 and 11, Linaweaver-Burk graphs were drawn at 5 different substrate concentrations for the enzyme's substrates CDNB and GSH, and $K_M$ and $V_{max}$ values were found for each substrate with the help of these graphs. The $K_M$ constants obtained for CDNB and GSH were 3.6 and 0.802 mM, respectively, and the $V_{max}$ values were 2.829 and 1.833 EU/mL, respectively. According to these results, it can be said that the GSH substrate, which has a lower $K_M$ constant, has a greater interest in the enzyme than the CDNB substrate. In the literature review, $K_M$ values for quail liver in GSH and CDNB substrates were 0.114 and 0.672 mM, respectively; The $V_{max}$ value was also 0.048 and 0.047 EU/mL [22], the $K_M$ values for albus fish liver were 0.35 and 0.42 mM [37], respectively, the $K_M$ values for GSH and CDNB for human blood serum were 4.11 and 2, respectively. 8 mM [34], $K_M$ constants 0.59 and 1.057 mM [21] for Lake Van fish gill, $K_M$ values 0.5 and 0.42 mM [37] for tilapia fish gill, 0.0395 for rainbow trout erythrocytes, respectively and 0.259 mM [36]. When our results were compared with the literature, it was seen that generally similar results were obtained.

**Acknowledgement**

This study was supported by Bingöl University BAP Coordination Unit. Bingöl University Projects Coordination Unit (Project number: BAP-FEF-2022.001).

**REFERENCES**



[1] Temel Y, Ayna A, Hamdi Shafeeq I, Ciftci M. In vitro effects of some antibiotics on glucose-6-phosphate dehydrogenase from rat (Rattus norvegicus) erythrocyte. Drug Chem. Toxicol. 2020; 43(2): 219-223.
[2] Bayindir S, Ayna A, Temel Y, Ciftci M. The synthesis of new oxindoles as analogs of natural product 3, 3′-bis (indolyl) oxindole and in vitro evaluation of the enzyme activity of G6PD and 6PGD. Turk. J. Chem. 2018;42(2): 332-345.
[3] Bayindir S, Temel Y, Ayna A, Ciftci M. The synthesis of N-benzoylindoles as inhibitors of rat erythrocyte glucose-6-phosphate dehydrogenase and 6-phosphogluconate dehydrogenase. J. Biochem. Mol. Toxicol. 2018;32(9): e22193.
[4] Autrup H. Genetic polymorphism in human xenobiotica matebolizing enzymes as susceptibility factors in toxic response. Mutat. Res. 2000;464: 65-76.
[5] Lee WM. Drug-induced hepatotoxicity. N Engl J Med. 2003;349:474-485.
[6] Sheehan D, Meade G, Foley VM, Dowd CA. Structure, function and evolution of glutathione transferases: implications for classification of nonmammalianmembers of an ancient enzyme superfamily. Biochem J. 2001;360:1-16.
[7] Özaslan MS, Demir Y, Küfrevioğlu O I, Çiftci M. Some metals inhibit the glutathione S-transferase from Va Lake fish gills. J Biochem Mol Toxicol. 2017;73:e21967.

[8] Espinoza HM, CR Williams and EP Gallagher. Effect of cadmium on glutathione S-transferase and metallothionein gene expression in Coho Salmon liver, gill and olfactory tissues. Aquat Toxicol. 2012;110: 37-44.
[9] Aksoy AS. Bazı flavonoidlerin sığır karaciğer glutatyon stransferaz enzimi üzerine etkilerinin araştırılması. (Yüksek Lisans Tezi), Balıkesir Üniversitesi Fen Bilimleri Enstitüsü Kimya Anabilim Dalı, Balıkesir; 2018.
[10] Hayes JD, Flanagan JU, Jowsey IR. Glutathione transferases. Annu. Rev. Pharmacol Toxicol. 2005;45: 51-88.
[11] Cnubben NHP, Rietjens IMCM, Wortelboer H, van Zanden J, van Bladeren J. The interplay of glutathione-related processes in antioxidant defense. Environ Toxicol Pharmacol. 2001;10:141-152.
[12] Armstrong RN. Structure, catalytic mechanism, and evolution of the glutathione transferases. Chem Res Toxicol. 1997;10(1):2-18.
[13] Baş O. Dinitrocresol'ün (Rat rattus norvegicus) Sıçan glutatyon S-transferaz enzim aktivitesine etkisi (Yüksek Lisans Tezi) Uludağ Üniversitesi Fen Bilimleri Enstitüsü, Bursa; 2006.
[14] Fleischner GK, Kamisaka IM, Arias IM. Immunoloanalysis of rats and human ligandins. Glutathione: Metabolism and Function, 1976; 229-235.
[15] Toribio F, Martinez-Lara E, Pascual P, Lopez-Barea J. Methods for purification of glutathione peroxidase and related enzymes. J Chromatogr B. 1996;684:77-97.
[16] Güvercin S, Erat M, Şakiroğlu H. Determination of some kinetic and characteristic properties of glutathione s-transferase from bovine erythrocytes. Protein Pept. Lett. 2008;15(1): 6-12.
[17] Laemmli DK, Lajmanovich RC, Andre´s M, Attademo AM, Peltzer PM, Junges CM. Cleavage of structural proteins during in assembly of the head of bacteriophage T4. Nature, 1970; 277, 680-685.
[18] Ahmed B. M, Temel Y, Çiftçi M. Purification and characterization glutathione S transferase enzyme from quail (Coturnix, coturnix japonica) heart and investigation the effect of some metal ions on enzyme activity. C S J. 2019;40(4):802-812.
[19] Bradford MM. A rapid and sensitive method for the quantitation of microgram quantities of protein utilizing the principle of protein-dye binding. Anal. Biochem. 1976;72:248-251.
[20] Habig WH, Pabst MJ, Jakoby WB. Glutathione S-transferases. The first enzymmatic step in mercapturic acid formation. J Biol Chem.1974;246:7130-7139.
[21] Lineweaver H, and Burk D. The determination of enzyme dissociation constants. J Am Chem Soc. 1934;56 (3):658-666.
[22] Awasthi YC, Dao DD, Saneto RP. Interrelationship between anionic and cationic forms of glutathione S-transferases ofhuman liver. Biochem J. 1980;191:1-10.
[23] Nelson DL and Cox MM. Lehninger Principles of Biochemistry, Fourth edition. W.H. Freeman and Company, New York; 2004.
[24] Zariç Y. Glutatyon S-Transferaz Enziminin Van Gölü İnci Kefali Balığı *(chalcalburnus Tarichi )*Solungacından Saflaştırılması, Karakterizasyonu, Bazı Metal Ve Pestisitlerin Enzim Aktivitesi Üzerine Etkilerinin İncelenmesi. (Yüksek Lisans Tezi), Ağrı İbrahim Çeçen Üniversitesi Fen Bilimleri Enstitüsü, Ağrı; 2018.
[25] Taysi MŞ, Temel Y. Glutathione S-transferase: Purification and characterization from quail (Coturnix coturnix japonica) liver and the impact of some metal ions on enzyme activity. Bionanoscience. 2021;11: 91-98.
[26] Gözükara ME. Biyokimya, Nobel Matbaacılık, İstanbul; 2011.
[27] Keha E, Küfrevioglu Öİ. Biyokimya, Aktif Yayınevi, Erzurum; 2009.
[28] Dawn B, Marks Allan D, Mark, Colleen M, Smith. Basic Medical Biochemistry a clinical approach. A Wawely Company; 1996.
[29] Loscalzo J, Freedman J. Purification and characterization of human platelet glutathione-S transferase. Blood, 1986; 67, 1595-1599.
[30] Arca P, Garcida P, Hardisson C, Suarez JE. Purification and study of a bacteril glutathione S-transferase Area de Microbiologia, Fac. med.1990;1:77-79.
[31] Iizuka M, Inoue Y, Murata K, Kimura A Purification and some properties of glutathione S-transferase from escherichia coli B. J Bacteriol Res. 1989;6039-6042.
[32] Hiratsuka A, Sebata N, Kawashima K, Okuda H, Ogura K, Watabe T, Satoh K, Hatayama I, Tsuchida S, Ann Ishikawa TA. New class of rat glutathione Stransferase Yrs-Yrs inactivating reactive sulfate esters as metabolites of carcinogenic arylmethanols. J B C. 1990;265(20):11973-11981.
[33] Barcena JAE, Martinez-Lara SG, George J, Lopez-Barea. Purification and characterization of multiple glutathione s transferase isoenzymes from grey mullet liver. CMLS. 1997;759-768.
[34] Novoa-Valinas MC, Perez-Lopez M, Melgar MJ. Compparative study of the prufication and characterization of the cytosolic glutathione S-transferase from two salmonid species: Atlantic salmon (Salmo solar) and Brown trout (Salmo Trutta). C B P. part C, 2002;131:207-213.
[35] Young PR, and Briedis AV. Purification and kinetic mechanism of the major glutathione S-transferase from bovine brain. Biochem J. 1989;257:541-548.
[36] Huang Q, Liang L, Wei T, Zhang D, Zeng QY. Purification and partial characterization of glutathione transferase from the teleost monopterus albus. C B P Part C. 2008;147:96-100.
[37] Türkanoğlu A. Human serum arylesterase and glutathione S-transferase activities in patients with ischemic stroke compared to healthy controls. Approval of the Thesis Master of Science in Biochemistry Department, Middle East Technical University, Ankara; 2007.

[38] Tekman B, Ozdemir H, Senturk M, Ciftci M. Purification and characterization of glutathione reductase from rainbow trout (Oncorhynchus mykiss) liver and inhibition effects of metal ions on enzyme activity. C B P Part C. 2008;148:117-121.
[39] Çomaklı V, Çiftçi M, Küfrevioğlu Öİ. Gökkuşağı alabalık eritrositlerinden glutatyon S-transferas enziminin saflaştırılması ve bazı antibiyotiklerin enzim aktivitesi üzerine etkilerinin incelenmesi. Hacettepe J Biol Chem. 2011; 39 (4): 413-419.
[40] Hamed RR, Maharem TM and Guinidi RAM. Glutathione and its related enzymes in the nile fish. Fish Physiol Biochem. 2004;30 (3-4): 189-199.
[41] Ayna A, Khosnaw L, Temel Y, Ciftci M. Antibiotics as inhibitor of glutathione S-transferase: biological evaluation and molecular structure studies. Curr Drug Metab. 2021; 22(4):308-314.

Cilt 12, Sayı 1, Sayfa 125-135, 2023 Volume 12, Issue 1, Page 125-135, 2023

Araştırma Makalesi https://doi.org/10.46810/tdfd.1244940 Research Article

Türk Doğa ve Fen Dergisi
Turkish Journal of Nature and Science
www.dergipark.gov.tr/tdfd

# Evaluation of the Effects of Ribavirin and Proanthocyanidin on the Clinical Outcome, Hematological and Biochemical Parameters, and Viral Shedding in Canine Distemper

**Şükrü DEĞİRMENÇAY[1*]**

[1] Atatürk University, Faculty of Veterinary Medicine, Department of Internal Medicine, Erzurum, Türkiye
Şükrü DEĞİRMENÇAY ORCID No: 0000-0002-3920-6343

**Corresponding author: s.degirmencay@atauni.edu.tr*

(Received: 30.01.2023, Accepted: 06.03.2023, Online Publication: 27.03.2023)

**Keywords**
Antiviral agents, Canine distemper virus, Proanthocyanidins, Ribavirin

**Abstract:** This study investigated the effects of ribavirin, proanthocyanidin, and ribavirin-proanthocyanidin in dogs naturally infected with canine distemper virus (CDV). Five groups were created, each with six dogs aged 2-6 months: one healthy control group and four patient groups. For ten days, the A group received classical treatment (CT) [fluid treatment and antibiotic], the A+R group received CT + ribavirin, the A+P group received CT + proanthocyanidin, A+R+P group received CT + ribavirin-proanthocyanidin. On days T0, T3, T7, and T10, hematological, biochemical, and clinical scores were done. These days and the fifth and tenth post-treatment days were also screened for CDV. Clinical improvement was best in the A+P, A+R, A, and A+R+P groups, respectively. The A+R group had fewer leucocytes, neutrophils, and monocytes ($P<0.05$). CK and CK-MB activity were significantly higher only in the A group ($P<0.01$), and decreased only in the A+R group as therapy progressed. Creatinine values were high in A+P and A+R groups ($P<0.01$). The lowest calcium value was in the A+R group ($P<0.01$). The least CDV presence was detected in the A+R group regarding viral shedding. As a result, using ribavirin or proanthocyanidin helped to lessen the severity of clinical findings, increase survival, and reduce viral shedding in dogs with CDV.



# Kanin Distemperde Ribavirin ve Proantosiyanidin'in Klinik Bulgular, Hematolojik ve Biyokimyasal Parametreler ve Viral Saçılım Üzerine Etkilerinin Değerlendirilmesi

**Anahtar Kelimeler**
Antiviral ajanlar, Canine distemper virus, Proantosiyanidinler, Ribavirin

**Öz:** Bu çalışma, canine distemper virus (CDV) ile doğal olarak enfekte olan köpeklerde ribavirin, proantosiyanidin ve ribavirin-proantosiyanidin kombinasyonunun etkilerini araştırdı. Her biri 2-6 aylık yaşta altı köpekten oluşan bir sağlıklı kontrol ve dört hasta grubu olmak üzere beş grup oluşturuldu. On gün boyunca A grubuna klasik tedavi (KT) [sıvı tedavisi ve antibiyotik], A+R grubuna KT + ribavirin, A+P grubuna KT + proantosiyanidin, A+R+P grubuna KT + ribavirin-proantosiyanidin uygulandı. T0, T3, T7 ve T10 günlerinde hematolojik ve biyokimyasal analizler ve klinik skorlama yapıldı. Bu günlerde ve tedaviden sonraki 5. ve 10. günlerde CDV varlığına bakıldı. Klinik skorlama A+P, A+R, A ve A+R+P gruplarının sırasıyla en iyi klinik iyileşmeyi gösterdiğini ortaya koydu. A+R grubunda toplam lökosit, nötrofil ve monositlerde düşüş gözlendi ($P<0.05$). Kreatin kinaz ve kreatin kinaz-myokardiyal band aktivitesi sadece A grubunda anlamlı olarak yüksek bulunurken ($P<0.01$), bu değerler sadece A+R grubunda tedavi ilerledikçe azaldı. Kreatinin değerleri A+P ve A+R gruplarında yüksekti ($P<0.01$). En düşük kalsiyum değeri A+R grubundaydı ($P<0.01$). Viral saçılım açısından en az CDV varlığı A+R grubunda tespit edildi. Sonuç olarak, CDV'li köpeklerde ribavirin veya proantosiyanidin kullanımı, klinik bulguların ciddiyetini azaltmaya, hayatta kalma oranını artırmaya ve viral saçılımı azaltmaya yardımcı oldu.

## 1. INTRODUCTION

Canine distemper (CD) is a worldwide, multisystemic, and potentially fatal viral disease of dogs. The causative agent is the *canine distemper virus* (*CDV*) which belongs to the genus morbillivirus from the *Paramyxoviridae* family [1,2]. CDV is an enveloped virus with a single-stranded, linear, negative-sense RNA genome [3].

Canine distemper is mostly transmitted via oronasal aerosols [4]. Viral shedding starts up to 5 days after the infection forms -before the clinical signs appear- with all excreta and secretions [5,6]. The duration of viral shedding might range from 1-2 weeks to 4 months [5,7]. Dogs of all ages are susceptible to the disease, but dogs aged 3-6 months are more vulnerable [7,8]. While most dogs develop a subclinical infection, only a few develop a rapidly progressive infection followed by death [5]. The clinical manifestations of CD are mainly related to the respiratory, gastrointestinal, and central nervous systems. During the acute infection, various clinical findings such as cutaneous rash, oculonasal discharge, conjunctivitis, anorexia, secondary bacterial infections, and neurological disorders occur [9]. Typical hematological findings are anemia, thrombocytopenia, absolute lymphopenia, neutropenia, and monocytopenia, especially in dogs with acute CDV infection [10]. Early cases are characterized by lymphopenia while late cases are by lymphocytosis [11]. Serum biochemical changes are usually nonspecific [12]. Hypoalbuminemia, hyperglobulinemia [13], or hypocalcaemia [13,14] have been reported. Some dogs may experience slight elevations in liver enzyme activity due to hypoxia or secondary infections caused by intestinal bacteria translocation [5].

Most treatments are ineffective; however, they should contain broad-spectrum antibiotics, balanced electrolyte solutions, and corticosteroids in some neurological form [4]. The clinical use of antiviral drugs in veterinary medicine is not common, and the number of controlled studies on the efficacy of these drugs is limited [15]. Ribavirin is an antiviral with a broad spectrum of activity against many RNA and DNA viruses, both in-vitro and in-vivo. The only commercially available and used compound with known antiviral activity against various members of the *Paramyxoviridae* family is ribavirin [16–18]. Ribavirin has been used in-vitro to treat CD and is reported to be very effective in inhibiting CDV replication [19]. Proanthocyanidin, a dimeric procyanidin obtained from the condensation of monomeric flavanols [20,21] possesses antioxidant, antibacterial, and antiviral activities [22–25] as well as immunomodulatory properties [26]. Proanthocyanidin has been found to inhibit CDV in vitro both at the early and late stages of viral replication [27].

To our knowledge, ribavirin and proanthocyanidin have not been used in clinical studies to treat dogs naturally infected with CDV. Therefore, this study aimed to evaluate how the therapeutic use of these medications affects clinical outcomes, hematological and biochemical parameters, and viral shedding. It was hypothesized that ribavirin would reduce viral shedding and increase survival rates. Likewise, it was assumed that proanthocyanidin would show similar effects thanks to its multiple properties.

## 2. MATERIAL AND METHOD

This study was approved by the Atatürk University Animal Experiments Local Ethics Committee (Decision number 2017/62), and for each dog, written informed consent was obtained from the owner.

### 2.1. Animals and Protocol Design

The study included 30 dogs, 2-6 months old, of any breed and sex (Table 1). Based on clinical examination, rapid test kit (Anigen Rapid CDV Ag Test Kit, Bionote, Korea) and PCR analysis results, complete blood cell count, and treatment applied, the dogs were divided into five groups A (n=6), A+R (n=6), A+P (n=6), A+R+P (n=6) and healthy (n=6). Dogs showing neurological signs before and at the beginning of treatment and previously vaccinated against CDV were excluded from the groups. All dogs received single subcutaneous ivermectin (0.2 mg/kg; Alfamec® 1%, Ege Vet) and a tablet comprising fenbendazole, pyrantel pamoate, and praziquantel (1 tablet/10 kg; Caniverm® 700 mg, Intermed) was given orally. The day after this procedure was regarded as the pre-treatment (T0). Dogs in the A group received the classical treatment [intravenous fluid therapy and antibiotic (7 mg/kg amoxicillin + 1.75 mg/kg clavulanic acid, once a day, subcutaneously) [28], (Synulox®, Zoetis, USA)] for ten days. In addition to the classical treatment, dogs in the A+R group received 30 mg/kg [29] ribavirin tablet (Copegus®, Roche, ABD), and dogs in the A+P group received 10 mg/kg [30] proanthocyanidin film tablet (Proanthocyanidin®, GNC, ABD), and dogs in the A+R+P group received 30 mg/kg ribavirin and 10 mg/kg proanthocyanidin for ten days. A detailed clinical examination was performed on each dog before and during treatment. The scoring system developed by Gill et al. [31] was modified, and a scoring table was created by grading rectal temperature, general condition, appetite, dehydration, vomiting, diarrhea, cough, ocular discharge, nasal discharge, dental problems, skin problems, neurological findings and death (Table 2).



### 2.2. Blood Sampling

Blood samples were taken from CDV-positive dogs on days 0 (T0), 3 (T3), 7 (T7), and 10 (T10) of treatment, whereas healthy dogs only had blood samples taken once. The *vena cephalica antebrachia* of all dogs was punctured, and blood samples were collected into EDTA vacutainers (Vacutainer, K2E 3.6 mg, BD, UK) and plain tubes (Vacutainer, BD, UK) for hematological and biochemical analyses. After leaving for ten minutes at room temperature for clotting, sera were obtained by centrifugation (Beckman Coulter, Allegra® X-30R, USA) at 3000 rpm for 10 minutes and stored at -80°C until being analysed. Hematological analyses were performed immediately.

### 2.3. Hematological Analyses

White blood cell (WBC), lymphocyte (LYM), monocyte (MON), neutrophil (NEU), eosinophil (EOS), basophil (BAS), red blood cell (RBC), and hemoglobin (HGB) counts, haematocrit (HCT), and platelet (PLT) levels were determined by a hematology analyser (Abacus Junior Vet5, Hungary).

**Table 1.** Breed, age and sex of dogs in groups.

| Animal No | Control | A | A+R | A+P | A+R+P |
|---|---|---|---|---|---|
| 1 | Mix, 2 mo, m | Kangal Mix, 2 mo, f | BC, 3 mo, male | Kangal, 2 mo, f | Mix, 3 mo, m |
| 2 | Mix, 5 mo, f | Mix, 4 mo, f | Terrier Mix, 6 mo, f | Mix, 3 mo, f | Mix, 4 mo, f |
| 3 | Mix, 2 mo, f | Kangal Mix, 2 mo, m | Kangal Mix, 4 mo, f | Mix, 2 mo, f | Mix, 5 mo, f |
| 4 | Mix, 4 mo, m | Mix, 2.5 mo, m | Mix, 2 mo, m | Mix, 4 mo, m | Mix, 2 mo, f |
| 5 | Mix, 2 mo, f | Mix, 2.5 mo, f | Mix, 4 mo, m | Mix, 5 mo, m | Mix, 3 mo, m |
| 6 | Kangal, 4 mo, f | Mix, 5 mo, f | Kangal Mix, 4.5 mo, f | Mix, 6 mo, m | Russian Poodle, 5.5 mo, m |

m: male; f: female; mo: month; BC: Border Collie

**Table 2.** Scoring system for clinical signs of canine distemper.

| Signs | Score Value | Signs | Score Value | Signs | Score Value | Signs | Score Value | Signs | Score Value | Signs | Score Value | Signs | Score Value |
|---|---|---|---|---|---|---|---|---|---|---|---|---|---|
| **Rectal temperature** | | **Nasal discharge** | | **Ocular discharge** | | **General condition** | | **Appetite** | | **Dehydration** | | **Skin problems** | |
| 37.1-39.3°C | 0 | No | 0 | No | 0 | Very good | 0 | Very good | 0 | No | 0 | No | 0 |
| 39.4-39.9°C | 1 | Serous | 1 | Mild | 1 | Good | 1 | Good | 1 | Mild | 1 | Paw pad hyp | 3 |
| 40.0-40.5°C | 2 | Seromucous | 1 | Moderate | 2 | Bad | 2 | Bad | 2 | Moderate | 2 | Nasal hyp | 3 |
| ≥40.5°C | 3 | Mucous | 2 | Severe | 3 | Very bad | 3 | Very bad | 3 | Severe | 3 | ST-pustule | 1 |
| ≤37.0°C | 3 | Mucopurulent | 3 | | | | | | | | | | |

| Signs | Score Value | Signs | Score Value | Signs | Score Value | Signs | Score Value | Signs | Score Value | Signs | Score Value |
|---|---|---|---|---|---|---|---|---|---|---|---|
| **Cough** | | **Fecal consistency** | | **Vomiting** | | **Neurologic findings** | | **Dental problems** | | **Death** | |
| No | 0 | Normal | 0 | No | 0 | No | 0 | No | 0 | No | 0 |
| Present | 2 | Watery | 1 | Present | 1 | Present | 3 | E and D hypoplasia | 3 | Present | 20 |
| Provoked cough | 1 | Bloody | 3 | | | | | | | | |

ST: skin thickening; E: enamel; D: dentin; Hyp: hyperkeratosis

### 2.4. Biochemical Analyses

Alanine aminotransferase (ALT), aspartate aminotransferase (AST), gamma-glutamyl transferase (GGT), alkaline phosphatase (ALP), creatinine (CREA), blood urea nitrogen (BUN), creatinine kinase (CK), creatinine kinase-MB (CK-MB), total protein (TP), albumin (ALB), amylase (AMY), cholesterol (CHOL), triglyceride (TRIG), glucose, phosphorus (P), calcium (Ca) and magnesium (Mg) concentrations in serum samples were determined by commercial kits using a biochemistry autoanalyzer (Mindray BS-300 Chemistry Analyser, China).

### 2.5. Reverse Transcriptase Polymerase Chain Reaction (RT-PCR) Assay

#### 2.5.1. Preparation of samples

Leukocyte samples and mucosal swab samples (combination of conjunctiva and nose) from dogs were used to test for CDV on days T0, T7, and T10, as well as on days 5 (PT5) and 10 (PT10) post-treatment. Mucosal swab samples were vortexed in 1 mL of phosphate-buffered saline (PBS) and centrifuged at 3000 rpm for 5 min. After centrifugation, 200 µl of supernatant was kept at -20 °C until extraction. Blood samples collected in EDTA vacutainers were centrifuged at 2000 rpm for 10 minutes. The buffy coat layer was placed in a tube containing 200 µl of isotonic PBS. Collected leukocytes were kept at -20º C until extraction.

#### 2.5.2. Extraction

The samples were removed from -20 ºC and dissolved at room temperature. After dissolution, 200 µl of each sample was taken into a new tube, and the extraction process was carried out using the GF-1 Viral Nucleic Acid Extraction kit (Cat: GF-RD-100, Vivantis, Malaysia) according to the manufacturer's protocol. The samples were stored at -20°C until cDNA synthesis after extraction.

#### 2.5.3. RT reaction (Complementary DNA synthesis, cDNA)

A reverse transcriptase enzyme was used to convert possible RNA to DNA after extraction. This process was carried out with the RevertAid First Strand cDNA Synthesis Kit (Cat. No. K1621, Thermo Fisher Scientific, Germany) according to the method prescribed by the company. The resulting cDNAs were stored at -20 ºC until the PCR process.

#### 2.5.4. PCR analyses

PCR reaction was conducted to obtain the relevant product of the hemagglutinin gene region of *Paramyxovirus*, using the primer and method reported by Trebbien et al. [32]. Positive PCR amplicons were separated on a 1.5% agarose gel by gel electrophoresis, and displayed under UV light (Figure 1).

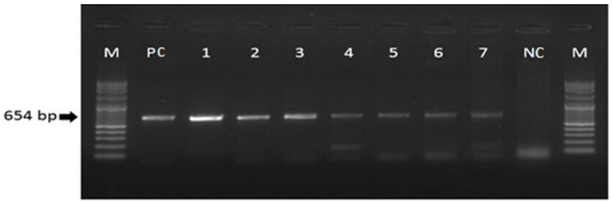


**Figure 1.** Gel image of PCR products made with the primers Zhao2010fwd and Bolt1997rev in the study of Trebbien et al. [32] with a product size of 654 bp. M: Marker (100 bp DNA Ladder), PC: Positive Control, NC: Negative Control, Study examples 1-3 (strong positive samples) and 4-7 (Weak positive samples).

### 2.6. Statistical Analysis

Statistical analysis was performed using IBM SPSS Statistics 25.0 (SPSS Inc., Chicago, IL, USA). The Shapiro-Wilk test was used to assess the distribution of data between groups, and it was determined that the data had a normal distribution. As a result, the One-way ANOVA was used to assess the data statistically. The statistical analysis evaluated treatments (A, A+R, A+P, A+R+P, and control groups) and sampling days (T0, T3, T7, and PT10) as primary effects, and the main effects were analysed independently. First, comparisons were done across treatment groups and then between data from the T0, T3, T7, and T10 sampling days within the same group. When the F-test for the main effect was significant, Duncan's Multiple Comparison Test was used to compare the means of the subclasses. All results were presented as the mean ± standard deviation (SD). A significance level of $P< 0.05$ was used for all statistical comparisons.

## 3. RESULTS

### 3.1. Clinical Status of the Dogs

A runny nose was observed in 19 of 24 dogs with CDV at T0. Ocular discharge and eye crust (16/24), high fever (14/24), cough, diarrhea, dehydration (12/24), skin problems (9/24), death (9/24), poor overall condition (4/24), vomiting, lack of appetite (2/24) and dental problems (2/24) were other clinical findings in dogs. According to clinical scores, the groups were the A+R+P group (349), A group (244), A+R group (188), and A+P group (182), in that order (Table 3). The difference between T10 and T0 was most pronounced in the A+R+P group, followed by the A group. The increase in the A+R and A+P groups was close to each other.

**Table 3.** Clinical score values of the treatment days of the groups.

| Groups | T0 | T3 | T7 | T10 | Total |
|---|---|---|---|---|---|
| A | 41 | 37 | 72 | 94 | **244** |
| A+R | 51 | 27 | 48 | 62 | **188** |
| A+P | 45 | 37 | 44 | 56 | **182** |
| A+R+P | 63 | 68 | 100 | 118 | **349** |

Following the initiation of the therapy, the general health of the dogs in the A+R+P group gradually declined. They also experienced a loss of appetite, bloody feces, severe dehydration, and mucopurulent nasal discharge. Dogs in group A had no improvement in cough despite treatment, nasal discharge, which was mostly serous at first, later turned into a mucopurulent consistency, and their general condition mostly deteriorated. In most dogs in the A+R group, prominent clinical findings at T0 were diarrhea and goopy eye discharge, and these problems mostly disappeared with treatment. Nasal discharge was a common clinical finding at T0 in all dogs in the A+P group. Even though the runny nose persisted throughout the treatment, the dogs' overall health improved significantly.

At T10, all dogs' body weights were generally reduced compared to T0 (Figure 2). In turn, the A+R and A+R+P groups had the most significant weight loss. The average body weight reduction was lowest in the A+P and A groups, respectively, and these groups often remained at their T0 weight.

During the 10-day treatment period, six out of six dogs (100%) in the A+P group, four out of six (46.6%) in the A and A+R groups, and two out of six (33.3%) in the A+R+P group survived.

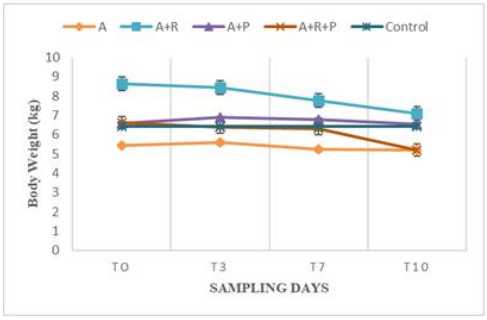


**Figure 2.** Mean body weight changes of the groups

### 3.2. Hematological Findings

In the A+R and A+R+P groups, WBC, LYM, NEU, and MON levels dropped as treatment progressed. However, it was found that in the A and A+P groups, these values increased as the treatment progressed. As the treatment progressed, a statistically significant decrease was detected in the levels of WBC, NEU ($P<0.05$) and MON ($P<0.01$) only in the A+R group. All patient groups had lower LYM counts than the control group on all treatment days.

All patient groups' RBC, HGB, and HCT values decreased statistically insignificantly during the treatment. The erythrocyte parameters of the A+R and A+R+P groups were generally higher than those in the A, A+P, and control groups. While PLT values increased gradually for group A, they decreased in other patient groups. Only the PLT values of the A group at T10 were the highest of all the groups ($P<0.05$). The statistically insignificant lowest PLT value in T10 was found in the A+R group (Table 4).

### 3.3. Biochemical Findings

During treatment, groups A and A+R+P had the highest ALT values ($P<0.05$), but ALT values decreased as treatment progressed. The A+R and A+P groups had very similar ALT values to the control group on all treatment days. Only in group A, the ALP value increased as the treatment days progressed ($P<0.05$). The group with the lowest ALP values was determined as the A+R group ($P<0.05$). The AST values of the A and A+R+P groups were higher than the control group and increased as the treatment progressed. AST values of the A+R group decreased. CK and CK-MB values of all patient groups were higher than the control group. Only in the A+R group did CK and CK-MB values decline with time and get close to the control group levels. The highest CK and CK-MB values were found in group A ($P<0.01$). The CREA levels of the A and A+R+P groups

were similar to those of the control group on all treatment days, but the CREA values were the highest in the A+P and A+R groups, respectively (P<0.01). As treatment progressed, CREA values increased only in the A+R group. CHOL values showed insignificant increases in all groups, but the groups with the least increase were A+R+P and A+P groups, respectively. Glucose values of all groups were found to be lower than the control group on all treatment days. While AMY values increased gradually in the A group, they first increased and then decreased in the other groups.

**Table 4.** Clinical score values of the treatment days of the groups.

| | | Groups | | | | | |
|---|---|---|---|---|---|---|---|
| Parameters | Day | A | A+R | A+P | A+R+P | Control | P |
| WBC | 0 | 10.56±3.31 | 13.24±5.10$^{A}$ | 13.82±13.81 | 24.94±20.49 | 11.52±3.07 | >0.05 |
| (x10$^3$ µL) | 3 | 12.89±8.53 | 8.26±2.83$^{B}$ | 11.67±5.99 | 18.33±7.96 | 11.52±3.07 | >0.05 |
| | 7 | 18.19±11.37 | 5.89±2.64$^{B}$ | 16.06±8.49 | 12.62±7.43 | 11.52±3.07 | >0.05 |
| | 10 | 17.91±9.91 | 7.63±2.41$^{B}$ | 17.87±9.45 | 12.90±17.44* | 11.52±3.07 | >0.05 |
| | P | >0.05 | **<0.05** | >0.05 | >0.05 | >0.05 | |
| LYM | 0 | 1.14±0.39 | 0.99±0.68 | 0.91±0.35 | 2.74±4.60 | 3.18±1.91 | >0.05 |
| (x10$^3$ µL) | 3 | 1.51±0.62 | 1.09±0.83 | 0.98±0.37 | 2.22±2.28 | 3.18±1.91 | >0.05 |
| | 7 | 2.54±2.82$^{ab}$ | 0.80±0.55$^{b}$ | 0.85±0.35$^{b}$ | 0.76±0.45$^{b}$ | 3.18±1.91$^{a}$ | **<0.05** |
| | 10 | 2.89±2.60 | 1.10±0.75 | 1.57±1.10 | 0.045±0.049* | 3.18±1.91 | >0.05 |
| | P | >0.05 | >0.05 | >0.05 | >0.05 | >0.05 | |
| NEU | 0 | 8.65±3.12 | 11.16±4.69$^{A}$ | 11.93±12.83 | 19.28±14.72 | 7.53±1.60 | >0.05 |
| (x10$^3$ µL) | 3 | 10.46±7.57 | 6.42±2.63$^{B}$ | 9.92±5.64 | 14.22±7.82 | 7.53±1.60 | >0.05 |
| | 7 | 14.70±9.19$^{a}$ | 4.47±2.59$^{B}$ | 14.04±8.23$^{a}$ | 10.62±6.41$^{ab}$ | 7.53±1.60$^{ab}$ | **<0.05** |
| | 10 | 13.93±7.48$^{a}$ | 5.52±1.52$^{B}$ | 15.20±8.22$^{a}$ | 11.89±16.24* | 7.53±1.60$^{ab}$ | **<0.05** |
| | P | >0.05 | **<0.05** | >0.05 | >0.05 | >0.05 | |
| RBC | 0 | 4.69±0.58$^{b}$ | 5.18±0.76$^{b}$ | 5.46±0.86$^{b}$ | 6.44±0.78$^{a}$ | 4.88±0.40$^{b}$ | **<0.01** |
| (x10$^6$ µL) | 3 | 4.61±0.47$^{b}$ | 5.34±0.86$^{ab}$ | 5.07±0.75$^{b}$ | 5.98±0.30$^{a}$ | 4.88±0.40$^{b}$ | **<0.01** |
| | 7 | 4.55±0.56 | 5.11±0.96 | 4.81±1.00 | 5.78±0.58 | 4.88±0.40 | >0.05 |
| | 10 | 4.26±0.55 | 5.00±1.62 | 4.30±0.77 | 5.41±0.48* | 4.88±0.40 | >0.05 |
| | P | >0.05 | >0.05 | >0.05 | >0.05 | >0.05 | |
| HGB | 0 | 8.38±1.38$^{b}$ | 10.03±1.60$^{b}$ | 9.78±1.68$^{b}$ | 12.56±2.39$^{a}$ | 9.21±1.17$^{b}$ | **<0.01** |
| (g/dL) | 3 | 7.88±0.98$^{c}$ | 10.31±2.13$^{ab}$ | 9.15±1.74$^{bc}$ | 11.73±1.42$^{a}$ | 9.21±1.17$^{bc}$ | **<0.01** |
| | 7 | 7.66±1.10$^{b}$ | 9.65±2.31$^{ab}$ | 8.71±1.93$^{b}$ | 11.05±1.07$^{a}$ | 9.21±1.17$^{ab}$ | **<0.05** |
| | 10 | 7.38±1.30 | 9.02±3.14 | 7.50±1.32 | 10.70±0.70* | 9.21±1.17 | >0.05 |
| | P | >0.05 | >0.05 | >0.05 | >0.05 | >0.05 | |
| HCT | 0 | 28.86±4.88$^{b}$ | 35.57±6.07$^{ab}$ | 34.72±6.49$^{ab}$ | 41.09±6.52$^{a}$ | 33.29±5.19$^{b}$ | **<0.05** |
| (%) | 3 | 27.56±4.08$^{b}$ | 35.89±6.18$^{a}$ | 31.65±6.16$^{ab}$ | 38.12±3.97$^{a}$ | 33.29±5.19$^{ab}$ | **<0.05** |
| | 7 | 26.79±4.73 | 34.39±7.55 | 29.71±7.38 | 36.51±3.81 | 33.29±5.19 | >0.05 |
| | 10 | 24.89±4.24 | 33.11±12.45 | 26.62±5.77 | 34.96±4.04* | 33.29±5.19 | >0.05 |
| | P | >0.05 | >0.05 | >0.05 | >0.05 | >0.05 | |
| PLT | 0 | 424±268 | 389±53 | 456±190 | 401±132 | 376±151 | >0.05 |
| (x10$^3$ µL) | 3 | 444±261 | 444±118 | 317±209 | 415±244 | 376±151 | >0.05 |
| | 7 | 484±143 | 343±164 | 252±172 | 268±205 | 376±151 | >0.05 |
| | 10 | 675±234$^{a}$ | 294±219$^{b}$ | 379±212$^{b}$ | 321±181* | 376±151$^{b}$ | **<0.05** |
| | P | >0.05 | >0.05 | >0.05 | >0.05 | >0.05 | |

WBC: white blood cell; LYM: lymphocyte; NEU: neutrophil, RBC: red blood cell; HGB: haemoglobin; HCT: haematocrit; PLT: platelet. $^{A, B}$ The means shown in different capital letters within the group (in the column) are statistically significant. $^{a, b}$ The means shown in different lowercase letters between the groups (on the line) are statistically significant. *The group A+R+P data from the 10th day were not statistically analysed because 2 dogs were still alive as a result of death in group A+R+P. Data are presented as the mean ± standard deviation

The highest AMY values were in the A+R+P group and this elevation was significant compared to the A and control groups (P<0.05). ALB values were low in all patient groups, but the low ALB values of the A+R and A+P groups at T0 and T10 were significant (P<0.05). P, Ca, and Mg values decreased numerically in the patient groups, but the A+R group's Ca value was lower on all treatment days compared to the control and A groups (P<0.01) (Table 5).

### 3.4. Virological Findings

Table 6 displays the PCR results for samples of mucosal swabs and leukocytes collected at T0, T7, T10, PT5, and PT10. In PCR analysis performed at T0, CDV was detected in mucosal swap samples but not in leukocyte samples in 6 of 24 dogs with CDV. On the other hand, CDV was found at T7 in the leukocyte samples of these six dogs. In four dogs in group A and two in the other groups, the viral load increased in leukocytes and mucosal swap samples in T7 and T10 compared to T0. When the PCR results of the groups were examined, the presence of CDV initially disappeared in the mucosal swap samples and then in the leukocyte samples. Among the treatment groups, the A+R and A+P groups were the best at reducing or stopping viral shedding, respectively. The CDV rapid test kit results were 100% accurate compared to the PCR results.

## 4. DISCUSSION

The results of this study revealed that ribavirin or proanthocyanidin may have positive effects on clinical outcomes, survival rate, viral shedding, and hematological and biochemical parameters in dogs naturally infected with CDV, consistent with the hypothesis.

In this study, 24 CDV-infected dogs exhibited various clinical symptoms in line with previous studies [33,34]. Ertürk [35] found that using antivirals like interferon,

**Table 5.** Comparison of biochemical parameters of the groups.

| | | Groups | | | | | |
|---|---|---|---|---|---|---|---|
| Parameters | Day | A | A+R | A+P | A+R+P | Control | P |
| ALT | 0 | 39.00±30.17$^{a}$ | 15.50±8.36$^{b}$ | 16.17±7.67$^{b}$ | 31.33±6.18$^{ab}$ | 15.83±8.97$^{b}$ | **<0.05** |
| (U/L) | 3 | 27.83±12.27$^{a}$ | 14.67±14.25$^{b}$ | 14.00±6.95$^{b}$ | 29.50±4.27$^{a}$ | 15.83±8.97$^{b}$ | **<0.05** |
| | 7 | 26.33±9.97$^{ab}$ | 16.00±8.92$^{b}$ | 17.17±7.88$^{b}$ | 28.50±6.31$^{a}$ | 15.83±8.97$^{b}$ | **<0.05** |
| | 10 | 28.60±8.98$^{a}$ | 17.75±5.96$^{b}$ | 15.50±4.50$^{b}$ | 34.00±8.48* | 15.83±8.97$^{b}$ | **<0.05** |
| | P | >0.05 | >0.05 | >0.05 | >0.05 | >0.05 | |
| ALP | 0 | 153±27$^{Ba}$ | 88±52$^{b}$ | 160±53$^{a}$ | 131±50$^{ab}$ | 158±33$^{a}$ | **<0.05** |
| (U/L) | 3 | 147±26$^{B}$ | 106±56 | 174±32 | 158±71 | 158±33 | >0.05 |
| | 7 | 171±23$^{AB}$ | 109±66 | 155±41 | 148±62 | 158±33 | >0.05 |
| | 10 | 192±27$^{Aa}$ | 77±83$^{b}$ | 149±40$^{a}$ | 127±141* | 158±33$^{a}$ | **<0.05** |
| | P | **<0.05** | >0.05 | >0.05 | >0.05 | >0.05 | |
| CK | 0 | 332±117 | 311±166 | 343±237 | 402±274 | 183±15 | >0.05 |
| (U/L) | 3 | 466±184$^{a}$ | 341±122$^{ab}$ | 314±74$^{bc}$ | 212±60$^{bc}$ | 183±15$^{c}$ | **<0.01** |
| | 7 | 443±187 | 239±73 | 270±104 | 524±565 | 183±15 | >0.05 |
| | 10 | 461±177$^{a}$ | 183±56$^{b}$ | 435±223$^{a}$ | 730±371* | 183±15$^{b}$ | **<0.01** |
| | P | >0.05 | >0.05 | >0.05 | >0.05 | >0.05 | |
| CK-MB | 0 | 81±31 | 129±118 | 75±54 | 88±69 | 54±13 | >0.05 |
| (U/L) | 3 | 110±50$^{a}$ | 80±34$^{ab}$ | 62±23$^{b}$ | 45±11$^{b}$ | 54±13$^{b}$ | **<0.01** |
| | 7 | 106±48 | 57±15 | 57±30 | 104±116 | 54±13 | >0.05 |
| | 10 | 113±46 | 53±25 | 94±55 | 137±50* | 54±13 | >0.05 |
| | P | >0.05 | >0.05 | >0.05 | >0.05 | >0.05 | |
| CREA | 0 | 0.67±0.17$^{b}$ | 1.44±1.49$^{b}$ | 2.71±1.11$^{a}$ | 0.63±0.14$^{b}$ | 0.62±0.15$^{b}$ | **<0.01** |
| (mg/dl) | 3 | 0.61±0.07$^{c}$ | 1.96±1.37$^{b}$ | 3.40±0.84$^{a}$ | 0.69±0.16$^{c}$ | 0.62±0.15$^{c}$ | **<0.01** |
| | 7 | 0.64±0.15$^{c}$ | 1.67±1.56$^{b}$ | 3.02±0.60$^{a}$ | 0.44±0.22$^{c}$ | 0.62±0.15$^{c}$ | **<0.01** |
| | 10 | 0.55±0.14$^{b}$ | 2.27±2.01$^{a}$ | 2.55±0.96$^{a}$ | 0.58±0.17* | 0.62±0.15$^{b}$ | **<0.01** |
| | P | >0.05 | >0.05 | >0.05 | >0.05 | >0.05 | |
| CHOL | 0 | 309±82$^{a}$ | 124±35$^{b}$ | 182±52$^{b}$ | 336±29$^{a}$ | 319±43$^{a}$ | **<0.01** |
| (mg/dl) | 3 | 318±77$^{a}$ | 181±49$^{b}$ | 188±31$^{b}$ | 346±64$^{a}$ | 319±43$^{a}$ | **<0.01** |
| | 7 | 388±84$^{a}$ | 175±41$^{b}$ | 206±69$^{b}$ | 330±61$^{a}$ | 319±43$^{a}$ | **<0.01** |
| | 10 | 379±68$^{a}$ | 206±66$^{b}$ | 197±55$^{b}$ | 351±25* | 319±43$^{a}$ | **<0.01** |
| | P | >0.05 | >0.05 | >0.05 | >0.05 | >0.05 | |
| GLUCOSE | 0 | 80.82±28.12$^{ab}$ | 62.83±19.04$^{b}$ | 69.55±13.60$^{b}$ | 78.76±13.25$^{ab}$ | 94.30±6.42$^{a}$ | **<0.05** |
| (mg/dl) | 3 | 71.60±13.55$^{b}$ | 81.46±13.55$^{ab}$ | 76.26±3.45$^{b}$ | 76.67±17.59$^{b}$ | 94.30±6.42$^{a}$ | **<0.05** |
| | 7 | 80.82±25.51$^{abc}$ | 69.55±6.35$^{bc}$ | 65.21±12.09$^{c}$ | 95.40±33.07$^{a}$ | 94.30±6.42$^{ab}$ | **<0.05** |
| | 10 | 55.47±15.39$^{c}$ | 79.30±11.38$^{ab}$ | 64.13±18.65$^{bc}$ | 58.17±18.98* | 94.30±6.42$^{a}$ | **<0.01** |
| | P | >0.05 | >0.05 | >0.05 | >0.05 | >0.05 | |
| AMY | 0 | 365±132 | 357±367 | 493±300 | 668±391 | 330±65 | >0.05 |
| (U/L) | 3 | 459±271$^{b}$ | 458±352$^{b}$ | 610±346$^{ab}$ | 923±356$^{a}$ | 330±65$^{b}$ | **<0.05** |
| | 7 | 405±98$^{b}$ | 519±348$^{ab}$ | 337±104$^{b}$ | 759±347$^{a}$ | 330±65$^{b}$ | **<0.05** |
| | 10 | 466±182 | 359±107 | 350±146 | 718±494* | 330±65 | >0.05 |
| | P | >0.05 | >0.05 | >0.05 | >0.05 | >0.05 | |
| ALB | 0 | 2.35±0.18$^{ab}$ | 1.90±0.619$^{c}$ | 2.05±0.18$^{bc}$ | 2.38±0.09$^{Aab}$ | 2.46±0.15$^{a}$ | **<0.05** |
| (mg/dl) | 3 | 2.40±0.23$^{a}$ | 2.41±0.22$^{a}$ | 1.86±0.20$^{b}$ | 2.38±0.19$^{Aa}$ | 2.46±0.15$^{a}$ | **<0.01** |
| | 7 | 2.33±0.28 | 2.13±0.48 | 1.95±0.40 | 2.11±0.22$^{B}$ | 2.46±0.15 | >0.05 |
| | 10 | 2.30±0.27$^{ab}$ | 2.07±0.33$^{bc}$ | 1.85±0.33$^{c}$ | 2.20±0.28* | 2.46±0.15$^{a}$ | **<0.01** |
| | P | >0.05 | >0.05 | >0.05 | **<0.05** | >0.05 | |
| Ca | 0 | 14.31±5.26$^{a}$ | 6.80±1.94$^{c}$ | 4.93±0.86$^{c}$ | 10.23±1.98$^{b}$ | 11.21±1.20$^{ab}$ | **<0.01** |
| (mg/dl) | 3 | 10.91±1.91$^{a}$ | 6.61±1.65$^{bc}$ | 5.36±1.17$^{c}$ | 8.10±2.06$^{b}$ | 11.21±1.20$^{ab}$ | **<0.01** |
| | 7 | 12.85±2.88$^{a}$ | 6.90±2.64$^{c}$ | 5.03±1.07$^{c}$ | 9.48±1.30$^{b}$ | 11.21±1.20$^{ab}$ | **<0.01** |
| | 10 | 11.44±2.90$^{a}$ | 3.80±2.54$^{b}$ | 4.83±1.12$^{b}$ | 9.15±0.49* | 11.21±1.20$^{ab}$ | **<0.01** |
| | P | >0.05 | >0.05 | >0.05 | >0.05 | >0.05 | |

ALT: Alanine aminotransferase; ALP: alkaline phosphatase; CK: creatinine kinase; CK-MB: creatinine kinase-MB; CREA: creatinine; CHOL: cholesterol; AMY: amylase; ALB: albumin; Ca: calcium $^{A, B}$ The means shown in different capital letters within the group (in the column) are statistically significant. $^{a, b}$ The means shown in different lowercase letters between the groups (on the line) are statistically significant. *The group A+R+P data from the 10th day were not statistically analysed because 2 dogs were still alive as a result of death in group A+R+P. Data are presented as the mean ± standard deviation.



oseltamivir, and famciclovir results in the best clinical outcome for dogs with parvoviral enteritis. Similarly, the A+P and A+R groups achieved the best clinical scores in this study, respectively.

Several therapeutic benefits of proanthocyanidin [26,27], such as antibiotic, antiviral, antioxidant, and immunomodulatory, may have contributed to this situation. Ribavirin has an immunomodulatory effect [36] and improved the clinical course in infants with severe bronchiolitis caused by a respiratory syncytial virus [37]. The properties mentioned above of ribavirin and its being an effective antiviral against CDV [19] may have contributed to the second-best clinical score in the A+R group. However, using ribavirin was found to cause weight loss. Dogs in the A+R group lost the most weight, followed by those in the A+R+P group. Like this, Weiss et al. [38] found that cats administered ribavirin at doses of 11, 22, and 44 mg/kg progressively lost weight and their appetite. With therapy, the clinical score of the A+R+P group increased steadily, and the dogs' overall condition quickly deteriorated. The high clinical score of the A+R+P group at T0 (Table 3) and an adverse drug interaction may have led to this outcome. 10 mg/kg proanthocyanidin and 30 mg/kg ribavirin, which we used in this study, do not have such side effects.

**Table 6.** PCR analysis results of CDV presence in mucosal swab and leukocyte samples and visual evaluation of PCR positivity of the groups.

| **Viral Shedding** | | **1** | | **2** | | **3** | | **4** | | **5** | | **6** | |
|---|---|---|---|---|---|---|---|---|---|---|---|---|---|
| **Groups** | **Day** | **MS** | **L** | **MS** | **L** | **MS** | **L** | **MS** | **L** | **MS** | **L** | **MS** | **L** |
| **A** | T0 | ++ | +++++ | ++++ | +++++ | + | + | +++ | N | +++++ | N | + | +++ |
| | T7 | N | N | +++ | +++++ | +++++ | +++++ | + | ++++ | ++ | +++ | ++++ | ++++ |
| | T10 | D | D | +++++ | +++ | D | D | ++++ | + | N | N | + | +++ |
| | PT5 | D | D | D | D | D | D | ++ | ++ | N | N | ++ | +++ |
| | PT10 | D | D | D | D | D | D | + | + | D | D | + | + |
| **A+R** | T0 | ++++ | +++++ | +++++ | ++ | +++++ | ++ | + | +++ | + | +++++ | ++++ | ++++ |
| | T7 | N | N | +++++ | N | N | + | + | +++ | N | +++++ | +++++ | +++++ |
| | T10 | N | N | D | D | D | D | +++ | +++++ | N | +++++ | +++++ | +++++ |
| | PT5 | N | N | D | D | D | D | ++ | + | N | ++ | ++++ | +++++ |
| | PT10 | N | N | D | D | D | D | D | D | N | N | D | D |
| **A+P** | T0 | ++++ | +++++ | + | N | ++++ | N | + | +++++ | +++++ | +++++ | ++++ | + |
| | T7 | ++ | + | ++ | ++ | ++++ | ++++ | +++++ | +++++ | +++++ | +++++ | + | + |
| | T10 | N | N | +++++ | +++++ | +++++ | +++++ | +++++ | +++++ | ++++ | ++++ | + | + |
| | PT5 | N | N | +++++ | +++++ | D | D | + | +++ | +++++ | +++++ | + | + |
| | PT10 | N | N | D | D | D | D | D | D | D | D | N | N |
| **A+R+P** | T0 | + | +++++ | +++ | ++++ | ++++ | +++ | ++ | ++ | ++++ | N | +++ | N |
| | T7 | +++++ | +++++ | N | N | +++++ | ++ | ++++ | ++++ | ++ | ++ | N | ++ |
| | T10 | D | D | N | N | D | D | D | D | D | D | N | N |
| | PT5 | D | D | D | D | D | D | D | D | D | D | D | D |
| | PT10 | D | D | D | D | D | D | D | D | D | D | D | D |

MS: Mucosal Swabs, L: Leucocyte layer, N: Negative, D: Death

Proanthocyanidin has reportedly been used safely and effectively for 24 weeks in dogs at doses of 4, 20, or 40 mg/kg [30]. Ribavirin has been shown to cause anemia in dogs with CDV when taken at a dose of 30 mg/kg for 15 days [29]. There isn't a study that combines the usage of these two medications in dogs, though. To better understand drug interactions, studies involving larger numbers of animals in groups might be advantageous.

All patient groups had lymphopenia, which is consistent with CD findings [5,11,34,39]. When the effects of the treatments on the hematological parameters of the groups were examined, significant decreases in WBC, NEU ($P<0.05$), and MON ($P<0.01$) values were observed only in the A+R group, and this decrease was attributed to the effects of ribavirin. Because ribavirin use has been associated with leukopenia in both humans [40] and cats [39]. This view is supported by the gradual decline in all leukocyte parameters in the A+R+P group utilizing ribavirin. The findings demonstrated that 30 mg/kg of ribavirin caused leukopenia, neutropenia, and monocytopenia in CDV-positive dogs. The dogs in the A+P and A+R+P groups had higher leukocyte parameters than those in the A+R group. This elevation indicated that the leukopenia-inducing effects of ribavirin and CD might be mitigated by proanthocyanidin's immunomodulatory properties [41] and antioxidant properties [42], which protect leukocyte cells.

The gradual decrease in erythrocyte parameters in all patient groups during the treatment was consistent with the reports of anemia in CD [4,11,34]. According to reports, ribavirin is directly toxic to erythrocytes, induces dose-related hemolysis and has adverse effects such as hemolytic anemia and bone marrow suppression [43,44]. However, it was found in this study that the groups using ribavirin had higher erythrocyte parameters than the other groups. These findings suggest that 1) By inhibiting CDV replication, ribavirin lessens the degree of anemia associated with the disease. 2) Blood RBC, HGB, and HCT values in dogs are not affected by ten days of treatment with 30 mg/kg ribavirin. 3) Ribavirin does not accumulate much in canine erythrocytes. The last two inferences can be explained as follows: Different erythrocyte affinities for isolation ribavirin cause different degrees of hematological toxicity in different species [38,44]. Some species, such as mice and rats, accumulate less ribavirin in their erythrocytes

than humans, resulting in fewer hemolytic effects [38]. Ribavirin-induced anemia is most severe in monkeys, followed by humans, rodents, and dogs [45]. In conclusion, it can be concluded that ribavirin at a dose of 30 mg/kg is safe to use in dogs with CDV and lessens the severity of CD-related anemia without producing evident hemolytic anemia.

When the high leukocyte levels are considered, a secondary bacterial infection [6] may be the reason for the high PLT values in group A. The reduction in PLT values in ribavirin-treated groups during treatment is consistent with reports that ribavirin produces thrombocytopenia [38,40].

An elevated serum AST activity and a higher ALT than AST [46] and high GGT activity [47] indicate liver disease in dogs. As is well known, liver enzyme activity is slightly elevated in CDV infection [13]. The AST and GGT activities of the treatment groups in this study did not differ statistically significantly. However, the ALT values of the A and A+R+P groups were higher than those of the other groups ($P<0.05$). Thus, the virus's effects on the liver could generate an increase in ALT. It has been demonstrated that proanthocyanidin [30] and ribavirin [29] had no influence on these enzyme levels in dogs. Similarly, in this study, the ALT activity of the A+R and A+P groups was nearly equivalent to that of the control group but lower than that of the A group ($P<0.05$). Moreover, these groups' final GGT and ALP activities were lower than those of the control group, and their ALT activities were lower than their AST activities. These findings suggest that using ribavirin or proanthocyanidin may be beneficial in reducing disease-related ALT elevations and has no adverse effects on the liver.

ALP activity increased during treatment in group A. ($P<0.05$). Enteritis and osteoclast, osteoblast, and osteocyte degeneration and necrosis caused by CDV [48] were suspected as potential causes of this condition. ALP activity was lower in T10 in the A+R group than in the other groups ($P<0.05$). This decrease may be due to ribavirin use. Because ribavirin has been linked to reduced bone ALP isoenzyme activity in people with chronic hepatitis C infection [49,50].

CDV can cause myocarditis in young dogs, but the histological changes in the myocardium are mild compared to myocarditis caused by parvovirus [51]. Increases in CK levels have been reported in some dogs experimentally infected with CDV [52]. Compared with the control group, CK, CK-MB ($P<0.01$), and AST, markers of myocardial damage [53] were higher in group A, providing evidence of myocarditis in CDV infection. In patients with hantavirus renal syndrome disease, ribavirin therapy has reportedly been associated with a decrease in CK-MB activity [54]. Confirming this information, CK and CK-MB activities decreased numerically in the A+R group as treatment progressed. Thus, it can be claimed that the using ribavirin in CDV infection effectively prevents cardiac damage.

According to reports, the CREA values were unaffected by using ribavirin in dogs and cats [29,55] or proanthocyanidin in dogs [30]. However, since ribavirin is excreted through the kidneys, it tends to accumulate in the kidneys in the presence of renal dysfunction [56]. Only the CREA values of the A+R group increased gradually during treatment. Considering the decrease in AST, CK, and CK-MB levels in the A+R group as the treatment continued, it was thought that the high CREA values in T0 might have been caused by muscle damage, and the high on other days ($P<0.01$) might have resulted from kidney damage in which ribavirin also played a role.

Anorexia, protein-losing enteropathies, hepatic disorders, maldigestion, and severe malnutrition can all cause hypocholesterolemia in dogs [57]. The A+R and A+P groups' CHOL levels at T0 were lower than those of the control group ($P<0.01$), and diarrhea and maldigestion were assumed to cause this decline. The low glucose, ALB, and TP levels ($P<0.05$) of these groups at T0 also support this inference. Proanthocyanidin has been observed to markedly lower CHOL levels in rats [58,59]. The A group's CHOL levels increased during the treatment, but the A+R+P group's CHOL levels reduced, while the A+P group's increase was the smallest. Therefore, it may be asserted that the use of proanthocyanidin prevents the increase of CHOL levels in dogs with CDV.

Mild AMY activity elevation occurs in dogs with acute pancreatitis, acute enteritis, perforated duodenal ulcers, intestinal torsion, and infarctions [46]. In group A, AMY values gradually increased, and most dogs had mild diarrhea. Inclusion bodies have been found in pancreatic tissue associated with CD [60,61]. Therefore, it was assumed that CDV-affected pancreatic tissue and enteritis caused this rise. Studies show that proanthocyanidin effectively reduced high levels of AMY and alleviated pancreatic damage in rats with acute pancreatitis [62]. At a dose of 30 mg/kg administered to rats, ribavirin was likewise seen not to damage the pancreas [63]. The AMY values of the A+R and A+P groups at T10 approached the control group values. These findings concluded that treating ribavirin or proanthocyanidin prevented the disease's associated elevations in AMY. The A+R+P group had higher AMY activity at T3 and T7 than the A and control groups ($P<0.05$). At the same time, the most severe diarrhea cases were detected in this group. Thus, at high AMY levels, pharmacological interactions between ribavirin and proanthocyanidin, CDV's impact on pancreatic tissue, and the presence of severe enteritis may have played a role.

Albumin levels are mostly decreased in renal glomerular diseases, protein-losing enteropathies, malnutrition, and liver diseases [46]. Hypoalbuminemia has been reported to occur in CD [13]. The ALB values are reported to be unaffected by the usage of ribavirin [29] or proanthocyanidin [30]. ALB, TP, and glucose levels were lower ($P<0.05$), and CREA levels were higher ($P<0.01$) in the A+R and A+P groups compared to the

control group, while there was no significant change in liver enzyme activities. These findings led to the inference that low ALB levels in these group would be caused by infection, malnutrition, and renal injury. The gradual decrease in TP and ALB values in the A+R+P group was attributed to the dogs having severe enteritis. Dogs with CDV [13] and cats receiving ribavirin [55] had decreased blood Ca levels. The A+R group exhibited the lowest Ca values. Ribavirin and CDV infection were suspected of contributing to this decline, in addition to the low baseline value.

Reportedly, CDV can be detected in whole blood samples two days after experimental infection in dogs, peaking on day six and dramatically declining on day twelve [64]. The absence of CDV in the leukocyte layer of six dogs at T0 can be attributed to the dogs being generally asymptomatic and not in the viremia stage. The increase in viral load in more dogs in group A in the following days of treatment showed that classical treatment was insufficient to reduce viral shedding. The highly antiviral effect of ribavirin and proanthocyanidin against CDV has been demonstrated [19,27,65]. Supporting this information, the best groups in lowering or stopping viral shedding were A+R and A+P, respectively. As a result, it can be argued that using ribavirin or proanthocyanidin in CD reduces CDV shedding. In PT10, no dogs survived in the A+R+P group, but two dogs survived in the A, A+R, and A+P groups. While viral shedding continued in group A, it had ceased in the other groups. However, in the A+R group, viral shedding ended earlier (T7). This action suggested that ribavirin was more efficient than proanthocyanidin at lowering and preventing viral shedding.

The study's shortcomings include the small number of animals in each group and the lack of inflammatory markers to evaluate treatment efficacy. This study, however, is regarded significant in terms of analysing the impact of ribavirin and proanthocyanidin use on clinical outcomes, hematological and biochemical parameters, viral shedding, and side effects in CDV-infected dogs.

## 5. CONCLUSION

Classical treatment was unable to enhance clinical outcomes, lessen viral shedding, or prevent cardiac damage. In terms of survival rates, it produced the same outcomes as ribavirin, nevertheless. Ribavirin administration to CDV-positive dogs caused leukopenia and weight loss, decreased serum Ca levels and was associated with kidney damage. On the other hand, ribavirin had no adverse effect on erythrocyte parameters, reduced the severity of CD-related anemia, did not induce liver damage, and had a beneficial effect in preventing cardiac damage and the rise in disease-associated AMY activity. The administration of proanthocyanidin in CDV-positive dogs was found to have good effects on causing an increase in leukocyte counts, preventing the rise in disease-related AMY activity, reducing CHOL levels, and did not cause liver and kidney damage. Proanthocyanidin and ribavirin achieved the most remarkable improvements in clinical course and survival rates, respectively. Ribavirin and proanthocyanidin produced the best results in terms of reducing or stopping viral shedding, respectively. Therefore, to limit the spread of the disease, it was considered beneficial to include ribavirin in the treatment, particularly in areas where dogs are collectively sheltered. Ribavirin-proanthocyanidin therapy decreased viral shedding, mitigated the leukopenia-inducing effects of ribavirin, did not result in liver or kidney damage, but quickly worsened the dogs' general health. It is advised to carry out experiments with more animals in the groups to corroborate the findings of this study and to gain comprehensive information about the pharmacokinetics and toxicity of combining these two medications.

## Acknowledgements

This study was self-funded and prepared depending on the Doctoral thesis of Şükrü Değirmençay. The author would like to express his gratitude to his thesis advisor, Prof. Dr M. Sinan Aktaş, for his guidance. The study's virological analysis was carried out by Assoc. Prof. Dr Mehmet Özkan Timurkan, for which the author is grateful.

## REFERENCES

[1] Beineke A, Puff C, Seehusen F, Baumgartner W. Pathogenesis and immunopathology of systemic and nervous canine distemper. Vet Immunol Immunopathol. 2009;127(1–2):1–18.
[2] Carpenter MA, Appel MJ, Roelke-Parker ME, Munson L, Hofer H, East M, et al. Genetic characterization of canine distemper virus in Serengeti carnivores. Vet Immunol Immunopathol. 1998;65(2–4):259–66.
[3] Kingsbury DW. Paramyxoviridae. Intervirology. 1978;10(3):137–52.
[4] Greene CE, Vandevelde M. Canine distemper. In: Greene CE, editor. Infectious diseases of the dog and cat. 4 th. St Louis,: Saunders; 2012. p. 25–42.
[5] Sykes JE. Canine distemper virus infection. In: Sykes JE, editor. Canine and feline infectious diseases. 1 st. St Louis: Saunders; 2014. p. 152–65.
[6] Leisewitz AL, Carter A, van Vuuren M, van Blerk L. Canine distemper infections, with special reference to South Africa, with a review of the literature. J S Afr Vet Assoc. 2001;72(3):127–36.
[7] Martella V, Elia G, Buonavoglia C. Canine distemper virus. Vet Clin North Am Small Anim Pr. 2008;38(4):787–97, vii–viii.
[8] Taylor S. Encephalitis, myelitis and meningitis. In: Couto CG, Nelson RW, editors. Small Animal Internal Medicine. 4th ed. St. Louis, Missouri: Mosby Elsevier; 2009. p. 1059–62.
[9] Krakowka S, Axthelm MK, Johnson GC. Canine distemper virus. In: Olsen RG, Krakowka S, Blakeslee JR, editors. Comparative Pathobiology of Viral Diseases. Boca Raton: CRC Press; 1985. p. 137–64.

[10] Shell LG. Canine distemper. Compend Contin Educ Pract Vet. 1990;12(2):173–9.
[11] Ezeibe MCO, Udegbunam RI. Haematology of dogs infected with canine distemper virus. Sokoto J Vet Sci. 2008;7(2):32.
[12] Greene GE, Appel M. Canine Distemper Virus. In: Greene GE, editor. Infectious Disease of the Dog and Cat. 2nd ed. Philadelphia, PA: Saunders; 1998. p. 1–22.
[13] Appel MJ. Pathogenesis of canine distemper. Am J Vet Res. 1969;30(7):1167–82.
[14] Weisbrode SE, Krakowka S. Canine distemper virus-associated hypocalcemia. Am J Vet Res. 1979;40(1):147–9.
[15] Hartmann K. Antiviral and immunomodulatory chemotherapy. In: Greene CE, editor. Infectious diseases of the dog and cat. 2013. p. 10–24.
[16] De Clercq E, Cools M, Balzarini J, Snoeck R, Andrei G, Hosoya M, et al. Antiviral activities of 5-ethynyl-1-beta-D-ribofuranosylimidazole-4-carboxamide and related compounds. Antimicrob Agents Chemother. 1991;35(4):679–84.
[17] Shigeta S, Mori S, Baba M, Ito M, Honzumi K, Nakamura K, et al. Antiviral activities of ribavirin, 5-ethynyl-1-beta-D-ribofuranosylimidazole-4-carboxamide, and 6'-(R)-6'-C-methylneplanocin A against several ortho- and paramyxoviruses. Antimicrob Agents Chemother. 1992;36(2):435–9.
[18] del Toro-Riera M, Macaya-Ruiz A, Raspall-Chaure M, Tallada-Serra M, Pasqual-Lopez I, Roig-Quilis M. [Subacute sclerosing panencephalitis: combined treatment with interferon alpha and intraventricular ribavirin]. Rev Neurol. 2006;42(5):277–81.
[19] Elia G, Belloli C, Cirone F, Lucente MS, Caruso M, Martella V, et al. In vitro efficacy of ribavirin against canine distemper virus. Antivir Res. 2008;77(2):108–13.
[20] Husain SR, Cillard J, Cillard P. Hydroxyl Radical Scavenging Activity of Flavonoids. Phytochemistry. 1987;26(9):2489–91.
[21] Fine AM. Oligomeric proanthocyanidin complexes: history, structure, and phytopharmaceutical applications. Altern Med Rev. 2000;5(2):144–51.
[22] Cheng HY, Lin CC, Lin TC. Antiviral properties of prodelphinidin B-2 3'-O-gallate from green tea leaf. Antivir Chem Chemother. 2002;13(4):223–9.
[23] Iwasawa A, Niwano Y, Mokudai T, Kohno M. Antiviral Activity of Proanthocyanidin against Feline Calicivirus Used as a Surrogate for Noroviruses, and Coxsackievirus Used as a Representative Enteric Virus. Biocontrol Sci. 2009;14(3):107–11.
[24] Takeshita M, Ishida Y, Akamatsu E, Ohmori Y, Sudoh M, Uto H, et al. Proanthocyanidin from blueberry leaves suppresses expression of subgenomic hepatitis C virus RNA. J Biol Chem. 2009;284(32):21165–76.
[25] Xu XY, Xie HH, Wang YF, Wei XY. A-Type Proanthocyanidins from Lychee Seeds and Their Antioxidant and Antiviral Activities. J Agric Food Chem. 2010;58(22):11667–72.
[26] Zhang XY, Li WG, Wu YH, Zheng TZ, Li W, Qu SY, et al. Proanthocyanidin from grape seeds potentiates anti-tumor activity of doxorubicin via immunomodulatory mechanism. Int Immunopharmacol. 2005;5(7–8):1247–57.
[27] Gallina L, Dal Pozzo F, Galligioni V, Bombardelli E, Scagliarini A. Inhibition of viral RNA synthesis in canine distemper virus infection by proanthocyanidin A2. Antivir Res. 2011;92(3):447–52.
[28] Allerton F. BSAVA Small Animal Formulary Part A: Canine and Feline. 10th ed. Allerton F, editor. Gloucester: British Small Animal Veterinary Association; 2020. 98 p.
[29] Mangia SH, Moraes LF, Takahira RK, Motta RG, Franco MMJ, Megid J, et al. The side effects of ribavirin, prednisone and DMSO in dogs naturally infected by canine distemper virus. Pesqui Vet Bras. 2014;34(5):449–54.
[30] Martineau A, Leray V, Lepoudere A, Blanchard G, Bensalem J, Gaudout D, et al. A mixed grape and blueberry extract is safe for dogs to consume. BMC Vet Res. 2016;12(1):162.
[31] Gill M, Srinivas J, Morozov I, Smith J, Anderson C, Glover S, et al. Three-year duration of immunity for canine distemper, adenovirus, and parvovirus after vaccination with a multivalent canine vaccine. J Appl Res Vet Med. 2004;2(4):227–34.
[32] Trebbien R, Chriel M, Struve T, Hjulsager CK, Larsen G, Larsen LE. Wildlife reservoirs of canine distemper virus resulted in a major outbreak in Danish farmed mink (Neovison vison). PLoS One. 2014;9(1):e85598.
[33] Gemma T, Watari T, Akiyama K, Miyashita N, Shin YS, Iwatsuki K, et al. Epidemiological observations on recent outbreaks of canine distemper in Tokyo area. J Vet Med Sci. 1996;58(6):547–50.
[34] Salem NY. Canine viral diarrhea: clinical, hematologic and biochemical alterations with particular reference to in-clinic rapid diagnosis. Glob Vet. 2014;13(3):302–7.
[35] Ertürk N. Köpeklerde parvoviral enteritisin tedavisinde antiviral kullanımının etkinliğinin değerlendirilmesi. Sağlık Bilimleri Enstitüsü, Veteriner İç Hastalıkları Anabilim Dalı. [Tez]: Erzurum: Atatürk Üniversitesi; 2015.
[36] Ogbomo H, Michaelis M, Altenbrandt B, Doerr HW, Cinatl Jr. J. A novel immunomodulatory mechanism of ribavirin in suppressing natural killer cell function. Biochem Pharmacol. 2010;79(2):188–97.
[37] Lindgren C, Grogaard J. [Ribavirin treatment of children with respiratory syncytial virus bronchiolitis]. Tidsskr Nor Laegeforen. 1994;114(17):1928–9.
[38] Weiss RC, Cox NR, Boudreaux MK. Toxicologic effects of ribavirin in cats. J Vet Pharmacol Ther. 1993;16(3):301–16.
[39] Axthelm MK, Krakowka S. Canine distemper virus-induced thrombocytopenia. Am J Vet Res. 1987;48(8):1269–75.
[40] Aydın M, Aksöz E, Korkut O, Akhan S. Farklı Pegile İnterferon-α Molekülleriyle Ribavirin Kombinasyonlarının Hematolojik Yan Etkiler

Açısından Karşılaştırılması. Klimik Derg. 2014;27(3):99–102.
[41] Liu YZ, Cao YG, Ye JQ, Wang WG, Song KJ, Wang XL, et al. Immunomodulatory effects of proanthocyanidin A-1 derived in vitro from Rhododendron spiciferum. Fitoterapia. 2010;81(2):108–14.
[42] Huang Y, Zhao H, Cao K, Sun D, Yang Y, Liu C, et al. Radioprotective Effect of Grape Seed Proanthocyanidins In Vitro and In Vivo. Oxid Med Cell Longev. 2016;2016:5706751.
[43] Kowdley K V. Hematologic side effects of interferon and ribavirin therapy. J Clin Gastroenterol. 2005;39(1 Suppl):S3-8.
[44] Canonico PG, Kastello MD, Spears CT, Brown JR, Jackson EA, Jenkins DE. Effects of ribavirin on red blood cells. Toxicol Appl Pharmacol. 1984;74(2):155–62.
[45] Lin C-C, Yeh L-T, Luu T, Lourenco D, Lau JYN. Pharmacokinetics and metabolism of [(14)C]ribavirin in rats and cynomolgus monkeys. Antimicrob Agents Chemother. 2003;47(4):1395–8.
[46] Turgut K. Karaciğer Hastalıkları ve Testleri. In: Turgut K, editor. Veteriner Klinik Laboratuvar Teşhis. 2. Baskı. Konya: Bahçıvanlar Basım Sanayi A.Ş.; 2000. p. 202–57.
[47] Özkanlar Y. Laboratuvar Değerler ve Sonuçların Yorumlanması. In: Özkanlar Y, editor. Küçük Hayvan Medikal Ayırıcı Tanı Bir Liste Kitabı. 1. Baskı. Malatya: Medipres; 2016. p. 263–301.
[48] Baumgartner W, Boyce R, Alldinger S, Axthelm M, Weisbrode S, Krakowka S, et al. Metaphyseal bone lesions in young dogs with systemic canine distemper virus infection. Vet Microbiol. 1995;44(2–4):201–9.
[49] Abenavoli L, Mazza M, Almasio P. The optimal dose of ribavirin for chronic hepatitis C: From literature evidence to clinical practice: The optimal dose of ribavirin for chronic hepatitis C. Hepat Mon. 2011;11(4):240–6.
[50] Moreira RO, Balduíno A, Martins HSLH, Reis JSN, Duarte MEL, Farias MLF, et al. Ribavirin, but not interferon alpha-2b, is associated with impaired osteoblast proliferation and differentiation in vitro. Calcif Tissue Int. 2004;75(2):160–8.
[51] Ware W. Cardiovascular System Disorders. In: Nelson R, Couto C, editors. Small Animal Internal Medicine. 5th ed. Canada: Elsevier Mosby; 2014. p. 141.
[52] Higgins RJ, Krakowka S, Metzler AE, Koestner A. Canine distemper virus-associated cardiac necrosis in the dog. Vet Pathol. 1981;18(4):472–86.
[53] Bakirel U, Gunes S. Value of cardiac markers in dogs with chronic mitral valve disease. Acta Vet Brno. 2009;59(2–3):223–9.
[54] Zhang Q, Tang R, Yuan G. [The treatment effect of ribavirin to hemorrhagic fever with renal syndrome on the kinetics of serum creatine phosphate kinase isoenzyme]. Chin J Exp Clin Virol. 1999;13(3):266–8.
[55] Bogdanchikova N, Vázquez-Muñoz R, Huerta-Saquero A, Pena-Jasso A, Aguilar-Uzcanga G, Picos-Díaz P, et al. Silver nanoparticles composition for treatment of distemper in dogs. Intern J Nanotechnol. 2016;13:227–37.
[56] Jain AB, Eghtesad B, Venkataramanan R, Fontes PA, Kashyap R, Dvorchik I, et al. Ribavirin dose modification based on renal function is necessary to reduce hemolysis in liver transplant patients with hepatitis C virus infection. Liver Transpl. 2002;8(11):1007–13.
[57] Robbins R, Viviano KR. Hypocholesterolemia and nonregenerative, suspected immune-mediated, anemia: Report of 3 canine cases. Can Vet J. 2017;58(10):1100–4.
[58] Mansouri E, Khorsandi L, Zare Moaiedi M. Grape Seed Proanthocyanidin Extract Improved some of Biochemical Parameters and Antioxidant Disturbances of Red Blood Cells in Diabetic Rats. Iran J Pharm Res IJPR. 2015;14(1):329–34.
[59] El-Adawi H, Mohsen M, Youssef D, El-Sewedy S. Study on the Effect of Grape Seed Extract on Hypercholestrolemia: Prevention and Treatment. Int J Pharmacol. 2006;2(6):593–600.
[60] Woo G, Jho Y, Bak E. Canine Distemper Virus Infection in Fennec Fox (Vulpes zerda). J Vet Med Sci. 2010;72(8):1075–9.
[61] Caswell J, Williams K. Respiratory System. In: Maxie M, editor. Jubb, Kennedy, and Palmer's Pathology of Domestic Animals. 6th ed. China: Elsevier; 2016. p. 575.
[62] Akyuz C, Sehirli A, Topaloglu U, Ogunc A, Cetinel S, Sener G. Protective Effects of Proanthocyanidin on Cerulein-induced Acute Pancreatic Inflammation in Rats. Gastroenterol Res. 2009;2:20–8.
[63] Motor S, Alp H, Senol S, Pinar N, Motor V, Kaplan I, et al. Comparison of the chronic effects of ribavirin and caffeic acid phenethyl ester (CAPE) on pancreatic damage and hepatotoxicity. Int J Clin Exp Med. 2014;7:1005–13.
[64] Sehata G, Sato H, Ito T, Imaizumi Y, Noro T, Oishi E. Use of quantitative real-time RT-PCR to investigate the correlation between viremia and viral shedding of canine distemper virus, and infection outcomes in experimentally infected dogs. J Vet Med Sci. 2015;77(7):851–5.
[65] Carvalho O V, Saraiva GL, Ferreira CGT, Felix DM, Fietto JLR, Bressan GC, et al. In-vitro antiviral efficacy of ribavirin and interferon-alpha against canine distemper virus. Can J Vet Res. 2014;78(4):283–9.

Cilt 12, Sayı 1, Sayfa 136-143, 2023 Volume 12, Issue 1, Page 136-143, 2023

Araştırma Makalesi https://doi.org/10.46810/tdfd.1206130 Research Article

Türk Doğa ve Fen Dergisi
Turkish Journal of Nature and Science
www.dergipark.gov.tr/tdfd

# Time-Dependent Change of Plant Nutrients in Italian Grass (*Lolium multiflorum*) after Foliar Fertilization

**Nureddin ÖNER[1], Ali Rıza DEMİRKIRAN[2*], Filiz ÖNER[3]**

[1] Muğla Sıtkı Koçman University, Fethiye Ali Sıtkı Mefharet Koçman Vocational School, Plant and Animal Production, Organic Farming Program, Muğla, Türkiye, e-mail: nureddinoner@mu.edu.tr
[2] Bingöl University, Agricultural Faculty, Soil Science and Plant Nutrition Department, Bingöl, Türkiye, e-mail: ademirkiran@bingol.edu.tr
[2] Muğla Sıtkı Koçman University, Agricultural Application and Research Center, Kötekli-Menteşe, Muğla, Türkiye, e-mail: filizoner@mu.edu.tr
Nureddin ÖNER ORCID No: 0000-0001-9314-8108
Ali Rıza DEMİRKIRAN ORCID No: 0000-0002-0086-0137
Filiz ÖNER ORCID No: 0000-0002-8885-6318

**Corresponding author: ademirkiran@bingol.edu.tr*

(Received: 17.11.2022, Accepted: 10.03.2023, Online Publication: 27.03.2023)

**Keywords**
*Lolium multiflorum*, Algae, Foliar fertilization, Plant nutrient

**Abstract:** This research was carried out in the Keyfoturağı area of Menteşe district of Muğla, Türkiye, in 2021 year to examine the effects of different fertilizer doses with algae on the ryegrass yield and plant nutrient content of Italian grass (*Lolium multiflorum* attain). The fertilizer applications as algae (A: 200 ml) and algae + fertilizer 1 (A+F1: A+500 ml urea, 400 ml $MgSO_4$, 300 ml $ZnSO_4$, 200 ml borax, 100 ml $FeSO_4$, 100 ml $MnSO_4$, 15 ml $CuSO_4$), algae + fertilizer 2 (A+F2: A+625 ml urea, 500 ml $MgSO_4$, 375 ml $ZnSO_4$, 250 ml borax, 125 ml $FeSO_4$, 125 ml $MnSO_4$, 25 ml $CuSO_4$) were applied at different rates to Italian grass plant. Then, the whole plant sample is taken for nine days from the first day and the plants were analyzed for the nutrient contents. According to the results of the research, The wet weight of plant, nitrogen (N), potassium (K), calcium (Ca), magnesium (Mg), sodium (Na), sulfur (S), boron (B), zinc (Zn), copper (Cu), iron (Fe) and manganese (Mn) contents in the plant were found to be statistically significant ($p<0.01$). The highest moisture in A and A+F1 applications, the highest N, Ca, and Mn contents at A+F1 application and the highest S, B, Zn, Cu, and Fe contents at A+F2 application, with the highest K content at A and Na content at control application were determined.



# Yaprak Gübrelemesinden Sonra İtalyan Çiminde (*Lolium multiflorum*) Bitki Besin Elementlerinin Zamana Bağlı Değişimi

**Anahtar Kelimeler**
*Lolium multiflorum*, Yosun, Yaprak gübreleme, Bitki besin elementi

**Öz:** Bu araştırma, 2021 yılında Muğla'nın Menteşe ilçesi Keyfoturağı mevkiinde farklı dozlarda yosun ve kimyasal gübrelerin İtalyan çiminde (*Lolium multiflorum* attain) çim verimi ve bitki besin maddesi içeriği üzerine etkilerini incelemek amacıyla yapılmıştır. Yosun (A: 200 ml), yosun + gübre 1 (A+F1: A+500 ml üre, 400 ml $MgSO_4$, 300 ml $ZnSO_4$, 200 ml boraks, 100 ml $FeSO_4$, 100 ml $MnSO_4$, 15 ml $CuSO_4$) ve yosun + gübre 2 (A+F2: A+625 ml üre, 500 ml $MgSO_4$, 375 ml $ZnSO_4$, 250 ml boraks, 125 ml $FeSO_4$, 125 ml $MnSO_4$, 25 ml $CuSO_4$) olarak belirlenen gübreler İtalyan çimi bitkisine uygulanmıştır. Daha sonra ilk günden itibaren dokuz gün boyunca tüm bitki örneği alınmış ve bitkilerin besin içerikleri analiz edilmiştir. Araştırma sonuçlarına göre, bitki yaş ağırlığı ile azot (N), potasyum (K), kalsiyum (Ca), magnezyum (Mg), sodyum (Na), kükürt (S), bor (B), çinko (Zn), bakır (Cu), demir (Fe) ve mangan (Mn) içerikleri istatistiksel olarak önemli bulunmuştur ($p<0.01$). En yüksek nem A ve A+F1 uygulamalarında, en yüksek N, Ca ve Mn içerikleri A+F1 uygulamasında ve en yüksek S, B, Zn, Cu ve Fe içerikleri A+F2 uygulamasında, en yüksek K içeriği A uygulamasında ve en yüksek Na içeriği kontrol uygulamasında belirlenmiştir.

## 1. INTRODUCTION

Soil unfertility processes occur through physical, chemical and biological (loss of biodiversity, loss of organic matter etc.) [1]. One of the important soil problems expressed by the United Nations Food and Agriculture Organization (FAO) is the loss of soil organic matter [2]. Organic matter affects the physical, chemical and biological properties of soils, increasing the cation exchange capacity, infiltration and water holding capacity of the soil, and being the main source of nutrients such as N, P, and S.

Many researchers have reported that chemical fertilizers and organic fertilizers are effective in increasing plant yield and soil properties as physical, chemical and biological. Numerous studies have been conducted on the positive effects of organic fertilizers with applying to the different plant growth [3, 4, 5, 6, 7, and 8].

Considering the effect of leonardite on nutrient contents of rye plant, it was reported that the applications were the positive effect on plant growth and increases the K, Mg, Ca, Mn and Fe contents of plant nutrient [9]. It was also reported that leonardite increases the dry matter and nutrient contents (N, P, K, Ca, Mg, Fe, Cu, Zn, and Mn) in the ryegrass [10].

An experiment was conducted to determine the effect of biostimulants (Algex, Tytanit and Asahi SL) and nitrogen on Italian ryegrass. Algex biostimulant to Italian ryegrass produced the most beneficial response in terms of the share of NDF, ADF, and ADL fractions in the plant dry matter. Increasing nitrogen rates significantly reduced the quantity of analyzed fiber fractions, and increased grass digestibility [11].

It was found that the P, K and Mg concentrations of the plant increased with the application of leonardite-humic acid and humate to grass [12]. When humic material was applied to the grass, taking of N and Ca increased and reported that there was no significant change in P, K and Fe contents, whereas some physical properties of the plant increased and some of them decreased [13].

In a research it was determined that the effect of slurry applied on its own and supplemented with mineral fertilizers or soil conditioners (UGmax and Humus Active) on the yield and some properties of *Lolium multiflorum* (Dukat var.) Interaction of slurry with soil conditioners resulted in a lower yield compared to the plot where slurry was used on its own. The highest total protein content was obtained to *Lolium multiflorum* treated with slurry supplemented with mineral fertilizers [14]. The increasing yield as a response to natural fertilizer applied to grassland was also recorded by Barszczewski et al. [15].

Kotlarz et al. [16] as well as Kasperczyk [17] confirm that the level of nitrogen fertilizer determines total protein content in forage. Many authors point out that total protein content is not always increased in proportion to the applied nitrogen [18, 19, and 20].

In this research, the effects of different fertilizer doses with algae on the ryegrass yield and plant nutrient content of Italian grass (*Lolium multiflorum*) was carried out in the Keyfoturağı area of Menteşe district of Muğla province, Türkiye, in 2021.

## 2. MATERIAL AND METHOD

This study was carried out in irrigated conditions in the producer area in the Keyfoturağı locality of Menteşe district of Muğla province in 2021. Italian Grass (*Lolium multiflorum*) was use in the study. The experiment on the winter ryegrass plant was established on 16 May 2021 after the first form. The size of each parcel is 100 m x 10 m = 1000 $m^2$ which completely randomized design with three replicates.

The fertilizer were applied as fertigation and doses given in Table 1. Fertilizer doses were determined by considering the amount of plant nutrients in the ryegrass plant [21], which was analyzed by cutting 5 cm above the soil surface when it was 15 cm before the experiment was established. The second sample in the plant was taken from the plant when it was 30 cm long before the first fertilizer application on 30 May 2021.

The applications of the experiment were planned for searching the effect of organic material (A, algae, DynaMix) and chemical fertilizer doses (F1 and F2) with constant rate of the algae and increasing chemical fertilizer.



**Table 1**. Algae and fertilizers used in the experiment and its amounts (g 100 $L^{-1}$ water)

| C (Control) | A (Algae, DynaMix) | A+F1 (Algae+ Fertilizers 1) | A+F2 (Algae+ Fertilizers 2) |
|---|---|---|---|
| Only water | 200 ml | 200 ml algae | 200 ml algae |
| | | 500 ml urea (46% N) | 625 ml urea |
| | | 400 ml $MgSO_4$ (9,6% Mg) | 500 ml $MgSO_4$ |
| | | 300 ml $ZnSO_4$ (22% Zn) | 375 ml $ZnSO_4$ |
| | | 200 ml Boraks (11,5% B) | 250 ml boraks |
| | | 100 ml $FeSO_4$ (17% Fe) | 125 ml $FeSO_4$ |
| | | 100 ml $MnSO_4$ (31% Mn) | 125 ml $MnSO_4$ |
| | | 15 ml $CuSO_4$ (25% Cu) | 25 ml $CuSO_4$ |

To the leaves on 30 May 2021; Control (C), algae (DynaMix, A) and algae + fertilizer 1 (A+F1), algae + fertilizer 2 (A+F2) were applied. A (DynaMix) was applied to 100 L of water in 200 ml, and A+F1 and A+F2 were applied in the ratios given in table 1 to urea, magnesium sulfate, zinc sulfate, borax, iron sulfate, manganese sulfate and copper sulfate. In practice, it was thrown with 25 L of water for each parcel. After the first form, 36 kg of ammonium sulfate and 35 kg of potassium sulfate were irrigated 3 times with a sprinkler irrigation system on 18 May 2021. After the first application, the effect of the applications on the plant nutrients in the ryegrass plant was investigated in the each samples taken by cutting from the soil surface after 9 days. After

harvesting on 09 June 2021, the drum mower attached to the tractor, which takes about 100 $m^2$ in each plot, was determined as kg $da^{-1}$ in wet weight. After 40 days of planting, the harvested ryegrass samples, which were cut 5 cm above the soil surface, were washed with tap water and distilled water, then dried at 70 ºC for 48 hours, ground and made ready for analysis.

In leaf samples, total N analysis was performed by kjeldahl method [22], total K, Ca, Mg, Na, S, Cu, Fe, Zn, Mn, B and Mo analyzes were performed in microwave (20 minute at 190 °C and 1600 W at 40 °C) by wet burning method with acid (0.5 g sample +2 ml $H_2O_2$ + 6 ml $HNO_3$), filtered with filter paper (whatman no; 42) and made up to 50 ml with distilled water [23] and was analyzed in the ICP-OES.

The data of the applications, leaf sampling times and application x leaf sampling times were statistically analyzed. All data obtained were statistically analyzed using one-way ANOVA with the SPSS statistical software package program (Version 22.0, SPSS Inc., Chicago, IL, USA). Duncan's test ($p < 0.05$ and $p < 0.01$) was performed to evaluate the difference of each treatment. The research design was confirmed a completely randomized design with four replications.

## 3. RESULTS

The yield data obtained in 0.2% A, 0.2% A+F1, 0.2% A+ F2 and control plots applied to the ryegrass plant were given in Table 2.

**Table 2**. The wet weights of plant, differences and increases by applications

| Applications | Wet weight (kg $da^{-1}$) | Difference in the wet weight | Increase (%) |
|---|---|---|---|
| **Control** | 1736.96 | 0 | 0 |
| **A** | 2251.30 | 515 | 29.61 |
| **A+F1** | 2241.28 | 505 | 29.03 |
| **A+F2** | 2270.14 | 534 | 30.69 |

As can be seen in Table 2, algae (DynaMix) application (0.2%) increased the wet weight of plant by 515 kg $da^{-1}$ (29.61%) compared to the control application. There was no difference between the application of only 0.2% algae and the application of 0.2% A+F1 and F2. Therefore, it can be say more economical to use 0.2% algae (DynaMix) alone. When the data obtained in the study were examined, the significant levels of applications in the Table 3 and 4, the effects of the different days in the Table 5, the fertilizer applications in the Table 6, and interactions between application and time in the Table 7 were given.

**Table 3**. The significant levels of moisture and macro nutrient contents of ryegrass with applications.

| Analyses / Application | Moisture | N | K | Ca | Mg | S |
|---|---|---|---|---|---|---|
| Fertilizer doses | ** | ** | ** | ** | ns | ** |
| Time of taking leaf samples | ** | ** | ** | ** | ** | ** |
| Interaction of fertilizer doses and sampling time | ** | ** | ** | ** | * | ** |

* p< 0.05, ** p< 0.01, ns;

**Table 4**. The significant levels of micro nutrient contents of ryegrass with applications.

| Analyses / Application | Na | B | Zn | Cu | Fe | Mn |
|---|---|---|---|---|---|---|
| Fertilizer doses | ** | ** | ** | ** | ** | ** |
| Time of taking leaf samples | ** | ** | ** | ** | ** | ** |
| Interaction of fertilizer doses and sampling time | ** | ** | ** | ** | ** | ** |

** p< 0.01, ns; non significant.

### 3.1. Moisture content

In three of the fertilizer applications, the amount of moisture obtained in the plant was higher than the control group. With high moisture, the plant received more water in the soil and therefore more plant nutrients with all three applications (Table 6). The highest moisture value was obtained in A and A+F1 applications. When we examine the effect of time on moisture, the lowest moisture value on the 1st day and the highest humidity value on the 2nd day were obtained (Table 5). As the number of days increased, the amount of moisture in the plant decreased. When we evaluated the interaction of time x fertilizer applications, except the control application on the 2nd day, the other three applications were in the highest three groups (Table 7).

### 3.2. Nitrogen content

The amount of nitrogen in the plant, which was low in the first days, reached the highest value in the 9th, 6th , 7th and 8th days, respectively (Table 5). There was approximately 52.2% nitrogen content increased between day 1 and day 8. This may be due to 500 g 100 $L^{-1}$ urea fertilizer in practice. While the lowest nitrogen amount was obtained with A application to ryegrass plant, the highest nitrogen amount was obtained in A+F1 application (Table 6).

A most regular distribution was not determined in the time x fertilizer interaction. The highest nitrogen value was obtained in the A+F1 application on the 8th day, and the lowest in the A application on the 2nd day (Table 7).

### 3.3. Potassium content

When we look at the potassium in the plant in general according to the days, the potassium amount, which was high in the first days, decreased with the increase in the number of days. The highest potassium value was obtained on the 1st day, and the lowest value was obtained on the 9th day (Table 5). When we evaluated the effect of the applied fertilizers on the amount of potassium, the A application reached the highest potassium concentration compared to the control and provided an increase of approximately 28%. The order of decrease in potassium amount continued as A+F2, A+F1 and control (Table 6).

In the sampling time x fertilizer type interaction, the highest potassium content was obtained with the A application on the 1st day, while the lowest potassium was obtained in the control application on the 4th, 6th and 9th days and in the A application on the 7th day (Table 7).

Similar to our study, Ren et al. [24] stated that nitrogen applications increased the potassium content in ryegrass leaves from 3.0% to 3.2%. DeConti et al. [25] determined that the copper and iron fertilizers they applied to the ryegrass plant increased the potassium content of the plants from 0.85% to 2.0%, and Yolcu et al. [9] reported that barn manure, zeolite and leonardite applied to ryegrass significantly increased potassium content in the above-ground parts of the plant.

### 3.4. Calcium content

The highest calcium value was obtained on the fourth day, and the lowest calcium ratio was obtained on the 3rd, 7th, 8th and 9th days, while the highest value was obtained on the 1st day (Table 5). When we evaluated the effect of fertilizers on calcium amount, the highest amount of calcium was obtained in A+F1 application, and the lowest in A and A+F1 applications (Table 6). In the time x fertilizer interaction, the highest value was obtained in the 4th day A+F1 application and the lowest value was obtained in the 7th day A+F2 application (Table 7).

Working on a similar subject, Ren et al. [24] reported that the calcium content in ryegrass leaves increased from 0.39% to 0.49% with nitrogen applications. DeConti et al. [25] stated that Cu and Fe fertilizers applied to ryegrass increased the calcium content of plants (from 0.60% to 0.66%). In another study, Yolcu et al. [9] reported that organic materials applied to ryegrass significantly increased the calcium in the plant.

### 3.5. Magnesium content

The effect of fertilizer applications on the amount of magnesium element in the plant was determined as the highest on the 1st day and the lowest on the 9th day, and a decrease of 33% occurred (Table 5). The effect of fertilizer doses was not found to be statistically significant (Table 3). Only three different groups were formed in the time x fertilizer type interaction (Table 7). There was a 48.57% decrease between the highest magnesium value and the lowest.

Ren et al. [24] reported that N increased the magnesium content in ryegrass leaves from 0.23% to 0.27%. DeConti et al. [25] reported that Cu and Fe increased in the magnesium content of the ryegrass plant from 0.17% to 0.23%. Yolcu et al. [9] also reported that organic materials applied to ryegrass significantly increased the magnesium in the plant.

### 3.6. Sulfur content

It was determined that the effect of fertilizer applications on the amount of sulfur in the plant decreased by 95.94% at the highest level on the 1st day and at the lowest level on the 5th and 6th days (Table 5).

In the A+F2 application, the highest sulfur content was determined in the control group and the lowest sulfur content (Table 6). This may be due to the presence of sulfur in the sulphate form in the applied fertilizers. In the time x fertilizer type interaction, the largest amount of sulfur was obtained in the A application on the 1st day. The lowest sulfur content was determined in all doses of the 5th and 6th days in the same group (Table 7).

Looking at the previous studies, the copper and iron fertilizers applied to the ryegrass plant caused a significant increase in the sulfur (from 0.21% to 0.36%) content [25]. It was reported that the organic materials applied to ryegrass significantly increased the sulfur in the above-ground parts of the plant [9].



### 3.7. Sodium content

Sodium element was determined at the lowest level in 2 days and at the lowest level in 8th and 9th days (Table 5). There was a 75.2% decrease between the highest and lowest sodium elements. While the highest sodium amount was determined in the control group, the sodium amount decreased with fertilizer application. The highest was determined in the control group and the lowest in the A+F2 application (Table 6).

Between the time and fertilizer type interaction, the highest values were determined in the control application on the 4th, 3rd, 2nd and 1st days, respectively, while the lowest values were determined in the 9 th day with A application (Table 7).

### 3.8. Boron content

In the ryegrass plant, the highest boron element was obtained on the 1st day and the lowest on the 4th day (Table 5). In 0.2% DynaMix + Fertilizer 2 application, the highest application was followed by A+F1, A and control groups, respectively, with a decrease (Table 6). In the time and fertilizer type interaction, the highest boron was

determined in the 1st day A+F2 application and the lowest in the 1st and 4th day control group. The presence of boron fertilizer in Fertilizer 1 and 2 applications resulted in higher boron content in these plots (Table 7).

According to Yolcu et al. [9] reported that barn manure, zeolite and leonardite applied to ryegrass significantly increased the tubing in the above-ground parts of the plant.

### 3.9. Zinc content

Zinc element concentration was determined to be the highest on the 1st day and the lowest on the 7th day (Table 5). Between the two times, there was a 51.07% reduction. In the A+F2 application, this highest application was followed by the A+F1, control and A application (Table 6).

In the interaction of time x fertilizer type, the highest amount of zinc was determined in the 1st day A+F2 application and the lowest in the 7th day control group. The use of zinc sulphate fertilizer containing zinc element in Fertilizer 1 and Fertilizer 2 applications increased zinc in these applications (Table 7).

Yolcu et al. [9] also reported that barn manure, zeolite and leonardite applied to ryegrass increased the zinc content in the above-ground parts of the plant.

### 3.10. Copper content

The effect of the applications on the amount of copper depending on time was determined at the highest level on the 1st day and at the lowest level on the 6th day (Table 5). In the A+F2 application, this highest application was followed by the A+F1, A and control application. The use of copper sulphate fertilizer in Fertilizer 1 and Fertilizer 2 applications increased the copper element in these applications (Table 6).

In the time x fertilizer type application, the highest copper amount was determined in the 1st day in the A+F2 application, and the lowest in the 5th and 9th days control group (Table 7). According to Yolcu et al. [9] reported that barn manure, zeolite and leonardite applied to ryegrass increased the copper content in the above-ground parts of the plant.

### 3.11. Iron content

While the highest amount of iron was obtained on the first day, the lowest value was obtained on the 7th day (Table 5). In the A+F2 application, this highest application was followed by the A+F1, A and control application. The use of ferrous sulphate fertilizer in Fertilizer 1 and Fertilizer 2 applications increased the concentration of iron element in these applications (Table 6).

Between the application of time and fertilizer variety interaction, the highest iron content was determined in the 1st day A+F2 application in the control group on the 6th day and the lowest iron content in the 9th day 0.2 A+F1 application (Table 7). According to Yolcu et al. [9] reported that barn manure, zeolite and leonardite applied to ryegrass significantly increased the iron content of the above-ground parts of the plant.

### 3.12. Manganese content

The highest manganese concentration was determined on the 1st day and the lowest on the 7th day in the ryegrass plant of the treatments (Table 5). In the A+F1 application, this highest application was followed by the A+F1, A and control application (Table 6).

The use of manganese sulfate fertilizer in F1 and F2 applications increased the concentration of manganese in these applications. In the application of time x fertilizer variety, the highest manganese content was determined in the 1st day A+F2 application and the lowest manganese content were determined in the 7th day A+F2, the 9th day A+F1 and the 8th day A applications (Table 7).

Ren et al. [24] stated that nitrogen applications caused an increase of up to 10 mg $kg^{-1}$ (from 22 mg $kg^{-1}$ to 32 mg $kg^{-1}$) manganese content in ryegrass leaves. According to Yolcu et al. [9] reported that barn manure, zeolite and leonardite applied to ryegrass significantly increased the manganese content in the above-ground parts of the plant.

Regarding the subject from previous studies, Fortún et al. [26] showed that humic acid applications obtained from different sources and methods to the ryegrass plant which in the above-ground parts increased the total macro element contents of the plant from 10% to 11.5%, and the micro element contents in total from 260 mg $kg^{-1}$ to 720 mg $kg^{-1}$.

The results were obtained in our research that was observed that organic (algae) and inorganic fertilization increased the macro and micro element contents of *Lolium multiflorum* plant. The moisture of plant and macro and micro element contents (nitrogen, potassium, calcium, sodium, sulfur, boron, zinc, copper, iron and manganese) were found statistically significant ($p<0.01$).

The increasing of wet weight of plant was found as 30.69% by fertilizer application (in A+F2). The macro and micro elements, N, K, Ca, Mg, S, B, Zn, Cu, Fe, and Mn contents, were increased as 4.4% (in A+F1), 38.46% (in A), 3.03% (in A+F1), 8.7% (in A+F2), 45.22% (in A+F2), 205.55% (in A+F2), 212.87% (in A+F2), 50.29% (in A+F2), 18.32% (in A+F2), and 43.94% (in A+F1), respectively.

The effect of sampling time (Table 5), applied foliar fertilizer (Table 6) and the interaction of time x fertilizer doses (Table 7) on plant nutrients in plant samples taken for nine days after A, A+F1 and A+F2 fertilizers applied foliar to ryegrass plant during one harvest were interpreted in order below Tables. Levels in the Tables 5-7 explained that were no connected by the same letters

were significantly different at p< 0.01 by Tukey's honestly significant difference test.

**Table 5.** The moisture and element contents of ryegrass in the different days

| Day | Moisture | N | K | Ca | Mg | Na | S | B | Zn | Cu | Fe | Mn |
|---|---|---|---|---|---|---|---|---|---|---|---|---|
| | | | % | | | | | mg kg$^{-1}$ | | | | |
| **1** | 79.84f | 0.43f | 2.87a | 0.72ab | 0.30a | 2730.42b | 4444.51a | 1.68a | 24.85a | 6.97a | 52.24a | 24.73a |
| **2** | 84.06a | 0.50e | 2.59b | 0.69b | 0.26ab | 3106.26a | 3683.15b | 1.17b | 21.39b | 4.66b | 50.03b | 20.64b |
| **3** | 82.26b | 0.60d | 2.37d | 0.61c | 0.23bc | 2266.55cd | 3276.13d | 1.08c | 19.65c | 4.66b | 38.72f | 18.68d |
| **4** | 82.53b | 0.43f | 2.44c | 0.76a | 0.24bc | 2488.76bc | 3393.15c | 0.75f | 15.43f | 4.03c | 39.65e | 19.23c |
| **5** | 81.53c | 0.48ef | 2.55b | 0.72ab | 0.25abc | 2093.63d | 180.35h | 0.93d | 16.84d | 3.51e | 40.96c | 18.39e |
| **6** | 81.33cd | 0.76b | 1.96f | 0.68b | 0.24bc | 2552.46b | 183.39h | 0.98d | 16.15e | 3.47e | 34.83h | 17.60f |
| **7** | 81.10d | 0.89a | 1.86g | 0.56c | 0.21c | 1820.03d | 2844.96f | 0.83e | 12.69h | 3.71d | 31.69ı | 13.78h |
| **8** | 81.06d | 0.90a | 2.19e | 0.58c | 0.22bc | 1018.22f | 3059.05e | 0.93d | 15.34f | 3.54e | 35.48g | 14.63g |
| **9** | 80.48e | 0.70c | 1.78h | 0.8c | 0.20c | 769.46f | 2602.34g | 0.94d | 14.89g | 3.63d | 40.40d | 14.62g |

**Table 6.** The means of moisture and element contents of ryegrass with fertilizer doses

| Application | Moisture | N | K | Ca | Mg | Na | S | B | Zn | Cu | Fe | Mn |
|---|---|---|---|---|---|---|---|---|---|---|---|---|
| **C** | 80.83c | 0.68b | 1.82d | 0.66ab | 0.23 | 3418.65a | 2079.88d | 0.72c | 11.97c | 3.42d | 38.32d | 14.61d |
| **A** | 82.07a | 0.46c | 2.52a | 0.64b | 0.23 | 1685.92b | 2560.19c | 0.74c | 11.30d | 3.70c | 38.91c | 15.63c |
| **A+F1** | 82.20a | 0.71a | 2.35c | 0.68a | 0.23 | 1809.62b | 2858.21b | 1.19b | 21.13b | 4.71b | 39.20b | 21.03a |
| **A+F2** | 81.20b | 0.67b | 2.47b | 0.64b | 0.25 | 1461.72c | 3020.40a | 1.48a | 25.48a | 5.14a | 45.34a | 20.87b |

**Table 7.** The interaction between time and fertilizer doses on the moisture and element contents of ryegrass

| Day | App. | Moisture | N | K | Ca | Mg | Na | S | B | Zn | Cu | Fe | Mn |
|---|---|---|---|---|---|---|---|---|---|---|---|---|---|
| **1** | **C** | 82.95fg | 0.37no | 1.74o | 0.61ek | 0.25ab | 5196.01b | 2640.2lm | 0.46t | 11.26t | 4.42g | 42.87h | 13.95tu |
| | **A** | 78.26v | 0.19pq | 3.69a | 0.69ag | 0.29ab | 847.33mq | 5337.5a | 0.95ık | 12.61r | 6.16d | 56.49b | 16.95jk |
| | **A+F1** | 83.69cd | 0.48km | 2.79de | 0.81ab | 0.29ab | 1904.27gj | 4745.0c | 2.48b | 36.54c | 8.05b | 51.54c | 31.59b |
| | **A+F2** | 74.45w | 0.68hı | 3.26b | 0.75ae | 0.35a | 2974.09de | 5055.3b | 2.84a | 38.97a | 9.25a | 58.07a | 36.44a |
| **2** | **C** | 82.35 hl | 0.40lm | 1.88no | 0.76ad | 0.27ab | 5433.65ab | 2667.2lm | 0.61qs | 12.85r | 3.48lm | 52.40c | 15.31nq |
| | **A** | 84.70ab | 0.11q | 3.17b | 0.64dj | 0.22ab | 648.11nq | 3465.3gı | 0.60rs | 10.37w | 3.26no | 40.25jk | 16.75jk |
| | **A+F1** | 84.92 a | 0.73gh | 2.56fg | 0.67bh | 0.25ab | 3015.21de | 4266.9d | 1.46e | 26.33e | 5.42e | 50.29d | 25.78c |
| | **A+F2** | 84.25ac | 0.75fg | 2.73df | 0.70ag | 0.30ab | 3328.08d | 4333.2d | 2.01d | 36.01d | 6.47c | 57.16ab | 24.73d |
| **3** | **C** | 80.64qs | 1.02ab | 1.77o | 0.65cı | 0.26ab | 5864.17a | 2780.2l | 0.57rt | 13.40q | 4.25gı | 41.11ıj | 16.94jk |
| | **A** | 84.14bc | 0.42lm | 2.99c | 0.62dk | 0.20b | 560.08oq | 3254.2jk | 0.74oq | 10.36w | 4.29gı | 30.74p | 15.14or |
| | **A+F1** | 82.35 hl | 0.57ıj | 2.26ıj | 0.52hk | 0.22ab | 2155.69fh | 3344.1ık | 0.74oq | 17.70k | 3.90j | 34.10n | 17.79ı |
| | **A+F2** | 81.90 jn | 0.40lm | 2.44gh | 0.65cı | 0.22ab | 486.26pq | 3726.0f | 2.26c | 12.14r | 6.21d | 48.91e | 24.86d |
| **4** | **C** | 81.00 or | 0.55jk | 1.34p | 0.80ab | 0.27ab | 6007.26a | 2479.1m | 0.46t | 11.64s | 4.33gh | 34.64n | 14.54st |
| | **A** | 82.30 hl | 0.50kl | 2.90cd | 0.81ab | 0.21b | 890.31lq | 3424.2hj | 0.77np | 10.97tu | 4.11ı | 39.18jl | 19.23g |
| | **A+F1** | 83.47de | 0.39mn | 2.62ef | 0.82a | 0.26ab | 2643.28ef | 4004.1e | 0.94ıl | 19.56ı | 4.13hı | 46.40f | 24.68d |
| | **A+F2** | 83.33ef | 0.27op | 2.90cd | 0.60fk | 0.22ab | 414.21pq | 3665.2fg | 0.81lo | 19.53ı | 3.55lm | 38.39l | 18.48h |
| **5** | **C** | 81.37np | 0.39mn | 2.63ef | 0.72af | 0.22ab | 787.02mq | 166.1p | 0.81lo | 10.74uv | 2.68s | 34.86n | 16.04lm |
| | **A** | 82.69gh | 0.50kl | 2.13ıl | 0.67bh | 0.25ab | 4379.25c | 152.0p | 0.67pr | 12.78r | 3.41mn | 38.24l | 15.57mo |
| | **A+F1** | 80.41rs | 0.55jk | 2.68ef | 0.79ac | 0.24ab | 1479.20ıl | 184.1p | 1.06gı | 19.01j | 3.62kl | 44.23g | 20.69f |
| | **A+F2** | 81.67lmo | 0.43lm | 2.77de | 0.69ag | 0.27ab | 1729.03hk | 219.3p | 1.19fg | 24.84f | 4.32gh | 46.52f | 21.25f |
| **6** | **C** | 79.64u | 1.02ab | 1.26p | 0.60fk | 0.24ab | 4461.75c | 119.2p | 0.51st | 9.89x | 2.83rs | 26.70s | 14.68qs |
| | **A** | 82.45hk | 0.28op | 2.16ık | 0.68ah | 0.23ab | 2046.05fı | 180.2p | 0.78mp | 11.90s | 2.94qr | 34.01n | 16.92jk |
| | **A+F1** | 82.50hı | 0.87cd | 2.29hı | 0.79ac | 0.26ab | 2441.32eg | 225.0p | 1.50e | 23.94g | 4.28gı | 42.19hı | 22.07e |
| | **A+F2** | 80.72ps | 0.88cd | 2.12ıl | 0.65cı | 0.23ab | 1260.73kn | 209.1p | 1.11fh | 18.85j | 3.82jk | 36.42m | 16.74jk |
| **7** | **C** | 80.36rt | 0.72gh | 2.06km | 0.62dk | 0.18b | 481.30pq | 2552.6m | 0.92jl | 9.08y | 3.02qr | 31.27op | 12.73v |
| | **A** | 80.15su | 1.03ab | 1.27p | 0.56gk | 0.26ab | 5095.82b | 2479.1m | 0.50st | 11.11t | 3.11oq | 36.16m | 13.32uv |
| | **A+F1** | 81.74lmn | 0.96ac | 2.27hj | 0.56gk | 0.21b | 979.01lp | 3563.0fh | 0.90jn | 15.71m | 5.55e | 28.40q | 16.50kl |

| | | | | | | | | | | | | | |
|---|---|---|---|---|---|---|---|---|---|---|---|---|---|
| | **A+F2** | 82.16 ım | 0.84ef | 1.84no | 0.49k | 0.18b | 724.00nq | 2785.2l | 1.02hj | 14.87o | 3.16op | 30.92p | 12.56w |
| **8** | **C** | 81.25nq | 0.97ac | 2.25ıj | 0.68ah | 0.23ab | 1129.27ko | 3380.1hk | 1.56e | 15.20n | 3.08oq | 32.32o | 14.88pr |
| | **A** | 81.78 kn | 0.63hj | 2.26ıj | 0.51ık | 0.18b | 384.27pq | 2260.2n | 0.57rt | 10.48vw | 2.86rs | 34.74n | 12.22w |
| | **A+F1** | 79.69tu | 1.07a | 1.95ln | 0.54gk | 0.18b | 871.44lq | 2595.6lm | 0.69or | 14.00p | 3.57lm | 26.01s | 14.20st |
| | **A+F2** | 81.53mo | 0.95bc | 2.29dı | 0.59fk | 0.29ab | 1687.92hk | 4000.3e | 0.88kn | 21.67h | 4.67f | 48.86e | 17.23ıj |
| | **C** | 77.95v | 0.68gı | 1.43p | 0.50jk | 0.18b | 1407.44jm | 1934.3o | 0.57rt | 13.67q | 2.72s | 48.72e | 12.43w |
| **9** | **A** | 82.16 ım | 0.48km | 2.10jl | 0.62dk | 0.19b | 322.06q | 2489.0m | 1.05hı | 11.08t | 3.16op | 40.42j | 14.61rs |
| | **A+F1** | 81.00or | 0.78eg | 1.72o | 0.61ek | 0.20b | 797.16mq | 2796.2l | 0.91jm | 17.37l | 3.87j | 29.63pq | 15.94ln |
| | **A+F2** | 80.80 ps | 0.85de | 1.89mo | 0.60fk | 0.22ab | 551.18oq | 3189.9k | 1.22f | 17.45kl | 4.78f | 42.82h | 15.51mp |

## 4. DISCUSSION AND CONCLUSION

In general, when the element contents of the above-ground parts of the ryegrass plant were taken into account with 9-day foliar fertilization applications, nitrogen increased in the plant mostly on the 7$^{th}$ and 8$^{th}$ days, whereas most of the other elements, namely K, Mg, S, B, Zn, Cu, Fe and Mn contents, increased on the 1$^{st}$ day. It has been understood that most of plant nutrient content increased on the 1$^{st}$ day was more fast uptake by algae application with chemical fertilizer. Results show that the nitrogen uptake in the fertilizer form examined in the ryegrass plant and within the 9-day period after the application is understood to be intensified on the 7$^{th}$ and 8$^{th}$ days. However, it was determined that the content of K and Mg elements was higher on the 2$^{nd}$ day, and the Ca and Mg elements were also higher on the 5$^{th}$ day.

The sodium content in plant was found to be the highest in the control application, and it was determined that the fertilizer applications decreased the sodium content. It has been found that sodium has the lowest content as a result of A+F2 application, that is, this application reduces the Na content. When examined as days, it was observed that the Na content was the highest on the 2$^{nd}$ day, and the sodium concentration was high on the 1$^{st}$, 4$^{th}$ and 6$^{th}$ days. It is also understood that with these applications, it may be possible to reduce the sodium intake of the plant in the soils have high sodium.

As result, the contents of most of the nutrients (S, B, Cu, Fe and Mn) and the moisture content of the plant were found to be at the lowest levels of the ryegrass plant in the unfertilized (control) plots. Among the fertilizer applications, it was understood that the application of algae extract (A) increased the moisture content and K content of the plant. It was observed that Fertilization 1 (A+F1) applications with algae extract (A), which is one of the added fertilizer applications, caused an increase in the moisture content, N, Ca and Mn contents of the plant. It was understood that Fertilization 2 (A+F2) applications together with algae extract (A), which is one of the added and incremental fertilizer applications, also caused an increase in the S, B, Zn, Cu and Fe contents of the plant.

As a conclusion, it was observed that algae and chemical fertilizer applications with algae were applicable in *Lolium multiflorum* plant, increased plant fresh weight and plant nutrient intake, and it was recommended as an available method.

## REFERENCES


[1] Gomiero T. Soil degradation, land scarcity and food security: Reviewing a complex challenge. Sustainability, 2016;8:281. https://doi.org/doi:10.3390/su8030281.

[2] Anonymous. General Directorate of Agrarian Reform. Global Soil Partnership and Turkey Soil Information System Book. (T.C. Tarım ve Orman Bakanlığı, Tarım Reformu Genel Müdürlüğü. Küresel Toprak Paydaşlığı ve Türkiye Toprak Bilgi Sistemi Kitabı. Uzerler Matbaa, in Turkish). Ankara; 2019.

[3] Kasap Y, Demirkıran AR, Şerbetçi A. The effect of differents level of phosphorus fertilizer on yield, quality and agricultural characteristics of some groundnut varieties under the ecological conditions of Kahramanmaraş. Turkish Journal of Agriculture and Forestry, 1999;23(supp. 4):777-784.

[4] Demirkıran AR, Sağlam MT. The effect of nitrogen and phosphorus fertilizers on color characteristics of *Capsicum annuum* under the ecological conditions of Kahramanmaraş. Bingöl Üniversitesi Fen Bilimleri Dergisi, 2003;1(1):1-10.

[5] Demirkiran AR, Uslu OS. Effects of nitrogen and phosphorus fertilization on micro nutrient contents of *Trifolium angustifolium* and *Lotus suaveolens* from *Fabaceae* on a grassland ecosystem: the case of Kahramanmaras, Eastern Mediterranean region of Turkey. Journal of Animal and Veterinary Advances, 2010;9(22):2863-2869.

[6] Demirkıran AR, Cengiz MÇ. Effects of different organic materials (gyttja, alsil, sea moss, humic acid, moss, peat) and chemical fertilizers on nutrition of pistachio (*Pistacia vera* L.). Bingöl University Journal of Science, 2010b;1(1):43-50.

[7] Özbay N, Ergun M, Demirkıran AR. Effect of commercial microbial fertilizer Sim Derma® (*Trichoderma harzianum*, Kuen 1585) on germination, growth and yield of spinach. Turkish Journal of Agricultural and Natural Sciences, 2018;5(4):482-491.

[8] Ateş K, Demirkıran AR, İnik O. Effects of some natural and artificial fertilizer applications to soil on yield parameters of strawberry plant. Turkish Journal of Nature and Science, 2019;8(2):23-28.
[9] Yolcu H, Seker H, Gullap MK, Lithourgidis A, Gunes A. Application of cattle manure, zeolite and leonardite improves hay yield and quality of annual ryegrass (*Lolium multiflorum* Lam.) under semiarid conditions. Australian Journal of Crop Science, 2011;5(8):926-931.
[10] Adiloğlu A, Bellitürk K, Adiloğlu S, Solmaz Y. The effect of increasing leonardit applications on dry matter yield and some nutrient elements contents of rye (*Secalecerale* L.) plant. Eurasian Journal of Forest Science, 2018;6 (1): 44-51.
[11] Godlewska A, Ciepiela GA. Italian ryegrass (*Lolium multiflorum* Lam.) fiber fraction content and dry matter digestibility following biostimulant application against the background of varied nitrogen regime. Agronomy, 2020;11(1):39.
[12] Cooper RJ, Liu C, Fisher DS. Influence of humic substances on rooting and nutrient content of creeping bentgrass. Crop Science, 1998;38(6):1639-1644.
[13] Maibodi N, Kafi M, Nikbakht A, Rejali F. Effect of foliar applications of humic acid on growth, visual quality, nutrients content and root parameters of perennial pyegrass (*Lolium perenne* L.). Journal of Plant Nutrition, 2015;38(2):224-236.
[14] Wiśniewska-Kadżajan B, Jankowski K. Effects of slurry and soil conditioners on the yield, protein and ash content in Italian ryegrass (*Lolium multiflorum* Lam.). Applied Ecology and Environmental Research, 2020;18(2):2259-2268.
[15] Barszczewski J, Wróbel B, Jankowska-Huflejt H. Economic effect of permanent meadow spreading with the meadow limb. Water-Environment-Rural Areas, 2011;3(35):21-37.
[16] Kotlarz A, Stankiewicz S, Biel W. Botanical and chemical composition of hay from a semi-natural meadow and its nutritional value for horses. Acta Sci. Pol., Zootechnica, 2010;9(4):119-128.
[17] Kasperczyk M. Yielding of mountain meadow depending on the course of meteorological conditions. Acta Agrophysica, 2004;3(2):263-269.
[18] Ciepiela AG. Reaction of selected grass species to nitrogen fertilization used in urea solution and in ammonium nitrate. Scientific Dissertation No. 76. AP, Siedlce, 2004.
[19] Jankowska J, Ciepiela AG, Kolczarek R, Jankowski K. Impact of the type of mineral fertilizer and nitrogen dose on yield and nutritional value of permanent meadow sward. Puławski Diary, 2008;147:125-138.
[20] Szkutnik J, Kacorzyk P, Szewczyk W. Change in total protein content and raw fiber depending on the level of fertilization and the development phase of grasses. Grassland in Poland, 2012;15:185-191.
[21] Hart, J. M., Mellbye, M. E., Young, W. C., & Silberstein, T. (2003). Nutrient management for annual ryegrass grown for seed: western Oregon, Oregon State University, Technical report: EM 8854.
[22] Bremner JM. Determination of nitrogen in soil by the kjeldahl method. The Journal of Agricultural Science, 1960;55(1):11-33.
[23] Kacar B, İnal A. Bitki Analizleri, Nobel Yayın, Ankara, 1998 (in Turkish).
[24] Ren AZ, Gao YB, Wang W, Wang JL, Zhao NX. Influence of nitrogen fertilizer and endophyte infection on ecophysiological parameters and mineral element content of perennial ryegrass. Journal of Integrative Plant Biology, 2009;51(1):75-83.
[25] De Conti L, Cesco S, Mimmo T, Pii Y, Valentinuzzi F, Melo GW, Brunetto G. Iron fertilization to enhance tolerance mechanisms to copper toxicity of ryegrass plants used as cover crop in vineyards. Chemosphere, 2020;243:125298.
[26] Fortún C, Rapsch S, Ascaso C. Action of humic acid preparations on leaf development, mineral elements contents and chloroplast ultrastructure of ryegrass plants. Photosynthetica, 1985;19(3):294-299.

Cilt 12, Sayı 1, Sayfa 144-152, 2023 Volume 12, Issue 1, Page 144-152, 2023

Araştırma Makalesi https://doi.org/10.46810/tdfd.1250042 Research Article

Türk Doğa ve Fen Dergisi
Turkish Journal of Nature and Science
www.dergipark.gov.tr/tdfd

# The Study of 2, 4-Diamino-6-methly-1, 3, 5-triazine on the Corrosion Inhibition of Mild Steel in The Hydrochloric Acid Medium: Integrated Theoretical and Experimental Investigations

**Reşit YILDIZ**[1*]

[1]Mardin Artuklu University, Faculty of Health Sciences, Department of Nutrition and Dietetics, Mardin, Türkiye
Reşit YILDIZ ORCID No: 0000-0001-5467-6821

[*]Corresponding author: *ryildiz80@gmail.com, resityildiz@artuklu.edu.tr*

(Received: 11.02.2023, Accepted: 14.03.2023, Online Publication: 27.03.2023)

**Keywords**
Corrosion, Adsorption, Mild steel, Inhibitor, Quantum chemical calculation,

**Abstract:** The aim of this study is the investigation of adsorption and corrosion behaviors of 2,4-Diamino-6-methly-1,3,5-triazine (2-DMT) on mild steel (MS) in 0.5 M HCI solution using many experimental and theoretical studies such as potentiodynamic polarization, electrochemical impedance spectroscopy (EIS), linear polarization resistance (LPR), adsorption isotherm, potential of zero charge (PZC), scanning electron (SEM), atomic force microscopies (AFM) and quantum chemical calculations. The results showed that 2-DMT has an outstanding anti-corrosion performance of 94.7% at an optimum concentration of 10 mM and the MS surface, which was exposed to the inhibited solution at 298 K, does not contain pits, cracks or deformations. Values of $i_{corr}$ are found to be 0.513, 0.216, 0.098, 0.072 and 0.039 mA $cm^{-2}$ for blank solution and each concentration of 2-DMT. Hydrogen volumes are 90 and 4.6 mL $cm^{-2}$ for blank solution and the existence of 10.0 mM 2-DMT, respectively. The observed adsorption is much more consistent with Langmuir. The high performance is explained by the effective adsorbing of organic matter to the MS surface. HOMO, LUMO energies and the energy gap ($\Delta E$) are -7.1980, -1.9959 and 5.2021 eV, respectively. Accordingly, it is suggested that this organic compound can be used in the industrial acid cleaning procedure.



# 2, 4-Diamino-6-metil-1, 3, 5-triazinin Yumuşak Çeliğin Hidroklorik Asit Ortamda Korozyon İnhibisyonu Üzerine Çalışması: Teorik ve Deneysel Araştırmaların Bütünleştirilmesi

**Anahtar Kelimeler**
Korozyon, Adsorbsiyon, Yumuşak çelik, İnhibitör, Kuantum kimyasal hesaplama,

**Öz:** Bu çalışmanın amacı, potansiyodinamik polarizasyon, elektrokimyasal empedans spektroskopisi (EIS), doğrusal polarizasyon direnci (LPR), adsorbsiyon izotermi, sıfır yük potansiyeli (PZC), taramalı elektron (SEM), atomik kuvvet mikroskopileri (AFM) ve kuantum kimyasal hesaplamaları gibi birçok deneysel ve teorik çalışma kullanılarak 0,5 M HCI çözeltisinde 2,4-Diamino-6-methly-1,3,5-triazinin (2-DMT) adsorbsiyon ve korozyon davranışlarının incelenmesidir. Sonuçlar, 2-DMT'nin 10 mM'lik optimum konsantrasyonda % 94,7'lik olağanüstü korozyon önleyici performansa sahip olduğunu ve 298 K'de inhibe edilmiş çözeltiye maruz kalan çelik yüzeyin çukurlar, çatlaklar veya deformasyonlar içermediğini göstermiştir. Asit çözeltisi ve 10 mM 2-DMT varlığındaki çözelti için, $i_{corr}$ değerleri 0,513, 0,216, 0,098, 0,072 ve 0,039 mA $cm^{-2}$ olarak bulundu. Hidrojen hacmi sırasıyla, asit çözeltisi ve 10 mM 2-DMT varlığındaki çözelti için 90 ve 4,6 mL $cm^{-2}$' dir. Gözlemlenen adsorbsiyon, Langmuir ile çok daha tutarlıdır. Yüksek performans, organik maddenin MS yüzeyine etkili bir şekilde adsorbe olmasıyla açıklanmaktadır. HOMO, LUMO enerjileri ve enerji aralığı ($\Delta E$) sırasıyla, -7,1980, -1,9959 ve 5,2021 eV' tur. Dolayısıyla, bu organik bileşiğin endüstriyel asitle temizleme işleminde kullanılabileceği önerilmektedir.

## 1. INTRODUCTION

Corrosion, which has an annual global cost of 2.5 trillion dollars, is defined as the loss of effectiveness of metals as a result of their interactions with their environment [1]. Even if this phenomenon is completely impossible to stop, studies to slow down corrosion continue intensively by many researchers [2-5]. One of the industrial areas where corrosion is effective is acid cleaning, pickling and descaling [6,7]. HCl and $H_2SO_4$ are used to clean the steel materials in this area as cleaning agents, therefore the corrosion is inevitable. Using organic corrosion inhibitors are an effective method in the slow down the corrosion [8-11]. These compounds adsorb on the steel surface effectively, form a protective film on the steel surface and by inhibiting the corrosion reactions, protect the steel from corrosion. This corrosion protection is described in the literature as: Conjugated bonds, polar groups such as N, O, P, S and π-delocalized electrons in inhibitor molecules are adsorption centres during the interaction of metal and inhibitor molecules [12-14]. Many organic compounds as corrosion inhibitors are studied to prevent the different metals as well as MS. As examples, pyrazole, benzimidazole, azoles, pyridine, schiff bases, amino acids, quinoline, quinoxaline, rhodanine, etc. In recent years, triazine derivatives as organic inhibitors showed high inhibition efficiency in acid solutions [15]. Triazine derivatives are also used in the medical field for anti-HIV, anticancer, antiinflammatory, analgesic antihypertensive, cardiotonic, neuroleptic, nootropic, antihistaminergic, tuberculostatic, antiviral, anti-protozoal, estrogen receptor modulators, antimalarial, cyclin-dependent kinase inhibitors, antimicrobial, antiparasitic, activities [16].

In this study, 2,4-Diamino-6-methyl-1,3,5-triazine, a triazine derivative, is tested as a potential organic corrosion inhibitor to specify the corrosion properties of MS in 0.5 M HCI solution using electrochemical techniques, SEM/AFM and quantum chemical calculation. As mentioned above, this compound is chosen as an inhibitor because it contains electron-donating groups and possible adsorption groups in the aromatic ring. Its cost is another reason. Hydrogen gas is also measured in inhibited and uninhibited solutions after 120 h exposure time. The inhibition mechanism is discussed in more detail by determining the charge of metal. Finally, this work is supplemented by quantum chemical calculation to better understand the relationship between structural, electronic properties and adsorption process.

## 2. MATERIAL AND METHOD

The chemical composition of MS used in this study is (w): Mn: 0.71%, Cu: 0.26%, Si: 0.24%, C: 0.18%, S: 0.04%, P: 0.19%, N: 0.20%, O: 0.41% and Fe (remainder). To get a clean surface before electrochemical measurements, emery papers are used, washed with ethanol and distilled water, respectively. The corrosive media is composed by 0.5 M HCI (Merck, 37% HCI) without and with concentrations of 0.5, 1.0, 5.0 and 10.0 mM 2-DMT. Gamry instrument potentiostat/galvanostat/ZRA/3000 is used for electrochemical measurements with three-electrode setup which consists of MS as working, platinum sheet as counter and Ag/AgCI (3M KCI) as reference electrode, respectively. Prior to each experiment, stable open circuit potential ($E_{ocp}$) is achieved after 1 h immersion time in both corrosive solutions. Tafel curves is gotten between -0.75 and -0.25 V with a scan rate of 1 mV $s^{-1}$. Frequency between $1x10^5$ Hz and $1x10^{-2}$ Hz is applied to get EIS diagrams with an amplitude of 5 mV. Moreover, EIS results are fitted by using equivalent circuit with the help of Zview2 software. Measurement of LPR is recorded from $E_{ocp}$ -0.01 V to $E_{ocp}$ +0.01 V at 1.0 mV $s^{-1}$. The effect of various immersion times (24, 48, 72, 96 and 120 h) on corrosion behavior of MS electrode in blank and with the existence of inhibitor (10.0 mM) are examined by EIS. Hydrogen gas is measured by an inverted tape measure at the end of 120 h in both uninhibited and inhibited solutions (10.0 mM). To determine the charge of metal in inhibited solution (10.0 mM) it is plotted polarization resistance ($R_p$) versus applied potential. All the electrochemical experiments are carried out under atmospheric conditions by repeating three times at 298 K. To analyze the morphologic structure and elemental analysis, SEM and AFM are performed by Leo Evo 40 and Park system XE-100 AFM, respectively. Electrochemical results are supplemented by quantum chemical calculation, namely the basis set B3LYP/6-311 ++ G (d, p) for all atoms with the Gaussian 09 program package (USA). Some electronic properties such as the energy of the highest molecular orbital ($E_{HOMO}$), lowest empty molecular orbital ($E_{LUMO}$), energy gap ($\Delta E$) between LUMO and HOMO and Mulliken charges on the backbone atoms, dipole moment ($\mu$), global hardness ($\eta$), global softness ($\sigma$), the fraction of electrons transferred ($\Delta N$) and absolute electronegativity ($\chi$) are determined. The chemical structure of the tested inhibitor is given in Figure 1.

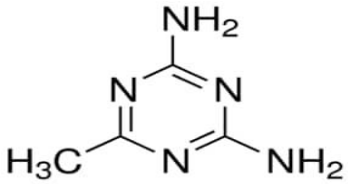


**Figure 1.** Chemical structure of 2,4-Diamino-6-methly-1,3,5-triazine (2-DMT)

## 3. DISCUSSION AND CONCLUSION

### 3.1. Tafel Results

The Tafel curve is the best method for determining of corrosion behavior of MS electrode in acid environment. Fig. 2 shows the Tafel curves of MS electrode in blank solution and with the existence of 0.5, 1.0, 5.0 and 10.0 mM 2-DMT.

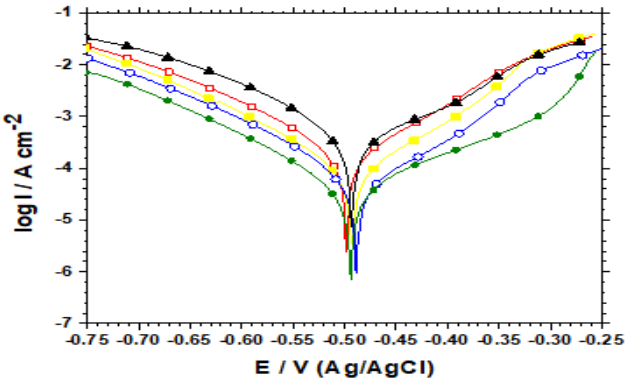


**Figure 2.** Tafel curves of MS electrode in 0.5 M HCI(▲) and with the existence of 0.5(□), 1.0(●), 5.0(○) and 10.0(●) mM 2-DMT

Prior to adding to the inhibitor in 0.5 M HCI solution, Fig. 2 clearly indicates that very high current density is obtained on MS electrode. When an inhibitor is added to a corrosive medium at concentrations of 0.5 to 10 mM, 2-DMT molecules influence the corrosion current density of the cathodic and anodic reactions, resulting in reducing the rate of anodic dissolution of the metal and cathodic reaction [17]. The highest decrease in current density is observed at the highest concentration (10 mM). The Tafel extrapolation method is used for the determination of corrosion current density ($i_{corr}$) and cathodic Tafel slopes ($b_c$). In addition, corrosion rate (CR) and inhibition efficiencies ($\eta$(%)) are also measured and related data are given in Table 1. The following formula is used for $\eta$(%).

$$\eta(\%)=(i^{o}_{corr}-i_{corr}inh/i^{o}_{corr})x100 \quad (1)$$

Here, $i^{o}_{corr}$ and $i_{corr}$ inh denote the corrosion current density of MS electrode in acid environment in the absence and presence of inhibitor, respectively. It is clearly seen from figure that characteristic behavior of Tafel curves does not change with the existence of different concentrations of 2-DMT in blank solution, implying that the same corrosion mechanism occurs in both corrosive media due to giving parallel lines. $b_c$ values support this behavior since there are small differences between MS electrode in blank solution and the existence of an inhibitor in blank solution (Table 1). This means that inhibitor molecules block the active centres of hydrogen evolution by adsorbing on the MS surface for the cathodic region, slow down the anodic dissolution of the MS for anodic region [18]. From Table 1, this inhibitor acts as a mixed-type inhibitor due to a maximum potential difference of 5 mV [19]. As can be seen in Table 1, values of $i_{corr}$ are found to be 0.5128, 0.2155, 0.0983, 0.07151 and 0.03861 mA cm$^{-2}$ for the blank solution and each concentration of 2-DMT. A decrease in $i_{corr}$ indicates the adsorption of inhibitor molecules onto MS surface. As for $\eta$, Table 1 shows the dependency of the inhibition efficiency on the inhibitor concentration. Inhibition efficiency increases from 58% to 92.4% in inhibited solution. This means that a stable inhibitor film forms on the MS surface and this film behaves like a preventative, resulting the reducing $i_{corr}$ values.

**Table 1.** Some data derived from Tafel curves of MS electrode in blank solution and with the existence of different concentrations 2-DMT at 298 K

| $C_{inh}$ (mM) | $E_{corr}$ (mV,Ag/AgCl) | $i_{corr}$ (mA cm$^{-2}$) | $bc$ (mV dec$^{-1}$) | CR (mpy) | $\eta$(%) |
|---|---|---|---|---|---|
| Blank | -493.7 | 0.5128 | 118.3 | 234.3 | - |
| 0.5 | -498.7 | 0.2155 | 108.5 | 98.49 | 58.0 |
| 1.0 | -492.4 | 0.0983 | 101.1 | 44.92 | 80.8 |
| 5.0 | -488.9 | 0.07151 | 102.6 | 32.68 | 86.0 |
| 10.0 | -493.9 | 0.03861 | 100.0 | 17.64 | 92.4 |

### 3.2. EIS and LPR Results

The relationship at the metal/solution interface can be elucidated by EIS. Nyquist and Bode plots of MS electrode in blank solution and with the addition of 0.5, 1.0, 5.0 and 10.0 mM 2-DMT are depicted in Fig. 3. The same shapes (one depressed semicircle) are seen for all electrodes in Bode plots (Fig. 3b), indicating that mechanism is controlled by charge transfer at the interface [20]. The reason why perfect semicircles are not obtained is due to the uneven charge distribution at the interface [21]. Impedance responses are fitted using equivalent circuit that is depicted in Fig. 3b as an inset. A single circuit is used in the fitting process. Because the most suitable fitting is obtained in this circuit. Fitting data are given in Table 2. Here $R_s$, $R_p$, CPE and $n$ denote solution resistance, polarization resistance that is containing charge transfer resistance ($R_{ct}$), diffuse layer resistance ($R_d$), the resistance of accumulated species ($R_a$) and film resistance ($R_f$), constant phase element and phase shift, respectively. The following formula is used for $\eta$.

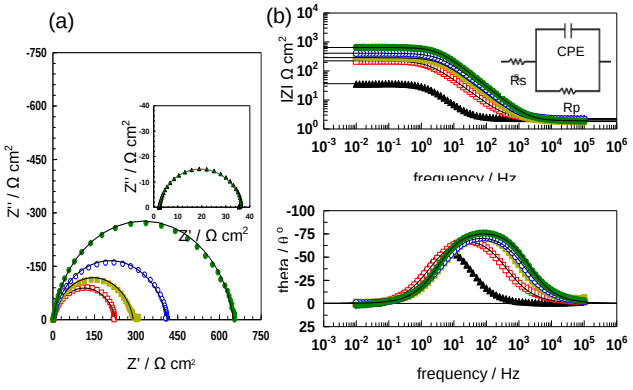


**Figure 3.** Nyquist (a) and Bode (b) plots of MS electrode (▲ or as inset) in 0.5 M HCI and with the existence of 0.5(□), 1.0(■), 5.0(○) and 10.0(●) mM 2-DMT. A related equivalent circuit is given in b as an inset.

**Table 2.** Some data derived from EIS and LPR for MS electrode in blank solution and with the existence of different concentrations 2-DMT at 298 K

| $C_{inh}$ (mM) | EIS | | | | | | | LPR | |
|---|---|---|---|---|---|---|---|---|---|
| | $R_s$ ($\Omega cm^2$) | $R_p$ ($\Omega cm^2$) | $CPE_{dl}$ $Y_o$ ( $x10^6$ $s^n$ $\Omega^{-1}$ $cm^{-2}$) | $n$ | $\eta$ (%) | $C_{dl}$ ($x10^6$ s $\Omega^{-1}$ $cm^{-2}$) | Fit error (chi-squared) | $R_p$ ($\Omega cm^2$) | $\eta$ (%) |
| Blank | 2.3 | 34 | 361 | 0.92 | | 248 | $4.2x10^{-3}$ | 37 | |
| 0.5 | 2.2 | 224 | 255 | 0.86 | 84.8 | 158 | $1.1x10^{-2}$ | 240 | 84.5 |
| 1.0 | 1.8 | 288 | 219 | 0.87 | 88.1 | 152 | $1.0x10^{-2}$ | 310 | 88.0 |
| 5.0 | 2.1 | 409 | 163 | 0.85 | 91.6 | 104 | $6.2x10^{-3}$ | 425 | 91.2 |
| 10.0 | 1.9 | 648 | 102 | 0.90 | 94.7 | 77 | $8.1x10^{-3}$ | 690 | 94.6 |

$$\eta\ \% = \left(\frac{R'_p - R_p}{R'_p}\right) \times 100 \quad (2)$$

$R_p$ and $R'_p$ denote the polarization resistance of MS electrode in blank solution and with the adding of 2-DMT, respectively. To calculate the CPE and double layer capacitance ($C_{dl}$), formulas are given below:

$$Z_{CPE}=Y_o^{-1}(jw)^{-n} \quad (3)$$

where $Y_o$, $j$, $w$ and $n$ are proportionality coefficient, $j^2 = -1$ imaginary number, angular frequency and phase shift, respectively.

$$C_{dl}=Y_o(w''_m)^{n-1} \quad (4)$$

$w''_m = 2\pi f_{max}$ (angular frequency), $f_{max}$ is the frequency at the maximum value of imaginary impedance [22]. As seen in Fig. 3a, the diameter of depressed semicircles which is directly related to $R_p$ values increases regularly with the adding of 0.5, 1.0, 5.0 and 10.0 mM 2-DMT in 0.5 M HCl, when compared to bare MS electrode. The increase in the diameter of the semicircle represents a measure of protection. This is supported by the increasing phase angles in the Bode curves (Fig. 3b). According to Table 2, when the concentration enhances from 0.5 to 10.0 mM, inhibition efficiency reaches its highest value from 84.8% to 94.7%. Here $n$ is related to the non-homogeneous nature of the semicircles which is a characteristic for solid metals [23]. Its value is between 0 and 1. As for $C_{dl}$ values, as expected, $C_{dl}$ values decrease with increasing 2-DMT concentration due to decreasing in the local dielectric constant and increasing the thickness of the double layer [24]. High inhibition efficiency and lower $C_{dl}$ values can be due to adsorption of inhibitor molecules onto the MS surface and by causing a protective layer, preventing the MS from corrosion [25]. Increments of phase angles prove the existence of surface protection (Fig. 3b). In the present work, as seen in Table 2, the results of LPR are very close to the results of EIS. A comparison of the protection ability of some triazine-containing compounds with 2,4-Diamino-6-methly-1,3,5-triazine are given in Table 3. Though researchers found very high inhibition efficiencies, as can be seen in Table 3, the inhibition ability of studied inhibitor is higher than those of the previously studied inhibitors. In general, inhibitors which have protection ability over 80% in acidic medium find place in industrial applications. This promising result once again exhibits the importance of this class of compounds for protecting metals in an acidic medium.

**Table 3.** Comparison of protection ability of 2-DMT with literature

| Inhibitor | Metal | Medium | $\eta$(%) | Ref |
|---|---|---|---|---|
| Triazine-glycine | Mild steel | 1.0 M HCl | 71.2 | [22] |
| 1,3,5-tri-p-tolyl-1,3,5-triazene | Brass | 0.5 M HCl | 76.0 | [26] |
| 6-methyl-5-[m-nitrostyryl]-3-mercapto-1,2,4-triazine | Tubing steel | 12% HCl | 87.1 | [27] |
| $N^2$-(4-(5-(4-methoxyphenyl)isoxazol-3-yl)phenyl)-$N^4$,$N^6$-diphenyl-1,3,5-triazine-2,4,6-triamine | Mild steel | 1 M HCl | 92.0 | [28] |
| 4-amino-6-methyl-3-thioxo-3,4-dihydro-1,2,4-triazin-5(2H)-one | Mild steel | 1.0 N HCl | 92.9 | [29] |
| 1,3,5-tris(4-methoxyphenyl)-1,3,5-triazine | N80 steel | 15% HCl | 93.2 | [30] |
| Hexahydro-1,3,5-p-aminophenyl-s-triazine | Mild steel | 1.0 N HCl | 96.1 | [31] |
| 2,4-Diamino-6-methly-1,3,5-triazine | Mild steel | 0.5 M HCl | 94.7 | This work |

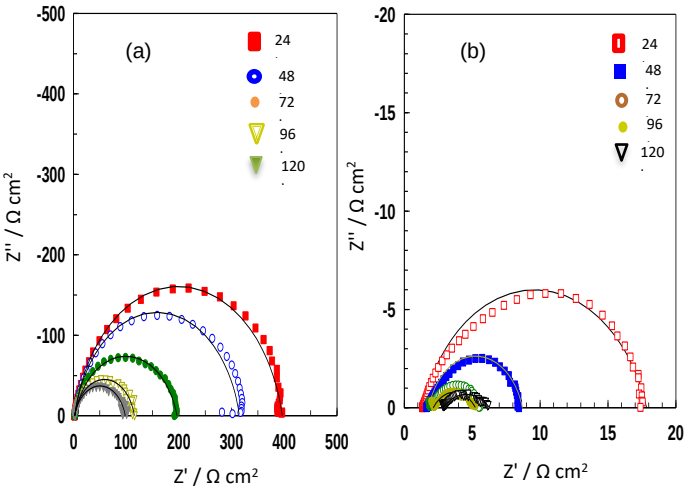


**Figure 4.** Nyquist plots of MS electrode (b) in 0.5 M HCl and with the existence of 10.0 mM 2-DMT (a) after different exposure times. Straight lines show the fitting curves.

Corrosion properties of MS in blank solution and with the existence of 10.0 mM 2-DMT are evaluated using EIS after 24, 48, 72, 96 and 120 h exposure times (long-immersion time) and related Nyquist diagrams are represented in Fig. 4. All EIS responses show the same behavior due to observing one depressed semicircle after long-immersion times. The acid solution damaged the bare MS heavily. Because $R_p$ values decreased from 17.0 $\Omega$ $cm^2$ to 3.3 $\Omega$ $cm^2$. Although polarization resistances decreased from 394 $\Omega$ $cm^2$ to 95 $\Omega$ $cm^2$ with the existence of 10.0 mM 2-DMT, polarization resistances are still higher when compared to those of blank solution results. Long-immersion time results showed that 2-

DMT underlines that it reduces the corrosion rate and the existence of an effective inhibition on the MS surface [32]. Besides, corrosion inhibition efficiencies are also calculated using equation 2, the values changed between 95.6% and 98.0%. LPR method supported by these values. To confirm the results of long-immersion time experiments obtained with EIS and LPR, the volume of hydrogen gas released at the MS electrode was measured at the end of 120 hours via an inverted tape measure and these results are given in Fig. 5. It is clearly seen from Fig. 5, while the hydrogen volume increased at the MS electrode as a result of corrosion, the hydrogen volume increased very slowly in the presence of 2-DMT. Measured volumes are 90 mL $cm^{-2}$ for blank solution and 4.6 mL $cm^{-2}$ for existence of 10.0 mM 2-DMT in 0.5 M HCI, respectively. These results confirm the results of long-immersion time experiments obtained with EIS and LPR.

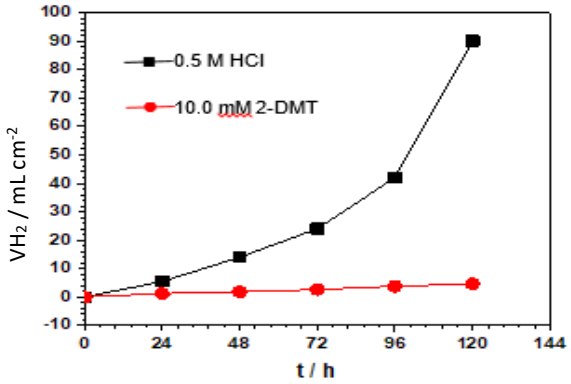


**Figure 5.** Hydrogen gas volume of MS electrode in 0.5 M HCI and with the existence of 10.0 mM 2-DMT after 120 h.

### 3.3. Thermodynamic Consideration

The most important event in the protection of the MS with the inhibitor is the adsorption of the inhibitor molecules on the metal surface. This event should be dealt with in detail. For this reason, in order to explain the adsorption process, several adsorption isotherms have been applied for this inhibitor and Langmuir isotherm provides the most suitable one. The plot of Langmuir isotherm ($C/\theta$ vs $C$) and related equation are given in Fig. 6. and below.

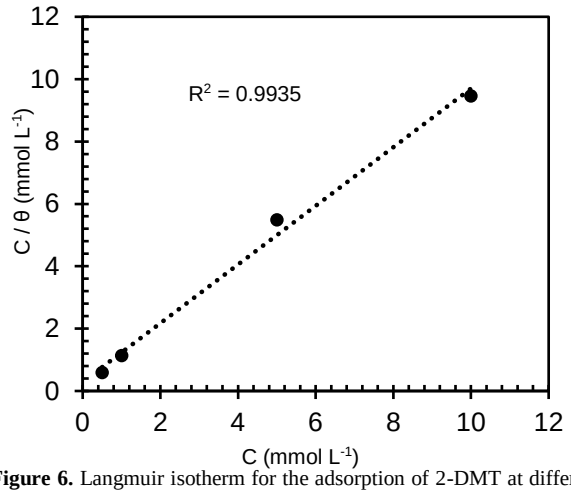


**Figure 6.** Langmuir isotherm for the adsorption of 2-DMT at different concentrations on the MS surface.

$$\frac{C_{(inh)}}{\theta} = \frac{1}{K_{(ads)}} + C_{(inh)} \quad (5)$$

$C_{inh}$, $\theta$ and $K_{ads}$ denote the concentration of inhibitor, degree of surface coverage and adsorption equilibrium constant, respectively. Intercept of equation 5 gives the $K_{ads}$ and its value is 3417 $M^{-1}$. This value is used for calculation of $\Delta G^o_{ads}$ in the following equation:

$$\Delta G^o_{ads} = -RT\ln(55.5K_{ads}) \quad (6)$$

$R$, $T$ and 55.5 denote the universal gas constant (8.314 J $mol^{-1}$ $K^{-1}$), temperature ($K$), and concentration $H_2O$, respectively. -30.11 kJ $mol^{-1}$ is found for $\Delta G^o_{ads}$. A negative sign shows the spontaneous adsorption and the value of $\Delta G^o_{ads}$ is between -20 kJ $mol^{-1}$ and -40 kJ $mol^{-1}$, indicating the mixed adsorption mode [33].

In addition to determining the adsorption process and calculating the thermodynamic parameters, a better understanding of the corrosion mechanism is required. We know that the adsorption of organic inhibitors to the metal surface occurs through electrostatic interactions [34]. In this study, to see whether there is an electrostatic interaction and to explain the inhibition mechanism, the surface charge of metal is measured using $E_{ocp}$ and $R_p$ with the existence of 10.0 mM 2-DMT and related figure is given below. The surface charge of metal is calculated as follows:

$$E_r = E_{ocp} - E_{pzc} \quad (7)$$

$E_r$ denotes the Antropov's rational corrosion potential [35]. $E_r$ is found to be 0.01 V (Ag/AgCI). This means that MS surface is charged with positive with the existence of inhibitor molecules. Mechanism can be described as follows: Negatively charged $CI^-$ ions can be adsorbed on positively charged MS surface at the firs step and the next step may be adsorption of the protonated inhibitor molecules [36]. Inhibitor molecules are protonated in the following way:

$$2\text{-DMT} + H^+ \leftrightarrow [2\text{-DMTH}]^+ \quad (8)$$

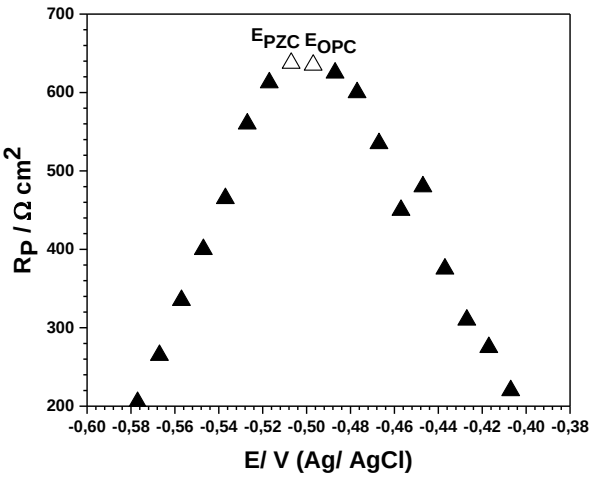


**Figure 7.** $R_p$ vs electrode potential for MS in 0.5 M HCl solution with the existence of 10 mM 2-DMT.

This electrostatic interaction (physical adsorption) forms a protective inhibitor film on the MS surface and this film prevents the metal from corrosion. In addition to the physical adsorption, functional groups such as amino, methyl and conjugated bonds lead to chemical adsorption on the MS surface, which contribute to the protective ability of inhibitor [34]. Same results are found in literature. For instance, a work by Gong et al. [37], inhibition abilities of 2-amino-4-(4-methoxyphenyl)-thiazole (MPT) and 2-amino-4-phenylthiazole (APT) were investigated for MS protection in acidic medium. $E_r$ values of these inhibitors are calculated positively, meaning that the surfaces of MS were positive charged after 1 h immersion. In another study, Ouakki et al. [38], investigated the corrosion inhibition performances of two organic compounds (2-(1,4,5-triphenyl-1H-imidazol-2-yl) phenol (P1) and 3-methoxy-4-(1,4,5-triphenyl-1H-imidazol-2-yl) phenol (P2)) for MS in 1.0 M HCl. Results showed that $CI^-$ ions will be the first to adsorb on MS surface and inhibitor in cationic form interacts with ions.

### 3.4. Surface Morphology Results

Figure 8 shows the SEM and AFM images of MS electrode in 0.5 M HCI and with the existence of 10.0 mM 2-DMT after 120 h. It is seen that MS surface is intensely corroded by acid environment after 120 h. Islands and cavities formed over the surface. Fortunately, as shown in Fig. 8c, the surface structure of the MS is smooth and some corrosion products are seen after adding 2-DMT. AFM images support the SEM results. Average roughness of bare MS and after adding 2-DMT are found to be 138.3 nm and 39.6 nm, respectively. As a result, 2-DMT significantly inhibited the MS corrosion in HCI environment.

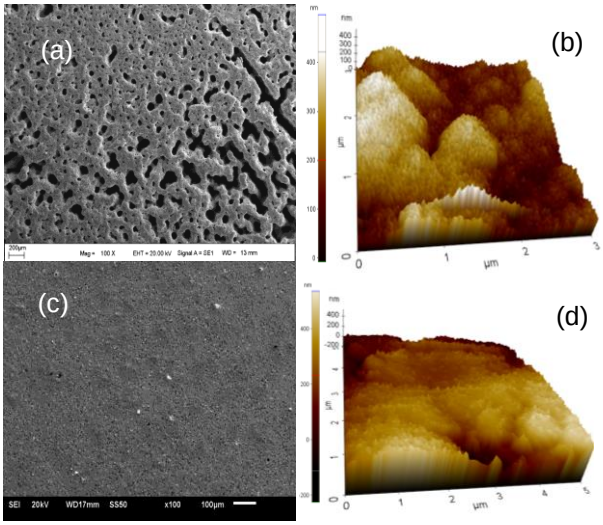


**Figure 8.** SEM (a,c) and 3D AFM (b,d) images of MS electrode in 0.5 M HCI (a,b) and with the existence of 10.0 mM 2-DMT (c,d) after 120 h.

### 3.5. Quantum Chemical Calculation Results

In addition to electrochemical experiments, quantum chemical calculation is performed to better understand the relationship between structural, electronic properties and adsorption process. Figure 9 depicts the structure of 2,4-Diamino-6-methly-1, 3, 5-triazine (2-DMT). B3LYP was used on the basis of DFT with a tuned of 6-311 ++ G (d, p) to obtain these geometries. Corrosion inhibitors have been extensively researched in heterocyclic chains, carboxyl, amines, conjugated bonds, and electronegative atom (N) [39-45]. These groups, according to the findings, acted as specific adsorption centres and rose to prominence. While the inhibitor mechanism anticorrosion inhibition is not fully understood, it can be stated that the inhibitor, in general, tends to offer electrons to the metal's unoccupied d orbital, and this trend increases as the magnitude of the orbital's energy of HOMO increases [46]. The values of absolute hardness ($\eta$), absolute electronegativity ($\chi$), fraction of transferred electrons ($\Delta N$) and absolute softness ($\sigma$) were calculated [47-52];

$$\Delta E = E_{LUMO} - E_{HOMO} \quad (9)$$

$$A = -E_{LUMO} \quad (10)$$

$$I = -E_{HOMO} \quad (11)$$

$$\eta = \frac{1}{2}(I - A) \quad (12)$$

$$\sigma = \frac{1}{\eta} \quad (13)$$

$$\chi = \frac{1}{2}(I + A) \quad (14)$$

$$\Delta N = \frac{\chi Fe - \chi inh}{2(\eta Fe + \eta inh)} \quad (15)$$



Table 4 shows the calculated parameters for this study, and Figure 9 shows the orbitals. The HOMO energy was -7.1980, as shown in Table 4. The HOMO was usually found in 2-DMT zones including atoms of N and a ring of heterocyclic. The energy of the LUMO was -1.9959 eV. The HOMO was discovered on the N terminals of the 2-DMT. In Table 4, the values for electronegativity were 4.5969 eV, hardness was 2.6010 eV, and softness was 0.3844. Adsorption appears to be appropriate for the interplay among not shared electron pairs of N atoms, electrons of the heterocyclic ring, and the metal's unoccupied d orbital. The molecules efficiency was also determined by examining the parameters of global reactivity. The energy gap ($\Delta E$) reflected the inhibitor molecule's reactivity to the metal. A low $\Delta E$ value indicated strong metal adsorption with high inhibitive efficiency. As the $\Delta E$ value decreases, the reactivity and tendency of electron donation increases. The dipole moment (3.1062 D) value can give an idea of the probability of the adsorption of molecules. The increased dipole moment could be attributed to dipole-dipole interactions between the molecules of inhibitor and the surface of the metal, resulting in increased inhibition. The processes of electron sharing between the inhibitor and the surface of metal can be argued as functions at the value $\Delta N$ listed in Table 4 with respect to Pearson theory [53]. The process of electron transfer is with respect to the electronegativity value ($\chi$), as well as the lower electronegativity as well as the higher transfer of electron. The fraction of electrons transferred, $\Delta N$

(0.4619) is important parameter to investigate corrosion inhibition. In the literature, it is claimed that high $\Delta N$ value help promote high adsorption to the MS surface, which is good inhibition and protection [53]. If $\Delta N$ is greater than zero, electrons move from inhibitors to the surface of metal atoms; otherwise, electrons move from the surface of the metal to molecules of the inhibitor [39, 54]. The inhibition efficiency and quantum parameters have a strong correlation.

**Table 4.** DFT/B3LYP/6-311G (++ d,p) method calculated quantum parameters for 2-DMT.

| Inhibitor | $E_{HOMO}$ (eV ) | $E_{LUMO}$ (eV) | $\Delta E$ (eV) | $\beta$ (eV) | $\gamma$ (eV) | $S$ ($eV^{-1}$) | $\Delta N$ | $\mu$ (Debye) |
|---|---|---|---|---|---|---|---|---|
| **2-DMT** | -7.1980 | -1.9959 | 5.2021 | 4.5969 | 2.6010 | 0.3844 | 0.4619 | 3.1062 |

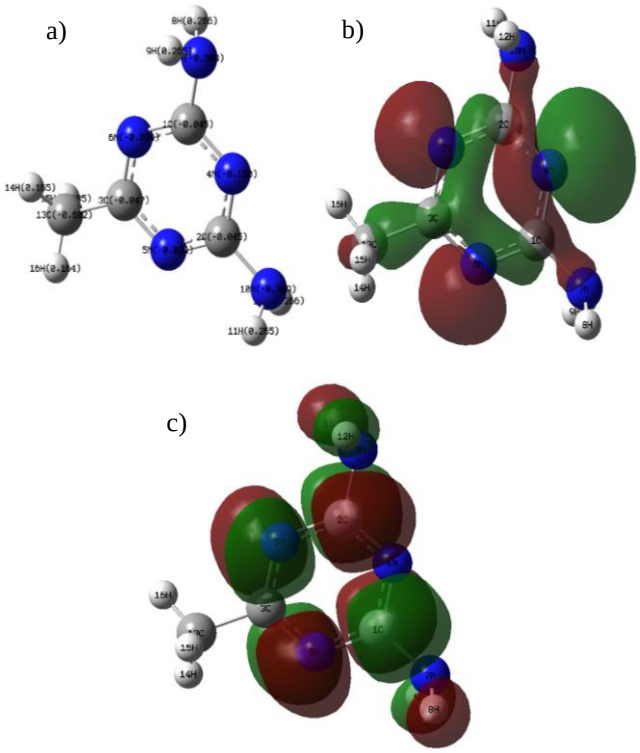


**Figure 9.** 2-DMT molecule structures with Mulliken charge (a), HOMO (b), and LUMO (c) orbitals.

## 4. CONCLUSION

A new organic compound as a corrosion inhibitor is studied for MS protection from acid corrosion using electrochemical, morphological and quantum chemical calculation methods. Following results can be drawn:

1. Tafel curves (cathodic and anodic) and Langmuir adsorption isotherm (physical and chemical adsorption) show that studied inhibitor is classified as mixed-type. Tafel curves do not change with the existence of different concentrations of 2-DMT in blank solution, implying that the same corrosion mechanism occurs in both corrosive media due to giving parallel lines.
2. While values of $i_{corr}$ decreased, $R_p$ values increased with the existence of 0.5, 1.0, 5.0 and 10.0 mM 2-DMT, indicating that a stable inhibitor film formed on the MS surface and this film behaves like a preventative.
3. The protection ability of some triazine-containing compounds are compared with 2,4-Diamino-6-methly-1,3,5-triazine and inhibition efficiency of studied inhibitor in this study is found higher than those of the previous studied inhibitors. This promising result once again exhibits the importance of this class of compounds for protecting metals in an acidic medium.
4. Although the diameter of semicircles of both bare MS and with the existence of 10.0 mM 2-DMT decreased after 120 h, the corrosion rate of MS electrode with the existence of 10.0 mM 2-DMT is slower than that of bare MS and very low hydrogen gas is obtained on the MS electrode with the existence of 10.0 mM 2-DMT.
5. The adsorption of inhibitor molecules on the MS surface is discussed in more detail and the existence of electrostatic and chemical interactions are confirmed by PZC results.
6. -30.11 kJ $mol^{-1}$ is found for $\Delta G^{o}_{ads}$. Negative sign shows the spontaneous adsorption.
7. SEM and AFM images confirm the existence of inhibition by 2-DMT due to obtaining smooth surface.
8. Quantum chemical calculation manifested that adsorption ability of inhibitor molecule is due to dipol moment and high value of $\Delta N$.



## Acknowledgement

I would like to thank Mardin Artuklu University for supporting this study.

## REFERENCES

[1] Koch G, Trends in oil and gas corrosion research and technologies. 1st ed. Elsevier Inc.; 2017.

[2] Rodriguez-Alonso L, Lopez-Sanchez J, Serrano A, de la Fuente OR, Galvan JC, Carmona N. Hybrid sol-gel coatings doped with non-toxic corrosion inhibitors for corrosion protection on AZ61 magnesium alloy. Gels 2022;8(34):1-12.

[3] Ouyang Y, Li LX, Xie ZH, Tang L, Wang F, Zhong CJ. A self-healing coating based on facile pH-responsive nanocontainers for corrosion protection of magnesium alloy. J. Magnes. Alloy. 2022;10:836-49.

[4] Jiang Y, Gao S, Liu Y, Huangfu H, Guo X, Zhang J. Enhancement of corrosion resistance of AZ31B magnesium alloy by preparing MgAl-LDHs coatings modified with imidazolium based dicationic ionic liquid, Surf Coating Technol 2022;440:128504.

[5] Tan B, Lan S, Zhang S, Deng H, Qiang Y, Fu A, Ran Y, Xiong J, Marzouki R, Li W. Passiflora edulia Sims leaves Extract as renewable and degradable inhibitor for copper in sulfuric acid

solution. Colloids Surfaces A Physicochem. Eng. Asp. 2022;645:128892.
[6] Sefaja J, Dernikovic B, Malina J, Lovrecek B. Investigation of steel corrosion in pickling solutions: Solutions with inhibitors. Surf. Technol. 1983;20(3):247–63.
[7] Goyal M, Kumar S, Bahadur I, Verma C, Ebenso E.E. Organic corrosion inhibitors for industrial cleaning of ferrous and non-ferrous metals in acidic solutions: A review. J. Mol. Liq. 2018;256:565–73.
[8] Yıldız R. An electrochemical and theoretical evaluation of 4,6-diamino-2-pyrimidinethiol as a corrosion inhibitor for mild steel in HCl solutions. Corrosion Sci. 2015;90:544-53.
[9] Ech-chihbi E, Nahl A, Salim R, Benhiba F, Moussaif A, El-Hajjaji F, et al. Computational, MD simulation, SEM/EDX and experimental studies for understanding adsorption of benzimidazole derivatives as corrosion inhibitors in 1.0 M HCl solution. J. Alloys Compd. 2020;844:155842.
[10] Fakhry H, El Faydy M, Benhiba F, Laabaissi T, Bouassiria M, Allali M, et al. A newly synthesized quinoline derivative as corrosion inhibitor for mild steel in molar acid medium: Characterization (SEM/EDS), experimental and theoretical approach. Colloids Surf, A Physicochem Eng Asp 2021:610:125746.
[11] Yıldız R, Döner A, Doğan T, Dehri İ. Experimental studies of 2-pyridinecarbonitrile as corrosion inhibitor for mild steel in hydrochloric acid solution. Corros. Sci. 2014;82:125-32.
[12] Ganapathi Sundaram R, Sundaravadivelu M. Anticorrosion activity of 8-quinoline sulphonyl chloride on mild steel in 1 M HCl solution. J. Metall 2016;8095206.
[13] Xhanari K, Finsgar M. Organic corrosion inhibitors for aluminium and its alloys in acid solutions: A review. RSC Adv. 2016;6(67):62833–57.
[14] Döner A, Kardaş G. N-Aminorhodanine as an effective corrosion inhibitor for mild steel in 0.5 M $H_2SO_4$. Corrosion Sci. 2011;53:4223–32.
[15] El-Faham A, Osman SM, Al-Lohedan HA, El-Mahdy GA. Hydrazino-methoxy-1,3,5-triazine derivatives' excellent corrosion organic inhibitors of steel in acidic chloride solution. Molecules 2016;21(6):714.
[16] Arshad M, Khan TA, Khan MA. 1,2,4-triazine derivatives: Synthesis and biological applications. Int. J. Pharm. Sci. 2014;5(4):149-62.
[17] Zarrok H, Oudda H, El Midaoui A, Zarrouk A, Hammouti B, Ebn Touhami M, Attayibat A, Radi S, Touzani R, Some new bipyrazole derivatives as corrosioninhibitors for C38 steel in acidic medium, Res. Chem. Intermed. 2012;38(8):2051–63.
[18] Bouoidina A, Ech-chihbi E, El-Hajjaji F, El Ibrahimi B, Kaya S, Taleb M, Anisole derivatives as sustainable-green inhibitors for mild steel corrosion in 1 M HCl: DFT and molecular dynamic simulations approach. J. Mol. Liq. 2021;324:115088.
[19] Murulana LC, Kabanda MM, Ebenso EE. Experimental and theoretical studies on the corrosion inhibition of mild steel by some sulphonamides in aqueous HCl. RSC Adv. 2015;36:28743–61.
[20] Li X, Deng S, Lin T, Xie X, Du G. 2-Mercaptopyrimidine as an effective inhibitor for the corrosion of cold rolled steel in $HNO_3$ solution. Corros. Sci. 2017;118:202-16.
[21] Li Y, Zhang S, Ding Q, Qin B, Hu L. Versatile 4, 6-dimethyl-2-mercaptopyrimidine based ionic liquids as high-performance corrosion inhibitors and lubricants. J. Mol. Liq. 2019;284:577–85.
[22] Seung-Hyun Y, Young-Wun K, Chung K, Nam-Kyun K, Joon-Seop K. Corrosion inhibition properties of triazine derivatives containing carboxylic acid and amine groups in 1.0 M HCl solution. Ind. Eng. Chem. Res. 2013;52(32):10880–89.
[23] Nassar IM, Abbas MA, Hamdy A, Elazabawy OE, Evaluating the inhibiting action of cds nanoparticles and cds/pmma hybrid for corrosion of carbon steel in acidic media, international journal of current research 2013;5:4327–37.
[24] Haque J, Ansari KR, Srivastava V, Quraishi MA, Obot IB. Pyrimidine derivatives as novel acidizing corrosion inhibitors for N80 steel useful for petroleum industry: A combined experimental and theoretical approach. J Ind Eng Chem, 2017;49:176-88.
[25] Ichchou I, Larabi L, Rouabhi H, Harek Y, Fellah A. Electrochemical evaluation and DFT calculations of aromatic sulfonohydrazides as corrosion inhibitors for XC38 carbon steel in acidic media. J. Mol. Struct. 2019;1198:126898.
[26] Singh P, Singh A, Quraishi MA. Inhibition effect of 1,3,5-tri-p-tolyl-1,3,5-triazene on the corrosion of brass in 0.5 M HCl solution. Res Chem Intermed 2014;40:595–4
[27] Migahed M, Nassar I. Corrosion inhibition of tubing steel during acidization of oil and gas wells. Electrochim. Acta 2008;53:2877–82.
[28] Yadav M, Kumar S, Tiwari N, Bahadur I, Ebenso EE. Experimental and quantum chemical studies of synthesized triazine derivatives as an efficient corrosion inhibitor for N80 steel in acidic medium. J. Mol. Liq. 2015;212:151–67.
[29] John S, Joseph A, Sajini T, Jose AJ. Corrosion inhibition properties of 1,2,4-Hetrocyclic systems: Electrochemical, theoretical and Monte Carlo simulation studies. Egypt. J. Pet. 2017;26:721–32.
[30] Salman M, Ansari KR, Haque J, Srivastava V, Quraishi MA, Mazumder MAJ, Ultrasound-assisted synthesis of substituted triazines and their corrosion inhibition behavior on N80 steel/acid interface. J Heterocyclic Chem. 2020;57:2157–72.
[31] Shukla SK, Singh AK, Quraishi MA. Triazines: Efficient corrosion inhibitors for mild steel in hydrochloric acid solution. Int. J. Electrochem. Sci. 2012;7:3371 – 89.
[32] Usman BJ, Gasem ZM, Umoren SA, Solomon MM. Eco-friendly 2-Thiobarbituric acid as a corrosion inhibitor for API 5L X60 steel in simulated sweet oilfield environment: Electrochemical and surface analysis studies. Scientific Reports, 2019;9:830.

[33] Gurjar S, Ratnani S, Kandwal P, Tiwari KK, Sharma A, Sharma SK. Experimental and theoretical studies of 1-Benzyl pyridazinium bromide as green inhibitor for mild steel corrosion. e-Prime - Advances in Electrical Engineering, Electronics and Energy 2022;2:100054.

[34] Shao H, Yin X, Zhang K, Yang W, Chen Y, Liu Y. N-[2-(3-indolyl)ethyl]-cinnamamide synthesized from cinnamomum cassia presl and alkaloid tryptamine as green corrosion inhibitor for Q235 steel in acidic medium. J. Mater. Res. Technol. 2022;20:916-33.

[35] Fuchs-Godec R. The adsorption CMC determination and corrosion inhibition of some N-alkyl quaternary ammonium salts on carbon steel surface in 2M $H_2SO_4$. Colloids Surf. A Physicochem. Eng. Aspects 2006;280:130–39.

[36] Kaya F, Solmaz R, Geçibesler İH. Adsorption and corrosion inhibition capability of Rheum ribes root extract (Işgın) for mild steel protection in acidic medium: A comprehensive electrochemical, surface characterization, synergistic inhibition effect, and stability study. J. Mol. Liq. 2023;372:121219.

[37] Gong W, Yin X, Liu Y, Chen Y, Yang W. 2-Amino-4-(4-methoxyphenyl)-thiazole as a novel corrosion inhibitor for mild steel in acidic medium. Progress in Organic Coatings 2019;126:150–61.

[38] M. Ouakki, M. Galai, M. Rbaa, Ashraf S. Abousalemd, B. Lakhrissi, M. Ebn Touhami, M. Cherkaoui, Electrochemical, thermodynamic and theoretical studies of some imidazole derivatives compounds as acid corrosion inhibitors for mild steel. J. Mol. Liq. 2020;319:114063.

[39] Alamiery A, A.B. Mohamad, A.A.H. Kadhum, M.S. Takriff. Comparative data on corrosion protection of mild steel in HCl using two new thiazoles. Data Brief 2022;40:107838.

[40] Wang C, Zou C, Cao Y. Electrochemical and isothermal adsorption studies on corrosion inhibition performance of β-cyclodextrin grafted polyacrylamide for X80 steel in oil and gas production. J. Mol. Struct. 2021;1228:129737.

[41] Ferraa S, Ouakki M, Barebita H, Nimour A, Cherkaoui M, Guedira T. Corrosion inhibition potentials of some phosphovanadate-based glasses on mild steel in 1 M HCl. Inorg. Chem. Commun. 2021;132:108806.

[42] El-Zekred MA, Nofal AM, Shalabi K, Fouda AS. Ficus carica extract as environmentally friendly inhibitor for the corrosion of L-80 carbon steel in 0.5 M $H_2SO_4$ media, J. Indian Chem. Soc. 2021;98.100128.

[43] Costa SN, Almeida-Neto FWQ, Campos OS, Fonseca TS, de Mattos MC, Freire VN., et al. Carbon steel corrosion inhibition in acid medium by imidazolebased molecules: Experimental and molecular modelling approaches. J. Mol. Liq. 2021;326:115330.

[44] Abdallah M, Gad EAM, Sobhi M, Al-Fahemi JH, Alfakeer MM. Performance of tramadol drug as a safe inhibitor for aluminum corrosion in 1.0 M HCl solution and understanding mechanism of inhibition using DFT. Egypt J. Pet. 2019;28:173–81.

[45] Sığırcık G, Yıldırım D, Tüken T. Synthesis and inhibitory effect of N,N'-bis(1-phenylethanol)ethylenediamine against steel corrosion in HCl Media. Corrosion Sci. 2017;120:184–93.

[46] Pour-Ali S, Hejazi S. Tiazofurin drug as a new and non-toxic corrosion inhibitor for mild steel in HCl solution: experimental and quantum chemical investigations. J. Mol. Liq. 2022;354:118886.

[47] Hegazy MA, Atlam FM. Three novel bolaamphiphiles as corrosion inhibitors for carbon steel in hydrochloric acid: Experimental and computational studies. J Mol. Liq. 2016;218:649–62.

[48] Yıldız R. Adsorption and inhibition effect of 2,4-diamino-6-hydroxypyrimidine for mild steel corrosion in HCl medium: experimental and theoretical investigation. Ionics 2019; 25:859–70.

[49] Verma C, Quraishi M, Singh A. 2-Amino-5-nitro-4, 6-diarylcyclohex-1-ene-1, 3, 3- tricarbonitriles as new and effective corrosion inhibitors for mild steel in 1 M HCl: Experimental and theoretical studies, J. Mol. Liq. 2015;212:804–12.

[50] Yıldız R, Doğru Mert B. Theoretical and Experimental Investigations on Corrosion Control of Mild Steel in Hydrochloric Acid Solution by 4-aminothiophenol. Anti-Corros Meth Mater. 2019;66:127–37.

[51] Keleşoğlu A, Yıldız R, Dehri İ, 1-(2-Hydroxyethyl)-2 Imidazolidinone as corrosion inhibitor of mild steel in 0.5 M HCl solution: thermodynamic, electrochemical and theoretical studies. J Adhes Sci Technol 2019;33:2010–30.

[52] Keleşoğlu A, Sığırcık G, Yıldız R, Dehri İ. Experimental and theoretical investigation of Pyrazinecarboxamide against mild steel corrosion. J Dispers Sci Technol 2023;44(2):329–341.

[53] Gomez B, Likhanova N, Dominguez-Aguilar M, Martinez-Palou R, Vela A, Gazquez JL. Quantum chemical study of the inhibitive properties of 2-pyridyl-azoles, J. Phys. Chem. B. 2006;110:8928-34.

[54] Tüzün B, Bhawsar J. Quantum chemical study of thiaozole derivatives as corrosion inhibitors based on density functional theory, Arab. J. Chem. 2021;14(2): 102927.

Cilt 12, Sayı 1, Sayfa 153-162, 2023 Volume 12, Issue 1, Page 153-162, 2023

Araştırma Makalesi https://doi.org/10.46810/tdfd.1205088 Research Article

Türk Doğa ve Fen Dergisi
Turkish Journal of Nature and Science
www.dergipark.gov.tr/tdfd

# Investigation of the Magnetic and Mechanical Properties of Nano-Y2O3 Doped Bismuth Based Superconductor Materials

**Emine Burcu CEVİZCİ [1*], Kemal KOCABAŞ[1], Sedat KURNAZ[2]**

[1] Dokuz Eylul University, Science Faculty, Physics Department, İzmir, Türkiye
[2] Kastamonu University, Central Research Laboratory, Kastamonu, Türkiye
Emine Burcu CEVİZCİ ORCID No: 0000-0002-1738-4130
Kemal KOCABAŞ ORCID No: 0000-0002-4443-0059
Sedat KURNAZ ORCID No: 0000-0003-3657-2628

**Corresponding author: cevizciburcu@gmail.com*

(Received: 15.11.2022, Accepted: 14.03.2023, Online Publication: 27.03.2023)

**Keywords**
nano- $Y_2O_3$, BSSCO, Critical Current Density, Hole concentration, Microhardnes

**Abstract:** The effects of nano-$Y_2O_3$ addition on the structural, superconducting, magnetic and mechanical properties of Bi-2223 superconducting system were investigated in this study. Bulk polycrystalline samples with general formula of $Bi_{1.8}Pb_{0.4}Sr_2Ca_2Cu_3O_{10+\delta}$ + ($Y_2O_3$) with ( x; weighted % 0.0-0.2-0.4-0.8-1.0) were prepared by solid state reaction method. X-ray diffraction (XRD), Scanning Electron microscope (SEM), Energy dispersive X-ray spectroscopy (EDX) measurement, Vibrating sample measurement (VSM), Resistance- temperature (ρ-T) measurement and Vickers microhardness measurement (VHM) were also used for samples structural characterizations. XRD patterns showed that both Bi -2223 and Bi-2212 phases are coexist in the samples. While a lattice parameter increased, c lattice parameter decreased with increasing nano- $Y_2O_3$ addition. In SEM photographs, it is seen that granular structure is plate-like in all samples. The presence of point particles on the layered particles has been seen more clearly with increasing $Y_2O_3$ addition. Hole concentration values that calculated from ρ-T measurement, ranges from 0.113 to 0.160. While amount of Y2O3 addition increased, critical transition temperatures decreased. VSM results showed that critical current density values increase with Y2O3 addition. VHM results showed that the hardness value increased until x= 0.4% additive sample and decreased after this value.



# Nano-Y2O3 Katkılı Bizmut Esaslı Süperiletken Malzemelerin Manyetik ve Mekanik Özelliklerinin İncelenmesi

**Anahtar Kelimeler**
nano- Y2O3, BSSCO, Kritik Akım Yoğunluğu, Delik konsantrasyon, Mikrosertlik

**Öz:** Bu çalışmada nano-$Y_2O_3$ ilavesinin Bi-2223 süperiletken sisteminin yapısal, süperiletken, manyetik ve mekanik özellikleri üzerindeki etkileri araştırılmıştır. Bi1.8Pb0.4Sr2Ca 2Cu3O10 + δ + ($Y_2O_3$) ile ( x; ağırlıkça % 0,0-0,2-0,4-0,8-1,0) genel formülüne sahip polikristal örnekler katıhal reaksiyon yöntemiyle hazırlandı. Örneklerin yapısal karakterizasyonları için X-ışını kırınımı (XRD), Taramalı Elektron mikroskobu (SEM), Enerji dağılımlı X-ışını spektroskopisi (EDX) ölçümü, Titreşimli numune ölçümü (VSM), Direnç-sıcaklık (ρ-T) ölçümü ve Vickers mikrosertlik ölçümü (VHM) yapılmıştır. XRD desenleri, örneklerde hem Bi -2223 hem de Bi-2212 fazlarının bir arada bulunduğunu gösterdi. Nano-Y ilavesinin artmasıyla a örgü parametresi artarken, c örgü parametresi azalmıştır. SEM fotoğraflarında tüm örneklerde tanecik yapısının plaka benzeri olduğu görülmekte ve katkı miktarındaki artmasıyla tabakalı yapı üzerinde nokta şeklinde partiküllerin varlığı daha net görülmektedir. ρ-T ölçümünden hesaplanan delik konsantrasyonu değerleri 0,113 ile 0,160 arasında değişmektedir. Nano-Y miktarı artarken kritik geçiş sıcaklıkları azalmıştır. VSM sonuçları Nano-Y eklenmesiyle kritik akım yoğunluğu değerlerinin arttığını göstermektedir. VHM sonuçları, sertlik değerinin x= % 0,4 katkılı örneğe kadar arttığını ve bu değerden sonra azaldığını göstermiştir.

## 1. INTRODUCTION

Superconducting materials are sometimes used as high-field magnets to store large amounts of energy. Therefore, superconductivity must persist up to high magnetic fields. High temperature superconductors have two critical field values: the lower critical ($H_{c1}$) and the upper critical magnetic ($H_{c2}$) field. When applied magnetic field (H) intensity is $H_{c1}<H<H_{c2}$, the magnetic field penetrates the superconductor and the superconductivity state is destroyed locally around a vortex [1]. Therefore, the superconducting state and the normal state coexist (mixed state). If the superconductor in the mixed state carries a carrying current, the electrons in the flux lines are exposed to the electromotive force depending on the direction of the magnetic field and the current. Electrons moving under the influence of this force cause ohmic losses. It is possible to eliminate these losses by preventing movement of the flux lines. Flux fixation is provided by various defects in the samples, such as impurities, dislocations, normal precipitates, voids, and grain boundaries. These impurities and defects are called needling centers. In this way, superconducting materials can maintain their superconductivity even at higher magnetic field values.

The critical current density $J_c$ can be increased by the formation of artificial active needling centers as they can prevent the movement of flux lines causing flux shift. Since dimensions of nano-sized particles are closer to the coherent length in relation to the characteristic Cooper pair size, nano doping in Type II superconductors can create stronger needling force in magnetic flux stabilization. The addition of nanoparticles to Bi-2223 superconducting phase plays an important role in flux stabilization and increasing critical current density [2]. Flux stabilization is due to nanoparticles being trapped inside the superconducting grains and producing crystal defects within superconducting particles by creating secondary phase defects [3]. For this reason, many studies have been carried out in the literature on the incorporation of different nano-sized elements into the BSCCO system. It is seen that some nanodopings, such as nano-Au [4], nano-Ag [5], nano-PbO–CdO composite [6], nano-$ZrO_2$ [7] and nano-Sn [8], improve the transport and superconduting properties of the system. The powders in the chemical composition of BiSrCaCuO (BSCCO), a Type II superconductor, have low toxicity. The high thermodynamic stability of the components of this material enables formation of high critical temperature ($T_c$) phases more easily [4]. Because of these properties, they are useful materials in terms of technological applications in order to increase cost efficiency in electricity consumption and to provide lossless power transfer. By improving the superconductivity, magnetic and mechanical properties of the system, it will increase the possibilities of use in industrial and medical applications.

In literature, it is seen that studies have been carried out on the improvement of the superconductivity and mechanical properties of Bi-2223 superconducting materials with micro-scale $Y_2O_3$ doping. In these studies, it is seen that the system improves the superconductivity and mechanical properties [9-12]. Suazlina et al. [13], reported the effects of $Y_2O_3$ nano particle addition in Bi-2212 superconductors. It was found that critical temperature and critical current density increased up to x=0.7 wt%. Again, in a study conducted by Oboudi in 2016 [14], nano $Y_2O_3$ was added to $Bi_{1,8}Pb_{0,4}Sr_2Ca_2Cu_3O_{10+y}$ superconductor samples with different weight percentages. As the additive ratio increased, the current density increased by 200% and superconductivity transition temperature increased by 3%. In both studies, it is seen that both critical temperature and critical current density values of BSCCO system with $Y_2O_3$ addittion increased. In our study, it is aimed to synthesize $Bi_{1,8}Pb_{0.3}Sr_2Ca_2Cu_3O_y$ superconducting ceramics by doping nano-$Y_2O_3$ with different weight percentages in order to improve the magnetic and mechanical properties of the obtained samples.

## 2. MATERIAL AND METHOD

$Bi_{1.8}Pb_{0.3}Sr_2Ca_2Cu_3O_y$ superconducting samples were synthesized using a solid state reaction method. In the first step of the synthesis process, $Y_2O_3$ nanoparticles were added by small weight percentages ($x$=0.2, 0.4, 0.6, 0.8, and 1.0 wt %). Stoichiometric amounts of starting high-purity (≥99.99%) $Bi_2O_3$, PbO, $SrCO_3$, $CaCO_3$, CuO (15–45 nm) and nanosized $Y_2O_3$ (18-38 nm) powders were thoroughly mixed. **Figure 1** has been given a schematic representation of the experimental process.



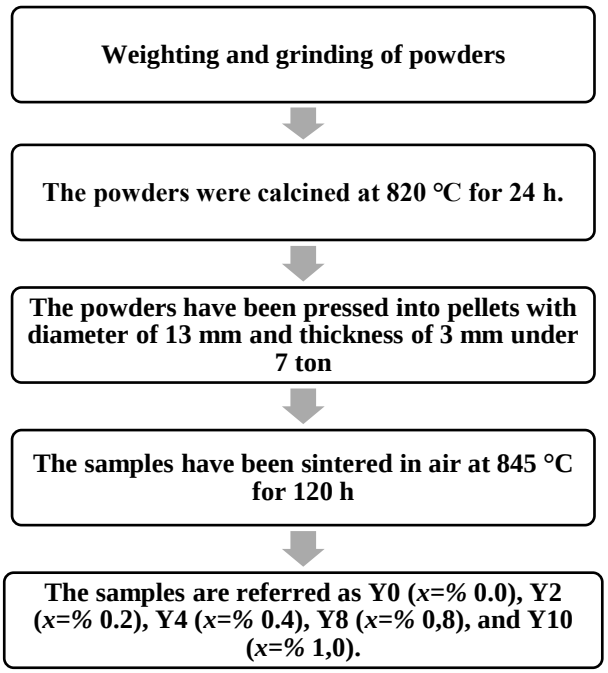


**Figure 1.** Experimental Procedure

The lattice parameters, the phase purity, crystal structure and grain size of samples were obtained from XRD. Phase analysis of the samples was determined with the help of X-PowderX program. The grain structure and surface morphology of the samples were examined with 10000x magnification by scanning electron microscope (SEM) photographs. Energy-dispersive spectrometry

(EDS) was applied for the elemental analysis of the samples. Magnetization curves of the samples depending on the magnetic field strength were taken with Vibrating Sample Magnetometer (VSM) measurements. Critical current density calculations of samples were made with the data obtained from the M-H curves and Bean Model [15]. Microhardness measurements of the samples were made with the Mitutoyo digital microhardness tester of the *HM-200* series.

## 3. RESULTS

The phase purity, the lattice parameters and crystal structure of samples were obtained from XRD patterns. XRD scans were made with $CuK_\alpha$ radiation between 3° to 70°. The wavelength used is $\lambda$=0.15406 nm. X-ray patterns of nano-$Y_2O_3$ addition samples are shown in **Figure 2.** In the XRD patterns, The peaks of Bi-2223 phase are labeled with open circle, the peaks of the Bi-2212 phase are labeled with filled circle, and the peaks of the $Ca_2PbO_4$ phase are labeled with filled diamond. XRD patterns showed that the majority phase consisted of Bi-2223 and Bi-2212 phases in all samples [16]. Impurity phase $Ca_2PbO_4$, which is accelerating the formation of the Bi-2223 phase, was observed at very low peak intensity at $2\theta$=17.80° in all samples except Y0 and Y2 samples [17]. No peaks of $Y_2O_3$ nanoparticles were found in the XRD model. This result showed that nano-$Y_2O_3$ addition did not enter the crystal structure. This may be due to the very small amount of additives made. The volume fraction and the lattice parameters of the samples are listed in **Table 1**.

**Table 1.** Lattice parameters and volume fraction of $Bi_{1.8}Pb_{0.4}Sr_2Ca_2Cu_3O_{10+\delta}$ + ($Y_2O_3$) samples

| Nano $Y_2O_3$ | a ( Å) | b (Å) | c (Å) | Volume Fraction (Bi-2223/Bi-2212) |
|---|---|---|---|---|
| **Y0** | 5.339 | 5.3995 | 37.0740 | 66.11/33.89 |
| **Y2** | 5.3488 | 5.3858 | 36.9768 | 63.92/36.08 |
| **Y4** | 5.3450 | 5.4081 | 36.8568 | 63.04/36.96 |
| **Y8** | 5.3488 | 5.3642 | 36.7716 | 59.02/40.98 |
| **Y10** | 5.3412 | 5.3764 | 36.7596 | 58.68/41.31 |

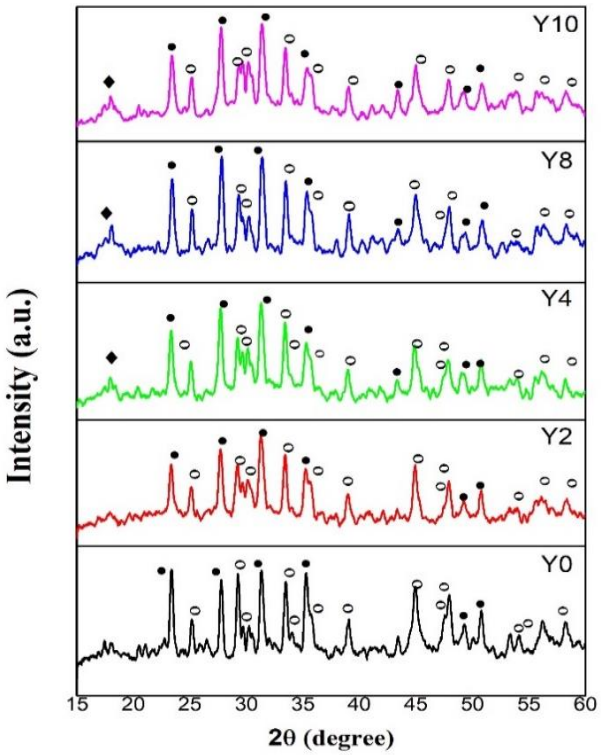


**Figure 2.** X-ray diffractometers at room temperature for the $Bi_{1.8}Pb_{0.4}Sr_2Ca_2Cu_3O_{10+\delta}$ + ($Y_2O_3$) with ( x; weighted % 0.0-0.2-0.4-0.8-1.0) , open circle Bi-2223 phase, filled circle Bi-2212 phase, filled diamond $Ca_2PbO_4$.

The volume ratio of Bi-2223 and Bi-2212 phases was calculated according to the equations below using the intensities of the peaks [18]:

$$Bi-[2223](\%) = \frac{\sum I\,(2223)}{\sum I(2223)+\sum I(2212)} x100 \quad (1)$$

$$Bi-[2212](\%) = \frac{\sum I\,(2212)}{\sum I(2223)+\sum I(2212)} x100 \quad (2)$$

where $I_{2223}$ and $I_{2212}$ are the intensities of the XRD peaks for Bi-2223 and Bi-2212 phases, respectively. It was observed that the percentage of Bi-2212 phase increases and the percentage of Bi-2223 phase decreases with increasing addition of nano- Y. We observed that the decrease in the volume fraction of the Bi-2223 phase in all doped samples was quite small [23]. These results showed that small amounts of nano-$Y_2O_3$ addition effectively contribute to the phase stability of BSCCO systems. Doping material slightly affected the low $T_c$ phase (Bi-2212) and high Tc phase (Bi-2223) ratios [19]. The cell parameters of all samples showed that the Bi-2223 phase is dominant. According to the calculated lattice parameters, the crystal lattice of all samples was found to be orthorhombic.

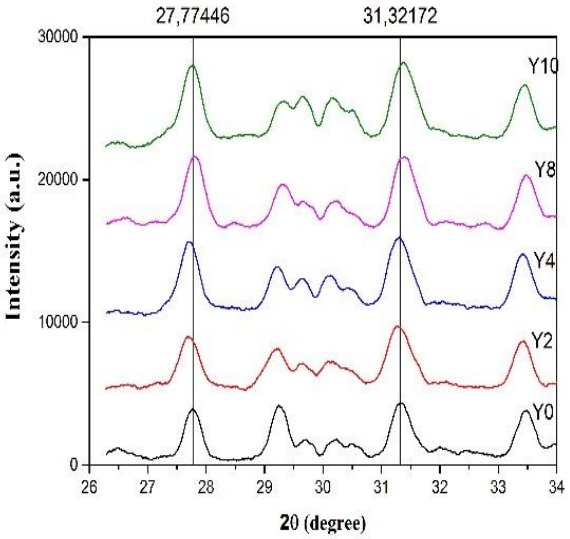


**Figure 3.** The peak shift of the strongest peaks due to the $Y_2O_3$ doping.

**Figure 3** has been showed that peak shift of the strongest peaks.Right and left shifts in the angle of the peaks are caused by point or dislocation defects, stress and strains that occur during the synthesis process. Defects in the structure cause the width of the peaks to increase, while the distortions in the lattice affect the peak positions. Shift in peak towards right is an indication of orthorhombic crystal formation tending the sample to attain superconducting state. When we looked at the positions of the peaks, we did not see that there is no significant peak shift. Accordingly, the orthorhombic structure continues to exist in all samples.

**Table 2. G**rain size, Critical current density and Critical temperature of $Bi_{1.8}Pb_{0.4}Sr_2Ca_2Cu_3O_{10+\delta}$ + ($Y_2O_3$) samples

| Nano $Y_2O_3$ | Grain size (nm) | Dislocation density δ (nm-2) | *Jc (0)* | *Tc*(on set) (Kelvin) |
|---|---|---|---|---|
| **Y0** | 49.88 | 0.000401 | 164.15 | 105 |
| **Y2** | 30.51 | 0.001074 | 211.11 | 109 |
| **Y4** | 30.39 | 0.001082 | 232.73 | 110 |
| **Y8** | 53.64 | 0.000347 | 177.96 | 75 |
| **Y10** | 35.08 | 0.000812 | 120.88 | 90 |

In **Table 1**, it is seen that there is no change the volume fraction of the 2223-phase in nano-$Y_2O_3$ addition samples compared to the undoped sample [14]. The nano-$Y_2O_3$ addition has been effectively added to the phase stability of the BSCCO systems. While parameters a and b did not change, a small decrease occurred in parameter c in nano-Y doped samples (**Figure 4**).
The reason for the small change in the c lattice parameter:

**1.** We think that the reason for the small change in the c parameter is due to the change in the hole concentration in the $CuO_2$ planes. The doped ions may change the spacing between CuO layers, afecting the charge transfer to CuO layers. The hole transfer from Cu planes to Bi–O bonds leads to the contraction of Bi–O layers, causing a decrease in c-axis [20].

**2.** The lattice distortions that manifest themselves in the formation of the modulated structure of the bismuth high temperature superconductors, as a rule, are attributed to the geometric mismatch between the $Bi_2O_2$ bismuth–oxygen and $CuO_2$ copper–oxygen blocks [21].

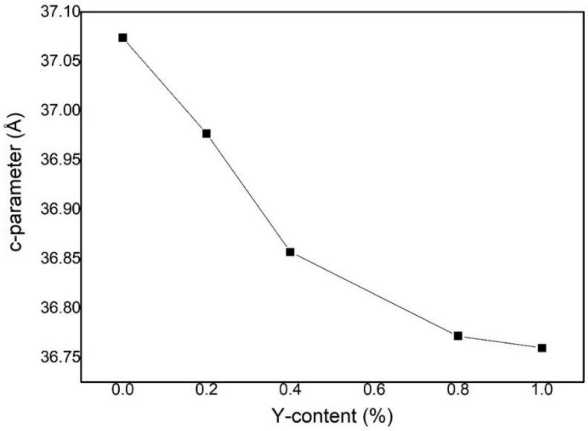


**Figure 4.** Variation of *c*-lattice parameters with nano-Y additive for Bi (Pb):2223 samples.

Grain size of the samples can be determined from XRD patterns using Scherrer Formula which is shown in Eq. (3) [22].

$$D = \frac{K\lambda}{B\cos(\theta)} \quad (3)$$

Here *D* is the mean size of grain, *B* is the line broadening at half the maximum intensity (FWHM) in radians, $\lambda$= 0.15406 nm is the X-ray wavelength and $\theta$ is the Bragg angle. K is Scherrer constant which depends on the crystallite shape and size distribution, indices of the diffraction line [23]. The value of the *K* constant, which ranges from 0.62 to 2.08, can be affected by microstrain in the crystal. In our study, we accepted *K* = 0.94 and the calculated values of *D* represent estimates. The Y4 sample has the smallest particle size and Y8 has the biggest particle size. This may be related to the grinding step of the samples during the preparation process. The particle sizes calculated from the XRD results and the particle development seen from the SEM photographs are similar.

In order to characterize the microstructure of the samples, SEM and EDX analyzes were made and the distribution of the elements in the structure was examined. EDX was used to confirm their chemical composition. SEM microscope images were taken and their morphologies and particle sizes were examined. In **Figure 5 (a-e)**, it is clearly seen that the structure is in a stratified form. This type of configuration is the general structure of the BSCCO system. It is observed that the layered structure continues to exist with increasing nano-$Y_2O_3$ addition. As from Y2 sample, while the layered structure still exists, the existence of agglomeration of small particles on the layered structures draws attention. With the increase in the amount of additive, the presence

of point particles on the layered particles is seen more clearly. This result can be thought to play a role in the formation of artificial needling centers on the samples due to the fact that the nano-dopeds could not enter the structure, but were trapped inside the superconductor grains, revealing the secondary phase defects and producing crystal defects in the superconducting particles [24]. It is thought that the black voids that occur in some places are considered as non-superconducting regions and that they are formed as a result of breaking the connections between the particles. when examined all SEM photos, It has been seen that with increasing nano-$Y_2O_3$ addition, the voids on the surface of the samples increase and cracks occur on the sample surface. The SEM results are well supported by the XRD results. In addition to the intergranular distribution of nanoparticles, the presence of nanoparticles can be observed in other parts of the microstructure of nano-$Y_2O_3$ addition samples. A increase in grain size was observed for Y8 and Y10 samples, which could reduce the superconductivity properties of the BSCCO system.

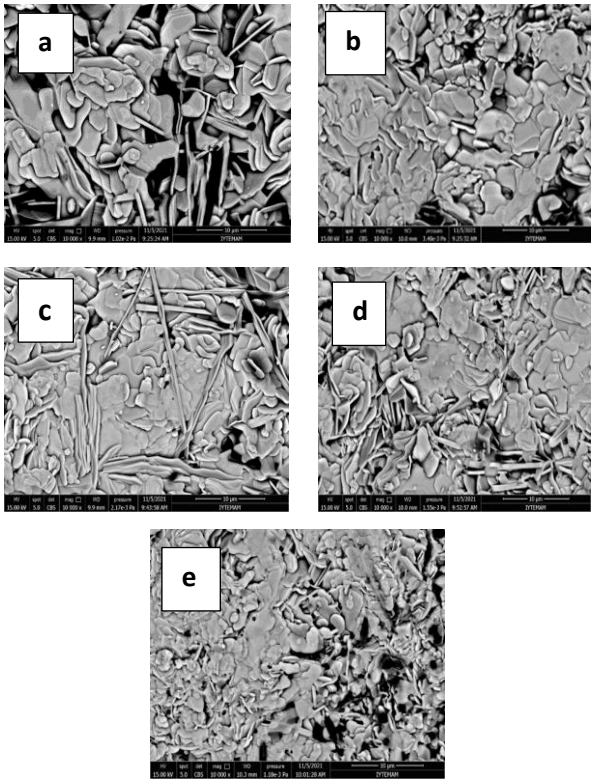


**Figure 5.** SEM images of **a** Y0, **b** Y2, **c** Y4, **d** Y8, and **e** Y10 samples.

According to the results of EDX elemental analysis in **Figure 6 (a-e)**, increase in the additive ratios (%) and the oxygen (O), Bismuth (Bi), Lead (Pb), Strontium (Sr), Calcium (Ca) and Copper (Cu) ratios (%) values in the samples did not change much. The EDX analysis results showed that element percentages are mostly in the desired composition for the prepared superconductor samples. The amount of Y on the sample surfacehas been increased with increasing nano-Y addition. The analysis on sample surface made at different points showed that Y elements in the doped samples are homogeneously distributed throughout the material as expected. In addition, there is no impurity formation in the material. Based on these facts, we can clearly state that the nano-$Y_2O_3$ element is evenly distributed in the structure.

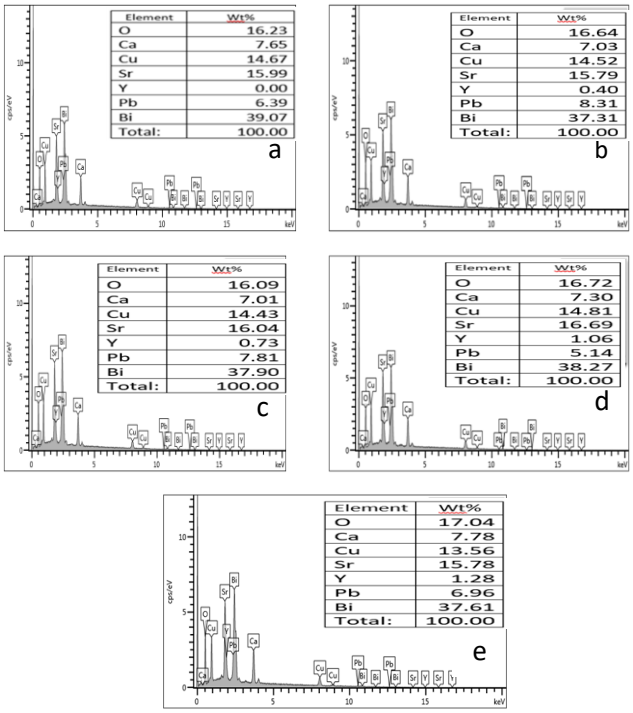


**Figure 6.** EDX graphs of **a** Y0, **b** Y2, **c** Y4, **d** Y8, and **e** Y10 samples

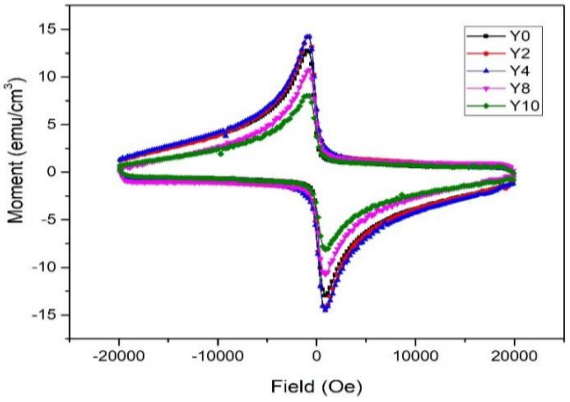


**Figure 7**. M-H graphs of Y0, Y2, Y4, Y8 and Y10 samples.

The magnetic moment responses of the samples against the external magnetic field applied to the samples were determined by M-H measurement with the VSM method. The obtained samples were subjected to M-H measurement with the Lake Shore VSM device at a temperature of 15 K, under a magnetic field between -20000 Oe and 20000 Oe. When the M-H curves of the samples are examined **(Figure 7)**, a hysteristic characteristic of diamagnetic properties of all samples is observed. For example, the magnetization curve is shaped as a loop, indicating presence of pinning centers on the surface of the material. According to the applied magnetic field, the magnetization values of the samples are listed as Y4, Y0, Y2, Y8 and Y10 from the largest to the smallest. No break was observed in the curves of the samples. This means that the impurity phases present in the structure are not evident. The magnetic values of all

samples decreased with the applied magnetic field exceeding 0 Oe. This situation is interpreted as the result of the decrease in the bond between the particles as a result of the agglomeration of the sample itself.

The magnetic field dependence of $J_c$ was calculated by using the experimental Bean model shown in Equation (4).

$$j_c = 20 \cdot \frac{\Delta M}{a\left(1-\frac{a}{3b}\right)} \quad (5)$$

$M$ value in the equation; It is the magnetization value obtained from the M-H curves. $\Delta M$ $[\Delta M = (M^+) - (M^-)]$ is the width of the magnetization curve during the decrease and increase of the area in emu/cm$^3$. $M^+$ and $M^-$ are the values of positive and negative region band of the magnetic response of samples against the external magnetic, respectively. The values of $a$ and $b$ (a < b) are the dimensions of the rectangular cross section of the sample perpendicular to the applied area in cm [25].

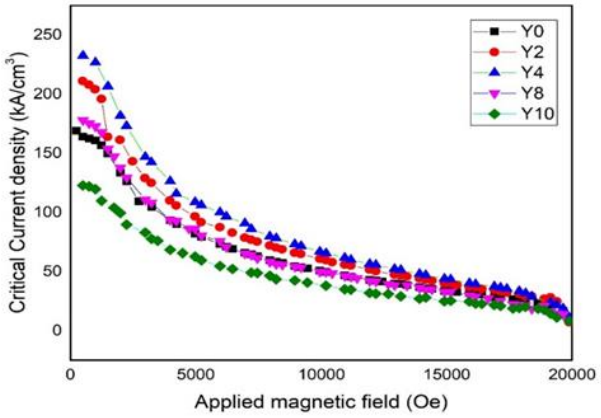


**Figure 8**. Field dependence of critical current density at 15 K for Y0, Y2, Y4, Y8 and Y10 samples

**Figure 8** showed that $J_c$ at 15 K of the samples containing pure and various amounts of nano-sized $Y_2O_3$. It is clearly seen in the graphs that the *Jc* values of the samples with granular structure decrease as the magnetic field increases. It can be thought that the reason for the decrease in the diamagnetic properties of the samples is due to the weakening of the interparticle bond [26]. In **Table 2**, the highest $J_c(0)$ value for sample Y4 is 232 kA/cm$^2$. Except for the Y10 sample, the critical current density value of all samples is higher than the undoped sample. Nano-$Y_2O_3$ addition has a positive contribution to the formation of artificial needling centers. The change in the critical current density depends on the formation of trapping centers in the structure and whether the interparticle bond is intact or not. However, since all of the samples were prepared under the same conditions, considering that the interparticle coupling would be similar in the samples. This irregular change in the critical current density values can only be explained by the increase and decrease in the trapping centers.

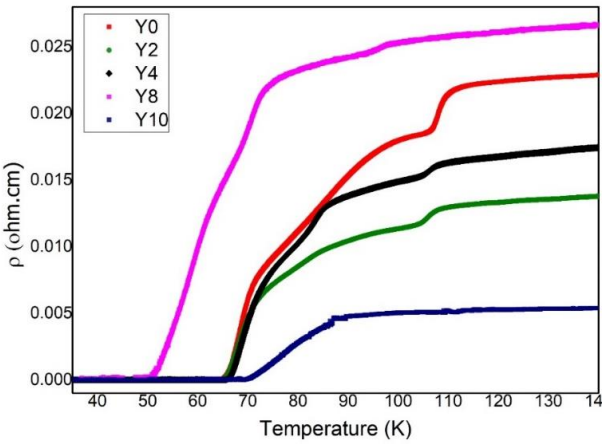


**Figure 9.** Resistivity temperature graph of Y0, Y2, Y4,Y8 and Y10 samples

Phase transitions that occur in superconducting materials can be determined from the resistivity measurements made depending on the temperature. Resistance temperature measurements were made with DC four probe method between 10 K and 300 K. The resistivity temperature graph of the Bi-based superconductor samples produced in this study is shown in **Figure 9** When the resistivity graph obtained as a function of temperature is examined, it is seen that all samples exhibit metallic behavior in regions above superconductivity transition temperature. With the addition of nano-$Y_2O_3$ addition in different percentages into the system, superconducting samples exhibit different behaviors in regions below the transition temperature.

$T_{c,onset}$ temperature value is that is the temperature at which the transition from the normal phase to the superconducting phase begins. $T_c^{offset}$ temperature value is the temperature value at which the superconducting phase transition is completed (R=0). The difference between $T_{c,onset}$ and $T_{c,offset}$ temperature values is shown with $\Delta T_c$.

$T_{c,onset}$ temperature value, which gives information about the superconducting phases, was the highest in the Y2 and Y4 sample. As seen in **Table 3**, $T_{c,onset}$ temperature values of Y2 and Y4 samples decrease slightly compared to the undoped sample. However, as the amount of additive increases, we see that the transition temperature to superconductivity decreases considerably. The intergrowth of impurity phases, weak bonding and structural distortions between impurities and superconducting grains can result in a decrease in $T_{c,onset}$ and $T_{c,offset}$ values, as well as an additional increase in the normal state resistivity value. Therefore, our resistivity results showed that the superconducting state was suppressed by increasing nano-$Y_2O_3$ addition in our system [27].

**Table 3**. $T_{c,onset}$, $T_{c,offset}$ and Hole concentration values of Y0, Y2, Y4, Y8, and Y10 samples

| | $T_{c,onset}$ (K) | $T_{c,offset}$ (K) | ΔT (K) | Hole concentration |
|---|---|---|---|---|
| **Y0** | 109.5 | 65 | 46.36 | 0.158 |
| **Y2** | 110 | 65 | 45.8 | 0.16 |
| **Y4** | 110 | 65 | 45.87 | 0.16 |
| **Y8** | 98 | 51 | 47 | 0.123 |
| **Y10** | 90 | 69 | 21 | 0.113 |

Hole concentration values ($p$) of the samples were calculated by using the following equation proposed by Persland et al [28].

$$p = 0.16-[(1-T_c/T^{max}{}_c)/82.6]^{1/2} \quad (4)$$

where $p$ is the carrier density (numbers of holes ); $T_c$ represents the critical temperature values of the samples. $T_c^{max}$ is taken as 110 K for the Bi-2223 system [29].

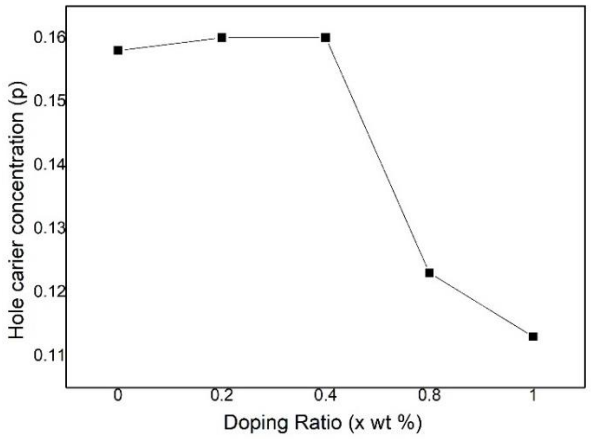


**Figure 10.** Hole concentration values of undoped and nano-$Y_2O_3$ added samples

**Figure 10** showed that hole carrier concentration values depending on the amount of additive. The hole concentration value ranges from 0.113 to 0.160. Hole concentration values of Y2 and Y4 samples are 0.16. Hole concentration values of Y8 and Y10 samples are 0.123 and 0.113, respectively. It is seen that the carrier density decreases after the value of nano-$Y_2O_3$ addition x=0.8 %. This result is in agreement with the XRD results. And this result supports our prediction that the decrease in c-parameter seen in XRD results may be due to the decrease in hole concentration [30].

$$H_v = 1854.4\left(\frac{F}{d^2}\right) \quad (GPa) \quad (5)$$

Vickers microhardness was calculated using the equation (5) given above [31]. The applied load is $F$ (N) and $d$ is the average diagonal length of the indentation impression (μm).

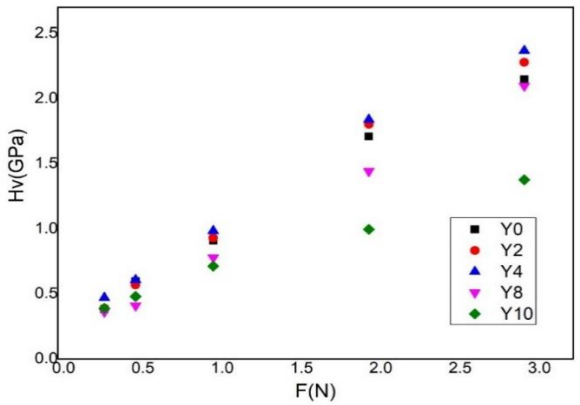


**Figure 11.** Variation of load dependent microhardness $H_v$ of nano-Y doped samples with applied load F.

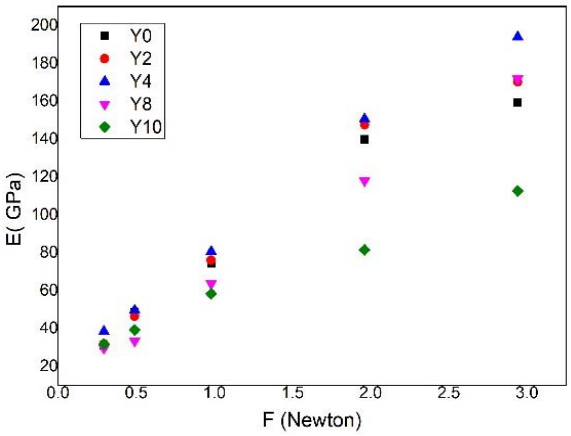


**Figure 12.** Variation of Young's modulus as a function of applied load



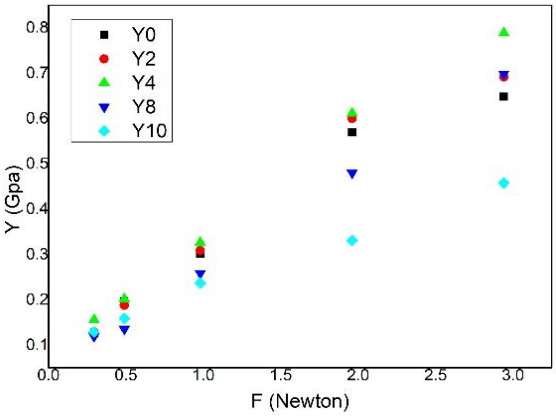


**Figure 13.** Variation of yield strength as a function of applied load

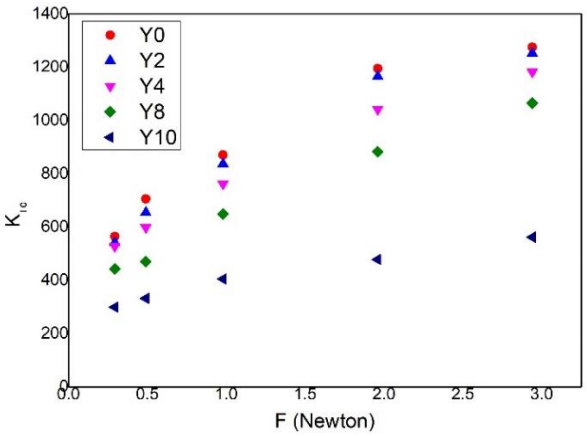


**Figure 14.** Variation of fracture toughness as a function of applied load

In **Figure 11**, The microhardness value increases non-linearly with the increasing applied force. Samples exhibiting this behavior, known as the reverse indentation size effect (RISE) in the literature, exhibit plastic deformation. The RISE behavior is a result of the bond strength between the superconducting grains and is caused by indentation-induced cracking [32]. Y4 sample has the highest hardness value. As supported by XRD results; compared to other nano-$Y_2O_3$ addition samples, the dislocation density of the Y4 sample is larger and the particle size is smaller. The dislocation density ($\delta$) was calculated using the formula $\delta=1/D^2$ and calculated data are presented in **Table 2**. It is known that crystalline size and dislocation density vary inversely. As the $\delta$ value increases, the crystallinity level decreases [20]. Among all samples, the highest dislocation density belongs to Y2 and Y4 samples. The high hardness value is due to the high dislocation density [33]. Increased dislocation movement cause the tiny cracks to propagate rapidly. As the particle size gets smaller, the bond between the superconducting particles gets stronger and the mechanical strength is expected to increase. The hardness value of the doped samples decreased after x = 0.4 % additive value. We think that the decrease in microhardness with increasing additive content may be due to weakening of the bond between superconducting grains and randomly distributed irregularities at grain boundaries [34]. In the surface micrographs of samples **(Figure 5 a-e)** showed that grain sizes, porosity and surface cracks increase as Y-content increases.

Elastic modulus ($E$), yield strength ($Y$) and fracture toughness ($K_{IC}$) values of samples are presented in **Table 4.** Elastik modulus, an intrinsic property of the material, gives the relative stiffness of the material. Elastic modulus is a measure of resistance to elastic deformation. As the value of the elastic modulus decreases, elasticity of the material increases. In the case of an increase in elastic modulus, it means that elasticity of the material decreases [35]. Elastic modulus were calculated from Equation 6. Yield Strength, which is the magnitude of the stress at which a samples loses its elasticity and turns into plastic, is calculated from Equation 7. Also fracture toughness values of samples were calculated from Equation 8. 'Fracture toughness' describes the resistance of brittle materials to propagation of cracks under an applied force [36]. Fracture toughness, which is an important parameter in material selection in superconducting applications, is one of the main mechanical properties of superconducting samples.

$$E=81.9635H_v \quad (6)$$

$$Y\approx H_V/3 \quad (7)$$

$$K_{IC}=\sqrt{2E\gamma}(\gamma \text{ is energy surface}) \quad (8)$$

Elastic modulus ($E$), yield strength ($Y$) and fracture toughness ($K_{IC}$) values increase with the increase in the applied load as seen in **Figure 11**, **Figure 12** and **Figure 13**. In addition, it is seen that $E$, $Y$ and $K_{IC}$ values increase up to x=0.4% additive value and decrease after x=0.4%.

It is seen in **Table 4** that hardness value increased until x = 0.4 % sample and decreased after this value. Especially the hardness value of Y10 sample is quite low compared to hardness values of all samples. When we add nano-$Y_2O_3$ at a certain rate, we see that the mechanical properties of the system are improved. After the amount of doping made after x= 0.4%, it affects the mechanical properties of the system negatively. We think that nano-dopings made in a certain amount can strengthen the interparticle connection by settling in the intergranular spaces. So we can say that nano-Y doping improves mechanical properties of BSCCO.

## 4. DISCUSSION AND CONCLUSION

In this study, $Bi_{1,8}Pb_{0,3}Sr_2Ca_2Cu_3O_y$ +$x$($Y_2O_3$) samples (where, $x$ = 0.0, 0.2, 0.4, 0.8 and 1.0 wt %) were prepared by solid state reaction method. The effects of $Y_2O_3$ nanoparticles addition on the microstructure, phase formation, critical temperature, critical current density and microhardness values were investigated and compared by using XRD, SEM-EDX, Vibrating sample measurements and Microhardness measurements. The results obtained in this study on BSCCO superconducting are summarized as given below.

XRD measurement results showed that the volume fraction of Bi-2223 phase was the highest in undoped samples. Increasing the amount of nano-$Y_2O_3$ addition decreased volume fraction of 2223 phase, a small extent. No peaks belong to $Y_2O_3$ nanoparticles were found in the XRD pattern. This showed that $Y_2O_3$ nanoparticles cannot enter the structure. It is seen that $a$ lattice parameter increased and $c$ lattice parameter decreased with the increase in the amount of nano-$Y_2O_3$ addition. This indicated that the nano-$Y_2O_3$ addition affected the BSSCO crystal structure to a small extent. When we looked at the positions of the strongest peaks to belong to BSSCO, we did not see that there is no significant peak shift. Accordingly, we have seen that the orthorhombic structure continues to exist in all samples.

**Table 4**. The calculated load dependent $H_v$, $E$, $Y$ and $K_{ıc}$ for Y0, Y2, Y4, Y8, and Y10 samples

| Force (N) | Hv (Gpa) | E (Gpa) | Y (Gpa) | Kıc (Pa/m$^{1/2}$) |
|---|---|---|---|---|
| **Y0** | | | | |
| 0.294 | 0.380 | 31.21 | 0.126 | 564.20 |
| 0.49 | 0.595 | 48.79 | 0.198 | 705.51 |
| 0.98 | 0.906 | 74.31 | 0.302 | 870.61 |
| 1.961 | 1.707 | 139.95 | 0.569 | 1194.79 |
| 2.941 | 1.945 | 159.42 | 0.648 | 1275.20 |
| **Y2** | | | | |
| 0.294 | 0.388 | 31.85 | 0.129 | 541.32 |
| 0.49 | 0.567 | 46.47 | 0.188 | 653.86 |
| 0.98 | 0.927 | 76.05 | 0.309 | 836.43 |
| 1.961 | 1.801 | 147.61 | 0.600 | 1165.37 |
| 2.941 | 2.076 | 170.18 | 0.692 | 1251.27 |
| **Y4** | | | | |
| 0.294 | 0.470 | 38.52 | 0.156 | 526.65 |
| 0.49 | 0.606 | 49.66 | 0.202 | 598.02 |
| 0.98 | 0.983 | 80.57 | 0.327 | 761.64 |
| 1.961 | 1.838 | 150.64 | 0.612 | 1041.47 |
| 2.941 | 2.367 | 194.01 | 0.789 | 1181.88 |
| **Y8** | | | | |
| 0.294 | 0.361 | 29.59 | 0.120 | 441.91 |
| 0.49 | 0.408 | 33.44 | 0.136 | 469.79 |
| 0.98 | 0.777 | 63.68 | 0.259 | 648.32 |
| 1.961 | 1.44 | 118.02 | 0.480 | 882.59 |
| 2.941 | 2.096 | 171.79 | 0.698 | 1064.82 |
| **Y10** | | | | |
| 0.294 | 0.388 | 31.80 | 0.129 | 298.40 |
| 0.49 | 0.479 | 39.26 | 0.159 | 331.55 |
| 0.98 | 0.712 | 58.35 | 0.237 | 404.23 |
| 1.961 | 0.994 | 81.47 | 0.331 | 477.61 |
| 2.941 | 1.374 | 112.61 | 0.458 | 561.54 |

When the surface morphology of the samples was examined with SEM photographs, it was seen that the particle structure was plate-like. EDX analysis showed that there is no impurity formation in the materials and nano-$Y_2O_3$ addition are evenly distributed in the structure. When the M-H curves of the samples are examined, all samples showed diamagnetic properties.

The highest critical current density value for sample Y4 is 232 kA/cm$^2$. Except for the Y10 sample, the critical current density value of all samples is higher than the undoped sample. Nano-$Y_2O_3$ addition has a positive contribution to the formation of artificial needling centers. According to the results obtained from DC measurements, $T_c^{onset}$ temperature values of Y2 and Y4 samples decrease slightly compared to the undoped sample. However, as the amount of additive increases, we see that the transition temperature to superconductivity decreases considerably. The hole concentration value ranges from 0.113 to 0.160. Hole concentration values of Y2 and Y4 samples are 0.16. Hole concentration values of Y8 and Y10 samples are 0.123 and 0.113, respectively. It is seen that the carrier density decreases after the value of nano-$Y_2O_3$ addition x=0.8 %. Vickers Microhardness measurement results showed that the microhardness value of the samples increases non-linearly with the increasing applied force. All samples exhibit RISE behavior. It is seen that the hardness values of the samples increase with increasing nano-$Y_2O_3$ addition.

**Acknowledgement**

We would like to thank Dokuz Eylül University faculty member Dr. Özlem Bilgili and İzmir University of Economics Faculty Member Hasan Durmuş for their valuable advice.



**REFERENCES**

[1] Kim CJ. Superconductor Levitation Concepts and Experiments (e Book). Springer Nature; 2019. https://doi.org/10.1007/978-981-13-6768-7

[2] Abou-Aly A, Abdel Gawad MMH, Awad R, G-Eldeen I. Improving the Physical Properties of (Bi, Pb)-2223 Phase by SnO2 Nano-particles Addition. J. Supercond. Nov. Magn.2011; 24, (7): 2077-84.

[3] Awad R. Study of the Influence of MgO Nano-Oxide Addition on the Electrical and Mechanical Properties of (Cu0.25Tl0.75)-1234 Superconducting Phase. J Supercond. Nov. Magn. 2008; 21: 461–6

[4] Öztornacı U, Özkurt B. The effect of nano-sized metallic Au addition on structural and magnetic properties of Bi1.8Sr2 AuxCa1.1Cu2.1Oy (Bi-2212) ceramics. Ceram. İnter. 2017; 43 (5): 4545-50.

[5] Mawassi R, Marhaba S, Roumié M Awad R, Korek M, Hassan I. Improvement of Superconducting Parameters of Bi 1.8Pb0.4Sr2Ca2Cu3O10+δ Added with Nano-Ag. J. Supercond. Nov. Magn. 2014; 27:1131–42.

[6] Yahya NAA, Al-Gaashani R, Abd-Shukor R. Synthesis and characterization of PbO–CdO nanocomposite and its effect on (Bi,Pb)-2223 superconductor. Appl. Phys. A. 2017;123-68.

[7] Jia ZY, Tang H, Yang ZQ, Xing YT, Wang YZ, Qiao GW. Effects of nano-ZrO particles on the

superconductivity of Pb-doped BSCCO. Phys. C. 2000; 337:130–2.

[8] Yıldırım G, Dogruer M, Karaboga F, Terzioglu C. Formation of nucleation centers for vortices in Bi-2223 superconducting core by dispersed Sn nanoparticles. J. All. Comp. 2014; 584: 344-51.

[9] Mohammed LA, Jasim KA. The substitutions of Strontium by yttrium and their effects on Bi2Sr2-xYxCa2Cu3O10+δ superconducting compound. Journal of Physics: Conference Series. 2021. 1879 (032069)

[10] Dong Y, Sun A, Xu B, Zhang H, Zhang M. Effect of the BSCCO superconducting properties by tiny Y2O3 addition. Mod. Phys. Let. B. 2016; 30 (26): 1650328/1-9.

[11] Khalil SM. Effect of Y3+ substitution for Ca on the transport and mechanical properties of Bi2Sr2Ca1−xYxCu2O8+δ system. J. Phys. Chem. Sol. 2003; 64 (5): 855-61.

[12] Sedky A. The impact of Y substitution on the 110 K high Tc phase in Bi (Pb):2223 superconductor. J. Phys. Chem. Sol. 2009;70: 483-88.

[13] Suazlina MA, Yusainee SYS, Azhan H, Abd-Shukor R, Mustaqim R. The Effects of Nanoparticle Addition in Bi-2212 Superconductors. 2014; 69 (2): 49–52.

[14] Oboudi SF. Synthesis and Magnetic Properties of Bi1.7Pb 0.3Sr2Ca2Cu3O10+δ Added with Nano Y. J. Supercond. Nov. Magn. 2017; 30: 1473–82.

[15] Durmus H, Kocabas K. The influence of Mn nanoparticles on superconducting properties and pinning mechanism of MgB2. J. Mater. Sci. Mater. Electr. 33 (21): 17079–89.

[16] Çorduk T, Bilgili O, Kemal K. Investigation of effects of MgO nanoparticles addition on the superconducting properties of Bi-2223 superconductors. J. Mater. Sci. Mater. Electr. 2017; 28 (11): 14689–95.

[17] Cevizci B, Bilgili O, Kemal K. The influence of Ag substitution on structural and mechanical properties of (Bi, Pb)-2223 ceramics. J.Mater. Sci. Mater. Elect. 2016; 27 (12), 13171-78.

[18] Bilgili O, Yurdaskal M. Effects of Graphene Oxide Doping on Magnetic and Structural Properties of Bi1.6Pb0.4Sr2Ca2Cu3Oy Superconductor. J.Elect. Mat.2021; 50: 4999–5006.

[19] Yildirim G, Dogruer M, Karaboga F, Terzioglu C. Formation of nucleation centers for vortices in Bi-2223 superconducting core by dispersed Sn nanoparticles. J. All. Comp.2014; 584: 344–51.

[20] Bilgili O. Structural and Electrical Properties of Nanosized Sm2O3 Doped Bi1.6Pb0.4Sr2Ca2Cu3Oy Superconductors .J. Low. Temp. Phys.2021; 204: 5-6.

[21] Shamray VF, Mikhailova AB, Mitin AV. Crystal structure and superconductivity of Bi-2223. Cryst Rep.2009; 54: 584–590.

[22] Scherrer P. Nachrichten von der Gesellschaft der Wissenschaften zu Göttingen. Mat. Phys. Klas. 1918; 2: 98-100.

[23] Langford J I, Wilson A J C Scherrer after Sixty Years: A Survey and Some New Results in the Determination of Crystallite Size. J. Appl. Cryst.1978; 11: 102-113.

[24] Abou-Aly A I, Abdel Gawad M M H, Awad R, G-Eldeen I. Improving the Physical Properties of (Bi, Pb)-2223 Phase by SnO2 Nano-particles Addition. J. Supercond. Nov. Magn. 2011; 24: 2077–84.

[25] Bean CP. Magnetization Of Hard Superconductors. Phys. Rev. Lett. 1962; 8 (6): 250-3.

[26] Yahya NAA, Abd-Shukor R. Effect of Different Nanosized MgO on the Transport Critical Current Density of Bi1.6Pb0.4Sr2Ca2Cu3O10 Superconductor. J. Supercond. Nov. Magn. 2014; 27: 329-35.

[27] Turk N, Gundogmus H, Akyol M, Yakıncı D, Ekicibil A, Ozcelik B. Effect of Tungsten (W) Substitution on the Physical Properties of Bi-(2223) Superconductors. J. Supercond. Nov. Magn. 2014; 27: 711–16.

[28] Persland M R, Tallon J L, Buckley R G, Liu R S, Floer N E. General trends in oxygen stoichiometry effects on Tc in Bi and Tl superconductors. Phys. C. 1191; 176 (1–3): 95–105.

[29] Bilgili O, Selamet Y, Kocabas K. Effects of Li Substitution in Bi-2223 Superconductors. J. Supercond. Nov. Magn. 2008; 21: 439–49.

[30] Saritekin N K, Tutuncu A T. Improving Superconductivity, Microstructure, and Mechanical Properties by Substituting Different Ionic Pb Elements to Bi and Ca Elements in Bi 2223 Superconductors. J. Supercond. Nov. Magn. 2022; 35: 2259–73.

[31] Uvarov V, Popov I. Metrological characterization of X-ray diffraction methods at different acquisition geometries for determination of crystallite size in nano-scale materials. Mater. Charac.2013; 85: 111-123.

[32] Safran S, Ozturk H, Bulut F, Ozturk O. The influence of re-pelletization and heat treatment on physical, superconducting, magnetic and micro-mechanical properties of bulk BSCCO samples prepared by ammonium nitrate precipitation method. Ceram. Inter. 2017; 43: 15586–92.

[33] Li H, Bradt R C. The effect of indentation-induced cracking on the apparent microhardness. J.Mat. Sci. 1966; 31: 1065-70.

[34] Ozturk O, Asikuzun E, Tasci A T, Gokcen T, Ada H, Koralay H, Cavdar S. Comparison of Vickers microhardness of undoped and Ru doped BSCCO glass ceramic materials. J.Mater. Sci. Mater. Elect. 2018; 29: 3957–66.

[35] Jones DRH, Ashby MF. Engineering Materials 1: An Introduction to Properties, Applications and Design. Chapter 3 - The Elastic Moduli. 5 th ed. Elsevier Science press; 2019. p.29-53.

[36] Jones DRH, Ashby MF. Engineering Materials 1: An Introduction to Properties, Applications and Design. Chapter 8 - Yield Strength, Tensile Strength, and Ductility. 5 th ed. Elsevier Science press; 2019. p.115-133.

Cilt 12, Sayı 1, Sayfa 163-170, 2023 Volume 12, Issue 1, Page 163-170, 2023

Araştırma Makalesi https://doi.org/10.46810/tdfd.1250739 Research Article

Türk Doğa ve Fen Dergisi
Turkish Journal of Nature and Science
www.dergipark.gov.tr/tdfd

# Investigation of Some Metabolic Enzyme Activities in Samples of Serum and Humor Aqueous of Cataract Cases with Pseudoexfoliation Syndrome

**Büşra ÇALIŞKAN[1*], Mine AKSOY[2], Muhammet Serhat ÖZASLAN[3], İlknur AKYOL SALMAN[1]**

[1]Atatürk University, School of Medicine, Department of Ophthalmology, Erzurum, Türkiye
[2]Atatürk University, Faculty of Science, Department of Chemistry, Erzurum, Türkiye
[3]Ardahan University, Nihat Delibalta Göle Vocational High School, Department of Pharmacy Services, Ardahan, Türkiye

Büşra ÇALIŞKAN ORCID No: 0000-0002-2350-184X
Mine AKSOY ORCID No: 0000-0002-2430-8769
Muhammet Serhat ÖZASLAN ORCID No: 0000-0002-5060-2048
İlknur AKYOL SALMAN ORCID No: 0000-0003-2079-6213

**Corresponding author: drbusracaliskan@gmail.com*

(Received: 17.02.2023, Accepted: 16.03.2023, Online Publication: 27.03.2023)

**Keywords**
Pseudoexfoliation syndrome, Carbonic anhydrase, Aldose reductase, Glutathione reductase, Paraoxonase

**Abstract:** Pseudoexfoliation syndrome (PEX) is a systemic disease that occurs as a result of aggregation of extracellular matrix material in ocular tissues and visceral organs. The etiopathogenesis of the PEX is not fully known. The purpose of our study is to examine the enzyme activities in some metabolic pathways that may be associated with etiopathogenesis. Carbonic anhydrase (CA), glutathione reductase (GR), aldose reductase (AR), paraoxonase (PON) enzymes activity in aqueous and serum samples, also serum selenium levels were investigated. According to the results, CA hydratase enzyme activity levels were higher in the serum samples with PEX compared to the control samples ($p < 0.05$). Aqueous CA hydratase and aqueous/serum PON, GR and AR activity levels did not differ significantly among the study samples ($p > 0.05$). Based on the relationship of carbonic anhydrase with aqueous production and glaucoma, increased serum CA hydratase activity may help to understand the PEX etiopathogenesis and mechanism of conversion to glaucoma.



# Psödoeksfoliasyon Sendromlu Katarakt Olgularının Serum ve Humor Aköz Örneklerinde Bazı Metabolik Enzim Aktivitelerinin Araştırılması

**Anahtar Kelimeler**
Psödoeksfoliasyon sendromu, Karbonik anhidraz, Aldoz redüktaz, Glutatyon redüktaz, Paraoksonaz

**Öz:** Psödoeksfoliasyon sendromu (PEX), ektraselüler matriks materyalinin oküler dokular ve visseral organlarda birikmesi sonucu ortaya çıkan sistemik bir hastalıktır. PEX'in etiyopatogenezi tam olarak bilinmemektedir. Çalışmamızın amacı, etyopatogenez ile ilişkili olabilecek bazı metabolik yolaklarda görev alan enzim aktivitelerinin değerlendirilmesidir. Bu amaçla; aköz ve serum örneklerinde karbonik anhidraz (CA), glutatyon redüktaz (GR), aldoz redüktaz (AR), paraoksonaz (PON) enzim aktiviteleri, ayrıca serum selenyum seviyeleri araştırılmıştır. Sonuçlara göre PEX'li örneklerde serum CA hidrataz enzim aktivite düzeyleri kontrol örneklerine göre daha yüksek tespit edildi ($p < 0.05$). Aköz CA hidrataz ve aköz/serum PON, GR ve AR aktivite seviyeleri, çalışma numuneleri arasında anlamlı farklılık göstermedi ($p > 0.05$). Karbonik anhidrazın aköz üretimi ve glokom ile ilişkisine dayanarak, artmış serum CA hidrataz aktivitesi, PEX'in etyopatogenezi ile glokoma dönüşüm mekanizmasının anlaşılmasına yardımcı olabilir.

## 1. INTRODUCTION

Pseudoexfoliation syndrome (PEX) is a systemic disease that known to occur with the aggregation of extracellular fibrillar material in visceral organs and ocular tissues. Although the cause of pathogenesis of PEX are unknown, it is thought that its formation may be relevant to environmental, genetic, viral infection, ischemia or immunological conditions [1-4]. In addition, increased oxidative damage and decreased cell protection

mechanism are thought to be one of the important pathogenetic factors [5]. It has been reported that oxidative stress is increased in eyes with PEX and decreased total antioxidant status in aqueous humor and serum. Ascorbic acid levels, an antioxidant, have been found to be decreased in aqueous samples of patients with PEX. Also, the concentration of 8-iso prostaglandin F2 alpha, which is an indicator of oxidative stress have been observed to increased in aqueous. All these studies have shown that oxidative damage due to free radicals plays an important role in the pathogenesis. [6, 7].

Although PEX occurs all over the world, its prevalence differs between countries and geographic regions [8]. PEX can present unilaterally or bilaterally. It is associated with the formation of cataracts and glaucomas. It is thought that the aqueous composition may be affected by changes in the iris vascular system and the blood-aqueous barrier, thus affecting lens metabolism and leading to earlier cataract formation [9].

Humor aqueous is bicarbonate-rich fluid that fills the space between the lens and cornea. The balance between the release and outflow of aqueous humor is closely related to intraocular pressure [10]. Decreased aqueous flow was observed in PEX positive eyes and it was concluded that aqueous humor production and composition were affected in PEX. Various studies have shown that the total aqueous protein quantity in the eyes is increased as a result of influencing the blood-aqueous barrier in PEX [11, 12]. Similarly, changes in the aqueous level of acid phosphatase [13], $\alpha_1$-lipoprotein and ceruloplasmin [14], $\alpha_1$-antitrypsin [15], transferrin [16], cellular⁄plasma fibronectin [17] and growth factors [18-20] have been reported.

CA is a metalloenzyme that contains $Zn^{2+}$ ions in its active site. CA is an important enzyme that reversibly catalyzes the reactions of hydration of carbon dioxide and dehydration of bicarbonate ion in the living. CA enzyme functions as a pH regulating enzyme in many tissues including erythrocytes [21, 22].

CA carries out bicarbonate transport through a rapid conversion pathway between $HCO_3^-$ and $CO_2$ across the ciliary epithelium. It affects liquid transport through optimum active transport of $Na^+$ by regulating pH with bicarbonate formation. Thus, it is directly related to aqueous production [23].

PON is a calcium-mediated esterase with antioxidant properties. It has been reported that there is a relationship between decreased activity of PON and increased oxidative stress in serum [24] [8] [9].

GR is a dimeric disulfide oxidoreductase that catalyzes the reduction of one molar equivalent of glutathione disulfide (GSSG) to two molar equivalents of reduced glutathione (GSH). It is known that GSH plays a critical role in maintaining the reducing environment of the cell and resisting oxidative stress by detoxifying some xenobiotics and heavy metals [25]. GR uses a FAD prosthetic assembly and NADPH to reduce GSSG to GSH [26]. Therefore, GR is essential in maintaining the GSH/GSSG intracellular ratio in the cell [27].

AR reduces various aldehydes using NADPH as the reductant. It is responsible for catalyzing the conversion of glucose to sorbitol in metabolism [28].

Selenium is an essential element that participates in the structure of many enzymes and acts as a cofactor. It is involved in many metabolic events such as antioxidant enzyme system, regulation of immune system and thyroid hormone system. Selenoproteins are proteins containing selenium in the form of selenocysteine in their active sites and play an important role in antioxidant defence [29].

In this study, aqueous and serum samples were examined from the cases cataract with PEX and the control group was selected from the cataract group without PEX. The aim of this study is to investigate the activities of CA, GR, AR, PON enzyme in patients and control groups. In addition, it was aimed to investigate the selenium levels in serum samples and to compare them with the control group.

## 2. MATERIAL AND METHOD

### 2.1. Materials

Paraoxon (diethyl p-nitrophenyl phosphate), NADPH (β-Nicotinamide adenine dinucleotide 2′-phosphate reduced tetrasodium salt hydrate), D,L-glyceraldehyde, 4-Nitrophenyl acetate, L-Glutathione oxidized and other chemicals were obtained from Sigma-Aldrich (Taufkirchen, Germany).



### 2.2. Sample Collection

Ethics committee report numbered B.30.2.ATA.0.01.00/176 was received for the conduct of the study. Patients who applied to Atatürk University Faculty of Medicine, Department of Ophthalmology with the complaint of low vision and were diagnosed with cataract were included in the study. The study population comprised 66 individuals, including 33 patients with cataract with PEX, 33 patients with age-related cataracts without PEX. Each participant underwent a full ophthalmologic examination. Individuals with ocular diseases such as glaucoma, corneal trauma, uveitis, diabetic retinopathy were excluded from the study. Also systemic, cronic and inflammatory diseases such as diabetes mellitus, liver-kidney failure, rheumatological diseases were excluded from the study.

Aqueous samples were obtained at the beginning of cataract surgery. About 100–150 µl of the aqueous humor was aspirated by utilizing a 30- gauge needle attached to a micro syringe under an operating microscope. Particular attention was paid to avoid touching the iris, lens, and corneal endothelium and to prevent the contamination of the aqueous sample by the irrigation fluid and blood from the conjunctiva. Venous blood samples (5 mL) were drawn from the participants. The blood samples were centrifuged for 15 min. The centrifuged serum samples

were distributed to Eppendorf tubes. The Eppendorf tubes containing both serum and aqueous samples were placed at 4 °C for 1 h. Then all samples were stored in the freezer at − 80 °C until the enzyme activity measurement [30].

### 2.3. Biochemical Analyses

For biochemical analysis, both hydratase and esterase activity of CA enzyme were investigated in serum and aqueous. Other enzyme activities were also examined in serum and aqueous.

#### 2.3.1. Principle of CA hydratase activity measurement method

Hydratase activity of CA was determined with the Wilbur-Anderson method [31]. In the method; the time taken for the pH to decrease from 8.2 to 6.3 due to the $H^+$ released as a result of the hydration of $CO_2$ is calculated using the bromine thymol blue indicator.

According to this method, an enzyme unit (EU) for CA activity is calculated by determining the $CO_2$ hydration time that occurs without the enzyme and the $CO_2$ hydration time with the enzyme. The formula EU= $((t_0-t_c)/t_c)$ was used to calculate the enzyme unit.

#### 2.3.2. Principle of CA esterase activity measurement method

It is the method that shows that it also has CA esterase activity. In principle, CA hydrolyzes p-nitro phenyl acetate, which is used as a substrate, to p-nitro phenol or p-nitro phenolate, which gives absorption at 348 nm [32]. The esterase activity of the CA was calculated in EU $mL^{-1}$ by applying the following formula:

$$EU/mL = \frac{\Delta OD}{5} \times \frac{V_T}{V_E} \times D_f$$

EU $mL^{-1}$: enzyme unit in 1 mL, ΔOD: absorbance change per minute, extinction coefficient ($M^{-1}.cm^{-1}$): 5, $V_T$= total cuvette volume, $V_E$ = the volume of enzyme sample $D_f$=dilution factor.

#### 2.3.3. Principle of PON enzyme activity measurement method

The activity measurement of PON is determined by measuring the absorbance change at 412 nm caused by p nitrophenol formed as a result of hydrolysis of paraoxon [33]. The activities of PON in EU $mL^{-1}$ were calculated by applying the following formula:

$$EU/mL = \frac{\Delta OD}{18.29} \times \frac{V_T}{V_E} \times 1000$$

EU $mL^{-1}$: Enzyme unit in 1 mL, ΔOD: absorbance change per minute, extinction coefficient ($M^{-1}.cm^{-1}$): 18.290, $V_T$: total cuvette volume, $V_E$: the volume of the enzyme sample, 1000: Enzyme unit conversion factor.

#### 2.3.4. Principle of AR enzyme activity measurement method

The AR enzyme activities were determined with a modified procedure used by Cerelli et al [28]. Activity measurement was carried out by considering the decrease in absorbance at 340 nm of the amount of NADPH spent in the reaction medium where DL-glyceraldehyde was used as the substrate. The activity of the enzyme was calculated in EU $mL^{-1}$ by applying the following formula:

$$EU/mL = \frac{\Delta OD}{6.22} \times \frac{V_T}{V_E} \times D_f$$

EU $mL^{-1}$: enzyme unit in 1 mL, ΔOD: absorbance change per minute, extinction coefficient ($M^{-1}.cm^{-1}$): 6.22, $V_T$= total cuvette volume, $V_E$ = volume of enzyme sample $D_f$=dilution factor.

#### 2.3.5. Principle of GR enzyme activity measurement method

Spectrophotometric method was used to measure the activity of GR enzyme. The method described by Carlberg and Mannervik is based on the absorbance of NADPH, which decreases due to the oxidation of NADPH at 340 nm in the presence of GSSG [26]. Absorbance decrease was recorded at 1-minute time intervals. The GR activities were calculated in EU $mL^{-1}$ by applying the following formula:

$$EU/mL = \frac{\Delta OD}{6.22} \times \frac{V_T}{V_E} \times D_f$$

EU $mL^{-1}$: enzyme unit in 1 mL, ΔOD: absorbance change per minute, extinction coefficient ($M^{-1}.cm^{-1}$): 6.22, $V_T$= total cuvette volume, $V_E$ = volume of enzyme sample $D_f$=dilution factor.



### 2.4. Determination of Selenium in Serum

Selenium levels analyzes of serum samples taken from the control group and patients with PEX were studied in the infrastructure of the Research Hospital Biochemistry laboratory.

### 2.5. Statistical Analysis

SPSS 20.0 software was used to analyze the data (SPSS Inc., Chicago, Illinois, USA). Each group was tested for normality. According to normality tests, only the groups of CA esterase aqueous sample, selenium serum sample are normally distributed ($p>0.05$, Table 1). Independent Samples t Test was used for group comparison of these two variables. Mann-Whitney U test was used for all other variables.

**Table 1.** Test of normality and homogeneity of variances

| | | | Shapiro-Wilk testi | | F-test | |
|---|---|---|---|---|---|---|
| **Variant** | **Samples** | **Groups** | **W** | **p-value** | **F** | **p-value** |
| CA Esterase | Serum | SC | 0.9202 | 0.01856 | 1.3587 | 0.3906 |
| | | SP | 0.95958 | 0.2515 | | |
| | Aqueous | AC | 0.94583 | 0.1005 | 0.89875 | 0.7646 |
| | | AP | 0.94421 | 0.0901 | | |
| CA Hydratase | Serum | SC | 0.90526 | 0.007312 | 0.36245 | 0.005258 |
| | | SP | 0.88312 | 0.001999 | | |
| | Aqueous | AC | 0.9565 | 0.2054 | 0.51173 | 0.06244 |
| | | AP | 0.92964 | 0.03418 | | |
| PON | Serum | SC | 0.90494 | 0.007173 | 0.99841 | 0.9964 |
| | | SP | 0.97432 | 0.608 | | |
| | Aqueous | AC | 0.65821 | 1.61e-07 | 1.4146 | 0.3316 |
| | | AP | 0.79135 | 2.217e-05 | | |
| AR | Serum | SC | 0.92692 | 0.028610 | 0.61508 | 0.1747 |
| | | SP | 0.89593 | 0.004185 | | |
| GR | Serum | SC | 0.95785 | 0.2245 | 0.76814 | 0.4598 |
| | | SP | 0.92223 | 0.02114 | | |
| | Aqueous | AC | 0.898 01 | 0.004732 | 1.0491 | 0.893 |
| | | AP | 0.9664 | 0.3876 | | |
| | | AP | 0.30499 | 2.254e-11 | | |
| Selenium | Serum | SC | 0.95593 | 0.1978 | 1.0013 | 0.9971 |
| | | SP | 0.95156 | 0.1478 | | |

SC: serum control group, SP: serum patient group, AC: aqueous control group, AP: aqueous patient group

## 3. RESULTS

Enzyme activities were studied in aqueous and serum samples of 66 individuals. The demographic data of the our study were previously given by Çalışkan *et al.* in the study that included same sample [30].

The test results of the group comparisons for each variant of the serum samples are presented in Table 2. When the table is examined, there is a statistically significant difference between PEX group and control patients regarding only the variables named CA hydratase ($p<0.05$).

The test results of group comparisons for each variable of aqueous samples are presented in Table 3. No statistically significant difference was observed between the groups in the test results ($p>0.05$).

**Table 2**. Enzyme activities comparisons in serum of patients with cataract with PEX and control subjects (cataracts without PEX).

| | | | Group Comparison | |
|---|---|---|---|---|
| **Variant** | **Groups** | **Median** | **Test statistics (u)** | **p-value** |
| CA Esterase | SC<br>SP | 0.72<br>0.77 | 631* | 0.267 |
| CA Hydratase | SC<br>SP | 20.39<br>41.61 | 815* | 0.0003967 |
| PON | SC<br>SP | 30.23<br>40.69 | 630.5* | 0.270 |
| AR | SC<br>SP | 0.14<br>0.13 | 512.5* | 0.680 |
| GR | SC<br>SP | 0.27<br>0.45 | 587* | 0.584 |
| Selenium | SC<br>SP | 77<br>75 | -0.033443** | 0.9734 |

*: Mann-Whitney U test, **: Independent Samples t-test
SC: serum control group, SP: serum patient group, AC: aqueous control group, AP: aqueous patient group

**Table 3.** Enzyme activities comparisons in aqueous samples of patients with cataract with PEX and control subjects (cataracts without PEX).

| | | | Group Comparison | |
|---|---|---|---|---|
| **Variant** | **Groups** | **Median** | **Test statistics (u)** | **p-value** |
| CA Esterase | AC<br>AP | 0.06<br>0.05 | 0.80197 | 0.4255 |
| CA Hydratase | AC<br>AP | 29.04<br>34.60 | 650 | 0.176 |
| PON | AC<br>AP | 11.37<br>11.41 | 833.5 | 0.272 |
| GR | AC<br>AP | 0.45<br>0.46 | 587.5 | 0.580 |

SC: serum control group, SP: serum patient group, AC: aqueous control group, AP: aqueous patient group

Hydratase activity of CA was found to be 46.5 EU $mL^{-1}$ in the PEX group and 27.3 EU $mL^{-1}$ in the control group in serum samples. According to the results, serum CA hydratase enzyme activity levels were significantly higher in the PEX group compared to the control group. ($p=0.013$).

Hydratase activity of CA was found to be 34.8 EU $mL^{-1}$ in the group of cataract cases with PEX and 29.1 EU $mL^{-1}$ in the group of cataract cases without PEX in aqueous samples.

Despite an increase in aqueous CA hydratase levels of the PEX group compared to control group, this increase did not create a statistically significant difference. ($p=0.176$). (Fig.1).

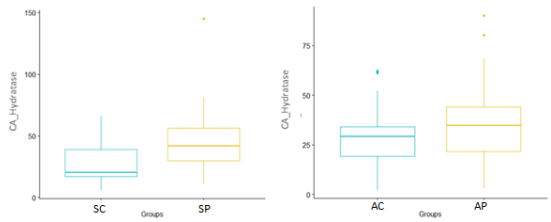


**Figure 1.** Carbonic anhydrase enzyme hydratase activities in serum and aqueous humor of patients with cataract with PEX and control subjects (cataracts without PEX). # Significantly elevated carbonic anhydrase enzyme hydratase activities in the serum of patients (Mann-Whitney U; p=0.013) compared with control subjects. (SC: Serum Control, SP: Serum PEX, AC: Aqueous Control, AP: Aqueous PEX)

AR activities were not detected in the study performed in aqueous samples of both groups.

## 4. DISCUSSION AND CONCLUSION

PEX, a systemic disease, occurs as a result of the aggregation of extracellular matrix material in the ocular and extraocular tissues in the body. Many ocular problems (corneal endotheliopathy, glaucoma, cataract, zonular instability, central retinal vein occlusion, decreased dilatation, and increased cataract surgery complication risk) are associated with PEX [34].

The pathogenesis and etiology of PEX are not yet fully known. It is argued that various factors have played a role in the etiology and pathogenesis of PEX, and it has been demonstrated by many studies that the aqueous content of patients with PEX is altered [35, 36]. A total of 269 protein groups were defined in the proteomic study conducted in patients with and without PEX, among patients with eye diseases such as cataracts and glaucoma. As a result of label-free protein quantification, no significant difference was observed between the aqueous humor proteomes of glaucoma and cataract. In the study, protein amounts were determined as 4.6±1.7 µg/mL in cases with cataract, 2.5±1.6 µg/mL in cases with pseudoexfoliative cataract, 4.3±1.8 µg/mL in cases with primary open angle glaucoma, and 2.7±0.7 µg/mL in cases with pseudoexfoliative glaucoma [37].

Oxidative stress (OS) results from excessive ROS formation or insufficient antioxidant defense. ROS production allows the presence of sufficient ROS to perform cellular signaling tasks. "Redox control" maintains the delicate balance between the advantageous and harmful effects of ROS, which is essential for the survival of living things. Redox control maintains homeostasis and protects against OS in living things. Overproduction of ROS damages cells by causing OS in them. As a result, cells have antioxidant defense systems to counteract excess ROS and maintain redox balance, both of which are essential for cell survival [38-40]. Several active oxidative agents are known to exist in aqueous humor, such as superoxide anions and hydrogen peroxide [41]. Therefore, oxidative markers in aqueous samples were frequently investigated in cases with PEX and/or glaucoma [42-44]. Until now, enzyme activities such as superoxide dismutase [44, 45], catalase [5, 43, 46], glutathione peroxidase [43, 46] and biomarkers such as malondialdehyde [44], glutathione [47, 48], nitric oxide [44] have been examined as oxidative stress markers. In addition, arylesterase and PON activities were measured in the study, which aimed to investigate the oxidative stress status of aqueous humor and serum in patients with PEX and pseudoexfoliative glaucoma (PEG). It was determined that total oxidative stress values were higher (< 0.05) in patients with PEX and PEG, and total antioxidant capacity, PON and ARE aqueous humor levels did not differ significantly between PEX and PEG groups [49]. In our study, the activities of PON and GR as oxidative markers were determined in serum and aqueous samples. The activities of PON and GR aqueous and serum samples did not differ significantly between cataract cases with PEX and control groups. In addition, in our study, AR levels were investigated in serum and aqueous samples, since both AR enzyme and oxidant-antioxidant pathways work in a NADPH-dependent manner [50]. There was no statistically significant difference between the two groups in serum AR levels (p=0.5235). AR enzyme activity was not detected in the study performed in aqueous samples of both groups. Aldose reductase (AR) is catalyzing the conversion of glucose to sorbitol in metabolism. During hyperglycemia the flux of glucose the polyol pathway increases significantly, leading to excessive formation of sorbitol. [51]. Since diabetic patients were excluded from the study population, aldose reductase enzyme activity may not have been detected under normoglycemic conditions in aqueous.

Serum and aqueous levels of trace elements have been evaluated by various studies in cases of cataract and PEX [52-55]. Selenium; It is an essential element that plays the role of a cofactor by participating in the structure of many enzymes. Along with various enzyme groups, it is also an engagement element for antioxidant enzymes [56]. In one study, selenium was investigated in the aqueous humor and serum of control groups and patients with PEX. The mean selenium levels in the serum of patients with PEX syndrome (115.25±25.20 µg/L) were found to be lower than the control group (124.25±14.40 µg/L), but no statistically significant result was obtained (P <.325) [57]. In our study, serum selenium levels for each group were found to be 80.2 µg/L in the control group and 80.5 µg/L in the PEX group. There was no statistically significant difference between the two groups in serum selenium levels (p: 0.9734).

Human CAs are metalloenzymes known for their ability to catalyze the hydration of $CO_2$ to bicarbonate anion and proton, and an association between glaucoma and the CA enzyme has been demonstrated [22, 58]. Inhibition of human CA isozymes such as hCA-I, II, IV, and XII, which reduces aqueous humor secretion and elevated intraocular pressure, is the mechanism of action of well-known anti-glaucoma agents [59]. Based on the relationship of carbonic anhydrase with aqueous production and glaucoma, in our study investigated the both activities of esterase and hydratase of CA in aqueous and serum

samples. According to the our results, a statistically significant difference was found in terms of CA hydratase activities in the serum samples of the patient group. Although there is no statistically significant difference, an increase in aqueous CA hydratase levels was also observed in patients with PEX.

PEX is known to be one of the most common causes of glaucoma. Progressive degeneration and obstruction occur with the accumulation of PEM in trabecular meshwork in PEX patients. Glaucoma can be seen in both eyes in cases with unilateral PEX or no glaucoma can be seen in all eyes with PEM suggests that the underlying cause may be due to different reasons. One of these reasons may be the increased activity of CA hydratase and the fact that this triggers the production of more aqueous in patients with PEX.

In conclusion, some oxidative markers and carbonic anhydrase activities were investigated in aqueous humor and serum samples of cataracts with PEX, in the control group without PEX. In addition, serum selenium levels were studied and compared with the control group. It is thought that the parameters obtained in our study may be related to the etiopathogenesis of pseudoexfoliation csyndrome and contain important findings in this respect. Especially, in the literature, we did not find a study on CA enzyme activity in serum and aqueous samples in patients with PEX. Therefore, we believe that this study can be a reference.

**Acknowledgement**

The authors thank Mr. Erkan OKTAY for their support in the statistical analysis of the article. This research did not receive any specific grant or project support. There is no statement of interest.

**REFERENCES**

[1] Damji KF, Bains HS, Amjadi K, Dohadwala AA, Valberg JD, Chevrier R, et al. Familial occurrence of pseudoexfoliation in Canada. Can J Ophthalmol. 1999;34(5),257-265.

[2] Konstas AG, Williamson TH. Coexistence of exfoliation syndrome, previous iris surgery and heterochromia. Acta Ophthalmol. 1993; 71(6),850-852.

[3] Orr AC, Robitaille JM, Price PA, Hamilton JR, Falvey DM, De Saint-Sardos AG, et al. Exfoliation syndrome: clinical and genetic features. Ophthalmic Genet. 2001;22(3),171-185.

[4] Ringvold A, Blika S, Elsas T, Guldahl J, Brevik T, Hesstvedt P, et al. The Middle-Norway eye-screening study. I. Epidemiology of the pseudo-exfoliation syndrome. Acta Ophthalmol. 1988;66(6):652-8.

[5] Koliakos GG, Befani CD, Mikropoulos D, Ziakas NG, Konstas. AGP. Prooxidant–antioxidant balance, peroxide and catalase activity in the aqueous humour and serum of patients with exfoliation syndrome or exfoliative glaucoma. Graefes Arch Clin Exp Ophthalmol. 2008;246:1477–1483.

[6] Koliakos GG, Konstas AGP, Schlötzer-Schrehardt U, et al. 8 isoprostaglandin F2α and ascorbic acid concentration in the aqueous humour of patients with exfoliaition syndrome. Br J Ophthalmol. 2003;87:353-6.

[7] Koliakos GG, Konstas GP, Schlötzer-Schrehardt U, Bufidis T et al. Ascorbic acid concentration is reduced in the aqueous humor of patients with exfoliation syndrome. American J Oph. 2002; 134;879-83.

[8] Ringvold A. Epidemiology of the pseudo-exfoliation syndrome. Acta Ophthalmol Scand. 1999;77(4),371-375.

[9] Sangal N, Chen TC. Cataract surgery in pseudoexfoliation syndrome. Semin Ophthalmol. 2014;29(5-6), 403-408.

[10] Goel M, Picciani RG, Lee RK, Bhattacharya SK. Aqueous humor dynamics: a review. Open Ophthalmol J. 2010;4,52-59.

[11] Kuchle M, Nguyen NX, Hannappel E, Naumann GO. The blood-aqueous barrier in eyes with pseudoexfoliation syndrome. Ophthalmic Res. 1995;27Suppl 1,136-142.

[12] Nguyen NX, Kuchle M, Martus P, Naumann GO. Quantification of blood-aqueous barrier breakdown after trabeculectomy: pseudoexfoliation versus primary open-angle glaucoma. J Glaucoma. 1999;8(1),18.

[13] Mizuno K, Hara S, Ishiguro S, Takei Y. Acid phosphatase in eyes with pseudoexfoliation. Am J Ophthalmol. 1980;89(4),482-489.

[14] Baba H. Investigation of the pathogenesis of glaucoma capsulare with special discussion of alpha-lp and cp in aqueous-humor. Graefes Archive for Clinical and Experimental Ophthalmology. 1982;218(6), 283-286.

[15] Smolenska-Janicowa D, Bernacka K. Relationship between exfoliation syndrome and autoimmunity. Results of the analysis of aqueous humor. Klin Oczna. 1982;84(4),99-100.

[16] Koliakos GG, Konstas AGP, Dimitrakoulias N, Triantos A, Kardasopoulos A, Dimitriadou A, et al. Possible role of transferrin in exfoliation syndrome. Acta Ophthalmol Scan. 1996;74(2), 155-159.

[17] Vesaluoma M, Mertaniemi P, Mannonen S, Lehto I, Uusitalo R, Sarna S,et al. Cellular and plasma fibronectin in the aqueous humour of primary open-angle glaucoma, exfoliative glaucoma and cataract patients. Eye(Lond). 1998;12,886-890.

[18] Ho SL, Dogar GF, Wang J, Crean J, Wu QD, Oliver N, et al. Elevated aqueous humour tissue inhibitor of matrix metalloproteinase-1 and connective tissue growth factor in pseudoexfoliation syndrome. Br J Ophthalmol. 2005;89(2),169-173.

[19] Koliakos GG, Schlotzer-Schrehardt U, Konstas AG, Bufidis T, Georgiadis N, Dimitriadou A. Transforming and insulin-like growth factors in the aqueous humour of patients with exfoliation syndrome. Graefes Arch Clin Exp Ophthalmol. 2001;239(7),482-487.

[20] Schlotzer-Schrehardt U, Zenkel M, Kuchle M, Sakai LY, Naumann GO. Role of transforming growth factor-beta1 and its latent form binding protein in pseudoexfoliation syndrome. Exp Eye Res. 2001;73(6),765-780.
[21] Aggarwal M, Boone CD, Kondeti B, McKenna R. Structural annotation of human carbonic anhydrases. J Enzyme Inhib Med Chem. 2013;28(2),267-277.
[22] Supuran CT, Scozzafava A. Carbonic anhydrase inhibitors and their therapeutic potential. Expert Opinion on Therapeutic Patents. 2000;10(5), 575-600.
[23] Dobbs PC, Epstein DL, Anderson PJ. Identification of isoenzyme C as the principal carbonic anhydrase in human ciliary processes. Invest Ophthalmol Vis Sci. 1979;18(8),867-870.
[24] Li HL, Liu DP, Liang CC. Paraoxonase gene polymorphisms, oxidative stress, and diseases. J Mol Med (Berl). 2003;81(12),766-779.
[25] Circu ML and Aw TY: Reactive oxygen species, cellular redox systems, and apoptosis. Free Radic Biol Med.2010;48(6):749-762.
[26] Carlberg I, Mannervik B. Purification and characterization of glutathione reductase from calf liver.An improved procedure for affinity chromatography on 2',5'-ADP-Sepharose-4B. Anal Biochem. 1981;116(2),531-536.
[27] Circu ML and Aw TY. Glutathione and modulation of cell apoptosis. Biochim Biophys Acta. 2012;1823(10): 1767-1777.
[28] Cerelli MJ, Curtis DL, Dunn JP, Nelson PH, Peak TM, Waterbury LD. Antiinflammatory and aldose reductase inhibitory activity of some tricyclic arylacetic acids. J Med Chem. 1986;29(11),2347-2351.
[29] Duntas LH, Benvenga S. Selenium: an element for life. Endocrine. 2015;48(3),756-775.
[30] Caliskan B, Ozaslan MS, Aksoy M, Salman IA. Prolidase activity in aqueous and serum samples of cataract cases with pseudoexfoliation syndrome. Exp Eye Res. 2022;214,108880.
[31] Wilbur KM, Anderson NG. Electrometric and colorimetric determination of carbonic anhydrase. J Biol Chem. 1948;176(1),147-154.
[32] Verpoorte JA, Mehta S, Edsall JT. Esterase activities of human carbonic anhydrases B and C. J Biol Chem. 1967;242(18), 4221-4229.
[33] Eckerson HW, Romson J, Wyte C, La Du BN. The human serum paraoxonase polymorphism: identification of phenotypes by their response to salts. Am J Hum Genet. 1983;35(2),214.
[34] Naumann GO, Schlotzer-Schrehardt U, Kuchle M. Pseudoexfoliation syndrome for the comprehensive ophthalmologist. Intraocular and systemic manifestations. Ophthalmology. 1998;105(6),951-968.
[35] Berlau J, Lorenz P, Beck R, Makovitzky J, Schlotzer-Schrehardt U, Thiesen HJ, et al. Analysis of aqueous humour proteins of eyes with and without pseudoexfoliation syndrome. Graefes Arch Clin Exp Ophthalmol. 2001;239(10),743-746.
[36] Schumacher S, Nguyen NX, Kuchle M, Naumann GO. Quantification of aqueous flare after phacoemulsification with intraocular lens implantation in eyes with pseudoexfoliation syndrome. Arch Ophthalmol. 1999;117(6),733-735.
[37] Kliuchnikova AA, Samokhina NI, Ilina IY, Karpov DS, Pyatnitskiy MA, Kuznetsova KG, et al. Human aqueous humor proteome in cataract, glaucoma, and pseudoexfoliation syndrome. Proteomics. 2016;16(13),1938-1946.
[38] Varışlı B, Caglayan C, Kandemir FM, Gür C, Ayna A, Genç A, et al. Chrysin mitigates diclofenac-induced hepatotoxicity by modulating oxidative stress, apoptosis, autophagy and endoplasmic reticulum stress in rats. Molecular Biology Reports. 2023;50(1), 433-442.
[39] Kucukler S, Benzer F, Yildirim S, Gur C, Kandemir FM., Bengu AS, et al. Protective effects of chrysin against oxidative stress and inflammation induced by lead acetate in rat kidneys: a biochemical and histopathological approach. Biological Trace Element Research. 2021;199(4),1501-1514.
[40] Caglayan, C., Kandemir, F. M., Darendelioğlu, E., Küçükler, S., & Ayna, A. Hesperidin protects liver and kidney against sodium fluoride-induced toxicity through anti-apoptotic and anti-autophagic mechanisms. Life Sciences. 2021;281,119730.
[41] Spector A, Garner WH. Hydrogen peroxide and human cataract. Exp Eye Res. 1981;33(6),673-681.
[42] Goyal A, Srivastava A, Sihota R, Kaur J. Evaluation of oxidative stress markers in aqueous humor of primary open angle glaucoma and primary angle closure glaucoma patients. Curr Eye Res. 2014;39(8),823-829.
[43] Uzun L, Duzguncinar O, Evren O, Demirpence E, Uzun A, Gürsel E. Antioxidant status in the aqueous humor of patients with exfoliation syndrome. MN Ophtalmol. 2006;13(4),273-278.
[44] Yagci R, Gurel A, Ersoz I, Keskin UC, Hepsen IF, Duman S, et al. Oxidative stress and protein oxidation in pseudoexfoliation syndrome. Curr Eye Res. 2006;31(12),1029-1032.
[45] DelaPaz MA, Epstein DL. Effect of age on superoxide dismutase activity of human trabecular meshwork. Invest Ophthalmol Vis Sci. 1996;37(9),1849-1853.
[46] Ferreira SM, Lerner SF, Brunzini R, Evelson PA, Llesuy SF. Antioxidant status in the aqueous humour of patients with glaucoma associated with exfoliation syndrome. Eye. 2009;23(8), 1691-1697.
[47] Costagliola C, Iuliano G, Menzione M, Rinaldi E, Vito P, Auricchio G. Effect of vitamin E on glutathione content in red blood cells, aqueous humor and lens of humans and other species. Exp Eye Res. 1986;43(6),905-914.
[48] Veach J. Functional dichotomy: glutathione and vitamin E in homeostasis relevant to primary open-angle glaucoma. Br J Nutr. 2004;91(6), 809-829.
[49] Dursun F, Vural Ozec A, Aydin H, Topalkara A, Dursun A, Toker MI, et al. Total oxidative stress, paraoxonase and arylesterase levels at patients with pseudoexfoliation syndrome and pseudoexfoliative glaucoma. Int J Ophthalmol. 2015;8(5),985-990.
[50] Srivastava SK, Ramana KV, Bhatnagar A. Role of aldose reductase and oxidative damage in diabetes

and the consequent potential for therapeutic options. Endocr Rev. 2005;26(3), 380-392.
[51] Singh M, Kapoor A, Bhatnagar A. Physiological and Pathological Roles of Aldose Reductase. Metabolites. 2021;27;11(10):655.
[52] Aydin E, Cumurcu T, Ozugurlu F, Ozyurt H, Sahinoglu S, Mendil D, Hasdemir E. Levels of iron, zinc, and copper in aqueous humor, lens, and serum in nondiabetic and diabetic patients: their relation to cataract. Biol Trace Elem Res. 2005;108(1-3),33-41.
[53] Dawczynski J, Blum M, Winnefeld K, Strobel J. Increased content of zinc and iron in human cataractous lenses. Biol Trace Elem Res. 2002;90(1-3),15-23.
[54] Gunduz G, Gunduz F, Yucel I, Senturk UK. Levels of zinc and magnesium in senile and diabetic senile cataractous lenses. Biol Trace Elem Res. 2003;95(2),107-112.
[55] Lakomaa EL, Eklund P. Trace element analysis of human cataractous lenses by neutron-activation analysis and atomic-absorption spectrometry with special reference to pseudoexfoliation of the lens capsule. Ophthalmic Res. 1978;10(5-6),302-306.
[56] Roman M, Jitaru P, Barbante C . Selenium biochemistry and its role for human health. Metallomics. 2014;6(1), 25-54.
[57] Yilmaz A, Ayaz L, Tamer L. Selenium and pseudoexfoliation syndrome. Am J Ophthalmol. 2011;151(2),272-276 e271.
[58] Aggarwal M, McKenna R. Update on carbonic anhydrase inhibitors: a patent review (2008-2011). Expert Opin Ther Pat. 2012;22(8),903-915.
[59] Carta F, Supuran CT, Scozzafava A. Novel therapies for glaucoma: a patent review 2007-2011. Expert Opin Ther Pat. 2012;22(1),79-88.